The Evolution of Complex DNAPL Releases: Rates of Migration and Dissolution

by

Gavin Peter Grant

A thesis submitted to the College of Science and Engineering in conformity with the requirements for the degree of Doctor of Philosophy

The University of Edinburgh
Edinburgh, Scotland, United Kingdom

October, 2005

DECLARATION

I hereby declare that all the material presented in this thesis is original, unless stated otherwise.

Author: Gavin Grant Date

ABSTRACT

A series of local and bench scale laboratory experiments and bench and field scale numerical simulations were conducted to develop a better understanding of the interrelationship between nonwetting phase (NWP) source zones and downgradient aqueous phase concentrations in saturated porous media contaminated by immiscible organic liquids. Specific emphasis was placed on the factors governing the rate of NWP source zone evolution and the factors governing the rate of mass transfer from the NWP to the aqueous phase.

Hysteretic NWP relative permeability-saturation (k_{rN}-S_W) relationships were measured at the local scale for six sands to examine the relationship between k_{rN}-S_W functions and porous media type. Parameterization of the measured constitutive relationships revealed a strong correlation between mean grain diameter and the maximum value of NWP relative permeability, $k_{rN}^{\max}$. The measured k_{rN}-S_W relationships, were validated through a bench scale experiment involving the infiltration, redistribution, and immobilisation of NWP in an initially water saturated heterogeneous porous medium. This match of simulation to experiment represents the first validation of a multiphase flow model for transient, fixed volume NWP releases. Multiphase flow simulations of the bench scale experiment were only able to reproduce the experimental observations, in both time and space, when the measured k_{rN}-S_W relationships were employed.

Two-dimensional field scale simulations of a fixed volume NWP release into a heterogeneous aquifer demonstrate the influence of spatially variable k_{rN}-S relationships correlated to porous media type. Both the volume of the NWP invaded porous media, and the length of time during which NWP is migrating, will be under predicted if variable (correlated) $k_{r,N}$ is not accounted for in the numerical model

formulation. This under prediction is exacerbated as the mean intrinsic permeability of the release location decreases.

A new, thermodynamically-based interfacial area (IFA) model was developed for use in the single-boundary layer expression of mass transfer as an alternative to existing empirical correlation expressions. The IFA model considers consistency and continuity of constitutive relationships, energy losses, effective specific interfacial area for mass transfer, and dissolution of residual NWP. A bench scale experiment involving the release and dissolution of a transient NWP source zone in heterogeneous porous media was conducted to evaluate the appropriateness of the developed IFA model when utilised to predict NWP dissolution rates. Comparison of measured downgradient dissolved phase concentrations and source zone NWP saturations in time and space with those from numerical simulations of the experiment reveal that the proposed IFA model is superior to both a local equilibrium assumption and existing empirical correlation expressions. This represents the first mass transfer model validated for the dissolution of a complex NWP source zone. Two-dimensional simulations at the field scale of multiphase flow and dissolution suggest that employing existing mass transfer expressions instead of the IFA model lead to incorrect predictions of the life spans of NWP source zones, downgradient dissolved phase concentrations, and the rate of mass flux through a downgradient boundary.

The practical implication of this research is that accurate numerical predictions of the evolution of a transient NWP source in porous media require consideration of k_{rN}-S relationships and NWP / aqueous phase IFA, as these factors dictate the rates of the key subsurface contaminant processes of migration and dissolution, respectively.

DEDICATION

Pour Alexandra, qui j'aime et admire, dans la mémoire du temps perdu, récupéré pendant un m888oment chaque fois que nous sommes ensemble.

"We sometimes disputed, and very fond we were of argument, and very desirous of confuting one another, which disputatious turn, by the way, is apt to become a very bad habit, making people often extremely disagreeable in company by the contradiction that is necessary to bring it into practice; and thence, besides souring and spoiling the conversation, is productive of disgusts and, perhaps enmities where you may have occasion for friendship… Persons of good sense, I have since observed, seldom fall into it, except lawyers, university men, and men of all sorts that have been bred at Edinborough."

B. Franklin, 1706-1790

ACKNOWLEDGEMENTS

Financial support for this research was provided, in part, by the School of Science and Engineering at the University of Edinburgh through a scholarship to the author. Additional funding was provided by The Royal Society, Nuffield Foundation, and the Natural Environment Research Council in the form of operating grants to the author's supervisor, Dr. J.I. Gerhard.

The author would like to acknowledge the support and valuable guidance provided by Dr. Jason Gerhard throughout this research. The effort and constructive input of the examination committee, Dr. Jim Smith and Dr. Jose Torero, is much appreciated. My gratitude is extended to Dr. Colin Cunningham and Dr. Peter Anderson at CLARRC for providing invaluable technical advice. The author acknowledges the guidance and support (through the donation of the local scale test cell and the cameras utilised in the light transmission system) from Dr. Bernard H. Kueper at Queen's University at Kingston, Ontario, Canada. The support of the entire groundwater research group is appreciated, with particular thanks to Ben Rotter, TiWee Pang, and Dr. Xiaomin Mao for their donation of CPU time. Thanks are given to Dr. Stan Reitsma at the University of Windsor, Ontario, Canada, for the measurement of capillary-pressure / saturation curves.

The author would also like to thank his extended family for their encouragement. Words are insufficient to express my appreciation for the unconditional and unending support of my wife, Alex.

FORWARD

This thesis has been written in manuscript format. Chapter 1 presents a general introduction to the research and Chapter 2 provides a review of the relevant literature. Chapters 3, 4, and 5 consist of manuscripts that are to be submitted to refereed journals within several weeks of completing this thesis. Chapter 6 provides a summary and general conclusion of the research. Appendices A through J provide additional information that was not included in the manuscripts:

- Appendix A – Laboratory Procedures
- Appendix B – Light Transmission / Image Analysis System
- Appendix C – Headspace Gas Chromatograph
- Appendix D – Non-reactive Tracer Test
- Appendix E – Numerical Model Verification and Performance Measures
- Appendix F – DNAPL3D-MT Supplemental Description
- Appendix G – Supplemental Study (Published Manuscript): *Sensitivity of Predicted DNAPL Source Zone Longevity to Mass Transfer Correlation Model* (Grant and Gerhard, 2004)
- Appendix H – Capillary Pressure – Saturation Data
- Appendix I – Nonwetting Phase Relative Permeability Cell Theory
- Appendix J – Uncertainty Analysis

TABLE OF CONTENTS

LIST OF TABLES

LIST OF FIGURES

NOTATION AND DEFINITION OF TERMS

Notation

Typical units are presented in brackets. [-] denotes a dimensionless parameter.

a^n specific interfacial area between the nonwetting phase and the wetting phase [cm^2/cm^3]

a^{wn} effective specific interfacial area between the nonwetting phase and the wetting phase [cm^2/cm^3]

a^w specific interfacial area of the bulk wetting phase in contact with the solid phase or the nonwetting phase [cm^2/cm^3]

a^s surface area of the solid phase [cm^2/cm^3]

C dissolved phase concentration [mg/l]

C_{NW} constant of integration that accounts for the contribution to interfacial area from the existence of spherical blobs of NWP residual [Pa]

C_s effective solubility [mg/l]

d_m mean grain size [μm]

D_m molecular diffusion coefficient [m^2/s]

D_L Longitudinal hydrodynamic dispersion [m]

D_T Transverse hydrodynamic dispersion [m]

g gravitational constant [m/s^2]

i aqueous phase gradient [m/m]

J solute mass flux [$kg/m^3.s$]; also, mean curvature of the nonwetting phase / wetting phase interface [m^{-1}]

K hydraulic conductivity [m/s]

k_i intrinsic permeability [m^2]

k_{ij} second-order intrinsic permeability tensor [m^2]

k_{la} average mass transfer coefficient for the nonwetting phase / wetting phase interface [m/s]

K_l lumped mass transfer term [s^{-1}]

k_r relative permeability [-]

$k_{r,W}$ wetting phase k_r [-]

$k_{r,N}$ nonwetting phase k_r [-]

k_{rN}^{i} spatially variable nonwetting phase k_r [-]

$k_{rN}^{\max}$ maximum achievable k_{rN} [-]

P_C capillary pressure [Pa]

P_D displacement capillary pressure [Pa]

P_E entry capillary pressure [Pa]

P_T terminal capillary pressure [Pa]

Q_W wetting phase source/sink flux [s^{-1}]

Q_N nonwetting phase source/sink flux [s^{-1}]

q_W wetting phase volume flux [m/s]

q_N nonwetting phase volume flux [m/s]

Sc Schmidt number [-]

S_e effective wetting phase saturation [-]

Sh Sherwood number [-]

S_N nonwetting phase saturation [-]

S_{Nr} residual nonwetting phase saturation [-]

$S_{Nr}^{\max}$ maximum achievable S_{Nr} [-]

S_r residual S_W [-]

S_W wetting phase saturation [-]

S_W^i current wetting phase saturation [-]

S_W' turn-around WP saturation from drainage to imbibition conditions [-]

S''_w turn-around WP saturation from imbibition to drainage conditions [-]

$S_{Wr}^{\max}$ $S_{Nr}^{\max}$ expressed in terms of S_W [-]

S_W^M emergence S_W [-]

S_W^X extinction S_W [-]

V_{avg} advective aqueous phase velocity [m/s]

α porous media compressibility [Pa^{-1}]; also, dispersivity [m]

β Haines jump energy dissipation factor [-]

β_w wetting phase compressibility [Pa^{-1}]

ΔS_W^{*d} incremental S_W target for drainage k_{rN} beyond emergence [-]

ΔS_W^{*i} incremental S_W target for imbibition k_{rN} beyond extinction [-]

κ terminal pressure to displacement pressure ratio [-]

μ_W wetting phase viscosity [Pa.s]

μ_N nonwetting phase viscosity [Pa.s]

λ_d Brooks-Corey drainage pore size distribution index [-]

λ_h horizontal correlation length [-]

λ_i Brooks-Corey imbibition pore size distribution index [-]

λ_v vertical correlation length [-]

ρ_W wetting phase density [kg/m^3]

ρ_N nonwetting phase density [kg/m^3]

σ interfacial tension [N/m]

θ_N DNAPL volume fraction [-]

ϕ porosity [-]

Φ_{NW} area under the P_C-S_W curve [Pa]

τ_d drainage nonwetting phase relative tortuosity exponent [-]

τ_i imbibition nonwetting phase relative tortuosity exponent [-]

Definition of Terms

aspect ratio	ratio of pore body to pore throat diameter;
continuous NWP	NWP that spans the macroscopic domain;
coordination number	number of pore throats connected to a pore body;
discontinuous NWP	sum of locally accessible and trapped NWP;
displacement pressure	macroscopic P_C obtained by extrapolating the drainage curve to $S_W = 1$;
DNAPL	denser-than-water nonaqueous phase liquid;
drainage	the displacement of wetting fluid by a nonwetting fluid;
emergence saturation	S_W on drainage at which NWP is first continuous across the macroscopic sample (i.e., $k_{rN} > 0$);
entry pressure	macroscopic P_C associated with S_W^M;
extinction saturation	S_W on imbibition at which NWP ceases being continuous across the macroscopic sample (i.e., $k_{rN} = 0$);
IFA	interfacial area;
IFTT	interfacial tracer technique;
imbibition	the displacement of nonwetting fluid by wetting fluid;
immobilisation	cessation of NWP migration;
infiltration	migration while NWP source is active;
k_{rN}-S_W	nonwetting phase relative permeability – saturation relationship;
k_{rW}-S_W	wetting phase relative permeability – saturation relationship;
LEA	local equilibrium assumption dissolution model;
LNAPL	lighter-than-water nonaqueous phase liquid;

main drainage	drainage associated with decreasing S_W from S_{Nr};
NAPL	nonaqueous phase liquid;
NMR	nuclear magnetic resonance;
NWP	nonwetting phase;
P_C-S_W	capillary pressure – saturation relationship;
primary drainage	increasing S_N from an initial state of complete WP saturation;
primary imbibition	increasing S_W from an initial state of complete NWP saturation;
PSD	pore size distribution;
PVI	photoluminescent volumetric imaging;
redistribution	migration subsequent to termination of the source;
REV	representative elementary volume;
REV_{LEA}	representative elementary volume associated with the validity of a LEA dissolution model;
REV_{mig}	representative elementary volume for accurately simulating NWP migration;
secondary drainage	drainage subsequent to primary or secondary imbibition;
secondary imbibition	imbibition subsequent to primary drainage;
terminal pressure	macroscopic capillary pressure associated with S_W^X;
WP	wetting phase;

CHAPTER 1 – INTRODUCTION

Groundwater contamination by nonaqueous phase liquids (NAPLs) residing in subsurface porous media is a significant health, economic and legal problem at numerous sites, particularly industrial sites, around the world (Freeze, 2000). NAPLs can be classified according to whether they are more dense (DNAPLs) or less dense (LNAPLs) than water. Hazardous DNAPLs such as chlorinated solvents (e.g. perchloroethylene, trichloroethylene, 1,2-dichloroethane), creosote, coal tar, polychlorinated biphenyl (PCB) oils, and some pesticides are recognized as some of the most health-threatening chemicals detected in groundwater (Mackay and Cherry, 1989). Although the recent discovery of the hazards associated with DNAPLs has significantly improved the use and handling procedures in industry, decades of unsafe practices have already led to significant environmental impacts. Leaking underground storage tanks, pipelines, and waste disposal ponds, as well as transportation accidents, accidental spills during use, and negligent use and disposal practices have all contributed to subsurface contamination by DNAPLs. DNAPLs are extremely difficult to locate and remediate and tend to act as long-term sources of groundwater contamination as a result of their physical, chemical and biological properties (Pankow *et al,* 1996).

A conceptual model of groundwater contamination by DNAPLs is presented by Kueper and Frind (1991a). During the release of DNAPLs at ground surface, DNAPLs migrate or flow through the subsurface as a separate fluid. If the release volume is sufficient, DNAPLs will penetrate the watertable and continue to migrate through the saturated zone due to fluid densities greater than that of water. In saturated porous media, DNAPLs are typically nonwetting with respect to water (i.e., DNAPLs are often defined as the nonwetting phase, NWP), and as such, displace

water from pore space during this infiltration phase under drainage processes. Following the termination of the source, the leading edge of the DNAPL body will continue to advance through the porous media. The presence of low permeability regions in the porous media will restrict advancement of the DNAPL and cause the formation of high saturation NWP pools. During this redistribution phase, water imbibition occurs along the trailing edge of the advancing DNAPL body where NWP saturations are decreasing. Complete imbibition results in the trapping of low NWP saturation residual in the form of disconnected blobs and ganglia. Eventually, the DNAPL will become immobilised in a complex pattern of disconnected residual and connected pool regions at hydrostatic equilibrium. The entire DNAPL body is a source zone for groundwater (i.e., aqueous phase) contamination that is composed of residual and pooled DNAPL source sub-zones. Dissolution of the DNAPL source zone results in the evolution of an aqueous phase contaminant plume. Transport of dissolved phase contaminants via groundwater to environmentally sensitive receptors is the primary hazard associated with DNAPL contamination scenarios.

Numerous physical experiments conducted in the laboratory (e.g. Schwille, 1988; Kueper *et al.*, 1989; Kueper and Frind, 1991a,b; Illangasekare *et al.,* 1995; Oostrom *et al.,* 1999; Gerhard and Kueper, 2003a,b; O'Carroll *et al.,* 2004) and in the field (Kueper *et al.,* 1993; Brewster *et al.,* 1995) have led to a detailed understanding of the factors that control the spatial distribution of DNAPLs released to the subsurface. However, very few of these studies (e.g. Gerhard and Kueper, 2003b,c; O'Carroll *et al.,* 2004) have examined the temporal aspects (rates) of DNAPL migration, and as such, understanding the factors affecting the timescales of DNAPL migration at the field scale is limited. The temporal aspects of DNAPL migration are of critical importance in addressing technical and financial questions of site

investigation and remediation, as well as in identifying legal responsibility for historical contamination cases.

The rate of DNAPL dissolution, or mass transfer between the NWP phase and the aqueous / wetting phase, WP, is also an area of much uncertainty, in spite of years of detailed research examining this phenomenon. This primarily stems from the inadequacy of the standard 'stagnant film' theory of dissolution and the important influence of NWP / WP interfacial area; a parameter that is exceedingly difficult to quantify at the scale of interest in describing DNAPL migration, dissolution and dissolved phase transport. Again, the temporal aspects of DNAPL dissolution are critical in addressing the technical, financial and legal issues common at a DNAPL contaminated site.

The goal of this research is to develop a better understanding of the interrelationship between DNAPL source zones and downgradient aqueous phase concentrations with specific emphasis on the factors governing the rate of DNAPL source zone evolution and the factors governing the rate of mass transfer from the DNAPL to the aqueous phase.

The rate of DNAPL migration through porous media is dependent, in part, on macroscopic relative permeability constitutive relationships. In particular, the temporal evolution of DNAPL has been demonstrated to be sensitive to the specific shape (i.e., curvature, endpoints, and hysteresis) of NWP relative permeability - saturation functions (Gerhard and Kueper, 2003b). Therefore, the first objective of this research is to conduct a series of experiments to examine the factors influencing the shape and end-point locations of the NWP relative permeability function. A series of six local scale experiments were carried out to meet this objective. The findings were validated with a two-dimensional bench scale flow cell experiment. The bench

scale experiment involved the release of a fixed volume of 1,2-dichloroethane into a saturated heterogeneous porous medium. A light transmission / image capture and analysis system was employed to track the migrating DNAPL and identify zones of transient saturation history in the flow cell for comparison with the results of a numerical simulator. Agreement between measured and simulated DNAPL distribution patterns in time and space would validate the findings of the NWP relative permeability local scale experiments and the constitutive relationships used to describe relative permeability.

The second objective of this research is to examine the significance of the shape and end-point locations of the NWP relative permeability function at the field scale. This objective was met by conducting a Monte Carlo suite of numerical simulations employing the characteristics of the NWP relative permeability curves measured in the local scale laboratory experiments.

The third objective of this research is to develop an expression for describing the rate of mass transfer from a transient DNAPL source. The bench scale flow cell experiment was also conducted to meet this third objective. Dissolved phase concentrations of 1,2-dichloroethane were measured in time and space throughout the experiment for comparison with data from a numerical simulation of the DNAPL release / dissolution employing the proposed mass transfer model.

To meet these objectives, and to confirm the experimental results, a numerical model (DNAPL3D-MT: a 3-dimensional 2-phase flow model with multispecies transport) was developed. A split-operator (SO) method (Barry *et al.*, 2002) was used to integrate the two phase flow model DNAPL3D (a 3-Dimensional, 2-Phase flow model) developed by Gerhard (1995, 2002) with the dissolved-phase transport code MT3D (Zheng, 1990). As well as incorporating numerous subroutines to link the

migration (DNAPL3D) and transport (MT3D) sub-models, DNAPL3D-MT also includes a revised porous media dependant relative permeability constitutive relationship and the developed mass transfer model.

The research is presented in this thesis as three theme-centred units. As outlined in Tables 1-1 and 1-2, Chapter 3 focuses on the factors affecting the rate of DNAPL migration and the validation of the NWP relative permeability constitutive relationships, and includes the relevant background, theory, local scale experimental results, and bench scale experimental results. Chapter 4 examines the significance of the revised relative permeability constitutive relationships at the field scale. Chapter 5 presents the developed dissolution model, and includes all relevant background, theory, bench scale experimental results and corresponding numerical simulations.

Table 1-1. Summary of Laboratory Experiments Conducted

Experiment	Laboratory Scale	Number of Experiments	Present In
NWP Relative Permeability	Local Scale	6	Chapter 3
Transient DNAPL Migration	Bench Scale	1	Chapter 3
Transient DNAPL Dissolution	Bench Scale	1	Chapter 5

Table 1-2. Summary of Numerical Simulations Performed

Simulation	Number of Dimensions / Scale	Number of Simulations	Present In
NWP Relative Permeability	2 / Field Scale and Bench Scale	30 + 10 Field Scale / 10 Bench Scale	Chapter 4
Transient DNAPL Migration	3 / Bench Scale	3	Chapter 3
Transient DNAPL Dissolution	3 / Bench Scale and 2 / Field Scale	9 Bench Scale / 3 Field Scale	Chapter 5

1.1 References

Barry, D.A., H. Prommer, C.T. Miller, P. Engesgaard, A. Brun, and C. Zheng, Modeling the fate of oxidizable organic contaminants in groundwater, *Advances in Water Resources, 25*, 945-983, 2002.

Brewster, M.L., A.P. Annan, J.P. Greenhouse, B.H. Kueper, G.R. Oldhoeft, J.D. Redman, and K.A. Sander, Observed migration of a controlled DNAPL release by geophysical methods, *Ground Water, 33*(6), 977-987, 1995.

Freeze, R.A., *The Environmental Pendulum: A Quest for the Truth About Toxic Chemicals, Human Health, and Environmental Protection,* 323 pp. University of California Press, Berkeley, CA., 2000.

Gerhard, J.I., A three-dimensional numerical model for simulating DNAPL migration in heterogeneous porous media, Master's thesis, Queen's Univ., Kingston, Ontario, Canada, 1995.

Gerhard, J.I., DNAPL infiltration, redistribution, and immobilization in porous media, Ph.D., thesis, Queen's Univ., Kingston, Ontario, Canada, 2002.

Gerhard, J.I., and B.H. Kueper, Capillary pressure characteristics necessary for simulation DNAPL infiltration, redistribution, and immobilization in saturated porous media, *Water Resources Research, 39*(8), SBH71-SBH717, 2003a.

Gerhard, J.I., and B.H. Kueper, Relative permeability characteristics necessary for simulating DNAPL infiltration, redistribution, and immobilization in saturated porous media, *Water Resources Research, 39*(8), SBH81-SBH816, 2003b.

Gerhard, J.I., and B.H. Kueper, Influence of constitutive model parameters on the predicted migration of DNAPL in heterogeneous porous media, *Water Resources Research, 39*(8), SBH41-SBH413, 2003c.

Illangasekare, T.H., J.L. Ramsey Jr., K.H. Jensen, and M.B. Butts, Experimental study of the movement and distribution of dense organic contaminants in heterogeneous aquifer, *Journal of Contaminant Hydrology, 20*, 1-25, 1995.

Kueper, B.H., W. Abbot, and G. Farquhar, Experimental observations of multiphase flow in heterogeneous porous media, *Journal of Contaminant Hydrology, 5*, 83-95, 1989.

Kueper, B.H., and E.O. Frind, Two phase flow in heterogeneous porous media: 1. Model development, *Water Resources Research, 27*(6), 1049-1057, 1991a.

Kueper, B.H., and E.O. Frind, Two phase flow in heterogeneous porous media: 2. Model application, *Water Resources Research, 27*(6), 1059-1070, 1991b.

Kueper, B.H., J.D. Redman, R.C. Starr, S. Reitsma, and M. Mah, A field experiment to study the behaviour of tetrachloroethylene below the watertable: Spatial distribution of residual and pooled DNAPL, *Journal of Ground Water, 31*(5), 756-766, 1993.

Mackay, D.M., and J.A. Cherry, Transport of organic contaminants in groundwater, *Environmental Science and Technology, 19,* 384-392, 1989.

O'Carroll, D.M., S.A. Bradford, and L.M. Abriola, Infiltration of PCE in a system containing spatial wettability variations, *Journal of Contaminant Hydrology, 73,* 39-63, 2004.

Oostrom, M., C. Hofstee, R.C. Walker, and J.H. Dane, Movement and remediation of trichloroethylene in a saturated heterogeneous porous medium, 1. Spill behaviour and initial dissolution, *Journal of Contaminant Hydrology, 37*(1-2), 159-178, 1999.

Pankow, J.F., S. Feenstra, J.A. Cherry, and M.C. Ryan, Dense chlorinated solvents in groundwater: Background and history of the problem, in: *Dense*

Chlorinated Solvents and Other DNAPLs in Groundwater, J.F. Pankow, and J.A. Cherry (Eds.), Waterloo Press, Portland, Oregon, pp 1-46, 1996.

Schwille, F., *Dense Chlorinated Solvents in Porous and Fractured Media Model Experiments*, 146 pp. Translated by J.F. Pankow, Lewis Publishers, Chelsea, MI, 1988.

Zheng, C., MT3D, *USEPA Report*, 1990.

CHAPTER 2 – LITERATURE REVIEW

This chapter summarizes the scientific literature relevant to the physical and chemical processes governing DNAPL migration, dissolution, and aqueous phase contaminant transport in porous media. The study of fluid flow through porous media has evolved as a distinct branch of fluid dynamics since the pioneering works of Henry Darcy (1803 - 1858). Contributions to the body of science covering fluid flow through porous media have come from the fields of petroleum reservoir engineering, soil and agricultural science, immiscible fluid physics and contaminant hydrogeology.

This review examines the current state of knowledge with respect to the fate of a dense non-aqueous phase liquid (DNAPL) in saturated porous media following a near surface release. The literature survey will discuss the theory and laboratory and numerical experiments conducted to predict this scenario with specific emphasis on the factors affecting the rates of subsurface processes.

2.1 DNAPL Migration

2.1.1 Migration at the Pore Scale

Understanding the physics of two phase flow at the pore scale is essential for understanding fluid flow at the local, bench and field scales. The factors governing fluid interactions at these large scales are the ensemble effects of pore scale mechanisms.

Multiphase flow in porous media is brought about by the relative influence of three critical forces: 1) gravity or buoyancy forces (related to the density differences of the fluids); 2) viscous dynamic forces (related to phase viscosities and pressure gradients); and, 3) capillary forces (related to the adhesive forces between fluid pairs and the porous media) (Rose, 1960). These forces interact with the physical

properties of the porous media to govern the flow of fluids in porous media (Pennell *et al.,* 1996).

2.1.1.1 Wettability

Wettability refers to the "tendency of one fluid to spread on or adhere to a solid surface in the presence of another immiscible fluid" (Craig, 1971). Immiscible fluids are classified as either wetting, nonwetting, or of intermediate wettability. The contact angle, a measure of wettability, is the angle that the interface between the two fluids makes with the solid surface (Hiemenz and Rajagopalan, 1997). If the contact angle approaches zero degrees, the fluid through which the angle is measured is termed the wetting phase (WP) and the second fluid is, therefore, termed the nonwetting phase (NWP). For contact angles less than 60 degrees, the fluids are deemed *strongly* wetting and *strongly* nonwetting. At a contact angle greater than 60 degrees, the fluids are deemed *weakly* wetting and *weakly* nonwetting, and as the contact angle approaches 90 degrees, the fluids are both considered to be of intermediate wettability (Dixit *et al.,* 1997).

2.1.1.2 Microscopic Capillary Pressure

When two fluid phases are present in porous media, they are separated by a fluid - fluid interface. The interface between the wetting and the nonwetting phase is curved, with the wetting phase on the convex side of the interface, and the nonwetting phase on the concave side of the interface. As such, a pressure discontinuity exists across this curved interface, where the nonwetting phase pressure is greater than the wetting phase pressure. A force balance across the interface at equilibrium derives the Young-Laplace equation (Hassanizadeh and Gray, 1993a):

$$P_N - P_W = \sigma \cdot J \tag{2-1}$$

where P_N and P_W are the nonwetting and wetting phase pressures on either side of the interface, σ is the interfacial tension, and J is the mean curvature of the interface. If J is defined as the mean interface curvature at a point, then Equation 2-1 gives the pressure difference at that point. If J is defined as the mean interface curvature of the entire interface ($J = 2\cos\theta / r$), where θ is the contact angle and r is the mean radius over the whole interface, then Equation 2-1 gives the average pressure difference over the interface (Corey, 1994).

During interface motion, Hassanizadeh and Gray (1993a) define microscopic capillary pressure, P_C, as an intrinsic property of the interface, such that:

$$P_C = \sigma \cdot J \tag{2-2}$$

P_C is unique from the pressure difference between the two fluids immediately on either side of the interface (Equation 2-1), however, $P_C = P_N - P_W$ and Equation 2-1 reduces to Equation 2-2 when equilibrium conditions exist (Hassanizadeh and Gray, 1993a).

2.1.1.3 Interface Movement

Movement of the fluid – fluid interface is caused by an increase or decrease in the phase pressure difference across the interface. For sufficiently small pressure changes, the interface contact point with the solid surface will resist translation (Hassanizadeh and Gray, 1993a). This phenomenon is described as "interface pinning" (Braun and Holland, 1994). As a consequence of interface pinning, slight pressure changes will cause a deformation of the interface and the contact angle such that the P_C of the interface is not unique to a given pressure difference of the fluids of a given microscopic saturation (Chatzis *et al.,* 1983). This phenomenon is described as contact angle hysteresis (Braun and Holland, 1994).

For sufficiently large pressure difference changes, the curvature will reach a maximum (P_C increasing during NWP invasion) or minimum (P_C decreasing during WP advancement) value before the interface physically translates to a new equilibrium position (Morrow, 1976). The stability of the new position of the interface is dependent on whether interface equilibrium is satisfied (i.e., whether the new microscopic P_C of the interface is equal to the pressure difference between the phases across the interface). Melrose (1970) explains that during NWP invasion, the maximum stable curvature is represented by the pore throat radius, and the minimum stable curvature is represented by the pore body radius.

The translation of the interface between one stable position and another is a rapid process (Haines, 1930). These rapid translations are often referred to as "Haines jumps" (Melrose, 1970) and are considered to be a thermodynamically irreversible process (Haines, 1930). As such, Haines jumps are responsible for macroscopic hysteresis, due entirely to the influence of pore geometry (i.e., the location and size of pore throats and bodies).

2.1.1.4 Drainage and Imbibition

Translation of the fluid - fluid interface is accompanied by a local region saturation change. If P_C increases, the interface moves such that wetting saturations decrease; a process referred to as "drainage". If P_C decreases, the interface moves such that wetting saturations increase; a process referred to as "imbibition".

During drainage, wetting fluid is displaced by nonwetting fluid according to two mechanisms: 1) piston-like displacement; and, 2) wetting phase film flow (Lowry and Miller, 1995). Piston-like displacement, the primary displacement mechanism, involves the advancement of the nonwetting phase through a series of Haines jumps. This displacement mechanism proceeds along a path of minimum energy such that

NWP advances past the largest pore throats first. However, the NWP flow path is restricted to the pore throats immediately adjacent to the NWP front, such that drainage is primarily controlled by pore throat radii and their connectivity at the pore scale (Fenwick and Blunt, 1988).

Drainage due to film flow occurs in strongly wetting systems where a continuous WP is present. Generally, film flow displacement occurs only at low wetting phase saturations and at time scales greater than those generally encountered in a contaminant hydrology context, as film flows are subject to a relatively large degree of viscous resistance due to their large surface area to volume ratios (Lowry and Miller, 1995). While the time scales for drainage film flow are not yet known (Lowry and Miller, 1995), measured 'residual' WP saturations can be defined as the wetting phase saturation where a transition between piston-like and film flow dominant displacement takes place. This would explain the fact that attempts to quantify residual WP saturations at the local scale are known to be highly dependent on the measurement method and time scales (Corey, 1994).

During imbibition, nonwetting fluid is displaced by wetting fluid according to two mechanisms: 1) piston-like displacement via stable advancement and unstable Haines jumps (Chatzis and Dullien, 1981); and, 2) choke-off within the pore throat (Mohanty *et al.,* 1987).

Piston-like displacement is the dominant mechanism during imbibition and is similar to piston-like displacement during drainage. Again, displacement proceeds along a path of minimum energy, however, stable interface positions during imbibition are controlled by pore body radii rather than pore throat radii. Similarly, the WP flow path is restricted to the pore bodies immediately adjacent to the WP

front, such that imbibition is primarily controlled by pore body radii and their connectivity at the pore scale (Chatzis and Dullien, 1981).

Choke-off is an imbibition mechanism whereby WP will spontaneously fill a pore throat occupied with NWP as a result of interface instability at the pore throat (Mohanty *et al.,* 1987). This phenomenon is only possible in strongly wetted systems where a continuous thin wetting film exists throughout the porous media (Mohanty *et al.,* 1987). Fenwick and Blunt (1988) state that microscopic P_C is usually higher at the 'head' of the fluid – fluid interface in a pore body, than at the pore throat between the 'neck' of the NWP and the WP film coating the soil grains. Therefore, imbibition by piston-like displacement is generally favoured. However, should the pore body be large enough relative to the size of the pore throat, the P_C of the head may fall below that of the neck, and film flow of WP will allow the growth of WP collars until the NWP in the pore body becomes disconnected. The ratio of the pore body size to the pore throat size is termed the 'aspect ratio', and high aspect ratios are typical of uniform porous media. Choke-off is essentially the rupturing of a NWP connection at a pore throat that occurs some distance behind the main NWP – WP interface. This process again depends on film flow, the timescales of which are unknown (Lowry and Miller, 1995). However, choke-off does proceed at a rate fast enough to be observed at the timescales typical of contaminant hydrogeology scenarios, as choke-off is the cause of one of the primary NWP trapping mechanisms commonly observed (Roof, 1970).

2.1.1.5 Residual formation

Residual is the relatively small volume of fluid that can not be completely removed from the pore space (i.e., becomes 'trapped') by any of the fluid displacement methods described above. Entrapment of the WP during drainage and

the NWP during imbibition are fundamentally different processes. WP trapping occurs along the sand grains, and in the corners between adjacent grains, and can possibly be eliminated at capillary pressures and time scales larger than those generally encountered in the context of contaminant hydrogeology (Corey, 1994). NWP trapping occurs in the pore body and is a function of contact angle and pore geometry. NWP trapping occurs by two different mechanisms: 1) 'Snap-off' (Roof, 1970); and, 2) 'Bypassing' (Chatzis and Dullien, 1983).

Snap-off is the trapping of NWP in a pore body by the choke-off mechanism (Roof, 1970). This process, therefore, requires strongly wetting conditions and a sufficiently high aspect ratio. Roof (1970) also indicates that snap-off is a function of the rate of meniscus movement: when choke-off proceeds slowly, movement of the main NWP – WP interface towards the pore throat may prevent trapping, while movement of the interface away from the pore throat will enhance trapping.

Bypassing is the trapping of larger blobs or ganglia of NWP (multiple pore volumes) and is entirely dependent on pore geometry (Chatzis and Dullien, 1983). During imbibition, WP will advance along the path of highest P_C; therefore, the advancing interface will follow the narrowest path of interconnected pores and pore throats. Depending on local pore geometry, piston-like displacement following the narrowest interconnected pathway may circumvent, or bypass, areas of the medium containing larger pores. Any NWP in this large pore area will be disconnected from the bulk NWP and trapped, as no further displacement of this volume of NWP is possible.

Both NWP trapping processes are governed by pore geometry. Chatzis and Dullien (1983) show that a high aspect ratio causes unstable neck capillary pressures and promotes trapping by snap-off, while a low aspect ratio encourages piston-like

displacement and favours trapping by bypassing. Wilson *et al.,* (1990) confirm this finding by showing that as aspect ratio decreases, the proportion of NWP trapped by bypassing relative to choke-off increases.

2.1.2 Migration at the Local Scale

2.1.2.1 Continuum Concept

While the study of phase interactions at the pore scale is essential for understanding the mechanisms that govern fluid flow, predicting migration patterns and timescales at such a fine scale is generally considered to be impractical. The continuum concept provides the theoretical framework for the scaling of pore scale (microns) processes to a more practical local scale (centimetre).

The continuum concept considers the fluid phases and the solid phase as spatially continuous across a macroscopic (local scale) volume of the subsurface. While it is clear that phase properties are spatially discontinuous at the pore scale, the continuum concept involves the spatial averaging of pore scale phase properties over a minimum volume of subsurface to give macroscopic or local scale property values. The minimum volume over which the macroscopic property values are valid (i.e., the volume above which the average property values do not vary) is the representative elementary volume (REV) (Bear, 1972). The REV is considered to be at the centimetre scale for properties such as porosity, permeability, and saturation, and it is at this scale that Darcy's law is considered to be valid (Bear, 1972).

2.1.2.2 Constitutive Relationships

Numerical modelling generally employs equations and parameters developed with a continuum approach, and most laboratory studies focus on the measurement of local scale parameter values. Constitutive relationships are the equations used in numerical models to describe local scale phenomena, and represent the point at which

physical measurements are incorporated into mathematical and numerical models (Reeves and Celia, 1996). Constitutive relationships are useful in that they describe processes at the local scale using fewer variables than would be necessary at the pore scale (Miller *et al.,* 1998).

For two phase flow, the required constitutive relationships in traditional models are the capillary pressure – saturation (P_C-S_W) function and the relative permeability – saturation (k_r-S_W) function (Kueper and Frind, 1992). Typically, numerical models employ a multiphase extension of Darcy's law, written in terms of fluid phase pressures and saturations (Kueper and Frind, 1992). The phase flow equations are coupled through the P_C-S_W function, which relates the contrast between fluid phase pressures and fluid saturations, and the k_r-S_W function is required for the parameterization of the generalised form of Darcy's law (Reeves and Celia, 1996). The constitutive relationships are linked through fluid phase saturation which provides further coupling of the flow equations through the additional constraint that phase saturations sum to unity (Reeves and Celia, 1996).

Figures 2-1 and 2-2 illustrate typical P_C - S_W and k_r - S_W curves, respectively. These figures highlight the parameters defined in the following sections and form the basis of the constitutive relationships of Gerhard and Kueper (2003a,b) which will be utilised throughout this thesis.

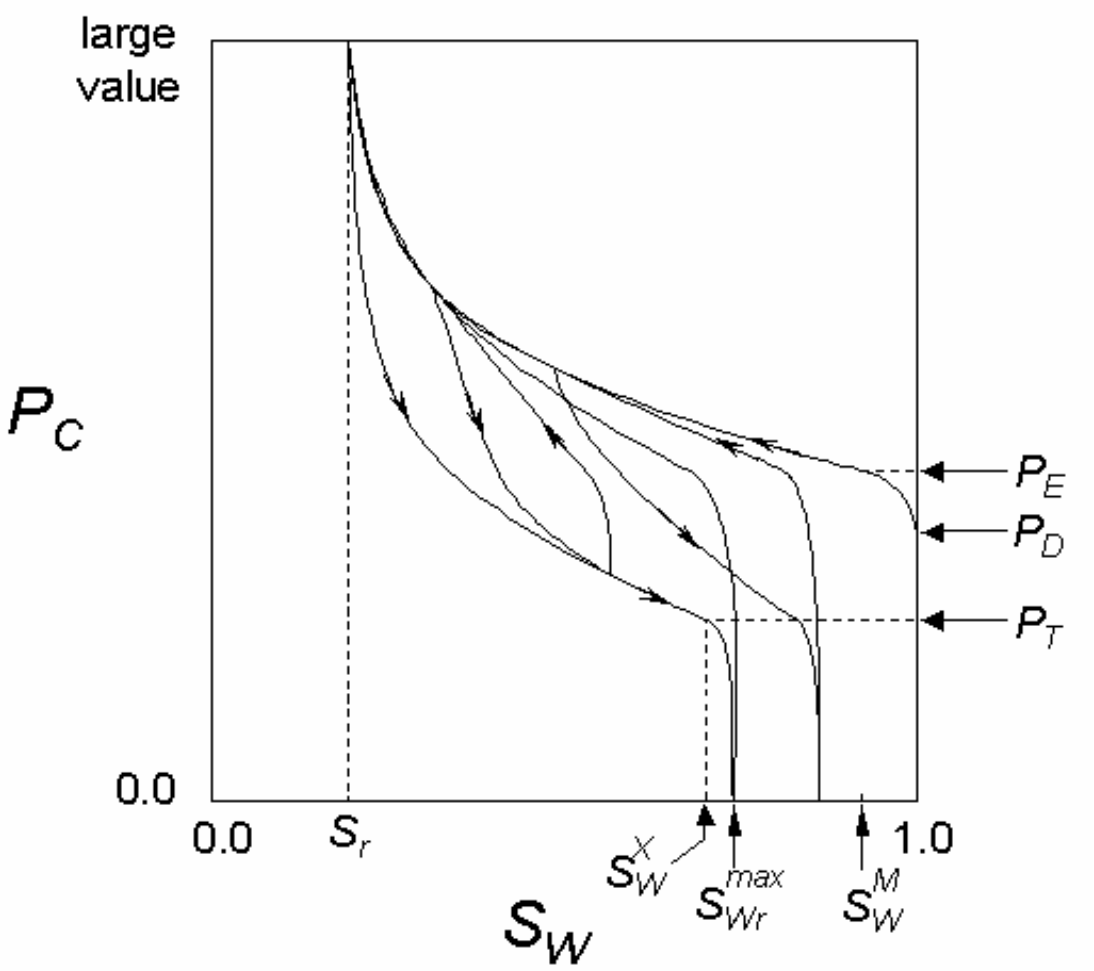

Figure 2-1. Typical capillary pressure-saturation curves.

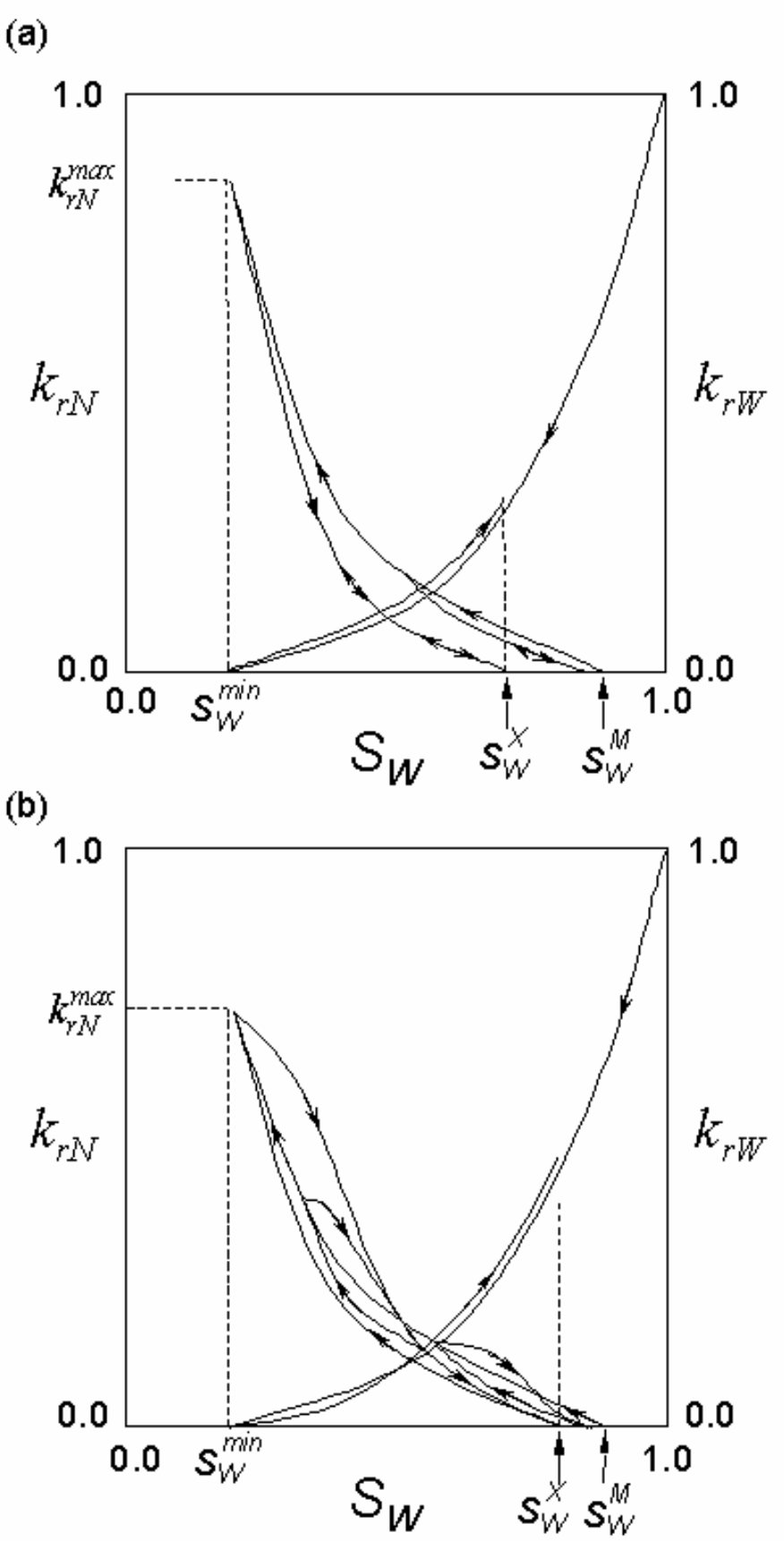

Figure 2-2. Typical nonwetting phase relative permeability-saturation relationships: (a) standard hysteresis pattern, (b) reverse hysteresis pattern.

2.1.2.3 Capillary Pressure – Saturation Relationships

Unlike porosity and saturation, for example, which are purely continuum concepts, capillary pressure is clearly defined at the pore scale (Section 2.1.1.2) as well as at the local scale. Analogous to P_C at the pore scale, P_C at the local scale is typically equated to the difference between the fluid pressures averaged over the REV (e.g. Melrose and Brandner, 1974; Morrow, 1976). In experiments measuring P_C-S_W functions, the fluid pressure differences across the REV are usually determined by observing external fluid reservoirs. This can be problematic when measuring P_C at near residual saturations. For example, NWP residual saturations are by definition discontinuous, however the pressure of discontinuous fluids can not be measured by observing external fluid pressures. As a consequence, capillary pressures are often determined to be equal to zero at residual NWP saturations, when the average P_C across the REV is a finite value equal to the average microscopic P_C of the residual blobs (Hassanizadeh and Gray, 1993a).

The local scale P_C-S_W relationship is hysteretic (i.e., not reversible) due to contact angle hysteresis and Haines jump, pore geometry induced, macroscopic hysteresis (see Section 2.1.1.3). For a given saturation, the drainage (WP saturation decreasing) capillary pressure will be larger than the imbibition (WP saturation increasing) capillary pressure.

2.1.2.3.1 Drainage

On drainage, NWP first invades the REV of strongly wetted porous media when the local P_C exceeds the capillary resistance of the largest pore throat (displacement pressure, P_D) exposed to the bulk NWP (Corey, 1994). Wetting phase saturations will decrease below unity as NWP invades the REV. If the porous media is characterised by a uniform pore size distribution (PSD), P_C above the P_D will result

in a continuous path of NWP across the REV (Corey, 1994). However, for non-uniform PSD porous media, a continuous pathway of NWP across the REV will only occur if the local P_C exceeds the capillary resistance of the smallest pore throat along the continuous NWP pathway (entry pressure, P_E). P_E corresponds to the first connected pathway of NWP across the REV, and therefore coincides with the first emergence of NWP relative permeability (k_{rN}) (Stonestrom and Rubin, 1989b). P_E is characterised by an inflection point on the drainage P_C-S_W curve. At P_C between P_D and P_E, invasion of the REV will only occur in the area immediately adjacent to the bulk NWP (locally accessible flow only) (Corey, 1994).

As P_C increases, WP saturations will decrease to a minimum, so-called "irreducible", or residual, S_W (S_r). As discussed in Section 2.1.1.5, the existence of an irreducible WP saturation is a matter of time scale and experimental method (Hassanizadeh and Gray, 1993a; Corey, 1994).

2.1.2.3.2 Imbibition

On imbibition, reduction in P_C will result in the displacement of NWP by the WP. As P_C decreases, the WP saturations will increase to a maximum value less than unity. WP saturations do not increase to unity following NWP invasion of the porous media, as total NWP displacement is limited by the presence of residual NWP, formed by the trapping mechanisms discussed in Section 2.1.1.5 (Wardlaw and Taylor, 1976). The P_C-S_W imbibition curve is offset from the drainage curve on the saturation axis by NWP trapping, and off-set on the P_C axis by hysteresis (Pickell *at al.,* 1966; Wardlaw and Taylor, 1976).

2.1.2.3.3 Residual

Residual NWP saturations are almost exclusively measured in the laboratory by first invading a WP saturated porous media with NWP fluid until with maximum

NWP saturation is reached; followed by a WP flood to displace NWP to residual saturations. Therefore, most NWP residual values reported in the literature represent the maximum possible S_{Nr} (Gerhard, 2002). S_{Nr} values for unconsolidated porous media have been found to be on the order of 14 and 16 % (Wilson *et al.,* 1990). This value has been shown to be independent of porous media grain size (Chatzis *et al.,* 1983) and permeability (Mayer and Miller*,* 1992) but sensitive to microscopic heterogeneities (Wilson *et al.,* 1990). Measurement of S_{Nr} for consolidated porous media (e.g. Morrow *et al.,*1988; Chatzis and Dullien, 1981; Naar *et al.,* 1962) have shown values of S_{Nr} to increase as a function of reduced aspect ratio and pore interconnectedness.

NWP residual saturation values have been shown by numerous researchers to be a function of saturation history (Pickell, *et al.,* 1966; Land, 1968; Wardlaw and Taylor, 1976; Chatzis and Dullien, 1981). In general, a higher maximum NWP saturation on drainage will result in a larger NWP residual saturation. As a consequence, the imbibition curve is scaled to the drainage – imbibition 'reversal point' to account for the saturation history dependency of the NWP residual saturation value.

Most multiphase flow numerical models utilise a non-linear description of the 'initial - residual relationship' proposed by Land (1968) (e.g. Lenhard and Parker, 1987; Lenhard, 1992; van Geel and Sykes, 1997; Rathfelder and Abriola, 1998). Regardless of the value of S_{Nr}, residual formation has been shown to occur during only the final stages of imbibition (Raimondi and Torcaso, 1964; Stonestrom and Rubin, 1989a; Lowry and Miller, 1995).

NWP residual formation is accompanied by an inflection point on the P_C-S_W imbibition curve. This inflection point has been defined as the terminal pressure, P_T,

and represents the average P_C of residual NWP, coincident with the essential completion of trapping, and thus, the extinction saturation on the $k_{rN} - S_W$ curve (Gerhard and Kueper, 2003a). Analogously to P_E, P_T is primarily dependent on pore geometry. Therefore it is expected that P_E and P_T are interrelated and similar functions of porous media geometry (Gerhard and Kueper, 2003a). The ratio of P_T and P_E, κ, has been shown to range from 0.55 – 0.65 (Gerhard and Kueper, 2003a).

2.1.2.3.4 Secondary Drainage

On secondary drainage, WP saturations decrease as NWP re-invades the REV. If imbibition has proceeded to NWP residual formation, local P_C must once again overcome the microscopic entry pressures of the pore throats along the continuous path of least resistance through the REV. Numerous researchers have found that entry pressure along secondary drainage is approximately equal to that of primary drainage (Pickell *et al.,* 1966; Wardlaw and Taylor, 1976; Colonna *et al.,* 1972; Stonestrom and Rubin, 1989a; Gerhard and Kueper, 2003a). However, if WP saturations start to increase prior to reaching the inflection point on the P_C-S_W imbibition curve, then a continuous NWP pathway exists and P_E will not have to be overcome to allow for the re-invasion of NWP.

2.1.2.3.5 Factors Affecting Capillary Pressure – Saturation Relationships

Capillary pressure – saturation relationships have been shown to be both qualitatively and quantitatively influenced by porous media properties including pore size distribution, connectivity, aspect ratio and wettability (e.g. Lowry and Miller, 1995; Corey, 1994; Powers *et al.,* 1996).

Pore size distribution is widely recognized as having a dominant influence on the shape of capillary pressure – saturation relationships. This phenomenon is reflected by the fact that most empirical descriptions of capillary pressure – saturation

incorporate a pore size distribution parameter (Corey, 1994). Lowry and Miller (1995) found that pore size distribution significantly influences the curvature of both the drainage and imbibition capillary pressure – saturation curves using pore network model simulations. As pore size distribution increases, the curvature of the relationship increases as a result of an increase in the number of large and small pore bodies and throats accessible at the extremes of capillary pressure (Lowry and Miller, 1995).

Lowry and Miller (1995) also conclude that pore connectivity (co-ordination number) significantly influences capillary pressure – saturation curves. That study notes that an increase in co-ordination number corresponds to an increase in the curvature of the drainage capillary pressure – saturation relationship. The curvature of the imbibition curve, however, was found to be independent of co-ordination number.

Lowry and Miller found that porous media aspect ratio, on the other hand, significantly affects the imbibition capillary pressure – saturation curve but has little influence on the shape of the drainage curve. Aspect ratio influences the prevalence of the choke-off NWP residual trapping mechanism (see Section 2.1.1.5). Lowry and Miller (1995) note that increased choke-off results in increased NWP residual values, increased imbibition curvature and a slightly increased terminal capillary pressure value. Increased aspect ratio was also noted by Morrow (1976) to increase the distance between the drainage and imbibition capillary pressure curves (i.e., increase the vertical hysteresis).

Capillary mechanisms, and thus capillary pressure – saturation relationships, are highly dependent on the wettability of the system (Morrow, 1976; Powers *et al.,* 1996). The standard P_C-S_W functions utilised in numerical simulators of two phase

flow typically assume strongly water wetting conditions. Powers *et al.* (1996) observed that the wettability of a system was variable for a given porous media, depending on the fluid - fluid pair combination. Phelan *et al.* (2004) note that wettability can vary with a variety of factors including: solid phase mineralogy (Anderson, 1986); surface roughness (Morrow, 1975); pH (Lord *et al.*, 1999); the presence of organic acids and bases (e.g. Dubey and Doe, 1993); exposure to coal tar (Powers *et al.,*1996; Villaume, 1985); exposure to synthetic gasoline (Powers and Tamblin, 1995); and exposure to surface active solutes (Gaudin and Decker, 1967; Jennings, 1975). Therefore, it is necessary to recognize that the applicability of the standard P_C-S_W function is often limited to idealised systems of silica sand and neat solvent – water fluid pairs. Wettability modified P_C-S_W functions have recently been incorporated into numerical models to account for variable wettability systems (e.g. O'Carroll *et al.,* 2004).

2.1.2.3.6 P_C-S_W Functions

Various workers have proposed empirical relationships that allow a mathematical function to be fit to experimental P_C-S_W data (e.g. Brooks and Corey, 1964; van Genuchten, 1980). Numerous other researchers have attempted to refine these relationships to account for hysteresis, terminal pressure, and other phenomenon observed in the laboratory (Luckner *et al.,* 1989; Gerhard and Kueper, 2003a). Numerical models generally employ either a van Genuchten (VG) – based constitutive model (e.g. Luckner *et al.,*1989; Lenhard *et al.,* 1991; Rathfelder and Abriola, 1998; Oostrom and Lenhard, 1998), or a Brooks-Corey (BC) - based constitutive model (e.g. Kueper and Frind, 1991a,b; Kueper and Gerhard, 1995; Gerhard and Kueper, 2003c). Recently, some VG-based models (e.g. O'Carroll *et al.,*

2004) have been updated to include a BC-based constitutive relationship or a modified VG-based relationship that explicitly accounts for displacement pressure.

Leverett (1941) presents a relationship allowing capillary pressure curves to be scaled as a function of permeability and interfacial tension. The Leverett function is useful in that it reduces the amount of physical measurement necessary for simulating two phase flow in heterogeneous porous media, and allows P_C-S_W functions measured using innocuous fluid - fluid pairs (e.g. water-air) to be translated for use in simulations involving more hazardous fluid - fluid pairs (e.g. chlorinated solvents in groundwater). The efficacy of the Leverett function has been demonstrated by numerous studies such as Schiegg (1984), Parker *et al.* (1987) and Kueper and Frind (1991a,b).

2.1.2.4 Relative Permeability – Saturation Relationships

Unlike the capillary pressure – saturation relationship, relative permeability is a continuum concept and is therefore only valid at the REV or local scale. Permeability, k, is an intrinsic property of a porous medium and is a measure of the ability to conduct fluid. From Darcy's law, it can be seen that flux of a single fluid through a homogeneous porous medium is proportional to the intrinsic permeability of the medium. This concept has been extended for multi-phase flow such that the flux of a given fluid is assumed to be proportional to the effective permeability of that fluid through the porous medium. Relative permeability, k_r, therefore, is defined as the ratio of effective permeability to intrinsic permeability. This approach assumes that, in strongly wetted media, the wetting and nonwetting fluids share the pore space as mutually exclusive interconnected flow pathways (Larson *et al.,* 1981a).

Larson *et al.* (1981a) state that relative permeability is affected by four key parameters: 1) pore size distribution; 2) the tortuosity of the effective saturation

pathways (which is a function of both phase saturation and saturation history); 3) the contribution of dead-end saturation (i.e., that proportion of connected phase in 'dead-end' pores that do not contribute to effective permeability); and, 4) NWP residual formation (i.e., the formation of discontinuous NWP that inhibits WP flow and doesn't contribute to NWP effective permeability).

In a two fluid – phase system, Bear (1972) and others note that the WP relative permeability, k_{rW}, and the NWP relative permeability, k_{rN}, do not sum to unity. Bear hypothesizes that this phenomenon is due to the viscosity difference between the fluids, which interfere with the ability of each fluid to flow. Scheidegger (1974) and Demond and Roberts (1987), however, explain that this phenomenon is due to increased tortuosity of the pathway of a fluid in the presence of another fluid.

2.1.2.4.1 Drainage

On drainage, wetting saturations will decrease below unity as NWP invades the REV. The NWP relative permeability will remain zero (i.e., 'local flow' only) until a continuous pathway of NWP exists across the REV (Wardlaw and Taylor, 1976; Thompson *et al.,* 1987). Once the local P_C exceeds the entry pressure of the REV, a continuous pathway of NWP across the REV will exist and the NWP relative permeability will immediately and abruptly increase to a finite, non-zero value (Stonestrom and Rubin, 1989b). The saturation corresponding to the first occurrence of non-zero NWP relative permeability corresponds to the "emergence saturation", S_W^M (Stonestrom and Rubin, 1989b).

As NWP further invades the REV, the WP relative permeability will decrease and the NWP relative permeability will increase to a maximum value ($k_{rN}^{\max}$) at the residual WP saturation. Geffen *et al.* (1951), examining NWP relative permeability from an oil reservoir engineering perspective, suggests that $k_{rN}^{\max}$ will approach unity

(100%) in strongly wetting systems because the WP, at residual saturations, will occupy the smallest pores and therefore not significantly block NWP flow (Geffen *et al.,* 1951; Demond and Roberts, 1987). However, Demond and Roberts (1993) suggest that $k_{rN}^{\max}$ values significantly less than unity are likely at the time-scales and flow rates typical in a contaminant hydrogeology context. While $k_{rN}^{\max}$ values of 1.0 are commonly employed in the petroleum literature (Anderson, 1987), numerous researchers report measured values of $k_{rN}^{\max}$ between 0.4 and 0.9 in the contaminant hydrogeology literature (Naar *et al.,* 1962; Stonestrom and Rubin, 1989b; Demond and Roberts, 1993; Gerhard and Kueper, 2003b; this study).

2.1.2.4.2 Imbibition

Decreasing capillary pressures and increasing WP saturations, subsequent to drainage, result in imbibition. In response to the advancement of WP into the REV, WP relative permeability will increase and NWP relative permeability will decrease to a finite minimum value. The NWP relative permeability abruptly drops to a value of zero at the extinction saturation, S_W^X; the saturation corresponding to the terminal pressure and the final loss of NWP continuity through the REV (Gerhard and Kueper, 2003a). As discussed in Section 2.1.2.3.3, the amount of trapped NWP residual on imbibition is a function of the maximum NWP saturation in the REV on drainage (i.e., the initial – residual relationship) (e.g. Land, 1968). As a result, the NWP relative permeability curve is scaled to the drainage – imbibition reversal point in a similar manner to the scaling of the capillary pressure – saturation curve.

2.1.2.4.3 Hysteresis

Consolidated porous media generally exhibit WP imbibition relative permeability greater than that exhibited for drainage (e.g. Geffen *et al.,* 1951; Osoba

et al., 1951; Land, 1968; Land, 1971, Amaefule and Handy, 1982; Braun and Holland, 1994), whereas unconsolidated porous media generally exhibit WP imbibition relative permeability less than that exhibited for drainage (Naar *et al.,* 1962; Demond and Roberts, 1991). However, the magnitude of WP hysteresis is generally considered to be slight (Anderson, 1987), and as such, numerical models capable of simulating two phase flow generally assume that a single function is sufficient for describing WP relative permeability for both drainage and imbibition conditions (e.g. Lenhard *et al.,* 1991; Kueper and Frind, 1991a,b; Rathfelder and Abriola, 1998; Oostrom and Lenhard, 1998; Kueper and Gerhard, 1995; Gerhard and Kueper, 2003c). The assumption, as stated by Demond and Roberts (1987), is that on average, the WP imbibes into and drains from essentially the same pore network.

NWP relative permeability hysteresis has been shown to be significantly greater than the hysteresis exhibited by the WP (Anderson, 1987; Demond and Roberts, 1987), although it is generally considered to be less than that observed in capillary pressure – saturation relationships (Bear, 1972; Corey, 1994). Once again, the pattern of hysteresis is variable and thought to be a function of porous media properties. The 'standard' pattern of hysteresis exhibits imbibition NWP relative permeability less than that exhibited for drainage. This hysteresis pattern has been observed in many petroleum studies in consolidated porous media (e.g. Geffen *et al.,* 1951; Osoba *et al.,* 1951; Naar *et al.,*1962; Land, 1968; Land, 1971; Talash, 1976; Amaefule and Handy, 1982; Jerauld and Salter, 1990; Fulcher *et al.,* 1985; Braun and Holland, 1994). The 'reverse' pattern of hysteresis exhibits imbibition NWP relative permeability greater than that exhibited for drainage. This hysteresis pattern has been observed for unconsolidated media by Naar *et al.* (1962), Stonestrom and Rubin

(1989b), Wei and Lile (1992), Lombard and Lenormand (1993), Gerhard and Kueper (2003b), and this study.

Dixit *et al.* (1997) conducted a series of pore network model simulations and determined that the pattern of hysteresis is governed by more sophisticated criteria than simply the consolidation state of the porous media. Dixit *et al.* (1997) conclude that the pattern of hysteresis is a function of 'effective' contact angle (which governs the primary NWP displacement mechanism on imbibition), co-ordination number (a measure of pore connectivity) and pore element volume and conductivity exponents (a surrogate measure of pore aspect ratio), and that unconsolidated media generally exhibit reverse hysteresis when flow bypassing is the dominant NWP residual formation mechanism and standard hysteresis when snap-off is the dominant mechanism. Dullien (1979) attribute the standard hysteresis pattern to trapping mechanisms occurring during imbibition (Land, 1968) that reduce the number of available NWP pathways while increasing the tortuosity of the remaining pathways; both of which act to reduce the effective permeability of the NWP on imbibition. Colonna *et al.* (1972) attribute the reverse hysteresis pattern to pore geometry hysteresis, indicating that for a given saturation, the wetting phase will occupy more of the larger pore spaces on drainage, but be restricted to the small pores and the points between sand grains on imbibition. This would leave larger flow pathways open to NWP during imbibition than during drainage.

2.1.2.4.4 k_r-S_W Functions

Various workers have proposed empirical relationships that allow a mathematical function to be fit to experimental k_r-S_W data (e.g. Brooks and Corey 1964; van Genuchten, 1980). These relative permeability constitutive relationships are integrated with extensions of the permeability functions proposed by either

Burdine (1953) or Mualem (1976). The most commonly used expression is the Brooks – Corey - Burdine relationship, however, the Brooks – Corey - Mualem, van Genuchten – Burdine, and van Genuchten – Mualem relationships have been used to varying degrees of success (e.g. O'Carroll *et al.,* , 2004).

Refinements of the traditional k_r-S_W constitutive relationships have been proposed by numerous authors to account for a number of factors, including: a more appropriate NWP effective tortuosity ratio – saturation relationship (Gerhard and Kueper, 2003b); and, relative permeability as a function of material wettability (e.g. Bradford *et al.,* 1997; Lenhard and Oostrom, 1998; Ustohal *et al.,* 1998).

2.1.2.4.5 Factors Affecting Relative Permeability – Saturation Relationships

Demond and Roberts (1987) present a review of k_r research conducted in the petroleum literature. This work describes the characteristics of typical relative permeability curves and summarizes the factors that qualitatively and quantitatively affect relative permeability, including: 1) intrinsic permeability; 2) pore properties; 3) viscosity ratio; 4) interfacial tension; and, 5) wettability.

Demond and Roberts (1987) conclude that, in general, the shape of relative permeability curves are not a function of intrinsic permeability. However, they note that intrinsic permeability is often an indication of other porous media properties that may affect k_r. For example, high intrinsic permeability may indicate well connected pores, which Morgan and Gordon (1970) show is associated with high relative permeability for a given WP saturation.

Pore properties that contribute to high relative permeability include high porosity, small aspect ratio, high co-ordination number (Wardlaw and Cassan, 1978), and lack of scale heterogeneity (Morrow, 1971). High coordination number implies high connectivity and few dead-end pores, while small aspect ratio and lack of scale

heterogeneity reduce the amount of NWP entrapment (Demond and Roberts, 1987). In addition, as the NWP tends to flow in the larger pores while the WP flows primarily in the smaller pores, pore-size distribution must have an effect on relative permeability (Demond and Roberts, 1987). Brooks and Corey (1964, 1966) note that porous media with narrow pore size distributions tends to exhibit a larger range of saturations over which two phase flow occurs, than media with wide pore size distributions. The influence of pore size distribution on relative permeability is further examined by Naar *et al.* (1962) with respect to $k_{rN}^{\max}$. Naar *et al.* (1962) concludes that uniform pore size distributions and / or lack of consolidation relate to decreased $k_{rN}^{\max}$.

Larson *et al.* (1981b) conclude that viscosity does affect relative permeability, but only at the low intrinsic permeabilities associated with consolidated porous media. For intrinsic permeabilities greater than that of silt, or for fluid-fluid pairs with less than 10-25% viscosity difference, the influence of viscosity on relative permeability is negligible (Demond and Roberts, 1987). Odeh (1959) found a sizeable enhancement of NWP relative permeability at WP residual saturations, however, the conclusion that viscosity is responsible for this enhancement has been criticised by Baker (1960) and Downie and Crane (1961). Rose (1960) points out that the influence of viscosity difference is a second-order effect, and thus is not likely to be observed with local scale experimental data.

A number of researchers have examined the influence of interfacial tension on relative permeability (Wycoff and Botset, 1936; Leverett, 1939; Lefebvre du Prey, 1973; Bardon and Longeron, 1978; Amaefule and Handy, 1981; Fulcher *et al.,* 1983). Bardon and Longeron (1978) conclude that at the limit of zero interfacial tension, the relative permeability of each phase would be equal to the phase saturation, and the

relative permeability curves would, consequently, be straight lines. However, Demond and Roberts (1987) conclude that even small interfacial tensions will significantly alter the shape of the relative permeability curves. Sufficiently great interfacial tensions are expected in all cases of two phase flow, with the possible exception of remediation scenarios involving surfactant flooding.

As separate relative permeability curves are specified for the NWP and the WP, obviously, wettability influences relative permeability. In fact, Demond and Roberts (1987) state that the relative permeability of a fluid is entirely independent of whether the fluid is aqueous or organic, and is entirely dependent on the wettability of that fluid in the porous media in question. As the relative permeability of a fluid is described by a NWP relative permeability curve if it is a nonwetting fluid, and by the WP relative permeability curve if it is a wetting fluid, then a fluid of intermediate wettability will likely exhibit relative permeability that is some average of the two relative permeability curves (Demond and Roberts, 1987). Relative permeability appears to be independent of contact angle and only the NWP shows hysteresis for $\theta < 49^{\circ}$ ($\theta > 138^{\circ}$), whereas, for intermediate contact angles, both the wetting and nonwetting curves display hysteresis (Demond and Roberts, 1987). As discussed in Section 2.1.2.4.3, Dixit *et al.,* (1997) note that the pattern of hysteresis is a function of 'effective' contact angle which is partially controlled by wettability.

2.1.3 Migration at the Laboratory and Field Scale

Numerous physical experiments have been conducted to examine the factors that affect the extent of NWP migration at the laboratory or bench scale (e.g. Schwille, 1988; Kueper *et al*., 1989; Illangasekare *et al.,* 1995; Hofstee *et al.,* 1997) and at the field scale (Kueper *et al.,* 1993; Brewster *et al.,* 1995). Numerical modelling studies examining the factors governing NWP migration (e.g. Kueper and

Frind, 1991b; Essaid *et al.*, 1993; Kueper and Gerhard, 1995; Dekker and Abriola, 2000; Lemke *et al.,* 2004) are also commonly conducted, as field experiments are generally prohibited, accidental spills are difficult to characterise (e.g. Poulson and Kueper, 1992; Kueper *et al.,* 1993; Essaid *et al.,* 1993) and field scale heterogeneity is rarely recreated in the lab (Kueper *et al.,* 1993; Kueper and Gerhard, 1995; Imhoff *et al.,* 2003).

Very few experiments, either physical or numerical, however, have specifically examined the factors governing the rate of NWP migration (Gerhard and Kueper, 2003c). For the most part, the physical experimental studies only focus on drainage processes, or lack the ability to measure time-varying NWP saturation distributions, and the numerical studies used models that have not been satisfactorily validated for redistribution and entrapment processes (Gerhard and Kueper, 2003c).

2.1.3.1 Spatial Distribution of NWP

Porous media heterogeneity with respect to permeability and capillary properties (e.g. Kueper *et al.,* 1993), source location, size and strength (e.g. Kueper and Gerhard, 1995), wettability (e.g. O'Carroll *et al.,* 2004), fluid properties (e.g. Kueper and Frind, 1991b), and hydraulic gradient (e.g. Dekker and Abriola, 2000) have been shown to greatly influence the patterns and spatial extent of NWP migration. However, the release of DNAPL into homogeneous porous media can nevertheless result in complex migration patterns (Kueper and Frind, 1988).

2.1.3.1.1 Homogeneous Porous Media

NWP releases to homogeneous porous media result in narrower, deeper, and more uniform distributions of NWP, than releases to heterogeneous porous media, as a result of lack of capillary barriers (e.g. Schwille, 1988; Kueper and Gerhard, 1995). However, displacement instability, or fingering, has been shown to occur in

homogeneous porous media, resulting in complex NWP migration patterns (Schwille, 1988; Kueper and Frind, 1988; Held and Illangasekare, 1995).

Under certain conditions the macroscopic interface between the WP and the NWP can become unstable, leading to a phenomenon referred to as 'fingering' (Kueper and Frind, 1992). Kueper and Frind (1988) provide a review of the criteria governing the occurrence of fingering. If destabilizing forces dominant over stabilising forces, small perturbations as a result of microscopic heterogeneities in an otherwise macroscopically homogeneous porous media will result in the formation of a finger (Kueper and Frind, 1988).

A homogeneous system, in which the NWP density is greater than the WP density, and the NWP viscosity is less than the WP viscosity, is unconditionally unstable, as destabilising forces dominate over stabilising forces. If the viscosity of the NWP is greater than that of the WP, then the viscosity difference will tend to stabilise the interface by counteracting the destabilising influence of the density difference. The dominance of the stabilising criteria versus the destabilising criteria in this scenario is governed by the relationship between the local interface velocity and the 'critical' velocity (Kueper and Frind, 1988). The wavelength or size of a finger, and thus the complexity of the migration pattern, is governed by the relationships between interfacial velocity, fluid-fluid viscosity difference, and interfacial tension (Kueper and Frind, 1988). Fingering in heterogeneous porous media is prevented if the length scale of the heterogeneity is equal to or less than the critical wavelength required to initiate fingering (Kueper and Frind, 1988).

2.1.3.1.2 Permeability and Capillary Property Heterogeneity

Schwille (1988) conducted the first comprehensive study of NWP migration in heterogeneous porous media in simplified bench scale experiments, demonstrating the

critical influence of low permeability capillary barriers. Further research by Kueper *et al.* (1989), Illangasekare *et al.* (1995), and Hofstee (1997) confirm the influence of capillary barriers and conclude the following characteristics of NWP migration: 1) NWP pools form upon low permeability capillary barriers; 2) horizontal migration of NWP occurs above capillary barriers; and, 3) entry of NWP into a low permeability capillary barrier only occurs when the capillary pressure of the NWP exceeds the entry pressure of the barrier.

Numerous experimental and numerical field studies have further examined the influence of permeability / capillary property variability on NWP migration patterns. Kueper *et al.* (1993) and Brewster *et al.* (1995) present the findings of a field experiment involving the release of tetrachloroethylene (PCE) below the watertable into a natural sand aquifer. Fine sampling and observation revealed that centimetre scale heterogeneities resulted in a complex network of branched, interconnected NWP migration pathways, in spite of the fact that the heterogeneities were only subtle, laminar variations in permeability / capillary properties.

2.1.3.1.3 Source Location, Size and Strength

Kueper and Gerhard (1995) present a study examining the influence of source release location, size and strength on the infiltration rate and degree of lateral spreading of a dense NWP liquid infiltrating into an initially wetting liquid saturated, heterogeneous porous media. The Monte Carlo suite of numerical simulations conducted in this study reveal that release location, and therefore the permeability / capillary properties, in the immediate vicinity of the release area, significantly influence the resultant pattern of NWP migration. Kueper and Gerhard (1995) note that migration pattern and infiltration rate variability decreases as the size of the source area increases. This is due to the fact that as the source area increases, an area

more characteristic of the average porous media heterogeneity is exposed to the source (Kueper and Gerhard, 1995). Kueper and Gerhard (1995) also found that increasing source strengths (i.e., source pressures / fluxes) were shown to cause an increase in the vertical migration, and decrease in the amount of lateral spread and degree of tortuosity, during an active NWP release.

Work presented by Dekker and Abriola (2000) indicate that the variability of migration patterns decreases as the variance of the permeability field (and capillary properties) decreases. They further conclude that NWP migration is also influenced by the mean and variance of subsurface permeability correlation length scales.

2.1.3.1.4 Wettability

The work of Bradford *et al.* (1998) and Phelan *et al.* (2004) revealed that spatially variable wettability properties can lead to pronounced capillary barriers. This work was confirmed through experimental observations of NWP retention within organic-wet sand lenses that acted to inhibit further NWP migration (O'Carroll *et al.,* 2004). While the traditional approach is to assume strongly water wet conditions, O'Carroll *et al.* (2004) illustrates the potential influence of subsurface wettability variations on NWP migration and entrapment.

2.1.3.1.5 Fluid Properties

Kueper and Frind (1991b) illustrate the influence of fluid physical properties on the behaviour of migrating NWP under drainage conditions. Gerhard *et al.* (1998) examines the influence of NWP density, viscosity, and interfacial tension on the behaviour of NWP migration during both infiltration and redistribution. These studies indicate that increased NWP density, decreased NWP viscosity, and reduced interfacial tension contribute to an increase in the mobility of the NWP both during drainage and imbibition.

2.1.3.1.6 Hydraulic Gradient

Gerhard *et al.* (1998) demonstrate the ability of high imposed hydraulic gradients to mobilise existing connected-phase DNAPL. Dekker and Abriola (2000), however, concluded that for hydraulic gradients up to 1%, the influence of hydraulic gradient on the pattern of NWP migration is negligible. Schwille (1988) and Held and Illangasekare (1995) observed no alteration of NWP migrations patterns as a result of the establishment of hydraulic gradients typical of ambient groundwater.

2.1.3.2 Times Scales of NWP Migration

2.1.3.2.1 Laboratory Studies

The magnitude of NWP migration time scales can be inferred by examining the results of numerous laboratory experiments. Schwille (1988) conducted an experiment involving the release of 24 litres of tetrachloroethylene (PCE) into a two-dimensional bench scale sand pack and noted that spreading on low permeability layers and at the bottom of the tank ceased after 21 hours. Held and Illangasekare (1995) conducted experiments involving the fixed volume release of NWP in a three-dimensional apparatus, and note that imbibition was occurring through much of the invaded material within 50 hours of the release and that saturations immediately below the source area approached residual levels. However, the focus of this study was to observe migration patterns: therefore, the possibility of continued migration of NWP in the lower part of the apparatus was not addressed (Gerhard, 2002). Hofstee (1997) conducted an experiment involving the pulse release of 225 ml of PCE into a one-dimensional column and note that water displacement, and thus NWP migration, ceased within a two day period. A second experiment by Hofstee (1997) involving the release of an additional 330 ml of PCE, subsequent to the first release of PCE into the one-dimensional column, required 12 days to reach static equilibrium. Hofstee

(1997) also conducted an experiment involving the release of 2.44 litres of PCE in a two-dimensional apparatus and found that static equilibrium conditions were established in the system seven days following the release of the NWP.

2.1.3.2.2 Field Studies

Brewster *et al.* (1995) monitored the release of 770 litres of PCE into an enclosed three-dimensional portion of the Border aquifer using geophysical techniques. The release took place for the first 6 hours of the experiment, and PCE migration was thought to be complete within approximately 573 hours, as indicated by geophysical data.

2.1.3.2.3 Numerical Studies

Numerical simulations of NWP release, redistribution and entrapment have typically utilised constitutive relationships that have not been validated with respect to the rates of NWP migration (e.g. Gerhard *et al.,* 1998; Bradford *et al.,* 1998; Rathfelder and Abriola, 1998; Dekker and Abriola, 2000; and Gerhard *et al.,* 2001). Therefore, the conclusions of these studies, with respect to the times scales of NWP migration, are generally considered to be unreliable. Gerhard *et al.* (1995) performed a simulation involving the release of 5.0 m^3 of DNAPL over 19.5 days into a two-dimensional heterogeneous porous medium and noted that redistribution of NWP ceased after 73 days. Dekker and Abriola (2000) performed a simulation involving the release of 75 L of DNAPL over 5 days into a two-dimensional heterogeneous porous media and state that redistribution of NWP ceased between 40 and 120 days. However, this study failed to identify how this range of cessation times was determined.

Gerhard and Kueper (2003c) were the first to examine the release of NWP in field scale numerical simulations utilising a simulator validated against one-

dimensional experiments with respect to spatial and temporal processes. This study revealed that for the particular set of fluid properties, porous media properties and source characteristics employed, migration of the highly mobile DNAPL employed into previously un-invaded territories of the porous medium ceased after 1.1 years, and that a state of static equilibrium existed after approximately 3.2 years.

2.1.4 Summary of Experimental Work Examining Migration

Experimental investigation into the factors influencing NWP migration have generally employed idealised representations of porous media consisting of large blocks of homogeneous sand (e.g. Kueper *et al*., 1989; Illangasekare *et al.,* 1995; Hofstee *et al.,* 1997; Rathfelder *et al.,* 2003; O'Carroll *et al.,* 2004). This approach has the advantage of simplifying the laboratory set-up and numerical model formulation, while allowing examination of the porous media properties, fluid properties and other factors that influence the pattern of NWP migration. Laboratory studies involving simplified heterogeneous systems such as this, however, are unable to explicitly examine the influence of centimetre-scale heterogeneities that have been shown to exist and affect migration patterns at the fields scale (Kueper *et al.,* 1993; Brewster *et al.,* 1995).

These studies generally focus on migration patterns, as opposed to migration rates, as a consequence of both the objective of the study and the fact that NWP data collection is rarely extensive enough, either spatially or temporally, to elucidate this issue. For example, Kueper and Frind (1989) conducted a laboratory scale flow cell experiment to validate a numerical model through visual observation of the front of NWP migration. Rathfelder *et al.* (2003) used a combination of visual observation and destructive sampling (following the complete cessation of NWP migration) to investigate the influence of surfactants on interfacial tension and the pattern of

migration. Illangasekare *et al.* (1995) utilised a dual-gamma attenuation system to measure very accurate NWP saturations, but were limited by the long exposure times required by the sampling system to only a few saturation surveys per experiment. None of these studies employed data collection methods adequate for measuring NWP saturations in space and time that would be necessary for evaluating the factors governing the rate of migration.

A light transmission image capture and analysis system was successfully employed by Gerhard and Kueper (2003b) in one-dimensional homogeneous porous media experiments specifically designed to examine the factors governing the rate of NWP migration. This system was shown to be ideal for performing this kind of study as there is no significant limit to the spatial discretisation and temporal frequency with which saturation measurements can be collected.

To date, no experimental study has been conducted to examine the factors governing the rate of NWP migration in multi-dimensional heterogeneous porous media.

2.2 Dissolution

2.2.1 DNAPL Dissolution at a Molecular Scale

Dissolution, or the transfer of mass between phases, is an endothermic process that proceeds according to the following steps (Schwarzenbach *et al.* 1993): 1) weak bonds between like molecules in the DNAPL are broken; 2) a cavity within the aqueous phase is formed; 3) the organic solute moves into the aqueous cavity; and, 4) weak bonds are formed between the organic solute and the surrounding water molecules. Transfer of the organic solute back into the DNAPL follows the reverse of these steps.

The rate of mass transfer between the phases determines the state of the process. When the rate of mass transferred to the aqueous phase is equal to the rate of mass transferred back to the DNAPL, a state of dynamic equilibrium exists such that the net rate of interphase mass transfer is zero, and the solute concentration in the aqueous phase is equal to effective solubility (Sale, 1998). Conversely, when there is a non-zero net rate of mass transfer from the DNAPL to the aqueous phase, a non-equilibrium condition exists and the aqueous concentration is less than the effective solubility.

Under steady-state conditions in a hydrogeological context, aqueous concentrations less than effective solubility are the result of advective and/or dispersive transport in the aqueous phase, and require that the net rate of mass transfer is equal to the rate of mass transport away from the DNAPL source zone. Therefore, the steady-state rate of DNAPL dissolution, or the bulk flux of mass transferred to the aqueous phase, is limited either by the rate of mass transport away from the source, or the rate of mass transfer at the DNAPL/water interface, which ever is the slower process (Sale and McWhorter, 2001).

2.2.2 Dissolution at the Macroscopic Scale

2.2.2.1 Boundary Layer Models

Mass transfer across the DNAPL/water interface is commonly described using a conventional single boundary layer, or stagnant film model (e.g. Hunt *et al.,* 1988; Miller *et al.,* 1990; Powers *et al.,* 1992; Imhoff, *et al.,* 1993). In this model, mass transferred from the bulk non-aqueous phase to the bulk aqueous phase is a result of a difference in chemical potential that occurs entirely in one phase or the other. An alternative to the single boundary layer approach is the dual boundary layer model,

where this chemical potential difference is apportioned between the phases (Brusseau, 1992).

For the single boundary layer model, the rate of mass transfer is a function of a driving force (concentration gradient) and an interfacial area between the two phases of concern (Miller *et al.,* 1990):

$$J = k_{la} a^n \left(C_s - C\right) \tag{2-3}$$

where J [$ML^{-3}T^{-1}$] is the solute mass flux from the DNAPL to the aqueous phase, k_{la} [LT^{-1}] is the average mass transfer coefficient for the DNAPL-water interface, a^n is the specific interfacial area [L^2L^{-3}} between DNAPL and groundwater for a REV, C_s [ML^{-3}] is the aqueous phase concentration that corresponds to the condition of thermodynamic equilibrium with the non-aqueous phase (i.e., effective solubility), and C [ML^{-3}] is the solute concentration in the bulk aqueous phase. Hunt *et al.* (1988) first applied this model to estimate NAPL dissolution rates.

2.2.2.2 Interfacial Area

Equation 2-3 is limited by the inherent difficulty in evaluating the specific interfacial area between the non-aqueous phase and the aqueous phase. Direct measurement of two-fluid interfacial areas is difficult (Morrow, 1970; Powers *et al.*, 1992). However, numerous emerging technologies have been developed to measure interfacial area, such as scanning electron microscopy (Gvirtzman *et al.,* 1987) non-intrusive fluorescence (Rashidi *et al.,* 1996), photoluminescent volumetric imaging (PVI) (Montemagno and Gray, 1995) and nuclear magnetic resonance (NMR) imaging (e.g. Ronen *et al.,* 1986; Majors *et al.,* 1997). These approaches are often tedious, expensive, and subject to other limitations (Dalla, *et al.,* 2002). For example, PVI methods require a medium with special optical properties and a long period of

time to obtain high-resolution images; a requirement that is not ideal for measuring interfacial areas of a transient DNAPL release in heterogeneous porous media.

Alternatively, interfacial areas can be approximated for use in numerical models for the evaluation of interfacial processes such as dissolution. Methods for approximating interfacial areas include the capillary tube model (Cary, 1994), the ideal soil model (Gvirtzman and Roberts, 1991), the interfacial tracer technique (IFTT) (Kim *et al.,* 1997; Saripalli *et al.,* 1998), and a thermodynamic approach (Leverett, 1941; Morrow, 1970; and, Bradford and Leij, 1997). Additionally, interfacial area can also be approximated from pore-scale network simulations (Dalla *et al.,* 2002; Reeves and Celia, 1996)

The capillary tube model uses experimental capillary pressure – saturation relationships to estimate the pore-size distribution according to the capillary law (Cary, 1994). The total interfacial area of the fluid-fluid interface is then obtained by summing up the hypothetical interfacial areas for all drained capillary tubes at a given capillary pressure (Bradford and Leij, 1997). This model simplifies the geometry of the porous medium and is further limited to assuming complete wetting of the solid.

The ideal soil model is based on the ideal soil concept of a homogeneous arrangement of identical spheres and involves the calculation of the volume and area of geometric shapes. This model is limited to scenarios of low wetting phase saturations where the wetting phase forms pendular rings between adjacent soil grains (Gvirtzman and Roberts, 1991).

The IFTT is an experimental approach, in which the retardation factor of a surface-reactive tracer (e.g. anionic surfactant), is determined from steady state column experiments for a given wetting phase saturation. The interfacial area is then calculated from the retardation factor and the adsorption coefficient for the tracer at

the fluid - fluid interface (Kim *et al.,* 1997). The IFTT method is limited to evaluating the effective interfacial area between fluids (i.e., the method neglects the interfacial area between the nonwetting fluid and the thin film of wetting fluid coating soil grains). However, this may be advantageous for evaluating the portion of the fluid-fluid interfacial area that is likely to contribute to substantial mass transfer.

The thermodynamic approach is based on equivalence between the change in interfacial energy and the mechanical work done on the system (Leverett, 1941; Morrow, 1970; and, Bradford and Leij, 1997). The total interfacial area is computed from the measured capillary pressure - wetting phase saturation curve. This method assumes energy dissipation to be negligible, however, Dalla *et al.* (2002) determined that energy dissipation during Haines jumps is significant and thus mechanical work done on the system is not completely converted into surface energy. In addition, Dalla *et al.,* (2002) determined that prediction of interfacial areas at low wetting saturations, where wetting phase geometries are pendular in shape, is unreliable at best. However, this method has the advantage of being highly suitable to complimenting constitutive relationships.

Pore-scale network modelling is useful for estimating interfacial areas in that the geometry of all menisci in the system can be calculated. These fluid - fluid interfaces, along with the pore system geometry, completely determine the boundaries delineating the spatial distribution of fluids within the network (Reeves and Celia, 1996). Although limited to representing the porous media as a network of geometrically shaped pores and pore throats, and utilising unproven 'rules' for pore snap-off and residual formation, this method is rigorous and often demonstrates excellent agreement with other methods used to quantify interfacial area, such as IFTT (Dalla *et al.,* 2002).

2.2.2.3 Correlation Expressions

Due to the complexities of measuring interfacial areas and the limitations associated with the methods for estimating interfacial areas, numerous researchers (e.g. Miller *et al.,* 1990; Powers *et al.,* 1992; Imhoff *et al.,* 1993; Saba and Illangasekare, 2000; Nambi and Powers, 2003) have opted to combine the mass transfer coefficient and the specific interface area in Equation 2-3 into a lumped mass transfer term, K_l [T^{-1}], such that:

$$J = K_l\left(C_s - C\right) \tag{2-4}$$

Miller *et al.* (1990) describe the lumped mass transfer rate coefficient as an empirically determined parameter and as such, extensive research has been conducted in regards to developing empirical models to predict its value (e.g. Miller *et al.,* 1990; Powers *et al.,* 1992; Imhoff *et al.,* 1993; Saba and Illangasekare, 2000; Nambi and Powers, 2003). Experimental studies conducted to determine the value of K_l typically involve centimetre scale columns packed with homogenous porous media containing constant (assumed) residual DNAPL saturations (Miller *et al.,* 1990; Powers *et al.,* 1992; Imhoff *et al.,* 1993). However, more recent work has seen the use of multi-dimensional bench scale flow cells (Saba and Illangasekare, 2000; Nambi and Powers, 2003) and has employed DNAPL saturations considered to be higher than residual values (Nambi and Powers, 2003). Miller *et al* (1990) and Imhoff *et al.* (1993) estimate K_l values in the range of 100-1000 day^{-1} from column studies; however, in these studies, constant seepage velocities were imposed on the column which are an order of magnitude greater than typical field values (Sale, 1998).

Justification for treating K_l as an empirical parameter is derived from the fact that for many multiphase systems, mass transfer near the interface between phases is the combined result of both advective and diffusive processes (and may be influenced

by other phenomena such as 'chemical kinetics' and 'density-motivated flow'), and is not simply a result of diffusive transport as assumed in the stagnant film theory (Miller *et al.,* 1990). Resolution of mass transfer under such circumstances requires an understanding of groundwater flow at a sub-REV scale. Therefore, when modelling mass transfer at the macroscopic scale, the stagnant film model itself reduces to an empirical tool.

The value of K_l, incorporating the unspecified specific surface area between phases, is typically determined from laboratory measurements that are characterised with a modified Sherwood number:

$$Sh = K_l d_m^2 D_m^{-1} \tag{2-5}$$

where Sh is the Sherwood number, d_m [L] is the mean particle diameter, and D_m [L^2T^{-1}] is the molecular diffusion coefficient for the soluble constituent (Miller *et al.*, 1990). Experimental determinations of the Sherwood number are usually presented in the form of traditional dimensionless groupings such as Schmidt, Peclet, and Reynolds numbers (Sale and McWhorter, 2001), and often contain a surrogate parameter for interfacial area such as DNAPL saturation or porous media structure.

Empirical models (referred to as correlation expressions) of Sh have been developed by numerous researchers (e.g. Miller *et al*., 1990; Parker *et al*.,1991; Powers *et al*., 1992; Gellar and Hunt, 1993; Imhoff *et al.*, 1993; Powers *et al*., 1994; Saba and Illangasekare, 2000; Nambi and Powers, 2003). With the exception of Powers *et al*. (1992), the correlation expressions are all a function of seepage velocity (through the Reynolds number) and DNAPL saturation. With the exception Miller *et al*. (1990) and Nambi and Powers (2003), the correlations also include porous media properties. For example, the correlation expression of Miller *et al*. (1990) is written as:

$$Sh = \beta_0 \, \mathrm{Re}^{\beta_1} \, \theta_n^{\beta_2} \, Sc^{1/2} \tag{2-6}$$

where β_0, β_1, and β_2 are empirical fitting parameters, Re is the Reynolds number, θ_n is the DNAPL volume fraction, and *Sc* is the Schmidt number.

Comparison of published correlation expressions has led to the conclusion that the expressions are only valid under very specific and narrow conditions, and in some cases may only be considered to be valid for the conditions under which they were derived (Grant and Gerhard, 2004 – see Appendix G). Imhoff *et al*. (1993) compares estimates of *Sh* calculated from the correlation expressions of Miller *et al*. (1990), Parker *et al*. (1991), Powers *et al*. (1992), and Gellar and Hunt (1993) and found that *Sh* values range over three orders of magnitude for a fixed set of conditions. Imhoff *et al*. (1993) attributes this lack of agreement to laboratory methods, including the different techniques used for establishing residual NAPL within the porous media.

Modelling studies comparing the above mentioned correlation expressions have shown that there are extremely large differences in the predicted time to complete DNAPL source dissolution in large scale (Zhu and Sykes, 2000) or heterogeneous (Mayer and Miller, 1996; Grant and Gerhard, 2004 - see Appendix G) systems. These comparative works imply that the ability to accurately predict the rate of DNAPL dissolution through correlation expressions is extremely limited, and that the determination of DNAPL source zone life spans will be impossible until such time as a comprehensive mass transfer expression is derived and validated.

2.2.3 Dissolution at the Super-Macroscale

Miller *et al*. (1990) and Imhoff *et al*. (1993) demonstrate that the scale of non-equilibrium conditions within an experimental column is on the order of centimetres for the seepage velocities and DNAPLs examined. At distances greater than a few centimetres, the solute concentration in the aqueous phase is equal to effective

solubility, and as such, the net rate of mass transfer beyond this distance is zero. Therefore, the bulk mass transfer rate, the product of the Darcy velocity and the aqueous phase solute concentration, is largely independent of K_l when distances of a few centimetres are considered (Sale, 1998). It is clear that the dependence of the bulk mass transfer rate on K_l is a function of the scale being considered.

A local scale equilibrium approach (LEA) allows the rate of mass transfer to be estimated based on an equilibrium partitioning relationship (e.g. Abriola, 1989; Seagren *et al.,* 1999; Sale and McWhorter, 2001) where the rate of mass flux from a DNAPL source zone is independent of the macroscopic mass transfer coefficient and is entirely dependent on advection - dispersion. However, the LEA requires the definition of the "local" scale, or REV, over which bulk mass transfer can be considered to be independent of K_l. This local scale is likely to be transient as the seepage velocity through a DNAPL source zone and the interfacial area between phases are both functions of DNAPL saturation, which will vary with time as dissolution proceeds. As noted by Miller *et al.* (1990) and Imhoff *et al.* (1993), the size of the local scale is generally in the order of a few centimetres.

2.2.4 Dissolution at the Field Scale

Miller *et al.* (1998) and others have observed that empirically derived mass transfer correlation expressions predict near-equilibrium concentrations within very short travel distances. This is consistent with the findings of Frind *et al*. (1999) where near-equilibrium concentrations were observed immediately downgradient of an emplaced uniform DNAPL source at the Borden field site. However, Mackey *et al.,* (1985) and Mercer and Cohen (1990) note that aqueous phase concentrations measured in observation wells rarely exceed 10% of the solubility at DNAPL

contaminated sites. This apparent inconsistency can be attributed to subsurface heterogeneity with respect to DNAPL distribution and groundwater flow.

Numerous researchers have examined the relationship between field scale dissolution rates and source zone architecture, hydraulic properties, and various other porous media and fluid properties (e.g. Parker and Park, 2004; Lemke *et al.,* 2004; Soga *et al.,* 2004). Field scale mass transfer rates are found to be orders of magnitude lower than local scale mass transfer rates as a result of 'flow-bypassing' attributed to effects of heterogeneity in DNAPL distributions and groundwater flow (Parker and Park, 2004). They are also a function of the scale being considered, as field scale mass transfer rates are dependent on the proportion of the DNAPL source zone occupied by DNAPL. Powers *et al.* (1998) and Soerens *et al.* (1998) showed that much of the apparent non-equilibrium dissolution can be explained by irregular NAPL distribution and flow heterogeneity. Brusseau *et al.* (2002) conducted intermediate-scale dissolution experiments and concluded that that dissolution behaviour is controlled by larger scale factors such as non-uniform NAPL distribution, permeability variation, and dilution associated with the aqueous phase sampling, and that local-scale mass transfer processes are generally of secondary importance. In general, while near-equilibrium mass transfer may occur at the local scale, field scale mass transfer is primarily controlled by advective – dispersive transport (Sale and McWhorter, 2001, Soga *et al.,* 2004).

Numerical / analytical modelling of field scale mass transfer requires a local scale (nodal scale) expression of mass transfer. To date, these studies have relied on a LEA (e.g. Sale and McWhorter, 2001) or an empirically derived mass transfer correlation expression (e.g. Parker and Park, 2004; Lemke *et al.,* 2004). Mayer and Miller (1996) and Saba and Illangasekare (2000) indicate that uncertainty in the local

scale correlation expression will have little effect on early time behaviour, but will result in gradually increasing uncertainty as DNAPL saturations become smaller and local mass transfer limitations become more significant. Evaluation of predicted field scale mass transfer rates is therefore limited by the variability and uncertainty associated with the employed correlation expression.

2.2.5 Summary of Experimental Work Examining Dissolution

Early work investigating dissolution focussed on the factors governing mass transfer at the local scale. Numerous researchers (e.g. Miller *et al.,* 1990, Parker *et al.,* 1991, Powers *et al.,* 1992; Gellar and Hunt, 1993, Imhoff *et al.,* 1993) derived correlation expressions describing the rate of mass transfer through the use of one-dimensional column studies. In addition to excluding the influence of flow dimensionality, these studies focused the dissolution of residual NWP blobs and ganglia.

More recent work has examined mass transfer from a low saturation NWP source in multi-dimensional systems utilising laboratory scale flow cells (Saba and Illangasekare, 2000; Nambi and Powers, 2003). Saba and Illangasekare (2000) derived a correlation expression by measuring aqueous phase concentrations downgradient of a residual NWP source zone in a simplified heterogeneous system comprising a well-defined coarse sand lens surrounded by a finer medium. The expression was validated in a second experiment involving three residual source zones of varying size. Nambi and Powers (2003) examined the influence of initial saturation on mass transfer using a simplified heterogeneous system similar to the one employed by Saba and Illangasekare (2000). Initial NWP saturations between 0.3 and 0.8 were employed, but early time behaviour showing near equilibrium mass transfer was ignored. Therefore, the applicability of the correlation expression derived in this

study is limited to NWP saturations less than approximately 0.35 (Nambi and Powers, 2003).

Further laboratory scale studies have attempted to illustrate the relationship between mass transfer rates and system hydrodynamics. Powers *et al.* (1998), for example, adopted a local equilibrium assumption and examined the influence of WP relative permeability on the rate of mass transfer from a high NWP saturation source zone emplaced in a simplified heterogeneous porous media (similar to the one used by Nambi and Powers (2003). While unable to accurately predict the dissolution behaviour of the NWP source zone, this study illustrated the importance of flow dimensionality and the influence of NWP presence on WP flow rates.

Numerical modelling studies examining NWP dissolution have either utilised a LEA, or have applied a local scale or laboratory scale derived empirical correlation expression (e.g. Mayer and Miller, 1996; Parker and Park, 2004; Grant and Gerhard, 2004 – see Appendix G). Application of these expressions often required extrapolation to NWP saturations much higher than the values used in their development, to flow systems of greater dimensionality, and to heterogeneous systems where the applicability of these expressions has not been tested.

Development of a mass transfer expression, empirical or otherwise, to describe the dissolution of a transient, variable saturation NWP body in realistic heterogeneous porous media is necessary before accurate predictions of the interrelationship between source zones and downgradient aqueous phase concentrations can be elucidated at the field scale.

2.3 Aqueous Phase Contaminant Transport

The processes governing aqueous phase contaminant transport at the local, laboratory and field scales will be discussed in this section.

2.3.1 Advection

Advection refers to the average bulk movement of the solute in flowing groundwater (Sudicky, 1986). The relationship between groundwater flow and the process of advection is direct, and knowledge about groundwater flow systems and rates is immediately transferable to understanding advection (Domenico and Schwartz, 1990). Accordingly, Darcy's law can be modified to give the advective (or average) velocity, V_{avg}, of an aqueous phase contaminant in the absence of other hydrophysical or chemical processes (Bear, 1972):

$$V_{avg} = \frac{q}{\phi} = -\frac{Ki}{\phi} \tag{2-7}$$

where q is the Darcy flux [LT^{-1}], ϕ is the porosity of the porous medium, K [LT^{-1}] is the hydraulic conductivity of the porous medium, and i [LL^{-1}] is the hydraulic gradient.

There are some situations where the advective velocity is different from the linear velocity described by Equation 2-7. Corey *et al.* (1963) and Krupp *et al.* (1972) discuss the transport of charged particles through clay materials. In their work, they found negatively charged ions to move faster than the groundwater in which they were dissolved, as the clay mineral electrical charges forced the dissolved molecules into the centre of the pore throats and bodies, where microscopic water velocities are at a maximum.

2.3.2 Dispersion

Spreading of aqueous phase concentrations about the average, or advective, position of the solute is caused by a process referred to as hydrodynamic dispersion (Sudicky, 1986). Longitudinal dispersion, D_L, or hydrodynamic dispersion along the direction of principle groundwater flow, can be written as (Bear, 1972):

$$D_L = \alpha \cdot V_{avg} + D_m \tag{2-8}$$

where $\alpha \cdot V_{avg}$ describes the mechanical mixing of solute by pore scale fluctuations in groundwater velocity quantified by the dispersivity parameter, α, and, D_m is the molecular diffusion parameter. Transverse dispersion, D_T, in the directions perpendicular to the principle direction of groundwater flow, is often assumed to be some fraction of the longitudinal dispersion (Bear, 1972).

The degree of dispersion in a given system is a function of porous media heterogeneity and the spatial structure of the hydraulic properties in the system (Sudicky, 1986). Numerous researchers have noted that dispersive transport is strongly dependent on the distribution of hydraulic conductivity (e.g. Schwartz, 1977; Gelhar *et al.,* 1979; Smith and Schwartz, 1980; Silliman and Simpson, 1987; Neuman, 1993). Dispersion is classically modelled as a Fickian process, such that dispersivity is then traditionally assumed to be a unique property of the porous medium at a particular scale of interest (Bear, 1972).

2.3.2.1 Dispersivity

Mechanical mixing, as quantified by the dispersivity parameter, α, is generated as a consequence of pore scale heterogeneities in an otherwise homogeneous local scale porous medium. These heterogeneities result in pore scale velocity differences and variability in tortuosity between flow channels (Domenico and Schwartz, 1990).

Dispersivity values are often determined by calibrating a solution of the advection-dispersion equation (Bear, 1972) to collected data (Sudicky, 1986). However, the scale dependence of dispersivity, as well as experimental deficiencies (such as lack of sufficient concentration data, or information regarding boundary conditions), often reduce the calibration of a dispersivity value to a curve fitting exercise (Sudicky, 1986).

Theoretical consideration of dispersivity reveals that the value of this parameter is scale dependent and will grow with solute residence time and displacement distance as the dispersion process develops (Sudicky, 1986). Dispersivity will reach an asymptotic maximum value slowly and may involve travel distances of many tens, or even hundreds of meters at some field sites (Dagan, 1982, 1984, 1986; Sudicky, 1983)

Recent advances in dispersion theory have allowed for the estimation of dispersivity values from the variability of aquifer hydraulic properties. Gelhar (1986) discusses a stochastic approach for estimating dispersivity when examining aqueous phase transport at the field scale. This approach is useful for quantifying average transport behaviour from statistically represented transport parameters and stochastic forms of the governing groundwater flow and aqueous phase transport equations (e.g. Gelhar *et al.,* 1979; Matheron and de Marsily, 1980; Güven *et al.,* 1984; Sudicky, 1984; Dagan, 1982; Gelhar and Axeness, 1983; Winter *et al.,* 1984).

2.3.2.2 Diffusion

Molecular diffusion results in solute mixing due to thermal kinetic energy - induced random molecular motions (Domenico and Schwartz, 1990). Diffusion is often expressed according to Fick's law that describes mass flux as proportional to a diffusion coefficient and a concentration gradient, similar to the single boundary layer model used to described rate limited mass transfer (Section 2.2.2.1). To account for diffusion of solute in a porous medium, Fick's law was modified by Whitaker (1967) to account for the fact that the liquid phase is enclosed by a porous solid.

2.3.3 Non-Fickian Behaviour

Non-ideal or non-Fickian aqueous phase transport has been observed by numerous researchers (e.g. Anderson, 1979; Barrow, 1989; Zinn *et al.,* 2004). This

type of behaviour is characterised by early breakthrough and 'tailing' of persistent, low solute concentrations over long periods of time that can not be accounted for in transport models employing traditional advective - dispersive formulations (Li *et al.,* 1994). Brusseau and Rao (1990) attribute this tailing phenomenon to several physical and chemical factors including heterogeneous hydraulic conductivity, heterogeneous soil chemical properties, and non - equilibrium sorption. While the chemical factors can be disregarded for the case of non reactive transport, or described explicitly (e.g. Brusseau, 1995), the physical factors alone, including solute movement between regions of high and low hydraulic conductivity, can cause non-ideal solute transport (e.g. Murali and Aylmore, 1980; Zinn *et al.,* 2004).

Aquifer heterogeneity resulting in non-Fickian behaviour, or tailing, is significant for porous media systems with large conductivity contrasts between adjacent sand types (Li *et al.,* 1994). Tailing is advection - dominated for conductivity contrasts of approximately one order of magnitude, and becomes increasingly diffusion - dominated as the conductivity contrast increases (Zinn *et al.,* 2004).

This phenomenon has prompted the development of a mass transfer – type model to describe mass transport into and out of low conductivity regions (Zinn and Harvey, 2003). A bicontinuum model is often used to characterise the system as containing a mobile region, where water and solute moves, and an immobile region, where the water and solute is stagnant except for diffusive transport (Rao *et al.,* 1980a,b).

2.3.4 Reactive Transport

In addition to the hydrophysical processes that result in transport, a solute will often react with the subsurface environment through a number of key transformation

processes, including: complexation (hydrolysis and acid – base reactions); oxidation – reduction; sorption - desorption; biodegradation; and, radioactive decay (Yeh and Tripathi, 1991).

Complexation is the process whereby simple cations and anions (sometimes call ligands) combine to form more complex ions (Domenico and Schwartz, 1990). This process is primarily a concern when investigating the transport of inorganic metal species in saline groundwater systems. However, hydrolysis and acid – base reactions can significantly affect the geochemical state of a subsurface system and impact the efficacy of chemical or biogeological remediation strategies.

Oxidation – reduction reactions involve the transfer of electrons from one compound to another. Oxidants such as potassium permanganate and Fenton's reagent are commonly used in DNAPL remediation scenarios as these compounds have been shown to effectively react with readily available chlorinated solvents (Seol *et al.,* 2003).

Sorption (and desorption) is the general term for the interaction (binding or association) of a solute with a solid surface. Sorption is often described by an isotherm relating the relationship between aqueous phase concentration and sorbed-phase concentration. This can take the form of a linear approximation, or a non-linear description such as the Langmuir, Freundlich, or Toth isotherms (Barry *et al.,* 2002). Other sorption isotherms are summarized by (Barry, 1992). Sorption is often modelled using a local equilibrium assumption (Miller and Weber, 1984; Bajracharya and Barry, 1993), however, numerous researchers have found it necessary to describe sorption as a rate-limited process in models describing the transport of transforming solutes (e.g. Eldor and Dagan, 1972; Lindstrom, 1976; Lassey, 1988; van Genuchten and Wagenet, 1989; Estrella *et al.,* 1993; Brusseau *et al.,* 1992). The sorption

phenomenon can cause the transport of a solute to be retarded relative to the rate of groundwater flow and in some cases, can even immobilise the solute (Domenico and Schwartz, 1990). In addition, numerous remediation schemes at contaminated sites, including zero-valent iron reductive dechlorination (Burris *et al.,* 1995) require adsorption to occur prior to the active transformation process.

Microbial mediated degradation of organic contaminants is essentially an oxidation – reduction process, where bacteria control the rate of the solute transformation process (Domenico and Schwartz, 1990). These processes are often a major factor in contaminant transformations, and play a central role in remediation schemes such as (active) bioremediation and monitored natural attenuation (Barry *et al.,* 2002). Besides reducing solute concentrations, biodegradation can also lead to secondary and tertiary reactions such as ion exchange, mineral precipitation and other process that further affect solute transport (Hunter *et al.,* 1998; Chapelle *et al.,* 1996).

Radioactive decay is only necessary to consider at sites contaminated with radioactive materials. Radioactive decay involves the transformation of an unstable isotope to a new, more stable isotope of the contaminant compound and is often modelled using a first-order expression quantified by an isotope half-life (Domenico and Schwartz, 1990).

2.4 Numerical Modelling of Subsurface Phenomena

2.4.1 Mass Balance Equations

The local-scale balance equations governing multiphase / multicomponent flow and transport in porous media can be derived by performing an appropriate averaging over the pore scale. This procedure is discussed by various authors including Hassanizadeh and Gray (1979a,b) and Marle (1982). Following the

derivation presented by Huyakorn and Pinder (1983), a mass balance equation for component κ in phase α can be written:

$$\frac{\partial}{\partial t}\left(\varepsilon_\alpha \rho_\alpha \varpi_\kappa^\alpha\right)+\frac{\partial}{\partial x_i}\left(\varepsilon_\alpha \rho_\alpha \varpi_\kappa^\alpha v_{\alpha,i}\right)-\frac{\partial}{\partial x_i} J_{\kappa,i}^\alpha = I_\kappa^\alpha + E_\kappa^\alpha \tag{2-9}$$

where ε_α is the fraction of bulk volume occupied by the α phase, ρ_α is the average mass density of the α phase, ω_κ is the mass fraction of component κ in the α phase, $\upsilon_{\alpha,i}$ is the velocity of the α phase in the ith direction, $J_{\kappa,i}{}^\alpha$ is the non-advective flux of κ in the α phase in the ith direction, $I_\kappa{}^\alpha$ represents the transfer of κ due to phase change and diffusion across the phase boundaries, and $E_\kappa{}^\alpha$ the external supply of κ to the α phase through biotic and abiotic transformations. Equation 2-9 is constrained by the fact that the mass fractions within a given phase sum to unity, the fractional phase volumes sum to unity, and the mass of a given component is conserved amongst the phases (Kueper and Frind, 1992).

Equation 2-9 requires knowledge of the velocity of the various phases. These are usually attained by a multi-phase extension of Darcy's law which can be written (Kueper and Frind, 1992):

$$v_{\alpha,i} = -\frac{K_{ij}^\alpha}{\varepsilon_\alpha}\left(\frac{\partial P_\alpha}{\partial x_j}+\rho_\alpha g \frac{\partial z}{\partial x_j}\right) \tag{2-10}$$

where P_α is the pressure of the α phase, g is acceleration due to gravity, z the vertical direction, and K_{ij}^α is the second rank hydraulic conductivity tensor given by:

$$K_{ij}^\alpha = \frac{k_{ij} k_{r,\alpha}}{\mu_\alpha} \tag{2-11}$$

where μ_α is the dynamic viscosity of the α phase, k_{ij} is the second rank intrinsic permeability tensor, and $k_{r\alpha}$ is the relative permeability to the α phase.

Equation 2-9 also requires a definition for the non-advective flux term, $J^{\alpha}_{k,i}$, that accounts for the hydrodynamic dispersion of component *k* within phase *α*. Under the assumption that hydrodynamic dispersion is Fickian in nature, $J^{\alpha}_{k,i}$ is represented by (Kueper and Frind, 1992):

$$J^{\alpha}_{k,i} = -\varepsilon_{\alpha}\tau_{\alpha,ij}D^{k,\alpha}_{o}\frac{\partial\left(\rho_{\alpha}\omega^{\alpha}_{k}\right)}{\partial x_{j}} - \varepsilon_{\alpha}D^{k,\alpha}_{m,ij}\frac{\partial\left(\rho_{\alpha}\omega^{\alpha}_{k}\right)}{\partial x_{j}} \qquad (2\text{-}12)$$

where $\tau_{\alpha,ij}$ is a tensor of phase tortuosity coefficients, $D^{k,\alpha}_{o}$ is the free molecular diffusion coefficient of *k* in *α*, and $D^{k,\alpha}_{m,ij}$ is a mechanical dispersion tensor of *k* in *α*.

2.4.2 Governing Equations

In some cases, Equation 2-9 can be simplified by decoupling phase behaviour from component behaviour. For modelling multiphase flow only, (e.g. Kueper and Frind, 1991a,b; Gerhard, 1995, 2002), it is assumed that partitioning and transformation of components does not significantly affect phase flow. This assumption is valid for low-solubility DNAPLs under conditions where migration time scales are relatively short (Kueper and Frind, 1992). For modelling multicomponent transport only (e.g. Falta *et al.* 1989; Mendoza and Frind, 1990a,b), it is assumed that the behaviour of certain phases occurs at time scales much shorter than that of component evolution. This assumption is valid, for example, when considering the early time dissolution rates of large immobile residual DNAPL source zones.

2.4.2.1 Multiphase Flow

Equation 2-9 can be summed over all components to give a mass balance for each phase of interest. Assuming laminar flow, incompressibility of the fluids and porous medium, and ignoring the source/sink terms, the continuity equations for mass

balance of the wetting (subscript 'W') and nonwetting (subscript 'N') phases, respectively, are given by (Bear, 1972):

$$\frac{\partial}{\partial x_i}\left[\frac{-k_{i,j}k_{r,W}}{\mu_W}\left(\frac{\partial P_W}{\partial x_j}+\rho_W g\frac{\partial z}{\partial x_j}\right)\right]-\phi\frac{\partial S_W}{\partial t}=0 \tag{2-13}$$

$$\frac{\partial}{\partial x_i}\left[\frac{-k_{i,j}k_{r,N}}{\mu_N}\left(\frac{\partial P_N}{\partial x_j}+\rho_N g\frac{\partial z}{\partial x_j}\right)\right]-\phi\frac{\partial S_N}{\partial t}=0 \tag{2-14}$$

As mentioned in Section 2.1.2, phase pressures are coupled through the relationship for capillary pressure:

$$P_C\left(S_W\right)=P_N-P_W \tag{2-15}$$

and phase saturations are related through:

$$S_W+S_N=1 \tag{2-16}$$

therefore, Equations 2-13 and 2-14 can be re-written to give the governing equations for two phase flow in porous media (Kueper and Frind, 1991a):

$$\frac{\partial}{\partial x_i}\left[\frac{-k_{i,j}k_{r,W}}{\mu_W}\left(\frac{\partial P_W}{\partial x_j}+\rho_W g\frac{\partial z}{\partial x_j}\right)\right]-\phi\frac{\partial S_W}{\partial t}=0 \tag{2-17}$$

$$\frac{\partial}{\partial x_i}\left[\frac{-k_{i,j}k_{r,N}}{\mu_N}\left(\frac{\partial\left(P_c+P_W\right)}{\partial x_j}+\rho_N g\frac{\partial z}{\partial x_j}\right)\right]+\phi\frac{\partial S_W}{\partial t}=0 \tag{2-18}$$

As discussed in Section 2.1.2, constitutive relationships describe the dependence of capillary pressure and phase relative permeability on phase saturation. As an example of the basic form of these constitutive relations, the Brooks-Corey capillary pressure curve for drainage is given by:

$$P_C=P_D\left(S_e\right)^{\frac{-1}{\lambda}} \tag{2-19}$$

where λ is the pore size distribution index on drainage, and S_e is the effective saturations defined by:

$$S_e = \frac{S_W - S_r}{1 - S_r} \tag{2-20}$$

The corresponding Brooks-Corey relative permeability curves are, for the wetting phase and nonwetting phase, respectively:

$$k_{rW} = S_e^{\frac{2+3\lambda}{\lambda}} \tag{2-21}$$

$$k_{rN} = (1 - S_e)^2 \left(1 - S_e^{\frac{2+\lambda}{\lambda}}\right) \tag{2-22}$$

As k_{rW}, k_{rN}, and P_C are all functions of S_W (e.g. Brooks and Corey, 1964, 1966), the two governing equations require simultaneous solutions for two unknowns (S_W and P_W).

2.4.2.2 Multicomponent Transport

Equation 2-9 can be summed over all phases to give a mass balance for each component of interest. Re-written in terms of aqueous phase concentrations, C_κ, of component, κ, Equation 2-9 becomes:

$$\frac{\partial}{\partial t}(\phi C_\kappa) + \frac{\partial}{\partial x_i}(\phi v_{\kappa,j} C_\kappa) - \frac{\partial}{\partial x_i}\left(\phi D_{ij} \frac{\partial C_\kappa}{\partial x_j}\right) = \sum R_n + q_s C_{\kappa,s} \tag{2-23}$$

where $\phi D_{ij} \frac{\partial C_\kappa}{\partial x_j} = J^\alpha_{\kappa,i}$, and D_{ij} is the hydrodynamic dispersion coefficient tensor, $\sum R_n = I^\alpha_\kappa$ is the chemical reaction term, and $q_s C_{\kappa,s} = E^\alpha_\kappa$, where q_s is the volumetric flow rate per unit volume of aquifer representing fluid sources (positive) and sinks (negative).

Considering the aqueous phase exclusively, and assuming Fickian hydrodynamic dispersion, D_{ij} is a function of groundwater velocity, as shown for one-dimensional flow in Equation 2-23. Groundwater velocity can be calculated according to Darcy's law (Bear, 1972):

$$v_{\kappa,j} = \frac{q_{\kappa,j}}{\phi} = -\frac{K_{ij}}{\phi}\frac{\partial h}{\partial x_j} \tag{2-24}$$

where h is hydraulic head, calculated from the solution of the groundwater flow equation (Bear, 1972):

$$\frac{\partial}{\partial x_j}\left(K_{ij}\frac{\partial h}{\partial x_j}\right) + q_s = S_s\frac{\partial h}{\partial t} \tag{2-25}$$

The chemical reaction term in Equation 2-23, R_n, can be used to include the effects of general biochemical and geochemical reactions (e.g. sorption and decay) which are generally expressed as functions of aqueous phase concentration. Therefore, the governing equations for each component require the solution of only one unknown (C_κ) for each equation.

2.4.3 Numerical Solution Techniques

The differential equations governing multiphase / multicomponent flow and transport often employ a numerical method, such as finite difference, finite element, or finite volume, to obtain an approximate solution (Kueper and Frind, 1992). These methods require the discretisation of the appropriate governing equations and the representation of the unknown variables at discrete points, or nodes, within the solution domain. A set of algebraic equations for the system can be obtained upon specification of boundary and initial conditions.

These differential equations are highly non-linear and generally require an implicit, iterative solution scheme such as Newton-Raphson iteration, which is generally regarded as one of the most robust (Huyakorn and Pinder, 1983).

Several 'compositional' models have been developed to solve the system of equations resulting from Equation 2-9 as presented above, including Abriola and Pinder (1985), Corapcioglu and Baehr (1987), Forsyth and Shao (1991), Sleep and

Sykes (1993), Huyakorn *et al.,* (1994a), Slough *et al.* (1999) and Reynolds and Kueper (2001). Rigorous models that simulate three-dimensional flow and transport of DNAPLs and aqueous phase contaminants in the saturated and unsaturated zones such as these, have extremely complex data requirements and are computationally intensive (e.g. Pinder and Abriola, 1986; Reeves and Abriola, 1988; Panday *et al*., 1997).

Some simulators (e.g. Reeves and Abriola, 1988; DNAPL3D-MT presented in this thesis) take advantage of the numerical simplifications presented by decoupling phase and component behaviour, and use a Split Operator (SO) routine to link the solutions of the isolated sets of equations presented in Sections 2.4.2.1 and 2.4.2.2. These simulators are able to model DNAPL migration, dissolution, and aqueous phase contaminant transport while minimizing the complexity of the data requirements associated with compositional models (see Appendix F).

Numerical models examining other subsurface processes, including density dependant flow coupled with aqueous phase transport (e.g. SEAWAT – Simpson, 2004), or aqueous phase transport coupled with biogeochemical reactions (e.g. Barry *et al.,* 2002) have successfully employed a SO routine. The primary disadvantage of implementing a SO approach is that an additional source of numerical error is introduced. This error is proportional to the numerical time step of the discrete approximation as a result of time-lagging the transport and migration sub-models (Barry *et al.,* 2002). Minimising the numerical time step will reduce this error.

2.5 References

Abriola, L.M., Modeling multiphase migration of organic chemicals in ground water systems – A review and assessment, *Environmental Health Perspective, 83,* 117-143, 1989.

Abriola L.M., and G.F. Pinder, A multiphase approach to the modelling of porous media contamination by organic compounds: 1. Equation development, *Water Resources Research, 21*(1), 11-18, 1985.

Amaefule, J.O., and L.L. Handy, The effect of interfacial tensions on relative oil-water permeabilities of consolidated porous media, SPE/DOE Paper 9783, SPE/DOE 2nd Joint Symposium on Enhanced Oil Recovery of the Society of Petroleum Engineers, Tulsa, 1981.

Amaefule, J.O., and L.L. Handy, The effect of interfacial tensions on relative oil/water permeabilities of consolidated porous media, *Society of Petroleum Engineering Journal, June,* 1982.

Anderson, M.P., Using models to simulate the movement of contaminants through ground water flow systems, *CRC Critical Reviews in Environmental Control, 9,* 97-156, 1979.

Anderson, W.G., Wettability literature survey Part 1: Rock/oil/brine interactions and the effects of core handling on wettability, *Journal of Petroleum Technology, 38,* 1125-1144, 1986.

Anderson, W.G., Wettability literature survey Part 5: The effects of wettability on relative permeability, *Journal of Petroleum Technology, 39,* 1453-1468, 1987.

Bajracharya, K., and D.A. Barry, Nonequilibrium solute transport parameters and their physical significance: Numerical and experimental results, *Journal of Contaminant Hydrology, 24*, 185-204, 1997.

Baker, P.E., Discussion of "Effect of viscosity ratio on relative permeability", *Journal of Petroleum Technology, 12,* 65-66.

Bardon, C. and D. Longeron, Influence of very low interfacial tensions on relative permeability, SPE Paper 7609, SPE 53rd Annual Technical Conference and Exhibition, Houston, 1978.

Barrow, N.J., Suitability of sorption-desorption models to simulate partitioning and movement of irons in soils, in *Inorganic Contaminants in the Vadose Zone,* B. Bar-Yosef, and N.J. Barrow (Eds), pp. 18-31, Springer-Verlag, New York, 1989.

Barry, D.A., Modelling contaminant transport in subsurface: Theory and computer programs, in *Modeling Chemical Transport in Soil: Natural and Applied Contaminants,* H. Ghadri, and C.W. Rose (Eds), pp. 105-144, Lewis Publishers, Boca Raton, FL., 1992.

Barry, D.A., H. Prommer, C.T. Miller, P. Engesgaard, A. Brun, and C. Zheng, Modeling the fate of oxidizable organic contaminants in groundwater, *Advances in Water Resources, 25*, 945-983, 2002.

Bear, J., *Dynamics of Fluids in Porous Media,* 764 pp., Dover, Mineola, N.Y., 1972.

Bradford, S.A., L.M. Abriola, and F.J., Leij, Wettability effects on two and three-fluid relative permeabilities, *Journal of Contaminant Hydrology, 28,* 171-191, 1997.

Bradford, S.A., and F.J. Leij, Estimating interfacial areas for multi-fluid soil systems, *Journal of Contaminant Hydrology, 27,*(1-2), 83-105, 1997.

Bradford, S.A., L.M. Abriola, and K.M. Rathfelder, Flow and entrapment of dense nonaqueous phase liquids in physically and chemically heterogeneous aquifer formations, *Advances in Water Resources, 22*, 117-132, 1998.

Braun, E.M., and R.F. Holland, Relative permeability hysteresis: Laboratory measurement and conceptual model, SPE 69th Annual Technical Conference and Exhibition, New Orleans, September 25-28, 1994.

Brewster, M.L., A.P. Annan, J.P. Greenhouse, B.H. Kueper, G.R. Oldhoeft, J.D. Redman, and K.A. Sander, Observed migration of a controlled DNAPL release by geophysical methods, *Ground Water, 33*(6), 977-987, 1995.

Brooks, R.H., and A.T. Corey, *Hydraulic Properties of Porous Media*, Hydrology Paper 3, Civil Engineering Department, Colorado State University, Fort Collins, 1964.

Brooks, R.H., and A.T. Corey, Properties of porous media affecting fluid flow, *Journal of Irrigation and Drainage Engineering, ASCE, 92*, 61-88, 1966.

Brusseau, M.L., Rate-limited mass transfer and transport of organic solutes in porous media that contains immobile immiscible organic liquids, *Water Resources Research, 28*(1), 22-45, 1992.

Brusseau, M.L., The effect of nonlinear sorption on transformation of contaminants during transport in porous media, *Journal of Contaminant Hydrology, 17*, 277-291, 1995.

Brusseau, M.L., and P.S.C. Rao, Modelling solute transport in structured soils: A review, *Geoderma, 46*, 169-192, 1990.

Brusseau, M.L., R.E. Jessup, and P.S.C. Rao, Modeling solute transport influenced by multi-process nonequilibrium and transformation reactions, *Water Resources Research, 28*(1), 175-182, 1992.

Brusseau, M.L., Z. Zhang, N.T. Nelson, R.B. Cain, G.R. Tick, and M. Oostrom, Dissolution of nonuniformly distributed immiscible liquid: intermediate-

scale experiments and mathematical modelling, *Environmental Science and Technology, 36,* 1033-1041, 2002.

Burdine, N.T., Relative permeability calculations from pore size distribution data, *Petroleum Transactions, AIME, 198*, 71-78, 1953.

Burris, D.R., T.J. Campbell, and V.S. Manoranjan, Sorption of trichloroethylene and tetrachloroethylene in a batch reactive metallic iron-water system, *Environmental Science and Technology, 29,* 2850-2855, 1995.

Cary, J.W., Estimating the surface area of fluid phase interfaces in porous media, *Journal of Contaminant Hydrology, 15*(4), 243-248, 1994.

Chapelle, F.H., S.K. Haack, P. Adriaens, M.A. Henry, and P.M. Bradley, Comparison of E_h and H_2 measurements for delineating redox processes in a contaminated aquifer, *Environmental Science and Technology, 30,* 3565-3569, 1996.

Chatzis, I., and F.A.L. Dullien, Mercury porosimetry curves of sandstones; mechanisms of mercury penetration and withdrawal, *Powder Technology, 29*, 117-125, 1981.

Chatzis, I., and F.A.L. Dullien, Dynamic immiscible displacement mechanisms in pore doublets: Theory versus experiment, *Journal of Colloid Interface Science, 91*(1), 199-222, 1983.

Chatzis, I., N.R. Morrow, and H.T. Lim, Magnitude and detailed structure of residual oil saturation, *Society of Petroleum Engineers AIME,* SPE Paper 10681, 1983.

Colonna, J., F. Brissaud, and J.L. Millet, Evolution of capillary and relative permeability hysteresis, *Society of Petroleum Engineers Journal, 12,* 28-38, 1972.

Corapcioglu, M.Y., and A.L. Baehr, A compositional multiphase model for groundwater contamination by petroleum products, 1. Theoretical considerations, *Water Resources Research, 23*(1), 191-200, 1987.

Corey, A.T., *Mechanics of Immiscible Fluids in Porous Media,* 252 pp., Water Resource Publications, Colorado, 1994.

Corey, J.D., D.R. Nielsen, and J.W. Biggar, Miscible displacement in saturated and unsaturated sandstone, *Soil Science of America Journal, 27,* 258-262, 1963.

Craig, F. F. Jr., The reservoir engineering aspects of waterflooding, *Society of Petroleum Engineers Monograph Series*, Richardson, TX, 3: 12-25, 1971.

Dagan, G., Stochastic modelling of groundwater flow by unconditional and conditional probabilities, 2, The solute transport, *Water Resources Research, 18*(4), 835-848, 1982.

Dagan, G., Solute transport in heterogeneous porous formations, *Journal of Fluid Mechanics, 145*, 151-177, 1984.

Dagan, G., Statistical theory of groundwater flow and transport: Pore to laboratory, laboratory to formation, and formation to regional scale, *Water Resources Research, 22*(9), 120S-134S, 1986.

Dalla, E., M. Hilpert, and C.T. Miller, Computation of the interfacial area for two-fluid porous medium systems, *Journal of Contaminant Hydrology, 56,* 25-48, 2002.

Dekker, T.J., and L.M. Abriola, The influence of field-scale heterogeneity on the infiltration and entrapment of dense, nonaqueous phase liquids in saturated formations, *Journal of Contaminant Hydrology, 42,* 197-218, 2000.

Demond A.H., and P.V. Roberts, Estimation of two phase relative permeability relationships for organic liquid contaminants, *Water Resources Research, 29*(4), 1081-1090, 1993.

Demond, A.H., and P.V. Roberts, An examination of relative permeability relations for two phase flow in porous media, *Water Resources Bulletin, 23*(4), 61-628, 1987.

Demond, A.H., and P.V. Roberts, Effect of interfacial forces on two-phase P_C-*S* relationships, *Water Resources Research, 27*(3), 423-437, 1991.

Dixit, A.B., S.R. McDougall, and K.S. Sorbie, A pore-level investigation of relative permeability hysteresis in water-wet systems, *Society of Petroleum Engineers,* SPE Paper 37233, 1997.

Domenico, P.A. and F.W. Schwartz, *Physical and Chemical Hydrogeology,* 824 pp., John Wiley and Sons, New York, N.Y., 1990.

Downie, J., and F.E. Crane, Effect of viscosity on relative permeability, *Society of Petroleum Engineers Journal, 1,* 59-60.

Dubey, S.T., and P.H. Doe, Base number and wetting properties of crude oils, *Society of Petroleum Engineering, Reservoir Engineering, 9,* 195-200, 1993.

Dullien, F.A.L., *Porous Media: Fluid Transport and Pore Structure*, 396 pp., Academic Press, New York, N.Y., 1979.

Eldor, M., and G. Dagan, Solutions of hydrodynamic dispersion in porous media, *Water Resources Research, 8*, 1316-1331, 1972.

Essaid, H.I., W.N., Herkelrath, and K.M. Hess, Simulation of fluid distributions observed at a crude oil spill site including hysteresis, oil entrapment, and spatial variability of hydraulic properties, *Water Resources Research, 29*(6), 1753-1770, 1993.

Estrella, M.R., M.L. Brusseau, R.S. Maier, I.L. Pepper, P.J. Wierenga, and R.M. Miller, Biodegradation, sorption, and transport of *2,4*-dichlorophenoxyacetic acid (*2,4*-D) in a saturated and unsaturated soil, *Applied Environmental Microbiology, 59*(12), 4266-4273, 1993.

Falta, R.W., I. Javandel, K. Pruess, and P.A. Witherspoon, Density-driven flow of gas in the unsaturated zone due to the evaporation of volatile organic compounds, *Water Resources Research, 25*(10), 2159-2169, 1989.

Fenwick, D.H., and M.J. Blunt, Three-dimensional modelling of three phase imbibition and drainage, *Advances in Water Resources, 21*(2), 121-143, 1998.

Forsyth, P.A., and B.Y. Shao, Numerical simulation of gas venting for NAPL site remediation, *Advances in Water Resources, 14*(6), 354-367, 1991.

Frind, E.O., J.W. Molsen, and M. Schirmer, Dissolution and mass transfer of multiple organics under field conditions: The Borden emplaced source, *Water Resources Research, 35*(3), 683-694, 1999.

Fulcher, R.A., Jr., T. Ertekin, and C.D. Stahl, The effect of the capillary number and its constituents on two-phase relative permeability curves, SPE Paper 12170, SPE 58th Annual Technical Conference and Exhibition, San Francisco, 1983.

Fulcher, R.A., Jr., T. Ertekin, and C.D. Stahl, Effect of capillary number and its constituents on two-phase relative permeability curves, *Journal of Petroleum Technology, February,* 249-260, 1985.

Gaudin, A.M, and T.G. Decker, Contact angles and adsorption in the system quartz-water-dodecane modified by dodecyl ammonium chloride, *Journal of Colloid Interface Science, 24,* 151-158, 1967.

Geffen, T.M., W.W. Owens, D.R. Parrish and R.A. Morse, Experimental investigations of factors affecting laboratory relative permeability measurements, *Transactions AIME, 192,* 99-110, 1951.

Gelhar, L.W., Stochastic subsurface hydrology from theory to applications, *Water Resources Research, 22*(9), 135S-145S, 1986.

Gelhar, L.W., A.L. Gujahr, and R.L. Naff, Stochastic analysis of macro-dispersion in a stratified aquifer, *Water Resources Research, 15*(6), 1387-1397, 1979.

Gelhar, L.W., and C.L. Axeness, Three-dimensional stochastic analysis of macrodispersion in aquifer, *Water Resources Research, 19*(1), 161-170, 1983.

Geller, J.T., and J.R. Hunt, Mass Transfer from nonaqueous phase organic liquids in water-saturated porous media, *Water Resources Research, 29*(4), 833-845, 1993.

Gerhard, J.I., DNAPL infiltration, redistribution, and immobilization in porous media, Ph.D. thesis, Queen's Univ., Kingston, Ontario, Canada, 2002.

Gerhard, J.I., B.H. Kueper, and G.R. Hecox, The influence of waterflood design on the recovery of mobile DNAPLs, *Ground Water, 36*(2), 283-292, 1998.

Gerhard, J.I., B.H. Kueper, G.R. Hecox, and E.J. Schwarz, Site-specific design for dual phase recovery and stabilization of pooled DNAPL, *Ground Water Monitoring and Remediation, Spring,* 71-88, 2001.

Gerhard, J.I., and B.H. Kueper, Capillary pressure characteristics necessary for simulation DNAPL infiltration, redistribution, and immobilization in saturated porous media, *Water Resources Research, 39*(8), SBH71-SBH717, 2003a.

Gerhard, J.I., and B.H. Kueper, Relative permeability characteristics necessary for simulating DNAPL infiltration, redistribution, and immobilization in saturated porous media, *Water Resources Research, 39*(8), SBH81-SBH816, 2003b.

Gerhard, J.I., and B.H. Kueper, Influence of constitutive model parameters on the predicted migration of DNAPL in heterogeneous porous media, *Water Resources Research, 39*(8), SBH41-SBH413, 2003c.

Grant, G.P., and J.I. Gerhard, The sensitivity of predicted DNAPL source zone longevity to mass transfer correlation model, in: Geoenvironmental Engineering: Integrated management of groundwater and contaminated land, Proceedings of the 4th British Geotechnical Association, Stratford-upon-Avon, UK, June 28-30, 2004.

Güven, O., F.J. Molz, and J.G. Melville, An analysis of dispersion in a stratified aquifer, *Water Resources Research, 20*(10), 1337-1354, 1984.

Gvirtzman, H., M. Magaritz, E. Klein, and A. Nader, A scanning electron microscopy study of water in soil, *Transport in Porous Media, 2*, 83-93, 1987.

Gvirtzman, H., and P.V. Roberts, Pore scale spatial analysis of two immiscible fluids in porous media, *Water Resources Research, 27*(6), 1165-1176, 1991.

Haines, W.B., Studies in the physical properties of soil: V. The hysteresis effect in capillary properties and the modes of moisture distribution associated therewith, *Journal of Agriculture Science, 20*, 97-116, 1930.

Hassanizadeh, M. and W.G. Gray, General conservation equations for multiphase systems 1. Averaging procedure, *Advances in Water Resources, 2,* 131-144, 1979a.

Hassanizadeh, M. and W.G. Gray, General conservation equations for multiphase systems 2. Mass, momenta, energy, and entropy equations, *Advances in Water Resources, 2,* 191-203, 1979b.

Hassanizadeh, S.M., and W.G. Gray, Thermodynamic basis of P_c in porous media, *Water Resources Research, 29*(10), 3389-3405, 1993a.

Heimenz, P.C., and R. Rajagopalan, *Principles of Colloid and Surface Chemistry,* xix 650 pp., Marcel Dekker, New York, 1997.

Held, R.J., and T.H. Illangasekare, Fingering of dense, nonaqueous phase liquids in porous media: 1. Experimental investigation, *Water Resources Research, 31*(5), 1213-1222, 1995.

Hofstee, C., Physics of DNAPL migration in porous media, Ph.D. thesis, Auburn Univ., Auburn, Alabama, 1997.

Hofstee, C., J.H. Dane, and W.E. Hill, Three fluid retention in porous media involving water, PCE and air, *Journal of Contaminant Hydrology, 25*, 235-247, 1997.

Hunt, J.R., N. Sitar, and K.S. Udell, Nonaqueous phase liquid transport and cleanup: 1. Analysis of mechanisms, *Water Resources Research, 24*(8), 1247-1258, 1988.

Hunter, K.S., Y. Wang, and P. van Cappellen, Kinetic modelling of microbially-driven redox chemistry of subsurface environments: Coupling transport, microbial metabolism and geochemistry, *Journal of Hydrology, 209,* 53-80, 1998.

Huyakorn, P.S. and G.F. Pinder, *Computational Methods in Subsurface Flow,* Academic Press, New York, N.Y., 1983.

Huyakorn, P.S., S. Panday, and Y.S. Wu, A three-dimensional multiphase flow model for assessing NAPL contamination in porous and fractured media: I. Formulation, *Journal of Contaminant Hydrology, 16*, 109-130, 1994.

Illangasekare, T.H., J.L. Ramsey Jr., K.H. Jensen, and M.B. Butts, Experimental study of the movement and distribution of dense organic contaminants in heterogeneous aquifer, *Journal of Contaminant Hydrology, 20*, 1-25, 1995.

Imhoff, P.T., P.R. Jaffe, and G.F. Pinder, An experimental study of complete dissolution of a nonaqueous phase liquid in saturated porous media, *Water Resources Research, 30*(2), 307-320, 1993.

Imhoff, P.T., A.S. Mann, M. Mercer, and M. Fitzpatrick, Scaling DNAPL migration from the laboratory to the field, *Journal of Contaminant Hydrology, 64,* 73-92, 2003.

Jennings, H.Y., A study of caustic solution-crude oil interfacial tensions, *Society of Petroleum Engineering Journal, 15*, 197-202, 1975.

Jerauld G.R., and S.J. Salter, The effect of pore-structure on hysteresis in relative permeability and capillary pressure: Pore level modelling, *Transport in Porous Media, 5,* 103-151, 1990.

Kim, H., P.S.C. Rao, and M.D. Annable, Gaseous tracer technique for estimating air-water interfacial areas and interface mobility, *Soil Science Society of America Journal, 63*, 1554-1560, 1999.

Krupp, H.K., S.W. Biggar, and D.R. Nielsen, Relative flow rates of salt in water and soil, *Soil Science of America Journal, 36,* 412-417, 1972.

Kueper, B.H., and E.O. Frind, An overview of immiscible fingering in porous media, *Journal of Contaminant Hydrology, 2*, 95-110, 1988.

Kueper, B.H., W. Abbot, and G. Farquhar, Experimental observations of multiphase flow in heterogeneous porous media, *Journal of Contaminant Hydrology, 5*, 83-95, 1989.

Kueper, B.H., and E.O. Frind, Two phase flow in heterogeneous porous media: 1. Model development, *Water Resources Research, 27*(6), 1049-1057, 1991a.

Kueper, B.H., and E.O. Frind, Two phase flow in heterogeneous porous media: 2. Model application, *Water Resources Research, 27*(6), 1059-1070, 1991b.

Kueper, B.H., and E.O. Frind, Numerical modelling of multiphase / multicomponent flow and transport in porous media: An overview, in: Proceedings of the International Conference on Subsurface Contamination by Immiscible Fluids, Calgary, Canada, April 18-20, 1992.

Kueper, B.H., J.D. Redman, R.C. Starr, S. Reitsma, and M. Mah, A field experiment to study the behaviour of tetrachloroethylene below the watertable: Spatial distribution of residual and pooled DNAPL, *Journal of Ground Water, 31*(5), 756-766, 1993.

Kueper, B.H., and J.I. Gerhard, Variability of point source infiltration rates for two-phase flow in heterogeneous porous media, *Water Resources Research, 31*(12), 2971-2980, 1995.

Land, C.S., Calculation of imbibition relative permeability for two- and three-phase flow from rock properties, *Transactions, American Institute of Mining, Metallurgical, and Petroleum Engineers, 243*, 149-156, 1968.

Land, C.S., Comparison of calculated with experimental imbibition relative permeability, *Society of Petroleum Engineers Journal,* 419-425, 1971.

Larson, R.G., L.E. Scriven, and H.T. Davis, Percolation theory of two phase flow in porous media, *Chemical Engineering Science, 36,* 57-73, 1981a.

Larson, R.G., L.E. Scriven, and H.T. Davis, Displacement of residual nonwetting fluid from porous media, *Chemical Engineering Science, 36,* 75-85, 1981b.

Lassey, K.R., Unidimensional solute transport incorporating equilibrium and rate-limited isotherms with first-order loss, 1. Model conceptualizations and analytic solutions, *Water Resources Research, 24*(3), 343-350, 1988.

Lefebvre du Prey, E.J., Factors affecting liquid-liquid relative permeabilities of a consolidated porous medium, *Society of Petroleum Engineers Journal, 13*(1), 39-47, 1973.

Lemke, L.D., L.M. Abriola, and P. Goovaerts, Dense nonaqueous phase liquid (DNAPL) source zone characterization: Influence of hydraulic property correlation on predictions of DNAPL infiltration and entrapment, *Water Resources Research, 40*(12), 1-18, 2004.

Lenhard, R.J., Measurement and modelling of three-phase saturation-pressure hysteresis, *Journal of Contaminant Hydrology, 9,* 243-269, 1992.

Lenhard, R.J., J.C. Parker, and J.J. Kaluarachchi, Comparing simulated and experimental hysteretic two phase transient fluid flow phenomena, *Water Resources Research, 27*(8), 2113-2124, 1991.

Lenhard, R.J. and M. Oostrom, A parametric model for predicting relative permeability-saturation-capillary pressure relationships of oil-water systems in porous media with mixed wettability, *Transport in Porous Media, 31,* 109-131, 1998.

Leverett, M.C., Flow of oil-water mixtures through unconsolidated sands, *Transactions of the American Institute of Mining Engineers, 132,* 149-171, 1939.

Leverett, M.C., Capillary behaviour in porous solids, *Transactions AIMME, 142*, 152-170, 1941.

Li, L., D.A. Barry, P.J. Culligan-Hensley, and K. Bajracharya, Mass transfer in soils with local stratification of hydraulic conductivity, *Water Resources Research, 30*(11), 2891-2900, 1994.

Lindstom, F.T., Pulsed dispersion of trace chemical concentrations in a saturated sorbing porous medium, *Water Resources Research, 12,* 229-238, 1976.

Lombard, J.M., and R. Lenormand, Fractional wettability and petrophysical parameters of porous media, in *Advances in Core Evaluation III: Reservoir Management*, Worthington, P.F., and C. Chardaire-Riviere (Eds), 411 pp., Gordon and Breach Science, Amsterdam, 1993.

Lord, D.L., A.H. Demond, and K.F. Hayes, Effects of organic base chemistry on interfacial tension, wettability, and capillary pressure in multiphase subsurface waste systems, *Transport in Porous Media, 38*(1-2), 79-92, 1999.

Lowry, M.I., and C.T. Miller, Pore scale modelling of nonwetting phase residual in porous media, *Water Resources Research, 31*(3), 455-473, 1995.

Luckner, L., M.Th. van Genuchten, and D.R. Nielsen, A consistent set of parametric models for the two phase flow of immiscible fluids in the subsurface, *Water Resources Research, 25*(10), 2187-2193, 1989.

Mackay, D.M., P.V. Roberts, and J.A. Cherry, Transport of organic contaminants in groundwater, *Environmental Science and Technology, 19*(5), 384-392, 1985.

Majors, P.D., P. Li, and E.J. Peters, NMR imaging of immiscible displacements in porous media, *Society of Petroleum Engineers Formation Evaluation, 12*(3), 164-139, 1997.

Marle, C.M., On macroscopic equations governing multiphase flow with diffusion and chemical reactions in porous media, *International Journal of Engineering Science, 20*(5), 643-662, 1982.

Matheron, G., and G. de Marsily, Is transport in porous media always diffusive? A counter-example, *Water Resources Research, 16*(5), 901-917, 1980.

Mayer, A.S., and C.T. Miller, The influence of mass transfer characteristics and porous media heterogeneity on nonaqueous phase dissolution, *Water Resources Research, 32*(6), 1551-1568, 1996.

Mayer, A.S., and C.T. Miller, The influence of porous medium characteristics and measurement scale on pore scale distributions of residual nonaqueous phase liquids, *Journal of Contaminant Hydrology, 11*, 189-213, 1992.

Melrose, J.C., Interfacial phenomena as related to oil recovery mechanisms, *The Canadian Journal of Chemical Engineering, 48*, 638-644, 1970.

Melrose, J.C., and C.F. Brandner, Role of capillary forces in determining microscopic displacement efficiency for oil recovery by waterflooding, *Journal of Canadian Petroleum Technology, 13*(4), 54-62, 1974.

Mendoza, C.A., and E.O. Frind, Advective-dispersive transport of dense organic vapours in the unsaturated zone, 1. Model development, *Water Resources Research, 26*(3), 378-387, 1990a.

Mendoza, C.A., and E.O. Frind, Advective-dispersive transport of dense organic vapours in the unsaturated zone, 2. Sensitivity analysis, *Water Resources Research, 26*(3), 388-398, 1990b.

Mercer, J.M., and R.M. Cohen, A review of immiscible fluids in the subsurface: Properties, models, characterisation, and remediation, *Journal of Contaminant Hydrology, 6,*107-163, 1990.

Miller, C.T., and W.J. Weber Jr., Modeling organic contaminant partitioning in ground water systems, *Ground Water 22*(5), 584-592, 1984.

Miller, C.T., M.M Poirier-McNeill, and A.S. Mayer, Dissolution of trapped nonaqueous phase liquids: Mass transfer characteristics, *Water Resources Research, 26*(11), 2783-2796, 1990.

Miller, C.T., G. Christakos, P.T. Imhoff, J.F. McBride, and J.A. Pedit, Multiphase flow and transport modelling in heterogeneous porous media: Challenges and approaches, *Advances in Water Resources, 21*(2), 77-120, 1998.

Mohanty, K.K., H.T. Davis, and L.E. Scriven, Physics of oil entrapment in water – wet rock, *Society of Petroleum Engineers, Reservoir Engineering, February,* SPE Paper 9406, 1987.

Montemagno, C.D., and W.G. Gray, Photoluminescent volumetric imaging – a technique for the exploration of multiphase flow and transport in porous media, *Geophysical Research Letters, 22*(4), 425-428, 1995.

Morgan, J.T., and D.T. Gordon, Influence of pore geometry on water-oil relative permeability, *Journal of Petroleum Technology, 22*, 1199-1208, 1970.

Morrow, N.R., Small-scale packing heterogeneities in porous sedimentary rocks, *American Association of Petroleum Geologists Bulletin, 55*(3) 514-522, 1971.

Morrow, N.R., Effects of surface roughness on contact angle with special reference to petroleum recovery, *Journal of Canadian Petroleum Technology, 14,* 42-53, 1975.

Morrow, N.R., P_C correlations for uniformly wetted porous media, *Journal of Canadian Petroleum Technology, October – December,* 1976.

Morrow, N.R., I. Chatzis, and J.J. Taber, Entrapment and mobilization of residual oil in bead packs, *Society of Petroleum Engineers,* SPE Paper 14423, 1988.

Mualem, Y., A new model for predicting the hydraulic conductivity of unsaturated porous media, *Water Resources Research, 12*(3), 513-522, 1976.

Murali, V., and L.A.G. Aylmore, No-flow equilibrium and adsorption dynamics during ionic transport in soils, *Nature, 283,* 467-469, 1980.

Naar, J., R.J. Wygal, and J.H. Henderson, Imbibition relative permeability in unconsolidated porous media, *Society of Petroleum Engineers Journal, March,* 1962.

Nambi, I.M., and S.E. Powers, Mass transfer correlations for nonaqueous phase liquid dissolution from regions with high initial saturations, *Water Resources Research, 39*(2), SBH41-SBH411, 2003.

Neuman, S.P., Eularian-Lagrangian theory of transport in space-time nonstationary velocity fields: Exact nonlocal formalism by conditional moments and weak approximation, *Water Resources Research, 29*(3), 633-645, 1993.

O'Carroll, D.M., S.A. Bradford, and L.M. Abriola, Infiltration of PCE in a system containing spatial wettability variations, *Journal of Contaminant Hydrology, 73,* 39-63, 2004.

Odeh, A.S., Effect of viscosity ratio on relative permeability, *Transactions of the American Institute of Mining Engineers, 216,* 346-353, 1959.

Oostrom, M., and R.J. Lenhard, Comparison of relative permeability-saturation-pressure parametric models for infiltration and redistribution of a light nonaqueous phase liquid in sandy porous media, *Advances in Water Resources, 21*(2), 145-157, 1998.

Osoba, J.S., J.G. Richardson, J.K. Kerver, J.A. Hafford, and P.M. Blair, Laboratory measurements of relative permeability, *Petroleum Transactions, AIME, 192,* 47-54, 1951.

Panday, S., Y.S. Wu, P.S. Huyakorn, S.C. Wade, and Z.A. Saleem, A composite numerical model for assessing subsurface transport of oily wastes and chemical constituents, *Journal of Contaminant Hydrology, 25*(1-2), 39-62, 1997.

Parker, J.C., R.J. Lenhard, and T. Kuppusamy, A parametric model for constitutive properties governing multiphase flow in porous media, *Water Resources Research, 23*(4), 618-624, 1987.

Parker, J.C., A.K. Katyal, J.J. Kaluarachchi, R.J. Lenhard, T.J. Johnson, K. Jayaraman, K. Unlu, and J.L. Zhu, Modeling multiphase organic chemical transport in soils and ground water, *Rep. EPA/600/2-91/042,* U.S. Environmental Protection Agency, Washington, D.C., 1991.

Parker, J.C., and E. Park, Modeling field-scale dense nonaqueous phase liquid dissolution kinetics in heterogeneous aquifers, *Water Resources Research, 40*(5), W051091-W0510912, 2004.

Pennell, K.D., G.A. Pope, and L.M. Abriola, Influence of viscous and buoyancy forces on the mobilization of residual tetrachloroethylene during surfactant flushing, *Environmental Science and Technology, 30*(4), 1328-1335, 1996.

Phelan, T.J., L.D. Lemke, S.A. Bradford, D.M. O'Carroll, and L.M. Abriola, Influence of textural and wettability variations on predictions of DNAPL persistence and plume development in saturated porous media, *Advances in Water Resources, 27,* 411-427, 2004.

Pickell, J.J., B.F. Swanson, and W.B. Hickman, Application of air-mercury and oil-air capillary pressure data in the study of pore structure and fluid distribution, *Society of Petroleum Engineers Journal, March*, 55-61, 1966.

Pinder, G.F., and L.M. Abriola, On the simulation of nonaqueous phase organic compounds in the subsurface, *Water Resources Research, 22*(9), 109S-119S, 1986.

Poulsen, M.M., and B.H. Kueper, A field experiment to study the behaviour of tetrachloroethylene in unsaturated porous media, *Environmental Science and Technology, 26*(5) 889-895, 1992.

Powers, S.E., L.M. Abriola, and W.J. Weber Jr., An experimental investigation of NAPL dissolution in saturated subsurface systems: Steady state mass transfer rates, *Water Resources Research, 28*(10), 2691-2706, 1992.

Powers, S.E., L.M. Abriola, W.J. Weber Jr., An experimental investigation of nonaqueous phase liquid dissolution in saturated subsurface systems: Transient mass transfer rates, *Water Resources Research, 30*(2), 321-332, 1994.

Powers S.E., and M.E. Tamblin, Wettability of porous media after exposure to synthetic gasolines, *Journal of Contaminant Hydrology, 19*, 105-125, 1995.

Powers, S.E., W.H. Anckner, and T.F. Seacord, Wettability of NAPL contaminated sands, *Journal of Environmental Engineering, 122*(10), 889-1119, 1996.

Powers, S.E., I.M. Nambi, and G.W. Curry, Non-aqueous phase liquid dissolution in heterogeneous systems: mechanisms and a local equilibrium modelling approach, *Water Resources Research, 34,* 3292-3302, 1998.

Raimondi, P., and M.A. Torcaso, Distribution of the oil phase obtained upon imbibition of water, *Society of Petroleum Engineers Journal, 49,* 1964.

Rao, P.S.C., R.E. Jessup, D.E. Rolston, J.M. Davidson, and D.P. Kilcrease, Experimental and mathematical description of nonadsorbed solute transfer by diffusion in spherical aggregates, *Soil Science Society of America Journal, 44,* 684-688, 1980a.

Rao, P.S.C., D.E. Rolston, R.E. Jessup, and J.M. Davidson, Solute transport in aggregated porous media: Theoretical and experimental evaluation, *Soil Science Society of America Journal, 44,* 1139-1149, 1980b.

Rashidi, M., A Tompson, T. Kulp, and L. Peurrung, 3-D microscopic measurement and analysis of chemical flow and transport in porous media, *Journal of Fluids Engineering – Transactions of the ASME, 118*(3), 470-480, 1996.

Rathfelder, K., and L.M. Abriola, The influence of capillarity in numerical modelling of organic liquid redistribution in two-phase systems, *Advances in Water Resources, 21*(2), 159-170, 1998.

Rathfelder, K.M., L.M. Abriola, M.A. Singletary, K.D. Pennell, Influence of surfactant-facilitated interfacial tension reduction on chlorinated solvent migration in porous media: observations and numerical simulation, *Journal of Contaminant Hydrology, 64*, 227-252, 2003.

Reeves, H.W., and L.M. Abriola, A decoupled approach to the simulation of flow and transport of non-aqueous organic phase contaminants through porous media, in: Proceedings of the 7th Conference on Computational Methods in Water Resources, Vol. 1., Cambridge, MA, USA, 147-152, 1988.

Reeves, P.C., and M.A. Celia, A functional relationship between capillary pressure, saturation, and interfacial area as revealed by a pore-scale network model, *Water Resources Research, 32*(8), 2345-2358, 1996.

Reynolds, D.A., and B.H. Kueper, Multiphase flow and transport in fractured clay/sand sequences, *Journal of Contaminant Hydrology, 51*(1-2), 41-62, 2001.

Ronen, D., M. Magaritz, N. Palder, and Y. Bachmat, The behaviour of groundwater in the vicinity of the watertable evidenced by specific discharge profiles, *Water Resources Research, 22*(8), 1217-1224, 1986.

Roof, J.G., Snapoff of oil droplets in waterwet pores, *Society of Petroleum Engineers Journal, 10*(1), 85-90, 1970.

Rose, W., Microscopic aspects of capillary imbibition, *Society of Petroleum Engineers AIME,* SPE Paper 1549G, 1960.

Saba, T., and T.H. Illangasekare, Effect of groundwater flow dimensionality on mass transfer from entrapped nonaqueous phase liquid contaminants, *Water Resources Research, 36*(4), 971-979, 2000.

Sale, T., Interphase mass transfer from single component DNAPLs, Ph.D. thesis, Colorado State Univ., Fort Collins, Colorado, USA, 1998.

Sale, T.C., and D.B. McWhorter, Steady state mass transfer from single-component dense nonaqueous phase liquids in uniform flow fields, *Water Resources Research, 37*(2), 393-404, 2001.

Saripalli, K.P., P.S.C. Rao, and M.D. Annable, Determination of specific NAPL-water interfacial areas of residual NAPLs in porous media using the interfacial tracers technique, *Journal of Contaminant Hydrology, 31*(3-4), 375-391, 1998.

Scheidegger, A.E., *The Physics of Flow Through Porous Media,* 353 pp., University of Toronto Press, Toronto, 1974.

Schiegg, H.O., Considerations on water, oil and air in porous media, *Water Science Technology, 17*, 467-476, 1984.

Schwartz, F., Macroscopic dispersion in porous media: The controlling factors, *Water Resources Research, 13*(4), 743-752, 1977.

Schwarzenbach, R., P.M. Gschwend, and D.M. Imboden, *Environmental Organic Chemistry,* John Wiley and Sons, New York, N.Y., 1983.

Schwille, F., *Dense Chlorinated Solvents in Porous and Fractured Media Model Experiments*, 146 pp. Translated by J.F. Pankow, Lewis Publishers, Chelsea, MI, 1988.

Seagren, E.A., B.E. Rittman, and A.J. Valocchi, A critical evaluation of the local-equilibrium assumption in modelling NAPL-pool dissolution, *Journal of Contaminant Hydrology, 39*(1-2), 109-135, 1999.

Seol, Y., H. Zhang, and F.W. Schwartz, A review of in situ chemical oxidation and heterogeneity, *Environmental and Engineering Geosciences, 9*(1), 37-49, 2003.

Silliman, S.E., and E.S. Simpson, Laboratory evidence of the scale effect of dispersion of solutes in porous media, *Water Resources Research, 23*(8), 1667-1673, 1987.

Simpson, M.J., SEAWAT-2000: Variable-density flow processes and integrated MT3DMS transport processes, *Ground Water, 42*(5), 642-645, 2004.

Sleep, B.E., and J.F. Sykes, Compositional simulation of groundwater contamination by organic compounds: 1. Model development and verification, *Water Resources Research, 29*, 1697-1708, 1993.

Slough, K.J., E.A. Sudicky, and P.A. Forsyth, Numerical simulation of multiphase flow and phase partitioning in discretely fractured geologic media, *Journal of Contaminant Hydrology, 40*(2), 107-136, 1999.

Smith, L., and F. Schwartz, Mass transport, 1, A stochastic analysis of macroscopic dispersion, *Water Resources Research, 16*(2), 303-313, 1980.

Soerens, T.S., D.A. Sabatini, and J.F. Harwell, Effects of flow-bypassing and nonuniform distribution on the mass transfer characteristics of NAPL dissolution, *Water Resources Research, 34,* 1657-1673, 1998).

Soga, K., J.W.E. Page, and T.H. Illangasekare, A review of NAPL source zone remediation efficiency and the mass flux approach, *Journal of Hazardous Materials, 110*, 13-27, 2004.

Stonestrom, D.A., and J. Rubin, Water content dependence of trapped air in two soils, *Water Resources Research, 25*(9), 1947-1958, 1989a.

Stonestrom, D.A., and J. Rubin, Air permeability and trapped-air content in two soil, *Water Resources Research, 25*(9), 1959-1969, 1989b.

Sudicky, E.A., An advection-diffusion theory of contaminant transport for stratified porous media, Ph.D. thesis, Univ. of Waterloo, Waterloo, Ontario, Canada, 1983.

Sudicky, E.A., A natural gradient experiment on solute transport in a sand aquifer: Spatial variability of hydraulic conductivity and its role in the dispersion process, *Water Resources Research, 22*(13), 2069-2082, 1986.

Talash, A.W., Experimental and calculated relative permeability data for systems containing low tension additives, SPE Symposium on Improve Oil Recovery, SPE Paper 5810, Tulsa, 1976.

Thompson, A.H., A.J. Katz, and R.A. Raschke, Estimation of absolute permeability from P_C measurements, SPE 62nd Annual Technical Conference and Exhibition, Dallas, September 27-30, 1987.

Ustohal, P., F. Stauffer, and T. Dracos, Measurement and modelling of hydraulic characteristics of unsaturated porous media with mixes wettability, *Journal of Contaminant Hydrology, 33,* 5-37, 1998.

van Geel, P.J., and J.F. Sykes, The importance of fluid entrapment, saturation hysteresis and residual saturations on the distribution of a lighter-than-water

nonaqueous phase liquid in a variably saturated sand medium, *Journal of Contaminant Hydrology, 24*, 249-270, 1997.

van Genuchten, M.Th., A closed-form equation for predicting the hydraulic conductivity of unsaturated soils, *Soil Science Society of America, 44*, 892-898, 1980.

van Genuchten, M. Th., and R.J. Wagenet, Two-site/two-region models for pesticide transport and degradation: Theoretical development and analytical solutions, *Soil Science Society of America Journal, 53,* 1303-1310, 1989.

Villaume, J.F., Investigations at sites contaminated with dense, nonaqueous phase liquids (NAPLs), *Ground Water Monitoring Review, 5*(2), 60-74, 1985.

Wardlaw, N.C., and R.P. Taylor, Mercury P_C curves and the interpretation of the pore structure and capillary behaviour in reservoir rocks, *Bulletin of Canadian Petroleum Geology, 24*(2), 225-262, 1976.

Wardlaw, N.C., and J.P. Cassan, Estimation of recovery efficiency by visual observation of pore systems in reservoir rock, *Bulletin of Canadian Petroleum Geologists, 26*(4), 572-585, 1978.

Wei, J.Z., and O.B. Lile, Influence of wettability and saturation sequence on relative permeability hysteresis in unconsolidated porous media, *Society of Petroleum Engineering,* SPE Paper 25282, 1992.

Whitaker, S., Diffusion and dispersion in porous media, *American Institute of Chemical Engineers Journal, 13,* 420-427, 1967.

Wilson, J.L., S.H. Conrad, W.R. Mason, W. Peplinski, and E. Hagan, Laboratory investigation of residual liquid organics from spills, leaks, and the disposal of hazardous wastes in groundwater, *EPA/600/6-90/004,* 267 pp., 1990.

Winter, C.L., C.M. Newman, and S.P. Neumann, A perturbation expansion for diffusion in a random velocity field, *SIAM, Journal of Applied Mathematics, 44*(2), 411-424, 1984.

Wyckoff, R.D., and H.G. Botset, The flow of gas-liquid mixtures through unconsolidated sands, *Physics, 7,* 325-345, 1936.

Yeh, G-T., and Tripathi, V.S., A model for simulating transport of reactive multispecies components: Model development and demonstration, *Water Resources Research, 27*(12), 3075-3094, 1991.

Zhu, J., and J.F. Sykes, Simple screening models of NAPL dissolution in the subsurface, *Journal of Contaminant Hydrology, 72,* 245-258, 2004.

Zinn B., and C.F. Harvey, When good statistical models of aquifer heterogeneity go bad: A comparison of flow, dispersion, and mass transfer in connected and multivariate Gaussian hydraulic conductivity fields, *Water Resources Research, 39*(3), SBH41-SBH418, 2003.

Zinn, B., L.C. Meigs, C.F. Harvey, R. Haggerty, W.J. Peplinski, and C. F. von Schwerin, Experimental visualization of solute transport and mass transfer processes in two-dimensional conductivity fields with connect regions of high conductivity, *Environmental Science and Technology, 38,* 3916-3926, 2004.

CHAPTER 3 – MULTIDIMENSIONAL VALIDATION OF A ROBUST NONWETTING PHASE RELATIVE PERMEABILITY CONSTITUTIVE RELATIONSHIP

3.1 Introduction

In the field of contaminant hydrogeology, little is known about the rate of migration and the time required for the immobilization of a dense, nonaqueous phase liquid (DNAPL) release to the subsurface. Numerous physical experiments (e.g. Schwille,1988; Kueper *et al*., 1989; Illangasekare *et al*., 1995; Oostrom *et al*., 1999; O'Carroll *et al*., 2004) and field studies (Kueper, *et al*., 1993; Brewster *et al*., 1995) have been conducted to examine the factors that govern the final distribution of a DNAPL body released to the subsurface, but few studies have collected data to examine the rate of migration (e.g. Illangasekare *et al*., 1995; Gerhard and Kueper, 2003b; O'Carroll *et al*., 2004). With the exception of Gerhard and Kueper (2003c), who conducted one-dimensional homogeneous porous media column experiments (Gerhard and Kueper, 2003b), numerical models employed for predicting DNAPL migration (e.g. Kueper and Frind, 1991b; Essaid *et al.*, 1993; Kueper and Gerhard, 1995; Gerhard *et al.,* 1998; White and Oostrom, 1998; Dekker and Abriola, 2000; Gerhard *et al.,* 2001; Lemke *et al.,* 2004) have not been validated for migration rates.

The rate of DNAPL migration through porous media is dependent, in part, on macroscopic relative permeability constitutive relationships. Relative permeability is defined as the ratio of effective permeability to absolute permeability (k_{abs}) for a given phase in a multiphase system. This parameter, a function of both saturation and saturation history, is particularly difficult to measure in the laboratory and, as such, very few studies have been conducted to specifically measure relative permeability functions in unconsolidated porous media (Naar *et al*., 1962; Lin *et al*., 1982;

Stonestrom and Rubin, 1989b; Demond and Roberts, 1993; Dury *et al*., 1999; Gerhard and Kueper, 2003b). This has prompted researchers to devise new methods of measuring relative permeability curves, with varying degrees of success (Dane *et al*., 1998, Kamon *et al*., 2003)

Relative permeability has been more thoroughly examined in the oil engineering literature (e.g. Osoba, *et al*., 1951; Land, 1971; Lefebvre du Prey, 1973; Amaefule and Handy, 1982; Fulcher *et al*., 1985; Braun and Holland, 1994). However, the characteristics of relative permeability curves for media with coordination numbers and pore aspect ratios typical of oil reservoir rock (Morgan and Gordon, 1970; Dixit *et al.,* 1997) limit the validity of extending this data to the field of contaminant hydrogeology at even a qualitative level.

Nonwetting phase (NWP) relative permeability has been shown to be a function of wetting phase (WP) saturation, S_W, and saturation history, with distinct non-zero endpoints of emergence saturation, S_W^M, and extinction saturation, S_W^X (see Gerhard and Kueper, 2003b, and Chapter 2 for a detailed description of the characteristics of NWP relative permeability curves). In unconsolidated porous media, NWP relative permeability (k_{rN}-S_W) functions generally exhibit a "reverse hysteresis pattern" where imbibition k_{rN} is greater than drainage k_{rN} for some or all of the relevant S_W range (see Figure 2-2a). The maximum value of NWP relative permeability, $k_{rN}^{\max}$, is coincident with the minimum possible S_W (i.e., residual wetting phase saturation, S_r) and the reversal point between the primary drainage curve and the secondary imbibition curve. For a strongly water wet system S_r is non-zero, as further reduction of S_W through film flow is not likely to occur for the fluids, porous media, and velocities typical of groundwater contamination scenarios. Although

$k_{rN}^{\max}$ values of 1.0 are commonly used in the petroleum literature, a non-zero S_r value dictates that $k_{rN}^{\max}$ must be less than unity.

The k_{rN}-S_W constitutive relationship of Gerhard and Kueper (2003a) on primary drainage is given by:

$$k_{rN} = k_{rN}^{\max}\left(1-\overline{S}_e^{*d}\right)^{2\tau_d}\left(1-\overline{S}_e^{*d^{(2+\lambda_d/\lambda_d)}}\right) \tag{3-1}$$

where τ_d is the drainage NWP relative tortuosity exponent, λ_d is the pore size distribution index associated with drainage processes, and $\overline{S}_e^{*d}$ is a scaled saturation variable for drainage:

$$\overline{S}_e^{*d} = \frac{S_W - S_r}{\left(S_W^M + \Delta\overline{S}_W^{*d}\right) - Sr} \qquad S_r \le S_W \le S_W^M \tag{3-2a}$$

$$\overline{S}_e^{*d} = 1 \qquad S_W^M \le S_W \le 1 \tag{3-2b}$$

in which $\Delta\overline{S}_W^{*d}$ is the drainage emergence fitting parameter that determines the amount that k_{rN} abruptly jumps from zero to a finite positive value when $S_W = S_W^M$.

On secondary imbibition, the k_{rN}-S_W constitutive relationship of Gerhard and Kueper (2003a) is given by:

$$k_{rN} = k'_{rN}\left(1-\hat{S}_e^{*i}\right)^{2\tau_i}\left(1-\hat{S}_e^{*i^{(2+\lambda_i/\lambda_i)}}\right) \tag{3-3}$$

where k'_{rN} is the k_{rN} associated with the reversal point between drainage and imbibition (i.e., $k_{rN}^{\max}$ when the reversal point is at $S_W = S_r$), τ_i is the imbibition NWP relative tortuosity exponent, λ_i is the pore size distribution index associated with imbibition processes, and $\hat{S}_e^{*i}$ is the imbibition k_{rN}-S_W initial – residual scaled effective saturation parameter, defined as:

$$\hat{S}_e^{*i} = \frac{S_W - S_r}{\left(S_W^X + \Delta S_W^{*i}\right) - Sr} \qquad S_r \leq S_W \leq S_W^X \tag{3-4a}$$

$$\hat{S}_e^{*i} = 1 \qquad S_W = S_W^X \tag{3-4b}$$

in which ΔS_W^{*i} is the imbibition extinction parameter. ΔS_W^{*i} is a fixed parameter that determines the amount that k_{rN} abruptly jumps from a finite positive value to zero when $S_W = S_W^X$

$k_{rN}^{\max}$ is a measure of the degree to which NWP flow is impeded (relative to saturated flow conditions) by the presence of residual WP (Gerhard and Kueper, 2003b). $k_{rN}^{\max}$ values of 1.0 are typical of numerical modelling studies employing a Burdine-based NWP relative permeability expression (e.g. White and Oostrom, 1998; Gerhard *et al.,* 1998; Gerhard *et al.,* 2001); however, values between 0.40 and 0.90 have been demonstrated to be more appropriate for unconsolidated porous media (Naar *et al.,* 1962; Stonestrom and Rubin, 1989b; Demond and Roberts, 1993; Gerhard and Kueper, 2003b – see Chapter 4 for a detailed list of $k_{rN}^{\max}$ values found in the contaminant hydrogeology literature). Residual WP presence causes increased tortuosity for the NWP flow paths, the extent of which must be determined experimentally. No experimental work has yet been carried out to systematically examine the factors that affect $k_{rN}^{\max}$ in the field of contaminant hydrogeology.

Demond and Roberts (1987) summarized a number of studies to examine the effects of intrinsic permeability, pore-size distribution, viscosity ratio, interfacial tension, and wettability on relative permeability curves. While the majority of the data examined in that review came from the petroleum literature, there was some evidence found in the work of Wardlaw and Cassan (1978) and Morgan and Gordon

(1970) to suggest that porous media properties may affect the shape and end-point locations of NWP relative permeability curves.

Numerical simulations have suggested that the migration rates of NWP releases are sensitive to k_{rN}-S_W function parameters, including $k_{rN}^{\max}$ (Gerhard and Kueper, 2003c). NWP relative permeability functions employed in numerical modelling studies of NWP migration are often described using geometry-based (Burdine, 1953; Mualem, 1976) or analogy-based (Lenhard and Parker, 1987; Luckner *et al*., 1989; Fischer *et al*., 1996; White and Oostrom, 1998; Gerhard *et al*., 1998; Gerhard *et al*., 2001) relationships. However, only the NWP relative permeability expression of Gerhard and Kueper (2003b, c), which accounts for all of the physics of two phase flow described above (including a distinct emergence and extinction saturation, a non-zero value of S_r, and a non-unity value of $k_{rN}^{\max}$) has been validated for one-dimensional migration in homogeneous porous media.

The goal of this study is two-fold: 1) to systematically examine the relationship between NWP relative permeability-saturation functions and porous media type, with specific emphasis on the factors affecting $k_{rN}^{\max}$; and, 2) to validate a numerical model, specifically the k_{rN}-S_W constitutive relationship proposed by Gerhard and Kueper (2003b) for a fixed volume DNAPL release in a two-dimensional heterogeneous porous medium, for the first time. The first objective will be carried out by measuring NWP relative permeability curves for six unconsolidated sands in a local scale flow cell. The second objective will be carried out by simulating a bench scale experiment using a numerical model equipped with the measured k_{rN}-S_W functions. The bench scale experiment will employ a heterogeneous porous medium composed of the six sand types examined in the local scale experiments. The validation will compare the numerically predicted and laboratory measured evolving

pattern of NWP migration, both spatially and temporally, from the start of the experiment until NWP migration has ceased.

3.2 Experimental Set-up

3.2.1 Materials

Six natural sands with single mesh number grain size distributions were employed in all experiments, referred to as the N10, N16, N20, N30, N40 and N50 sands corresponding to the standard mesh number retaining each sand type. The six sands used in the experiments were separated from four different source sands. The N10 sand was separated from Leighton Buzzard DA 8/16 silica sand (WBB Minerals, Brookside Halls, Cheshire, UK), the N16 and N20 sands were separated from Chelford BS 14/22 silica sand (WBB Minerals, Brookside Halls, Cheshire, UK), the N30 and N40 sands from Chelford D30 silica sand (WBB Minerals, Brookside Halls, Cheshire, UK), and the N50 sand from Lochaline L60A silica sand (Tarmac Central Ltd., Stoke-on-Trent, Staffordshire, UK). According to documentation received from WBB Minerals and Tarmac Ltd., each of the source sands contain >97% silicon dioxide and the grain shape is classified as 'very rounded'. Photomicrographs of the N10, N30 N40 and N50 sands, however, reveal that the N10 sand is considerably less 'round' and has a much rougher surface than any of the other sand types examined (see Appendix A). Each of the sands was acid washed in a 0.1M HCL solution, triple rinsed with deionised water and dried prior to use in order to remove any organic material or iron oxides coating the grains.

The NWP employed in the local scale experiments was Hydrofluoroether (HFE) 7500 (3M Specialty Fluids, St. Paul, MN., USA). HFE 7500 (3-ethoxy-1,1,1,2,3,4,4,5,5,6,6,6-dodecafluoro-2-trifluoromethyl-hexane) is a clear, colourless, inert liquid that is totally immiscible in water. Two-dimensional flow-cell

experiments have shown that this class of fluorocarbons behaves very similarly to chlorinated solvents in saturated porous media (Miller, 1997). The NWP employed in the bench scale experiments was analytical reagent grade 1,2-dichloroethane (1,2-DCE) (Fisher Scientific Limited, Loughborough, Leicestershire, UK). Both the 1,2-DCE used in the bench scale experiments and the HFE 7500 used in the local scale experiments were dyed to solubility with Oil Blue A powder (Octel-Starreon, Littleton, CO). Deionised water was employed as the wetting phase. Table 3-1 lists the measured properties of dyed HFE 7500, 1,2-DCE and water. All physical properties were measured using the blue-dyed NWP previously equilibrated with the wetting phase. To ensure constant fluid properties, the laboratory was maintained at 22.0 ± 1.0 ^{o}C throughout the experiments.

Table 3-1. Fluid Properties

Property	Value	Temperature (ºC)
HFE 7500* Density	1.620 ± 0.002 g/ml	22
HFE 7500* Viscosity[1]	1.25 ± 0.02 cP	22
1,2-DCE* Density	1.259 ± 0.002 g/ml	22
1,2-DCE* Viscosity[1]	0.89 ± 0.02 cP	22
Water† Density	0.997 ± 0.002 g/ml	22
Water† Viscosity[1]	0.96 ± 0.02 cP	22
Water† / HFE 7500* Interfacial Tension[2]	23.0 ± 1.0 mN/m	22
Water† / 1,2-DCE* Interfacial Tension[2]	22.3 ± 0.5 mN/m	22
Solubility of HFE 7500 in Water[3]	0.006 ppm	20
Solubility of Water in HFE 7500[3]	45 ppm	20
Solubility of 1,2-DCE in Water[4]	1260 ppm	15
HFE 7500 Vapour Pressure[3]	6 mm Hg	20
1,2-DCE Vapour Pressure[5]	87 mm Hg	25

Note: Measurement of fluid properties is described in Appendix A
* Dyed and equilibrate with water for 24 hrs.
† Deionised and equilibrated with dyed HFE 7500 / 1,2-DCE for 24 hrs.
[1] Gardner Bubble Viscometer (Pacific Scientific, Silver Spring, MD)
[2] Kruss™ ring tensiometer (Hamburg, Germany)
[3] Data provided (3M Specialty Fluids, St. Paul, MN.)
[4] Lange's Handbook of Chemistry, 1987, McGraw-Hill, New York.
[5] Patty's Industrial Hygiene and Toxicology, 1982, John Wiley Sons, New York.

3.2.2 Methods

3.2.2.1 Local Scale Experiments

Local scale experiments were conducted to measure k_{rN}-S_W curves for each of the sands described above. Each experiment measured a complete primary drainage k_{rN}-S_W curve from total WP saturation of the porous media to the maximum possible NWP saturation corresponding to S_r, and a secondary imbibition k_{rN}-S_W curve from S_r to S_W^X. The experiment involving the N20 sand was repeated to confirm the results of the original N20 curve (data not shown). Excellent repeatability for the two experiments was achieved. The local scale experiments were conducted in a square flow cell with a 5 cm x 1 cm internal cross section and a sand pack height of 5cm. Details of the experimental apparatus can be found in Appendix A, and information regarding the experimental procedure can be found in Appendix I; these details are not presented here as the method has been published previously (Gerhard and Kueper, 2003a,b).

3.2.2.2 Bench Scale Experiments

The bench scale experiments were conducted to validate the constitutive relationships of the numerical model (discussed below) employing the k_{rN}-S_W functional parameters measured in the local scale experiments. The bench scale experiments were conducted in a flow cell with a 210 cm x 1 cm internal horizontal cross section and a height of 100 cm, as illustrated in Figure 3-1. The apparatus was constructed from aluminium, stainless steel, Viton©, and toughened plate glass. Only stainless steel, Viton©, and the toughened glass, however, were used in constructing the interior of the cell, as they are generally considered to be un-reactive with 1,2-dichloroethane (1,2-DCE). The aluminium was used in the construction of the frame which acts to support the rest of the apparatus.

The front and back panels of the flow cell were toughened glass, as in the local scale cell, to allow the transmission of light from a 40 tube fluorescent light bank (see Appendix A). Attenuation of transmitted light (i.e., a reduction in the light intensity measured by the light transmission / image analysis system described in Appendix B) caused by the presence of the blue-dyed 1,2-DCE was used as a means of tracking the location of the NWP throughout the experiment. Glass *et al.* (1989) used a similar system to correlate the presence of NWP to changes in measured light intensity.

The glass plates were held in place by a support strip through which cushioned bolts were tightened to hold the glass against a 1 cm thick stainless steel spacer, sealed with Viton©. Screened access ports were located at 10 cm intervals along the perimeter of the frame. The side ports were used for the connection of constant head tank tubing and head measurement tubing. The top and bottom ports were used during sand pack saturation. A DNAPL injection system was inserted through an access port located along the top of the apparatus, 0.5 m from the left boundary of the sand pack, to a depth of 3.0 cm below the top of the sand.

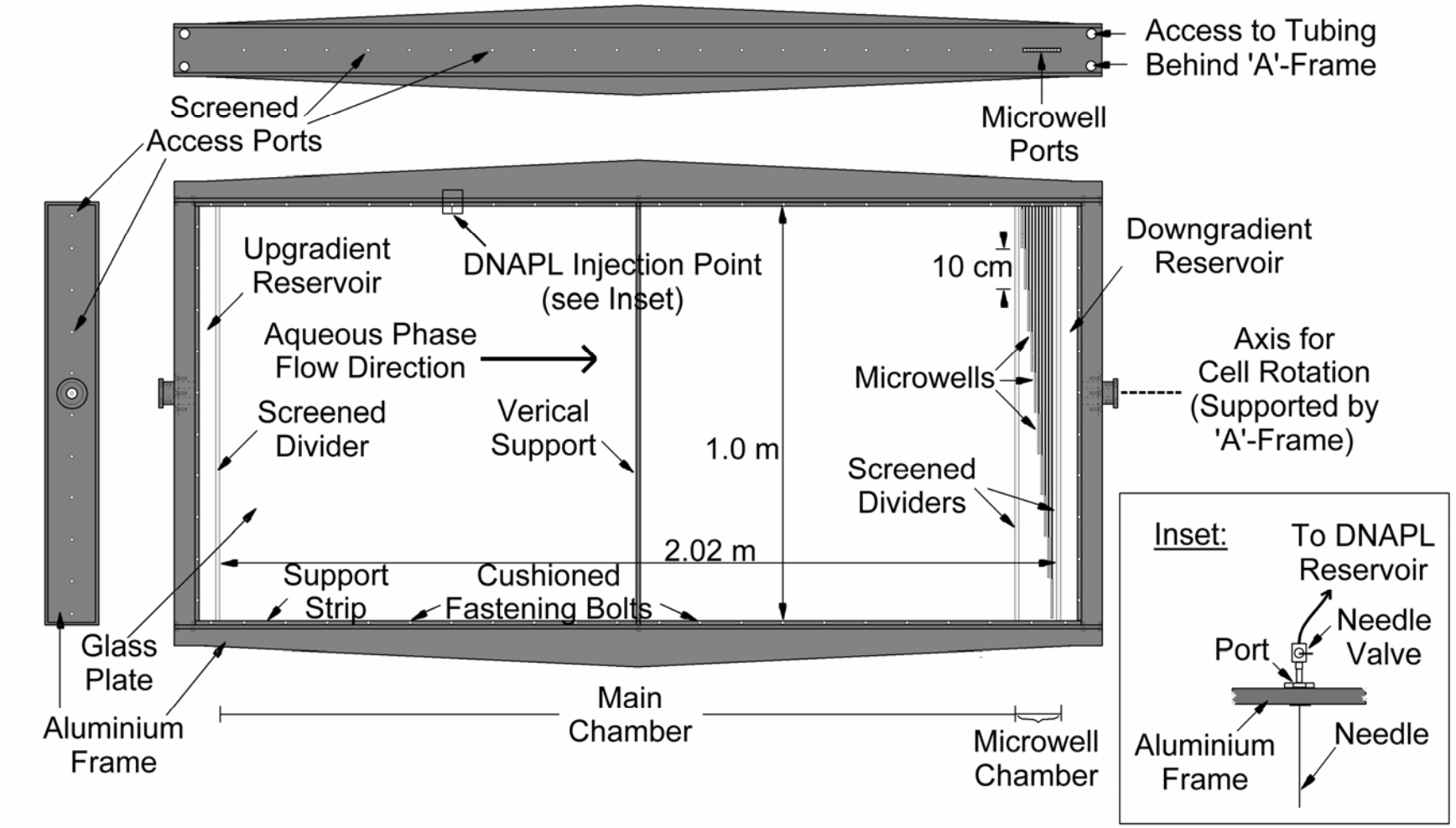

Figure 3-1. Schematic of the bench scale apparatus illustrating left side, top, and front views. The inset presents a detailed illustration of the NWP injection manifold, whose location is identified in the front view.

The interior of the apparatus was divided into four sections with screened dividers located at four centimetres, 196 cm, and 206 cm from the left hand side of the apparatus. The left and right most areas were used exclusively as water reservoirs that were directly connected to constant head tanks. This ensured a constant head along the entire height of the sand pack. The constant head tank connected to the left most water reservoir (upgradient boundary) was set at an elevation 0.02 m great than that of the tank connected to the right most reservoir (downgradient boundary), to establish a hydraulic gradient (i = 0.01) from left to right across the sand pack. The remaining areas have been termed the 'main chamber' and the 'microwell chamber'. The main chamber was packed with a heterogeneous sand pack, and the microwell chamber contains the microwells inserted in a homogeneous sand pack (not utilised in these experiments).

The main chamber of the apparatus was packed with sand in 5 cm by 5 cm blocks of homogeneous sand to create an over-all heterogeneous porous medium. As in the packing of the local scale apparatus, each 5 cm by 5cm block was packed in 0.5 cm lifts of moist, fully compacted sand. Two thin (1 mm thick) reinforced stainless steel dividers (1 metre long by 1 cm wide – i.e., the thickness of the space between the glass plates) were inserted into the cell to define the width of the 5 cm by 5 cm block. The height of the 5 cm by 5 cm block was defined by a grid drawn with removable ink on the front glass panel. Moist sand was dropped from the top of the apparatus and a 1 metre long tamping device was inserted between the paired dividers for each 0.5 cm lift added to the block space. The bottom row of sand was packed first, and each subsequent row of sand was packed on top of the previously emplaced row. The main chamber of the flow cell was packed to a total depth of 0.91 meters.

Packing the bench scale apparatus was complicated by the fact that the addition of sand and water to the cell increases the pressure on the glass front and back panels which causes them to deflect in an outwards direction. This deflection not only increases the thickness of the sand pack, but also causes slumping, or a reduction in the height of the sand pack. The result is thick non-horizontal layers of sand across the apparatus. Attempts were made to minimize this affect throughout the packing procedure, including the installation of a stainless steel vertical support strip along the centre of the front and back glass plates of the apparatus to limit the amount of glass deflection (see Appendix A).

Once the packing was completed, the cell was sealed along the top boundary with a Viton© / stainless steel barrier containing access ports, the water was drained from the cell, and compressed air was forced through the sand pack to dry it prior to re-saturation. To re-saturate the sand pack, carbon dioxide (CO_2) was flushed through the flow cell for 48 hours, followed by a slow, upwards displacement of CO_2 with distilled, deaired water. This procedure is well established for preventing the formation of trapped bubbles, since de-airing the water and filling the void space with high solubility carbon dioxide ensures that trapped bubbles will quickly dissolve into the water and be carried out of the system should any form during the saturation procedure.

The single phase average permeability of the heterogeneous sand pack in the bench scale apparatus was calculated from data collected from a non-reactive tracer test. The tracer test was also utilised to quantify the degree of glass deflection resulting from the addition of sand and water to the apparatus (see Appendix D).

The bench scale flow cell was packed with 5cm x 5cm blocks of homogeneous sand utilising the six sand types examined in the local scale experiments to generate a

larger scale heterogeneous sand pack. A spatially correlated numerical intrinsic permeability field was generated using FGEN 9.1 (Robin *et al.,* 1991) assuming an exponential autocorrelation function. After the method of Silliman (2001), each node in the numeric field was binned into one of six groups of equal size corresponding to the intrinsic permeability of the sand types measured in the local scale experiments. The binned permeability field was used as a map during the emplacement of the homogeneous blocks of sand in the bench scale flow cell. The predetermined pattern of the sand emplacement gave a heterogeneous medium that can be characterised with a mean $\ln k$ = -23.09 m^2, a variance of $\ln k$ = 0.24 m^2, a horizontal correlation length, λ_H = 15.2 cm, and a vertical correlation length, λ_V = 2.8 cm which closely matched the targeted statistical parameter values. The end result is a heterogeneous porous media statistically similar to a fine to coarse sand aquifer with correlation lengths appropriately proportioned to the size of the apparatus, according to dimensioning suggestions proposed by Welty and Elsner (1997).

During the bench scale experiment, a constant flux source of 1,2-DCE was activated through the DNAPL injection point (see Figure 3-1). The source was active at a rate of 90 ml/hr for 130 minutes, such that 194.6 ml of 1,2-DCE was injected into the flow cell. The light transmission / image analysis system described in Appendix B was utilised to capture images of the flow cell throughout the experiment and to track the progress of the advancing NWP. Images were collected during NWP injection and subsequent re-distribution following termination of the source, until migration of the NWP ceased.

Although an aqueous phase gradient was applied across the flow cell and 1,2-DCE is slightly soluble in water, the timescales of the migration experiment conducted herein (on the order of 24 hours) were such that the evolving NWP

distribution was assumed to be unaffected by dissolution while migration was active. Numerical simulations that account for dissolution, presented in Chapter 5, confirm this assumption.

3.2.2.3 Numerical Modelling

The numerical model utilised in this study is the three-dimensional, finite difference, two phase flow model DNAPL3D (Gerhard *et al.,* 1998) (the migration sub-model of DNAPL3D-MT presented in Chapter 5 and Appendix F), modified to accommodate spatially variable relative permeability functional relationships. Details regarding the numerical formulation of DNAPL-3D can be found elsewhere (Gerhard *et al.,* 1998; Appendix F).

DNAPL3D was utilised to simulate the bench scale flow cell experiment. To correctly account for the nonuniform thickness of the sand pack, due to glass deflection as a result of sand and water pressures exerted on the cell, the experiment was simulated in three dimensions. The solution domain employed was 202 cm wide by 91 cm high by 3 cm thick. The amount of glass deflection as a function of location in the flow cell was independently determined from the tracer test (see Appendix D). The obtained function was employed in constructing the numerical domain such that it determined, for each location in vertical cross-section, the proportion of the 3 cm domain thickness occupied by porous media versus that occupied by the glass plates. The domain was discretised into 220,584 nodes with a nodal spacing of 1 cm horizontally, 1 cm vertically, and 0.25 cm in the third dimension.

The experimental results will be compared both spatially and temporally to the results of three numerical simulations of the bench scale experiment: 1) 'validation simulation'– where the independently measured $k_{r,N}$ - S_W curves are employed in the numerical model and the simulation is run without any calibration; 2) 'Burdine

simulation'– where $k_{r,N}$ values at S_W^M and S_W^X are equal to zero, and a $k_{rN}^{\max}$ value of unity is assumed, as in the Burdine (1953) permeability model (e.g. White and Oostrom, 1998; Gerhard *et al.,* 1998; Gerhard *et al.,* 2001); and, 3) 'N16 simulation' – where the measured N16 $k_{r,N}$ - S_W curve is utilised throughout the model domain, thereby removing the influence of porous media type on $k_{rN}^{\max}$, S_r and the associated curvature parameters. These comparisons will enable a direct evaluation of both the form of the $k_{r,N}$ - S_W function, as well as the accuracy of the measurements which quantified a dependence of $k_{rN}^{\max}$ on porous media type.

3.3 Results

3.3.1 Local Scale Experiments

3.3.1.1 Drainage and Imbibition k_{rN}-S_W Relationships

Figure 3-2 and 3-3 present the measured NWP relative permeability curves for the six sands for drainage and imbibition, respectively (plotted separately, and without error bars for clarity; see Appendix J for discussion of measurement uncertainty). The figures also plot the corresponding best-fit curves of the k_{rN}-S_W function of Gerhard and Kueper (2003b), while Table 3-2 details the best-fit function parameters. The best-fit parameter values were determined through a standard non-linear least squares fitting routine with the end-points of the curves constrained by the measured data.

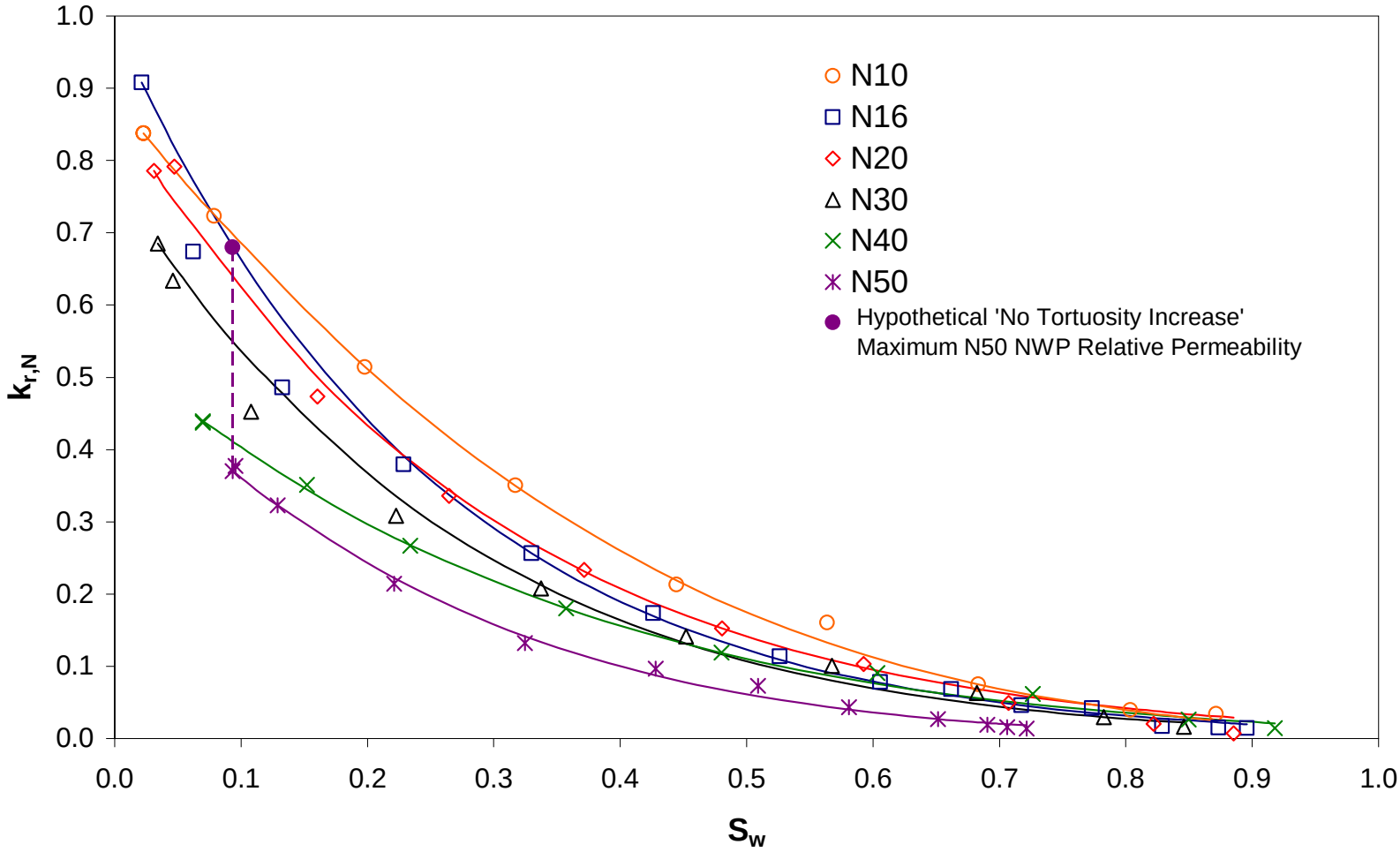

Figure 3-2. Main drainage NWP relative permeability – saturation (k_{rN}-S_W) relationship as a function of porous media type; including best-fit curves for each sand type using Equation 3-1.

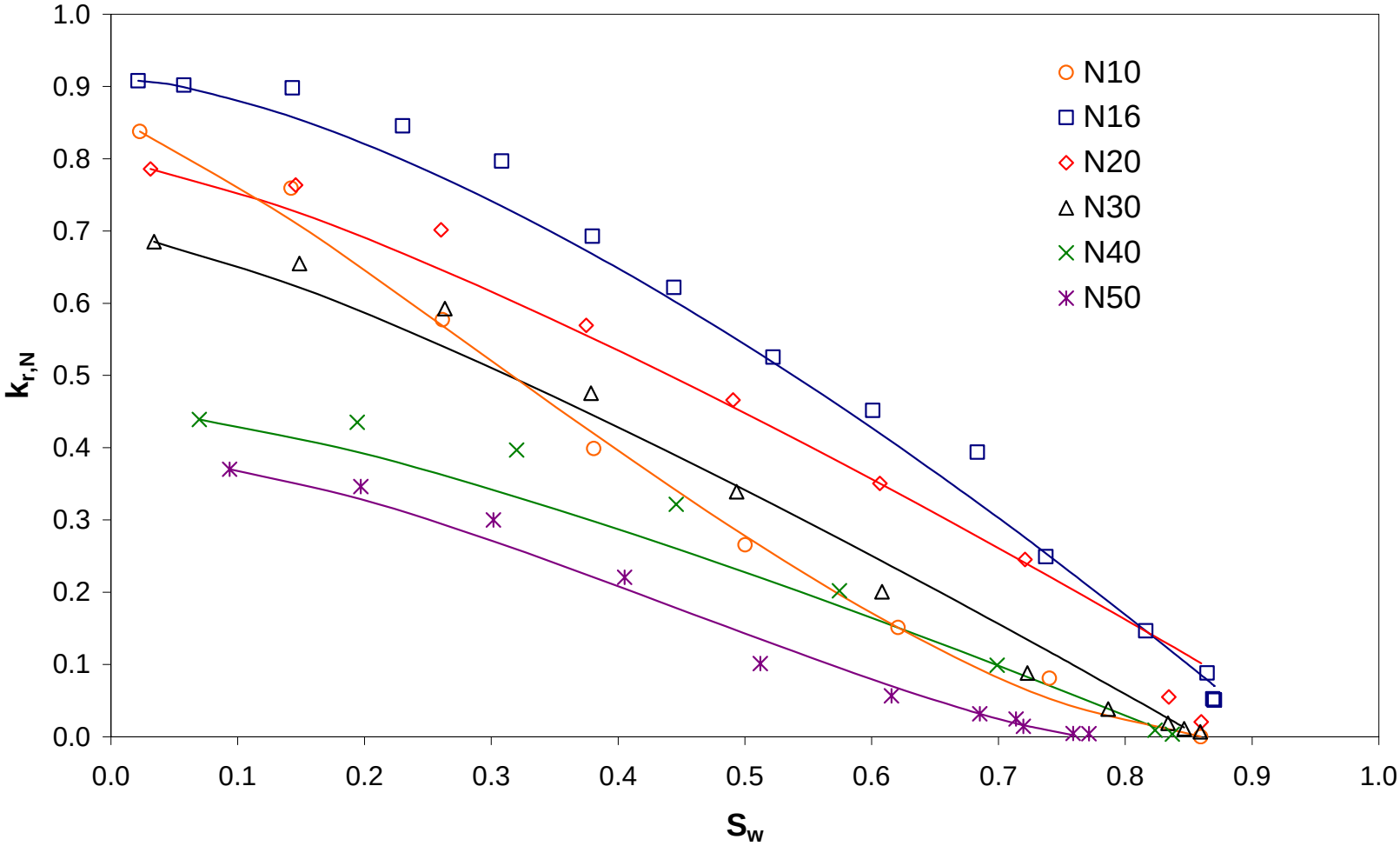

Figure 3-3. Secondary imbibition NWP relative permeability – saturation (k_{rN}-S_W) relationship as a function of porous media type; including best-fit curves for each sand type using Equation 3-3.

Table 3-2. Experimentally Derived $k_{rN} - S_W$ Parameter Values

Parameter	Values					
	N10	**N16**	**N20**	**N30**	**N40**	**N50**
Mean Particle Diameter (μm)	2180	1295	1015	700	513	363
k_{abs} (m^2)	2.62×10^{-10}	1.90×10^{-10}	1.81×10^{-10}	7.10×10^{-11}	7.41×10^{-11}	1.84×10^{-11}
Porosity	0.35	0.38	0.34	0.33	0.31	0.36
$k_{rN}^{\max}$	**0.84**	**0.91**	**0.79**	**0.69**	**0.44**	**0.37**
S_r	0.023	0.022	0.031	0.034	0.070	0.093
S_W^M	0.87	0.90	0.89	0.85	0.92	0.72
S_W^X	0.86	0.87	0.86	0.86	0.84	0.77
λ_d / λ_i [1]	3.7 / 5.0	3.4 / 4.4	4.1 / 8.4	4.4 / 9.6	4.8 / 8.1	4.4 / 3.6
ΔS_W^{*d} [2]	0.69	4.68	3.83	2.87	2.06	1.40
ΔS_W^{*i} [2]	0.004	0.049	0.098	0.000	0.005	0.000
τ_d [3]	1.89	10.98	7.99	6.65	4.14	3.79
τ_i [3]	0.30	0.00	0.00	0.00	0.00	0.19

[1] Brooks-Corey (1964) drainage / imbibition pore size distribution index; determined through analysis of measured P_C-S_W curves (see Appendix H)

[2] Curvature fitting parameters (see Gerhard and Kueper, 2003b)

[3] Drainage and imbibition tortuosity exponents (see Gerhard and Kueper, 2003b)

The figures illustrate a clear trend in the shape and end-point locations of the $k_{r,N}$ - S_W curves as a function of porous media type. The figures and the table indicate that the emergence and extinction saturations (S_W^M and S_W^X, respectively) are generally unaffected by porous media type, but the turn-around points between drainage and imbibition (i.e., $k_{rN}^{\max}$ and S_r) appear to be a function of mean grain diameter. As a result, a number of the best-fit curvature parameters presented in Table 3-2 (i.e., ΔS_W^{*d} and τ_d), which are affected by the value of $k_{rN}^{\max}$, also appear to be a function of mean grain diameter.

3.3.1.2 $k_{rN}^{\max}$ as a Function of Mean Grain Diameter

$k_{rN}^{\max}$ is a particularly sensitive parameter that varies from a value of 0.91 for the N16 sand to 0.37 for the N50 sand (see Table 3-2). These findings imply that in small particle size sands, the NWP relative permeability will be disproportionately lower at a given NWP saturation, than for larger particle size sands; particularly as the NWP saturation increases towards residual wetting phase levels.

This phenomenon can best be explained by consideration of Figure 3-4 which plots pore size distribution curves for hypothetical 'fine' and 'coarse' grained sands, expressed in terms of 'frequency of occurrence' versus 'pore radius' assuming normally distributed pore sizes ranging from zero (i.e., the contact between adjacent sand grains) to a hypothetical maximum, r_{max} (for which it is reasonable to assume increases with increasing sand grain diameter).

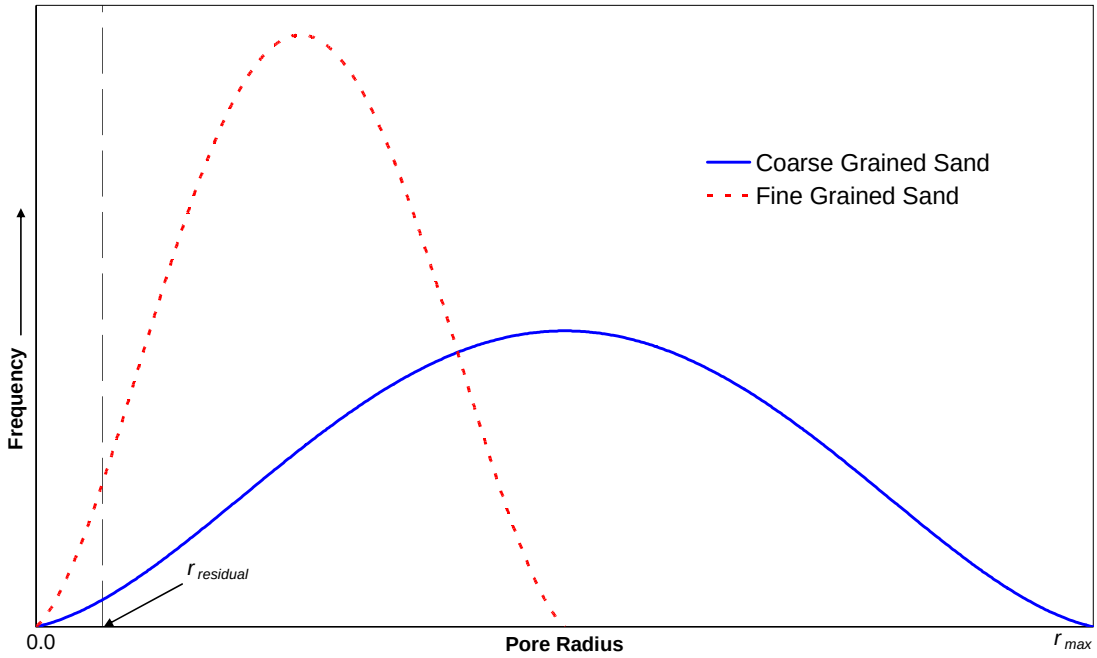

Figure 3-4. Pore size distribution curves for hypothetical 'fine' and 'coarse' grained sands.

As NWP invades the porous medium, WP saturation decreases, primarily through piston-like displacement, until S_r is attained and the WP is trapped in the smallest corners between sand grains or exists as thin films coating the sand grains (see Chapter 2 for a detailed discussion of wetting phase displacement mechanisms). S_r is achieved at high capillary pressures approaching infinity where all P_C - S_W curves, regardless of sand type, converge. The WP thus exists in the smallest pore spaces between the sand grains (pore spaces smaller than a definable $r_{residual}$) and can not be removed at the time scales and pressures typical of contaminant hydrogeology systems. As the minimum pore radius for both sands is zero (i.e., the contact point between adjacent sand grains), and the maximum pore radius is larger for the coarse sand than it is for the fine sand, the proportion of pore radii smaller than $r_{residual}$ is greater for the fine sand than it is for the coarse sand. As a result, the fraction of original pore space available for NWP flow is proportionally reduced for the fine grained sand relative to the coarse grained sand. This phenomenon was observed in the experimental data as S_r increases with decreasing mean grain size.

However, the resulting increase in S_r does not explain the full extent of $k_{rN}^{\max}$ reduction for finer sands. As an example, Figure 3-2 plots the expected value of $k_{rN}^{\max}$ for the N50 sand when only this reduction in pore space available for NWP flow is considered to have an effect on $k_{rN}^{\max}$ with reference to the N16 sand; in such a case it would be expected that the N50 $k_{rN}^{\max}$ value would plot on the N16 curve as shown. In fact, there is an additional effect: the decrease in pore space will exacerbate the degree of tortuosity of the NWP flow path (Gerhard and Kueper, 2003b discusses the relationship between tortuosity and $k_{rN}^{\max}$). The increase in NWP tortuosity reduces the value of $k_{rN}^{\max}$ further, as illustrated by the value of $k_{rN}^{\max}$ actually measured for the N50 sand (Figure 3-2).

In general, it can be said that a reduction in pore space available for NWP flow at residual WP saturations, combined with the effect this has on NWP flow path tortuosity, manifests itself as a decrease in $k_{rN}^{\max}$ as a function of decreasing mean grain diameter of the porous medium. A numerical relationship between $k_{rN}^{\max}$ and mean grain diameter, including data from other studies, is presented in Chapter 4.

3.3.1.3 k_{rN} Hysteresis

Figures 3-2 and 3-3 show a significant degree of reverse hysteresis between drainage and imbibition conditions for each of the very rounded sand types (i.e., the N16, N20, N30, N40 and N50 sands), which is comparable in character to the hysteresis pattern of k_{rN}-S_W curves measured by other researchers with similarly shaped unconsolidated sand grains (e.g. Naar *et al.,* 1962; Stonestrom and Rubin, 1989b; Wei and Lile, 1992).

The N10 sand, however, while also exhibiting reverse hysteresis pattern, shows a smaller degree of hysteresis between drainage and imbibition. The N10 sand is physically different from the other sand types as noted in the photomicrographs presented in Appendix A. It is considerably less 'round', and as a result, the difference between the size of the 'pore throats' and 'pore bodies' (i.e., the aspect ratio) is likely to be significantly less than the rest of the sands.

As discussed by Melrose (1970), the stable position of the NWP / WP interface during drainage occurs in the pore throat, and the stable position of the interface during imbibition appears in the pore body. As the pore throat and pore body radii are more similar for the N10 sand, the position of the interface during drainage and imbibition will be more similarly located than in the other sands. Therefore, the degree of NWP tortuosity, and the value of $k_{r,N}$, will be more similar for a given NWP saturation between drainage and imbibition conditions; thus hysteresis is reduced compared to the other (high aspect ratio) sands.

3.3.2 Bench Scale Experiments

Figure 3-5 shows the sand type distribution emplaced in the bench scale flow cell and identifies a number of 'key' locations by number that will be highlighted throughout the discussion of the bench scale experiments. Figure 3-5 also identifies the proportion of the domain that will be the focus of the following sections, as NWP migration takes place entirely within this area.

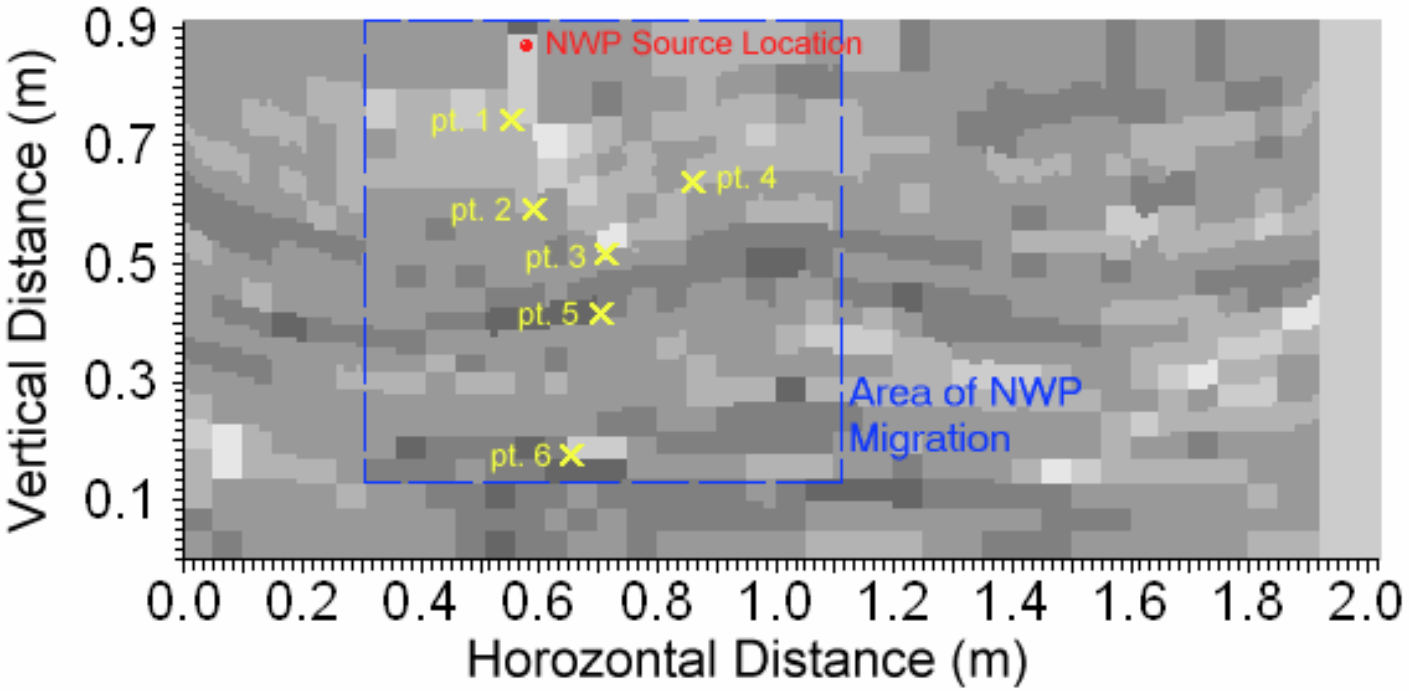

Figure 3-5. Visual depiction of the bench scale experimental apparatus identifying 'key' locations (by number) to be discussed in the text; the grey scale represents the different sand types emplaced in the apparatus and the blue box outlines the area of NWP migration.

3.3.2.1 Spatial Comparison: Validation Simulation

Figure 3-6a illustrates the NWP saturation distribution 130 minutes after the start of the experiment (corresponding to the time at which the NWP source condition was terminated). This figure is a photograph of the experimental apparatus collected with the light transmission / image analysis system that has been digitally enhanced to make the presence / absence of NWP more distinct. The figure illustrates that the NWP migrated in a generally downwards direction from the source location, spreading laterally upon low hydraulic conductivity sand types (i.e., at Points 2 and 3).

Figure 3-6b shows the predicted NWP saturation distribution of the validation simulation when the numerical model employs the measured $k_{r,N}$ - S_W functions. The background greyscale in the figure identifies the sand types. As can clearly be seen, there is excellent agreement between the predicted location of NWP from the simulation and the actual location of NWP as seen in Figure 3-6a. At Point 3, for example, breakthrough of NWP into the N40 sand has only just occurred 130 minutes after the start of the experiment, as predicted by the validation simulation.

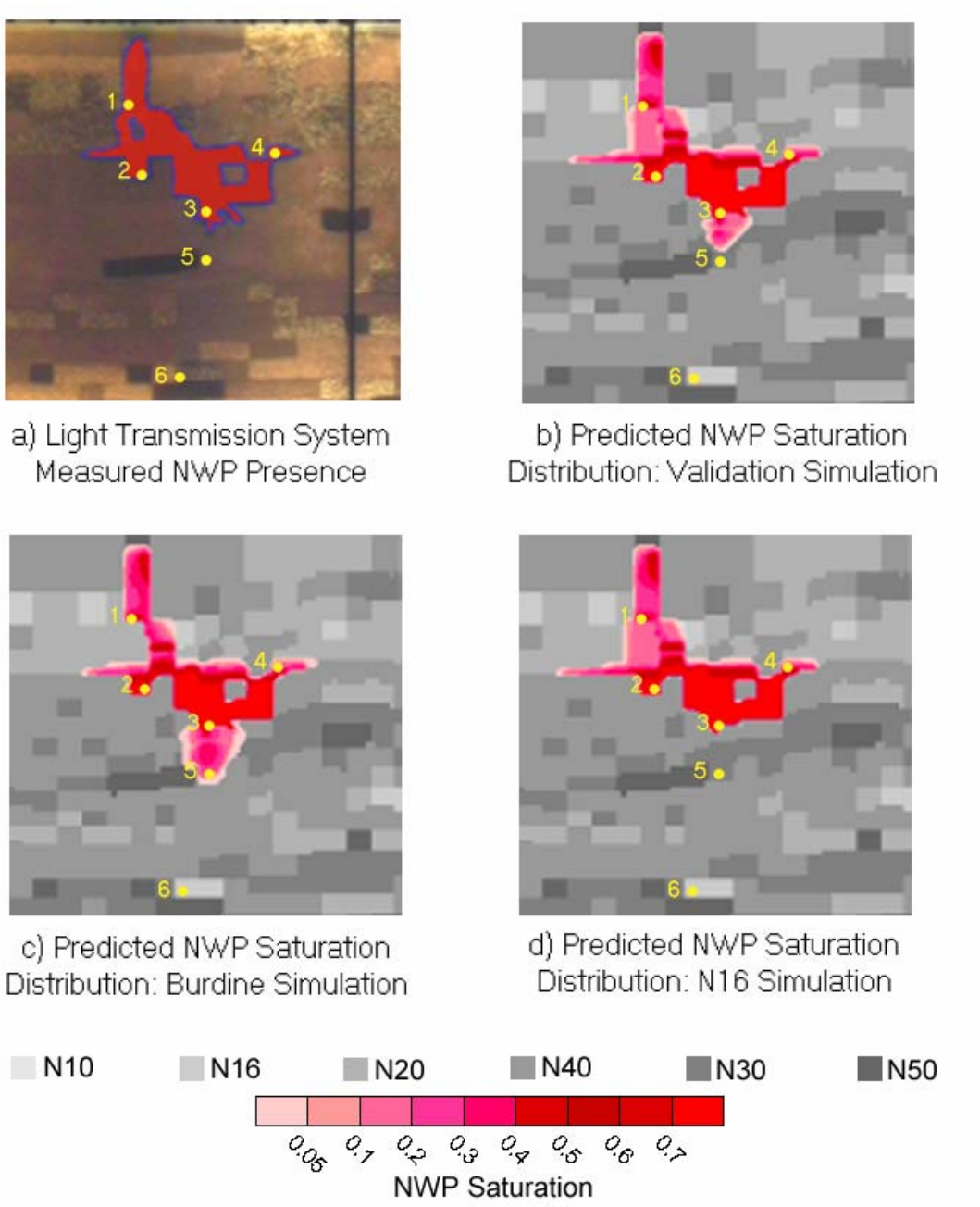

Figure 3-6. Laboratory measured and numerical model predictions of NWP presence at *t* = 130 minutes (immediately following termination of the source) in the bench scale experimental apparatus.

Figures 3-7a and 3-7b present the actual NWP distribution and the validation simulation predicted NWP distribution, respectively, 24 hours after the start of the experiment / simulation. All NWP migration has ceased by this time. As can clearly be seen, when the numerical model employs the measured $k_{r,N}$ - S_W functions, there is excellent agreement between the final predicted and actual NWP distributions.

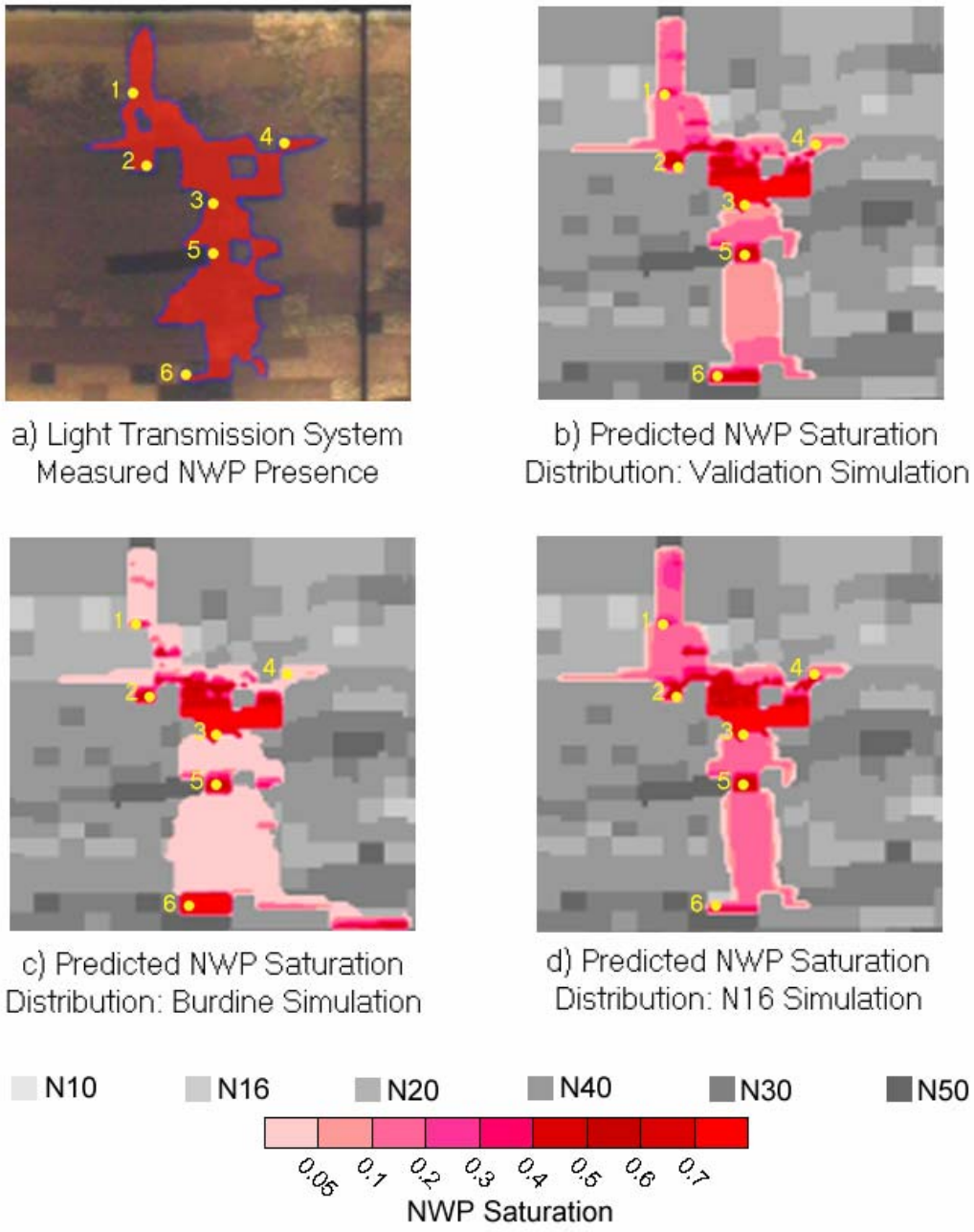

Figure 3-7. Laboratory measured and numerical model predictions of NWP presence at *t* = 24 hours (following complete cessation of migration) in the bench scale experimental apparatus.

Figure 3-8 compares the saturation history of the experimental and predicted NWP saturation distributions of the validation simulation. Point-by-point intensity versus time plots created using the light transmission / image analysis system (Appendix B) were used to delineate zones of high NWP saturation (on drainage), zones of reducing NWP saturation (on imbibition), and zones of residual NWP saturation.

The experimental data presented in Figure 3-8 shows that NWP has passed through the high permeability sands surrounding Point 1, leaving behind a trail of low saturation residual NWP. Beneath this location, high NWP saturations have accumulated above low permeability sands at Points 2 and 3. At Point 3, for example, high NWP saturations persist following the complete cessation of migration as a result of NWP flow path cut-off. Following termination of the source, the capillary pressure in the N40 sand beneath this location decreases to the terminal pressure (P_T), trapping a high NWP saturation pool above. This pattern of residual and decreasing NWP saturations on imbibition above areas of high NWP saturation on drainage (trapped above low permeability sand types) is repeated throughout the sand pack at Points 2, 3, 5, and 6.

Comparison of the saturation history zones between the experimental and predicted results indicates that the model accurately predicts zones of high and low NWP saturation. For example, the numerical model accurately predicts zones of high NWP saturation above low permeability sand types at Points 2, 3, 5 and 6, and correctly predicts residual saturations beneath Point 3, and between Points 5 and 6.

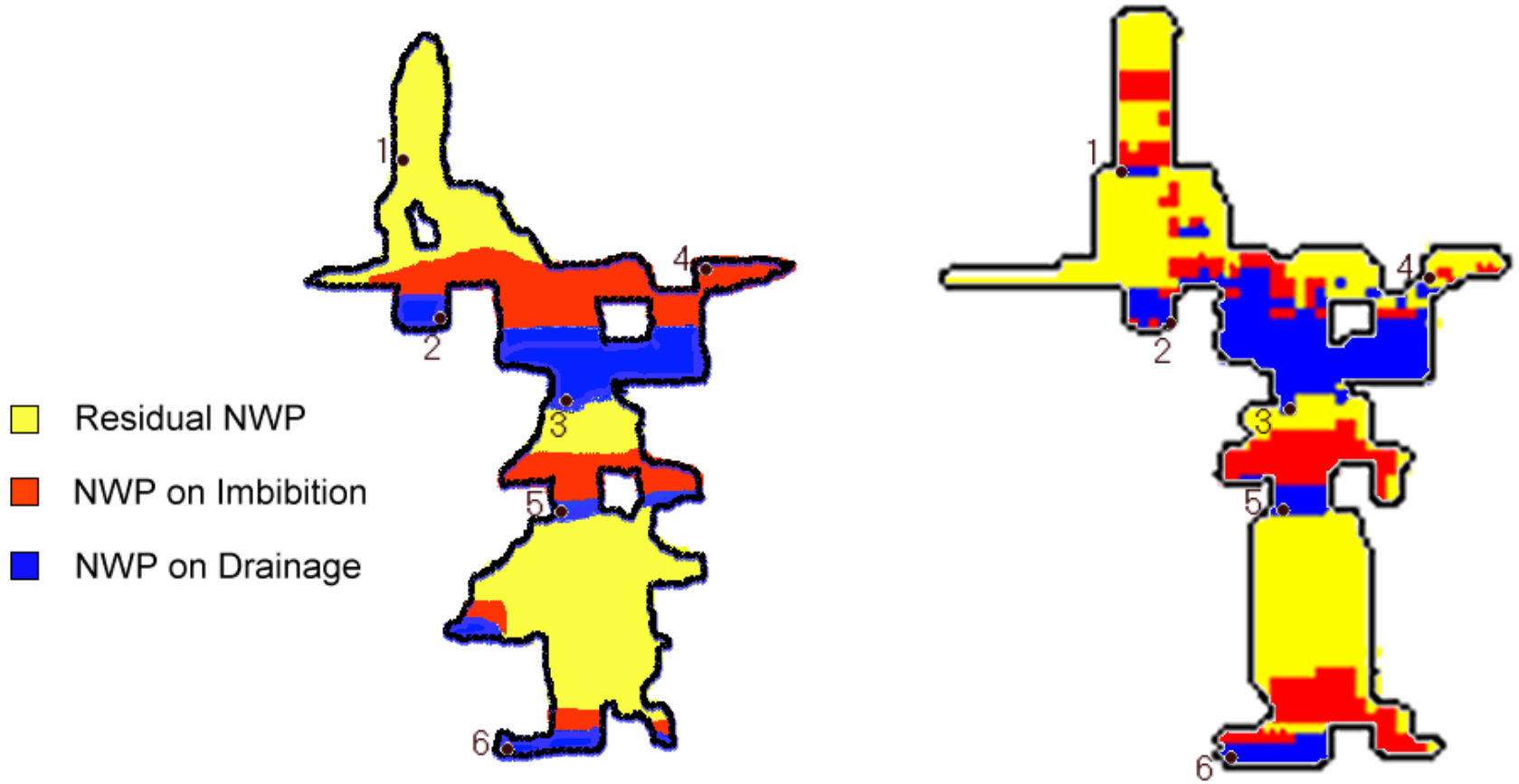

Figure 3-8. Comparison of saturation history zones between experimental results (left hand diagram) and the validation simulation predictions (right hand diagram) at *t* = 24 hours.

3.3.2.2 Spatial Comparison: 'Burdine' and 'N16' Simulations

Figure 3-6c shows the predicted NWP saturation distribution when the Burdine $k_{r,N}$ - S_W function is employed throughout the domain by the numerical model at t = 130 minutes. Comparison of this figure to Figure 3-6a reveals discrepancies at both Points 1 and 3. At Point 1, the numerical model fails to predict breakthrough of NWP into the N20 sand. The Burdine simulation over predicts the rate of NWP flow through the N16 and N10 sands to the right of Point 1 such that NWP saturations, and therefore pressures, do not increase at Point 1 to a level sufficient to overcome the displacement pressure of the N20 sand. At Point 3, the numerical model over predicts the degree of breakthrough at t = 130 minutes. The Burdine simulation over predicts the rate of NWP flow at low WP saturations such that NWP saturations and pressures increase at this location faster than determined experimentally; thus the predicted breakthrough of NWP to the N40 sand beneath Point 3 occurs earlier than in the experiment.

Figure 3-6d shows the predicted NWP saturation distribution when the N16 $k_{r,N}$ - S_W function is employed throughout the domain by the numerical model at t = 130 minutes. Comparison of this figure to Figure 3-6a reveals a discrepancy at Point 3: the N16 simulation does not predict any breakthrough at Point 3 into the N40 sand. The N16 simulation over predicts the rate of NWP migration through the N20 sand, therefore the NWP spreads further laterally to the left of Point 2 in this simulation relative to the validation simulation. As a result, NWP saturations and pressures have not increased rapidly enough at Point 3 to overcome the displacement pressure of the N40 sand prior to termination of the source at t = 130 minutes.

The final NWP distribution at t = 24 hours is well predicted by the N16 simulation (Figure 3-7d), but there remain a number of discrepancies between the

final NWP distribution predicted by the Burdine simulation (Figure 3-7c) and the experimental results (Figure 3-7a). In the Burdine simulation, breakthrough has still not occurred at Point 1. In addition, the Burdine simulation predicts NWP migration to the right of Point 6, towards the centre of the flow cell. Once again, the Burdine $k_{r,N}$ - S_W function over predicts the rate of NWP flow at low WP saturations. As a result, a larger proportion of the released volume migrates beneath Point 3 prior to source termination. This additional volume of NWP is forced to migrate through the coarser sands to the right of Point 6.

3.3.2.3 Temporal Comparison: Validation Simulation

Figures 3-9 through 3-11 plot normalized light intensity on the left-hand vertical axis (current light intensity at a location in the sand pack divided by the maximum intensity at that location) as recorded by the light transmission / image analysis system, together with a plot of validation simulation predicted NWP saturation on the right-hand vertical axis, both as a function of time (note the logarithmic scale to show both early and late time behaviour). As the NWP utilised in the bench scale experiment was dyed blue, the presence of NWP decreases the amount of light that is able to pass through the domain to be recorded by the light transmission / image analysis system. Therefore, a decrease in light intensity indicates the arrival of NWP, and an increase in light intensity indicates a reduction in NWP saturation, at a particular location in the domain.

Figure 3-9 shows the intensity / saturation profile for a location 2 cm beneath Point 1 for the experiment and the validation simulation. As can clearly be seen, the first arrival of NWP at this location in the experiment, as indicated by a sharp drop in light intensity at t = 0.1 hours, coincides well with the arrival of NWP predicted by the variable k_{rN} simulation. The increase in light intensity at t = 3.5 hours coincides

with a predicted decrease in NWP saturation for the validation simulation following termination of the source and change to imbibition flow conditions.

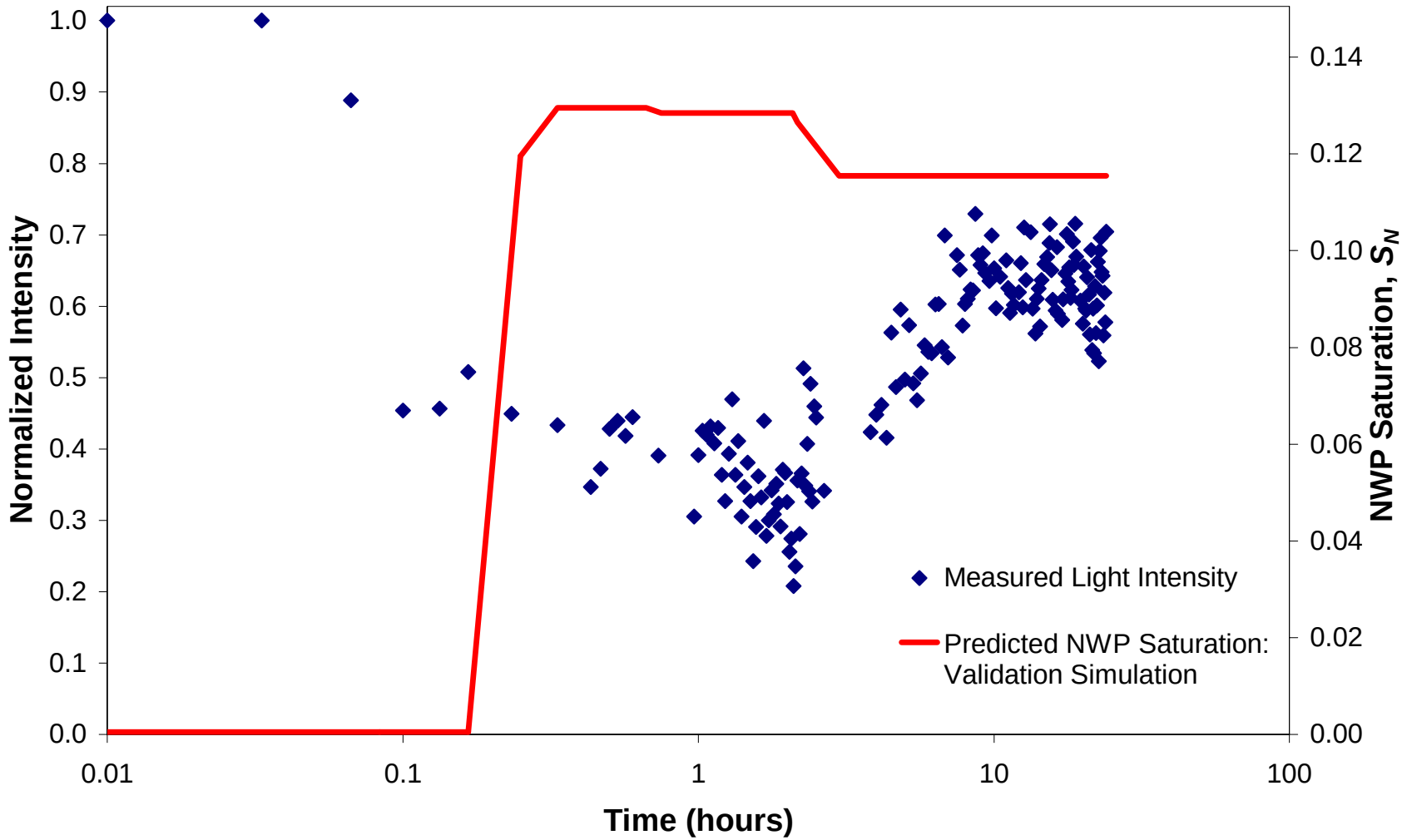

Figure 3-9. Intensity (dots; left hand axis) / saturation (solid line; right hand axis) profile for a location 2 cm beneath Point 1.

Figure 3-10 shows the intensity / saturation profile at Point 3 for the experiment and the validation simulation. Once again, the rapid decrease in light intensity, indicating the arrival of NWP at this location in the experiment at t = 0.5 hours, coincides with a rapid increase in NWP saturation predicted by the numerical model. At this location, the measured light intensity profile indicates that, in contrast to the saturation history of the location examined in Figure 3-9, NWP saturations do not decrease following first invasion; this behaviour is (also) accurately predicted by the validation simulation.

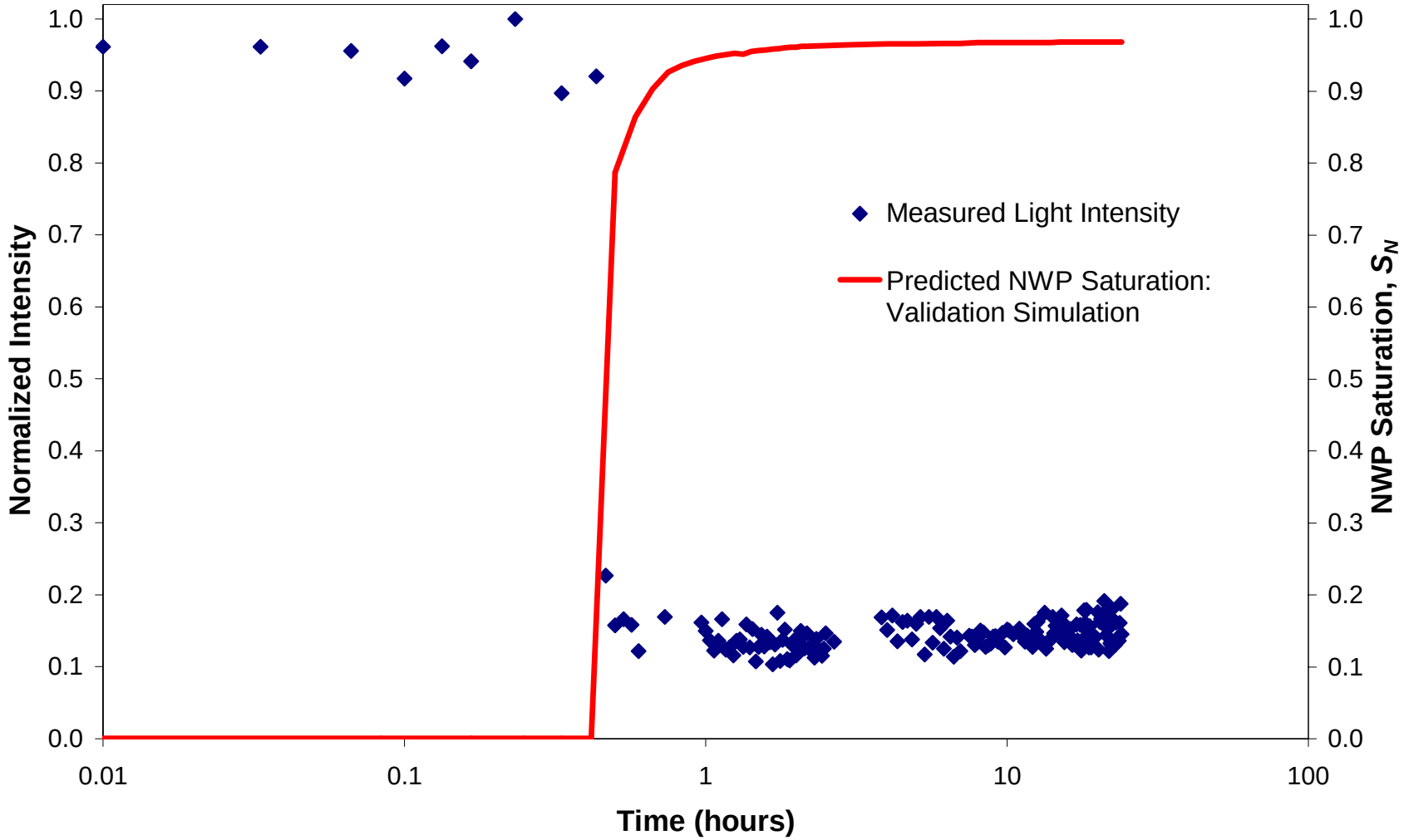

Figure 3-10. Intensity (dots; left hand axis) / saturation (solid line; right hand axis) profile at Point 3.

Figure 3-11 shows the intensity / saturation profile at a location 7 cm beneath Point 3 for the experiment and the validation simulation. Similar to Figures 3-9 and 3-10, the decrease in light intensity at this location coincides with the predicted arrival of NWP. This not only confirms the ability of the simulator to predict the rate of migration to this location, but implicitly confirms the ability of the simulator to accurately predict the time of NWP breakthrough to the N40 sand beneath Point 3.

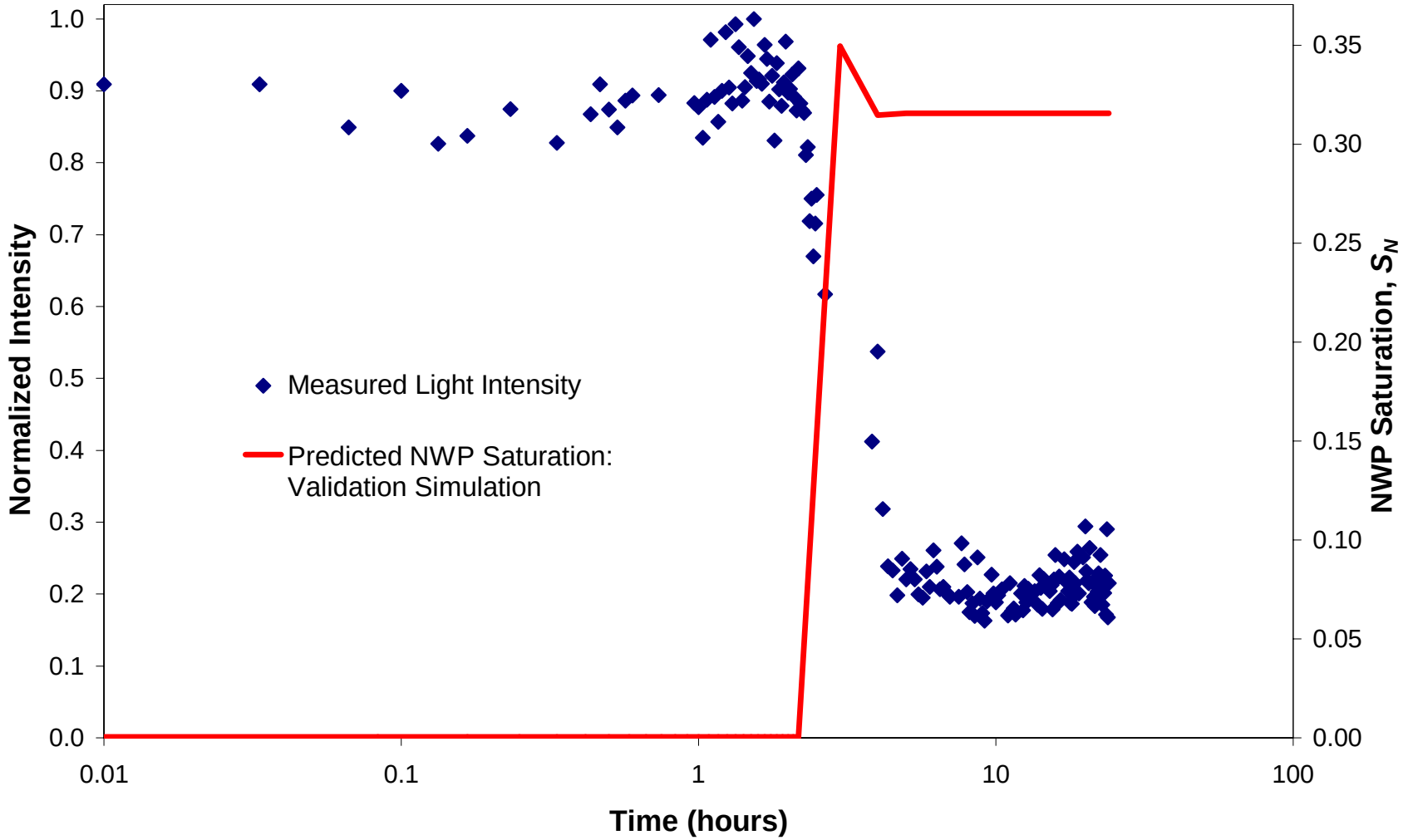

Figure 3-11. Intensity (dots; left hand axis) / saturation (solid line; right hand axis) profile for a location 7 cm beneath Point 3.

Table 3-3 summarizes the NWP arrival times for all the key locations identified in Figure 3-5. At Points 1, 2 and 4, the validation simulation over predicts the arrival time, while at Points 3, 5, and 6, the simulation under predicts the arrival time. However, the differences in the predicted arrival times at Points 1 through 5 are all less than 2.57% of the total NWP migration time, with no discernable discrepancy at Point 2 and a discrepancy of 0.07% at Point 4.

The predicted NWP arrival time at Point 6, however, is significantly different than the actual arrival time (71.11% discrepancy). While the final distribution of NWP is very well predicted by the simulation employing the measured $k_{r,N}$ - S_W functions, the rate of migration through the area of N40 sand between Points 5 and 6, is not well predicted by any of the NWP relative permeability expressions. During flow cell sand packing, each layer of sand was emplaced in 5 cm vertical intervals. This method inadvertently put very slight horizontal bedding interfaces between an otherwise continuous vertical section of N40 sand between Points 5 and 6. These subtle interfaces between identical sands are not explicitly incorporated into the numerical model, yet DNAPL migration is notoriously sensitive to such minor (grain-scale) heterogeneity (Kueper *et al.,* 1989). As a result, the experiment exhibited NWP saturations building up and spreading laterally at each of these discontinuities (clearly apparent through examination of the light transmission / image analysis system images), resulting in retardation of the NWP vertical advancement that is not predicted by the models. While such models are generally incapable of reproducing unstable displacement behaviour in homogeneous (or, in this case, homogenous sub-regions of) bench scale experiments, it is expected that such homogeneity (above the REV scale) is unrealistic in the field (Kueper *et al.,* 1989). The extensive analysis

provided demonstrates that the model is accurate in space and time where porous media properties are independently measured and accounted for.

Table 3-3. Arrival Times at Key Points in the Bench Scale Flow Cell

Location	Actual Arrival Time (min)	Validation Simulation Predicted Arrival Time (min)	Difference in Arrival Times (% of Total Migration Time)
pt. 1	4	6	0.14
pt. 2	20	20	0.00
pt. 3	28	26	0.14
pt. 4	100	101	0.07
pt. 5	170	133	2.57
pt. 6	1180	156	71.11

3.3.2.4 Temporal Comparison: 'Burdine' and 'N16' Simulations

Intensity / saturation profiles created for the Burdine and N16 simulations (not presented) show some differences in the predicted temporal behavior of the migrating NWP relative to experimental results. For example, the profile for the location 2 cm beneath Point 1 (examined for the validation simulation in Figure 3-9) shows no predicted NWP arrival in the Burdine simulation, as breakthrough at Point 1 has been shown not to occur. Also, the predicted arrival time of NWP in the N16 simulation is over predicted at the location 7 cm beneath Point 3 (examined for the validation simulation in Figure 3-11) as a result of the later breakthrough time predicted at Point 3.

These results are summarized in Table 3-4 which presents breakthrough times (i.e., the time at which NWP pressure increases above the displacement pressure of the sand type immediately below a particular location) for the three simulations for comparison with actual, measured breakthrough times. Breakthrough times at Points 1 and 3 are accurately predicted in the validation simulation. Of importance in the results of the other simulations is the lack of breakthrough of NWP at Point 1 in the

Burdine simulation and the failure of the N16 simulation to predict breakthrough at Point 3 prior to termination of the source at t = 130 minutes. In general, however, the N16 breakthrough times compare as well as the validation simulation to the actual breakthrough times. As discussed in detail in Chapter 4, differences in arrival times, breakthrough times, and migration cessation times between simulations employing variable (i.e., the validation simulation) versus constant (i.e., N16 simulation) k_{rN} are sensitive to the permeability of the source node and surrounding area at the bench scale. In some cases, including the permeability field constructed in the bench scale apparatus, the differences in release behaviour characteristics for these two cases are slight. However, Table 3-4 confirms that the proposed $k_{r,N}$ - S_W function is better able to predict the timescales of NWP migration than is the Burdine-based function.

Table 3-4. Breakthrough Times at Key Points in the Bench Scale Flow Cell

Location	Breakthrough Times (min)			
	Actual	Validation Simulation	Burdine Simulation	N16 Simulation
Pt. 1	13	13.43	∞	13.00
Pt. 3	119	124.37	125.33	131.30

3.4 Conclusions

Measurement of hysteretic k_{rN}–S_W constitutive relationships for six sand types of varying mean grain diameter revealed a dependence of the function shape and end-points - in particular, the maximum NWP relative permeability, $k_{rN}^{\max}$ - on porous media type. In the bench scale experiment, the majority of NWP flow occurred in the high permeability / coarse sands connected to the source location (i.e., the N10, N16 and N20 sands) where this dependence is not as pronounced as in the low permeability / finer sands examined (i.e., the N30, N40 and N50 sands). Therefore, the bench scale experiment did not well illustrate (through comparison of the validation simulation and N16 simulation predictions to experimental results) the

influence of porous media type-dependent k_{rN} –S_W relationships on predictions of a NWP release. However, Chapter 4 will examine the implications of porous media type-dependent k_{rN} –S_W functions on the distribution and time-scales of NWP migration at the field scale, and in bench scale experiments where NWP flow occurs in porous media where $k_{rN}^{\max}$ values are significantly less than 1.0.

The bench scale experiment provides the first robust data set suitable for validating multiphase flow numerical models for the case of a finite volume DNAPL release into saturated, heterogeneous porous media. Spatial and temporal comparisons demonstrate the validity of the k_{rN} -S_W constitutive relationships of Gerhard and Kueper (2003b) for complex DNAPL migration in heterogeneous porous media in at least two dimensions. Simulations, in which the model employed an analogy-based relative permeability function based on an extension of the work of Burdine (1953), revealed that accurate prediction of the pattern of NWP migration, as well as temporal aspects such as key location arrival time and breakthrough time was not possible. The numerical model requires utilisation of a robust k_{rN}–S_W constitutive relationship that accounts for all the physics of two phase flow in porous media at the local scale (e.g., Gerhard and Kueper, 2003b) and k_{rN}–S_W function parameter values explicitly determined for the porous media being examined.

3.5 References

Amaefule, J.O., and L.L. Handy, The effect of interfacial tensions on relative oil/water permeabilities of consolidated porous media, *Society of Petroleum Engineering Journal, June,* 1982.

Braun, E.M., and R.F. Holland, Relative permeability hysteresis: Laboratory measurement and conceptual model, SPE 69th Annual Technical Conference and Exhibition, New Orleans, September 25-28, 1994.

Brewster, M.L., A.P. Annan, J.P. Greenhouse, B.H. Kueper, G.R. Oldhoeft, J.D. Redman, and K.A. Sander, Observed migration of a controlled DNAPL release by geophysical methods, *Ground Water, 33*(6), 977-987, 1995.

Brooks, R.H., and A.T. Corey, *Hydraulic Properties of Porous Media*, Hydrology Paper 3, Civil Engineering Department, Colorado State University, Fort Collins, 1964.

Burdine, N.T., Relative permeability calculations from pore size distribution data, *Petroleum Transactions, AIME, 198*, 71-78, 1953.

Dane, J.H., C. Hofstee, and A.T. Corey, Simultaneous measurement of capillary pressure, saturation, and effective permeability of immiscible liquids in porous media, *Water Resources Research, 34*(12), 3687-3692, 1998.

Dekker, T.J., and L.M. Abriola, The influence of field-scale heterogeneity on the infiltration and entrapment of dense, nonaqueous phase liquids in saturated formations, *Journal of Contaminant Hydrology, 42,* 197-218, 2000.

Demond A.H., and P.V. Roberts, Estimation of two phase relative permeability relationships for organic liquid contaminants, *Water Resources Research, 29*(4), 1081-1090, 1993.

Demond, A.H., and P.V. Roberts, An examination of relative permeability relations for two phase flow in porous media, *Water Resources Bulletin, 23*(4), 61-628, 1987.

Dixit, A.B., S.R. McDougall, and K.S. Sorbie, A pore-level investigation of relative permeability hysteresis in water-wet systems, *Society of Petroleum Engineers,* SPE Paper 37233, 1997.

Dury, O., U. Fischerm and R. Schulin, A comparison of relative nonwetting phase permeability models, *Water Resource Research, 35*(5), 1481-1493, 1999.

Essaid, H.I., W.N., Herkelrath, and K.M. Hess, Simulation of fluid distributions observed at a crude oil spill site including hysteresis, oil entrapment, and spatial variability of hydraulic properties, *Water Resources Research, 29*(6), 1753-1770, 1993.

Fischer, U., R. Schulin, M. Keller, and F. Stauffer, Experimental and numerical investigation of soil vapour extraction, *Water Resources Research, 32*(12), 3413-3427, 1996.

Fulcher, R.A., Jr., T. Ertekin, and C.D. Stahl, Effect of capillary number and its constituents on two-phase relative permeability curves, *Journal of Petroleum Technology, February,* 249-260, 1985.

Gerhard, J.I., B.H. Kueper, and G.R. Hecox, The influence of waterflood design on the recovery of mobile DNAPLs, *Ground Water, 36*(2), 283-292, 1998.

Gerhard, J.I., and B.H. Kueper, Capillary pressure characteristics necessary for simulation DNAPL infiltration, redistribution, and immobilization in saturated porous media, *Water Resources Research, 39*(8), SBH71-SBH717, 2003a.

Gerhard, J.I., and B.H. Kueper, Relative permeability characteristics necessary for simulating DNAPL infiltration, redistribution, and immobilization in saturated porous media, *Water Resources Research, 39*(8), SBH81-SBH816, 2003b.

Gerhard, J.I., and B.H. Kueper, Influence of constitutive model parameters on the predicted migration of DNAPL in heterogeneous porous media, *Water Resources Research, 39*(8), SBH41-SBH413, 2003c.

Gerhard, J.I., B.H. Kueper, G.R. Hecox, and E.J. Schwarz, Site-specific design for dual phase recovery and stabilisation of pooled DNAPL, *Groundwater Monitoring and Remediation, 21*(2), 71-99, 2001.

Glass, R.J., T.S. Steenhuis, and J.-Y. Parlange, Mechanism for finger persistence in homogeneous, unsaturated, porous media: Theory and verification, *Soil Science, 148*(1), 60-70, 1989.

Illangasekare, T.H., J.L. Ramsey Jr., K.H. Jensen, and M.B. Butts, Experimental study of the movement and distribution of dense organic contaminants in heterogeneous aquifer, *Journal of Contaminant Hydrology, 20*, 1-25, 1995.

Kamon, M., K. Endo, and T. Katsumi, Measuring the k-s-p relations on DNAPLs migration, *Engineering Geology, 70*(3-4), 351-363, 2003.

Kueper, B.H., W. Abbot, and G. Farquhar, Experimental observations of multiphase flow in heterogeneous porous media, *Journal of Contaminant Hydrology, 5*, 83-95, 1989.

Kueper, B.H., and E.O. Frind, Two phase flow in heterogeneous porous media: 2. Model application, *Water Resources Research, 27*(6), 1059-1070, 1991b.

Kueper, B.H., J.D. Redman, R.C. Starr, S. Reitsma, and M. Mah, A field experiment to study the behaviour of tetrachloroethylene below the watertable: Spatial distribution of residual and pooled DNAPL, *Journal of Ground Water, 31*(5), 756-766, 1993.

Kueper, B.H., and J.I. Gerhard, Variability of point source infiltration rates for two-phase flow in heterogeneous porous media, *Water Resources Research, 31*(12), 2971-2980, 1995.

Land, C.S., Comparison of calculated with experimental imbibition relative permeability, *Society of Petroleum Engineers Journal,* 419-425, 1971.

Lefebvre du Prey, E.J., Factors affecting liquid-liquid relative permeabilities of a consolidated porous medium, *Society of Petroleum Engineers Journal, 13*(1), 39-47, 1973.

Lemke, L.D., L.M. Abriola, and P. Goovaerts, Dense nonaqueous phase liquid (DNAPL) source zone characterization: Influence of hydraulic property correlation on predictions of DNAPL infiltration and entrapment, *Water Resources Research, 40*(12), 1-18, 2004.

Lenhard, R.J., and J.C. Parker, A model for hysteretic constitutive relations governing multiphase flow: 2. Permeability saturation relations, *Water Resources Research, 23*(12), 2197-2206, 1987.

Lin, C., G.F. Pinder, and E.F. Wood, Water and trichloroethylene as immiscible fluids in porous media, Research Report 83-WR-2, Princeton University, Princeton, New Jersey, USA, 1982

Luckner, L., M.Th. van Genuchten, and D.R. Nielsen, A consistent set of parametric models for the two phase flow of immiscible fluids in the subsurface, *Water Resources Research, 25*(10), 2187-2193, 1989.

Melrose, J.C., Interfacial phenomena as related to oil recovery mechanisms, *The Canadian Journal of Chemical Engineering, 48*, 638-644, 1970.

Miller, C.D., Immiscible fluids in layered porous media: Examples of accessibility and hysteresis, M.Sc. thesis, Colorado State University, Fort Collins, 1997.

Morgan, J.T., and D.T. Gordon, Influence of pore geometry on water-oil relative permeability, *Journal of Petroleum Technology, 22*, 1199-1208, 1970.

Mualem, Y., A new model for predicting the hydraulic conductivity of unsaturated porous media, *Water Resources Research, 12*(3), 513-522, 1976.

Naar, J., R.J. Wygal, and J.H. Henderson, Imbibition relative permeability in unconsolidated porous media, *Society of Petroleum Engineers Journal, March,* 1962.

O'Carroll, D.M., S.A. Bradford, and L.M. Abriola, Infiltration of PCE in a system containing spatial wettability variations, *Journal of Contaminant Hydrology, 73,* 39-63, 2004.

Oostrom, M., C. Hofstee, R.C. Walker, and J.H. Dane, Movement and remediation f trichloroethylene in a saturated porous medium. 1. Spill behaviour and initial dissolution, *Journal of Contaminant Hydrology, 37,* 159-178, 1999.

Osoba, J.S., J.G. Richardson, J.K. Kerver, J.A. Hafford, and P.M. Blair, Laboratory measurements of relative permeability, *Petroleum Transactions, AIME, 192,* 47-54, 1951.

Robin, M.J.L., E.A. Sudicky, R.W. Gillham, and R.G. Kachanowski, Spatial variability of Strontium distribution coefficients and their correlation with hydraulic conductivity in the Canadian Forces Base Borden aquifer, *Water Resources Research, 27*(10), 2619-2632, 1991.

Schwille, F., *Dense Chlorinated Solvents in Porous and Fractured Media Model Experiments*, 146 pp. Translated by J.F. Pankow, Lewis Publishers, Chelsea, MI, 1988.

Silliman, S.E., Laboratory study of chemical transport to wells within heterogeneous porous media, *Water Resources Research, 37*(7), 1883-1892, 2001.

Stonestrom, D.A., and J. Rubin, Air permeability and trapped-air content in two soil, *Water Resources Research, 25*(9), 1959-1969, 1989b.

Wardlaw, N.C., and J.P. Cassan, Estimation of recovery efficiency by visual observation of pore systems in reservoir rock, *Bulletin of Canadian Petroleum Geologists, 26*(4), 572-585, 1978.

Wei, J.Z., and O.B. Lile, Influence of wettability and saturation sequence on relative permeability hysteresis in unconsolidated porous media, *Society of Petroleum Engineering,* SPE Paper 25282, 1992.

Welty, C., and M.M. Elsner, Constructing correlated random fields in the laboratory for observations of fluid flow and mass transport, *Journal of Contaminant Hydrology, 202*(1-4), 192-211, 1997.

White, M.D., and M. Oostrom, Modelling surfactant-enhanced nonaqueous phase liquid remediation of porous media, *Soil Science, 163*, 931-940, 1998.

CHAPTER 4 – FIELD SCALE IMPACTS OF SPATIALLY VARIABLE RELATIVE PERMEABILITY IN HETEROGENEOUS MULTIPHASE SYSTEMS

4.1 Introduction

Numerous physical experiments have been conducted to examine the factors that affect the extent of nonwetting phase (NWP) migration at the laboratory or bench scale (e.g. Schwille, 1988; Kueper *et al*., 1989; Illangasekare *et al.,* 1995; Hofstee *et al.,* 1997) and at the field scale (Kueper *et al.,* 1993; Brewster *et al.,* 1995). Numerical modelling studies examining the factors governing NWP migration (e.g. Kueper and Frind, 1991b; Essaid *et al.*, 1993; Kueper and Gerhard, 1995; Dekker and Abriola, 2000; Lemke *et al.,* 2004) are also commonly conducted, as field experiments are generally prohibited, accidental spills are difficult to characterise (e.g. Poulson and Kueper, 1992; Kueper *et al.,* 1993; Essaid *et al.,* 1993) and field scale heterogeneity is rarely recreated in the lab (Kueper *et al.,* 1993; Kueper and Gerhard, 1995; Imhoff *et al.,* 2003).

Very few experiments, either physical or numerical, have specifically examined the factors governing the rate of NWP migration at the field scale (Gerhard and Kueper, 2003c). Physical experiments conducted to date generally focus on drainage processes (e.g. Kueper and Frind, 1991a), and lack the ability to measure time-varying NWP saturation distributions and therefore rely on system endpoints (e.g. Rathfelder *et al.,* 2003). In addition numerical studies previously published often have not been satisfactorily validated for redistribution and entrapment processes (Gerhard and Kueper, 2003c).

The saturation-dependent rate of DNAPL migration through porous media is typically described by macroscopic relative permeability constitutive relationships.

Gerhard and Kueper (2003b) developed an analogy - based relative permeability constitutive model that was validated for transient, hysteretic two phase flow in one-dimensional homogeneous porous media experiments. That study demonstrated that failing to account for key relative permeability constitutive relationship characteristics prevents a numerical model from successfully reproducing the spatial and temporal behaviour observed in laboratory experiments.

The experiments conducted in Chapter 3 further validated the constitutive relationships developed by Gerhard and Kueper (2003a,b) for NWP flow in a two-dimensional heterogeneous porous media at the bench scale. In addition, this study revealed that the shape and end-point locations of the NWP relative permeability, $k_{r,N}$, functions are dependent on porous media type. However, it is not known whether this dependence is significant for predicting the evolution of field scale NWP releases. Typically, while capillary pressure-saturation relationships are scaled to local intrinsic permeability in multiphase flow modelling, a single relative permeability-saturation relationship is assumed to apply throughout a heterogeneous domain.

The purpose of this study is to examine the influence of variable relative permeability as a function of porous media type on predictions of fixed-volume DNAPL releases in heterogeneous porous media at the field and bench scale. Three suites of numerical simulations are carried out in multiple realisations of a spatially correlated, random hydraulic conductivity field to meet this objective. In this way, it can be determined if this newly discovered aspect of relative permeability is critical and therefore needs to be measured and incorporated into field scale numerical simulators for practical applications.

4.2 Maximum NWP Relative Permeability

Nonwetting phase relative permeability has been shown to be a function of wetting phase (WP) saturation, S_W, and saturation history, with distinct non-zero endpoints of emergence saturation (S_W^M) and extinction saturation (S_W^X) (Gerhard and Kueper, 2003b). In unconsolidated porous media, NWP relative permeability (k_{rN}-S_W) functions generally exhibit a "reverse hysteresis pattern" where imbibition k_{rN} is greater than drainage k_{rN} for some or all of the relevant S_W range. The 'turn-around point' between primary drainage and main secondary imbibition conditions is marked by the minimum WP residual saturation, S_r, and the maximum NWP relative permeability, $k_{rN}^{\max}$. Figure 4-1 presents a typical reverse hysteresis pattern NWP relative permeability curve and identifies the endpoint parameters S_W^M, S_W^X, S_r, and $k_{rN}^{\max}$ (see Gerhard and Kueper, 2003b for a detailed description of the other parameters defining NWP relative permeability curves).

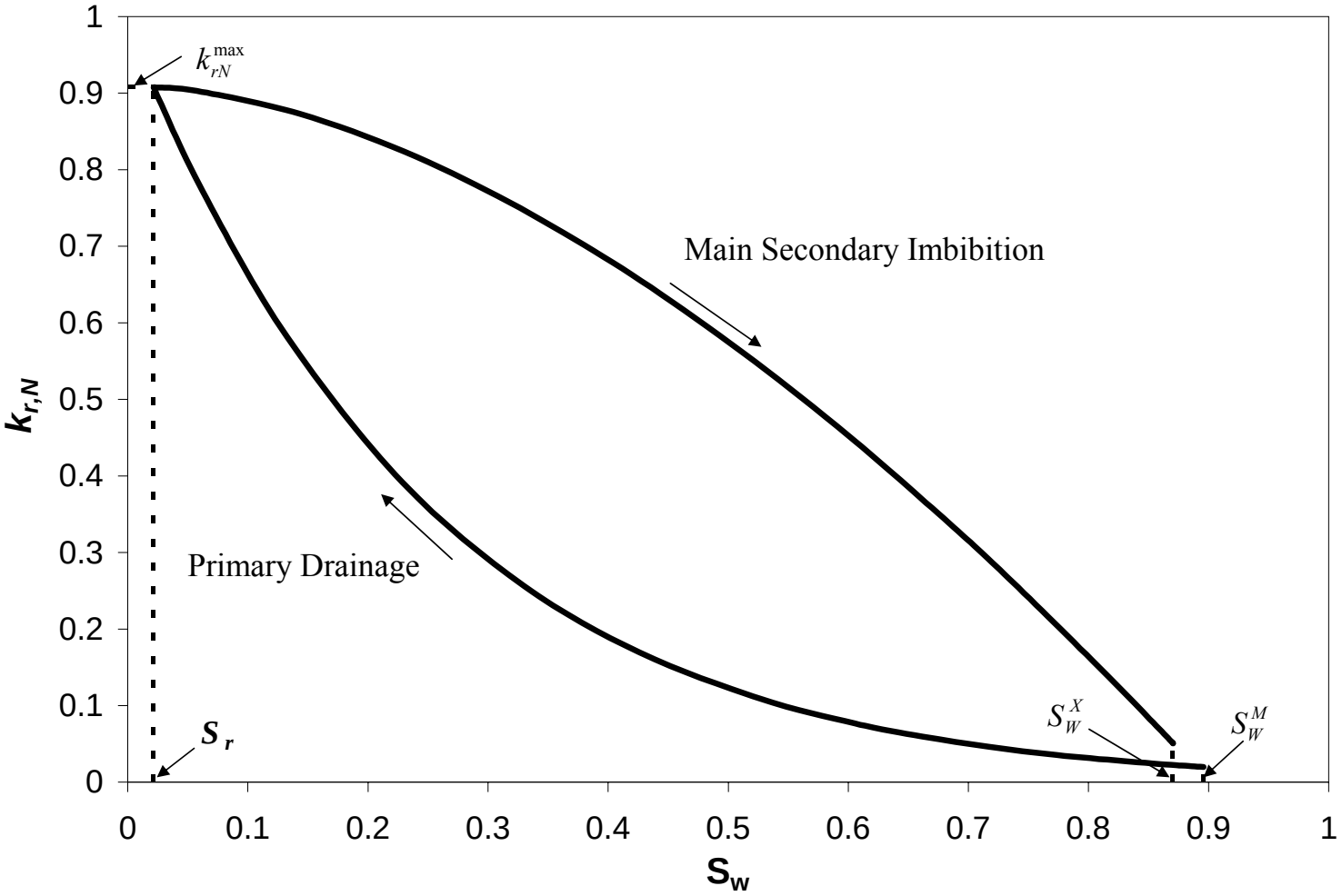

Figure 4-1. Typical reverse hysteresis pattern NWP relative permeability curve.

Numerical models often employ $k_{rN}^{\max}$ values of 1.0 (e.g., Kueper and Frind, 1991a; Rathfelder *et al.,* 2003; Lemke *et al.,* 2004; O'Carroll *et al.,* 2004) in spite of the fact that published NWP relative permeability curves typically exhibit $k_{rN}^{\max}$ values less than unity (e.g. Naar *et al*., 1962; Lin *et al*., 1982; Stonestrom and Rubin, 1989; Demond and Roberts, 1993; Dury *et al*., 1999; Gerhard and Kueper, 2003b). Geffen *et al.* (1951), examining NWP relative permeability from an oil reservoir engineering perspective, suggests that $k_{rN}^{\max}$ will approach unity (100%) in strongly wetting systems because the WP, at residual saturations, will occupy the smallest pores and therefore not significantly block NWP flow (Geffen *et al.,* 1951; Demond and Roberts, 1987). However, Demond and Roberts (1993) suggest that $k_{rN}^{\max}$ values significantly less than unity are likely as further reduction of WP saturations below S_r through film flow is not likely to occur at the time-scales and flow rates typical in a contaminant hydrogeology context.

Chapter 3 presents a series of experiments examining the influence of porous media size on NWP relative permeability. NWP relative permeability curves were measured for six sands of differing mean grain size, referred to as the N10, N16, N20, N30, N40 and N50 sands corresponding to the mesh number that retains each of the sands. The experimental curves were fit with the relative permeability constitutive relationships presented in Gerhard and Kueper (2003b).

Each of the sands exhibited a roughly consistent emergence saturation and extinction saturation, but showed a distinct trend for $k_{rN}^{\max}$, the corresponding wetting phase residual saturation, and a number of the function curvature parameters related to $k_{rN}^{\max}$ (i.e., the NWP relative tortuosity exponent, τ, and the incremental saturation target beyond emergence / extinction, ΔS_W^* - see Gerhard and Kueper, 2003a) as a

function of mean grain diameter (see Chapter 3). The N10 sand relative permeability curve also exhibited a decreased degree of hysteresis, relative to the other sand types, that has been attributed to the fact that this sand was considerably less 'round' and had a much rougher surface than any of the other sand types examined (see Appendix A). However, the experimental results reveal that $k_{rN}^{\max}$ values ranged from 0.37 for the fine grained N50 sand to 0.91 for the coarse grained N16 sand.

Table 4-1 presents a summary of all readily available $k_{rN}^{\max}$ values extracted from $k_{r,N}(S_W)$ curves reported in the contaminant hydrogeology literature for unconsolidated porous media, and the experimental conditions under which they were measured. As can clearly be seen, $k_{rN}^{\max}$ values can vary over a considerable range, and appear to be a function of porous media type. Chapter 3 presents a detailed discussion of the influence of mean grain diameter on the relative proportion of pore space occupied by the WP at residual WP saturations. It is this relative volume of trapped WP, and its resulting intereference with NWP flow (via pathway blockage and increased NWP tortuosity), that results in the variability of $k_{rN}^{\max}$ as a function of porous media type.

Figure 4-2 plots the $k_{rN}^{\max}$ values presented in Table 4-1 as a function of porous media mean grain diameter, including the results of the experiments conducted in Chapter 3, but omitting studies for which porous media mean grain diameter was not reported or could not be inferred. $k_{rN}^{\max}$ values range from 0.22 for a Borden aquifer sand with a mean grain diameter of 380 μm (Demond and Roberts, 1993) to 0.91 for the N16 sand (mean grain diameter = 1295 μm) of this study. The included data have been fit with a Pearl curve best-fit function to relate mean grain diameter to $k_{rN}^{\max}$. A Pearl curve was selected because upper and lower bounds of $k_{rN}^{\max}$ can be specified to

influence the shape of the best-fit function and limit $k_{rN}^{\max}$ to values greater than zero and less than unity regardless of mean grain size. $k_{rN}^{\max}$ is expected to asymptotically approach an upper limit with increasing mean grain diameter as the influence of WP film presence on the rate of NWP flow becomes negligible. $k_{rN}^{\max}$ is also expected to asymptotically approach a lower limit greater than zero with decreasing mean grain diameter to a grain size too fine for any WP displacement to be possible (except through film flow). Best-fit upper and lower limits for the Pearl function describing the data presented in Figure 4-2 were 0.95 and 0.3, respectively.

With the exception of the $k_{rN}^{\max}$ value reported by Gerhard and Kueper (2003b) for an artificially engineered wide pore-size distribution (PSD) sand, the reported $k_{rN}^{\max}$ values demonstrate a clear trend that is well characterised by the Pearl curve. Figure 4-2 presents the Pearl curve best-fit function as well as R^2 values for both the entire data set presented in Table 4-1 as well as only the experimental data collected in this study. The best-fit Pearl function is also given in Equation 4-1:

$$k_{rN}^{\max} = 0.3 + \left[\frac{0.95 - 0.3}{1 + 25.87 \cdot e^{-0.00469 \cdot d_m}} \right] \tag{4-1}$$

where d_m is the mean grain diameter.

Table 4-1. Summary of $k_{rN}^{\max}$ Data for Unconsolidated Porous Media Available in the Contaminant Hydrogeology Literature

Data Source	Porous Media Description	Fluid Pair	Residual WP Saturation	Intrinsic Permeability (m^2)	Porosity	Mean Grain Diameter (μm)	$k_{rN}^{\max}$
This Study	N10 sand	water / HFE-7500	0.023	2.62×10^{-10}	0.36	2180	0.84
	N16 sand		0.022	1.90×10^{-10}	0.38	1295	0.91
	N20 sand		0.031	1.81×10^{-10}	0.34	1015	0.79
	N30 sand		0.034	7.10×10^{-11}	0.33	700	0.69
	N40 sand		0.070	7.40×10^{-11}	0.31	513	0.44
	N50 sand		0.093	1.84×10^{-11}	0.36	363	0.37
Gerhard and Kueper (2003b)	Narrow PSD silica sand	water / HFE-7200	0.130	2.10×10^{-10}	0.32	960	0.85
	Wide PSD silica sand		0.050	1.25×10^{-11}	0.25	350	0.8
Demond and Roberts (1993)	Well sorted quartz sand – Borden Aquifer	*n*-dodecane / water	0.086	8.50×10^{-12}	0.33	380[a]	0.38
		o-xylene / water	0.220	8.80×10^{-12}			0.40
		n-butyl acetate / water	0.250	7.80×10^{-12}			0.22
Lin *et al.* (1982)	Fisher S-150	water / TCE	0.350	ND	ND	215[b]	0.40
Stonestrom and Rubin (1989b)	Oakley sand	water / air	0.280	1.28×10^{-11}	0.37	553[c]	0.69
Naar *et al.* (1962)	Glass spheres – Large PSD	oil / air	0.110	ND	ND	ND	0.88

Notes: ND – No Data; [a] a median grain size range for this sand was reported as 70 – 690 μm in Demond and Roberts (1991), however, no indication was made as to specific mean grain size of the samples tested for NWP relative permeability, therefore, the average of the reported mean grain diameter will be assumed for each reported $k_{rN}^{\max}$ value; [b] Fisher S-150 is described as a fine sand, but coarser than 80 mesh (180 μm) (Fisher Scientific, International Ltd., NH, USA). As fine sands are defined as ranging in grain diameter from 120 μm to 250 μm (Folk, 1980), the S-150 sand was assumed to range from 180 μm to 250 μm; therefore, the mean grain diameter of this sand type was taken to be 215 μm; [c] as determined from the particle size distribution chart presented in Stonestrom (1987).

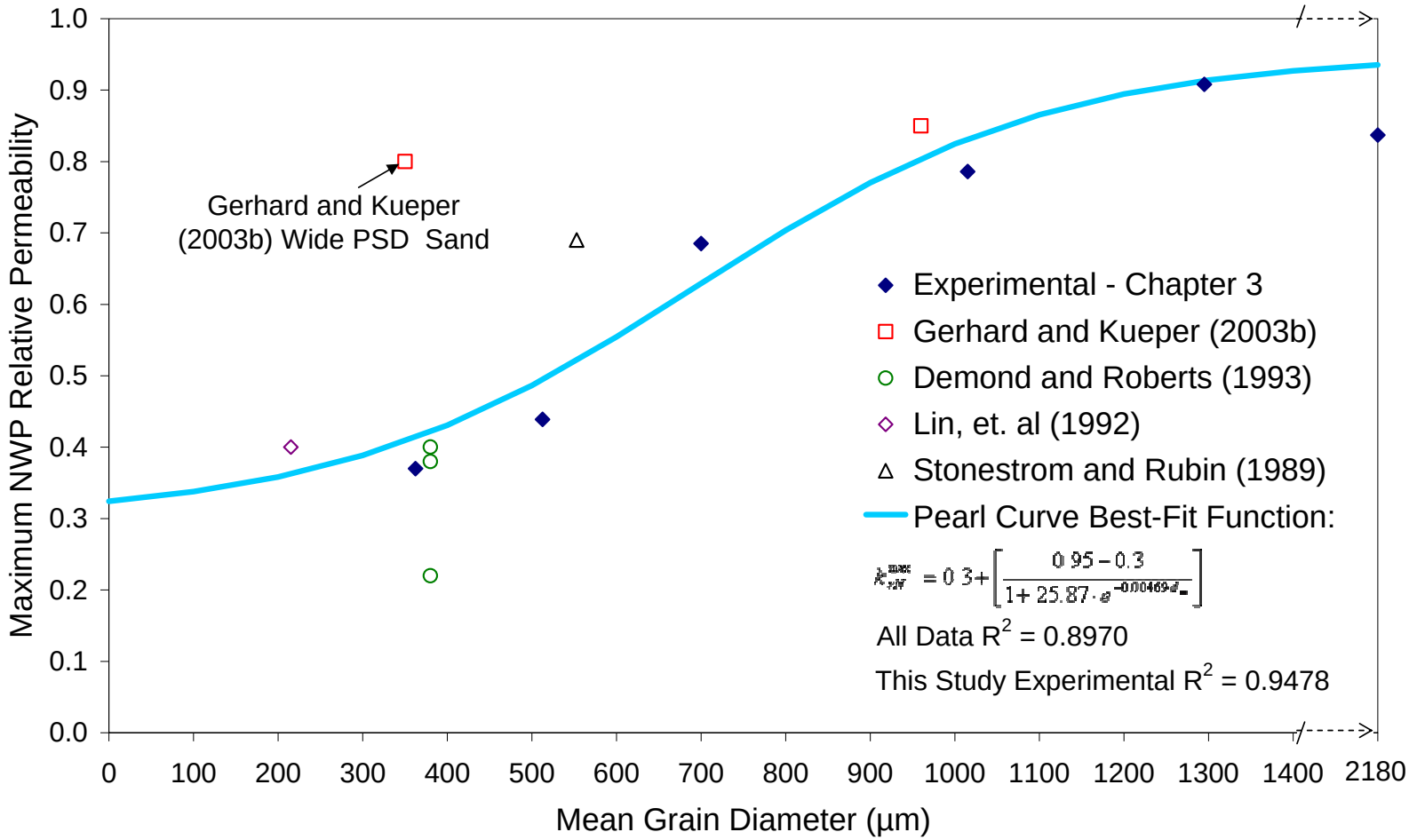

Figure 4-2. $k_{rN}^{\max}$ **as a function of porous media mean grain diameter.**

In addition to assuming a $k_{rN}^{\max}$ value of unity, most numerical models employ a non-hysteretic relative permeability curve (e.g. Kueper and Frind, 1991a; Rathfelder *et al.,* 2003; Lemke *et al.,* 2004; O'Carroll *et al.,* 2004). In addition, with the exception of O'Carroll *et al.* (2004) who distinguished between NWP relative permeability curves for organic-wet versus water-wet materials when attempting to simulate a DNAPL release in a bench scale flow cell experiment, none of these studies have examined the influence of variable NWP relative permeability on the timescales and migration patterns of a DNAPL release in heterogeneous porous media.

Variability of k_{rW} is also expected, however much less data is available to confirm this. In any case, it is expected that for simulations of NWP releases in heterogeneous materials, subtle details of k_{rW} shape variability will not be significant.

4.3 Methods

4.3.1 Model Formulation

The numerical model utilised in this study is the three-dimensional, finite difference two phase flow model DNAPL-3D (Gerhard *et al.,* 1998) (the migration sub-model of DNAPL3D-MT presented in Chapter 5 and Appendix F), modified to accommodate spatially variable relative permeability functional relationships. Details regarding the numerical formulation of DNAPL-3D can be found elsewhere (Gerhard *et al.,* 1998; Appendix F), therefore, only a brief overview of the model will be presented here.

The continuity equations for mass balance of a wetting (subscript 'W') and nonwetting (subscript 'N') phase, given laminar flow conditions and the assumption of no mass transfer between phases can be written (Bear, 1972):

$$-\frac{\partial}{\partial x_i}\left[\rho_W q_{Wi}\right]+Q_W=\frac{\partial}{\partial t}\left[\phi\rho_W S_W\right] \qquad i=x,y,z \tag{4-2}$$

$$-\frac{\partial}{\partial x_i}\left[\rho_N q_{Ni}\right]+Q_N=\frac{\partial}{\partial t}\left[\phi\rho_N S_N\right] \qquad i=x,y,z \tag{4-3}$$

where ρ_W and ρ_N are the wetting and nonwetting phase densities, q_{Wi} and q_{Ni} are the respective fluxes, Q_W and Q_N are the respective phase source / sink terms, t is time, x, y, and z are the spatial coordinates, ϕ is the porosity of the porous medium, and S_W and S_N are the respective phase saturations.

Substituting the multi-phase extension of Darcy's law into Equations 4-2 and 4-3, assuming wetting phase and porous medium compressibility (i.e., accounting for storage effects), and noting that phase pressures are coupled through the relationship for capillary pressure, $P_C(S_W)=P_N-P_W$, and that phase saturations are related through $S_W+S_N=1$, the problem reduces to the simultaneous solution of:

$$\frac{\partial}{\partial x_i}\left[\frac{-k_{i,j}k_{r,W}}{\mu_W}\left(\frac{\partial P_W}{\partial x_j}+\rho_W g\frac{\partial z}{\partial x_j}\right)\right]+S_w(\alpha+\phi\beta_W)\frac{\partial P_W}{\partial t}-\phi\frac{\partial S_W}{\partial t}=0 \quad i,j=x,y,z \tag{4-4}$$

$$\frac{\partial}{\partial x_i}\left[\frac{-k_{i,j}k^i_{r,N}}{\mu_N}\left(\frac{\partial(P_c+P_W)}{\partial x_j}+\rho_N g\frac{\partial z}{\partial x_j}\right)\right]+(1+S_W)(\alpha)\frac{\partial P_W}{\partial t}+\phi\frac{\partial S_W}{\partial t}=0 \quad i,j=x,y,z \tag{4-5}$$

where k_{ij} is a second – order tensor defining porous media intrinsic permeability, $k_{r,W}$ is the relative permeability to the wetting phase, k^i_{rN} is the spatially variable relative permeability to the nonwetting phase, μ_W and μ_N are the respective phase viscosities, P_W is the wetting phase pressure, P_C is the capillary pressure, α is the porous medium compressibility, β_W if the wetting phase compressibility, and g is acceleration due to gravity.

The capillary pressure – saturation and relative permeability – saturation constitutive relationships presented in Gerhard and Kueper (2003a) and (2003b), respectively, close the presented system of equations. A seven – point node centred,

finite difference scheme was utilised to discretise Equations 4-4 and 4-5. The developed numerical scheme is fully implicit with second - order accurate spatial operators and a first – order accurate temporal derivative (Rosenburg, 1969). The internode absolute permeabilities are calculated using harmonic means, and the internode relative permeabilities are upstream – weighted with respect to fluid saturation (Aziz and Settari, 1979). The set of Equations 4-4 and 4-5 are nonlinear due to the dependence of capillary pressure and relative permeability on saturation. The nonlinearities are handled with full Newton-Raphson iteration, and the preconditioned system is solved with a modified ORTHOMIN routine (Behie and Forsyth, 1984). Thus, the model solves the evolution of phase saturations and pressures in space and time. Dissolution is ignored as it is assumed that mass transfer influences on NWP migration is minimal at the timescales of infiltration and redistribution.

4.3.2 Spatially Variable Relative Permeability

Numerical modelling studies in heterogeneous porous media are often conducted using realisations of a porous media as characterised by statistical measures of intrinsic permeability, k_i (e.g. Kueper and Gerhard, 1995; Gerhard and Kueper, 2003c; Lemke *et al.,* 2004; and Phelan *et al.,* 2004). Porous media properties, including displacement pressure (Kueper and Gerhard, 1995), porosity (Lemke, *et al.,* 2004), and wettability (Phelan *et al.,* 2004), are often correlated to the k_i field to examine the influence of the spatial variability of these parameters on NWP flow. Similarly, the k_i fields generated for this study will be correlated to mean grain diameter, d_m, through the Kozeny – Carmen equation (Bear, 1972):

$$k = \frac{d_m^2}{180} \frac{n^3}{(1-n)^2} \tag{4-6}$$

where n is porosity.

Combining Equation 4-6 with Equation 4-1 gives the functional relationship between k_i and $k_{rN}^{\max}$:

$$k_{rN}^{\max} = 0.3 + \left[\frac{0.9 - 0.3}{1 + 25.87 \cdot e^{-0.00469 \cdot \left[k \frac{\left(180(1-n)^2\right)}{n^3} \right]^{\frac{1}{2}}}} \right] \tag{4-7}$$

Since $k_{rN}^{\max}$ provides a key endpoint for the k_{rN} - S_W function (much like P_d with the P_C-S_W curve), this effectively correlates the entire $k_{rN}(S_W)$ curve to k_i, creating a spatially variable k_{rN} field.

As presented in Chapter 3, the experimental results also showed a distinct trend for wetting phase residual saturation, and the relative permeability curvature parameters τ and ΔS_W^*, as a function of mean grain diameter; this is as expected since these parameters are inherently linked to $k_{rN}^{\max}$. This study will employ a constant drainage and imbibition pore size distribution index throughout the simulation domain (λ_d = 4.0 and λ_i = 3.0; see Table 4-2). When this approach is adopted, the best-fit functions for the k_{rN} - S_W data presented in Chapter 3 show constant τ and ΔS_W^* on drainage and variable τ and ΔS_W^* on imbibition (this contrasts with the trends exhibited in Chapter 3 when independently measured pore size distribution index values were utilised). Therefore, for the purposes of numerical modelling, the parameters, S_r, τ_i, and ΔS_W^{*i} will be correlated to $k_{rN}^{\max}$ as described by the equations in Table 4-2.

4.3.3 Simulations Conducted

Three suites of numerical simulations, encompassing a total of 52 porous media realisations and 104 individual simulations were conducted in this study. The

general format for each suite was to statistically compare results from NWP releases in identical heterogeneous porous media domains assuming either a constant NWP relative permeability field (i.e., a single NWP relative permeability curve was assumed to be valid across the entire solution domain), or a variable NWP relative permeability field (i.e., NWP relative permeability was assumed to vary spatially as a function of porous media mean grain diameter). The former represents the best current modelling approach to multiphase systems (when complex hysteresis is accounted for), while the latter acknowledges the newly revealed dependence of local $k_{rN}^{\max}$ on porous media type.

Table 4-2 lists the NWP relative permeability parameter values or functional relationships required by the constitutive relationship of Gerhard and Kueper (2003b) employed for both the constant NWP relative permeability simulations and the variable (correlated) NWP relative permeability simulations. The $k_{rN}^{\max}$ utilised throughout the simulation domain for the constant $k_{r,N}$ simulations is 0.91, and the $k_{rN}^{\max}$ utilised throughout the variable $k_{r,N}$ simulations is given by Equation 4-7.

Table 4-2. Constitutive Relationship Parameters for Constant and Variable NWP Relative Permeability

Parameter	Notation	Value	
		Constant $k_{r,N}$	Variable $k_{r,N}$
Porosity	ϕ	0.35	0.35
Emergence saturation	S_W^M	0.86	0.86
Maximum NWP residual saturation (extinction saturation)	$\left(1 - S_W^X\right)$	0.16	0.16
Wetting phase residual saturation	S_r	0.022	$S_r = 0.0188 \cdot k_{rN}^{\max(-1.606)}$
Terminal / entry pressure ratio	κ	0.62	0.62
Brooks – Corey drainage PSD index	λ_d	4.0	4.0
Brooks - Corey imbibition PSD index	λ_i	3.0	3.0

Drainage NWP relative tortuosity exponent	τ_d	3.0	3.0
Imbibition NWP relative tortuosity exponent	τ_i	0.02	$\tau_i = 0.0148 \cdot k_{rN}^{\max(-3.225)}$
Incremental saturation target for drainage beyond emergence	ΔS_W^{*d}	1.0	1.0
Incremental saturation target for imbibition beyond extinction	ΔS_W^{*i}	0.05	$\Delta S_W^{*i} = 0.059 \cdot k_{rN}^{\max(1.601)}$

Suite 1 (Very Fine to Fine Sand Aquifer, 60 simulations): each of 30 realisations of a heterogeneous k_i field were employed for a pair of identical NWP releases, the first accounting for variable relative permeability and the second assuming constant relative permeability. Using a mean ln(k_i) of -26.8 m^2, the resultant range of intrinsic permeabilities for Suite 1 is characteristic of a fine to very fine sand aquifer. The aim of this suite was to understand the significance of accounting for variable relative permeability at the field scale.

Suite 2 (Coarse Sand Aquifer, 24 simulations): these releases were repeated for 12 of the k_i fields utilised in Suite 1, except that the k_i values were increased by two orders of magnitude. This has the effect of increasing the mean ln(k_i) to -22.2 m^2 but retaining the subsurface correlation structure of the original fields. The resultant range of intrinsic permeabilities for Suite 2 is characteristic of a coarse sand to gravel aquifer. . The aim of this suite was to investigate the influence of mean aquifer permeability on the significance established with Suite 1.

Suite 3 (Bench Scale Flow Cell, 20 simulations): 10 pairs of releases (variable versus constant k_{rN} - S_W) were conducted using a consistent subdomain of 10 of the k_i fields utilised in Suite 2. The goal of this suite was to allow a comparison of the role of variable k_{rN} - S_W in DNAPL releases at the field scale to those at the bench scale. In effect, this aims to answer the question of whether experimentalists, who

typically employ two-dimensional experimental flow cells at this scale, packed with such coarse sands, would be able to discern the influence of variable k_{rN} - S_W.

All three suites of simulations employed random, spatially correlated k_i fields generated using FGEN 9.1 (Robin *et al.,* 1991) assuming an exponential autocorrelation function. The Leverett (1941) function and a dimensionless displacement pressure (P_{CD}) equal to 0.18557 (Kueper and Frind 1991b) were used to correlate displacement pressure to k_i.

The Suite 1 and 2 (Field Scale) simulations were conducted in a two-dimensional vertical cross-section solution domain 60 m wide by 30 m high. The domain was discretised into 57,600 nodes with a nodal spacing of 0.250 m horizontally and 0.125 m vertically. The Suite 3 (Bench Scale) simulations were conducted in a two-dimensional vertical cross-section solution domain 5 m wide by 3 m high. This domain was discretised into 6000 nodes with a nodal spacing of 0.05 m both horizontally and vertically. For all simulation suites, the domain was initially fully saturated with water and was assigned wetting phase pressures that increased hydrostatically from a watertable coincident with the top boundary. The side boundaries were characterised by fixed wetting phase pressures that increased hydrostatically from 0.0 Pa at the top boundary while permitting the flux of either phase. The bottom boundary was set as impermeable to both fluids.

For Suites 1 and 2, the source boundary was 20 nodes (5.0 m) wide The release was simulated by fixing the flux of NWP through a source located centrally along the top boundary. Fixing the total rate of NWP invasion was necessary to ensure that an identical DNAPL volume entered the domain in an identical amount of time for all simulations. It is acknowledged that an imposed NWP flux source condition is less realistic than one that is constant capillary pressure (Reynolds and

Kueper, 2002). To mimic the realistic input of DNAPL across a wide source area, the fraction of total flux through each source node was weighted according to intrinsic permeability:

$$Flux_{Node} = Flux_{Total} \cdot \left(\frac{k_{Node}}{\sum_{i=1}^{N} k_i} \right) \tag{4-8}$$

where $Flux_{Node}$ is the flux of NWP through a given source node, $Flux_{Total}$ is the total flux through the source boundary, k_{Node} is the intrinsic permeability of a given source node, and N is the total number of nodes in the NWP source boundary. This technique successfully reproduces NWP infiltration behaviour characteristic of more realistic constant capillary pressure source boundaries (e.g., Gerhard and Kueper, 1995).

In each case, a 1,2-DCE DNAPL source was initiated at time t = 0 and was eliminated at t= 5 days, representing the release of 6.25 m^3, or 30 drums, of DNAPL in the field. For Suite 3, the source boundary was a single node (0.05 m) wide, initiated at time t = 0 that was eliminated at t= 20 minutes, representing the release of 1.5 litres of DNAPL in the bench scale apparatus.

Table 4-3 lists the numerical model input parameters utilised for the various suites of simulations.

Table 4-3. Numerical Model Input Parameters

Parameter	Value		
	Suite 1	Suite 2	Suite 3
Wetting phase density	1000 kg/m^3	1000 kg/m^3	1000 kg/m^3
Nonwetting phase density	1260 kg/m^3	1260 kg/m^3	1260 kg/m^3
Wetting phase viscosity	0.001 Pa.s	0.001 Pa.s	0.001 Pa.s
Nonwetting phase viscosity	0.000887 Pa.s	0.000887 Pa.s	0.000887 Pa.s
Interfacial Tension	0.02 N/m	0.02 N/m	0.02 N/m
Matrix compressibility	1.0 x 10^{-7} pa^{-1}	1.0 x 10^{-7} pa^{-1}	1.0 x 10^{-7} pa^{-1}
Wetting phase compressibility	4.4 x 10^{-10} pa^{-1}	4.4 x 10^{-10} pa^{-1}	4.4 x 10^{-10} pa^{-1}

Mean ln k_i	-26.8 m^2	-22.2 m^2	-22.2 m^2
Variance ln k_i	2.0	2.0	2.0
Horizontal correlation length	5.0 m	5.0 m	0.5 m
Vertical correlation length	0.5 m	0.5 m	0.12 m
Horizontal nodal spacing	0.25 m	0.25 m	0.05 m
Vertical nodal spacing	0.125 m	0.125 m	0.05 m
Number of nodes (horizontal)	240	240	100
Number of nodes (vertical)	240	240	60
Dimensionless displacement Pressure	0.18557	0.18557	0.18557

The simulations were analysed for the evolving spatial and temporal characteristics of the migrating NWP body. In particular, the endpoints of migration were compared using the ultimate volume of porous media invaded and the time required for the effective cessation of NWP migration.

4.4 Results

4.4.1 Suite 1

4.4.1.1 Qualitative Results

Figure 4-3a illustrates the NWP saturation distribution after five days (corresponding to the time at which the NWP source condition was terminated) accounting for variable (correlated) k_{rN} for Realisation 2. The background grey scale in the figure represents the intrinsic permeability distribution employed for this realisation, with darker shades corresponding to lower k_i values. Figure 4-3b shows the NWP saturation distribution of the same release in Realisation 2 when constant k_{rN} is assumed in the simulation. The NWP saturation distribution in these two figures is very similar. The boundary condition selected for the source ensures that the majority of NWP enters the domain through the higher k_i nodes. In these nodes, the differences between the $k_{rN}^{\max}$ values in the variable and constant $k_{r,N}$ models are minimal.

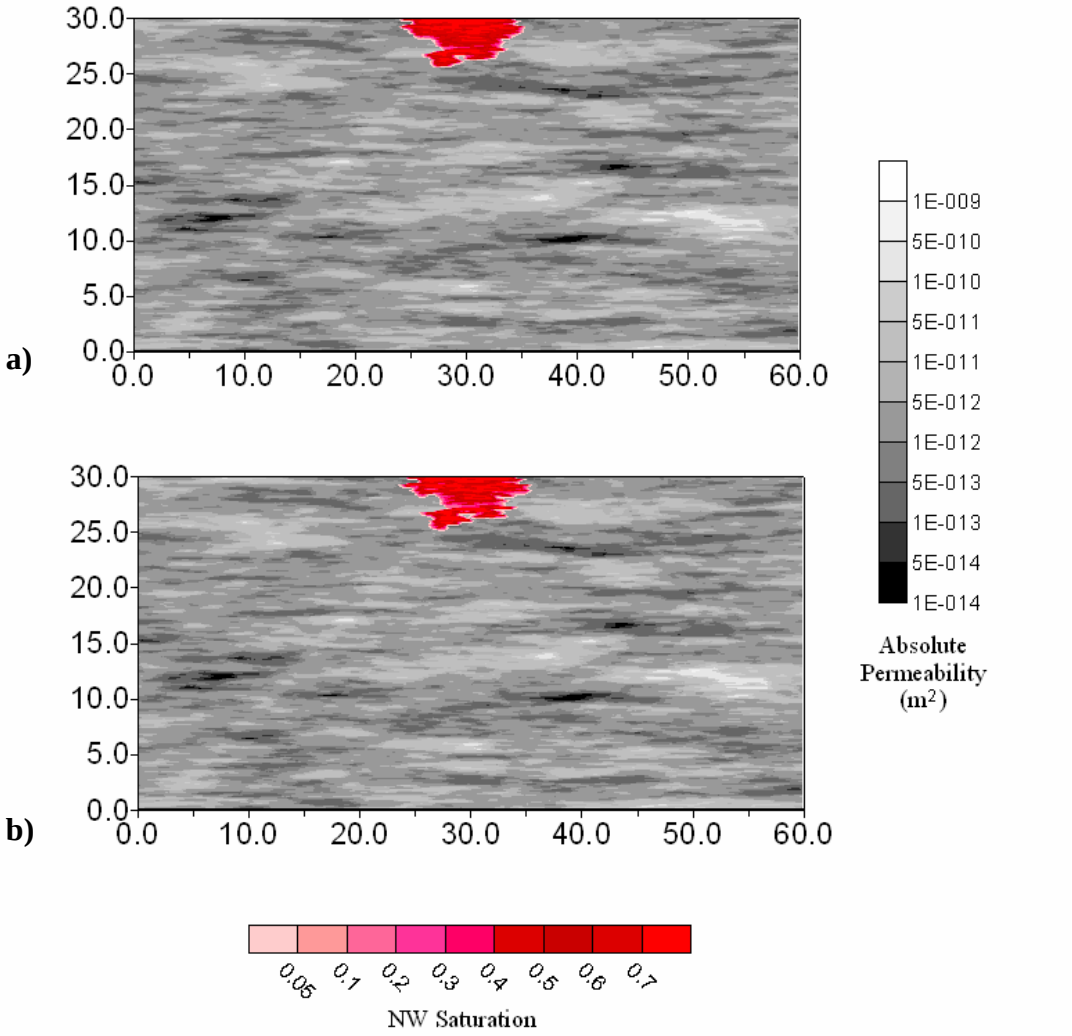

Figure 4-3. NWP saturation distribution for Suite 1, Realisation 2, following 5 days of simulation time: a) accounting for variable $k_{r,N}$; and, b) assuming constant $k_{r,N}$.

Figures 4-4a and 4-4b present the NWP saturation distributions for the variable $k_{r,N}$ case and the constant $k_{r,N}$ case for Realisation 2 following 12 weeks of simulation time, respectively. For the constant $k_{r,N}$ simulation, 12 weeks represents the time at which the number of invaded nodes is 90% of the total that will ultimately be invaded by NWP (i.e., the 90% migration cessation time, t_{90}). However, the t_{90} for the variable $k_{r,N}$ simulation is approximately 1.5 years. The figures illustrate significant differences in the NWP distribution at this time between the two cases. The NWP has migrated further from the source boundary after 12 weeks of migration when constant $k_{r,N}$ is assumed, than when variable $k_{r,N}$ is accounted for in the

simulation. In addition, the saturation distribution of invaded nodes between the two cases shows significant differences. A greater proportion of the invaded nodes have a high NWP saturation (i.e., greater than approximately 0.5) in the variable $k_{r,N}$ case than in the constant $k_{r,N}$ case.

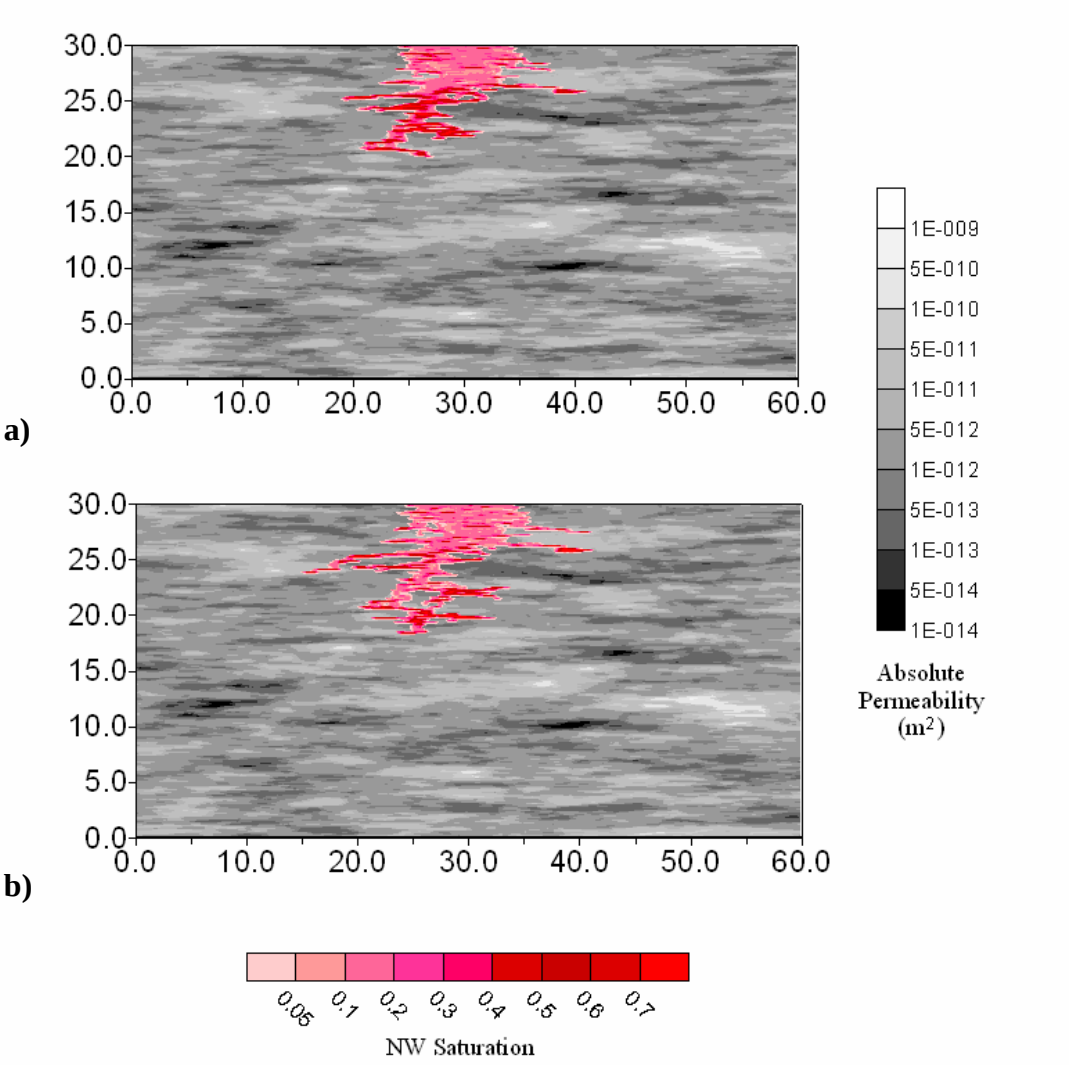

Figure 4-4. NWP saturation distribution for Suite 1, Realisation 2, following 12 weeks of simulation time: a) accounting for variable $k_{r,N}$; and, b) assuming constant $k_{r,N}$.

Figures 4-5a and 4-5b present the NWP saturation distributions for the variable $k_{r,N}$ case and the constant $k_{r,N}$ case for Realisation 2 following 57 years of simulation time, respectively. This time represents the t_{100} for the simulation accounting for variable $k_{r,N}$. The t_{100} for the constant $k_{r,N}$ case, however, occurred after only five years of simulation time. The two figures show differences in the

distribution of NWP following the complete cessation of migration. The NWP migration pattern is deeper and narrower when variable $k_{r,N}$ is accounted for in the simulation, than the distribution pattern that evolves assuming constant $k_{r,N}$.

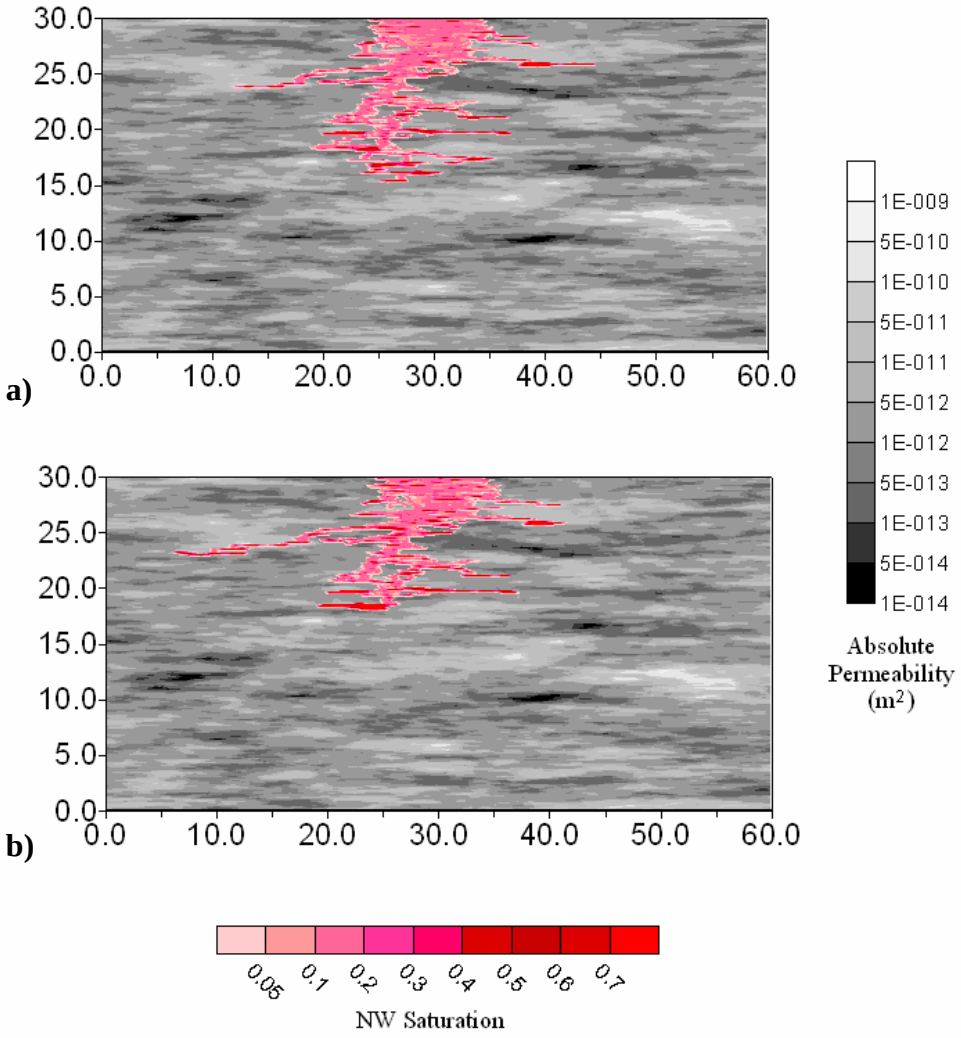

Figure 4-5. NWP saturation distribution for Suite 1, Realisation 2, following 57 years of simulation time: a) accounting for variable $k_{r,N}$; and, b) assuming constant $k_{r,N}$.

The qualitative descriptions included above were found to generally hold for the remaining 29 realisations of Suite 1. Although $k_{r,N}$ is a rate term in the governing equations describing two phase flow, variability of this parameter can have a significant effect on the distribution pattern of the NWP, in addition to significantly affecting NWP migration rates.

The effects of variable $k_{r,N}$ are further illustrated through the use of invasion profiles. Figure 4-6 presents NWP invasion profiles in terms of the absolute number of nodes invaded versus time on the horizontal logarithmic scale. This figure illustrates the advancement of the NWP through the solution domain for all of the realisations examined in Suite 1. However, due to the large number of simulations, conclusions regarding the behaviour of the invading NWP are difficult to make. Therefore, Figure 4-7 plots a subset of the data presented in Figure 4-6. This figure plots the invasion profiles for both variable and constant $k_{r,N}$ for Realisations 2, 5 and 20. Realisation 2 was featured in the discussion above, Realisation 5 represents the simulation set corresponding to the minimum total number of nodes invaded, and Realisation 20 represents the simulation set corresponding to the maximum total number of nodes invaded. In each case, the total number of nodes invaded is greater, and the overall rate of advancement is slower (as evidenced by a reduced profile slope), when variable $k_{r,N}$ is accounted for than when constant $k_{r,N}$ is assumed. This trend was observed for the remaining realisations examined.

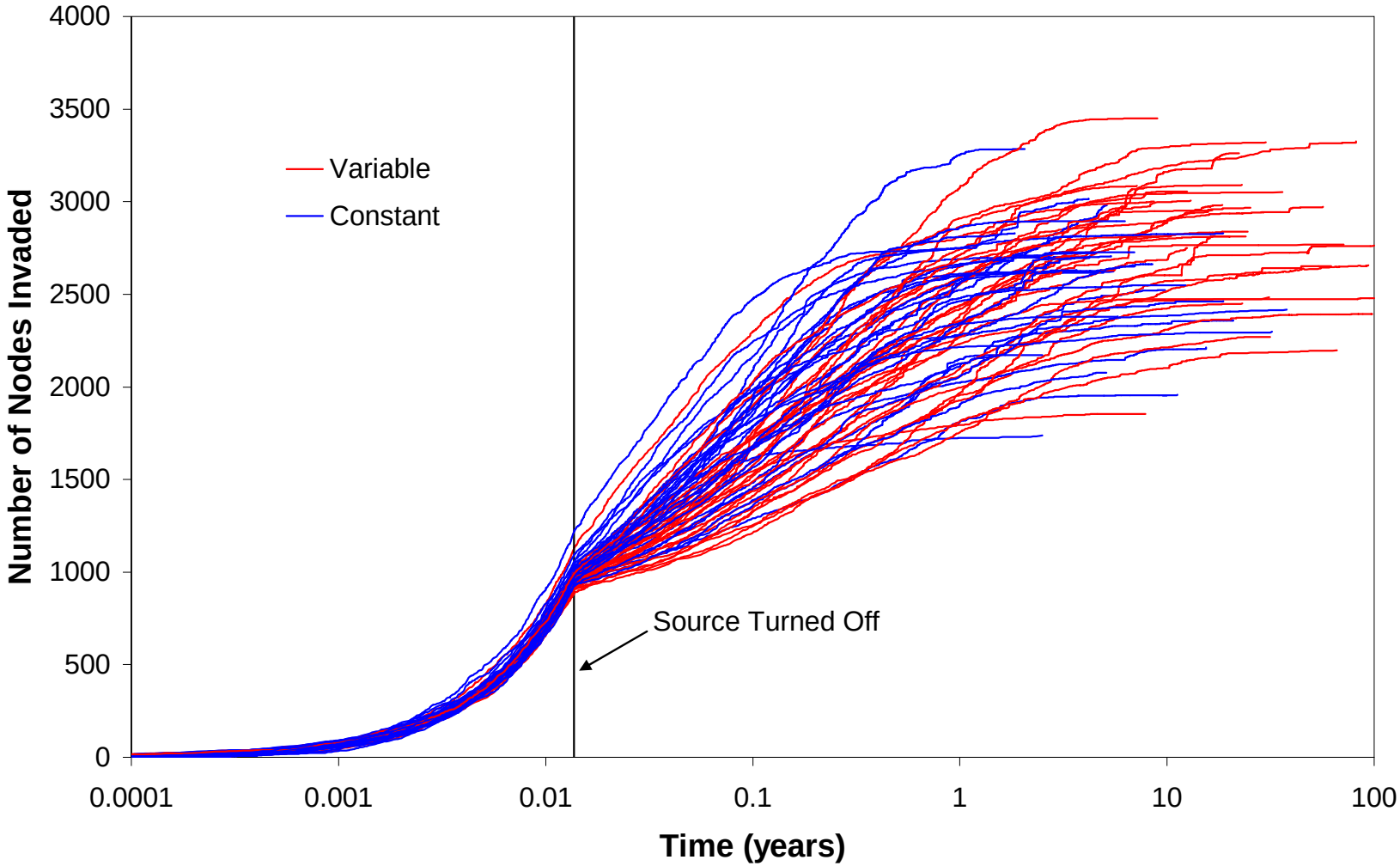

Figure 4-6. Invasion profiles for all Suite 1 data: absolute rate of invasion.

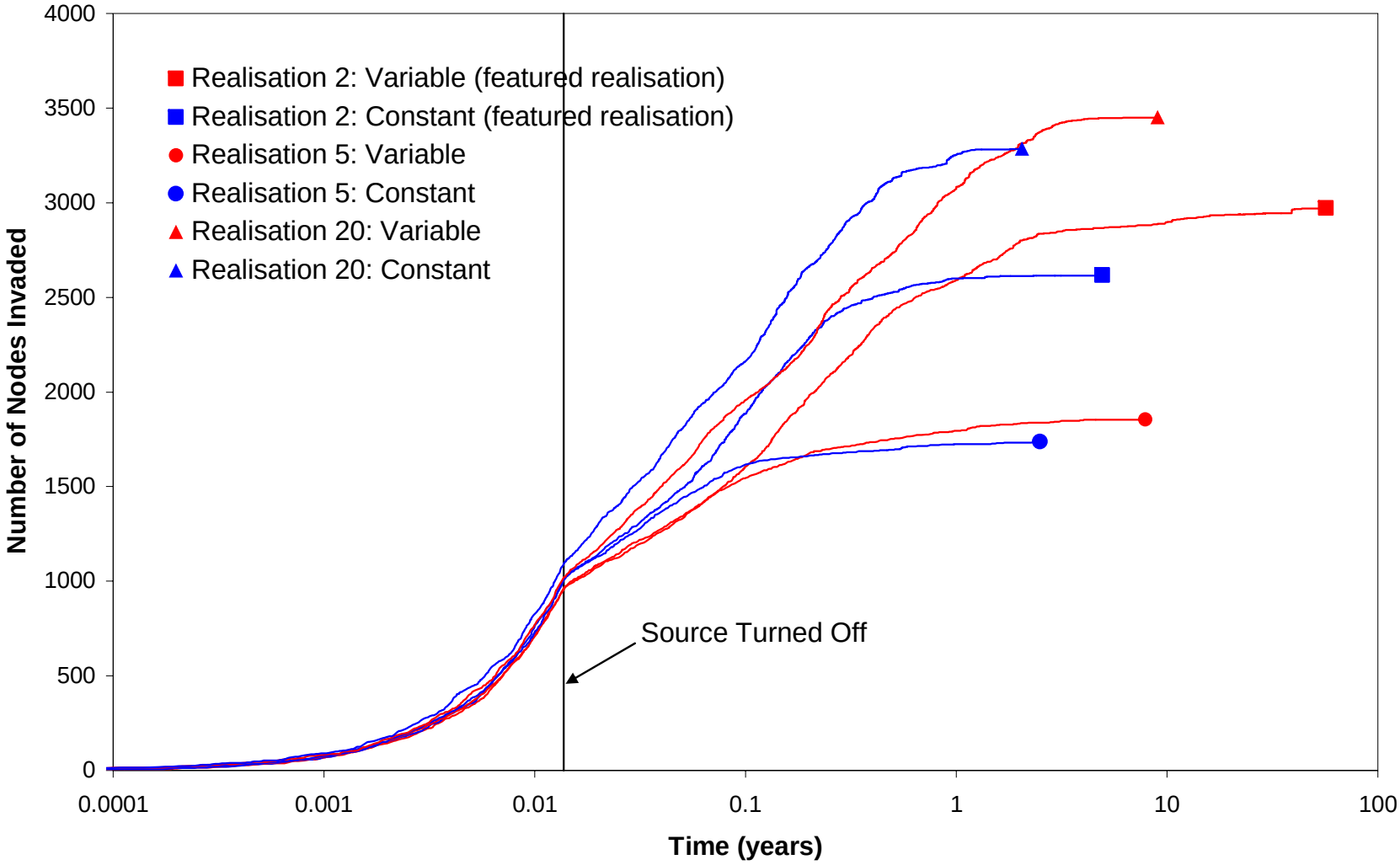

Figure 4-7. Invasion profiles for selected Suite 1 data: absolute rate of invasion.

To confirm that the increase in migration cessation time for the variable $k_{r,N}$ simulations is not simply a consequence of the increased number of nodes invaded, Figure 4-8 presents a summary of the relative invasion profiles for the Suite 1 simulations. Relative invasion profiles plot the number of nodes invaded, normalised to the total number of nodes invaded for each simulation, as a function of time on a logarithmic scale. Figure 4-8 illustrates the minimum, mean and maximum rate of NWP advancement for the constant and variable $k_{r,N}$ cases (30 simulations in each case). While the range of relative invasion profiles overlaps for the two cases examined, the mean relative invasion profile for the variable $k_{r,N}$ simulations is distinctly different from the mean relative invasion profile for the constant $k_{r,N}$ simulations.

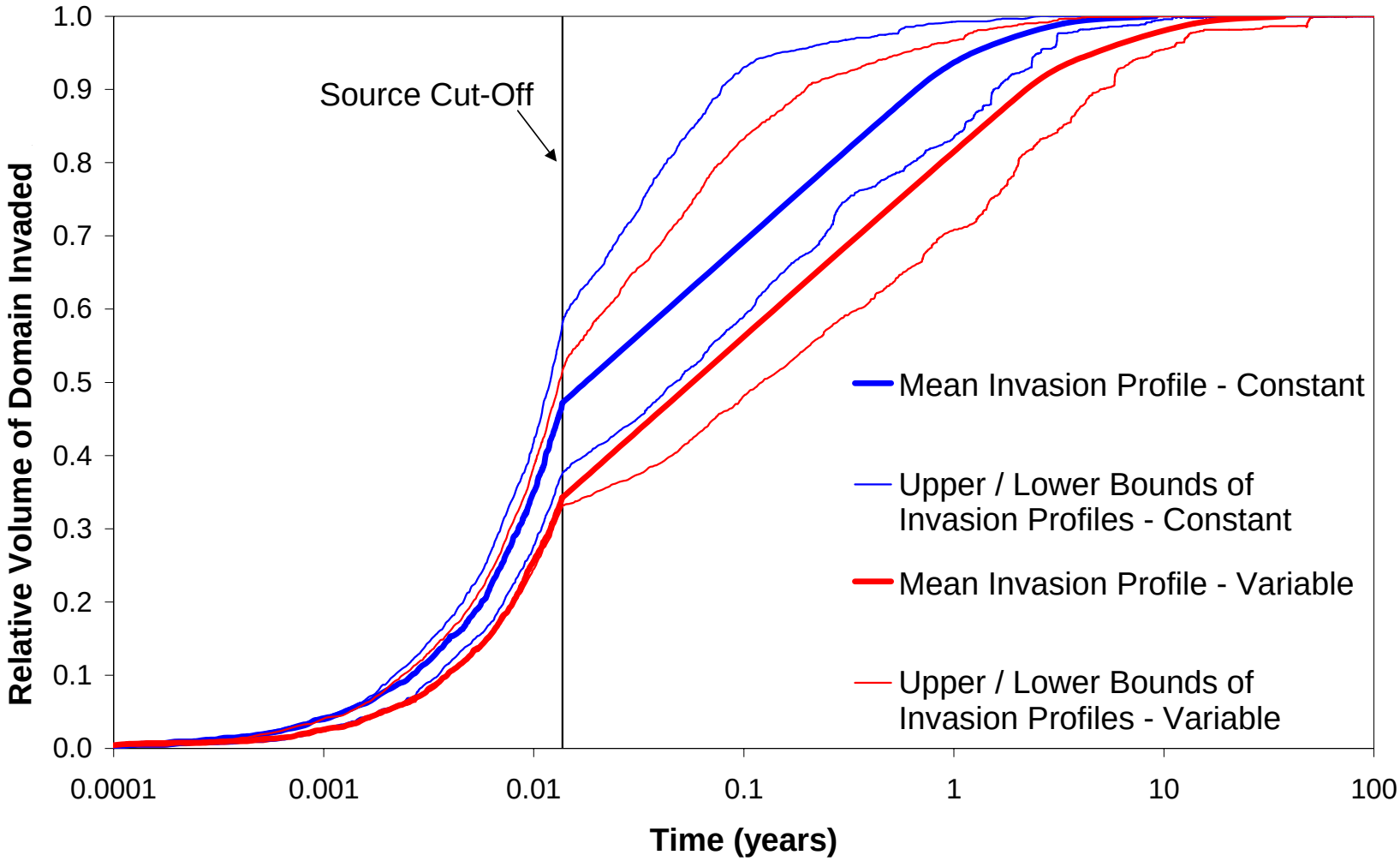

Figure 4-8. Invasion profiles for Suite 1 data: relative rate of invasion.

4.4.1.2 Quantitative Results

Figure 4-9 presents a plot of the cumulative average number of nodes invaded as a function of the number of realisations examined in Suite 1. As can clearly be seen, the cumulative average number of nodes invaded is insensitive to the addition of realisations to the data set beyond approximately 25 realisations, indicating that a data set of 30 realisations is sufficiently large from which to draw statistical conclusions about the influence of variable $k_{r,N}$ on the migration of NWP.

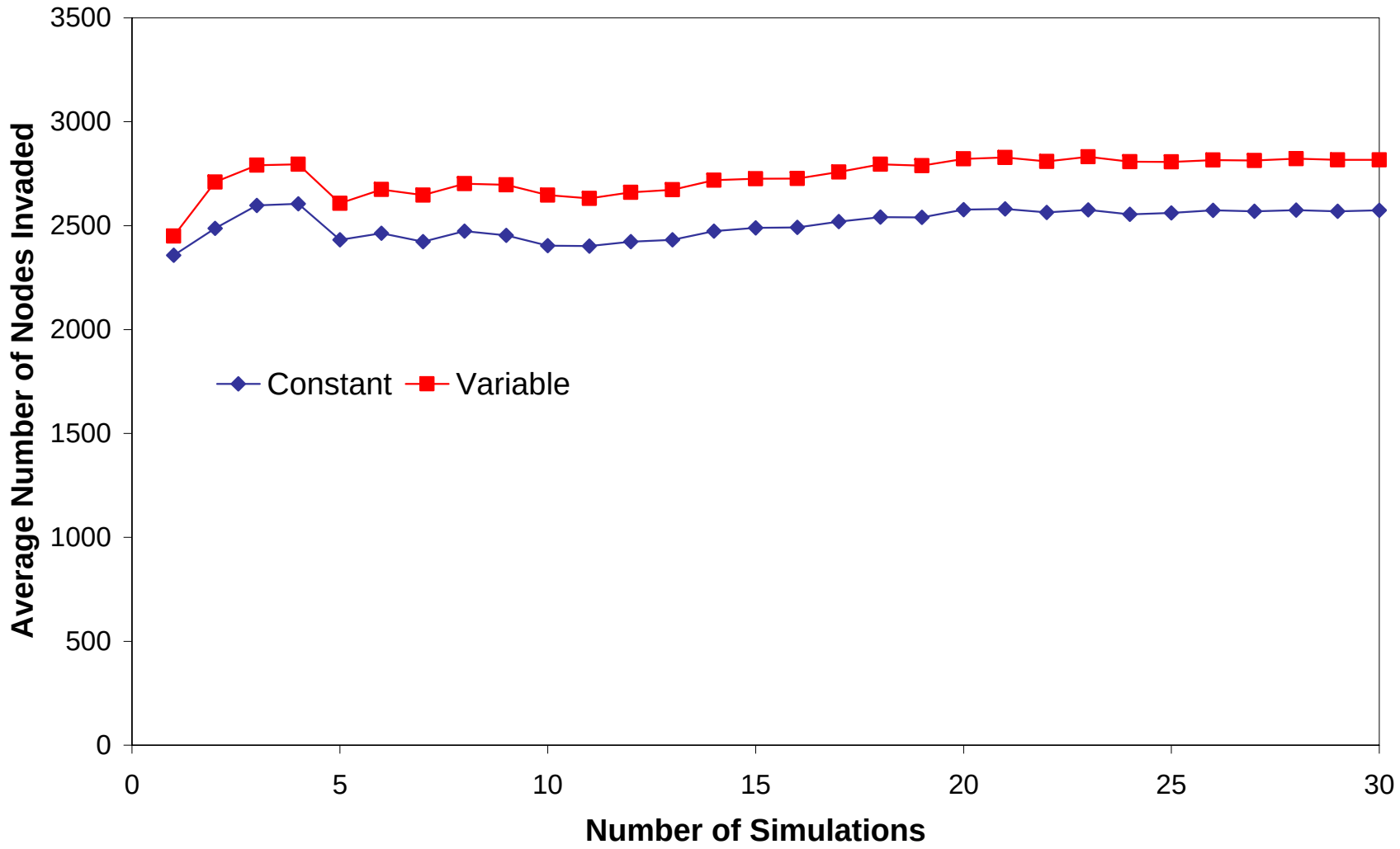

Figure 4-9. Number of nodes invaded: cumulative average as a function of the number of realisations examined.

Figure 4-10 compares the total number of nodes invaded between the constant $k_{r,N}$ case and the variable $k_{r,N}$ case for each of the 30 realisations of Suite 1. For each realisation, the total number of nodes invaded is greater when variable $k_{r,N}$ is accounted for than when constant $k_{r,N}$ is assumed, regardless of the extent of NWP migration (which varies from 1855 nodes invaded for variable $k_{r,N}$ Realisation 5 to 3451 nodes invaded for variable $k_{r,N}$ Realisation 20). The difference in number of nodes invaded between the two cases ranges from 63 (2.28% of the total number of nodes invaded for the variable $k_{r,N}$ case) for Realisation 25 to 490 (14.8%) for Realisation 23, with the average difference equal to 242.9 nodes (8.6%, or 7.6 m^3 of porous media), indicating that the total volume of the domain invaded is sensitive to the variability of $k_{r,N}$ in the Suite 1 simulations. In practical terms, this suggests that ignoring variable $k_{r,N}$ will result in under predicting the extent of DNAPL migration by 9% on average for a location exhibiting a similar mean and distribution of permeability.

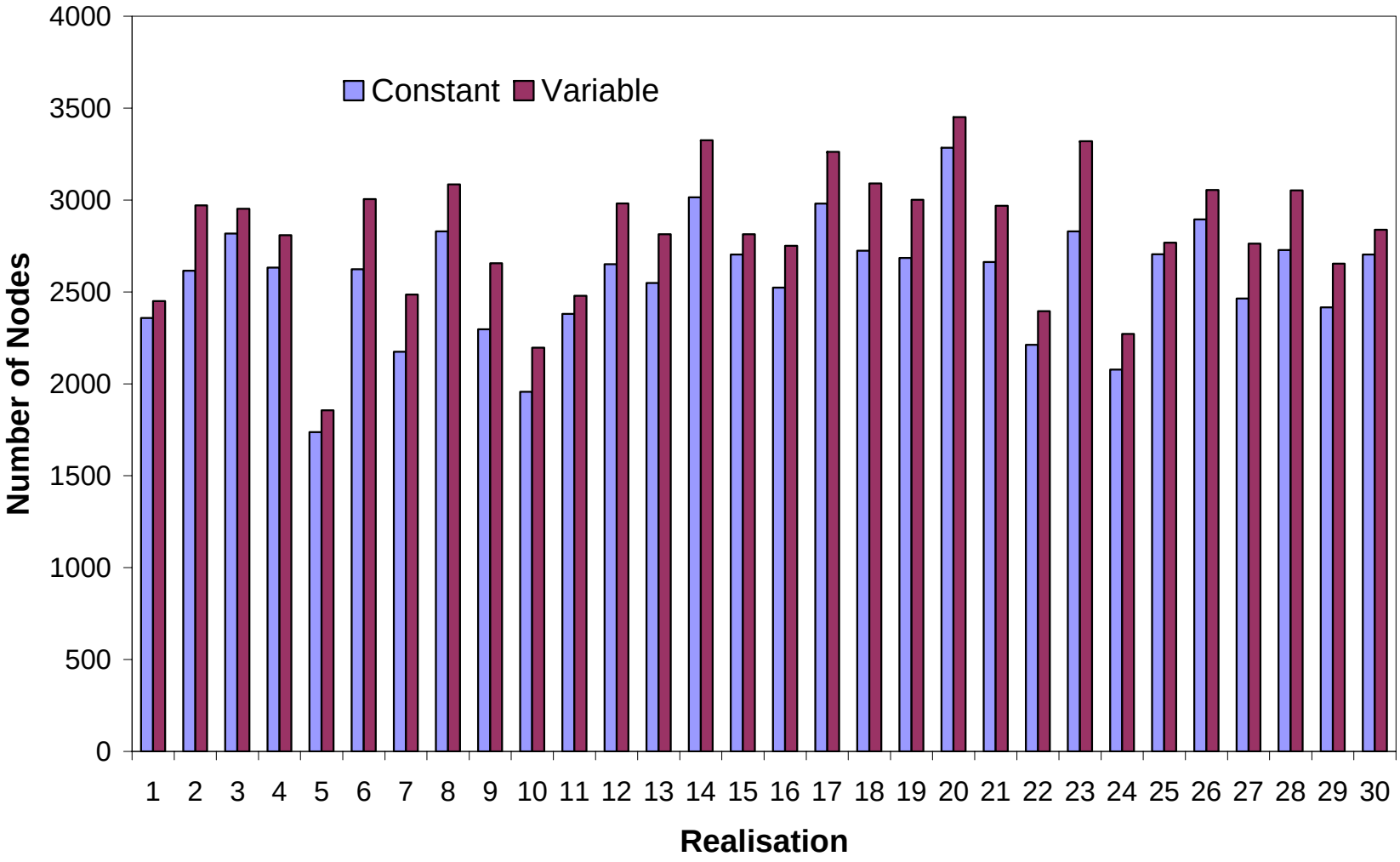

Figure 4-10. Comparison of the total number of nodes invaded: Suite 1.

Figures 4-11 through 4-14 compare the 90%, 95%, 99%, and 100% migration cessation times (t_{90}, t_{95}, t_{99} and t_{100}), respectively, between the constant $k_{r,N}$ case and the variable $k_{r,N}$ case for each of the 30 realisations of Suite 1. As can clearly be seen, for each realisation, regardless of the cessation time considered, migration through the domain will cease earlier if constant $k_{r,N}$ is assumed, than if variable $k_{r,N}$ is accounted for in the simulation.

The difference in t_{90} ranges from 0.12 years for Realisation 2 to 3.6 years for Realisation 4, with an average difference of 1.5 years. The average t_{90} for the simulations assuming constant $k_{r,N}$ is 32% of the average migration time for the simulations accounting for variable $k_{r,N}$.

The difference in t_{95} ranges from 0.42 years for Realisation 5 to 11.2 years for Realisation 4, with an average difference of 3.5 years. The average t_{95} for the simulations assuming constant $k_{r,N}$ is 26% of the average migration time for the simulations accounting for variable $k_{r,N}$.

The difference in t_{99} ranges from 1.18 years for Realisation 5 to 45.7 years for Realisation 14, with an average difference of 10.7 years. The average t_{99} for the simulations assuming constant $k_{r,N}$ is 24% of the average migration time for the simulations accounting for variable $k_{r,N}$.

The difference in t_{100} ranges from 0.28 years for Realisation 16 to 82.6 years for Realisation 22, with an average difference of 28.1 years. The average t_{100} for the simulations assuming constant $k_{r,N}$ is 24% of the average migration time for the simulations accounting for variable $k_{r,N}$.

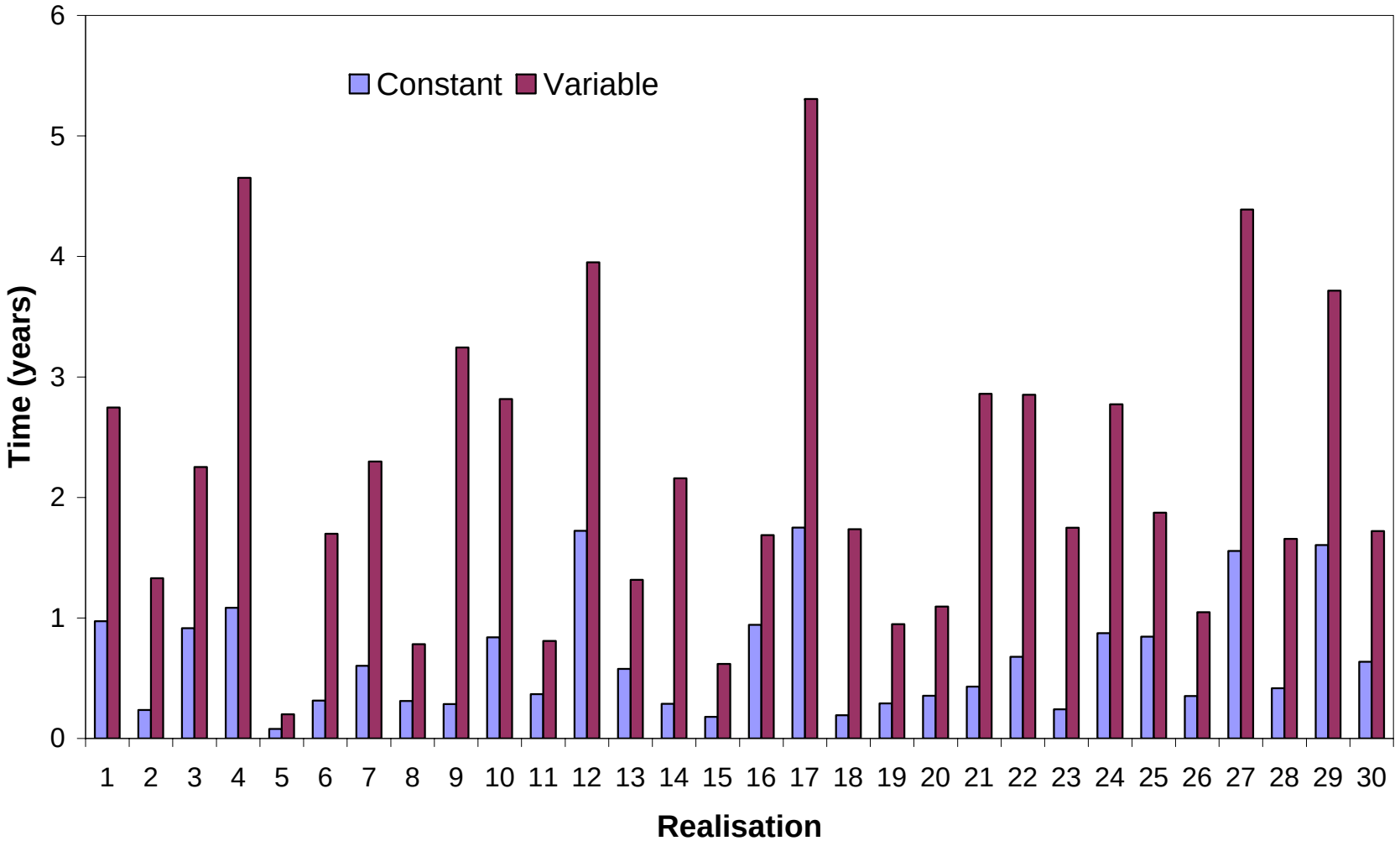

Figure 4-11. Comparison of the 90% cessation times: Suite 1.

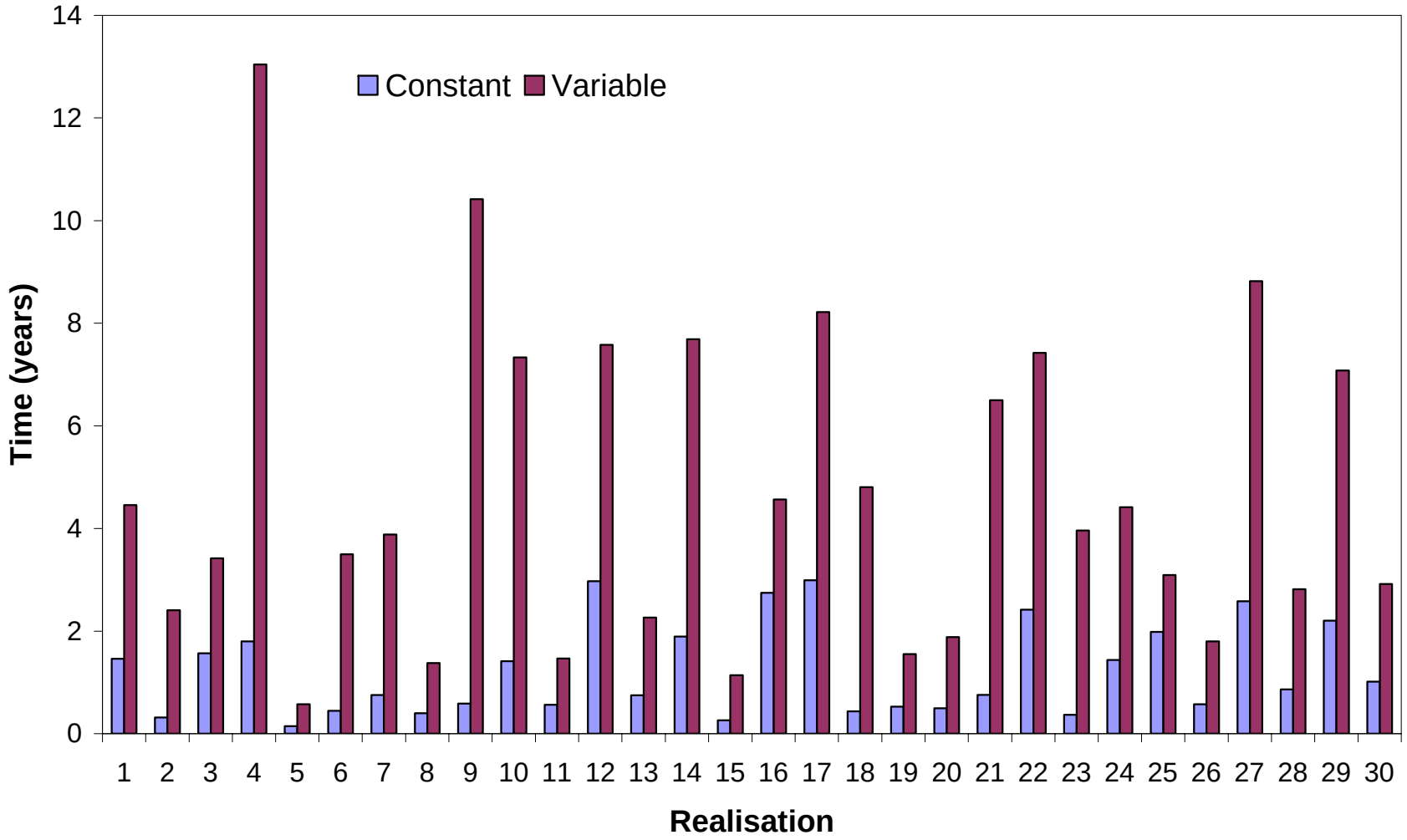

Figure 4-12. Comparison of the 95% cessation times: Suite 1.

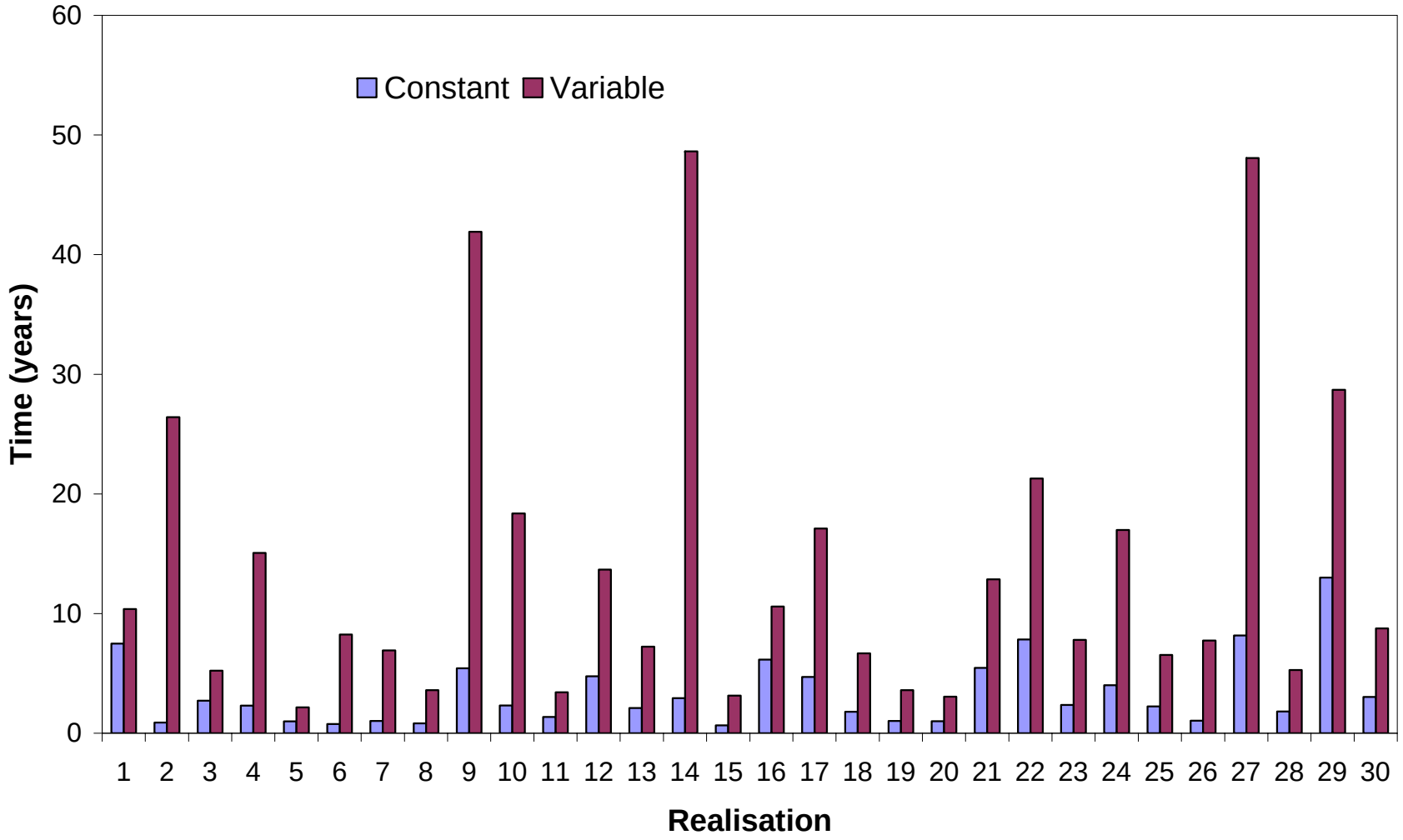

Figure 4-13. Comparison of the 99% cessation times: Suite 1.

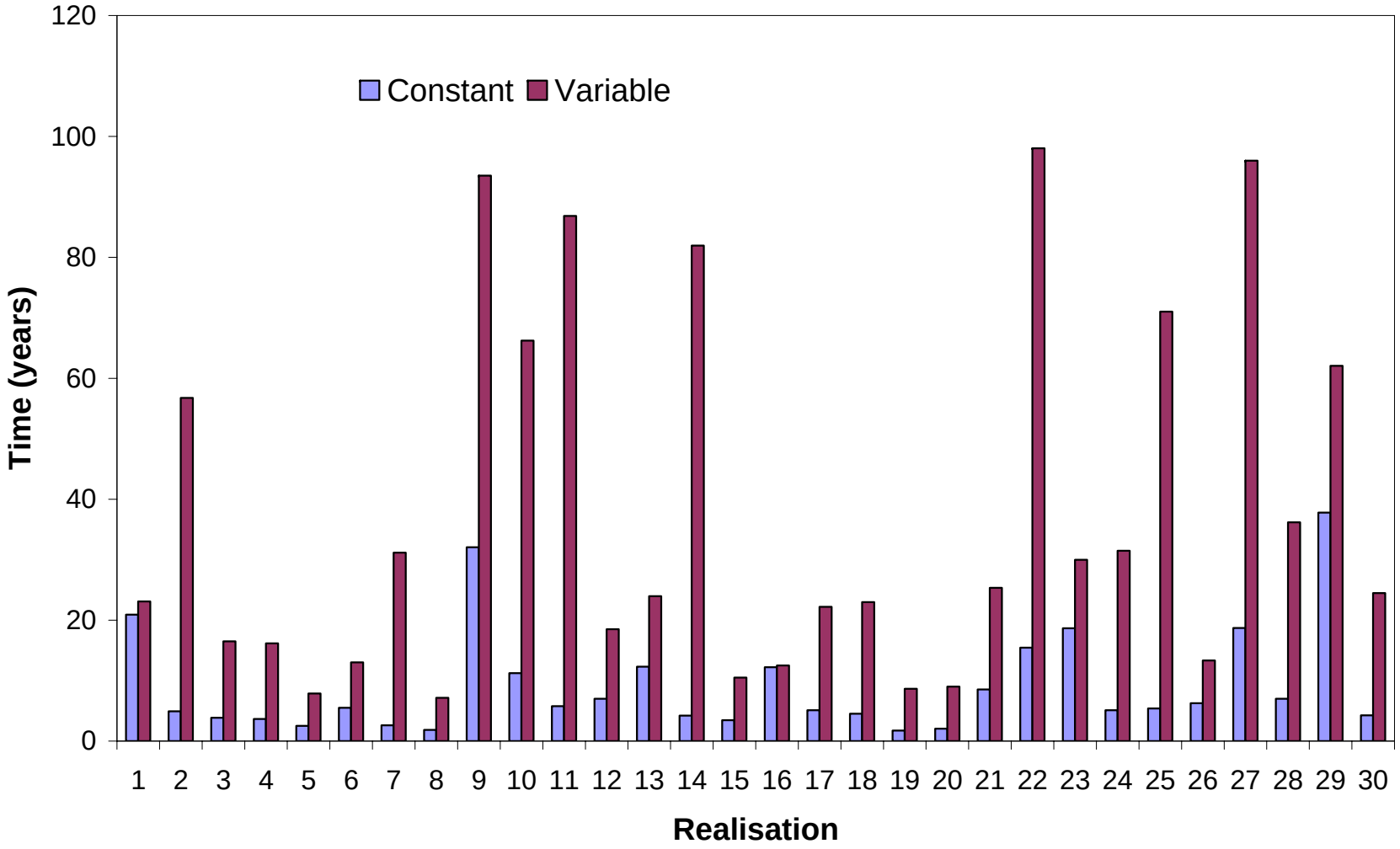

Figure 4-14. Comparison of the 100% cessation times: Suite 1.

Table 4-4 is a summary of the results presented in Figures 4-10 through 4-14, indicating the mean, minimum and maximum total number of nodes invaded, as well as the mean, minimum and maximum t_{100}, t_{99}, t_{95}, and t_{90} for both the constant $k_{r,N}$ simulations and the variable $k_{r,N}$ simulations for the 30 realisations of Suite 1.

Table 4-4. Summary of Numerical Modelling Results: Suite 1 Simulations

Comparison		Constant $k_{r,N}$	Variable $k_{r,N}$	Ratio (Constant / Variable)
Total Number of Nodes Invaded	Mean	2574.3	2817.2	0.91
	Minimum	1737 (Realisation 5)	1855 (Realisation 5)	0.94
	Maximum	3285 (Realisation 20)	3485 (Realisation 20)	0.94
90% Cessation Time (years)	Mean	0.7	2.2	0.32
	Minimum	0.08 (Realisation 5)	0.20 (Realisation 5)	0.40
	Maximum	1.8 (Realisation 17)	5.3 (Realisation 17)	0.34
95% Cessation Time (years)	Mean	1.2	4.7	0.26
	Minimum	0.15 (Realisation 5)	0.57 (Realisation 5)	0.26
	Maximum	3.0 (Realisation 17)	13.0 (Realisation 4)	0.23
99% Cessation Time (years)	Mean	3.3	14.0	0.24
	Minimum	0.64 (Realisation 15)	2.16 (Realisation 5)	0.30
	Maximum	13.0 (Realisation 29)	48.1 (Realisation 27)	0.27
100% Cessation Time (years)	Mean	9.1	37.2	0.24
	Minimum	1.71 (Realisation 19)	7.15 (Realisation 8)	0.24
	Maximum	37.8 (Realisation 29)	98.0 (Realisation 22)	0.39

The mean number of nodes invaded for the constant $k_{r,N}$ simulations is 2574.3 (4.47% of the domain) and the mean number of nodes invaded for the variable $k_{r,N}$ simulations is 2817.2 (4.89%). The difference in mean number of nodes invaded between the constant $k_{r,N}$ simulations and the variable $k_{r,N}$ simulations were found to be statistically significant to 1% by null hypothesis testing.

The mean t_{90}, t_{95}, t_{99} and t_{100} assuming constant $k_{r,N}$ were found to be 32%, 26%, 24%, and 24% of the cessation times accounting for variable $k_{r,N}$, respectively. Null hypothesis testing indicates that these differences are statistically significant to 1%. Clearly, the influence of properly accounting for variable $k_{r,N}$ on the predicted total number of nodes invaded, and the time to NWP migration cessation, is statistically significant. In practical terms, this means that ignoring variable $k_{r,N}$ will result in under predicting the time for migration cessation by 74% on average for an aquifer with similar permeability characteristics.

4.4.2 Suite 2

4.4.2.1 Qualitative Results

Figures 4-15a and 4-15b present the NWP saturation distributions for Realisation 2 of Suite 2 following five days of simulation time (corresponding to the time at which the NWP source condition was terminated) for the variable $k_{r,N}$ case and the constant $k_{r,N}$ case, respectively. The k_i field defining Realisation 2 of Suite 2 is identical to the k_i field defining Realisation 2 of Suite 1 (utilised as the example realisation in Section 4.4.1.1), except that the k_i values have been increased by two orders of magnitude. The pattern of k_i, however, is identical, such that comparisons between the simulations conducted in Suite 1 / Realisation 2 and the simulations conducted in Suite 2 / Realisation 2 will directly reveal the effect of higher k_i on the trends observed for the Suite 1 simulations.

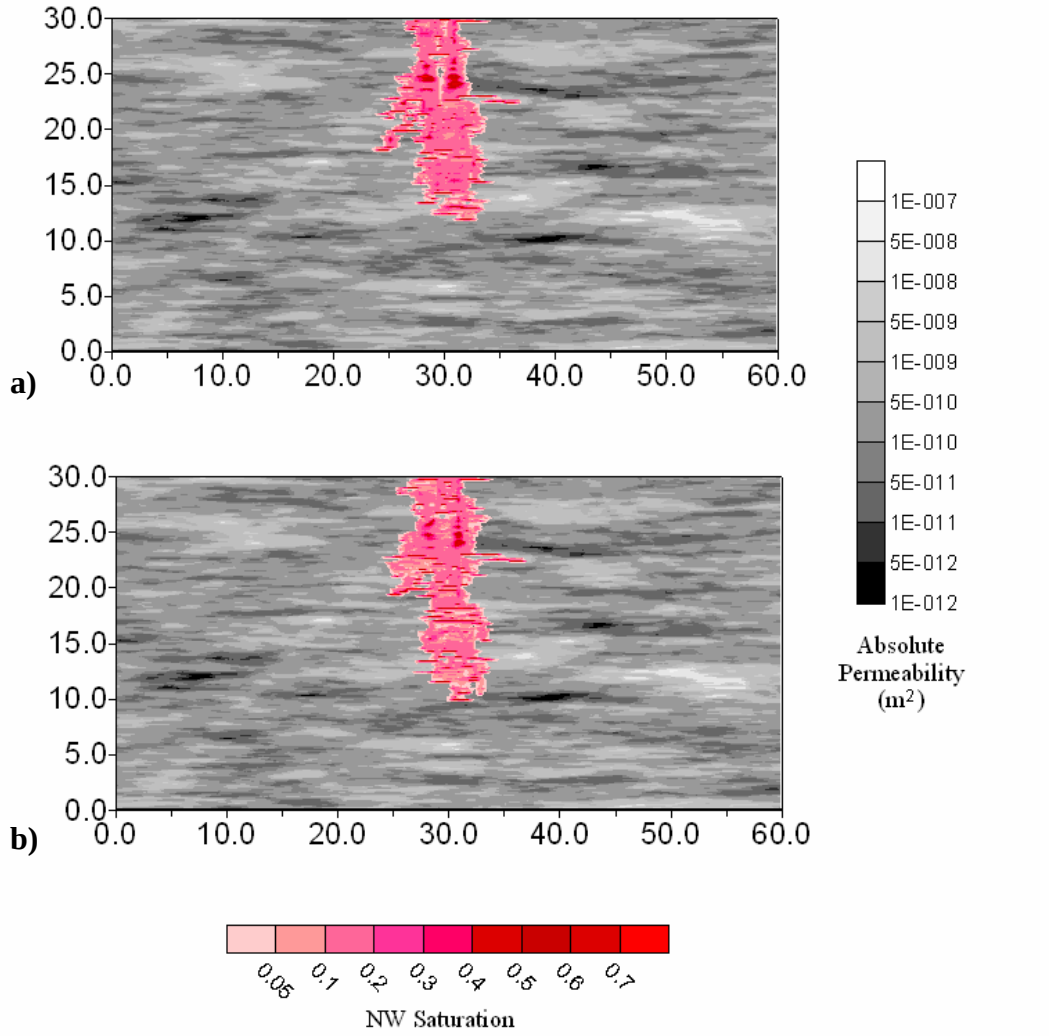

Figure 4-15. NWP saturation distribution for Suite 2, Realisation 2, following 5 days of simulation time: a) accounting for variable $k_{r,N}$; and, b) assuming constant $k_{r,N}$.

As can clearly be seen in Figures 4-15a and 4-15b, the difference in the NWP saturation distribution between the variable $k_{r,N}$ simulation and the constant $k_{r,N}$ simulation is negligible. Not only does the source condition ensure that the majority of NWP enters the domain through the highest k_i nodes, as in Suite 1, but even the relatively low k_i nodes in the source boundary for the variable $k_{r,N}$ case will have high $k_{rN}^{\max}$ values, and therefore k_{rN} functions similar to those used in the constant $k_{r,N}$ simulation.

Figures 4-16a and 4-16b present the NWP saturation distributions for the variable $k_{r,N}$ case and the constant $k_{r,N}$ case for Realisation 2 of Suite 2 following one week of simulation time, respectively. One week of simulation time represents the t_{95} for both simulations, in contrast to the Suite 1 simulations where the t_{95} were significantly different for Realisation 2 (0.3 years for the constant $k_{r,N}$ case, and 2.4 years for the variable $k_{r,N}$ case). As in Figures 4-15a and 4-15b, the distribution of NWP is very similar between the two simulations, indicating negligible affects of variable $k_{r,N}$ on the pattern of migration.

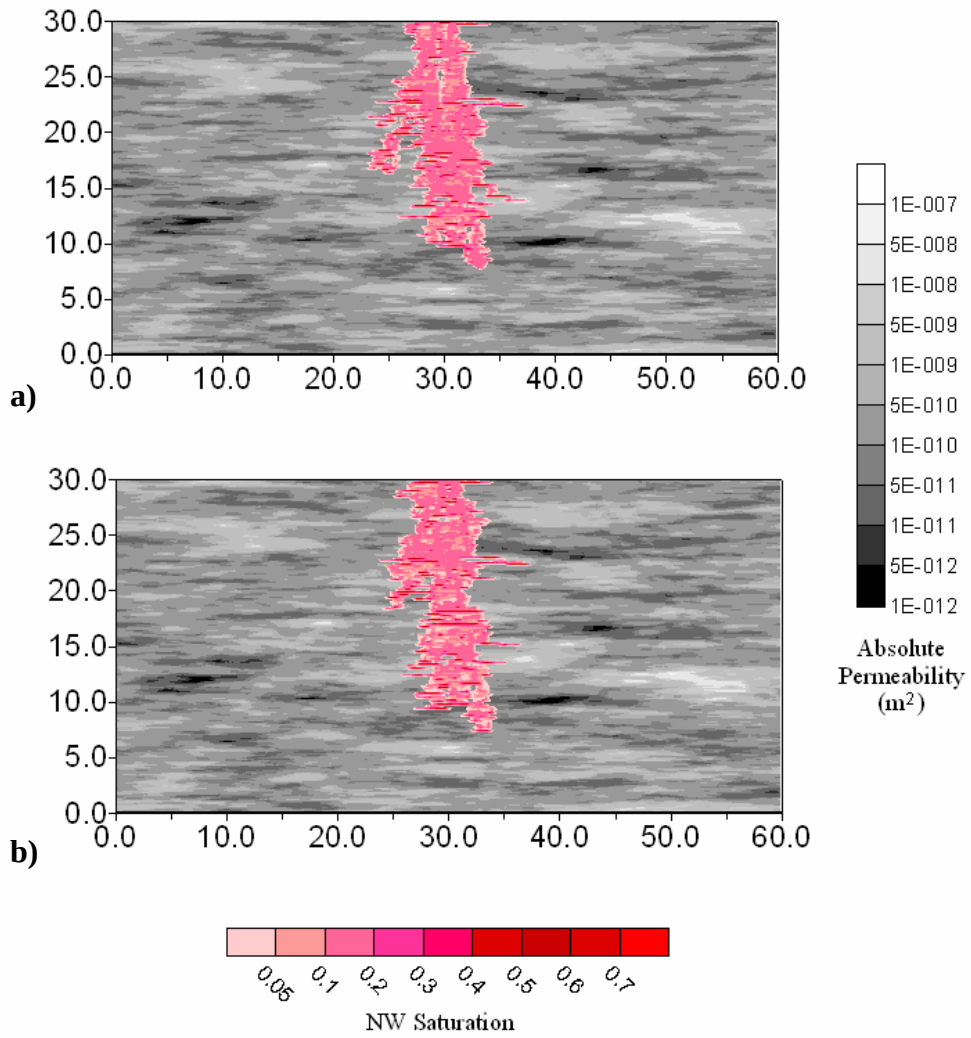

Figure 4-16. NWP saturation distribution for Suite 2, Realisation 2, following 1 week of simulation time: a) accounting for variable $k_{r,N}$; and, b) assuming constant $k_{r,N}$.

Figures 4-17a and 4-17b present the NWP saturation distributions for the variable $k_{r,N}$ case and the constant $k_{r,N}$ case following 4 weeks of simulations time, corresponding to the time of complete NWP migration cessation for both cases. Once again, the distribution of NWP is very similar between the two simulations, indicating that variable $k_{r,N}$ has no significant affect on either the pattern of NWP migration, or the timescale of NWP migration for this Suite of simulations.

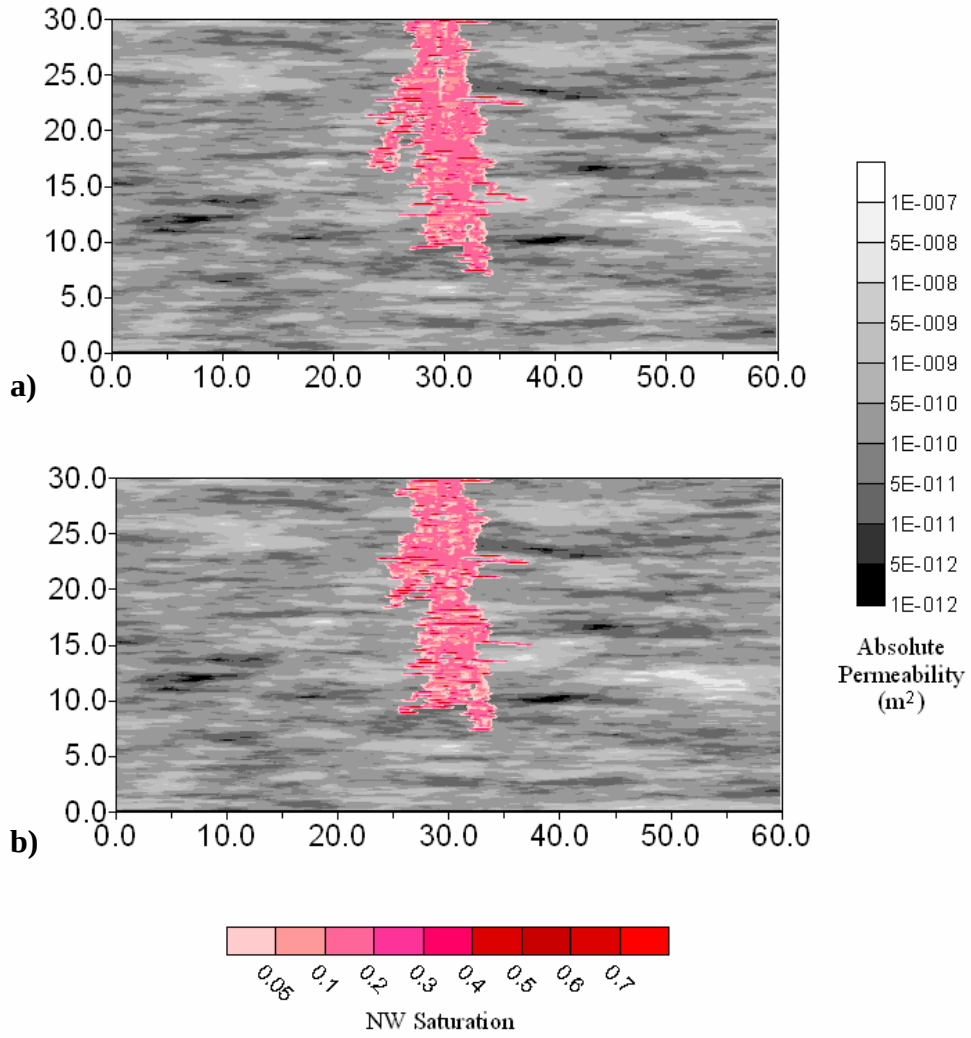

Figure 4-17. NWP saturation distribution for Suite 2, Realisation 2, following 4 weeks of simulation time: a) accounting for variable $k_{r,N}$; and, b) assuming constant $k_{r,N}$.

Comparison of Figures 4-17a and 4-17b and Figures 4-5a and 4-5b illustrate another important factor governing the predicted migration patterns of a NWP release in heterogeneous porous media. In the relatively low k_i simulations of Suite 1, the

NWP tends to migrate a greater distance laterally, and a shorter distance vertically, than the same release of NWP in the relatively high k_i simulations of Suite 2. This is a result of the increase in displacement pressures associated with lower k_i materials in the Suite 1 realisations, in addition to the fact that the lower k_i materials of Suite 1 limit the rate of NWP flux so that horizontal spreading necessarily occurs simultaneously to vertical penetration.

The qualitative descriptions included above were found to generally hold for the remaining 11 realisations of Suite 2. In general, the high k_i of the Suite 2 realisations led to high $k_{rN}^{\max}$ values and therefore minimal variation of the k_{rN} function throughout the solution domain for the variable $k_{r,N}$ case. Therefore, the differences in migration patterns and cessation times between the constant $k_{r,N}$ case and the variable $k_{r,N}$ case are negligible.

4.4.2.2 Quantitative Results

Figure 4-18 compares the total number of nodes invaded between the constant $k_{r,N}$ case and the variable $k_{r,N}$ case for each of the 12 realisations of Suite 2. Eight of the twelve realisations show that the total number of nodes invaded is greater when variable $k_{r,N}$ is accounted for in the simulation than when constant $k_{r,N}$ is assumed, however, Realisations 6, 7, 9, and 10 show the reverse relationship. The difference in number of nodes invaded ranges from 12 (0.3% of the total number of nodes invaded for the variable $k_{r,N}$ case) for Realisation 9 to 257 (6.17%) for Realisation 1, with the average difference equal to 66 nodes (1.63%) indicating that the total volume of the domain invaded is insensitive to the variability of $k_{r,N}$ in the Suite 2 simulations.

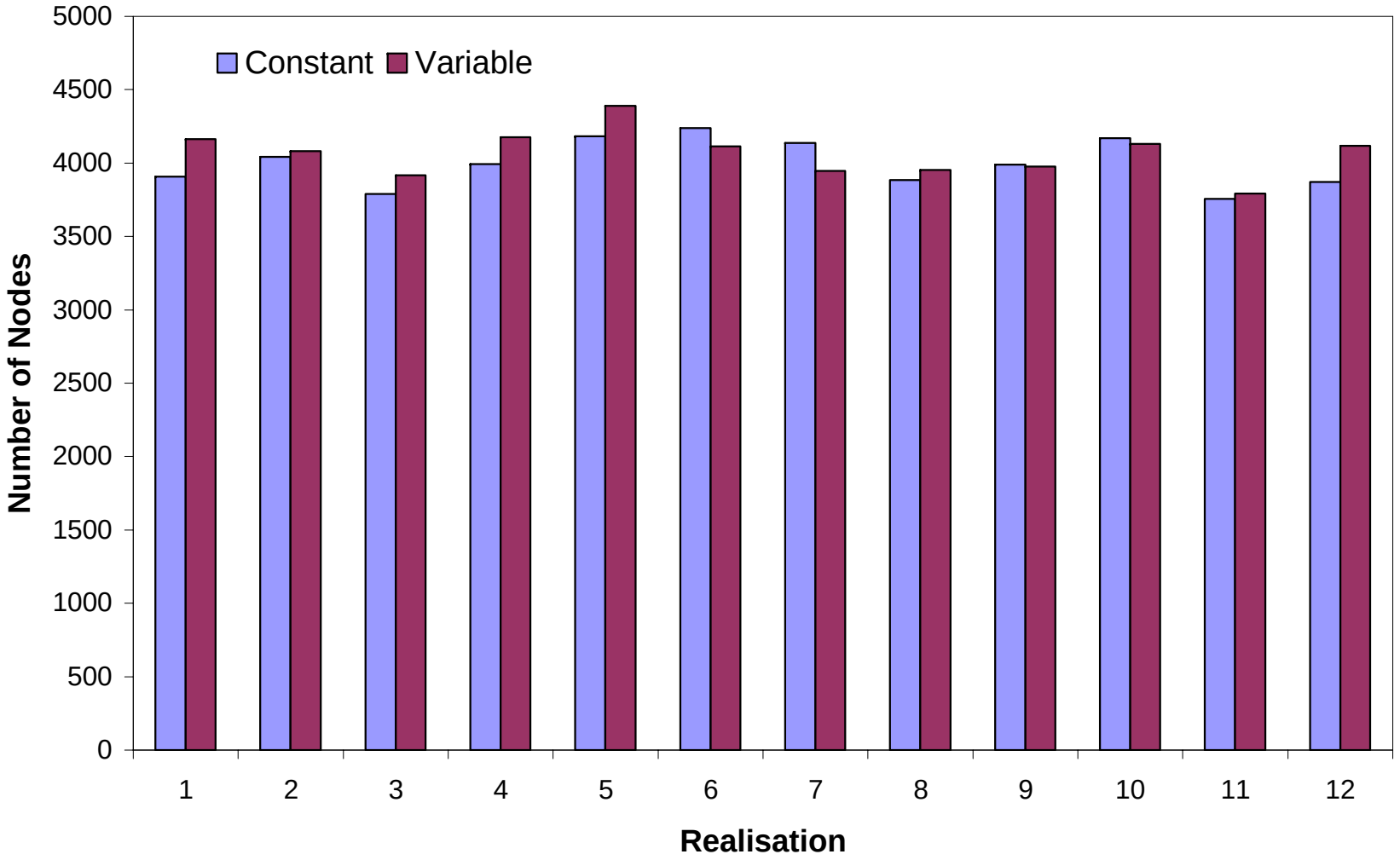

Figure 4-18. Comparison of the total number of nodes invaded: Suite 2.

Figures 4-19 through 4-22 compare the t_{90}, t_{95}, t_{99}, and t_{100}, respectively, between the constant $k_{r,N}$ case and the variable $k_{r,N}$ case for each of the 12 realisations of Suite 2. While Figure 4-19 shows the t_{90} for every realisation to be greater for the variable $k_{r,N}$ case than for the constant $k_{r,N}$ case, Figures 4-20 through 4-22 show the reverse to be true for the t_{95} of Realisation 7, the t_{99} of Realisations 4, 5, 8, and 9, and the t_{100} of half of the realisations examined: numbers 3, 4, 5, 7, 8, and 11. This trend indicates that predictions regarding the cessation of NWP migration are sensitive to the numerical domain realisation and the degree of $k_{r,N}$ function variability in the region encountered by the advancing NWP.

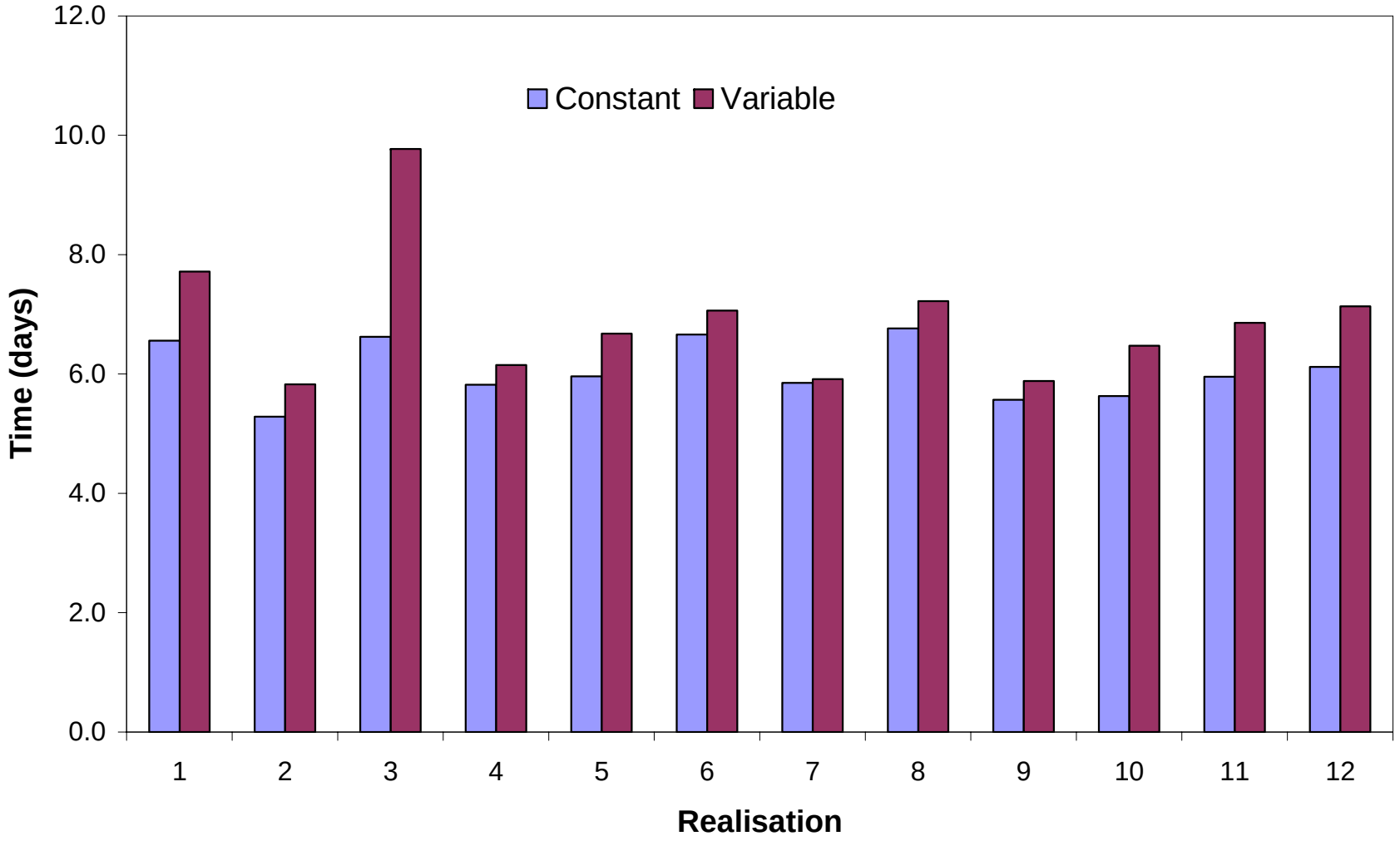

Figure 4-19. Comparison of the 90% cessation times: Suite 2.

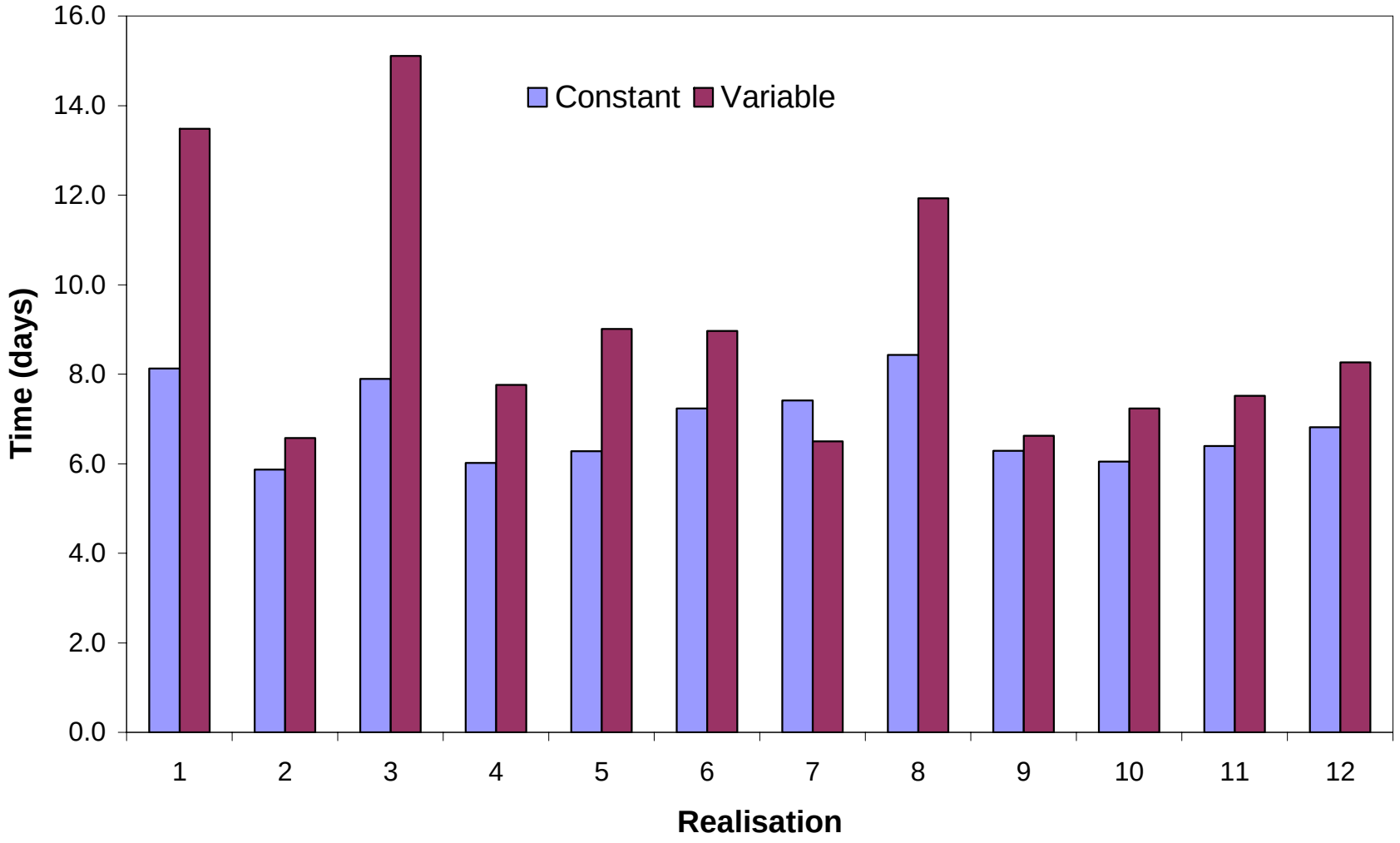

Figure 4-20. Comparison of the 95% cessation times: Suite 2.

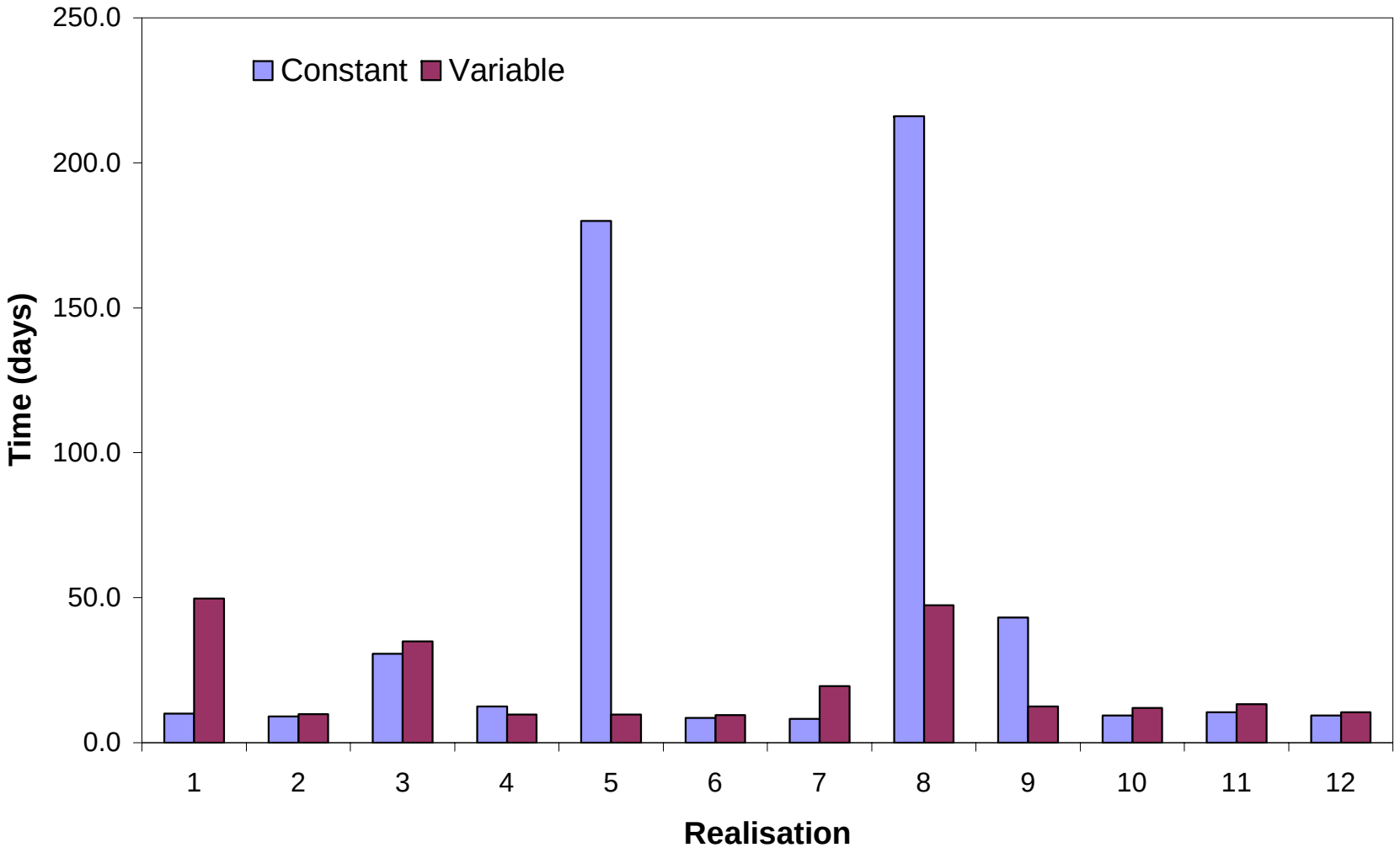

Figure 4-21. Comparison of the 99% cessation times: Suite 2.

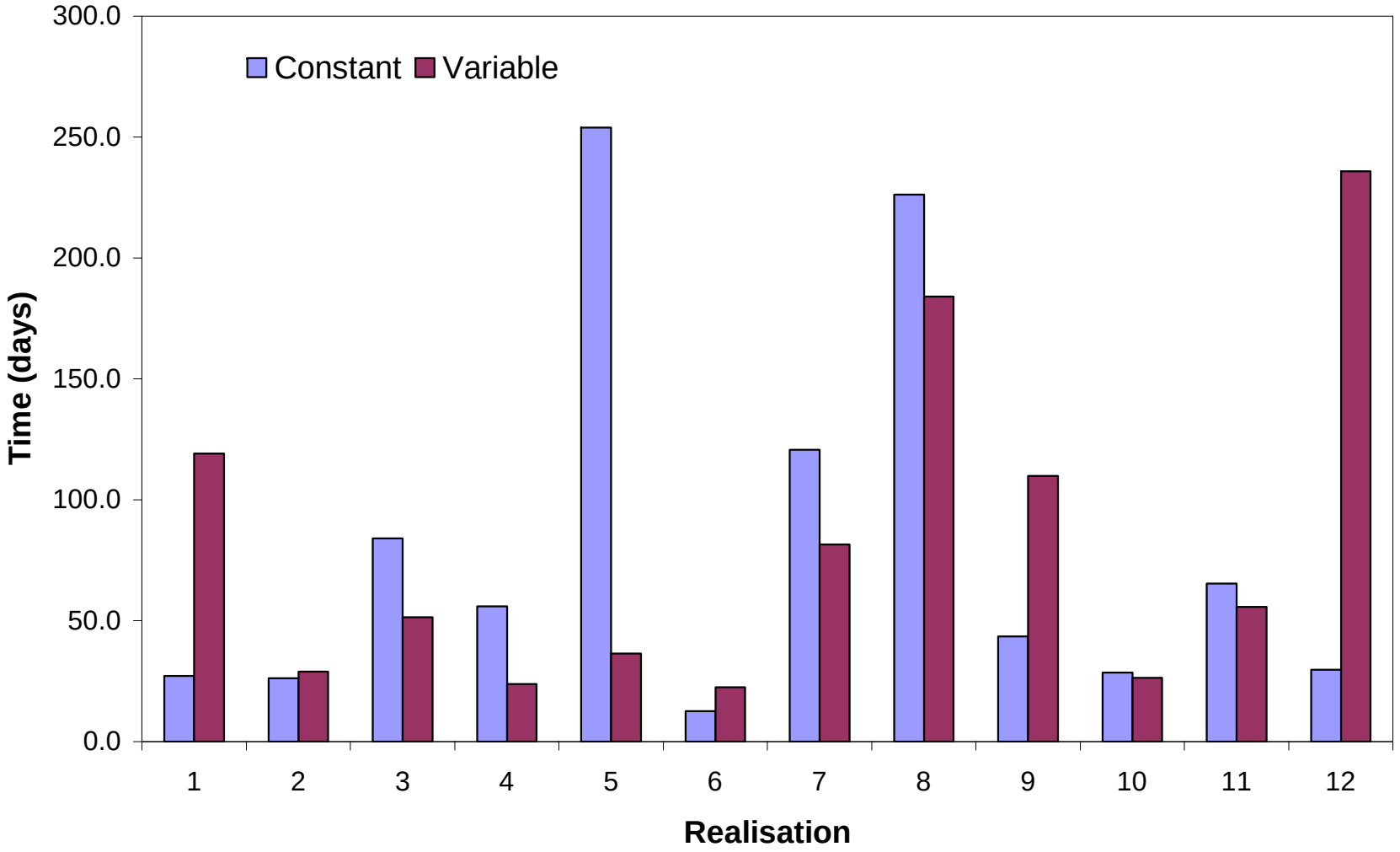

Figure 4-22. Comparison of the 100% cessation times: Suite 2.

Table 4-5 is a summary of the results presented in Figures 4-18 through 4-22, indicating the mean, minimum and maximum total number of nodes invaded, as well as the mean, minimum and maximum t_{100}, t_{99}, t_{95}, and t_{90} for both the constant $k_{r,N}$ simulations and the variable $k_{r,N}$ simulations for the 12 realisations of Suite 2.

Table 4-5. Summary of Numerical Modelling Results: Suite 2 Simulations

Comparison		Constant $k_{r,N}$	Variable $k_{r,N}$	Ratio (Constant / Variable)
Total Number of Nodes Invaded	Mean	3996.8	4063.3	0.98
	Minimum	3757 (Realisation 11)	3795 (Realisation 11)	0.99
	Maximum	4240 (Realisation 6)	4389 (Realisation 5)	0.97
90% Cessation Time (days)	Mean	6.1	6.9	0.88
	Minimum	5.3 (Realisation 2)	5.8 (Realisation 2)	0.91
	Maximum	6.8 (Realisation 8)	9.8 (Realisation 3)	0.69
95% Cessation Time (days)	Mean	6.9	9.1	0.76
	Minimum	5.9 (Realisation 2)	6.5 (Realisation 7)	0.91
	Maximum	8.4 (Realisation 8)	15.1 (Realisation 3)	0.56
99% Cessation Time (days)	Mean	45.6	19.9	2.29
	Minimum	8.2 (Realisation 7)	9.5 (Realisation 6)	0.86
	Maximum	216.0 (Realisation 8)	49.7 (Realisation 1)	4.35
100% Cessation Time (days)	Mean	81.2	81.3	1.00
	Minimum	12.7 (Realisation 6)	22.5 (Realisation 6)	0.56
	Maximum	254.0 (Realisation 5)	235.8 (Realisation 12)	1.08

The mean number of nodes invaded for the constant $k_{r,N}$ simulations is 3996.8 (6.9% of the domain) and the mean number of nodes invaded for the variable $k_{r,N}$ simulations is 4063.3 (7.1%). The difference in mean number of nodes invaded between the constant $k_{r,N}$ simulations and the variable $k_{r,N}$ simulations was found to be statistically insignificant by null hypothesis testing at the 5% significance level.

This suggest that on average, variable $k_{r,N}$ has little affect on the predicted volume of porous media invaded for a NWP release in relatively high k_i porous media.

The mean t_{90} and t_{95} assuming constant $k_{r,N}$ were found to be 88% and 76% of the cessation times accounting for variable $k_{r,N}$, respectively. Null hypothesis testing indicates that these differences are significant to 1%. However, the differences in the magnitudes of the migration time (mean t_{90} and t_{95} differences are 0.8 days and 2.2 days, respectively) are small relative to timescales of other subsurface process (e.g. dissolution). Differences in the t_{99} and t_{100} were found to be statistically insignificant by null hypothesis testing at the 5% significance level. In general, differences in migration times between the two cases were significant on a realisation by realisation basis, but are clearly of little practical importance (on the order of a few days), relative to the differences observed in the Suite 1 simualtions (on the order of years and decades), when predicting NWP migration at the field scale.

4.4.3 Comparison of Suite 1 and 2 Simulations

The two-order of magnitude difference in k_i values between the Suite 1 and Suite 2 simulations has significantly affected the conclusions that can be drawn about the influence of variable $k_{r,N}$ on the release of a DNAPL at the field scale. While the influence of variable $k_{r,N}$ is clearly reduced as k_i increases, the effect of increasing k_i on the overall character of the pattern of NWP migration is even more pronounced. In the relatively low k_i simulations of Suite 1, the timescales of active NWP migration are on the order of years. In contrast, the relatively high k_i simulations of Suite 2 demonstrate cessation of migration on the order of days, regardless of the assumption of constant versus variable $k_{r,N}$. In addition, the final pattern of NWP distribution is shallower and wider in the Suite 1 simulations, and deeper and narrower in the Suite 2

simulations as a direct consequence of the difference in mean k_i, in spite of assumptions of constant versus variable k_{rN}.

4.4.4 Suite 3

4.4.4.1 Qualitative Results

Figures 4-23a and 4-23b present the NWP saturation distributions for Realisation 5 of Suite 3 (bench scale simulations) following 20 minutes of simulation time (corresponding to the time at which the NWP source condition was terminated) for the variable $k_{r,N}$ case and the constant $k_{r,N}$ case, respectively. The NWP saturation distributions for the two cases of this realisation are very similar. This similarity can be explained by the fact that the source node and the nodes immediately adjacent to the source location have a relatively high k_i. Therefore, the $k_{rN}^{\max}$ values in this region for the variable $k_{r,N}$ simulation are similar in magnitude (between approximately 0.8 and 0.9) to the $k_{rN}^{\max}$ value used throughout the constant $k_{r,N}$ simulation domain (0.91); thus, the effect of variable $k_{r,N}$ for this realisation, while the source is active, is minimal. Examination of the simulations performed using other realisations of Suite 3 indicate that the k_i of the source node can cause significant differences in the NWP migration pattern while the source is active, depending on the individual realisation utilised.

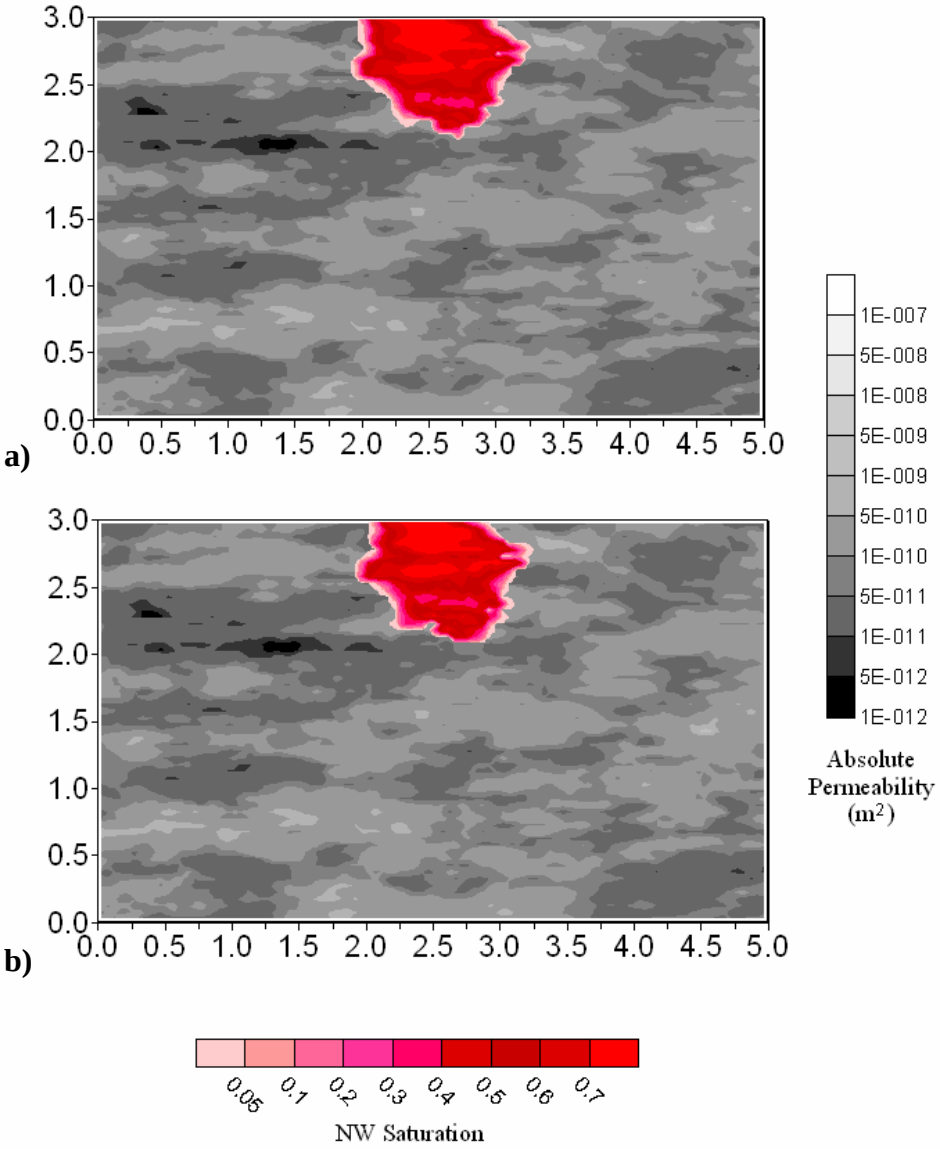

Figure 4-23. NWP saturation distribution for Suite 3, Realisation 5, following 20 minutes of simulation time: a) accounting for variable $k_{r,N}$; and, b) assuming constant $k_{r,N}$.

Figures 4-24a and 4-24b present the NWP saturation distributions for the variable $k_{r,N}$ case and the constant $k_{r,N}$ case, respectively, for Realisation 5 following 6 hours of simulation time. For the constant $k_{r,N}$ simulation, 6 hours represents the t_{99}. However, the t_{99} for the variable $k_{r,N}$ simulation is approximately 21 hours. The figures illustrate significant differences in the NWP distribution at this time between the two cases. The NWP has migrated to the bottom boundary of the solution domain after 6 hours of migration time when constant $k_{r,N}$ is assumed, while the NWP in the

variable $k_{r,N}$ simulation has migrated to a point approximately 0.6 m from the bottom of the domain. While 0.6 m is only a slight difference at the scale of the simulations performed in Suites 1 and 2, this difference in migration pattern is significant at the bench scale.

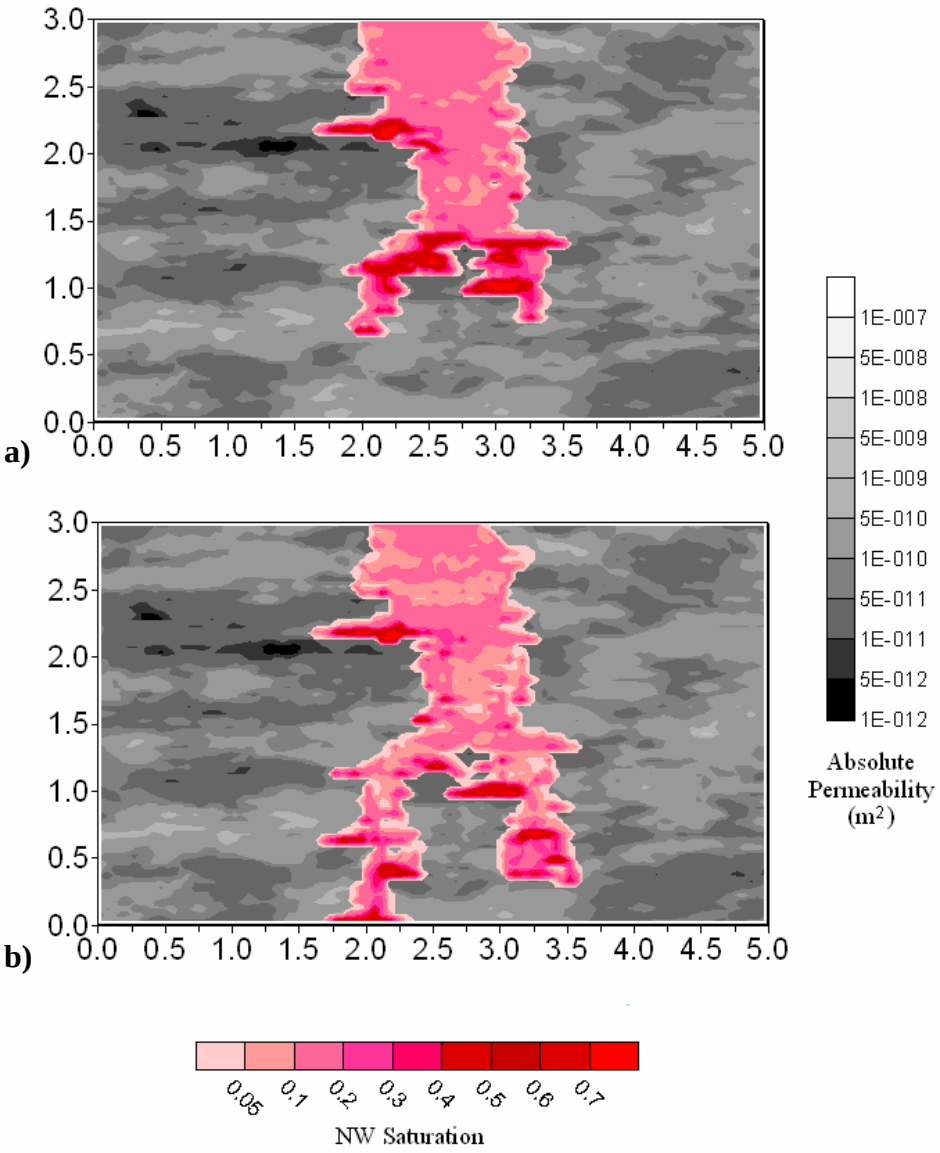

Figure 4-24. NWP saturation distribution for Suite 3, Realisation 5, following 6 hours of simulation time: a) accounting for variable $k_{r,N}$; and, b) assuming constant $k_{r,N}$.

Figures 4-25a and 4-25b present the NWP saturation distributions for the variable $k_{r,N}$ case and the constant $k_{r,N}$ case for Realisation 5 following 57 hours of simulation time, respectively. This time represents the t_{100} for the simulation

accounting for variable $k_{r,N}$. However, the t_{100} for the constant $k_{r,N}$ case occurred after only 9 hours of simulation time. The two figures show only very slight differences in the distribution of NWP following the complete cessation of migration.

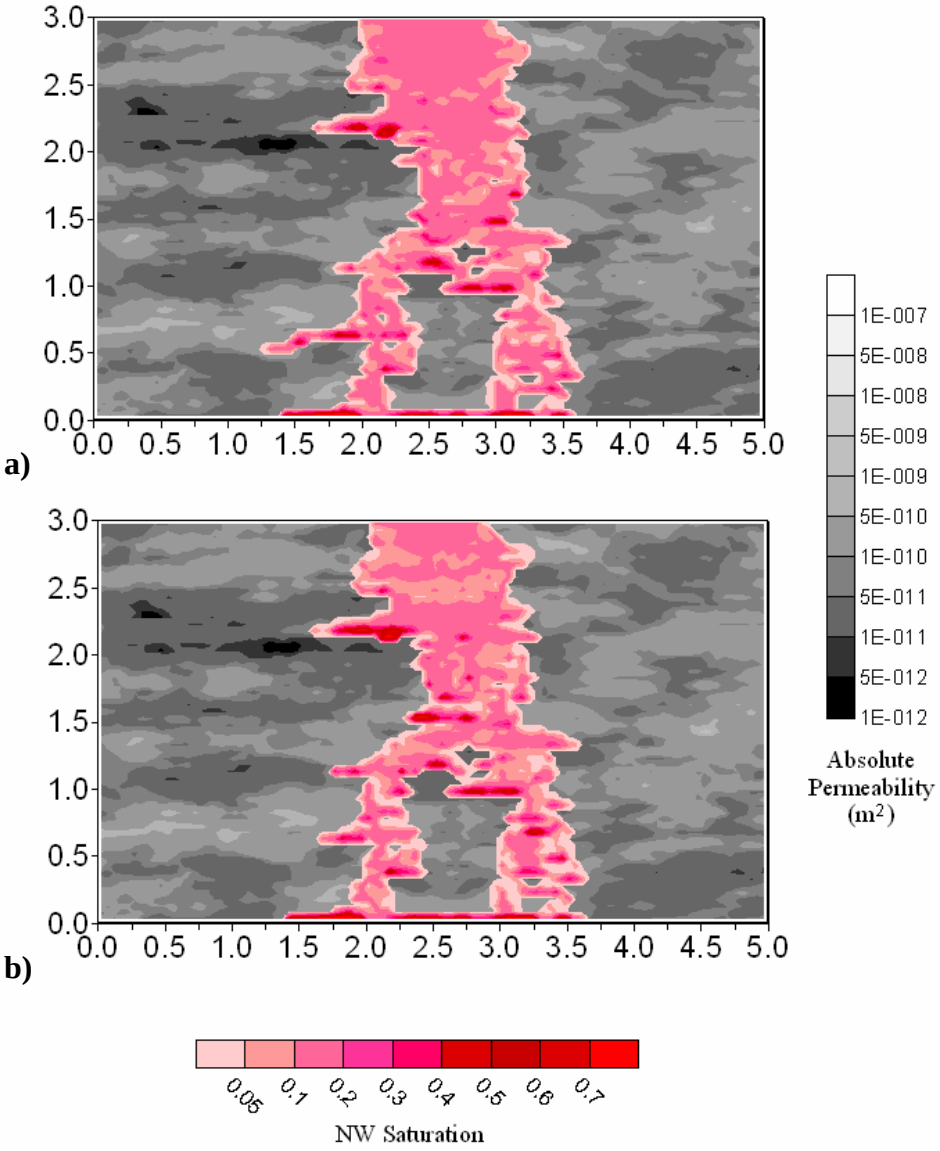

Figure 4-25. NWP saturation distribution for Suite 3, Realisation 5, following 57 hours of simulation time: a) accounting for variable $k_{r,N}$; and, b) assuming constant $k_{r,N}$.

In general, differences in the time scales of migration and the pattern of migration between the constant $k_{r,N}$ simulations and the variable $k_{r,N}$ simulations were found to be strongly dependent on the k_i of the source node and the nodes adjacent to the source. As NWP was released through a single node for this suite of simulations,

the $k_{rN}^{\max}$ value in the source boundary had a larger impact on the overall advancement of the NWP through the solution domain, than any single node in the wide source boundary for the Suite 2 simulations.

4.4.4.2 Quantitative Results

Figure 4-26 compares the total number of nodes invaded between the constant $k_{r,N}$ case and the variable $k_{r,N}$ case for each of the 10 realisations of Suite 3. Six of the ten realisations show that the total number of nodes invaded is greater when constant $k_{r,N}$ is assumed than when variable $k_{r,N}$ is accounted for in the simulation. However, Realisations 1, 5, and 8 show the reverse relationship, and Realisation 2 shows an identical number of nodes invaded for the two cases. The difference in number of nodes invaded ranges from zero for Realisation 2 to 53 (5.2% of the total number of nodes invaded for the variable $k_{r,N}$ case) for Realisation 9, with the average difference equal to 14.8 nodes (1.3%) indicating that the total volume of the domain invaded is insensitive to the variability of $k_{r,N}$ in the Suite 3 simulations. This insensitivity to variability of $k_{r,N}$ was also observed in the Suite 2 simulations which utilised realisations of an k_i field identical in mean and variance to the realisations of this suite of simulations.

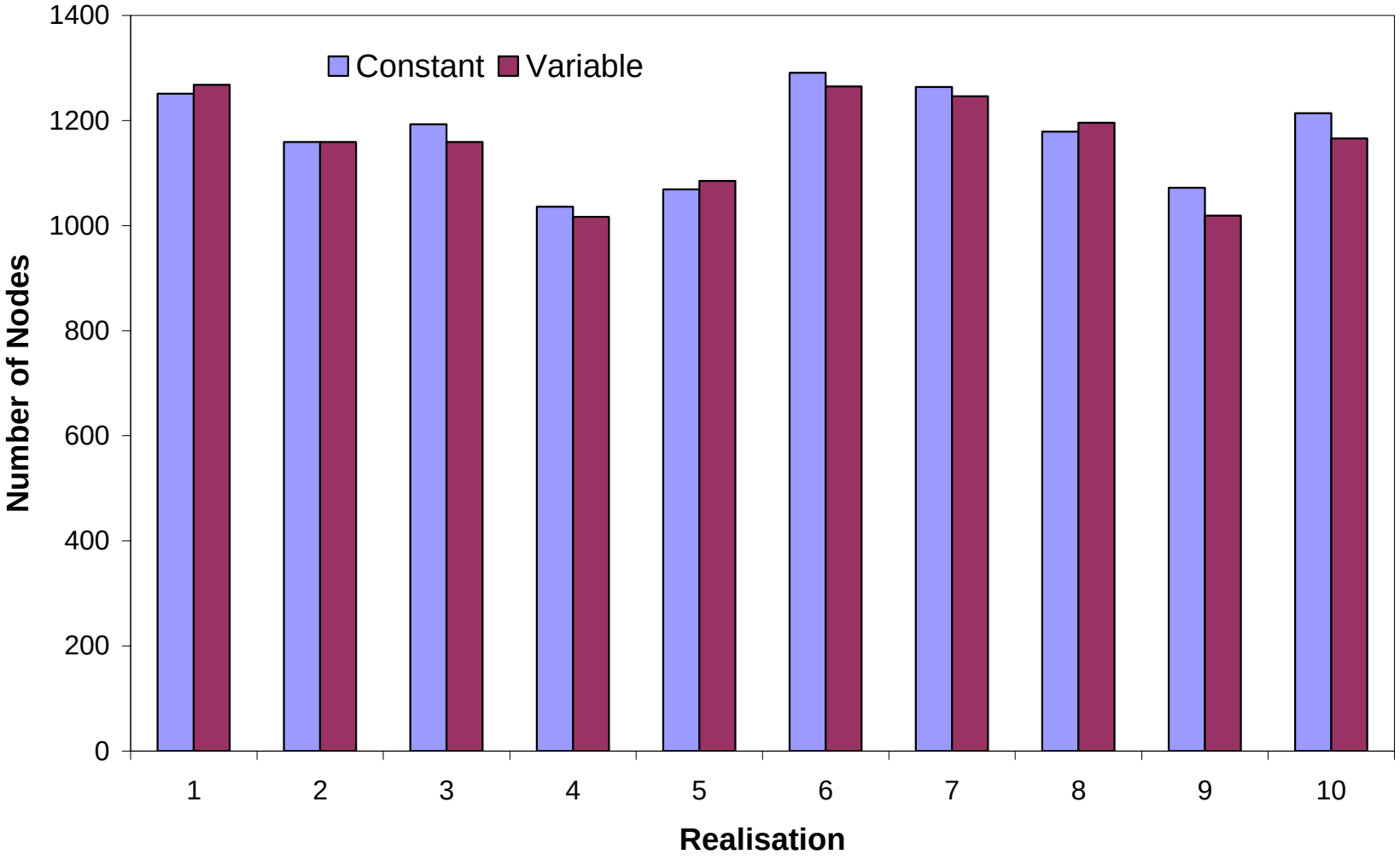

Figure 4-26. Comparison of the total number of nodes invaded: Suite 3.

Figures 4-27 through 4-30 compare the t_{90}, t_{95}, t_{99}, and t_{100}, respectively, between the constant $k_{r,N}$ case and the variable $k_{r,N}$ case for each of the 10 realisations of Suite 3. As can clearly be seen, for each realisation of the t_{90} and t_{95} figures, migration through the domain will cease earlier if constant $k_{r,N}$ is assumed, than if variable $k_{r,N}$ is accounted for in the simulation. The difference in t_{90} ranges from 1.9 hours for Realisation 1 to 13.8 hours for Realisation 7, with an average difference of 7.0 hours. The average t_{90} for the simulations assuming constant $k_{r,N}$ is 60% of the average migration time for the simulations accounting for variable $k_{r,N}$. The difference in t_{95} ranges from 2.6 hours for Realisation 7 to 24.4 hours for Realisation 2, with an average difference of 10.1 hours. The average t_{95} for the simulations assuming constant $k_{r,N}$ is 63% of the average migration time for the simulations accounting for variable $k_{r,N}$.

The relationship between t_{99} and t_{100} for the assumption of constant $k_{r,N}$ versus variable $k_{r,N}$ is fairly erratic. Cessation of migration generally occurs earlier if constant $k_{r,N}$ is assumed than when variable $k_{r,N}$ is accounted for in the simulation, with the exception of two realisations when migration is 99% ceased (Realisations 2 and 7) and for one realisation when migration is 100% ceased (Realisation 4). This inconsistency indicates that predictions regarding the cessation of NWP migration are sensitive to the numerical domain realisation and the degree of $k_{r,N}$ function variability in the region encountered by the advancing NWP.

The sensitivity of these results to the specific domain realisation utilised is exemplified by comparing the difference in complete (100%) migration cessation times for Realisations 4 and 7. Realisation 4 shows NWP migration continuing for 5.6 hours longer if constant $k_{r,N}$ is assumed, but Realisation 7 shows NWP migration continuing for 561.0 hours longer if variable $k_{r,N}$ is accounted for in the simulation.

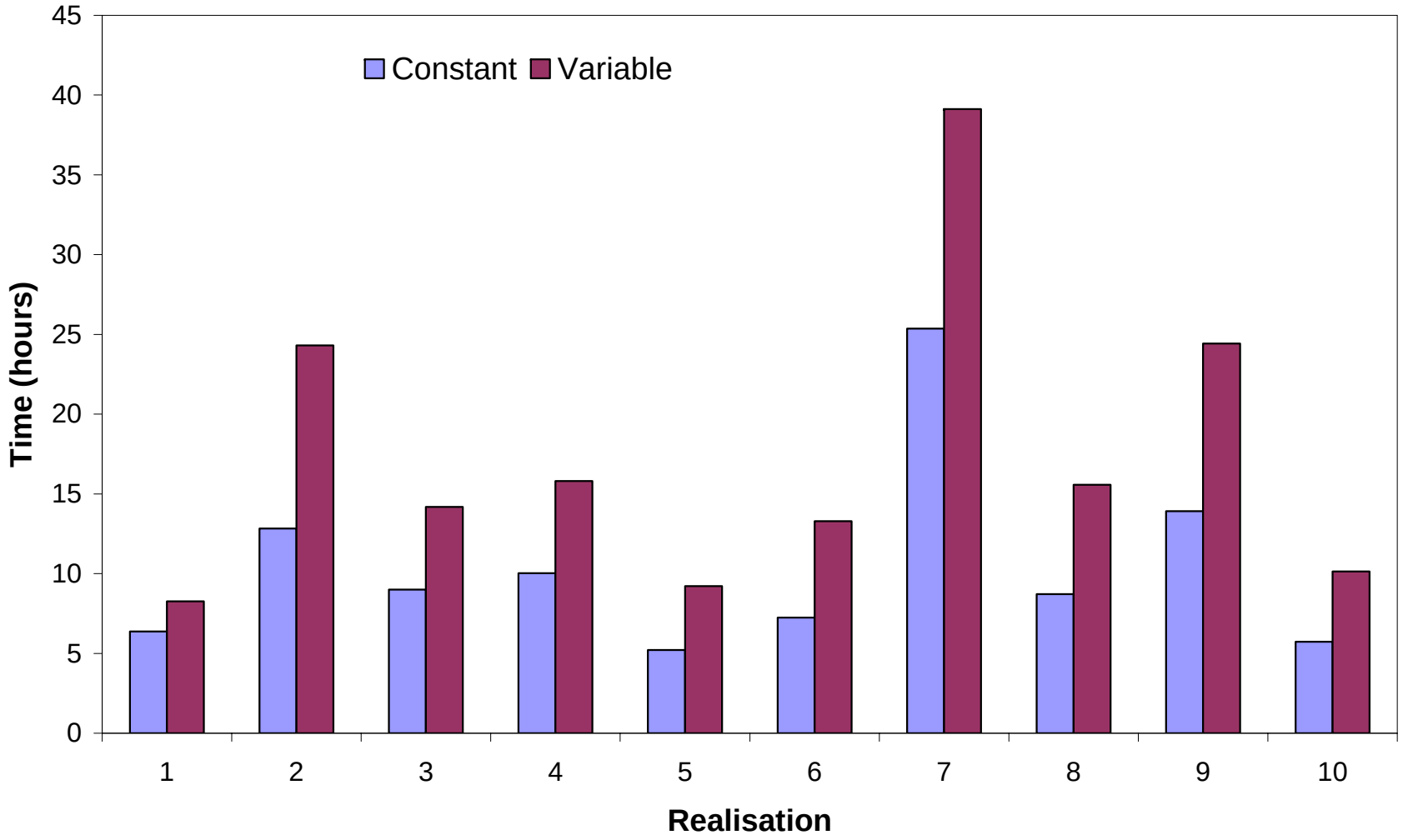

Figure 4-27. Comparison of the 90% cessation times: Suite 3.

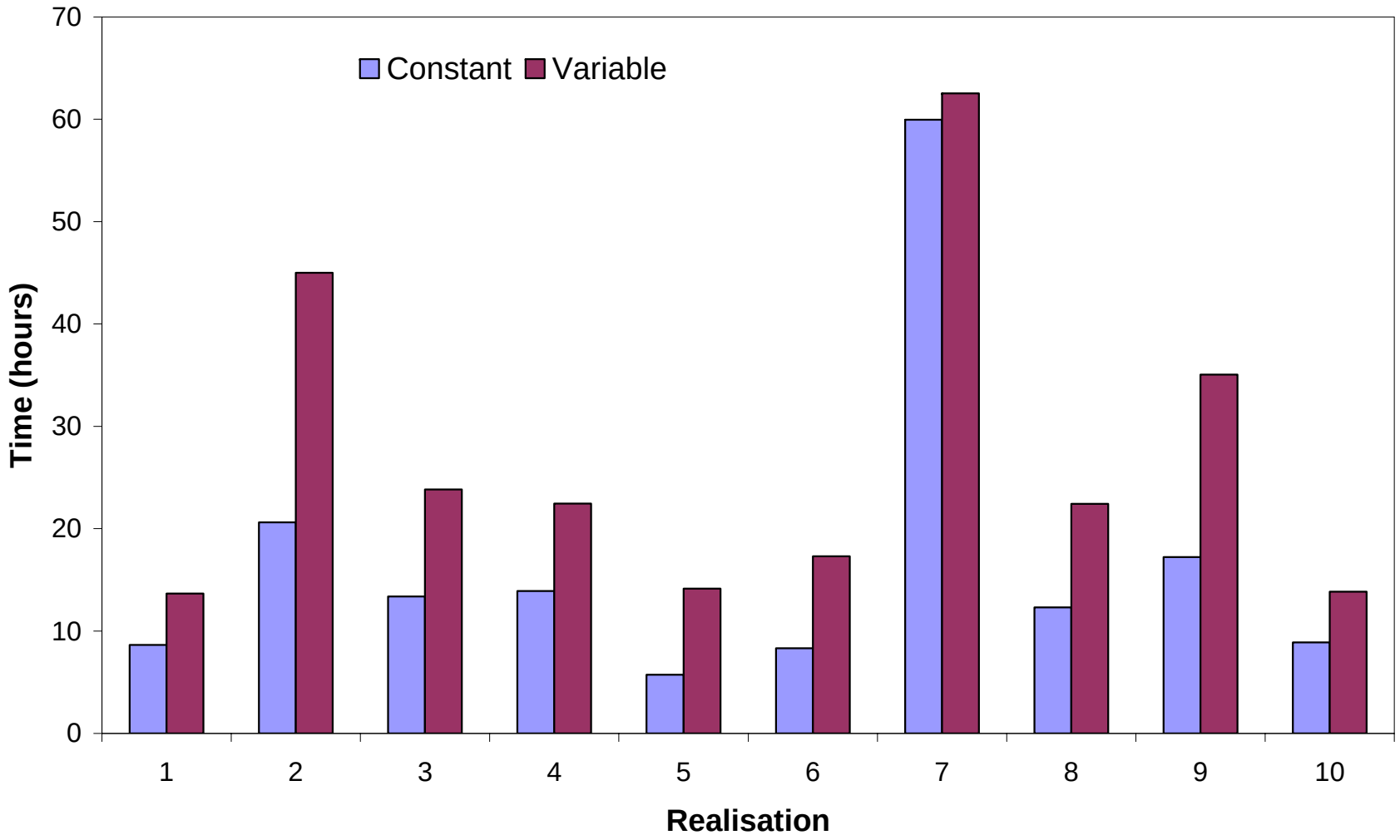

Figure 4-28. Comparison of the 95% cessation times: Suite 3.

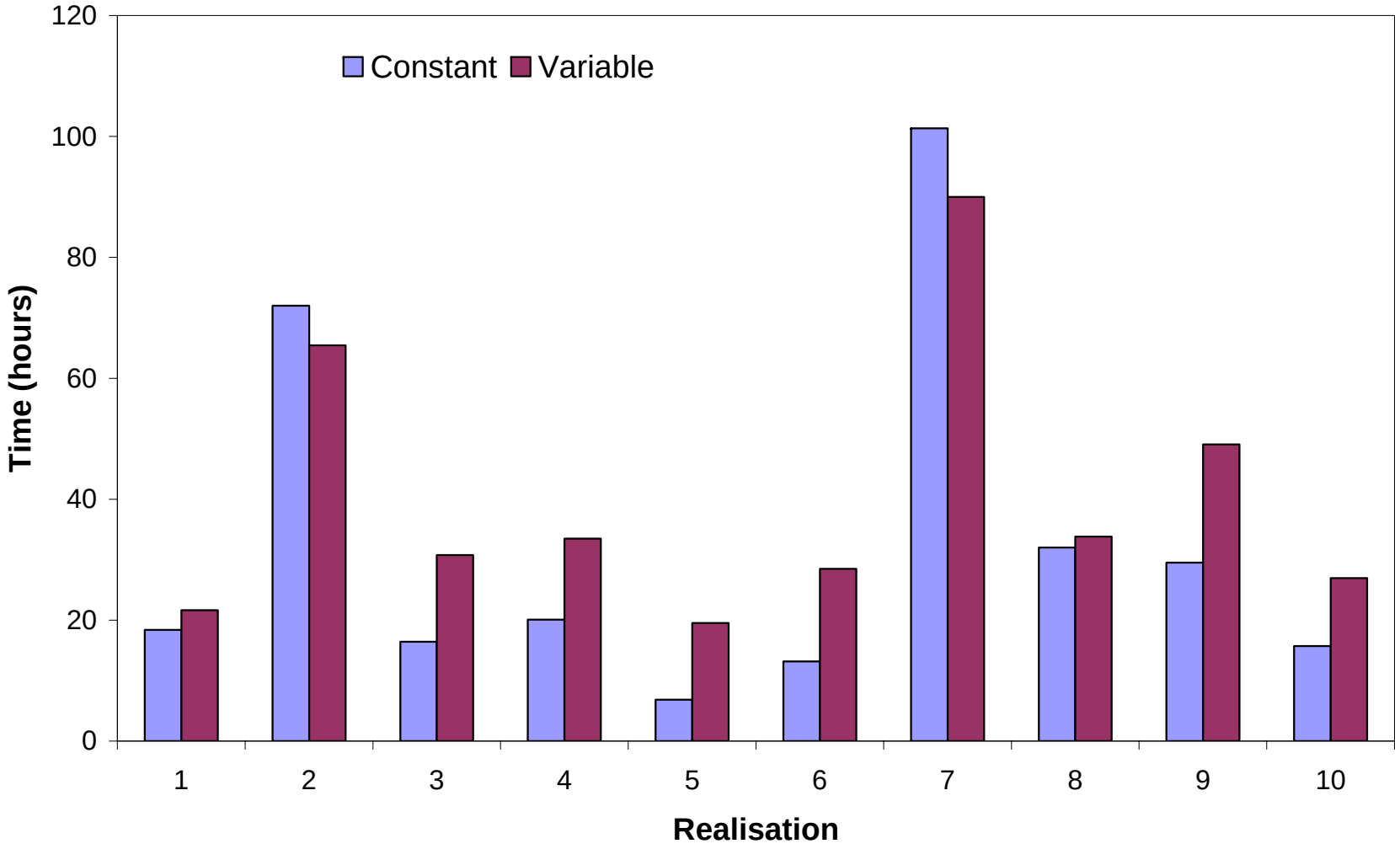

Figure 4-29. Comparison of the 99% cessation times: Suite 3.

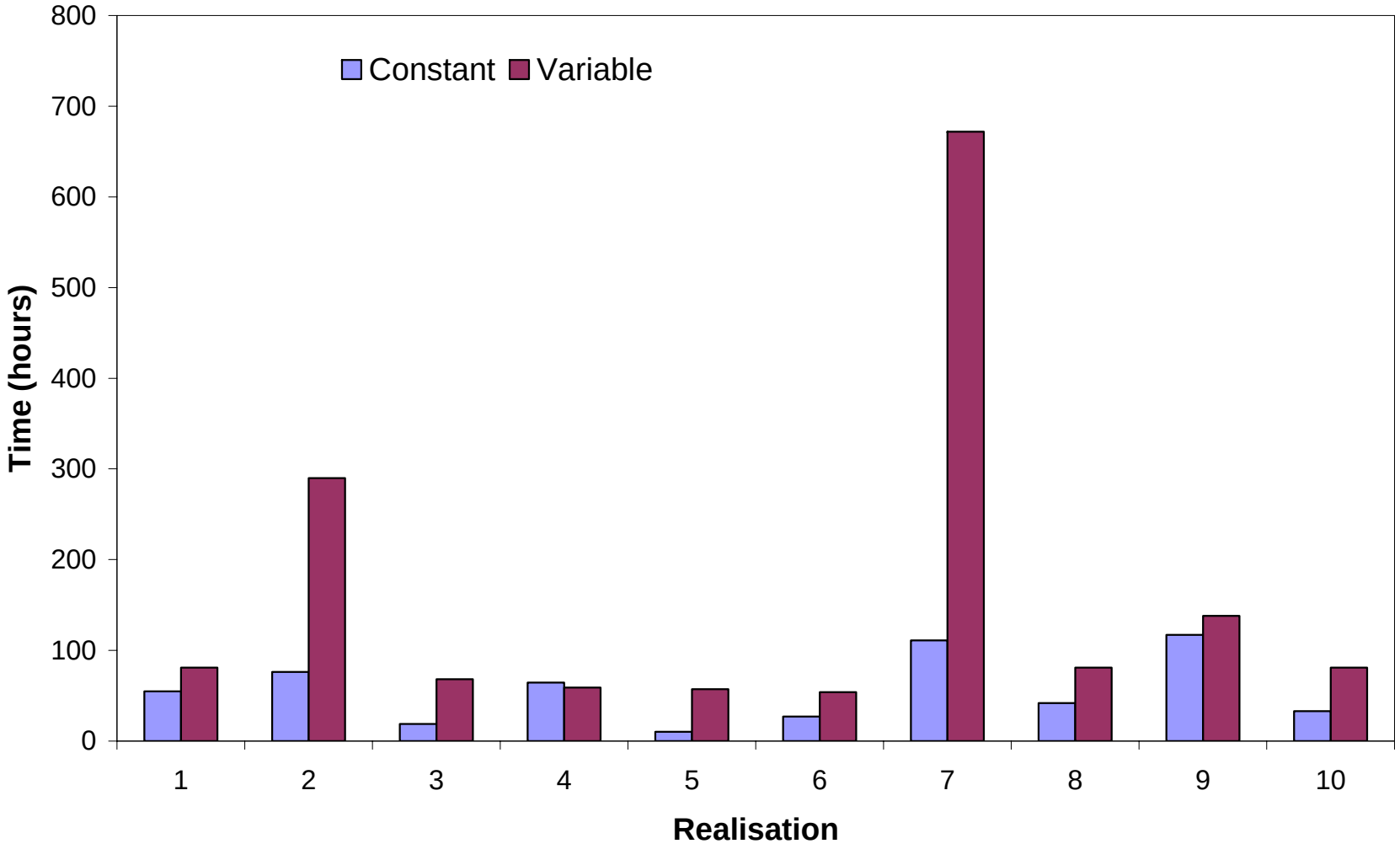

Figure 4-30. Comparison of the 100% cessation times: Suite 3.

Table 4-6 is a summary of the results presented in Figures 4-26 through 4-30, indicating the mean, minimum and maximum total number of nodes invaded, as well as the mean, minimum and maximum t_{100}, t_{99}, t_{95}, and t_{90} for both the constant $k_{r,N}$ simulations and the variable $k_{r,N}$ simulations for the 10 realisations of Suite 3.

Table 4-6. Summary of Numerical Modelling Results: Suite 3 Simulations

Comparison		Constant $k_{r,N}$	Variable $k_{r,N}$	Ratio (Constant / Variable)
Total Number of Nodes Invaded	Mean	1172.8	1158.0	1.01
	Minimum	1036 (Realisation 4)	1017 (Realisation 4)	1.02
	Maximum	1291 (Realisation 6)	1268 (Realisation 1)	1.02
90% Cessation Time (hours)	Mean	10.4	17.4	0.60
	Minimum	5.2 (Realisation 5)	8.27 (Realisation 1)	0.63
	Maximum	25.4 (Realisation 7)	39.1 (Realisation 4)	0.65
95% Cessation Time (hours)	Mean	16.9	27.0	0.63
	Minimum	5.7 (Realisation 5)	13.7 (Realisation 1)	0.42
	Maximum	60.0 (Realisation 7)	62.5 (Realisation 7)	0.96
99% Cessation Time (hours)	Mean	32.5	40.0	0.81
	Minimum	6.8 (Realisation 5)	19.5 (Realisation 5)	0.35
	Maximum	101.4 (Realisation 7)	90.0 (Realisation 7)	1.13
100% Cessation Time (hours)	Mean	55.4	158.1	0.35
	Minimum	10.2 (Realisation 5)	54.0 (Realisation 6)	0.19
	Maximum	117.0 (Realisation 9)	672.0 (Realisation 7)	0.17

The mean number of nodes invaded for the constant $k_{r,N}$ simulations is 1172.8 (19.5% of the domain) and the mean number of nodes invaded for the variable $k_{r,N}$ simulations is 1158.0 (19.3%). The difference in mean number of nodes invaded between the constant $k_{r,N}$ simulations and the variable $k_{r,N}$ simulations was found to be statistically insignificant by null hypothesis testing at the 5% significance level,

indicating that on average, variable $k_{r,N}$ has little affect on the predicted volume of porous media invaded for a NWP release in high k_i porous media at the bench scale.

The mean t_{90} and t_{95} assuming constant $k_{r,N}$ were found to be 60% and 63% of the cessation times accounting for variable $k_{r,N}$, respectively. Null hypothesis testing indicates that these differences are significant to 5%. While the mean t_{99} and t_{100} for constant $k_{r,N}$ were found to be 81% and 35% of the t_{99} and t_{100} for variable $k_{r,N,}$ respectively, the cessation times are highly sensitive to the specific domain realisation. As a result, the variance of the cessation times is appreciably large that the differences in the t_{99} and t_{100} are statistically insignificant by null hypothesis testing at the 5% significance level.

In some realisations, however, there are large differences in migration cessation times between the constant $k_{r,N}$ case and the variable $k_{r,N}$ (e.g., t_{100} for Realisation 7). Migration cessation times are under predicted for certain realisations, over predicted for others, and show no significant difference for the remainder of realisations. The significance of variable $k_{r,N}$ is dominated by the intrinsic permeability of the source node, and the nodes immediately surrounding the source at the bench scale. Therefore, researchers employing two-dimensional heterogeneous sand packs must consider variable $k_{r,N}$, as it may significantly affect the ability of a numerical simulator to predictthe results of a NWP release experiment: the influence of variable $k_{r,N}$ will depend on the specific pattern of heterogeneity employed in the experimental apparatus.

4.5 Conclusions

The Suite 1 simulations reveal that spatially variable $k_{r,N}$, correlated to porous media type, can significantly impact predictions of the pattern and timescales of a NWP release in a fine to very fine sand aquifer at the field scale. Null hypothesis

testing revealed that the assumption of constant $k_{r,N}$ throughout the solution domain will lead to under predictions of the volume of porous media invaded and the timescales of NWP migration. In general, the volume of NWP invaded porous media will be under predicted by approximately 9%, and the length of time during which NWP is migrating will be under predicted by a factor of approximately four, if variable (correlated) $k_{r,N}$ is not accounted for in the formulation of the numerical model.

The Suite 2 simulations revealed that accounting for variable $k_{r,N}$ is less important in a coarse sand to gravel (on average) aquifer at the field scale. High k_i implies a greater proportion of high $k_{rN}^{\max}$ values, and a relatively uniform distribution of $k_{r,N}$ throughout the domain. Therefore, the relative permeability characteristics of the domain more closely resemble the typical assumption of constant, high $k_{rN}^{\max}$ NWP relative permeability.

In contrast to the conclusions drawn for the Suite 2 simulations, the Suite 3 simulations reveal that variable $k_{r,N}$ can significantly affect predictions of the timescales of NWP invasion when considering migration at the bench scale, for a given realisation, even for relatively high k_i domains. At this scale, the influence of a single node, particularly the source node, or a node in the immediate vicinity of the source, can have a disproportionate influence on the prediction of a NWP release. A low k_i node (and the low $k_{rN}^{\max}$ value associated with this node) in the vicinity of the source, will significantly affect the rate of migration, and therefore, the timescales of NWP migration through the domain.

The implications are that numerical simulators should incorporate the relationship between k_{rN}-S_W and porous media type in order to be reliable across the widest range of subsurface environments and at a variety of scales. This suggests that

further local scale experiments would be valuable to enlarge the database of k_{rN}-S_W curve parameters across a wider range of porous media types. This may require new experimental techniques as currently measuring such curves in anything other than medium sand would be challenging.

4.6 References

Aziz, K., and A. Settari, *Petroleum Reservoir Simulation,* 476 pp., Applied Science, London, 1979.

Bear, J., *Dynamics of Fluids in Porous Media,* 764 pp., Dover, Mineola, N.Y., 1972.

Behie, G.A., and P.A. Forsyth, Incomplete factorization methods for fully implicit simulation of enhanced oil recovery, *SIAM J. Science and Statistical Computation, 5*(3), 543-561, 1984.

Brewster, M.L., A.P. Annan, J.P. Greenhouse, B.H. Kueper, G.R. Oldhoeft, J.D. Redman, and K.A. Sander, Observed migration of a controlled DNAPL release by geophysical methods, *Ground Water, 33*(6), 977-987, 1995.

Dekker, T.J., and L.M. Abriola, The influence of field-scale heterogeneity on the infiltration and entrapment of dense, nonaqueous phase liquids in saturated formations, *Journal of Contaminant Hydrology, 42,* 197-218, 2000.

Demond, A.H., and P.V. Roberts, An examination of relative permeability relations for two phase flow in porous media, *Water Resources Bulletin, 23*(4), 61-628, 1987.

Demond A.H., and P.V. Roberts, Estimation of two phase relative permeability relationships for organic liquid contaminants, *Water Resources Research, 29*(4), 1081-1090, 1993.

Demond, A.H., and P.V. Roberts, Effect of interfacial forces on two-phase P_C-S relationships, *Water Resources Research, 27*(3), 423-437, 1991.

Dury, O., U. Fischerm and R. Schulin, A comparison of relative nonwetting phase permeability models, *Water Resource Research, 35*(5), 1481-1493, 1999.

Essaid, H.I., W.N., Herkelrath, and K.M. Hess, Simulation of fluid distributions observed at a crude oil spill site including hysteresis, oil entrapment, and spatial variability of hydraulic properties, *Water Resources Research, 29*(6), 1753-1770, 1993.

Folk, R.L., *Petrology of Sedimentary Rocks,* 182 pp., Hemphill Publishing Company, Austin, Texas, 1980.

Geffen, T.M., W.W. Owens, D.R. Parrish and R.A. Morse, Experimental investigations of factors affecting laboratory relative permeability measurements, *Transactions AIME, 192,* 99-110, 1951.

Gerhard, J.I., B.H. Kueper, and G.R. Hecox, The influence of waterflood design on the recovery of mobile DNAPLs, *Ground Water, 36*(2), 283-292, 1998.

Gerhard, J.I., and B.H. Kueper, Capillary pressure characteristics necessary for simulation DNAPL infiltration, redistribution, and immobilization in saturated porous media, *Water Resources Research, 39*(8), SBH71-SBH717, 2003a.

Gerhard, J.I., and B.H. Kueper, Relative permeability characteristics necessary for simulating DNAPL infiltration, redistribution, and immobilization in saturated porous media, *Water Resources Research, 39*(8), SBH81-SBH816, 2003b.

Gerhard, J.I., and B.H. Kueper, Influence of constitutive model parameters on the predicted migration of DNAPL in heterogeneous porous media, *Water Resources Research, 39*(8), SBH41-SBH413, 2003c.

Hofstee, C., J.H. Dane, and W.E. Hill, Three fluid retention in porous media involving water, PCE and air, *Journal of Contaminant Hydrology, 25*, 235-247, 1997.

Illangasekare, T.H., J.L. Ramsey Jr., K.H. Jensen, and M.B. Butts, Experimental study of the movement and distribution of dense organic contaminants in heterogeneous aquifer, *Journal of Contaminant Hydrology, 20*, 1-25, 1995.

Imhoff, P.T., A.S. Mann, M. Mercer, and M. Fitzpatrick, Scaling DNAPL migration from the laboratory to the field, *Journal of Contaminant Hydrology, 64,* 73-92, 2003.

Kueper, B.H., W. Abbot, and G. Farquhar, Experimental observations of multiphase flow in heterogeneous porous media, *Journal of Contaminant Hydrology, 5*, 83-95, 1989.

Kueper, B.H., and E.O. Frind, Two phase flow in heterogeneous porous media: 1. Model development, *Water Resources Research, 27*(6), 1049-1057, 1991a.

Kueper, B.H., and E.O. Frind, Two phase flow in heterogeneous porous media: 2. Model application, *Water Resources Research, 27*(6), 1059-1070, 1991b.

Kueper, B.H., J.D. Redman, R.C. Starr, S. Reitsma, and M. Mah, A field experiment to study the behaviour of tetrachloroethylene below the watertable: Spatial distribution of residual and pooled DNAPL, *Journal of Ground Water, 31*(5), 756-766, 1993.

Kueper, B.H., and J.I. Gerhard, Variability of point source infiltration rates for two-phase flow in heterogeneous porous media, *Water Resources Research, 31*(12), 2971-2980, 1995.

Lemke, L.D., L.M. Abriola, and P. Goovaerts, Dense nonaqueous phase liquid (DNAPL) source zone characterization: Influence of hydraulic property correlation on

predictions of DNAPL infiltration and entrapment, *Water Resources Research, 40*(12), 1-18, 2004.

Lin, C., G.F. Pinder, and E.F. Wood, Water and trichloroethylene as immiscible fluids in porous media, Research Report 83-WR-2, Princeton University, Princeton, New Jersey, USA, 1982

Naar, J., R.J. Wygal, and J.H. Henderson, Imbibition relative permeability in unconsolidated porous media, *Society of Petroleum Engineers Journal, March,* 1962.

O'Carroll, D.M., S.A. Bradford, and L.M. Abriola, Infiltration of PCE in a system containing spatial wettability variations, *Journal of Contaminant Hydrology, 73,* 39-63, 2004.

Phelan, T.J., L.D. Lemke, S.A. Bradford, D.M. O'Carroll, and L.M. Abriola, Influence of textural and wettability variations on predictions of DNAPL persistence and plume development in saturated porous media, *Advances in Water Resources, 27,* 411-427, 2004.

Poulsen, M.M., and B.H. Kueper, A field experiment to study the behaviour of tetrachloroethylene in unsaturated porous media, *Environmental Science and Technology, 26*(5) 889-895, 1992.

Rathfelder, K.M., L.M. Abriola, M.A. Singletary, K.D. Pennell, Influence of surfactant-facilitated interfacial tension reduction on chlorinated solvent migration in porous media: observations and numerical simulation, *Journal of Contaminant Hydrology, 64*, 227-252, 2003.

Reynolds, D.A., and B.H. Kueper, Multiphase flow and transport in fractured clay/sand sequences, *Journal of Contaminant Hydrology, 51*(1-2), 41-62, 2001.

Robin, M.J.L., E.A. Sudicky, R.W. Gillham, and R.G. Kachanowski, Spatial variability of Strontium distribution coefficients and their correlation with hydraulic

conductivity in the Canadian Forces Base Borden aquifer, *Water Resources Research, 27*(10), 2619-2632, 1991.

Rosenburg, D.U., Methods for the Numerical Solution of Partial Differential Equations, 128 pp., Elsevier Science, New York, 1969.

Schwille, F., *Dense Chlorinated Solvents in Porous and Fractured Media Model Experiments*, 146 pp. Translated by J.F. Pankow, Lewis Publishers, Chelsea, MI, 1988.

Stonestrom, D.A., Co-determination and comparisons of hysteresis-affected parametric functions of unsaturated flow: Water-content dependence of matric pressure, air-trapping, and fluid permeabilities in a non-swelling soil, Ph. D., thesis, Stanford University, Stanford, CA., USA, 1987.

Stonestrom, D.A., and J. Rubin, Air permeability and trapped-air content in two soil, *Water Resources Research, 25*(9), 1959-1969, 1989b.

CHAPTER 5 – VALIDATION OF AN INTERFACIAL AREA MODEL FOR THE EXPLICIT DESCRIPTION OF RATE LIMITED MASS TRANSFER IN MULTIPHASE SYSTEMS

5.1 Introduction

A significant amount of theoretical and laboratory research has been conducted to study the process of Dense Non-Aqueous Phase Liquid (DNAPL) dissolution. This area of study has received a great deal of attention because dissolved phase constituents are the primary hazard associated with DNAPL contaminated sites and are often quantified in the field as a measure of the efficacy of remediation efforts.

DNAPL dissolution is often described using either a Local Equilibrium Assumption (LEA) (e.g. Abriola, 1989; Seagren *et al.,* 1999; Sale and McWhorter, 2001) or an empirical rate-limited expression based on the single boundary layer model (e.g. Hunt *et al.,* 1988; Miller *et al.,* 1990; Powers *et al.,* 1992; Imhoff, *et al.,* 1993), or the dual boundary layer model (Brusseau *et al.*, 1992).

The LEA allows the rate of mass transfer to be estimated based on an equilibrium partitioning relationship (e.g. Abriola, 1989), whereas for the single boundary layer model, the rate of mass transfer is a function of a driving force (concentration gradient) and the interfacial area between the two phases of concern (Miller *et al.,* 1990):

$$J = k_{la} a^n \left(C_s - C\right) \tag{5-1}$$

where J $[ML^{-3}T^{-1}]$ is the solute mass flux from the DNAPL to the aqueous phase, k_{la} $[LT^{-1}]$ is the average mass transfer coefficient for the DNAPL-water interface, a^n is the total specific interfacial area $[L^2L^{-3}]$ between DNAPL and groundwater for a representative elementary volume (REV), C_s $[ML^{-3}]$ is the aqueous phase

concentration that corresponds to the condition of thermodynamic equilibrium with the non-aqueous phase (i.e., effective solubility), and C [ML^{-3}] is the solute concentration in the bulk aqueous phase. As direct measurement of two-fluid interfacial area is difficult (Morrow, 1970; Powers *et al.*, 1992), most researchers combine the average mass transfer term and the specific interfacial area term into a lumped mass transfer term, $K_l = k_{la}\, a^n$, and evaluate this parameter through the use of 'correlation expressions' of the Sherwood number, *Sh*.

Although Equation 5-1 has been shown to be theoretically simplistic (Miller *et al.,* 1990), it has been successfully utilised by a number of researchers as an empirical tool for describing rate-limited mass transfer (e.g. Miller *et al.,* 1990; Parker *et al.,* 1991; Powers *et al.,* 1992; Gellar and Hunt, 1993; Imhoff *et al.,* 1993; Powers *et al.,* 1994; Saba and Illangasekare, 2000; Nambi and Powers, 2003). However, these studies have primarily examined the dissolution of a fixed source of residual saturation DNAPL (e.g. Miller *et al.,* 1990; Powers *et al.,* 1992; Imhoff *et al.,* 1993; Powers *et al.,* 1994; Saba and Illangasekare, 2000), often in only one-dimensional systems (e.g. Miller *et al.,* 1990; Powers *et al.,* 1992; Imhoff *et al.,* 1993; Powers *et al.,* 1994). To date, no one to the authors' knowledge has conducted a detailed study to examine the dissolution of a transient near-surface DNAPL release that has resulted in a complex suite of pools and residual distributed through heterogeneous porous media and exhibiting complex, realistic saturation history.

The suitability of any expression or model for dissolution depends on the scale at which it is applied. In the LEA, the rate of mass flux from a DNAPL source zone is independent of the macroscopic mass transfer coefficient and is entirely dependent on advection and dispersion within the aqueous phase. However, the LEA requires the definition of the "local" scale, or REV (REV_{LEA}), over which bulk mass transfer

can be considered to be independent of K_l. The size of this REV is likely to evolve, as the seepage velocity through a DNAPL source zone and the interfacial area between phases are both functions of DNAPL saturation, which will vary with time as dissolution proceeds. As noted by Miller *et al.* (1990) and Imhoff *et al.* (1993), the size of the REV_{LEA} is generally on the order of a few centimetres.

At scales smaller than a few centimetres, a rate-limited description of mass transfer is necessary (Imhoff *et al.,* 1993). However, numerical modelling studies that compare published correlation expressions have shown dissolution rates to be highly sensitive to the local scale expression utilised to predict behaviour in large scale (Zhu and Sykes, 2000) or heterogeneous (Mayer and Miller, 1996; Grant and Gerhard, 2004 - see Appendix G) systems. Imhoff *et al.* (1993) compares estimates of *Sh* calculated from the correlation expressions of Miller *et al.* (1990), Parker *et al.* (1991), Powers *et al.* (1992), and Gellar and Hunt (1993) and found that *Sh* values range over three orders of magnitude for a fixed set of conditions. While Imhoff *et al.* (1993) attributes this lack of agreement to laboratory methods, including the different techniques used for establishing residual NAPL within the porous media, it is clear that the correlation expressions are only valid under very specific conditions, and in some cases may only be considered valid under the conditions under which they were derived (Grant and Gerhard, 2004 – see Appendix G).

Describing dissolution at the laboratory and field scale is further complicated by the fact that large-scale mass transfer rates are often found to be orders of magnitude lower than local scale mass transfer rates as a result of 'flow-bypassing'. Field scale mass flux can be described according to (Falta *et al.,* 2005):

$$M_{field} = \hat{q}_W A C_{avg} \tag{5-2}$$

where M_{field} is the field scale mass flux (MT^{-1}), $\hat{q}_W$ is the global aqueous phase Darcy flux (LT^{-1}), A is the given cross-sectional area of a control plane perpendicular to the mean groundwater flow direction (L^2), and C_{avg} is the average aqueous phase concentration (M^3L^{-3}). Equation 5-2 reveals that field scale mass flux is increased with an increase in either average aqueous phase concentration or global aqueous phase flux. However, for groundwater passing through a complex DNAPL source zone, both of these are determined by the summation of the (non-trivial) spatially and temporally variable local scale concentrations and fluxes. Local scale aqueous phase flux in a multiphase system is given by the two phase extension of Darcy's law, such that (Bear, 1970):

$$q_w = \frac{-k_{abs}k_{r,W}}{\mu_W}\left(\frac{dP_W}{dx} + \rho_W g \frac{dz}{dx}\right) \tag{5-3}$$

where k_{abs} is the local intrinsic permeability, $k_{r,W}$ is the local relative permeability to the aqueous phase which is a function of the local saturation, μ_W is the aqueous phase viscosity, P_W is the local aqueous phase pressure and g is acceleration due to gravity. Thus, it is at the local scale that multiphase flow processes and interphase mass transfer processes interact, dictating the observed fate of contaminant mass at the field scale. For example, if the gradient is increased across a highly NWP-saturated pool, the increased local scale aqueous phase flux will accelerate local dissolution, causing NWP saturations to decrease and $k_{r,W}$ to increase, thereby further increasing local mass flux rates (i.e., reducing flow bypassing) and correspondingly causing field scale mass flux rates, M_{field}, to increase.

Flow-bypassing is attributed to the effects of heterogeneity in DNAPL distributions and groundwater flow (Parker and Park, 2004). Brusseau *et al.* (2002) conducted intermediate-scale dissolution experiments and concluded that overall

(bench scale or higher) dissolution behaviour is controlled by larger scale factors such as non-uniform NAPL distribution, permeability variation, and dilution associated with aqueous phase sampling, and that local-scale mass transfer processes are generally of secondary importance. Therefore, even if near-equilibrium mass transfer occurs at the local scale, field scale mass transfer is primarily controlled by advective – dispersive transport (Sale and McWhorter, 2001, Soga *et al.,* 2004).

The gross influence of flow-bypassing on numerical model predictions of mass transfer rates at the laboratory and the field scale does not need to be estimated if DNAPL migration is simulated at a scale fine enough to precisely describe the architecture of the source zone. As migration has been shown to be governed by porous media heterogeneity at the centimetre scale (Kueper *et al.* 1993; Brewster *et al.* 1995), it is possible that the REV required to precisely describe DNAPL migration (REV_{mig}) may be smaller than the scale above which dissolution can be adequately described using a LEA (i.e., $REV_{mig} < REV_{LEA}$). REV_{LEA} is variable as a result of the interplay between saturation, interfacial area, and groundwater velocity; therefore, the most rigorous method for simulating both DNAPL migration and dissolution would be to define the system at a scale equal to REV_{mig} and utilise a rate-limited expression for mass transfer. To simulate DNAPL migration and dissolution at a sub REV_{LEA} scale, you need a reliable mass transfer model; but, as we have seen above, correlation expressions are too limited. No robust dissolution model yet exists to cover the range of saturations and conditions encountered for a transient DNAPL release at this scale.

A truly scale-independent rate limited mass transfer expression is desirable for use in numerical simulations at the field scale. A mass transfer expression such as this may be possible by developing a methodology for independently approximating the specific interfacial area between the DNAPL and the aqueous phase (see Equation

5-1). Such an approximation would allow for the explicit evaluation of the average mass transfer coefficient for the DNAPL-water interface, k_{la}, for the REV. Correlation expressions do not explicitly determine the value of k_{la}: however, k_{la} is expected to be a proportionality constant for a given system that is only dependent on the fluid pair in question (Powers *et al.,* 1991).

Numerous methods exist for approximating interfacial area including the capillary tube model (Cary, 1994), the ideal soil model (Gvirtzman and Roberts, 1991), the interfacial tracer technique (IFTT) (Kim *et al.,* 1999; Saripalli *et al.,* 1998), or the thermodynamic approach (Leverett, 1941; Morrow, 1970; and, Bradford and Leij, 1997). However these methods have a number of drawbacks, as the capillary tube and ideal soil models rely on assumptions of an idealised porous media, the IFTT is better suited to approximating average interfacial area at the field scale, and the thermodynamic approach assumes an equality between mechanical work done on the system and change in interfacial area (Dalla *et al.,* 2002).

The purpose of this study is to derive and validate an expression describing rate-limited mass transfer that includes an appropriate and explicit description of DNAPL/aqueous phase interfacial area, referred to herein as the current model. Data from two-dimensional bench scale experiments examining the dissolution of a transient DNAPL source in heterogeneous porous media will be compared to numerical simulation results to carry out this objective. Numerical simulations will also be conducted to examine the influence of the derived expression on the timescales of DNAPL dissolution at the field scale.

5.2 Interfacial Area Approximation

As discussed in detail in Chapter 2, interfacial area (IFA) plays a critical role in governing trans-interfacial processes such as dissolution. While numerous methods

exist for approximating interfacial area (see Chapter 2), comparison with experimental (e.g. IFTT), or numerical (pore-network model) calculations indicate that existing models are inadequate for predicting interfacial areas at the level of precision required in many groundwater contamination scenarios (Dalla *et al.,* 2002). This section will present the development of a new IFA model that, when incorporated into numerical models, will allow prediction of the rate-limited mass transfer throughout a complex, realistic DNAPL source zone.

5.2.1 Basic Thermodynamic Interfacial Area Model

The current IFA model is based upon the thermodynamic treatment of two-fluid capillary pressure - saturation relations; elements of this approach are presented by Leverett (1941), Morrow (1970) and Bradford and Leij (1997). The thermodynamic approach is based upon an assumption of equality between mechanical work done on the system and change in interfacial area (Dalla *et al.,* 2002). Notably, Leverett (1941) proposed that the former is proportional to the area under the capillary pressure – saturation curve. The thermodynamic model is used as the basis for the current IFA model as it is theoretically sound and it relies solely on calculations involving data that is readily available for most systems of interest, namely fluid properties and capillary pressure – saturation relationships.

The current IFA model will significantly modify and expand the basic thermodynamic model in order to more completely and consistently describe mass transfer throughout the range of possible saturations and saturation history. This expansion includes 5 major changes: 1) to provide consistency with the constitutive relationships necessary for simulating DNAPL migration in heterogeneous porous media; 2) to provide continuity of saturation history; 3) to account for Haines Jump energy losses (as identified by Dalla *et al.,* 2002); 4) to consider only the effective

specific interfacial area between the bulk nonwetting phase (NWP) and the bulk WP; and, 5) to describe the change in interfacial area resulting from the dissolution of residual NWP.

5.2.2 Modification 1: Consistency with Constitutive Relationships

Leverett (1941) first presented a thermodynamic approach for estimating IFA that was relatively basic. Assuming complete wetting of the solid by the wetting fluid, no NWP residual formation, and capillary pressures defined for $S_r < S_W \leq 1.0$, total specific interfacial area (i.e., the total interfacial area per unit volume of porous media), a^n [L^2L^{-3}], can be calculated according to (Leverett, 1941):

$$a^n(S_W) = \frac{\Phi_{NW}(S_W)}{\sigma_{NW}} \qquad S_r < S_W \leq 1.0 \qquad (5\text{-}4)$$

where σ_{NW} is the interfacial tension between the NWP and the WP, and $\Phi_{NW}(S_W)$ is the area under the capillary pressure - saturation curve:

$$\Phi_{NW}(S_W) = -\int_X^{S_W} P_C(S_W)\,dS_W \qquad (5\text{-}5)$$

where X is equal to the value of S_W when $P_C = 0$, and $P_C(S_W)$ is the capillary pressure - saturation function for drainage or imbibition.

Bradford and Leij (1997) modified Equation 5-4 for the case of imbibition so as to account for the formation of NWP residual; that work suggests total specific interfacial area can be more accurately calculated according to:

$$a^n(S_W) = \frac{\Phi_{NW}(S_W) + C_{NW}}{\sigma_{NW}} \qquad S_r < S_W \leq 1.0 \qquad (5\text{-}6)$$

where C_{NW} is a constant of integration that accounts for the contribution to interfacial area from the existence of spherical blobs of NWP residual: $C_{NW} = 0$ on drainage and imbibition until first NWP residual formation where $C_{NW} > 0$, and remains so on all subsequent drainage/imbibition cycles. While this represents a useful advance, this

model remains insufficient because it fails to account for the influence of saturation history on the amount of work applied to, and from, the system.

The present work uses the constitutive model of Gerhard and Kueper (2003a,b), further developed in Chapter 3, which contains the key characteristics necessary for DNAPL migration in heterogeneous porous media. Importantly in this context, that constitutive model fully accounts for complex saturation history and physically realistic and mathematically consistent endpoints for the $P_C(S_W)$ and $k_{rN}(S_W)$ functions. Equation 5-4 can be further modified for consistency with this constitutive model by re-defining X as $S_W = 1.0$ and defining Equation 5-4 as valid on drainage:

$$\Phi_{NW}(S_W) = -\int_{X}^{S_W} P_C(S_W) dS_W \qquad S_r < S_W \leq S_W^M \qquad (5\text{-}7)$$

where S_W^M is the WP saturation when P_C equals the entry pressure, P_E, and on imbibition:

$$\Phi_{NW}(S_W) = -\int_{X}^{S_W} P_C(S_W) dS_W \qquad S_r < S_W \leq S_W^X \qquad (5\text{-}8)$$

where S_W^X is the WP saturation when P_C equals the terminal pressure, P_T.

Figure 5-1 presents a hypothetical capillary pressure - saturation diagram and Figure 5-2 presents the corresponding interfacial area - saturation diagram according to the basic thermodynamic model, modified for the presence of NWP residual and consistency with the constitutive relationships employed in this study. In the basic thermodynamic IFA model presented in Figure 5-2, C_{NW} is zero during primary drainage and main imbibition, but is calculated according to the method of Bradford and Leij (1997) at first NWP residual formation. This is seen in Figure 5-2 as an abrupt increase in interfacial area at the WP saturation corresponding to the formation of NWP residual.

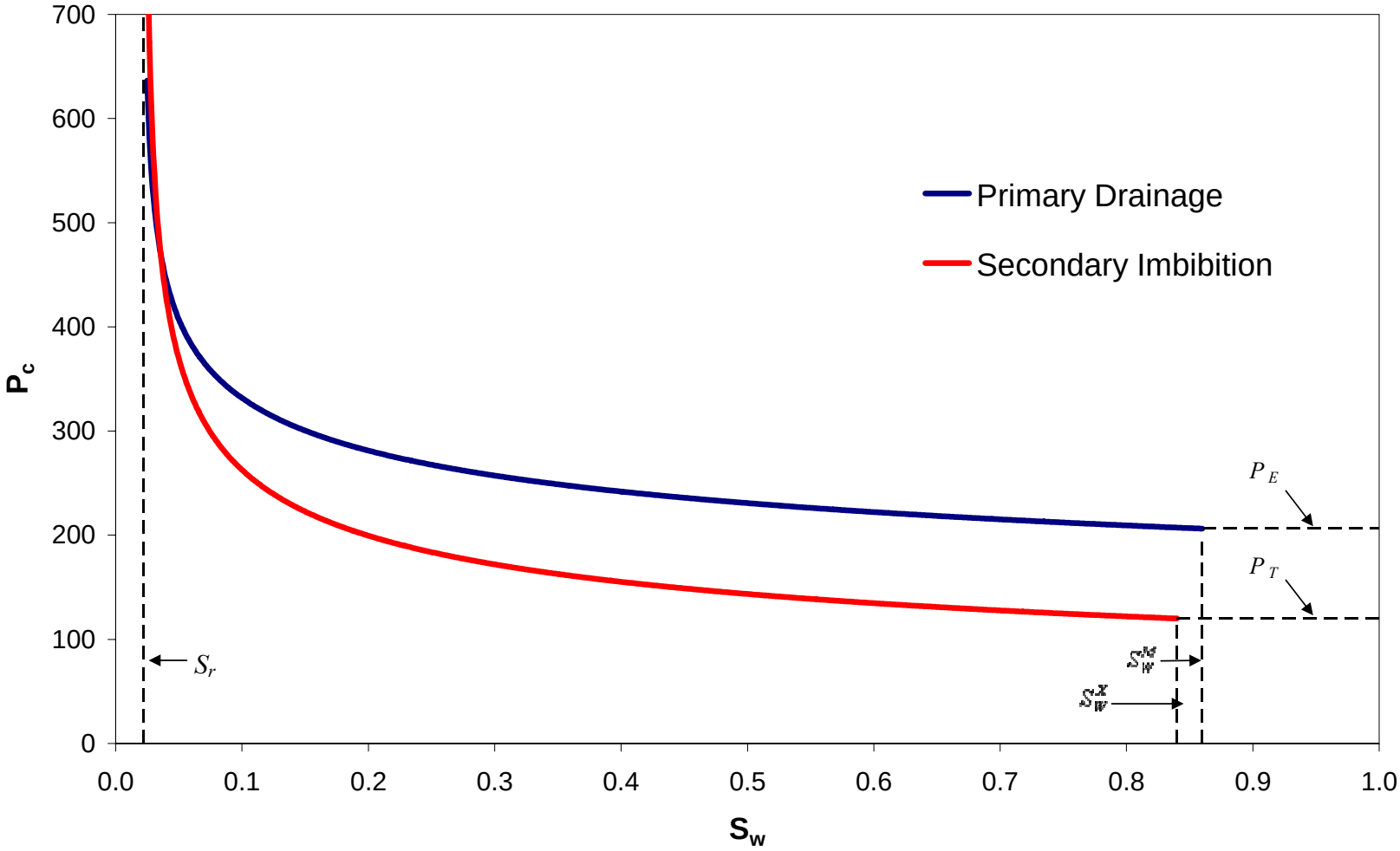

Figure 5-1. Hypothetical capillary pressure – saturation curve.

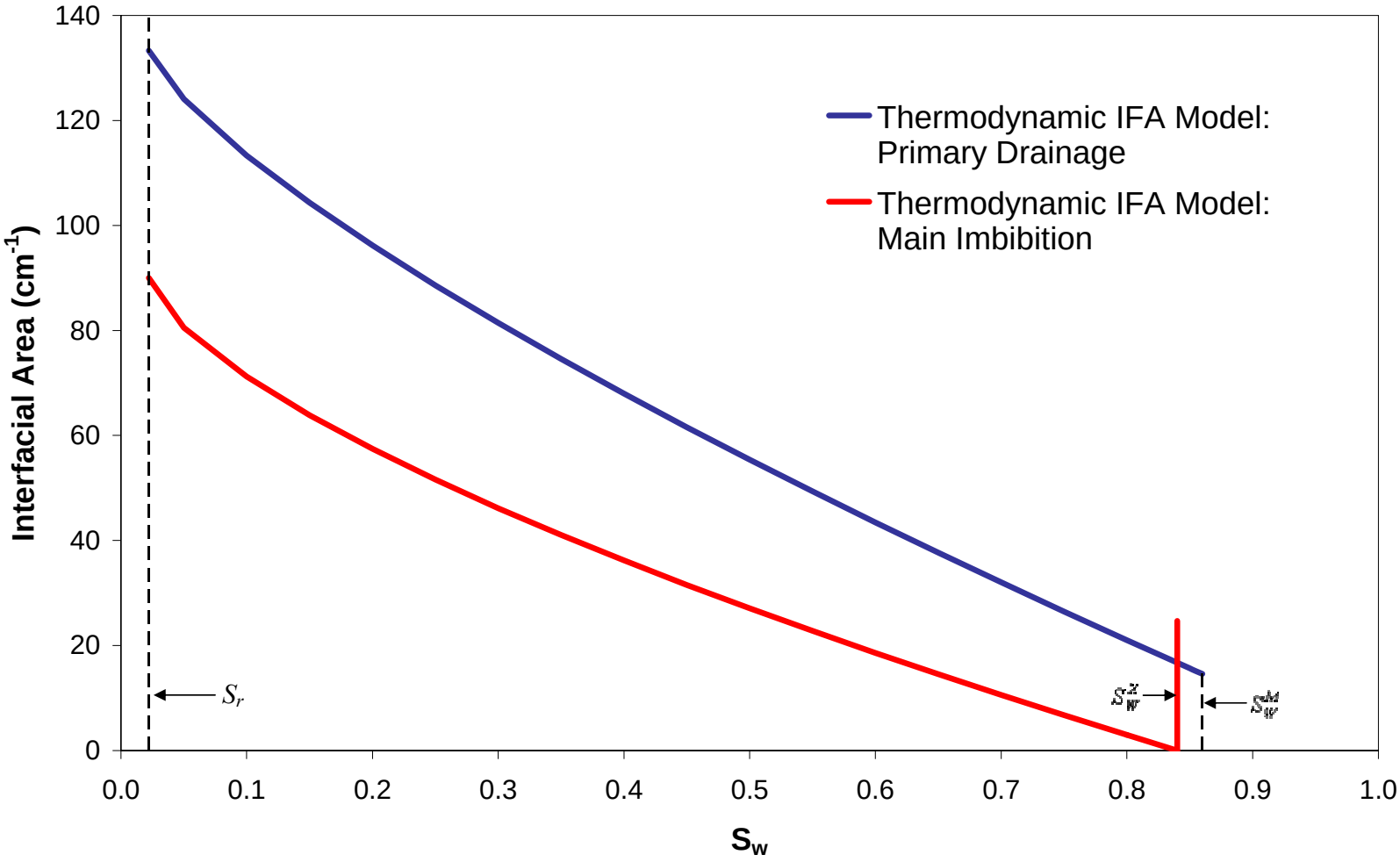

Figure 5-2. Thermodynamic IFA model corresponding to the hypothetical capillary pressure – saturation curve.

5.2.3 Modification 2: Continuity and Saturation History Considerations

The thermodynamic IFA models presented by Leverett (1941) and Bradford and Leij (1997) in Equations 5-4 and 5-6, respectively, show a discontinuity in total specific interfacial area at $S_W = S_r$ between drainage and imbibition conditions (see Figure 5.2). This discontinuity results from the independent consideration of the drainage and imbibition curves. These previous works have failed to consider the continuity of saturation history, which is essential to transient multiphase flow releases. In other words, these models do not consider the influence that evolving NWP saturations have on the cumulative work applied to the system of fluids and porous media. Morrow (1970) in analysing surface free energy (which is proportional to IFA) revealed the necessity of considering saturation history.

According to the basic thermodynamic model of Leverett (1941) and Bradford and Leij (1997), drainage interfacial area is proportional to the area under the drainage P_C - S_W curve from $S_W^i < S_W < 1.0$ (where S_W^i is an arbitrary intermediate WP saturation greater than or equal to S_r), and is a measure of the work applied to the system (Equation 5-4). Interfacial area during imbibition is calculated in an analogous manner such that the interfacial area is proportional to area under the imbibition P_C - S_W curve from $S_W^i < S_W < S_W^X$ (i.e., area 'C' in Figure 5-3). However, when considering transient fluid saturations in a contaminant hydrogeology context, where NWP is typically introduced into a WP-saturated system, imbibition processes cannot be considered independently of drainage processes in this manner. It is here hypothesized that interfacial area during imbibition should be calculated as the difference in work applied *to the system* during drainage, minus the work done *by the system* on the surroundings during imbibition. By this reasoning, imbibition

interfacial area is proportional to the area under the drainage curve from $S_r < S_W < 1.0$, minus the area under the imbibition curve from $S_r < S_W < S_W^i$ (i.e., area 'ABCD' minus area 'B' in Figure 5-3).

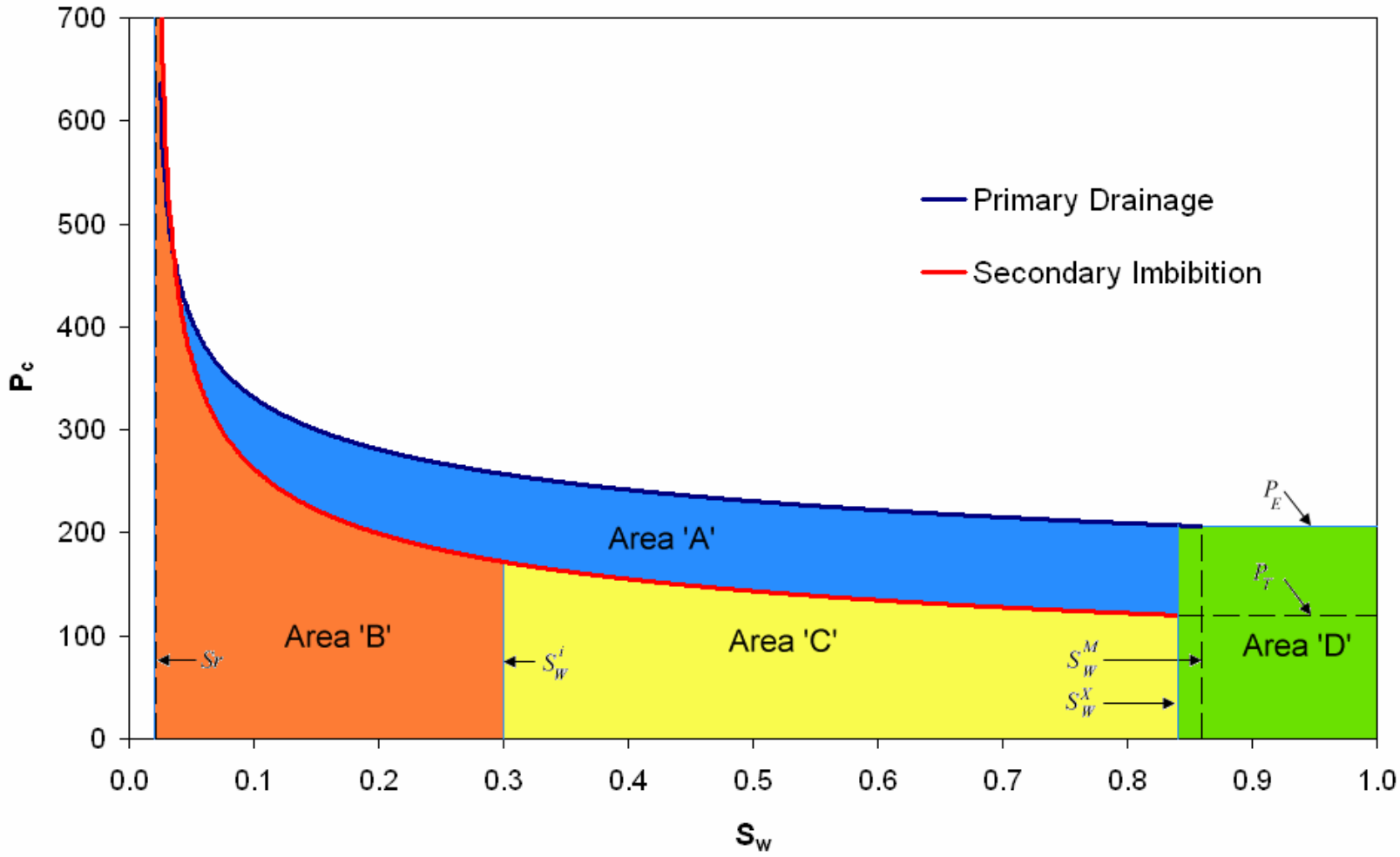

Figure 5-3. Calculation of interfacial area as proportional to area under the P_C - S_W curve.

As a consequence of applying this method for the determination of total specific interfacial area during imbibition, interfacial area from the existence of NWP residual is automatically determined (i.e., area 'D' in Figure 5-3), therefore eliminating the need to approximate C_{NW} in Equation 5-6.

Figure 5-4 presents the interfacial area - saturation diagram corresponding to the P_C - S_W function presented in Figure 5-1 calculated according to the basic thermodynamic method, further modified for systems involving transient fluid saturations. The total specific interfacial area presented in this figure is proportional to the sum of the work applied to the system during drainage, minus the work done by the system during imbibition.

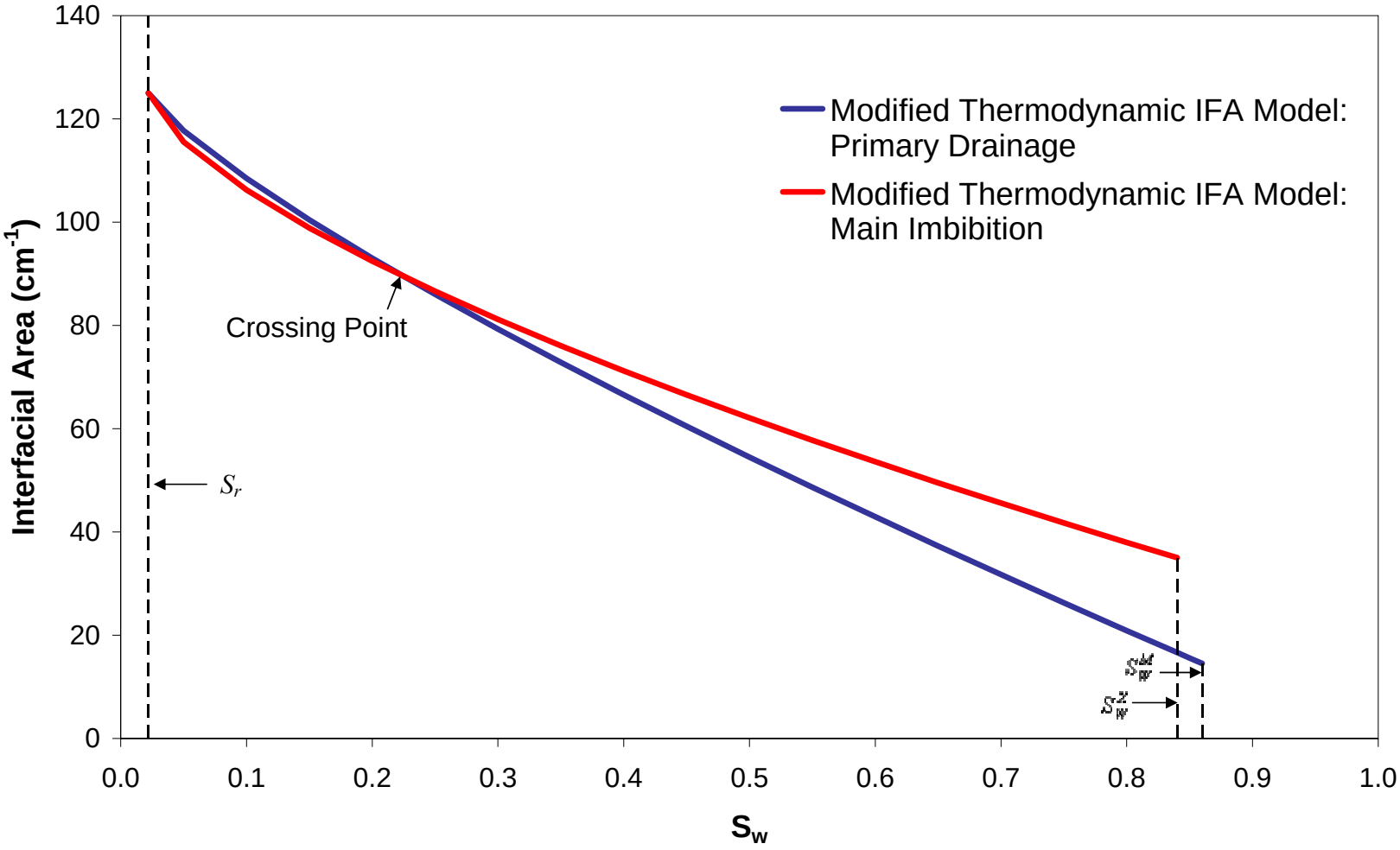

Figure 5-4. Thermodynamic IFA model for systems accounting for continuity of saturation history.

Figure 5-4 shows the imbibition interfacial area curve crossing the drainage interfacial area curve near S_r, such that imbibition interfacial areas are higher than drainage interfacial areas over the majority of WP saturations. This occurs because the formation of residual dictates that imbibition interfacial areas will be greater than drainage interfacial areas at and near NWP residual. Note, however, that the location of the crossing point is a function of the shape of the P_C - S_W curve. For example, a decrease in the pore size distribution index during imbibition would cause the crossing point to shift towards higher WP saturations.

5.2.4 Modification 3: Haines Jump Energy Dissipation

Dalla *et al.* (2002) note that energy dissipation during Haines jumps is significant; thus mechanical work done on the system is not completely converted into surface energy (as is assumed in the basic thermodynamic IFA model). Through pore network modelling, that work illustrates that the conversion of mechanical work to interfacial free energy varies between approximately 0.54 for low WP saturations and 0.74 for high WP saturations with an average conversion rate of approximately 0.6. This incomplete conversion of mechanical energy into interfacial free energy results in an overestimation of interfacial area by the traditional thermodynamic approach. To account for these findings, a Haines jump energy dissipation factor, β, is here proposed, such that:

$$a^n = \beta \cdot \frac{\Phi_{NW}(S_W)}{\sigma_{NW}} \tag{5-9}$$

A value of 0.6 will be assumed for β throughout this study.

5.2.5 Modification 4: Effective Specific Interfacial Area

Dalla *et al.* (2002) note that "effective" specific interfacial area (i.e., total specific interfacial area minus the interfacial area between the NWP and the WP films

coating the solid phase) is a better estimate of interfacial area as measured by Kim *et al.* (1999) using the IFTT (see Figure 14, Dalla *et al.,* 2002). As the IFTT is predicated on the transfer of mass from the WP to the NWP (i.e., the sorption of a WP-borne tracer to the NWP), effective specific interfacial area is also a better measure of the interfacial area governing mass transfer from the NWP to the WP (i.e., dissolution), and will be adopted in the current IFA model.

Dalla *et al.* (2002) calculate effective specific interfacial area, a^{wn}, according to:

$$a^{wn} = \frac{1}{2}\left(a^{n} - a^{s} + a^{w}\right) \tag{5-10}$$

where a^{n} is the total specific NWP interfacial area, a^{s} is the specific surface area of the solid phase (SP), and a^{w} is the specific interfacial area of the bulk WP in contact with the SP or the NWP (see Figure 5-5). While a^{n} can be approximated using the thermodynamic method outlined above and a^{s} can be approximated assuming an ideal soil model, no method is currently available for approximating a^{w}. However, in pore network model simulations, such as those performed by Dalla *et al.* (2002) and Reeves and Celia (1996), values of a^{n}, a^{s}, and a^{w} can be calculated directly.

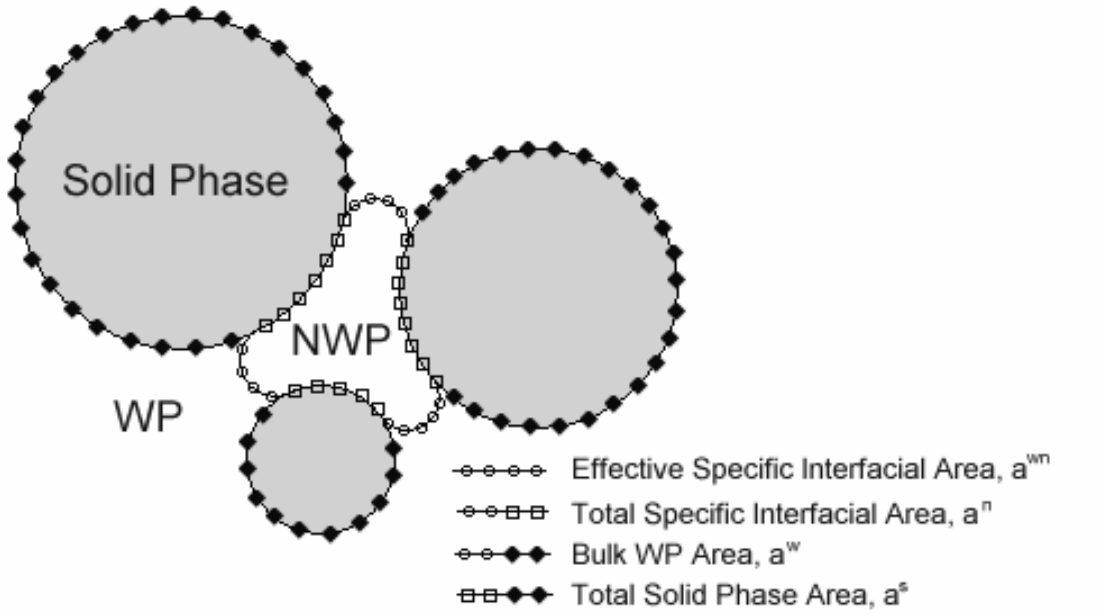

Figure 5-5. Illustration of the method for calculating effective interfacial area, a^{wn}; after Dalla *et al.* (2002).

Figure 5-6 is a partial reproduction of Figures 14 and 15 from Dalla *et al.* (2002) which plots a^n versus a^{wn} (following 'Richardson extrapolation'; see Dalla *et al.,* 2002) for WP saturations between 0.0 and 1.0 during primary drainage. As can clearly be seen, the total specific interfacial area, a^n, increases as WP saturation decreases across the entire range of saturations, as expected from examination of Equations 5-4 and 5-5 and Figure 5-4. However, the plot of a^{wn} shows a maximum effective specific interfacial area at a wetting phase saturation significantly greater than zero, and zero effective interfacial area at $S_W = 0.0$. As S_W approaches zero, the bulk WP is removed from the system and the NWP is only in contact with the WP film coating the solid phase.

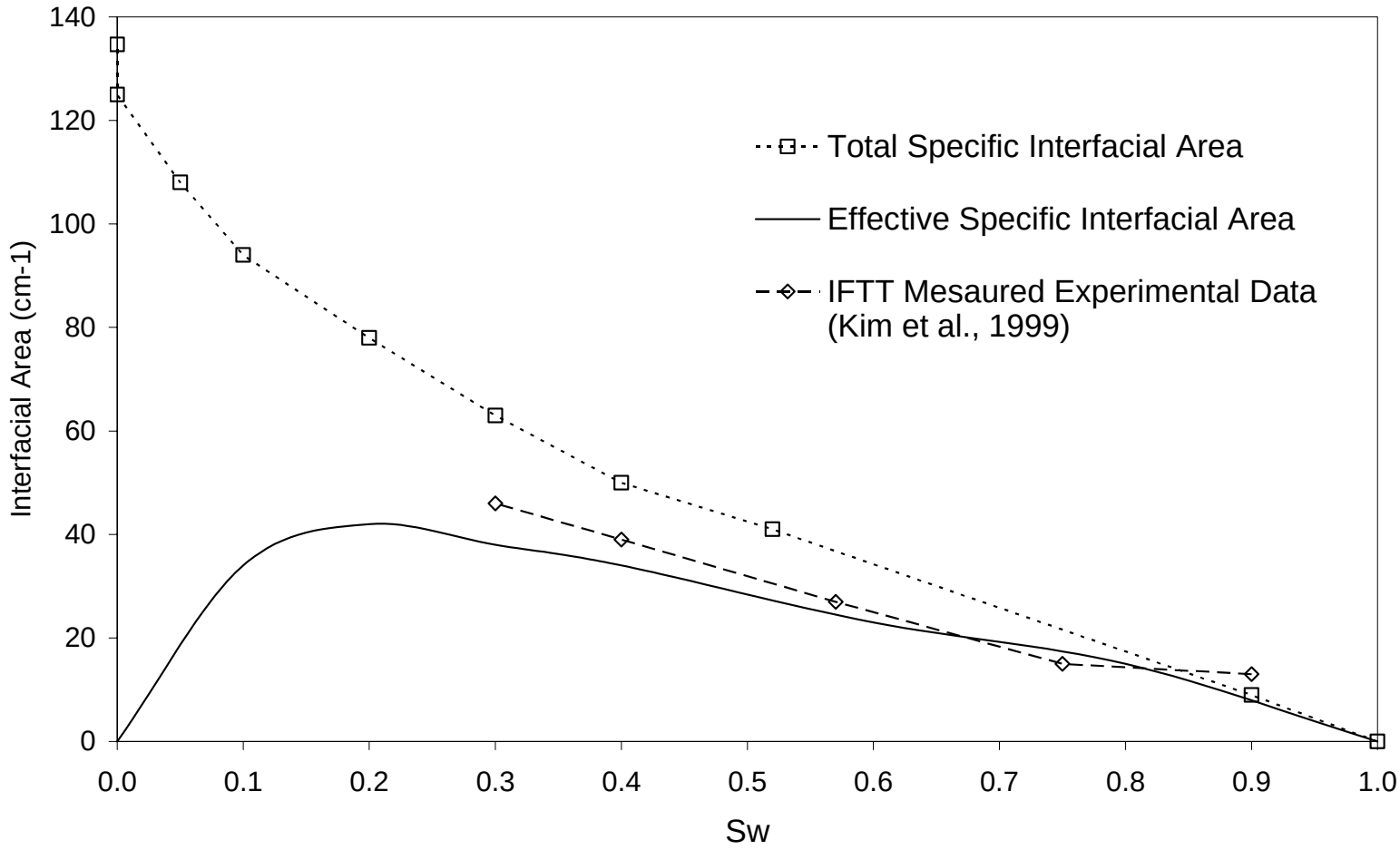

Figure 5-6. Simulated effective specific interfacial area and total specific interfacial area using a pore network model; after Dalla *et al.* (2002).

Using pore-scale network models, Reeves and Celia (1996), Kawanishi *et al.* (1998) and Dalla *et al.* (2002) all calculate effective specific interfacial areas that reach a maximum at wetting phase saturations greater than zero. For the pore network systems examined, it was consistently found that the maximum effective specific interfacial area occurs at WP saturations between 0.2 and 0.3 on drainage, and between 0.3 and 0.4 on imbibition.

Using the data presented in Figure 5-6, Figure 5-7 plots the ratio a^{wn}/a^{n} as a function of S_W, and a fourth order polynomial best-fit function. In the absence of a direct method for obtaining a^{w}, this best-fit function will be used to determine effective specific interfacial area from a thermodynamic approximation of total specific interfacial area. Note that for consistency with the constitutive relationships employed in this study, the endpoint $S_W = S_r$ is employed rather than $S_W = 0$, which is unrealistic. It is reasonable that zero effective interfacial area is coincident with S_r since only WP films are present (and therefore negligible mass transfer occurs) at this hypothetical asymptote of the P_C (S_W) curve.

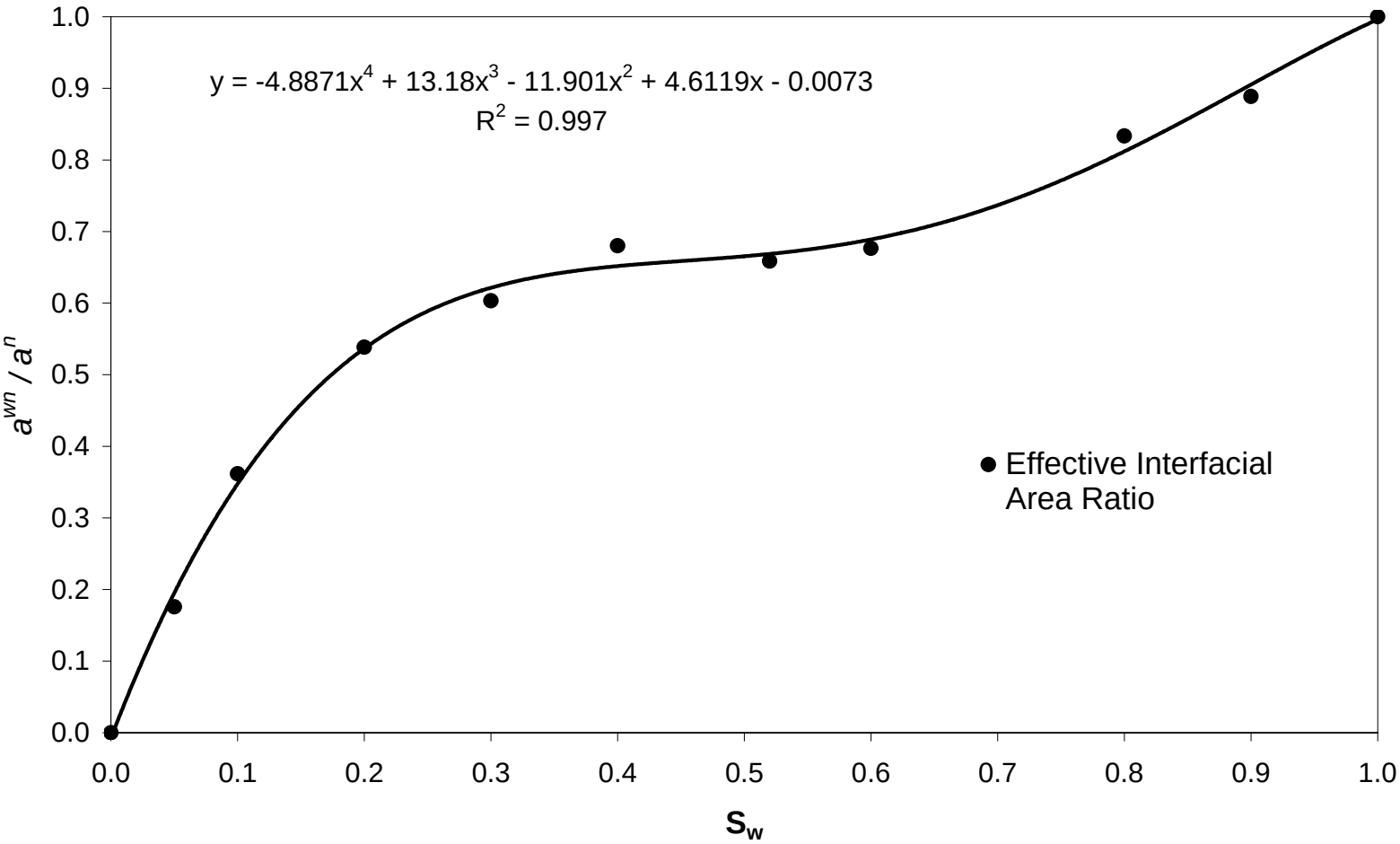

Figure 5-7. Ratio of effective specific interfacial area to total specific interfacial area as a function of WP saturation using the data of Dalla *et al.* (2002).

5.2.6 Modification 5: Dissolution of NWP Residual

A number of studies have specifically examined the dissolution of residual NWP (e.g. Miller *et al.*, 1990; Imhoff *et al.,* 1993; Nambi and Powers, 2003). Miller *et al.* (1990) illustrate a near linear decrease of Sherwood Number (and therefore lumped mass transfer rate coefficient, K_l), with decreasing NWP residual saturations. However, the dissolution correlation expression proposed by Miller *et al.* (1990) includes an NWP saturation exponent of 0.6. Imhoff *et al.* (1993) also note that for low NWP saturations (i.e., NWP residual), interfacial area decreases with decreasing NWP saturation. That study included a NWP saturation exponent of 0.87 in the proposed correlation expression, which is valid for NWP saturations less than 0.04. Nambi and Powers (2003) propose a correlation expression with a NWP saturation exponent of 1.24; however, that study examined rate limited mass transfer for NWP saturations less than 0.3. As controversy surrounds the value of the NWP saturation exponent, a linear relationship between effective specific interfacial area and WP saturations above S_W^X will be assumed in the current IFA model.

5.2.7 Current Thermodynamic Interfacial Area Model

Figure 5-8 presents the current IFA model incorporating modifications to the basic thermodynamic model as described in Sections 5.2.1 to 5.2.6. The labels indicate WP saturation history pathway. This figure plots the effective IFA curve for a complete cycle through primary drainage (path 1), secondary imbibition (path 2) and main drainage (path 3), as well as an example curve for primary drainage (path A), secondary imbibition (path B) and main drainage (path C) corresponding to WP saturation 'turn-around' points for $S_W > S_r$ on drainage (i.e. S'_W), and $S_W < S_W^X$ (i.e. S''_w) on imbibition (see Gerhard and Kueper, 2003a, for details regarding the locations

identified in the figure). The paths identified on Figure 5-8 correspond to the capillary pressure paths identified in Figure 5-9.

The current IFA model is summarised as:

$$\text{Effective IFA} = a^{wn}\left(S_W^i\right) = \psi\left(S_W^i\right)\cdot\beta\cdot\frac{\left[\Phi_{NW}\left(S_W\right)\right]^{d,i,d*}}{\sigma_{NW}} \tag{5-11}$$

where $\psi\left(S_W^i\right)$ is the effective/total interfacial area ratio given by:

$$\psi\left(S_W\right) = -4.8871\cdot\left(S_W^i\right)^4 + 13.18\cdot\left(S_W^i\right)^3 - 11.901\cdot\left(S_W^i\right)^2 + 4.6119\cdot\left(S_W^i\right) - 0.0073 \tag{5-12}$$

The superscripts *d, i, d** denote primary drainage, secondary and all subsequent imbibition, and main and all subsequent drainage conditions, respectively, and S_W^i is the current WP saturation.

On primary drainage:

$$\left[\Phi_{NW}\left(S_W\right)\right]^d = -\int_{S_W=1.0}^{S_W^i}\left[P_C\left(S_W\right)dS_W\right]^d \qquad S_r \le S_W^i < S_W^M \tag{5-13}$$

On secondary and all subsequent imbibition:

$$\left[\Phi_{NW}\left(S_W\right)\right]^i = \left[-\int_{S_W=1.0}^{S_W'}\left[P_C\left(S_W\right)dS_W\right]^d\right] - \left[-\int_{S_W^i}^{S_W'}\left[P_C\left(S_W\right)dS_W\right]^i\right] \quad S_W' \le S_W^i < S_W^X \tag{5-14}$$

$$\left[\Phi_{NW}\left(S_W\right)\right]^i = \left(\frac{1-S_W^i}{1-S_W^X}\right)\cdot\left[-\int_{S_W=1.0}^{S_W'}\left[P_C\left(S_W\right)dS_W\right]^d\right] - \left[-\int_{S_W^X}^{S_W'}\left[P_C\left(S_W\right)dS_W\right]^i\right] \quad S_W^X < S_W^i \tag{5-15}$$

where S_W^X is scaled to the turn-around saturation (from primary drainage to imbibition), S_W' (see Gerhard and Kueper, 2003a).

On main and all subsequent drainage:

$$\left[\Phi_{NW}\left(S_W\right)\right]^{d*} = \left[-\int_{S_W=1.0}^{S_W'}\left[P_C\left(S_W\right)dS_W\right]^d\right] - \left[-\int_{S_W''}^{S_W'}\left[P_C\left(S_W\right)dS_W\right]^i\right] + \left[-\int_{S_W''}^{S_W^i}\left[P_C\left(S_W\right)dS_W\right]^d\right]$$
$$S_r \le S_W^i < S_w'' \tag{5-16}$$

where S_w'' is the turn-around saturation (from imbibition to main drainage).

In summary, total work is always calculated as a continuous summation incorporating all saturation history up to the current WP saturation. Only the primary drainage and secondary imbibition curves are utilised in the calculation; scanning curves of the $P_C(S_W)$ model (Gerhard and Kueper, 2003a) are not used. Following primary drainage, effective IFA follows a path with varying WP saturation bounded by the main secondary imbibition and main drainage curve of Figure 5-8:

$$\left[a^{wn}\left(S_W^i\right)\right]^i < a^{wn}\left(S_W^i\right) < \left[a^{wn}\left(S_W^i\right)\right]^{d*} \tag{5-17}$$

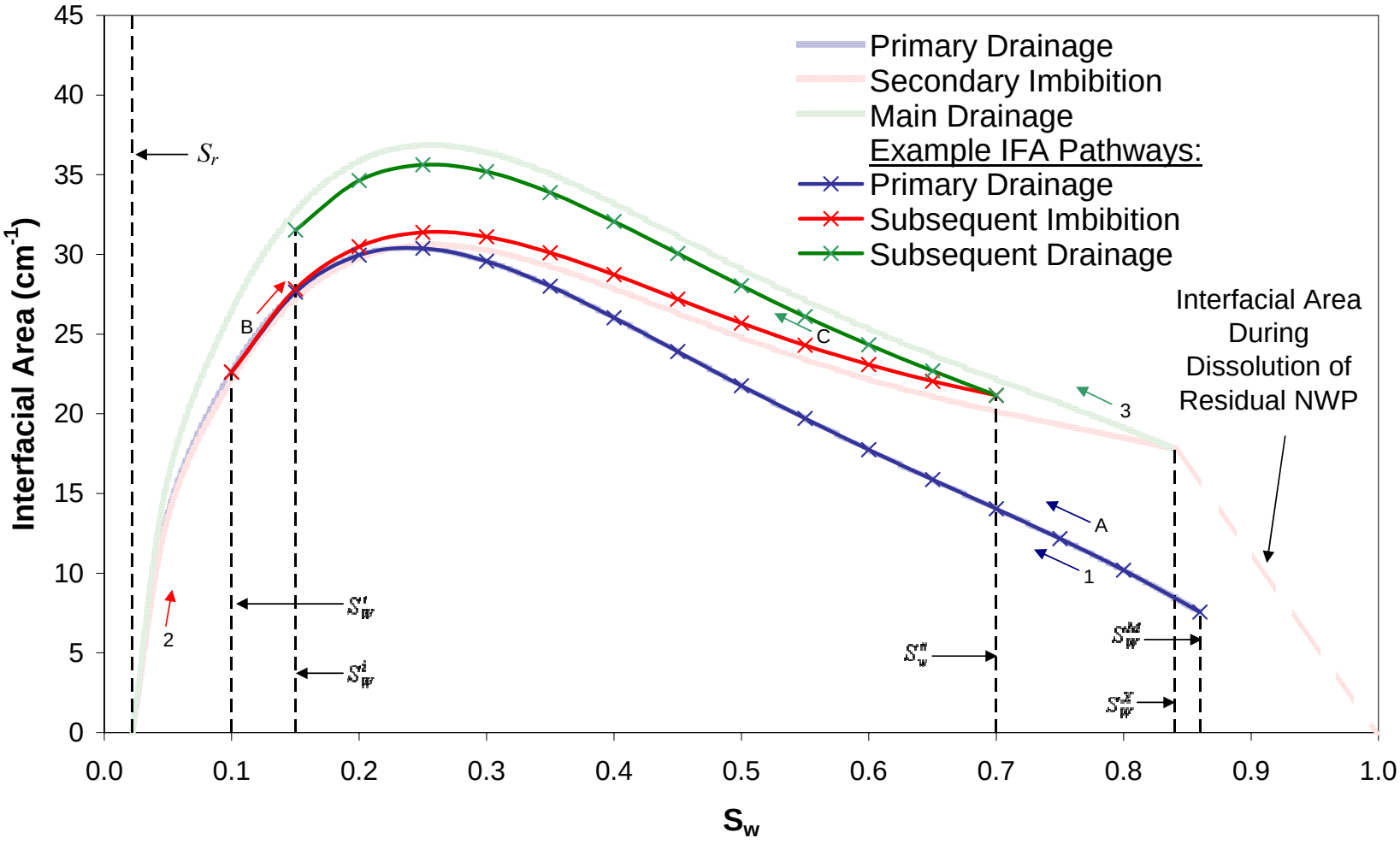

Figure 5-8. Proposed IFA model corresponding to the hypothetical capillary pressure – saturation curve.

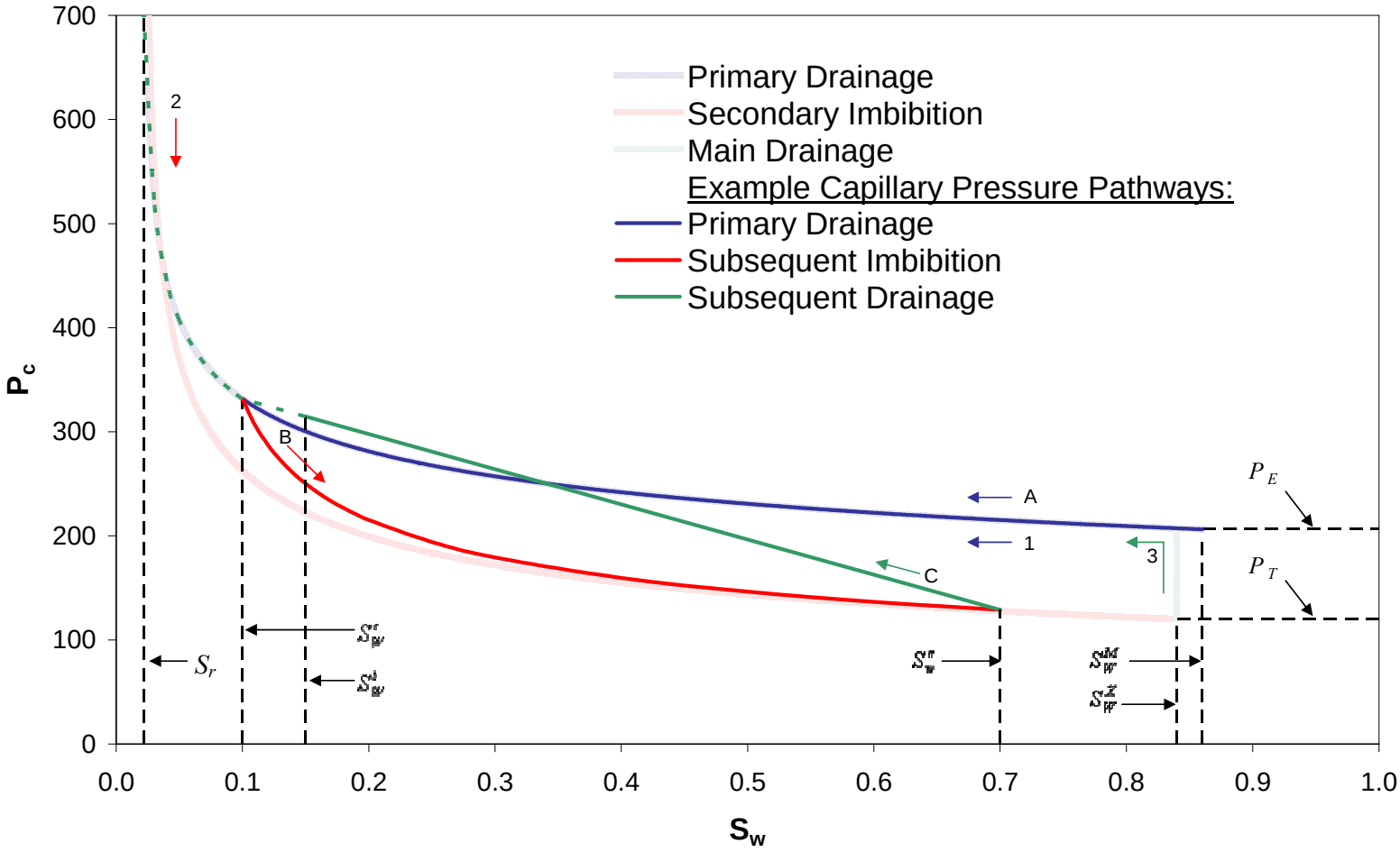

Figure 5-9. Saturation history pathways along the hypothetical capillary pressure – saturation curve (after Gerhard and Kueper, 2003a).

5.3 Experimental Setup

5.3.1 Materials

Six natural sands with single mesh number grain size distributions were employed in the bench scale experiments, referred to as the N10, N16, N20, N30, N40 and N50 sands corresponding to the standard mesh number retaining each sand type. The six sands used in the experiments were separated from four different source sands. The N10 sand was separated from Leighton Buzzard DA 8/16 silica sand (WBB Minerals, Brookside Halls, Cheshire, UK), the N16 and N20 sands were separated from Chelford BS 14/22 silica sand (WBB Minerals, Brookside Halls, Cheshire, UK), the N30 and N40 sands from Chelford D30 silica sand (WBB Minerals, Brookside Halls, Cheshire, UK), and the N50 sand from Lochaline L60A silica sand (Tarmac Central Ltd., Stoke-on-Trent, Staffordshire, UK). According to documentation received from WBB Minerals and Tarmac Ltd., each of the source sands contain >97% silicon dioxide and the grain shape is classified as 'rounded'. Photomicrographs of the N10, N30 N40 and N50 sands, however, reveal that the N10 sand is considerably less 'round' and has a much rougher surface than any of the other sand types examined (see Appendix A). Each of the sands was acid washed in a 0.1M HCL solution, triple rinsed with deionised water and dried prior to use to remove any organic material or iron oxides coating the grains.

The NWP employed in the bench scale experiments was analytical reagent grade 1,2-dichloroethane (1,2,DCE) (Fisher Scientific Limited, Loughborough, Leicestershire, UK) that was dyed to solubility with Oil Blue A powder (Octel-Starreon, Littleton, CO). Deionised water was employed as the wetting phase. Table 5-1 lists the measured properties of dyed 1,2-DCE and water. All physical properties were measured using the blue-dyed NWP previously equilibrated with the wetting

phase. To ensure constant fluid properties, the laboratory was maintained at 22.0 ± 1.0 ^{o}C throughout the experiments.

Table 5-1. Fluid Properties

Property	Value	Temperature (ºC)
1,2-DCE* Density	1.259 ± 0.002 g/ml	22
1,2-DCE* Viscosity[1]	0.887 ± 0.02 cP	22
Water† Density	0.997 ± 0.002 g/ml	22
Water† Viscosity[1]	0.959 ± 0.02 cP	22
Water† / 1,2-DCE* Interfacial Tension[2]	22.3 ± 0.5 mN/m	22
Solubility of 1,2-DCE in Water[3]	1260 ppm	15
1,2-DCE Vapour Pressure[4]	87 mm Hg	25

Note: Measurement of fluid properties is described in Appendix A
* Dyed and equilibrate with water for 24 hrs.
† Deionised and equilibrated with dyed 1,2-DCE for 24 hrs.
[1] Gardner Bubble Viscometer (Pacific Scientific, Silver Spring, MD)
[2] Kruss™ ring tensiometer (Hamburg, Germany)
[3] Lange's Handbook of Chemistry, 1987, McGraw-Hill, New York.
[4] Patty's Industrial Hygiene and Toxicology, 1982, John Wiley Sons, New York.

5.3.2 Methods

The bench scale experiments were conducted to validate the new thermodynamically based IFA model, through the analysis of spatially and temporally variable aqueous phase concentrations, and thus mass transfer rates, from a transient NWP source zone with a complex distribution of saturation and saturation history. Details regarding the construction of the flow cell used in the bench scale experiment can be found in Chapter 3 and Appendix A.

The bench scale flow cell was packed with 5cm x 5cm blocks of homogeneous sand utilising the six sand types examined in the local scale experiments of Chapter 3 to generate a larger scale heterogeneous sand pack. A spatially correlated numerical intrinsic permeability field was generated using FGEN 9.1 (Robin *et al.,* 1991) assuming an exponential autocorrelation function. After the method of Silliman (2001), each node in the numeric field was binned into one of six groups of equal size corresponding to the intrinsic permeability of the sand types measured in the local

scale experiments. The binned permeability field was used as a map during the emplacement of the homogeneous blocks of sand in the bench scale flow cell. The predetermined pattern of the sand emplacement gave a heterogeneous medium that can be characterised with a mean $\ln k$ = -23.09 m^2, a variance of $\ln k$ = 0.24 m^2, a horizontal correlation length, λ_H = 15.2 cm, and a vertical correlation length, λ_V = 2.8 cm which closely matched the targeted statistical parameter values. The end result is a heterogeneous porous media statistically similar to a fine to coarse sand aquifer with correlation lengths appropriately proportioned to the size of the apparatus, according to dimensioning suggestions proposed by Welty and Elsner (1997).

During the experiment, a constant flux source of 1,2-DCE was activated through the DNAPL injection point (see Figure 3-1 in Chapter 3). The source was active at a rate of 90 ml/hr for 130 minutes, such that 194.6 ml of 1,2-DCE was injected into the flow cell. The light transmission / image analysis system described in Appendix B was utilised to capture images of the flow cell throughout the experiment and to track the progress of the advancing / dissolving NWP. Images were collected during NWP injection and subsequent re-distribution following termination of the source, until the entire source zone had dissolved to the aqueous phase.

An aqueous phase gradient of 0.01 was applied across the flow cell to enable the un-aided or natural dissolution of the NWP source zone. Aqueous phase samples were collected from nine active microwells at the downgradient end of the flow cell for analysis by gas chromatography. The microwells were emplaced in homogeneous N16 sand within the 'microwell chamber' (see Appendix A). The microwell sampling system is illustrated in Figure 5-10.

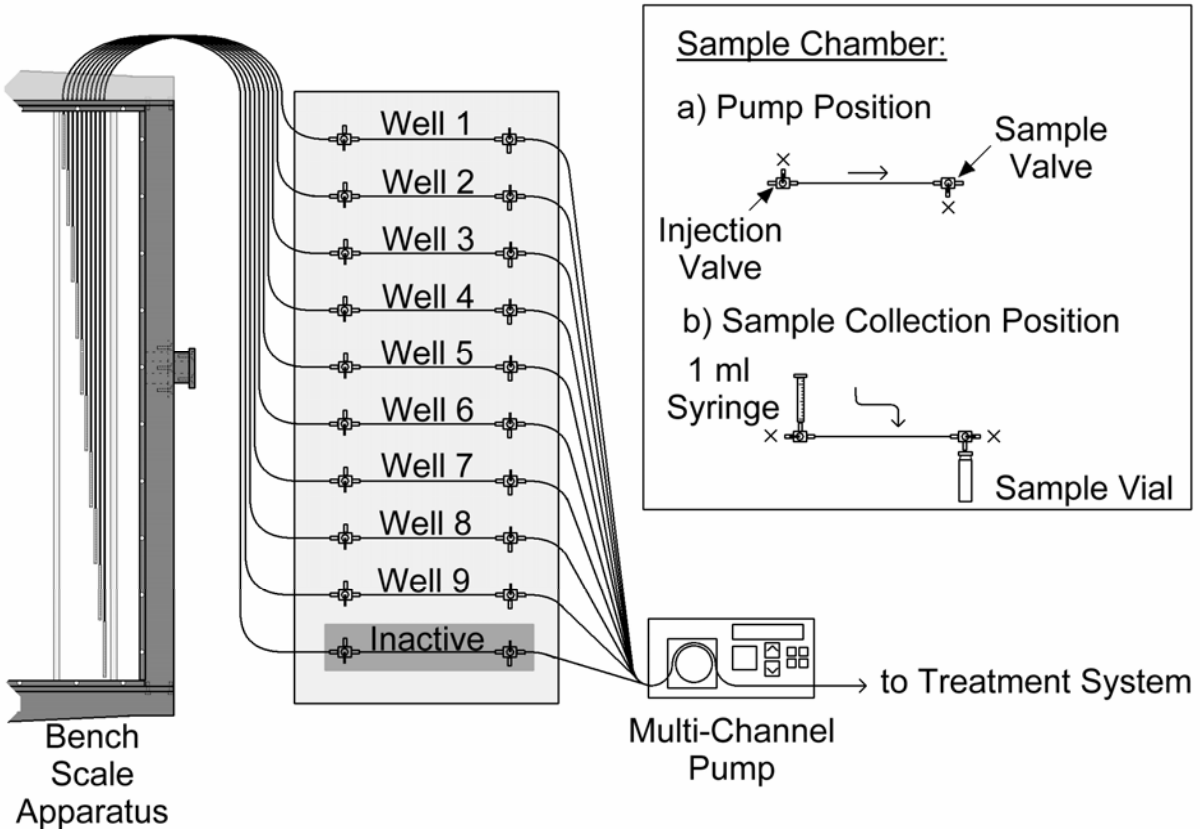

Figure 5-10. Bench scale apparatus microwell sampling system, including the nine active, and one inactive microwell: a) pump position – valve positioning during microwell pumping; b) sample collection position – valve position during sample vial filling.

A 10-channel multi-channel Watson-Marlow 505s digital pump (Falmouth, Cornwall, UK) was used to pump the samples from the microwells to the sample chambers. Although the downgradient boundary condition for the cell during the experiment was constant head, the boundary condition was changed to constant flux while sampling took place. In order to prevent disruption of the flow field, the flow rate leaving the constant head boundary prior to sampling was measured and the pump rate was set to extract aqueous phase from the cell at the same rate. Therefore, while the boundary condition was changed during sampling, the effect on aqueous phase flow and dissolved phase transport was negligible.

The pumping time was adjusted according to the measured flow rate so that the sample removed from the sample chamber was the same parcel of water previously at the microwell screens when pumping commenced. The materials used and the distance between the top of the screen and the sample valve is identical for each of the microwells. Thus all samples collected from each of the screened areas arrive at the sample chambers at exactly the same time.

The sample chamber volume is 1.2 ml. To collect a sample, the pump was stopped, the boundary condition was returned to constant head, and the sample chamber was isolated from the microwells by adjusting the valves at either end of the sample chamber. An empty 1 ml syringe, with the plunger extended to the 1 ml mark, was locked onto the injection valve. The injection valve was opened, a headspace sample vial was placed beneath the sample valve, the sample valve was opened, and the plunger was depressed to push a 1ml sample into the headspace vial. This process was repeated for each of the sample chambers.

The microwell method of aqueous phase sampling was adopted because it provided the highest control of the rate and location of sample collection. A direct

syringe method (such as a syringe inserted through a port installed in the glass plate) would collect a sample in a radial pattern around the location of the syringe point. This would disrupt the flow field in the cell, as each syringe would act as a point sink, and would smear the region over which the sample was collected, complicating the process of numerically simulating the laboratory results. In addition, the direct syringe method would require the installation of ports through the glass which would interfere with the light transmission system and weaken the glass plate.

Table 5-2 lists the number of aqueous phase samples and sample frequency for the bench scale experiment.

Table 5-2. Aqueous Phase Sampling Frequency

Interval	Sample Frequency	Number of Sampling event	Total Number of Samples
0-24hr	2 hours	12	108
24hr – 1week	12 hours	12	108
24hr – 6week	24 hours	41	369

The aqueous phase samples were analysed by headspace gas chromatography (GC) with flame ionization detection (FID). The analysis employed an Equity™-1 fused silica capillary column (Supelco, Bellefont, PA) in a Perkin-Elmer 8700 GC with a Perkin-Elmer HS-101 headspace autosampler. Because the analysis was for a single volatile species only (1,2-DCE), no oven ramping was necessary and the analysis protocol was optimized for time efficiency. The GC oven temperature was maintained at 80 ºC for 5 minutes, the injector port was set to 150 ºC and the detector port was set to 250 ºC. The employed carrier gas was ultra-high-purity helium (column pressure equal to 10 psi). The autosampler needle temperature, sample temperature and transfer temperature were all set at 25 ºC and the thermostat time was set for 5 minutes. Following this procedure, analysis time for a single sample was approximately 18 minutes. Matrix spike (MS) recoveries between 90 and 110% of

expected values and matrix spike duplicate (MSD) differences less than 5.04% were observed for all 1-2-DCE analysis in the water/1,2-DCE system. The Method Detection Limit (MDL) and Limit of Quantification (LOQ), calculated according to a method based on a student 't' statistical analysis of data (WDNR PUBL-TS-056; 40CFR136), were 0.585 mg/l and 1.46 mg/l, respectively. Details regarding the performance of the GC can be found in Appendix C.

5.4 Numerical Modelling

The numerical model developed for this study is the three-dimensional, finite difference two phase flow model DNAPL3D-MT (see Appendix F). DNAPL3D-MT is an efficient three-dimensional numerical model capable of simulating two phase flow, mass transfer and reactive transport. This model was developed for the simulation of DNAPL infiltration and redistribution, rate limited or instantaneous mass transfer between the non-aqueous and aqueous phases, and advective – dispersive aqueous phase transport of contaminants in heterogeneous porous media.

DNAPL3D-MT is composed of a migration sub-model (DNAPL3D: Gerhard et al., 1998) and a dissolved phase transport sub-model (MT3D: Zheng, 1990) linked through a mass transfer expression (see Appendix F). Details regarding the numerical formulation of the migration sub-model DNAPL3D can be found elsewhere (Gerhard *et al.,* 1998; Appendix F; Chapter 3) and Zheng (1990) provides details regarding the transport sub-model MT3D. The linking of the sub-models follows a standard split operator (SO) approach (e.g. Barry *et al.*, 2002), whereby a time step of DNAPL migration is followed by dissolved phase transport conducted over the same time period. This time-lagging of the transport and migration sub-models introduces a source of error proportional to the numerical time step size (Barry *et al.,* 2002). Information regarding mass transfer and the linking of the two sub-models can be

found in Appendix F. Appendix E presents information regarding the verification of the sub-models through comparison to analytical solutions of simple migration, mass transfer and aqueous phase transport scenarios, and includes details regarding the numerical accuracy of the model.

DNAPL3D-MT was utilised to simulate the bench scale flow cell experiment. To correctly account for the nonuniform thickness of the sand pack, due to glass deflection as a result of sand and water pressures exerted on the cell, the experiment was simulated in three dimensions. The solution domain employed was 202 cm wide by 91 cm high by 3 cm thick. The amount of glass deflection as a function of location in the flow cell was independently determined from a tracer test (see Appendix D). The obtained function was employed in constructing the numerical domain such that it determined, for each location in vertical cross-section, the proportion of the 3 cm domain thickness occupied by porous media versus that occupied by the glass plates. The domain was discretised into 220,584 nodes with a nodal spacing of 1 cm horizontally, 1 cm vertically, and 0.25 cm in the third dimension.

The NWP relative permeability constitutive parameter values utilised in the bench scale simulations were as determined at the local scale for the six sand types in Chapter 3 (see Table 3-2). The capillary pressure – saturation constitutive parameter values utilised were as determined at the local scale for the six sand types (see Appendix H). The transport parameters utilised in the simulations were calculated from the non-reactive tracer test presented in Appendix D.

5.4.1 Validation Simulations

Numerical simulations of the bench scale experiment were conducted with DNAPL3D-MT employing different mass transfer models: 1) 'IFA model' (proposed herein); 2) 'LEA' (local equilibrium assumption); and, 3) 'Correlation model'

(empirical model of Saba and Illangasekare, 2000) to describe mass transfer. As detailed in Section 5.2.7, the proposed IFA model contains one unknown parameter, the average mass transfer coefficient, k_{la}, which was not explicitly determined for this fluid pair; therefore this constant is determined by calibration to the experiment.

The correlation model of Saba and Illangasekare (2000) was selected for comparison as it is one of the few empirical expressions of rate limited mass transfer that has been derived in more than one dimension and is designed for scaling to systems of proportions different from those used in the derivation of the expression. However, this expression was derived for the case of residual NWP dissolution, and at a length scale greater than that utilised for numerical modelling in this study. The mass transfer correlation model is (Saba and Illangasekare, 2000):

$$Sh = 11.34\,\mathrm{Re}^{0.2767}\,Sc^{0.33}\left(\frac{d_m\theta_N}{\tau L}\right)^{1.037} \tag{5-18}$$

where Sh is the Sherwood number, Re is the Reynolds number, Sc is the Schmidt number, d_m is the mean grain diameter, θ_N is the volumetric NAPL content, τ is the tortuosity of the sand, and L is the length of the contaminated numerical soil block in the flow direction.

The tortuosity parameter, τ, has not been explicitly evaluated in this study. Therefore, the simulations utilising the correlation model of Saba and Illangasekare (2000), will assume that wetting phase tortuosity, τ = 2.0, as was utilised in the derivation of the expression. For comparison, a simulation of the bench scale experiment was also carried out using the correlation model of Saba and Illangasekare (2000) where the wetting phase tortuosity is equal to the NWP tortuosity as determined in the local scale $k_{rN} - S_W$ experiments of Chapter 3 (variable as a function of sand type; see Table 3-2).

The experimental results were compared, both spatially and temporally, to the results of the four numerical simulations. Such comparisons enable a direct evaluation of the suitability of these models for describing mass transfer in heterogeneous porous media at the bench scale.

5.4.2 Sensitivity to IFA Model Formulation

A series of simulations of the bench scale experiment were also conducted to examine the sensitivity of the assumptions made in deriving the IFA expression (see Section 5.2). The proposed IFA model results will be compared to four simulations. The 'No Haines Jump Energy Dissipation' simulation will assume that the Haines jump energy dissipation factor, β, is set to a value of 1.0 (in the validation simulation, $\beta = 0.6$). The 'Total Interfacial Area' simulation will assume that the entire NWP / WP interface (including the area between the NWP and WP films coating the porous media) is calculated. The 'Constant Residual Interfacial Area' simulation will assume that interfacial area does not change as residual NWP dissolves (i.e., the IFA line in Figure 5-8 from $S_w'' < S_W < 1.0$ will be horizontal), as opposed to the validation simulation where a linear relationship between IFA and NWP saturation is assumed for NWP saturations less than residual resulting from dissolution. The 'No Saturation History' simulation will assume that IFA is calculated according to the method of Leverett (1941) and Bradford and Leij (1997), such that saturation history is not considered, and both drainage and imbibition interfacial area is proportional to the area under the drainage P_C - S_W curve from $S_W^i < S_W < 1.0$ (where S_W^i is an arbitrary intermediate WP saturation greater than or equal to S_r).

A second series of sensitivity simulations was carried out to evaluate sensitivity to the value of k_{la} employed. Simulations of the bench scale experiment utilizing four k_{la} values (2 x 10^{-7} m/s, 3 x 10^{-7} m/s, 4 x 10^{-7} m/s, and 5 x 10^{-7} m/s) as

well as the LEA (which represents the upper bound of k_{la}) were compared to carry out this evaluation.

5.4.3 Field Scale Sensitivity Simulations

A series of field scale simulations were conducted to examine the influence of the mass transfer model selected in a numerical simulator on predicted source zone life spans and dissolution behaviour. Simulations employing the proposed IFA model were compared to simulations utilizing a LEA and the correlation expression of Saba and Illangasekare (2000) in two-dimensional heterogeneous porous media at the field scale. The simulations employed random, spatially correlated k_i fields generated using FGEN 9.1 (Robin *et al.,* 1991) assuming an exponential autocorrelation function. The solution domain was 60 m wide by 30 m high. The domain was discretised into 57,600 nodes with a nodal spacing of 0.250 m horizontally and 0.125 m vertically. The domain was initially fully saturated with water and was assigned wetting phase pressures that increased hydrostatically from a watertable coincident with the top boundary. The side boundaries were characterised by fixed wetting phase pressures that established a hydraulic gradient of 0.01 from left to right across the domain while permitting the flux of either phase. The bottom boundary was set as impermeable to both fluids.

The source boundary was 20 nodes (5.0 m) wide. The release was simulated by fixing the flux of NWP through a source located between 17.5 and 22.5 m from the left side of the domain along the top boundary (i.e., centred 10 m left of the domain midpoint). Fixing the total rate of NWP invasion was necessary to ensure that an identical DNAPL volume entered the domain in an identical amount of time for all simulations. However, it is acknowledged that an imposed NWP flux source condition is less realistic than one that is constant capillary pressure (Reynolds and

Kueper, 2002). Therefore, to mimic the realistic input of DNAPL across a wide source area, the fraction of total flux through each source node was weighted according to intrinsic permeability:

$$Flux_{Node} = Flux_{Total} \cdot \left(\frac{k_{Node}}{\sum_{i=1}^{N} k_i} \right) \tag{5-19}$$

where $Flux_{Node}$ is the flux of NWP through a given source node, $Flux_{Total}$ is the total flux through the source boundary, k_{Node} is the intrinsic permeability of a given source node, and N is the total number of nodes in the NWP source boundary. In each case, the source was initiated at time $t = 0$ and was eliminated at t= 5 days, representing the release of 8.334 m^3, or 40 drums, of DNAPL (1,2-dichloroethane) in the field. Table 5-3 lists the numerical model input parameters utilised for the simulations. The NWP relative permeability constitutive parameter values utilised in the field scale simulations are identical to the parameter values used for the variable $k_{r,N}$ case examined in Chapter 4.

Table 5-3. Numerical Model Input Parameters

Parameter	Value
Wetting phase density	1000 kg/m^3
Nonwetting phase density	1260 kg/m^3
Wetting phase viscosity	0.001 Pa.s
Nonwetting phase viscosity	0.000887 Pa.s
Interfacial Tension	0.02 N/m
Solubility	8520 kg/m^3
Dispersivity	0.015 m
Free liquid diffusion coefficient	9.908 x 10^{-10} m^2/s
Matrix compressibility	1.0 x 10^{-7} Pa^{-1}
Wetting phase compressibility	4.4 x 10^{-10} Pa^{-1}
Mean ln k_i	-25.7 m^2
Variance ln k_i	2.0
Horizontal correlation length	5.0 m
Vertical correlation length	0.5 m

Horizontal nodal spacing	0.25 m
Vertical nodal spacing	0.125 m
Number of nodes (horizontal)	240
Number of nodes (vertical)	240
Dimensionless displacement pressure	0.18557

5.5 Results

5.5.1 Bench Scale Experiment

5.5.1.1 Downgradient Dissolved Phase Concentrations

Figure 5-11 shows the location of the microwells in the bench scale flow cell, the final simulated NWP saturation distribution following cessation of migration, the sand type distribution emplaced in the cell (background grey-scale), and the identification of three 'dissolution zones', which will be considered in the discussion to follow. Zone 1 encompasses the region dominated by a small pool located near the bottom of the flow cell. Zone 2 corresponds to the area of highest NWP mass and includes the large pool located between 0.5 and 0.7 m from the bottom boundary of the flow cell as well as a large area exhibiting residual NWP beneath this pool. Zone 3 is located at the top of the flow cell, and includes a region of exclusively residual NWP saturations.

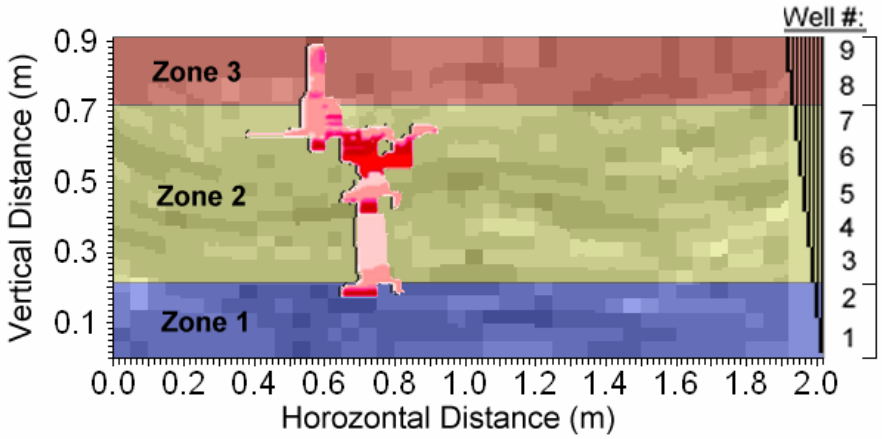

Figure 5-11. Simulation domain overview identifying 'dissolution zones' utilised in the discussion of mass transfer rate.

Figure 5-12 plots the average concentration of aqueous phase 1,2-DCE from samples collected from each of the active microwells, exiting the downgradient (right most) boundary of the bench scale flow cell, including error bars (see Appendix J for determination of experimental errors). The breakthrough curve shows dissolved phase 1,2-DCE first exiting exit the flow cell approximately 6 hours after the start of the experiment. Concentrations rise sharply to approximately 30% of C_S at t_1 = 20 hours. The peak concentration at t_1 is followed by a steep decrease in concentration to time t_2 = 84 hours. Dissolved phase 1,2-DCE concentrations plateau between t_2 and time t_3 = 192 hours, where the concentrations decrease once more until time t_4 = 264 hours. Relatively constant average effluent concentrations continue beyond t_4 until approximately 672 ± 12 hours (4 weeks) following the start of the experiment, which is approximately 18 hours after the time of complete NWP dissolution. Mass balance error between the amount of NWP 1,2-DCE released to the flow cell, and the cumulative aqueous phase mass exiting the cell as estimated by integrating under the curve in the figure was approximately 16% (i.e., 16% of the mass released to the flow cell was not recovered in the dissolved phase samples). This error is likely due to an

occasional inadvertent introduction of small air bubbles into the sample chamber (see Figure 5-10) which would disrupt the pumping of the aqueous phase parcel of water from the microwell to the sample chamber.

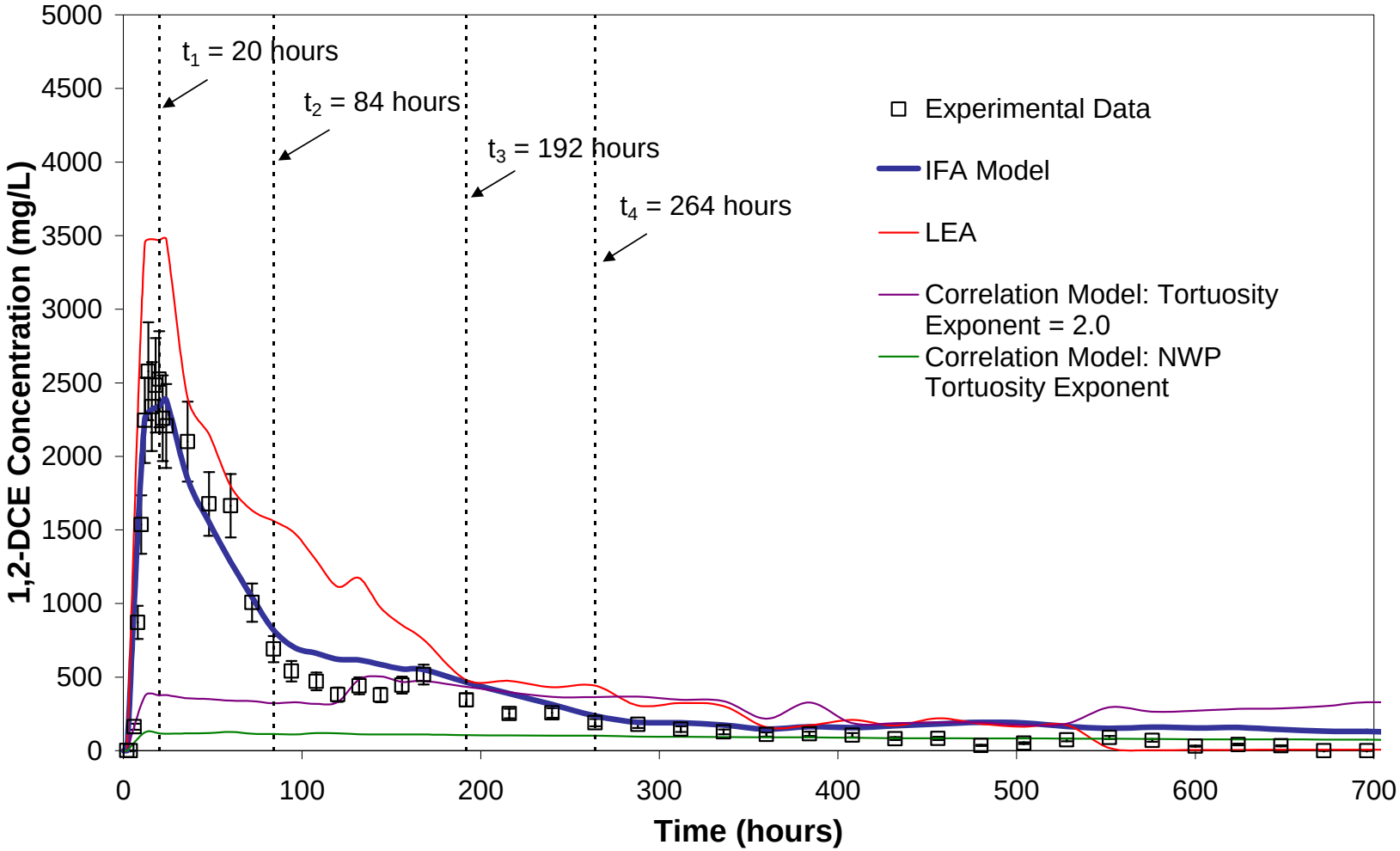

Figure 5-12. Measured and numerically predicted average 1,2-DCE concentration at the downgradient boundary of the bench scale flow cell.

Figure 5-12 also plots the DNAPL3D-MT predicted average downgradient boundary 1,2-DCE concentration utilising: 1) the proposed IFA model in conjunction with a best-fit value of k_{la} = 3 x 10^{-7} m/s; 2) a local equilibrium assumption of mass transfer; 3) the correlation model with τ = 2.0; and, 4) the correlation model with τ equal to the sand type, and saturation history, specific NWP tortuosity exponent as determined in Chapter 3.

The figure demonstrates that the 'IFA model' simulation is in excellent agreement with the experimental results. The peak concentration occurs at near identical times (t_1) for both the experimental and IFA model predicted results, and the magnitude of the peak is nearly identical as well (2580 mg/l and 2380 mg/l, respectively) with the 'IFA model' under predicting the peak concentration by only 7.8%. The 'IFA model' simulation also accurately predicts the breakthrough curve significant changes in slopes at times t_1 and t_2. Moreover, it also properly predicts the subtle slope changes at t_3 and at t_4.

However, the IFA model continues to predict 1,2-DCE concentrations exiting the flow cell after 672 hours (4 weeks) of simulation time. At this time, the simulation predicts that approximately 12% of the released NWP volume has yet to dissolve. As the experimental mass balance error was approximately 16%, it is possible that experimental error is the reason for the discrepancy between the predicted (12% of the release volume) and actual (0%) mass present in the flow cell 672 hours following the start of the experiment.

Figure 5-12 demonstrates that the other mass transfer models are significantly less successful at reproducing the experimental results. The LEA simulation predicts much higher peak concentrations (3480 mg/l) than actually measured (2580 mg/l) - an overestimation of approximately 34.9% - and generally over predicts the average

downgradient concentration exiting the flow cell throughout the simulation. As a result of the over predicted aqueous phase concentrations, the simulation predicts total NWP mass removal at approximately 552 hours: five days earlier than measured experimentally.

The model under predicts the mass transfer rate when the correlation model of Saba and Illangasekare (2000) is utilised for each value of τ selected for the aqueous phase tortuosity in this study. As a result, no peak concentration is predicted at time t_1, and the $\tau = 2.0$ simulation and the simulation where τ is equal to the NWP tortuosity value predict approximately 66% and 40%, respectively, of the NWP mass released to the domain remaining in the flow cell following the experimentally determined time for complete source zone dissolution ($t = 672$ hours).

Figures 5-13 through 5-16 show the measured and model predicted aqueous phase 1,2-DCE concentrations for each of the zones identified in Figure 5-11, at time t_1 (20 hours), t_2 (84 hours), t_3 (192 hours), and t_4 (264 hours), respectively. The Zone 1 concentrations are the average dissolved phase concentrations measured at microwells 1 and 2, the Zone 2 concentrations are the average of microwells 3, 4, 5, 6, and 7, and the Zone 3 concentrations are the average of microwells 8 and 9.

Figure 5-13 illustrates the ability of the IFA model to most accurately predict the aqueous phase concentrations in Zones 2 and 3 at time t_1. In Zone 1, however, the IFA model over predicts the concentrations at this time. This, however, is a result of discrepancies in NWP migration modelling, and in no way is associated with the mass transfer description. As discussed in detail in Chapter 3, subtle bedding interfaces were inadvertently formed in a homogeneous N40 sand region above the pool in Zone 1; these microlayers were not explicitly incorporated into the numerical model preventing the migration model from reproducing the transient arresting of NWP upon

them. As a result, the numerical model predicts NWP presence in this zone after approximately 2.6 hours, in contrast to the experimentally measured arrival time at approximately 19.7 hours. Therefore, the model predicts aqueous phase concentrations in Zone 1, prior to the actual arrival time of NWP in this area. The measured aqueous phase concentrations in Zone 1 presented in Figure 5-13 are a result of dispersion from Zone 2 above. However, the shape of the concentration breakthrough curve for Zone 1 is well predicted by the IFA model simulation; it is simply offset by approximately 17 hours (figure not shown). Further evidence for the accuracy of the IFA model is that the predicted peak concentration in Zone 1 is 950 mg/l, which is in excellent agreement with the actual peak concentration of 985 mg/l (a discrepancy of approximately 3.6%). In general, the LEA over predicts aqueous phase concentrations, and the two correlation model simulations under predict the aqueous phase concentration in each of the three zones.

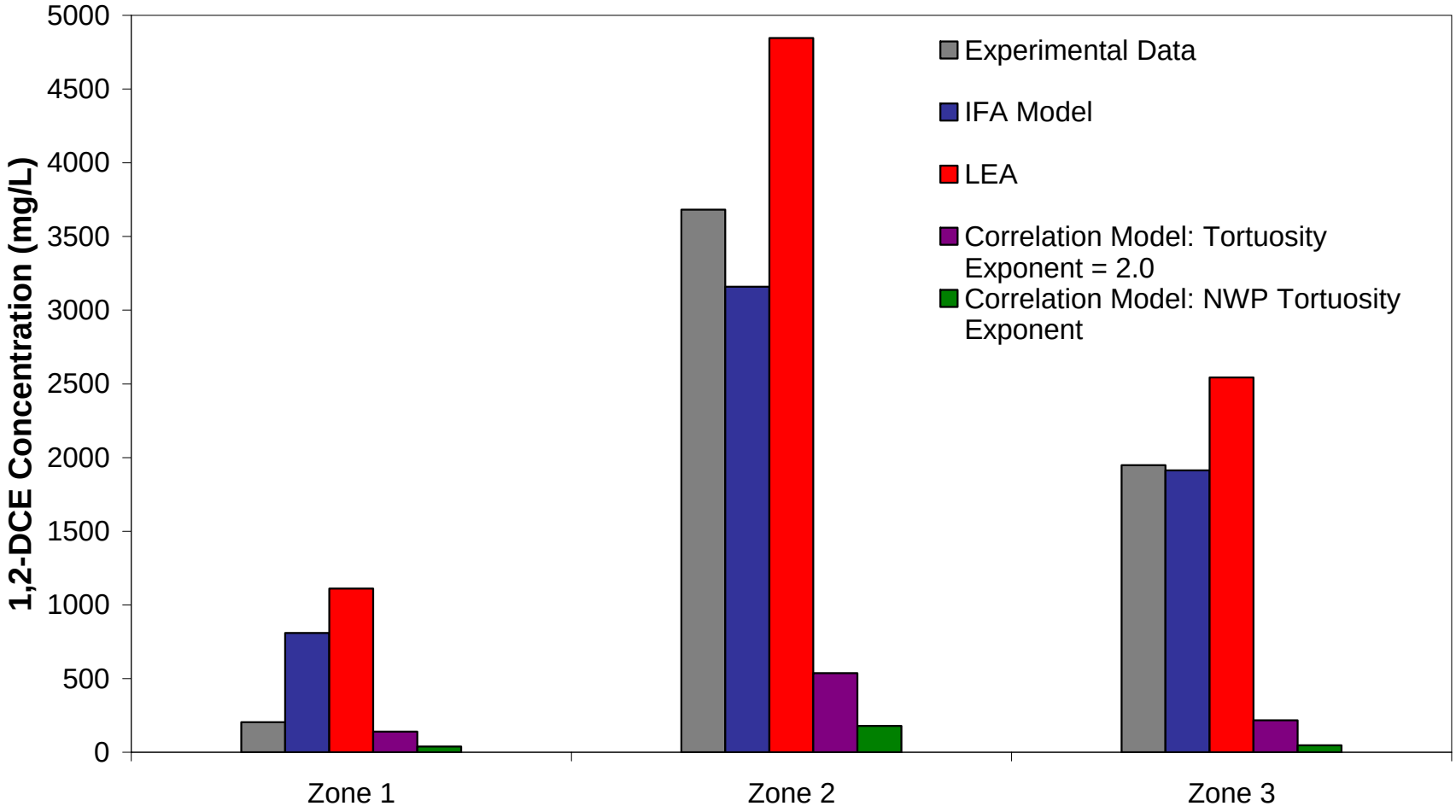

Figure 5-13. Predicted and actual aqueous phase concentrations in Zones 1, 2 and 3, at time t_1 (20 hours).

In Figure 5-14, the IFA model most accurately predicts the measured downgradient concentrations in Zones 1 and 2 at time t_2 relative to the other simulations conducted. In Zone 3, however, the IFA model over predicts the aqueous phase concentration. This is a result of an overestimation by DNAPL3D-MT of the volume of NWP located in this Zone. As discussed in detail in Chapter 3 and Appendix D, the degree of glass plate deflection and the resultant volume of the porous media at each location in the apparatus were determined experimentally. The results of this study indicate that the volume of porous media, and therefore the volume of NWP at residual saturations within Zone 3, was over estimated. Therefore, the numerical model predicts NWP presence in Zone 3 at time t_2, and dissolved phase concentrations in excess of those measured experimentally. Figure 5-18, presented in the following section, illustrates the difference in measured and predicted NWP presence in Zone 3 at time t_2. As in Figure 5-13, the LEA assumption over predicts the aqueous phase concentrations, and the two correlation model simulations under predict the aqueous phase concentrations.

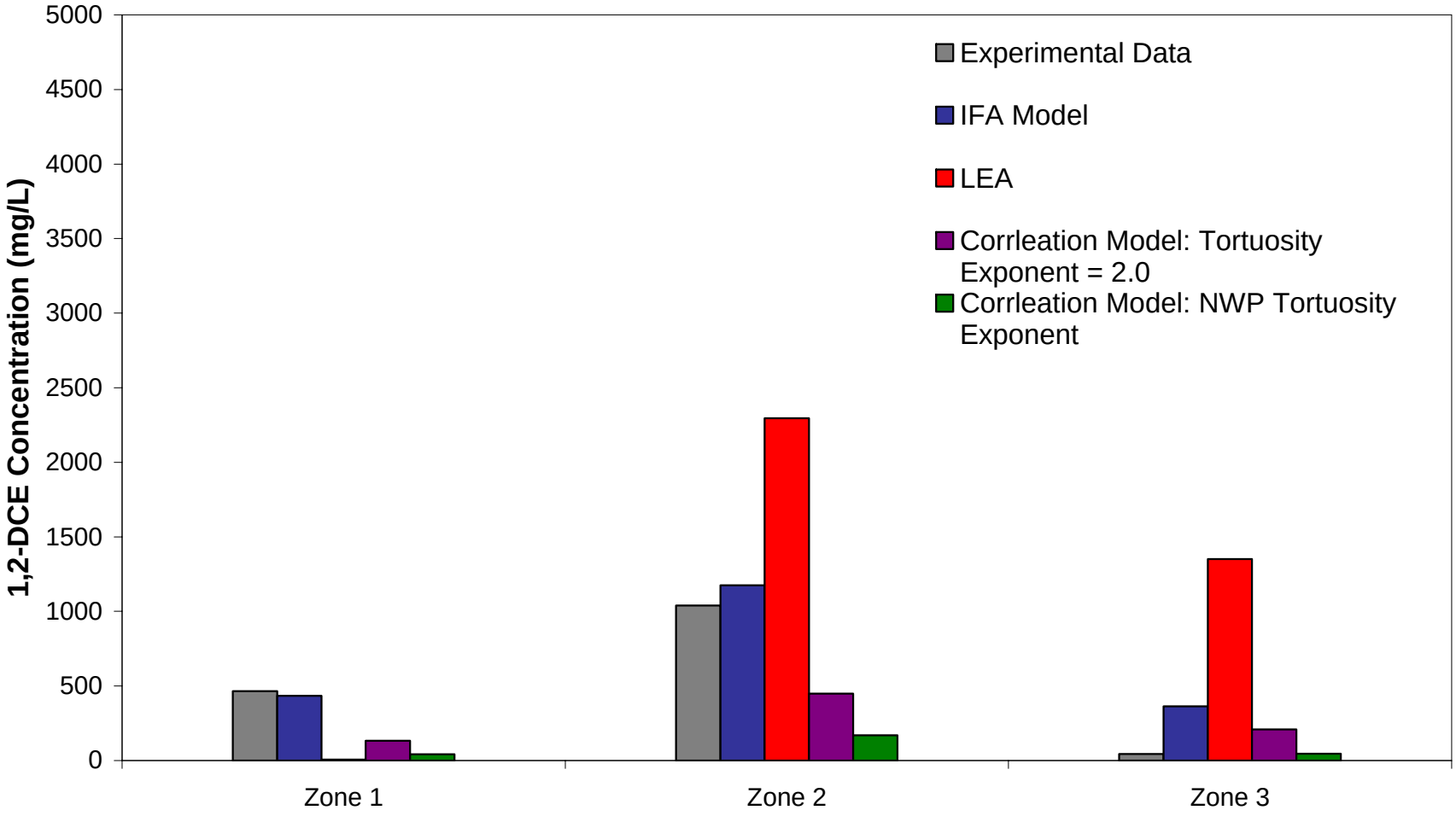

Figure 5-14. Predicted and actual aqueous phase concentrations in Zones 1, 2 and 3, at time t_2 (84 hours).

As seen in Figure 5-15, the IFA model accurately predicts the measured dissolved phase concentrations for the three zones examined at time t_3. The LEA assumption predicts no aqueous phase 1,2-DCE in Zones 1 and 3, as this mass transfer model over predicts the rate of mass flux, such that no NWP source exists in these zones at this time. In contrast, the predicted aqueous phase concentrations at t_3 for the two correlation model simulations are almost completely unchanged from the predicted concentrations at time t_1 and t_2. In this figure, the correlation model simulations appear to accurately predict the measured concentrations, but the concentration breakthrough curve of Figure 5-15 indicates that this is merely coincidence. The measured concentrations happen reduce to a level comparable to the generally constant and low aqueous phase concentrations predicted by the correlation models at time t_3.

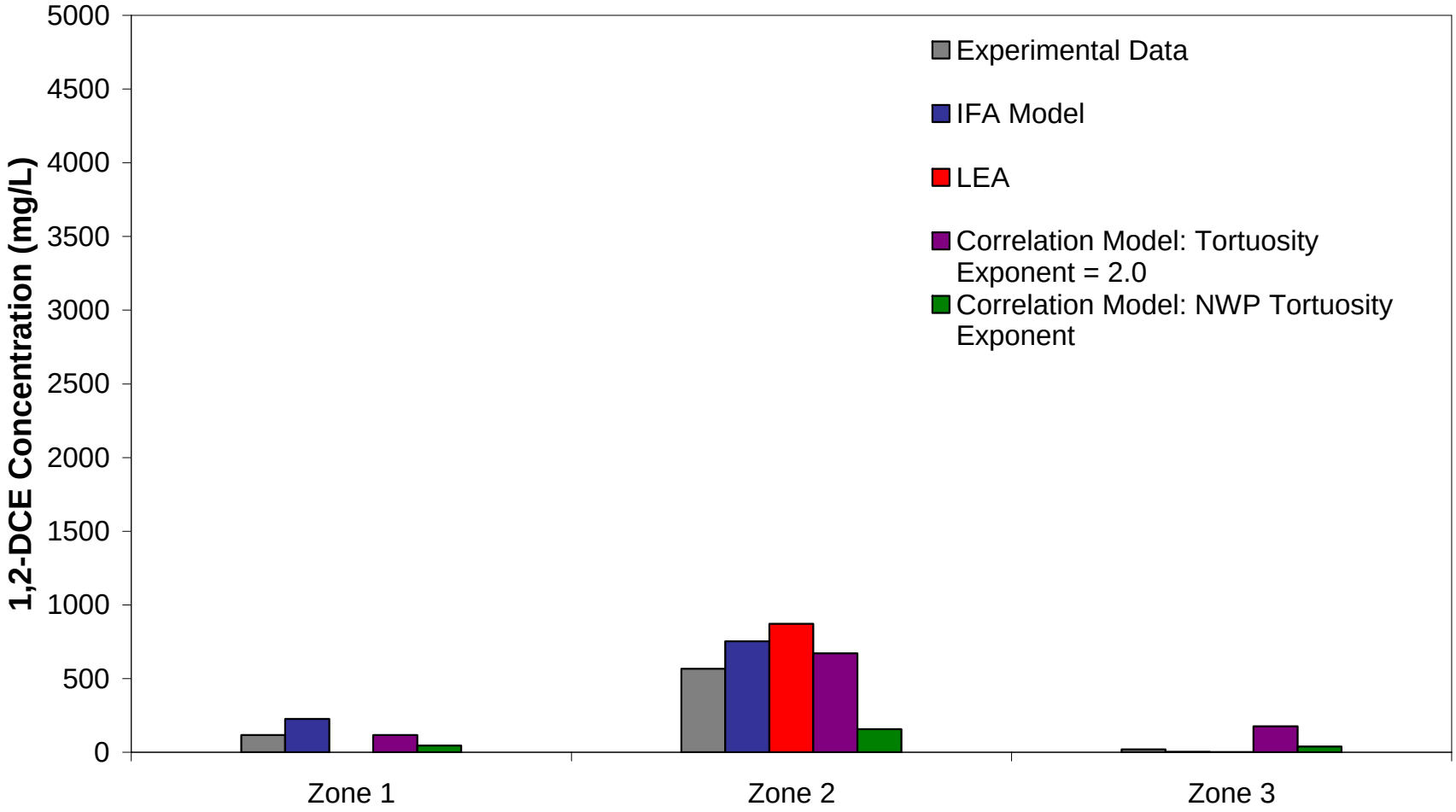

Figure 5-15. Predicted and actual aqueous phase concentrations in Zones 1, 2 and 3, at time t_3 (192 hours).

As seen in Figure 5-16, the IFA model once again accurately predicts the measured dissolved phase concentrations for the three zones examined at time t_4. The LEA assumption over predicts the aqueous phase concentrations in Zone 2, and predicts no 1,2-DCE presence in Zones 1 and 3, as at time t_3. Similarly, the predicted concentrations from the correlation model simulations are virtually unchanged at this time.

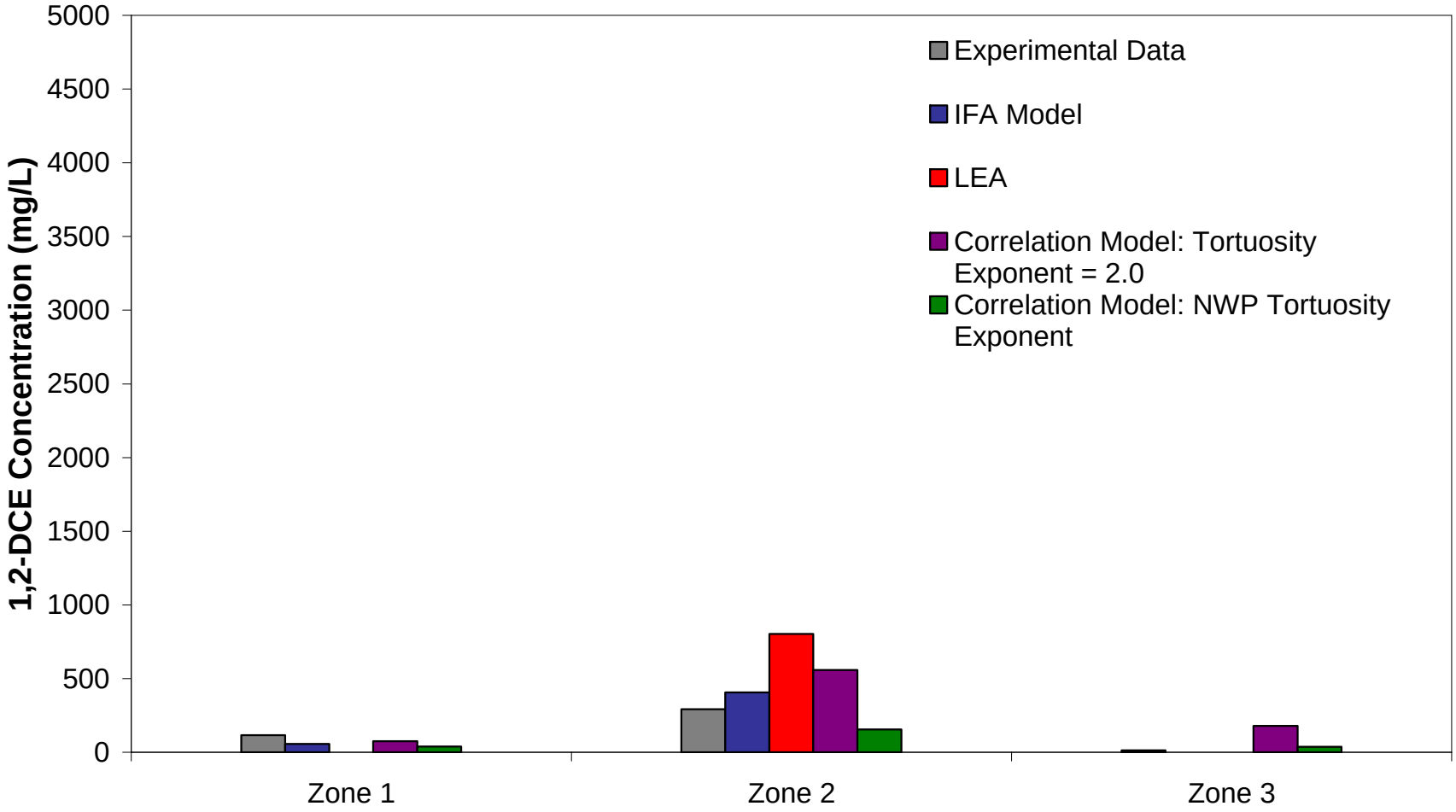

Figure 5-16. Predicted and actual aqueous phase concentrations in Zones 1, 2 and 3, at time t_4 (264 hours).

5.5.1.2 NWP Saturation Distribution

Figures 5-17 through 5-20 compare the experimental and IFA model, LEA, and $\tau = 2.0$ correlation model predicted NWP saturation distributions at times t_1, t_2, t_3, and t_4 respectively.

As can clearly be seen in Figure 5-17, the IFA model simulation well predicts the presence of NWP within the experimental apparatus. The only discrepancy occurs within Zone 3, near the top of the domain, where the IFA model predicts residual saturations where NWP was not detected by the light transmission / image analysis system. However, as discussed in Chapter 3, the light transmission system is insensitive to the presence low saturation NWP. In addition, the dissolution of NWP causes the precipitation of the blue dye that was used in the colouration of the 1,2-DCE, which further limits the sensitivity of the light transmission system. Visual observations made during the experiment made it clear that NWP was indeed present at this location at t_1, as accurately predicted by the IFA model simulation. As anticipated, the high mass flux rates of the LEA simulation results in the prediction of complete NWP dissolution in large areas of the NWP source, particularly in Zones 1 and 3. The correlation model ($\tau = 2.0$) also well predicts the NWP saturation distribution at time t_1.

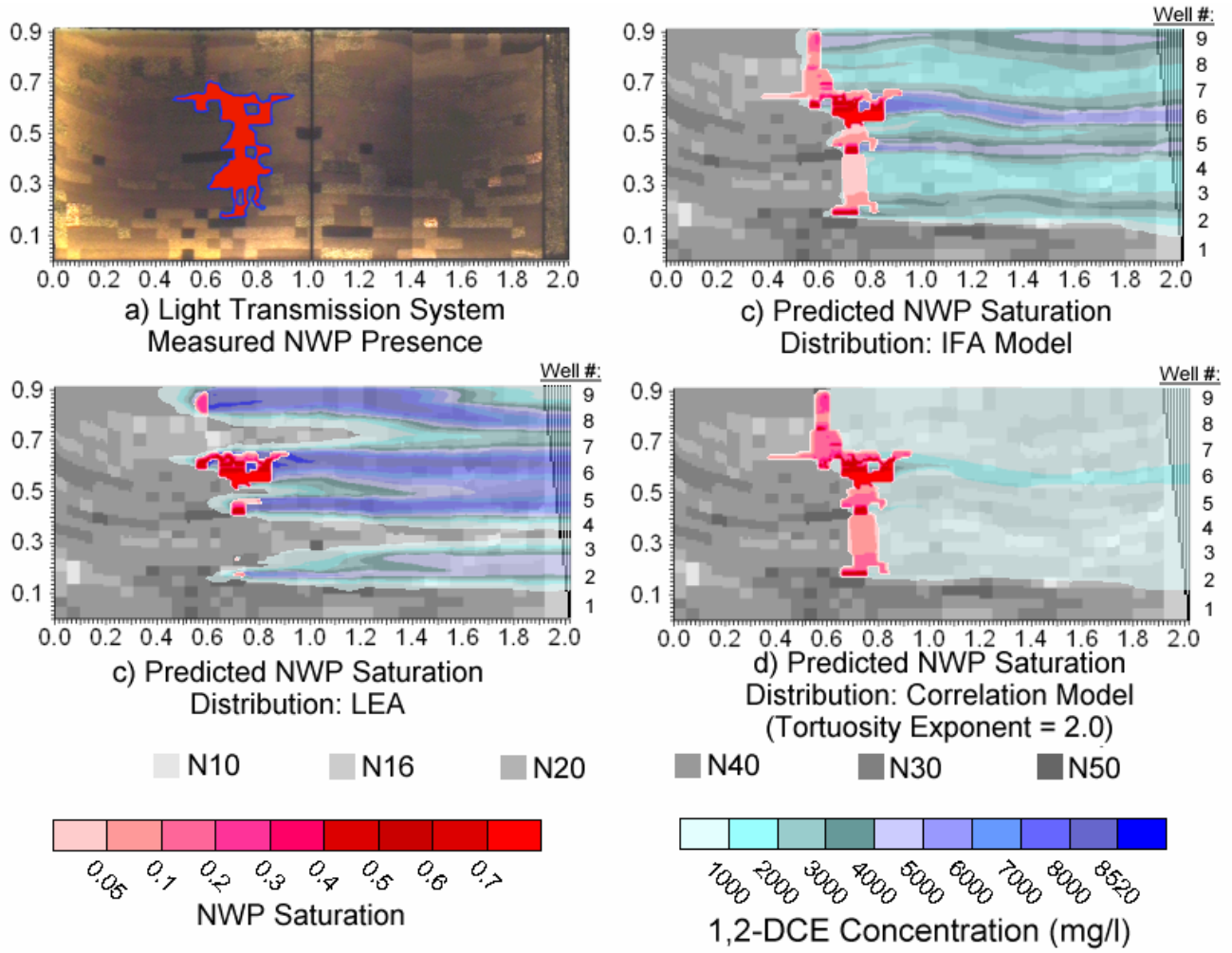

Figure 5-17. Laboratory measured and numerical model predictions of NWP presence at time t_1 in the bench scale experimental apparatus.

Figure 5-18 compares the actual and predicted presence of NWP at time t_2. The IFA model simulation predicts the existence of three pooled NWP regions - a large area within Zone 2, a smaller area immediately beneath this first area, and a small area within Zone 1 at the bottom of the domain – that are similar in shape and location to the actual location of NWP within the experimental apparatus. The LEA assumption predicts that the pool in Zone 3 at the bottom of the domain has already completely dissolved by time t_2, and the correlation model simulation predicts virtually no change in the pattern of NWP, and very little change in predicted NWP saturations between this figure and Figure 5-17 illustrating model predictions at time t_1.

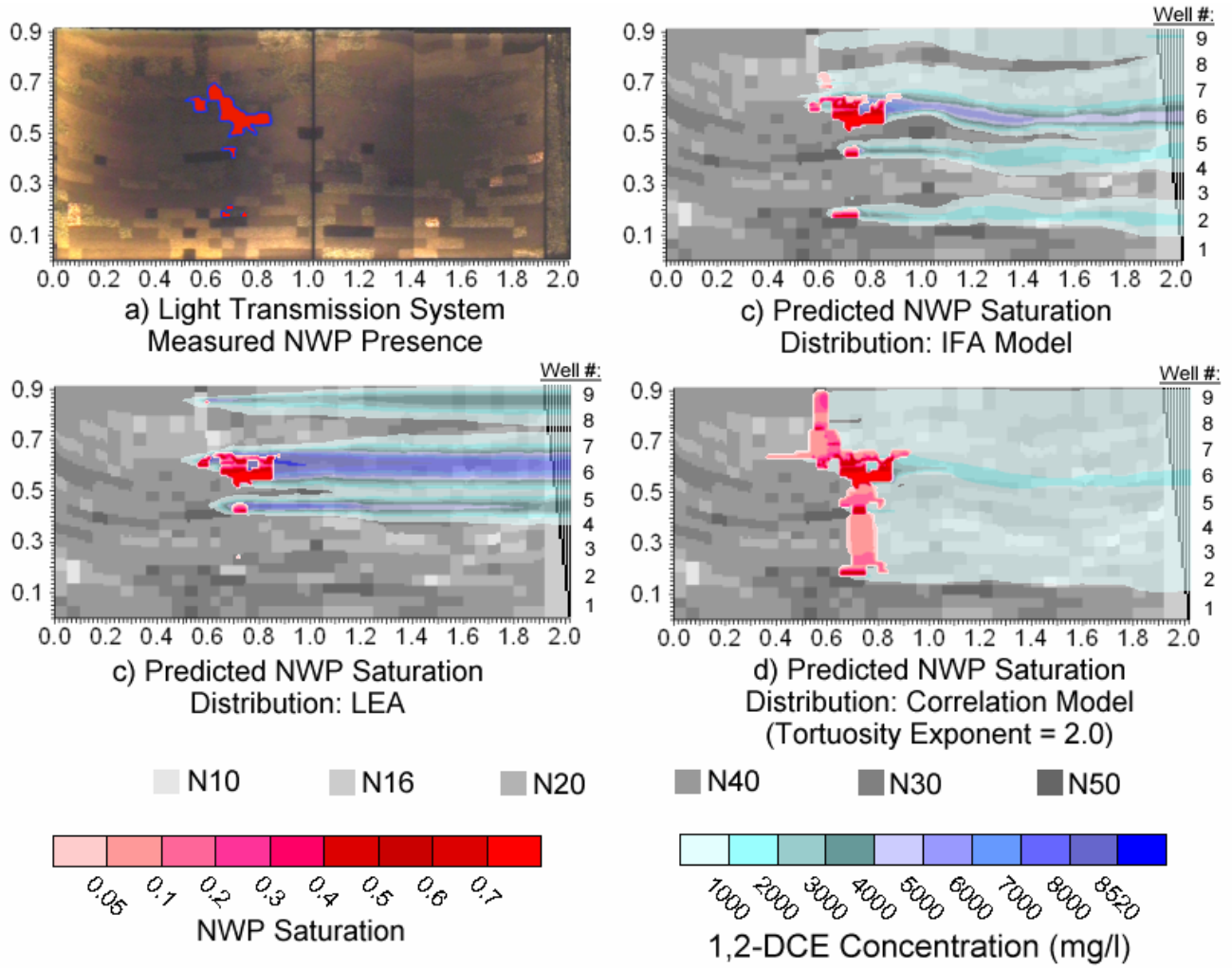

Figure 5-18. Laboratory measured and numerical model predictions of NWP presence at time t_2 in the bench scale experimental apparatus.

At time t_3 illustrated in Figure 5-19, the same three areas of NWP described for Figure 5-18 are still present within the experimental apparatus. Once again, the IFA model accurately predicts NWP at these locations. The LEA assumption predicts the existence of only the largest pool in Zone 2, and the correlation model predicts very little change in the pattern of NWP since the cessation of migration at approximately 2.6 hours.

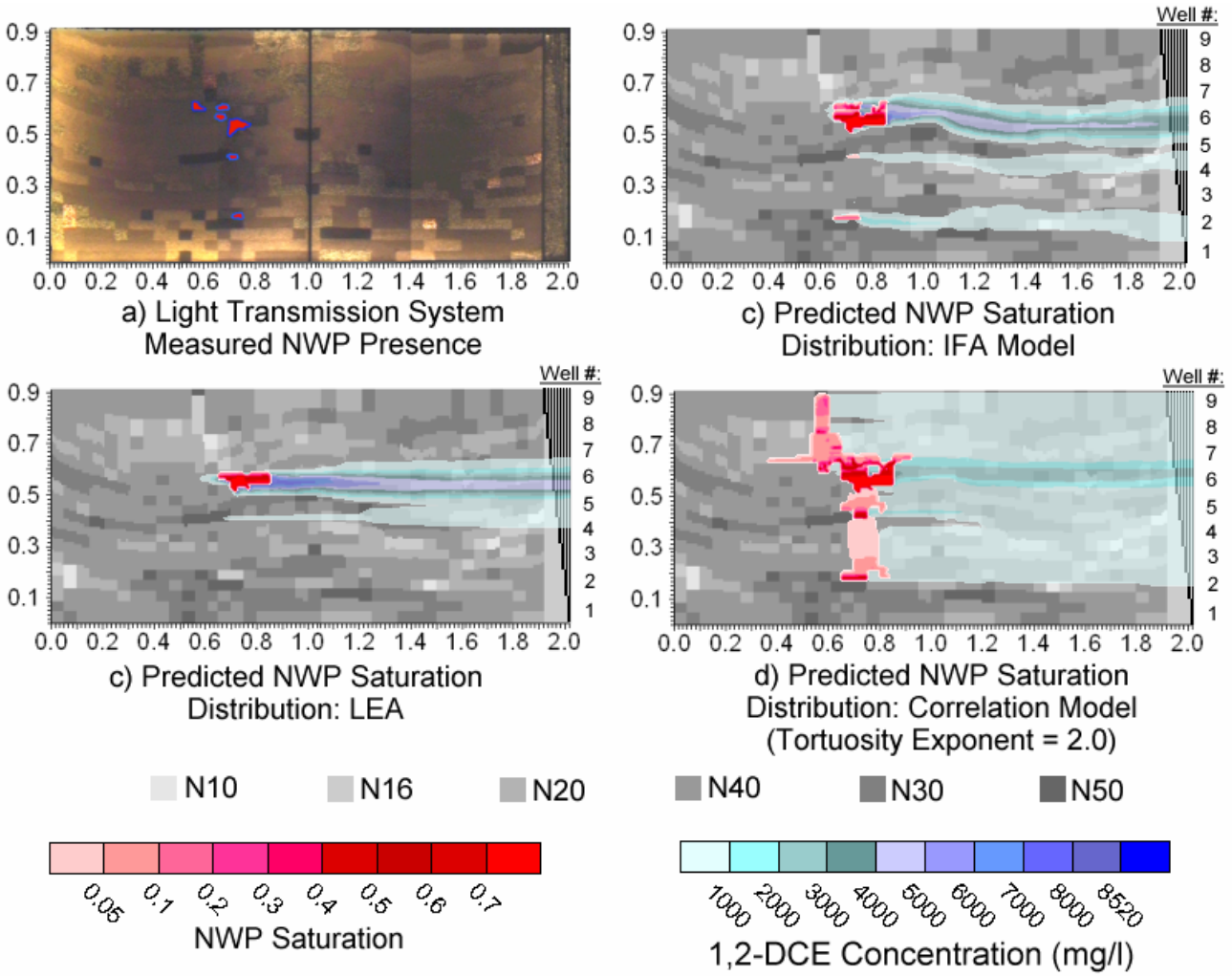

Figure 5-19. Laboratory measured and numerical model predictions of NWP presence at time t_3 in the bench scale experimental apparatus.

Figure 5-20 shows the actual and predicted presence of NWP in the domain at time t_4. The IFA model predicts NWP saturations within the Zone 1 pool at this time, in contrast to experimental results. However, the predicted NWP saturations are on the order of approximately 0.05, indicating that the pool in this zone has almost completely dissolved. The LEA accurately predicts the continued presence of the large Zone 2 pool, as the other initial areas of NWP presence have already completely dissolved by this time. However, even after 264 hours, there is no substantial change in the predicted NWP distribution when the correlation model is used in the simulation.

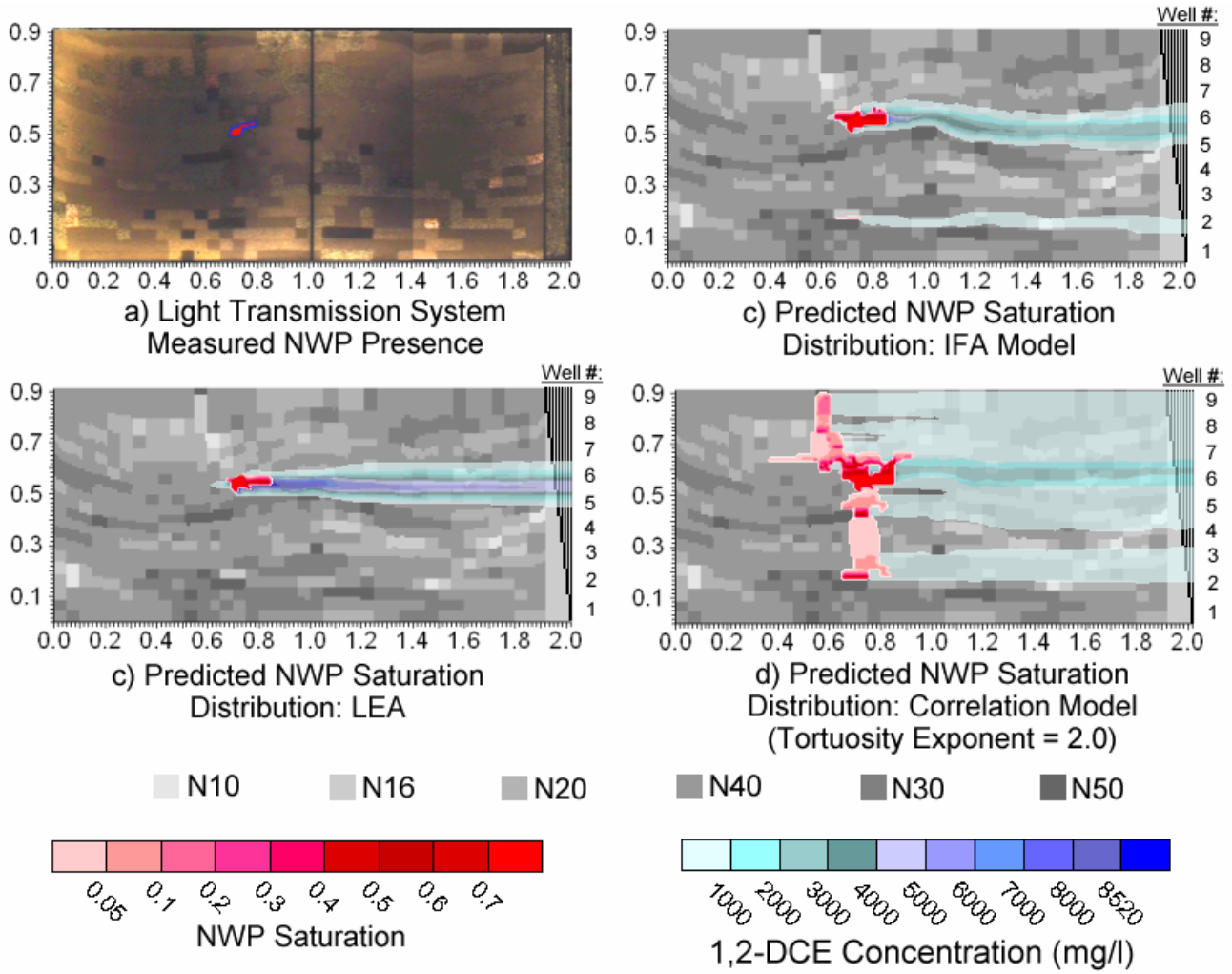

Figure 5-20. Laboratory measured and numerical model predictions of NWP presence at time t_4 in the bench scale experimental apparatus.

These analyses of source zone evolution thus lead to the same conclusion as those of downgradient concentrations: the IFA model simulation most accurately predicts mass transfer. The LEA assumption over predicts the mass transfer rate, and therefore under predicts the life span of the identified pooled regions. In contrast, the low mass transfer rates predicted by the correlation model simulation lead to a large over prediction of the life spans of both residual and pooled NWP regions within the domain. In fact, the correlation model predicts that the pattern of NWP within the domain remains virtually unchanged from the time of complete migration cessation until time t_4, as examined in Figure 5-20.

5.5.1.3 Sensitivity to IFA Model Assumptions

A sensitivity analysis was carried out to examine the relative importance of the assumptions made in the derivation of the proposed IFA model. Figure 5-21 compares the predicted concentration breakthrough curve for the bench scale experiment using the proposed IFA model with four alternative simulations: 1) the 'No Haines Jump Energy Dissipation' simulation that assumes that the Haines jump energy dissipation factor, β, is set to a value of 1.0 (in the validation simulation, β = 0.6); 2) the 'Total Interfacial Area' simulation that assumes that the entire NWP / WP interface (including the area between the NWP and WP films coating the porous media) is calculated; and, 3) the 'Constant Residual Interfacial Area' simulation that assumes that interfacial area does not change as residual NWP dissolves (i.e., the IFA line in Figure 5-8 from $S_w'' < S_W < 1.0$ will be horizontal), as opposed to the validation simulation where a linear relationship between IFA and NWP saturation is assumed for NWP saturations less than residual resulting from dissolution; and, 4) the 'No Saturation History' simulation that assumes that IFA is calculated according to the method of Leverett (1941) and Bradford and Leij (1997), such that saturation history

is not considered, and both drainage and imbibition interfacial area is proportional to the area under the drainage P_C - S_W curve from $S_W^i < S_W < 1.0$ (where S_W^i is an arbitrary intermediate WP saturation greater than or equal to S_r).

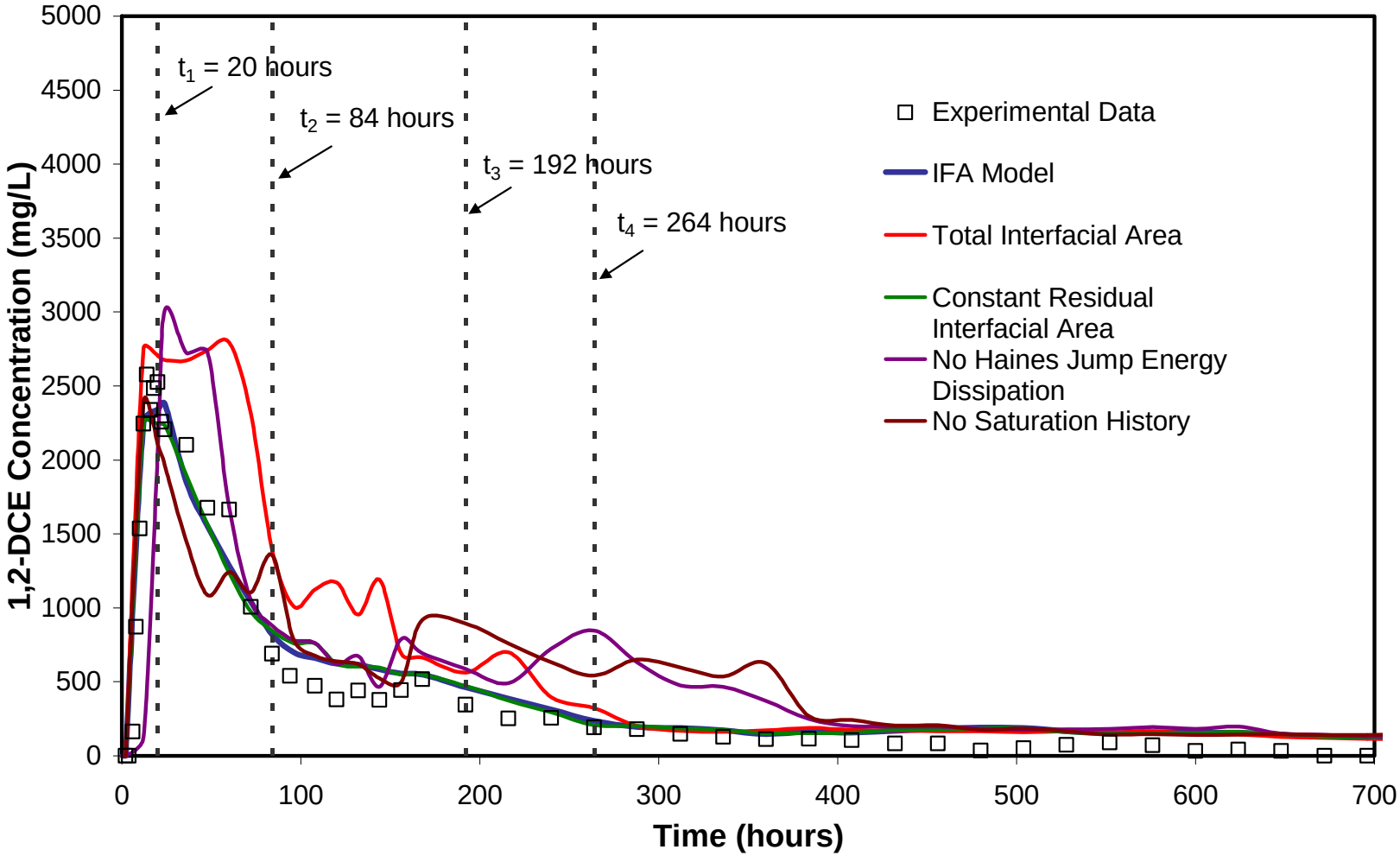

Figure 5-21. Sensitivity of numerically predicted average 1,2-DCE concentration at the downgradient boundary of the bench scale flow cell to IFA model assumptions.

As can clearly be seen in the figure, the complete IFA model (i.e., as derived) gives the best prediction of the dissolution behaviour observed in the bench scale flow cell. The 'constant residual interfacial area' simulation matches the complete IFA model simulation almost exactly, with only minor differences near time t_1 and just after time t_2. This indicates that the dissolution behaviour of the transient NWP release in heterogeneous porous media conducted in the bench scale experiment is insensitive to the local scale description of interfacial area at residual NWP saturations.

The 'total interfacial area' and the 'no Haines jump energy dissipation' simulations, however, are distinctly different from the IFA model prediction of average downgradient aqueous phase concentration. Both of these simulations predict generally higher aqueous phase concentrations than does the IFA model simulation. The 'total interfacial area' simulation predicts higher concentrations than the IFA model at early time, when saturations are approaching WP residual levels. This is expected, as maximum interfacial areas are estimated at residual WP saturations for the 'total interfacial area' model, in contrast to the IFA model which predicts maximum areas at WP saturations between approximated 0.2 and 0.4.

The 'no Haines jump energy dissipation' simulation also shows a higher peak concentration, but deviates further from the IFA model prediction at both early and late time. At early time, the first arrival time of aqueous phase 1,2-DCE is significantly later than predicted by the other sensitivity analysis simulations. At late time, a secondary peak of concentration at time t_4 is predicted (that is not observed in the complete IFA model simulation). As discussed in the following section, the interfacial area description affects local dissolution rates that in turn affect NWP saturations during migration. As a result, local scale mass transfer impacts the bench

scale aqueous phase flow field and ultimately bench scale mass transfer rates. The differences in early and late time dissolution behaviour predicted with the 'no Haines jump energy dissipation' simulation is a combination of local scale mass transfer differences and bench scale aqueous phase flow affects.

The 'no saturation history' is also distinctly different from IFA model simulation. At early time, when a large proportion of the NWP in the domain is under drainage conditions, the 'no saturation history' simulation is similar in shape and character to the IFA model aqueous phase concentration prediction. However at late time, when saturations decrease as a result of dissolution, and imbibition dominates, the 'no saturation history' simulation over predicts the aqueous phase concentrations exiting the downgradient boundary of the domain.

5.5.1.4 Sensitivity to the Value of k_{la}

Figure 5-22 plots the predicted average aqueous phase 1,2-DCE concentration exiting the downgradient boundary of the flow cell as a function of time for the IFA model simulations utilising four different k_{la} values: 2 x 10^{-7} m/s, 3 x 10^{-7} m/s, 4 x 10^{-7} m/s, and 5 x 10^{-7} m/s; the LEA simulation is also plotted for comparison purposes. The figure clearly demonstrates that the predicted concentration profile is highly sensitive to the value of k_{la}, for the (notably small) range of values examined in this study. The effect of k_{la} is not trivial; the predicted dissolution behaviour (encompassing numerous benchmarks values such as the peak concentration, the rate of concentration decrease following the peak, the life span of the source zone, etc.) is not linearly related to changes in k_{la}. Clearly the appropriate value of k_{la} is not only expressed directly at the local scale of mass transfer, but is also expressed by the ensemble dissolution behaviour of the entire NWP source zone. The change in bench scale dissolution characteristics is a function of both the local scale mass transfer rate,

and the effect this local scale rate has on the evolution of a transient NWP source zone and the resulting aqueous phase flow field.

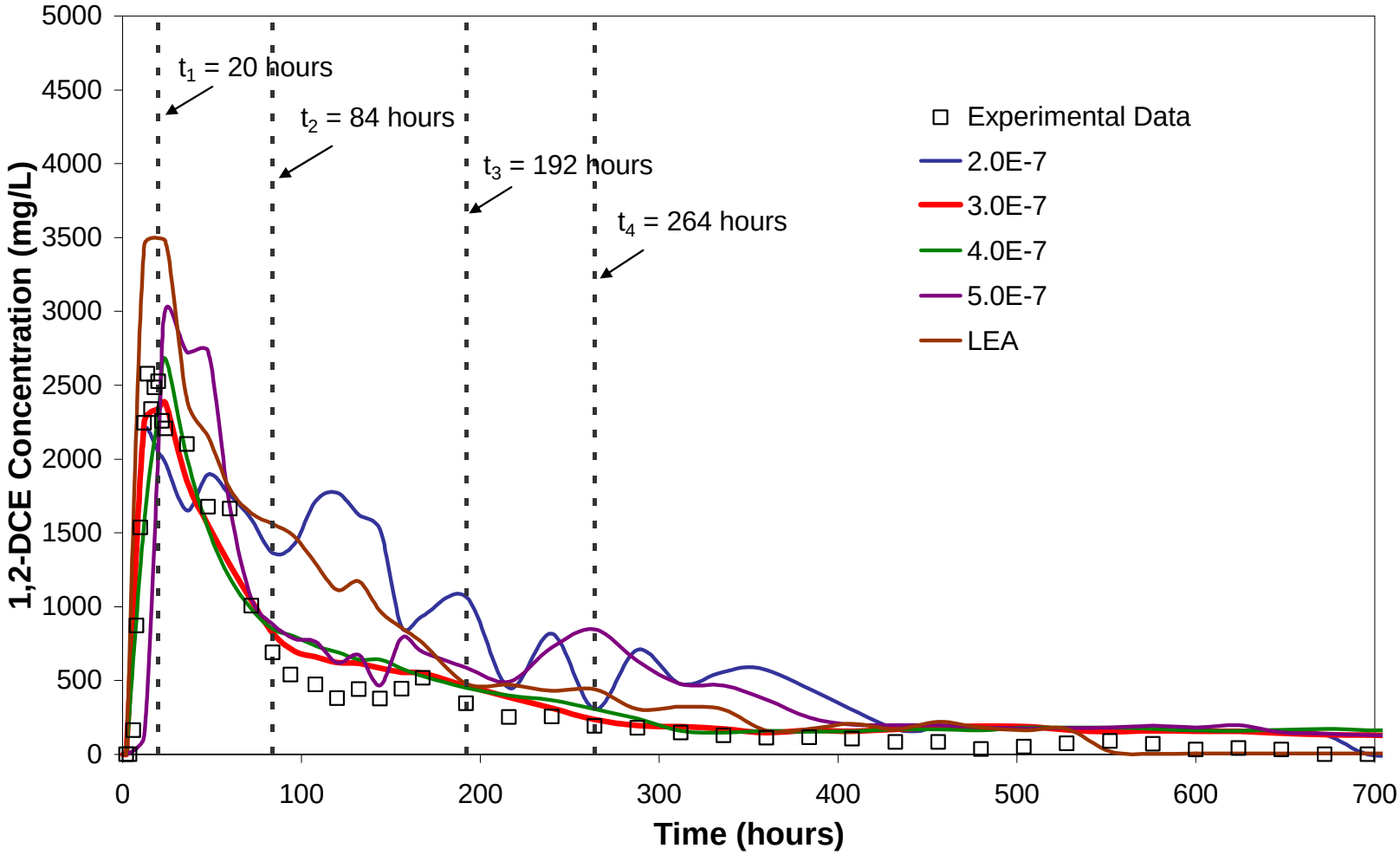

Figure 5-22. Sensitivity of numerically predicted average 1,2-DCE concentration at the downgradient boundary of the bench scale flow cell to the value of k_{la}.

This phenomenon is illustrated in Figure 5-23 which plots the predicted NWP vertical first moment as a function of time during this first 24 hours of the bench scale experiment. This figure shows the average vertical position of the source zone for the four IFA model simulations, the LEA simulation, and a simulation where dissolution is not considered. While the selection of the mass transfer expression was observed to not significantly affect 'key location' arrival and breakthrough times (as discussed in Chapter 3) and the general outline of the NWP source, Figure 5-23 illustrates that local scale mass transfer has a direct affect on the distribution of mass within the NWP source zone. Following the complete cessation of migration at approximately 2.6 hours, the predicted vertical first moment is shown to increase for faster descriptions of mass transfer, with the range bounded by the minimum mass transfer rate (zero) for the 'no dissolution' simulation and the maximum local scale mass transfer rate for the LEA simulation. Increasing the local scale mass transfer rates increases the rate of NWP mass reduction beneath NWP pool regions following termination of the source condition; in particular, the large NWP pool region in Zone 2. As the NWP flow path beneath the pool region in Zone 2 is cut off at an earlier time, the mass of NWP retained above this pooled region is consequently increased (figure not shown).

This shift in the distribution of saturations within the source zone has a significant affect on the aqueous flow field. For example, Figure 5-22 shows higher average downgradient 1,2-DCE concentrations at time t_3 for the IFA model simulation in conjunction with a k_{la} value of 2×10^{-7} – the minimum k_{la} value examined - than for any of the other IFA model simulations. In this simulation, a larger proportion of mass has migrated deep within the flow cell (see Figure 5-23). The higher saturation Zone 1 pool and the ensuing lower aqueous phase flow rate through this area, results

in a longer pool life span emanating from this zone. As a result, NWP mass is still dissolving from this area, contributing to the bench scale average aqueous phase concentrations leaving the flow cell at t_3, in contrast to the other simulations examined in this sensitivity analysis.

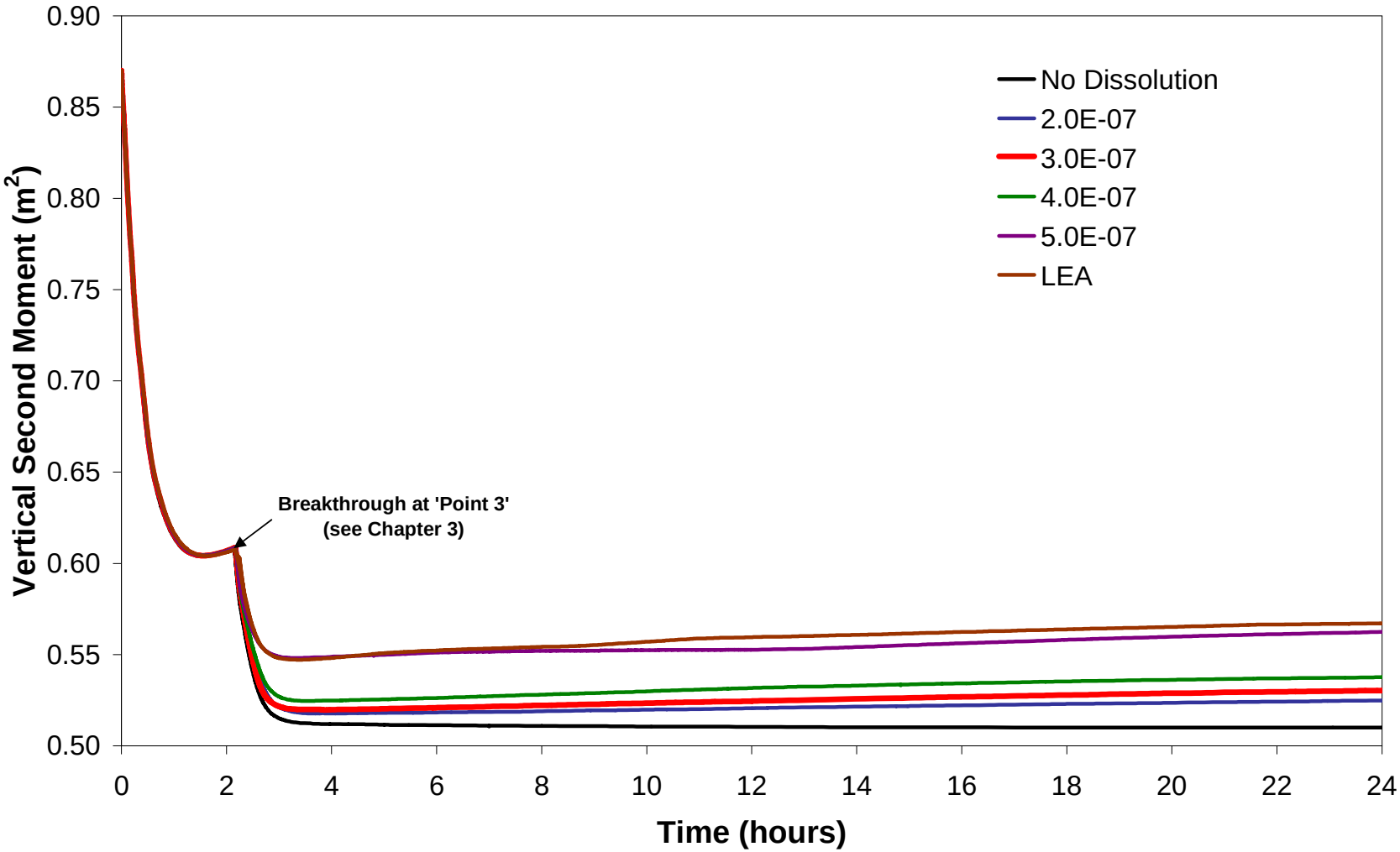

Figure 5-23. Vertical first moment of the NWP versus time as a function of local scale mass transfer rate.

General conclusions regarding the influence of k_{la} on bench scale mass transfer rates are difficult to make. The interplay between local scale mass transfer, distribution of NWP saturations, and bench scale aqueous phase flow is dynamic and complex with compounding (feedback) interactions. However, the multifarious nature of this relationship reveals that the overall average downgradient concentration is a relatively unique signal that is quite sensitive to most aspects of a local scale mass transfer model. The unique fit of the observed signal by the simulation with k_{la} = 3 x 10^{-7} m/s among all the sensitivity runs examined, provides confidence in both the IFA model itself and the calibrated k_{la} value determined in this study, as slight deviations from this value lead to significant changes in the character of the predicted dissolution breakthrough curve as seen in Figure 5-22.

5.4.2 Field Scale Simulations

5.5.2.1 Predicted Mass Transfer Rates

Figure 5-24 plots the volume of NWP present within the simulation domain as a function of time for the field scale simulations conducted: IFA model, correlation model, and LEA assumption. This figure illustrates a more rapid decrease in source volume for the correlation model simulation than for either the IFA model or the LEA simulation. In fact, the LEA predicts the slowest field scale mass transfer rates, as illustrated by Figure 5-24, in spite of the fact that the LEA represents the maximum local scale mass transfer rate possible.

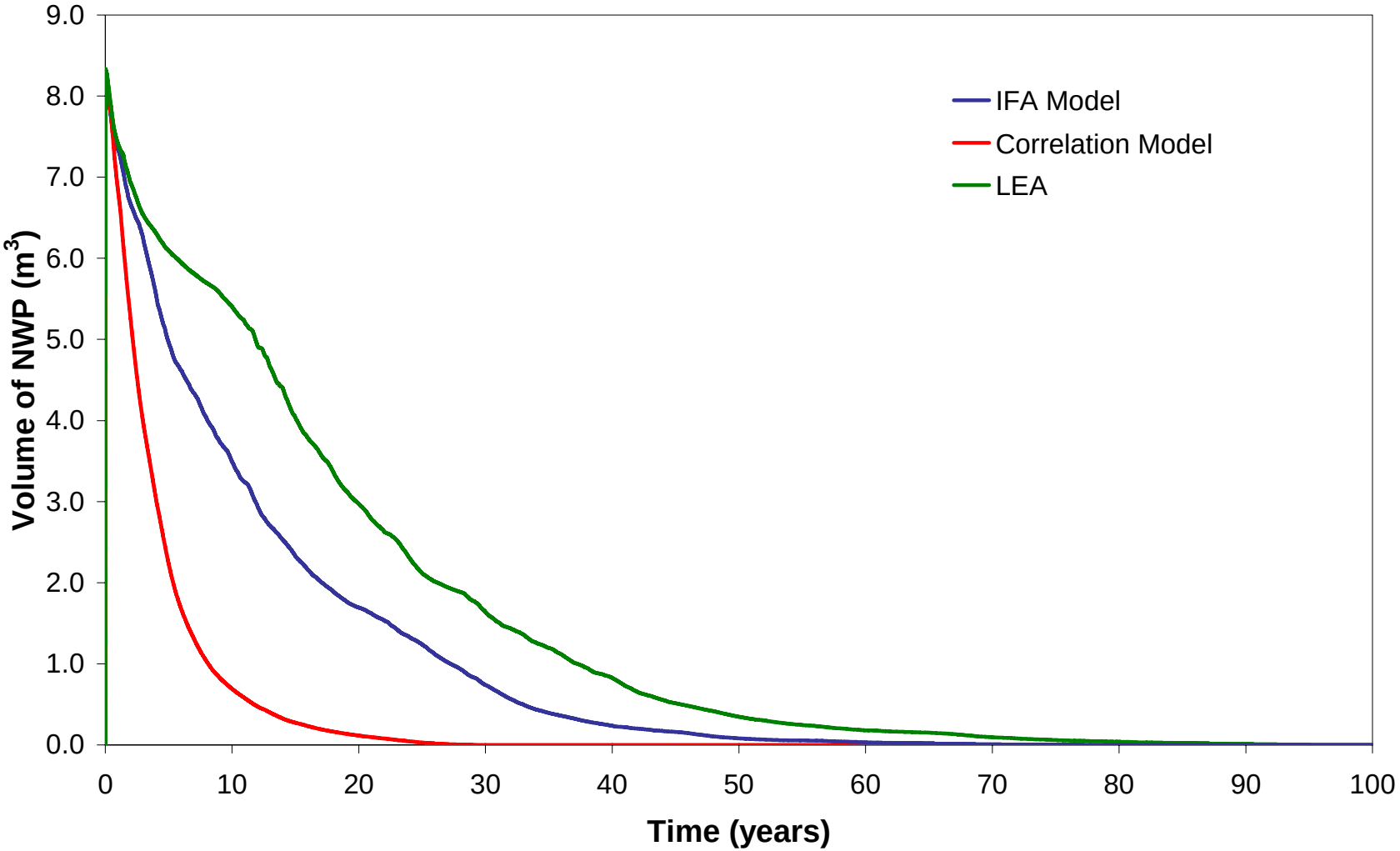

Figure 5-24. Volume of NWP within the field scale simulation domain as a function of time.

This phenomenon is due to differences in aqueous phase velocities through the source zone; a more detailed explanation is provided with reference to Figure 5-25 which sketches the relationship between NWP saturations, groundwater flow rates and (spatially variable) aqueous phase concentrations within a two-dimensional source zone for both a LEA and a rate-limited mass transfer case. As illustrated, the aqueous phase concentration exiting the source zone in the LEA case is at the solubility limit. As the LEA assumes the instantaneous transfer of mass to the aqueous phase, dissolution - and therefore NWP saturation reduction - is always limited to the leading edge of the NWP source. Groundwater velocity through the source zone is governed, in part, by the presence of NWP: velocity is proportional to WP relative permeability which is a function of S_W. Therefore, as the NWP saturation at the downgradient end of the source remains unaffected by mass transfer in the LEA case (see Figure 5-25b), the downgradient NWP saturations in a two-dimensional source zone ultimately limit the velocity of groundwater, and consequently the overall rate of mass flux from the source zone.

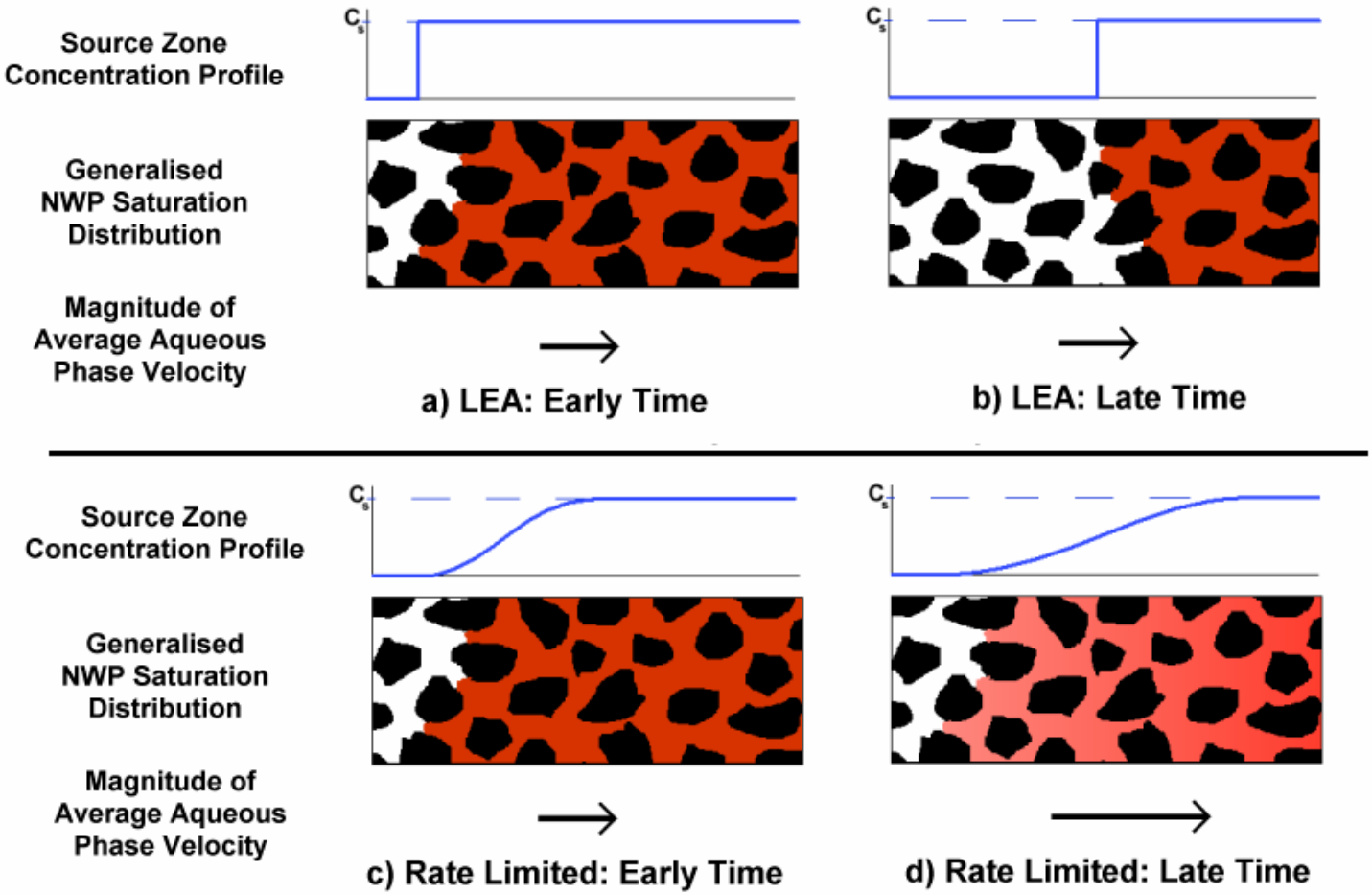

Figure 5-25. Hypothetical source zone evolution for a LEA and a rate limited mass transfer model.

In contrast, as illustrated in Figure 5-25c and d, the rate limited case does not assume instantaneous mass transfer. Therefore NWP mass reductions can occur across a larger proportion of the source zone. If mass transfer occurs across the entire source zone, then the aqueous phase concentration exiting the source will be below the solubility limit. However, for large source zones, aqueous phase concentrations will approach the solubility limit and therefore not be significantly different from those predicted for the LEA case. The larger scale difference between the two cases, therefore, is the fact that mass is removed from part or all of the source zone in the rate limited case. As a result, rate limited mass transfer will lead to a corresponding increase in groundwater flow rate through the source (see Figure 5-25d). Thus, the mass transfer rate from the source (which is a function of both the aqueous phase concentration and the groundwater velocity – see Equation 5-2) will be equal or similar for the two cases at early time, and greater for the rate limited case at late time (see Figure 5-25).

Figure 5-26 is a plot of groundwater volumetric flux exiting the downgradient boundary for each of the field scale simulations. The figure demonstrates that, despite identical constant head boundary conditions, the aqueous phase flow rate is greatest for the correlation model and slowest for the LEA assumption. This figure further emphasizes the significant influence the local scale mass transfer expression has on the aqueous phase flow field and, therefore, on field scale mass flux and the life span of the source zone.

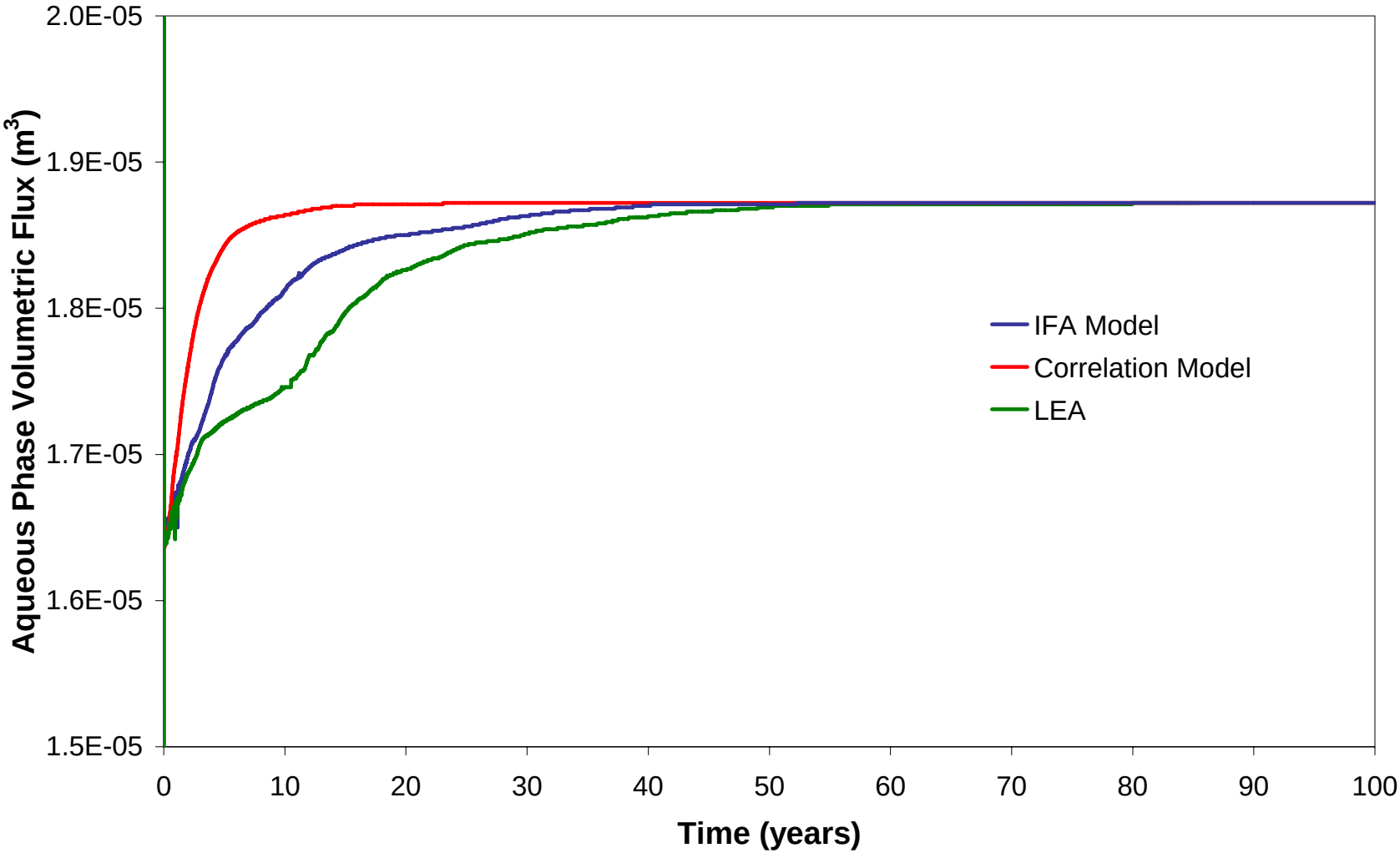

Figure 5-26. Groundwater volumetric flux exiting the downgradient constant head boundary of the field scale simulation domain.

The predicted field scale mass transfer rate of the IFA model simulation is in between the rate predicted for the LEA and correlation model simulations (Figure 5-24). The IFA model is a rate limited case, but the local scale mass transfer rate is greater than for the correlation model (see Figure 5-24). Thus, the phenomenon described above is observed for the IFA model simulation, but to a lesser degree than predicted for the correlation model case.

In three-dimensional simulations of mass transfer, it is anticipated that the field scale dissolution of NWP will be dominated by the transfer of mass at the outer boundaries of source zones and sub-zones (as opposed to within the source as described above). Therefore, advection - dispersion will play a more pronounced role, and the LEA will likely exhibit field scale mass transfer rates greater than predicted for either of the rate limited cases. Note that this does not diminish the significance of the conclusions presented in this work. Aqueous phase velocity-controlled mass flux through source zones is still significant in that (a) almost all simulations conducted in this context are performed in two dimensions, and (b) such effects will dominate in three dimensions when source zones are extensive, confined by low permeability strata, and in the vicinity of high gradients (e.g., waterflooding). Moreover, the presented IFA model, while validated in two dimensions, is expected to be equally appropriate for three-dimensional simulations.

5.5.2.2 NWP Saturation and Aqueous Phase Concentration Distributions

Figures 5-27 through 5-29 plot the predicted NWP saturation and aqueous phase concentration distributions for the three field scale simulations after 4 months, 1 year, and 20 years, respectively. Following the termination of the source after 5 days of simulations time, there was no significant difference in the magnitude and distribution of NWP within the simulation domain.

As seen in Figure 5-27, the rate limited simulations (the IFA model and the correlation model) show aqueous phase concentrations at four months extending further downgradient from the source than observed in the LEA simulation. Although not readily apparent, NWP saturations in the rate limited simulations are, by this time, on the order of 10 to 15 percent lower than in the LEA simulation in certain high permeability areas. As a consequence, groundwater velocities through these zone are higher and aqueous phase 1,2-DCE has transported further after four months.

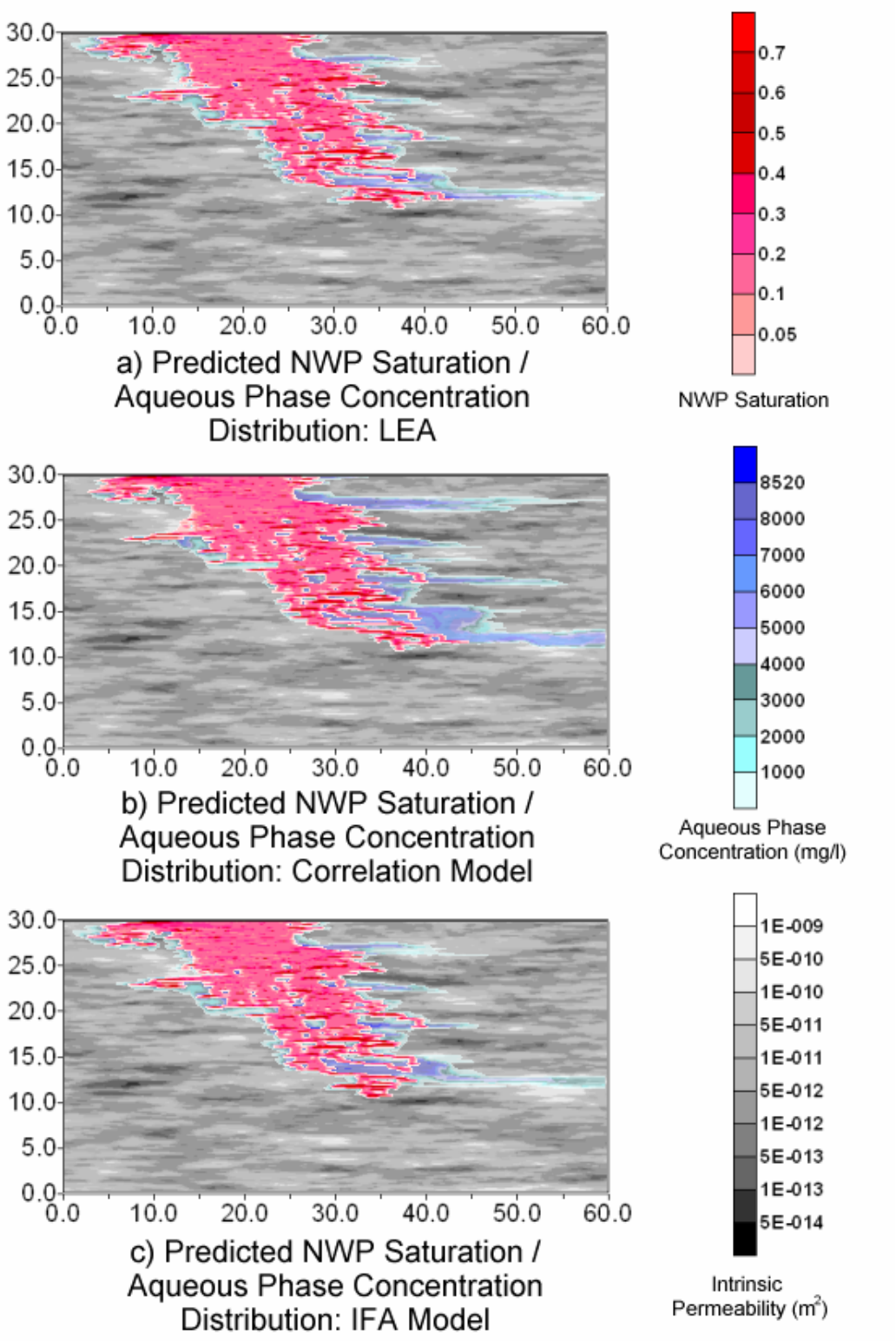

Figure 5-27. Numerical model predictions of NWP presence after 4 months.

In Figure 5-28, the relative reduction in NWP saturations anticipated for the rate limited cases are more clearly evident. Increased groundwater flow has led to an increase in the field scale mass transfer rate. This phenomenon is most apparent in the correlation model simulation (see Figure 5-25b).

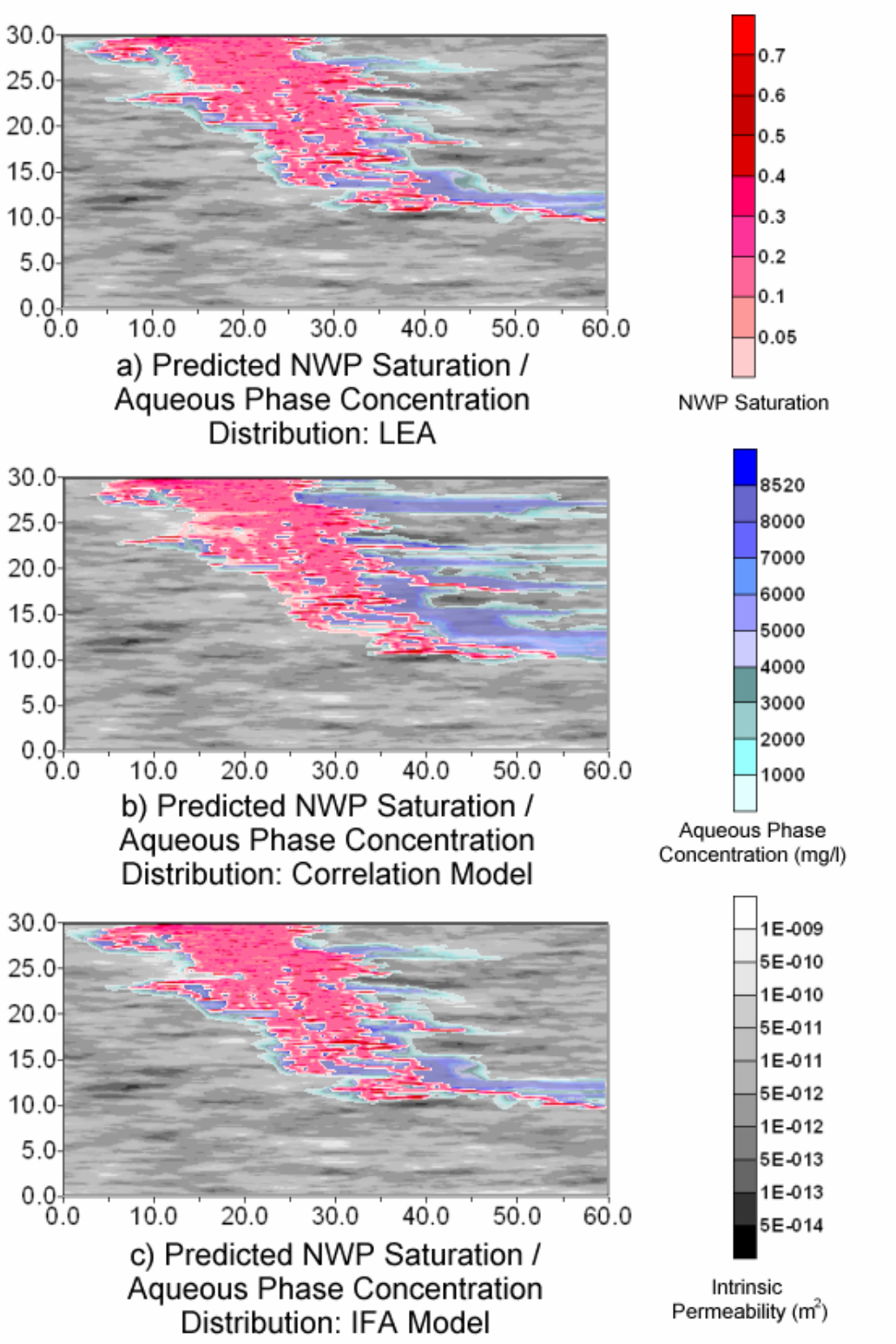

Figure 5-28. Numerical model predictions of NWP presence after 1 year.

Figure 5-29 demonstrates the sensitivity of predicted source zone life span to the description of local scale mass transfer. The correlation model simulation predicts near complete source zone dissolution after 20 years. In contrast, the LEA simulation predicts approximately 35% of the release volume remaining in the model domain at this same time.

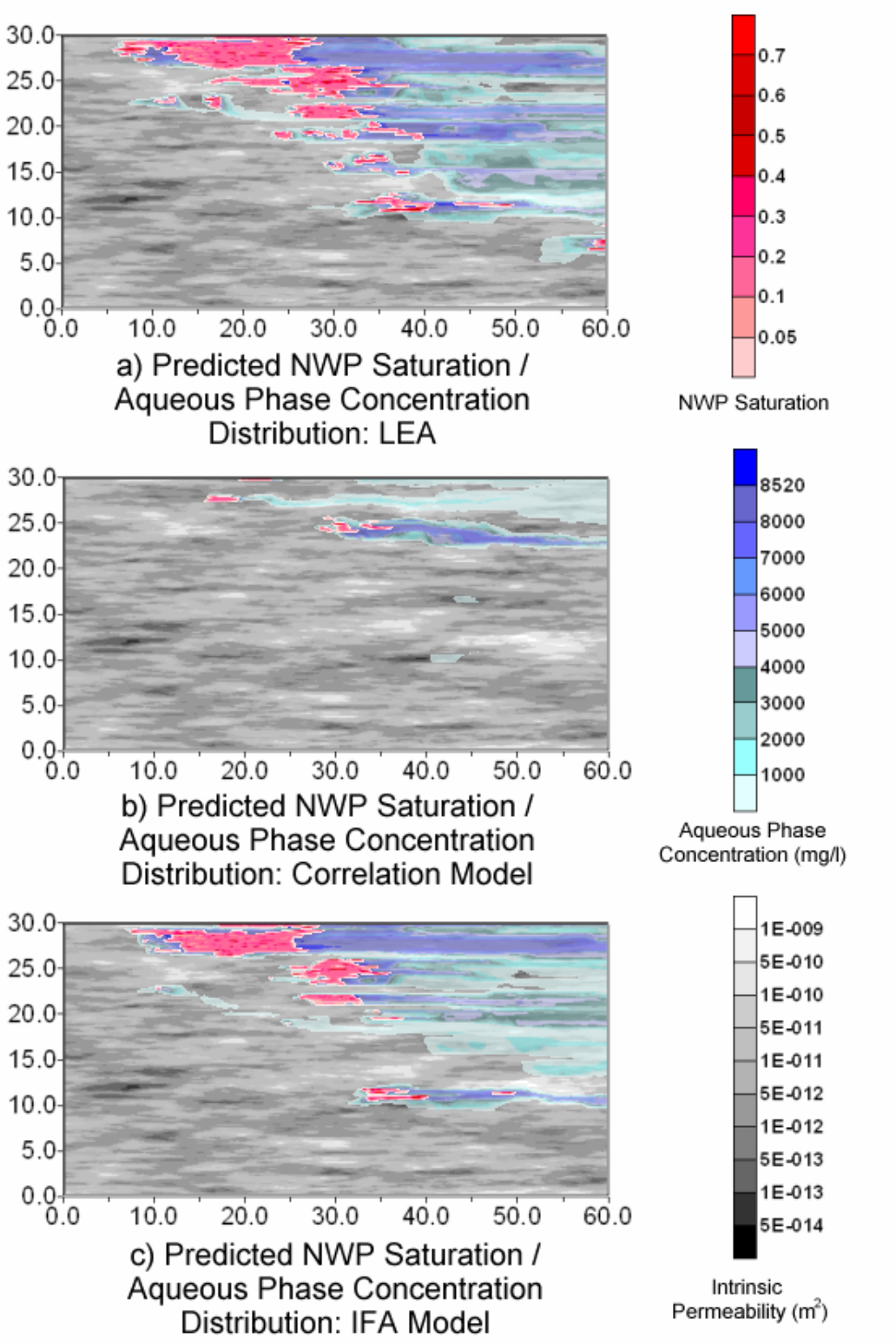

Figure 5-29. Numerical model predictions of NWP presence after 20 years.

5.6 Conclusions

A new, thermodynamically-based interfacial area (IFA) model was developed for use in the single-boundary layer expression of mass transfer as an alternative to existing empirical correlation expressions. The IFA model considers consistency and continuity with multiphase flow constitutive relationships, energy losses, effective specific interfacial area for mass transfer, and dissolution of residual NWP. The model is easily implemented within a numerical model that couples multiphase flow and dissolution, containing only a single additional parameter (constant) that applies for a given wetting-nonwetting fluid pair: k_{la}.

A two-dimensional bench scale experiment involving the release and dissolution of a transient NWP source zone in heterogeneous porous media was conducted to evaluate the validity of the developed IFA model when utilised to predict NWP dissolution rates. In absence of independent data, the model was calibrated to the experiment via a water-1,2DCE k_{la} value determined to be 3×10^{-7} m/s. Comparison of measured downgradient dissolved phase concentrations and source zone NWP saturations in time and space with those from numerical simulations of the experiment reveal that the proposed IFA model is superior to both a local equilibrium assumption and existing empirical correlation expressions.

Sensitivity analysis revealed an important characteristic of mass transfer at the bench scale: that the local scale mass transfer expression can significantly affect the distribution of NWP in a transient release, the aqueous phase flow field, and ultimately, bench scale mass transfer characteristics. As a result, the average downgradient concentration is demonstrated to be a sensitive signal against which to evaluate coupled multiphase flow / mass transfer models. This analysis further confirmed the appropriateness of the best-fit k_{la} value, and revealed that the only

component of the IFA model which is inconsequential is that associated with residual NWP saturations.

Two-dimensional simulations at the field scale of multiphase flow and dissolution demonstrate that the assumed local mass transfer expression has a significant effect on the predicted life span of the source zone and on the rate of mass flux through the downgradient boundary. In contrast to intuitive expectations, the local equilibrium assumption results in predictions of reduced global flux and increased source longevity relative to rate-limited mass transfer models. The IFA model, properly accounting for the evolving groundwater flow field, predicts source longevity that is intermediate between the LEA assumption and those resulting from empirically derived correlations expressions.

It was already known that accurate multiphase flow modelling of NWP source zones required detailed accounting of intrinsic permeability and constitutive relationships at the local scale. This work implies that when coupling such models with dissolution to examine mass fate, it is necessary to use a rate-limited approach at the local scale that links interfacial area to nonwetting phase saturations, saturation history, and aqueous phase relative permeability. Only with this comprehensive approach are predications able to properly account for the influence of local mass flux on global mass flux through modification of the groundwater flow field. The presented IFA model is expected to be equally applicable in three dimensions, although it remains to be seen whether a LEA or other simpler approaches may be sufficient (due to the expected increased significance of flow around rather than through source zones) in contrast to two dimensions where such approaches clearly are not sufficient.

5.7 References

Abriola, L.M., Modeling multiphase migration of organic chemicals in ground water systems – A review and assessment, *Environmental Health Perspective, 83,* 117-143, 1989.

Barry, D.A., H. Prommer, C.T. Miller, P. Engesgaard, A. Brun, and C. Zheng, Modeling the fate of oxidizable organic contaminants in groundwater, *Advances in Water Resources, 25*, 945-983, 2002.

Bradford. S.A., and F.J. Leij, Estimating interfacial area for multi-fluid soil systems, *Journal of Contaminant Hydrology, 27*, 83-105, 1997.

Brewster, M.L., A.P. Annan, J.P. Greenhouse, B.H. Kueper, G.R. Oldhoeft, J.D. Redman, and K.A. Sander, Observed migration of a controlled DNAPL release by geophysical methods, *Ground Water, 33*(6), 977-987, 1995.

Brusseau, M.L., R.E. Jessup, and P.S.C. Rao, Modeling solute transport influenced by multi-process nonequilibrium and transformation reactions, *Water Resources Research, 28*(1), 175-182, 1992.

Brusseau, M.L., Z. Zhang, N.T. Nelson, R.B. Cain, G.R. Tick, and M. Oostrom, Dissolution of nonuniformly distributed immiscible liquid: intermediate-scale experiments and mathematical modelling, *Environmental Science and Technology, 36,* 1033-1041, 2002.

Cary, J.W., Estimating the surface area of fluid phase interfaces in porous media, *Journal of Contaminant Hydrology, 15*(4), 243-248, 1994.

Dalla, E., M. Hilpert., and C.T. Miller, Computation of the interfacial area for two-fluid porous medium systems, *Journal of Contaminant Hydrology, 56*, 25-48, 2002.

Falta, R.W., P.S. Rao, and N. Basu, Assessing the impacts of partial mass depletion in DNAPL source zones: 1. Analytical modelling of source strength functions and plume response, *Journal of Contaminant Hydrology, 78,* 259-280, 2005.

Grant, G.P., and J.I. Gerhard, The sensitivity of predicted DNAPL source zone longevity to mass transfer correlation model, in: Geoenvironmental Engineering: Integrated management of groundwater and contaminated land, Proceedings of the 4th British Geotechnical Association, Stratford-upon-Avon, UK, June 28-30, 2004.

Geller, J.T., and J.R. Hunt, Mass Transfer from nonaqueous phase organic liquids in water-saturated porous media, *Water Resources Research, 29*(4), 833-845, 1993.

Gerhard, J.I., B.H. Kueper, and G.R. Hecox, The influence of waterflood design on the recovery of mobile DNAPLs, *Ground Water, 36*(2), 283-292, 1998.

Gerhard, J.I., and B.H. Kueper, Capillary pressure characteristics necessary for simulation DNAPL infiltration, redistribution, and immobilization in saturated porous media, *Water Resources Research, 39*(8), SBH71-SBH717, 2003a.

Gerhard, J.I., and B.H. Kueper, Relative permeability characteristics necessary for simulating DNAPL infiltration, redistribution, and immobilization in saturated porous media, *Water Resources Research, 39*(8), SBH81-SBH816, 2003b.

Gvirtzman, H., and Roberts, P.V., Pore scale spatial analysis of two immiscible fluids in porous media, *Water Resources Research, 22*(5), 1165-1176, 1991.

Hunt, J.R., N. Sitar, and K.S. Udell, Nonaqueous phase liquid transport and cleanup: 1. Analysis of mechanisms, *Water Resources Research, 24*(8), 1247-1258, 1988.

Imhoff, P.T., P.R. Jaffe, and G.F. Pinder, An experimental study of complete dissolution of a nonaqueous phase liquid in saturated porous media, *Water Resources Research, 30*(2), 307-320, 1993.

Kawanishi, T., Y. Hayashi, P.V. Roberts, and M.J. Blunt, Fluid-fluid interfacial area during two and three phase fluid displacement in porous media: a network model study. GQ98. International Conference and Special Seminars on Groundwater Quality: Remediation and Protection. 1998.

Kim, H., P.S.C. Rao, and M.D. Annable, Gaseous tracer technique for estimating air-water interfacial areas and interface mobility, *Soil Science Society of America Journal, 63*, 1554-1560, 1999.

Kueper, B.H., J.D. Redman, R.C. Starr, S. Reitsma, and M. Mah, A field experiment to study the behaviour of tetrachloroethylene below the watertable: Spatial distribution of residual and pooled DNAPL, *Journal of Ground Water, 31*(5), 756-766, 1993.

Leverett, M.C., Capillary behaviour in porous solids, *Transactions AIMME, 142,* 152-170, 1941.

Mayer, A.S., and C.T. Miller, The influence of mass transfer characteristics and porous media heterogeneity on nonaqueous phase dissolution, *Water Resources Research, 32*(6), 1551-1568, 1996.

Miller, C.T., M.M Poirier-McNeill, and A.S. Mayer, Dissolution of trapped nonaqueous phase liquids: Mass transfer characteristics, *Water Resources Research, 26*(11), 2783-2796, 1990.

Morrow, N.R., Physics and thermodynamics of capillary action in porous media, *Industrial Engineering Chemistry Research, 62*(6), 32-56, 1970.

Nambi, I.M., and S.E. Powers, Mass transfer correlations for nonaqueous phase liquid dissolution from regions with high initial saturations, *Water Resources Research, 39*(2), SBH41-SBH411, 2003.

Parker, J.C., A.K. Katyal, J.J. Kaluarachchi, R.J. Lenhard, T.J. Johnson, K. Jayaraman, K. Unlu, and J.L. Zhu, Modeling multiphase organic chemical transport in soils and ground water, *Rep. EPA/600/2-91/042,* U.S. Environmental Protection Agency, Washington, D.C., 1991.

Parker, J.C., and E. Park, Modeling field-scale dense nonaqueous phase liquid dissolution kinetics in heterogeneous aquifers, *Water Resources Research, 40*(5), W051091-W0510912, 2004.

Powers, S.E., C.O. Loureiro, L.M. Abriola, and W.J. Weber Jr., Theoretical study of nonequilibrium dissolution on nonaqueous phase liquids in subsurface systems, *Water Resources Research, 27*(4), 463477, 1991.

Powers, S.E., L.M. Abriola, and W.J. Weber Jr., An experimental investigation of NAPL dissolution in saturated subsurface systems: Steady state mass transfer rates, *Water Resources Research, 28*(10), 2691-2706, 1992.

Powers, S.E., L.M. Abriola, W.J. Weber Jr., An experimental investigation of nonaqueous phase liquid dissolution in saturated subsurface systems: Transient mass transfer rates, *Water Resources Research, 30*(2), 321-332, 1994.

Reeves, P.C., and M.A. Celia, A functional relationship between capillary pressure, saturation, and interfacial area as revealed by a pore-scale network model, *Water Resources Research, 32*(8), 2345-2358, 1996.

Reynolds, D.A., and B.H. Kueper, Multiphase flow and transport in fractured clay/sand sequences, *Journal of Contaminant Hydrology, 51*(1-2), 41-62, 2001.

Robin, M.J.L., E.A. Sudicky, R.W. Gillham, and R.G. Kachanowski, Spatial variability of Strontium distribution coefficients and their correlation with hydraulic conductivity in the Canadian Forces Base Borden aquifer, *Water Resources Research, 27*(10), 2619-2632, 1991.

Saba, T., and T.H. Illangasekare, Effect of groundwater flow dimensionality on mass transfer from entrapped nonaqueous phase liquid contaminants, *Water Resources Research, 36*(4), 971-979, 2000.

Sale, T.C., and D.B. McWhorter, Steady state mass transfer from single-component dense nonaqueous phase liquids in uniform flow fields, *Water Resources Research, 37*(2), 393-404, 2001.

Saripalli, K.P., P.S.C. Rao, and M.D. Annable, Determination of specific NAPL-water interfacial areas of residual NAPLs in porous media using the interfacial tracers technique, *Journal of Contaminant Hydrology, 31*(3-4), 375-391, 1998.

Seagren, E.A., B.E. Rittman, and A.J. Valocchi, A critical evaluation of the local-equilibrium assumption in modelling NAPL-pool dissolution, *Journal of Contaminant Hydrology, 39*(1-2), 109-135, 1999.

Silliman, S.E., Laboratory study of chemical transport to wells within heterogeneous porous media, *Water Resources Research, 37*(7), 1883-1892, 2001.

Soga, K., J.W.E. Page, and T.H. Illangasekare, A review of NAPL source zone remediation efficiency and the mass flux approach, *Journal of Hazardous Materials, 110*, 13-27, 2004.

Welty, C., and M.M. Elsner, Constructing correlated random fields in the laboratory for observations of fluid flow and mass transport, *Journal of Contaminant Hydrology, 202*(1-4), 192-211, 1997.

Zheng, C. MT3D U.S.E.P.A. Report 1990.

Zhu, J., and J.F. Sykes, The influence of NAPL dissolution characteristics on field-scale contaminant transport in the subsurface, *Journal of Contaminant Hydrology, 41,* 133-154, 2000.

CHAPTER 6 – CONCLUSIONS

The goal of this research was to develop a better understanding of the interrelationship between DNAPL source zones and downgradient aqueous phase concentrations with specific emphasis on the factors governing the rate of DNAPL source zone evolution and the factors governing the rate of mass transfer from the DNAPL to the aqueous phase.

The first objective of this research was to validate a numerical model, specifically the k_{rN}-S_W constitutive relationship proposed by Gerhard and Kueper (2003b) for a fixed volume DNAPL release in a two-dimensional heterogeneous porous medium, for the first time. A bench scale flow cell experiment involving the release of a fixed volume of 1,2-dichloroethane into a heterogeneous porous medium was carried out to meet this objective. A light transmission / image analysis system was employed in these experiments to track the migrating DNAPL and identify zones of transient saturation history in the flow cell for comparison with the results of a numerical simulator. The excellent match between observed and simulated behaviour represents the first validation of a multiphase flow model for a finite volume, complex NWP release in heterogeneous porous media.

Simulations employing an analogy-based relative permeability function based on an extension of the work of Burdine (1953) revealed that accurate prediction of the pattern of NWP migration, as well as temporal aspects such as key location arrival time and breakthrough time, require utilisation of a robust k_{rN} –S_W constitutive relationship that accounts for all the physics of two phase flow in porous media at the local scale (e.g. Gerhard and Kueper, 2003a,b) and k_{rN} –S_W function parameter values explicitly determined for the porous media being examined.

Local scale experiments conducted to measure the k_{rN}–S_W function parameter values utilised in the numerical model, revealed a relationship between NWP relative permeability function shape and end-point locations, in particular, the maximum NWP relative permeability, $k_{rN}^{\max}$, on porous media type. A clear trend of decreasing $k_{rN}^{\max}$ with decreasing mean grain size was observed.

The second objective of this research was to examine the significance of the shape and end-point locations of the NWP relative permeability function at the field scale. This objective was met by conducting three Monte Carlo suites of numerical simulations employing the characteristics of the NWP relative permeability curves measured in the local scale laboratory experiments (i.e., $k_{rN}^{\max}$ as a function of mean grain size). The first suite of simulations reveal that spatially variable $k_{r,N}$, correlated to porous media type, can significantly impact predictions of the pattern and timescales of a NWP release in a fine to very fine sand aquifer at the field scale. Null hypothesis testing revealed that the assumption of constant $k_{r,N}$ throughout the solution domain will lead to under predictions of the volume of porous media invaded and of the timescales of NWP migration. In general, the volume of NWP invaded porous media will be under predicted by approximately 9%, and the length of time during which NWP is migrating will be under predicted by a factor of approximately four, if variable (correlated) $k_{r,N}$ is not accounted for in the formulation of the numerical model for the aquifer characteristics employed.

The second suite of simulations revealed that accounting for variable $k_{r,N}$ is less important in a coarse sand to gravel (on average) aquifer at the field scale. Higher k_i implies a greater proportion of higher $k_{rN}^{\max}$ values (i.e., nearer to 1.0), and thus a relatively uniform distribution of $k_{r,N}$ throughout the domain. Therefore, the relative permeability characteristics of the domain more closely resemble the typical

assumption of constant, high $k_{rN}^{\max}$ NWP relative permeability. In contrast to the conclusions drawn for the second suite of simulations, the third suite of simulations revealed that variable $k_{r,N}$ can significantly affect predictions of the timescales of NWP invasion when considering migration at the bench scale, even for relatively high k_i domains. At this scale, the influence of a single node, particularly the source node, or a node in the immediate vicinity of the source, can have a disproportionate influence on the prediction of a NWP release. A low k_i node (and the low $k_{rN}^{\max}$ value associated with this node) in the vicinity of the source, will significantly affect the rate of migration and, therefore, the timescales NWP migration through the domain. All multiphase flow models concerned with proper spatial and temporal migration of NWP in saturated porous media will need to account for this phenomenon.

The third objective of this research was to develop a global expression for describing the rate of mass transfer from a complex, realistic DNAPL source zone. A new, thermodynamically based interfacial area approximation method was developed that is consistent with the constitutive relationships required for multiphase flow, considers continuity of saturation history; accounts for Haines Jump energy losses, specifically estimates effective specific interfacial area with respect to mass transfer, and describes the change in interfacial area resulting from the dissolution of residual NWP.

This new model was then validated against the results of a bench scale experiment. Dissolved phase concentrations of 1,2-dichloroethane were measured in time and space throughout the experiment for comparison with data from a numerical simulation of the DNAPL release / dissolution employing the proposed mass transfer model. The results of the model validation indicate that a LEA or a currently available correlation model are incapable of describing the dissolution of a transient

NWP source in heterogeneous porous media to the level of accuracy attained when using the new thermodynamically based IFA model. This represents the first interfacial area model that is demonstrated to permit accurate use of the single boundary layer mass transfer expression across the spectrum of possible local NWP configurations. Moreover, this represents the first multiphase flow, mass transfer, and aqueous phase transport model validated for the dissolution of a complex, realistic, multi-dimensional NWP source zone.

The sensitivity of predicted aqueous phase concentrations to the assumptions made during the derivation of the IFA model reveal the importance of utilising an effective, as opposed to total, specific interfacial area estimate, of accounting for Haines jump energy losses and continuity of saturation history, and the insensitivity of overall dissolution rates to the approximation of interfacial area for NWP residual blobs. Simulations at the field scale of multiphase flow and dissolution demonstrate that the assumed local mass transfer expression has a significant effect on the predicted life span of the source zone and on the rate of mass flux through the downgradient boundary. In contrast to intuitive expectations, the local equilibrium assumption results in predictions of reduced global flux and increased source longevity relative to rate-limited mass transfer models. The IFA model, properly accounting for the evolving groundwater flow field, predicts source longevity that is intermediate between the LEA assumption and those resulting from empirically derived correlations expressions.

This work implies that when simulating mass transfer and aqueous phase transport from a complex, evolving NWP source zone, it is necessary to use a rate-limited approach at the local scale that links interfacial area to nonwetting phase saturations, saturation history, and aqueous phase relative permeability. Only with

this comprehensive approach, that couples NWP migration and dissolution at compatible scales, are predications able to properly account for the influence of local mass flux on global mass flux through modification of the groundwater flow field.

APPENDIX A –LABORATORY PROCEDURES

A.1 Apparatus

A.1.1 Local Scale Apparatus

The NWP relative permeability experiments are described, in part, in the Methods section of Chapter 3. Additional details are provided in this section. Figure A-1 presents a schematic of the local scale flow cell. This cell was on loan to the University of Edinburgh from Queen's University at Kingston, Ontario, Canada. The apparatus was constructed from aluminium except the front and back panels, which were constructed from plate glass, and the right and left boundaries of the sand pack, which were bounded by porous ceramic, as illustrated in the figure. The porous ceramic, separating the wetting fluid reservoirs from the sand pack, were cut from a ceramic plate (Hoskins Scientific, Burlington, Ontario) chosen for maximum permeability and a sufficiently high entry pressure to prevent DNAPL invasion. The glass front and back plates allowed the passage of light from a 40 fluorescent tube light bank, such that the cell simultaneously acted as a calibration device for light transmission properties as a function of NWP saturation. However, as discussed in Appendix B, the light transmission / image analysis system was only utilised as a NWP tracking and saturation history zone delineation device during the bench scale flow cell experiment, therefore, the calibration curves generated during the local scale experiments were not utilised. The upper endplate, containing bounding screens for the sand pack, was detachable, to allow access to the interior of the cell for packing and cleaning.

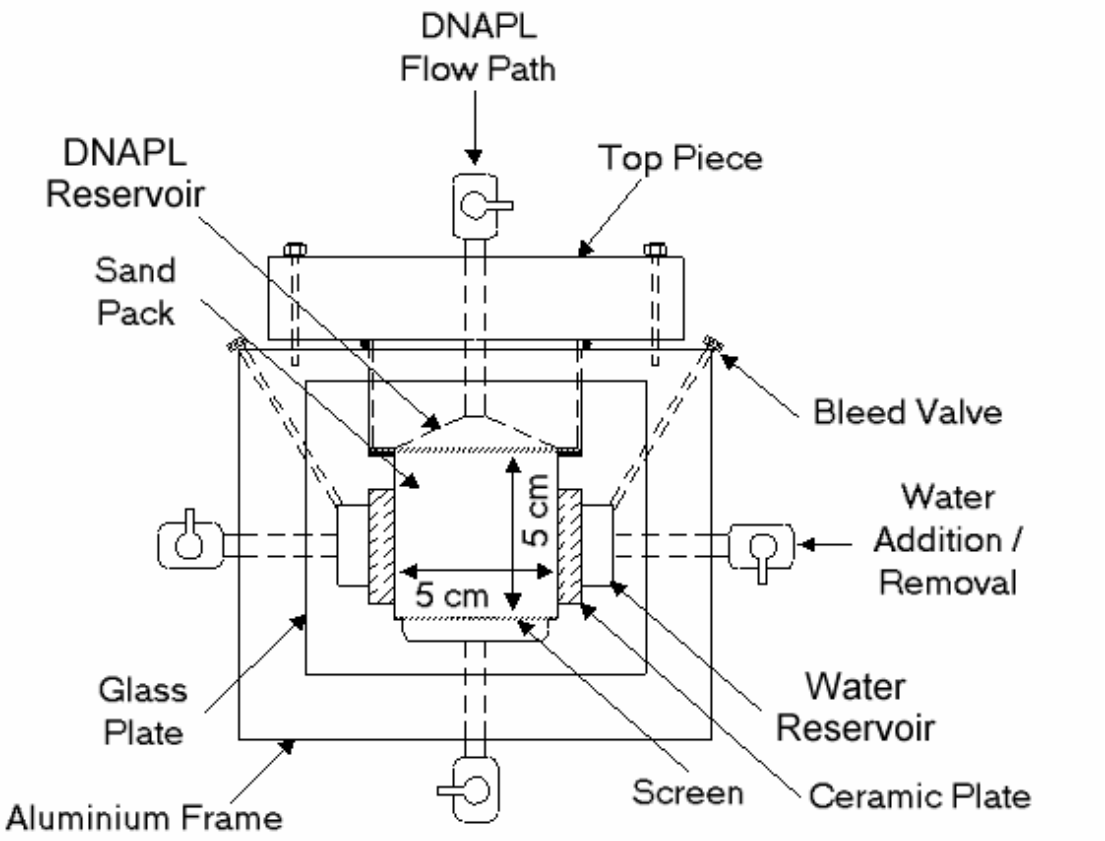

Figure A-1. Schematic of local scale NWP relative permeability apparatus.

Figure A-2 presents a schematic of the experimental setup for the NWP relative permeability experiments. The water flow pathways were constructed of copper pipe and inflexible high density polyethylene to eliminate volume changes in the tubing during the addition or removal of water. The DNAPL flow pathways were constructed of Tygon© tubing that was exposed to blue dyed HFE-7500 prior to the start of experiments. This exposure resulted in the transfer of blue dye to the Tygon© tubes to minimize the loss of dye from the NWP during the experiments, and prevent dye transfer from affecting the calibration of the light transmission / image analysis system.

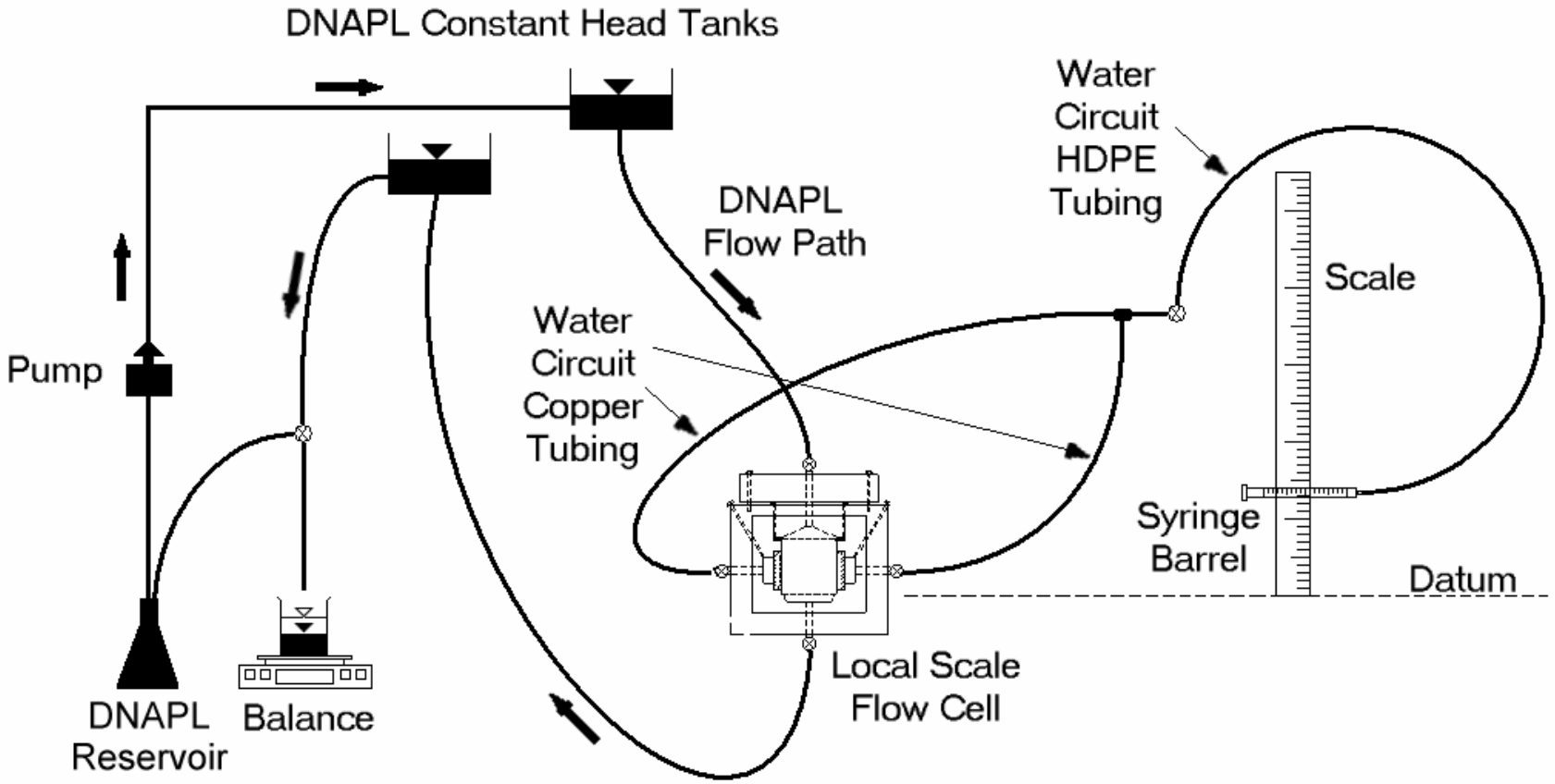

Figure A-2. Experimental setup for the local scale NWP relative permeability experiments.

A.1.2 Bench Scale Apparatus

The transient DNAPL release and dissolution experiment is described, in part, in the Methods sections of Chapters 3 and 5. Additional details regarding the bench scale apparatus used in this experiment are provided in this section.

Figure A-3 presents an overview schematic of the bench scale flow cell. The apparatus was constructed from aluminium, stainless steel, Viton©, and toughened plate glass. Only stainless steel, Viton©, and the toughened glass, however, were used in constructing the interior of the cell, as they are generally considered to be un-reactive with 1,2-dichloroethane (1,2-DCE). The aluminium was used in the construction of the frame which acts to support the rest of the apparatus.

The front and back panels of the flow cell were toughened glass, as in the local scale cell, to allow the transmission of light from a 40 tube fluorescent light bank (see Appendix B). The glass plates were held in place by a support strip through which cushioned bolts were tightened to hold the glass against a 1 cm thick stainless steel spacer, sealed with Viton©.

Screened access ports were located at 10 cm intervals along the perimeter of the frame. The side ports were used for the connection of constant head tank tubing and head measurement tubing. The top and bottom ports were used during sand pack saturation (see Section A.6). A DNAPL injection system was inserted through an access port located along the top of the apparatus, 0.5 m from the left boundary of the sand pack, to a depth of 3.0 cm below the top of the sand.

The cell was able to rotate about its horizontal axis, to enable the packing of sand in the microwell chamber (see Section A.4.2). The microwells were used for aqueous phase sampling as discussed in Section A.10.2.2.

The interior of the apparatus was divided into four sections with screened dividers located at four centimetres, 196 cm, and 206 cm from the left hand side of the apparatus. The left and right most areas were used exclusively as water reservoirs that were directly connected to constant head tanks. This ensured a constant head along the entire height of the sand pack at the left (upgradient) and right (downgradient) boundaries. The remaining areas have been termed the 'main chamber' and the 'microwell chamber'. The main chamber was packed with a heterogeneous sand pack, and the microwell chamber contains the microwells inserted in a homogeneous sand pack (see Section A.4.2).

A stainless steel vertical support strip was placed along the centre of the front and back glass plates of the apparatus. This support strip was installed to limit the amount of glass deflection during sand emplacement and throughout the experiments (see Section A.4.2 and Appendix D).

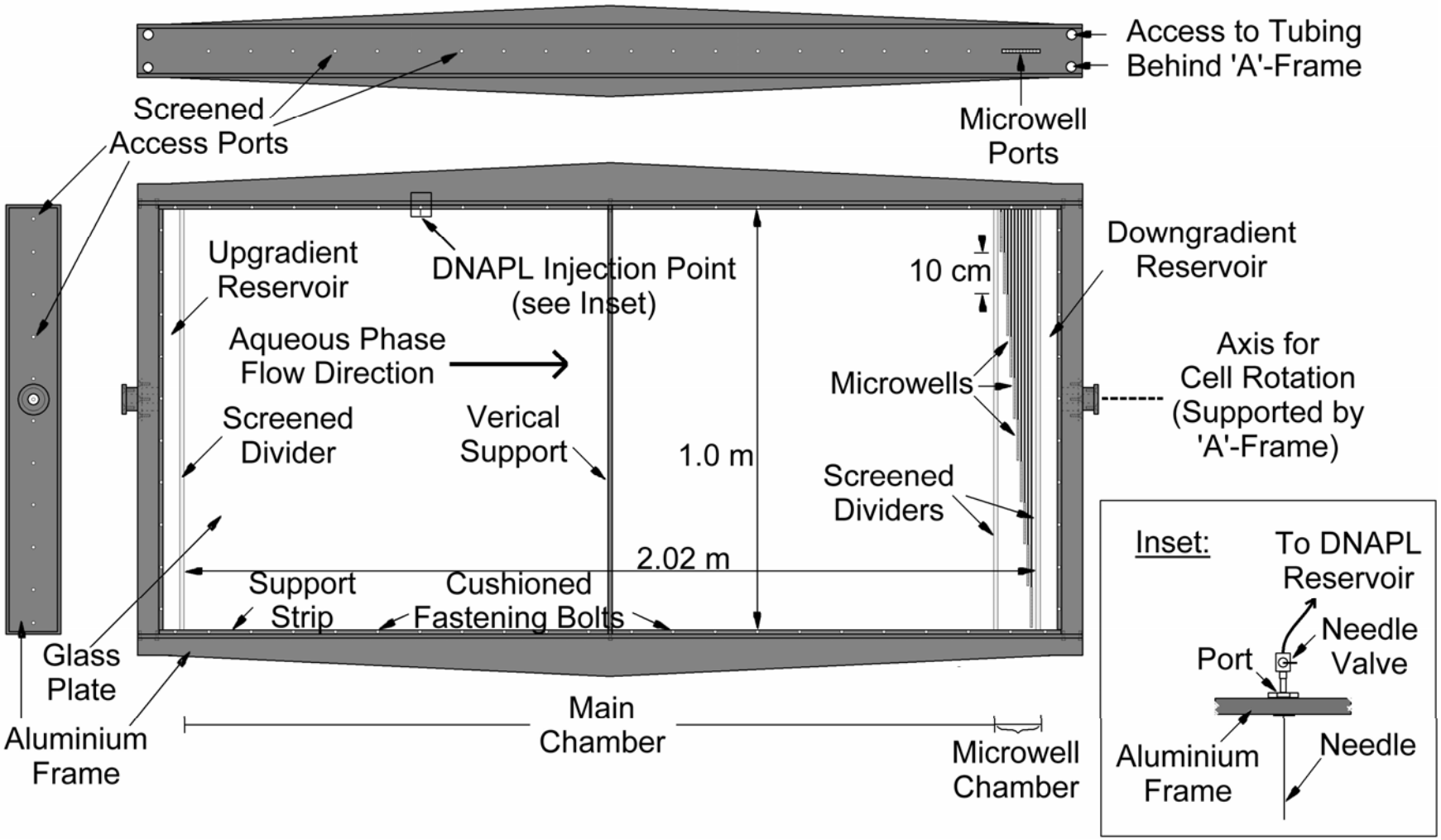

Figure A-3. Schematic of bench scale apparatus.

Figure A-4 illustrates the laboratory setup for the two-dimensional bench scale experiment including the light transmission / image analysis system. Details regarding the light bank shown in Figure A-4 are discussed in Appendix B. The water flow pathways were constructed of Tygon© tubing, however the DNAPL flow pathways were constructed of Viton© tubing to prevent deterioration of the DNAPL injection system during the experiment, as Viton© is more chemically resistant to 1,2-DCE than is Tygon©. The water flow pathways were attached to aqueous phase constant head tanks to establish a hydraulic gradient across the cell. Aqueous phase flow rates were measured gravimetrically (see Section A.7.2).

The DNAPL injection system acted as a constant flux source to the apparatus. A pump was used to inject DNAPL from a DNAPL reservoir to the sand pack through the injection system.

The cameras of the light transmission / image analysis system (see Appendix B) were placed at a height equal to the mid-point of the sand pack, located 2.67 m from the front glass plate. For the focal length of the cameras, this separation distance gave full coverage of the sand pack, including a 5% horizontal overlap.

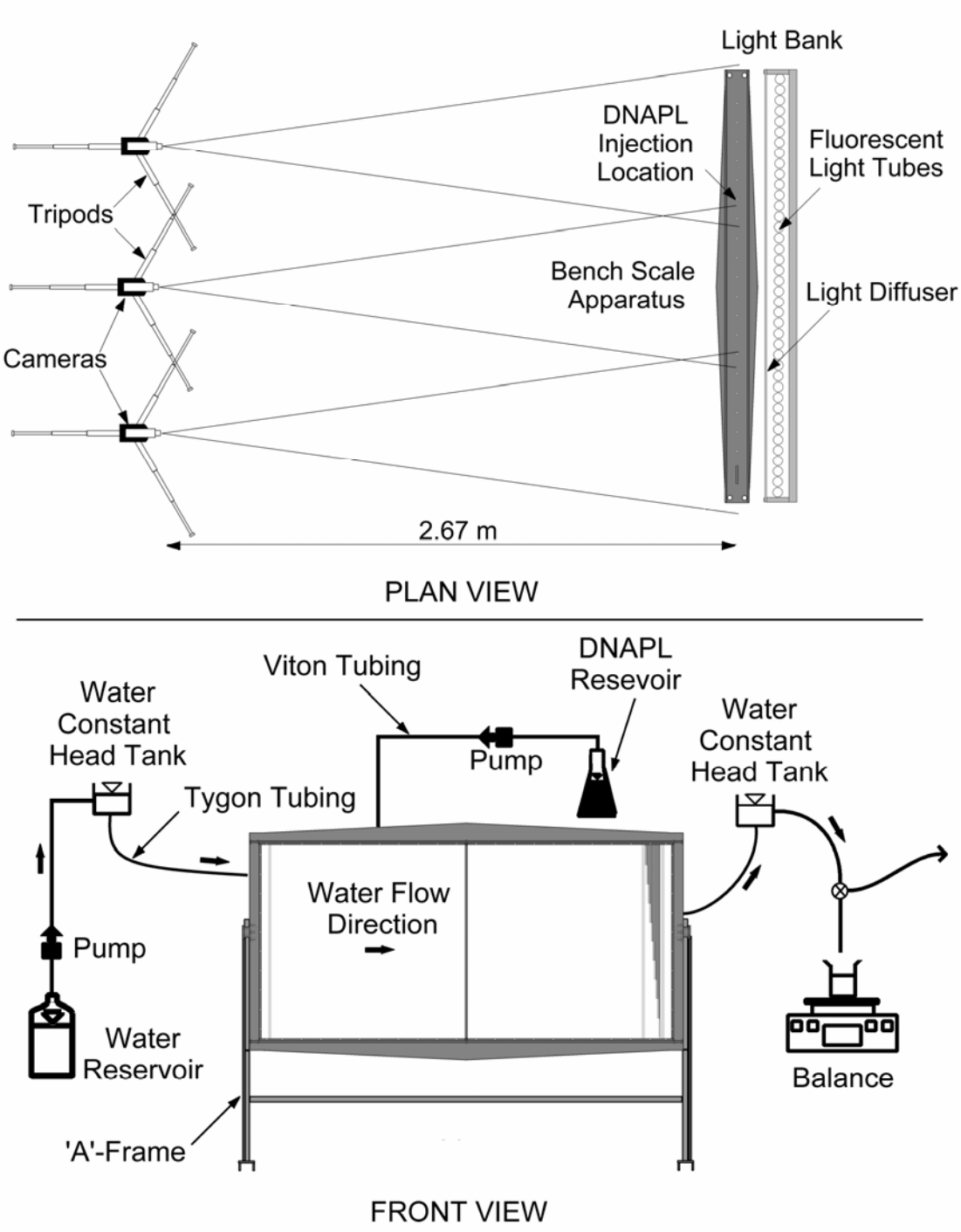

Figure A-4. Experimental setup for the bench scale experiments.

A.2 Fluids

Properties of the nonwetting and wetting fluids employed in the local scale NWP relative permeability experiments, blue-dyed HFE-7500 and water, respectively, are presented in Chapter 3, and the properties of the nonwetting and wetting fluids employed in the bench scale transient DNAPL release / dissolution experiments, blue-dyed 1,2-DCE and water, respectively, are presented in Chapters 3 and 5. Fluid density was measured by 5 repeat measurements of fluid mass for a known volume, for each of the temperatures examined. Interfacial tension between water and 1,2-DCE, water and HFE-7500, and surface tension between air and water was measured by 5 repeat measurements using a Kruss™ ring tensiometer (Hamburg, Germany). Viscosity of each of the fluids was measured by 5 repeat measurements using a Gardner Bubble Viscometer (Pacific Scientific, Silver Spring, MD).

Figure A-5 illustrates measured fluid density as a function of temperature along with density data available in the literature. None of the three fluids used in the experiments show significant variability with respect to density as a function of temperature. Other fluid properties, such as interfacial tension and viscosity, were also found to be relatively insensitive to temperature; however, temperature was controlled in the laboratory to 22.5 degrees Celsius (± 1° C) to ensure constant fluid properties and to limit the affect of temperature variability on dissolution rates.

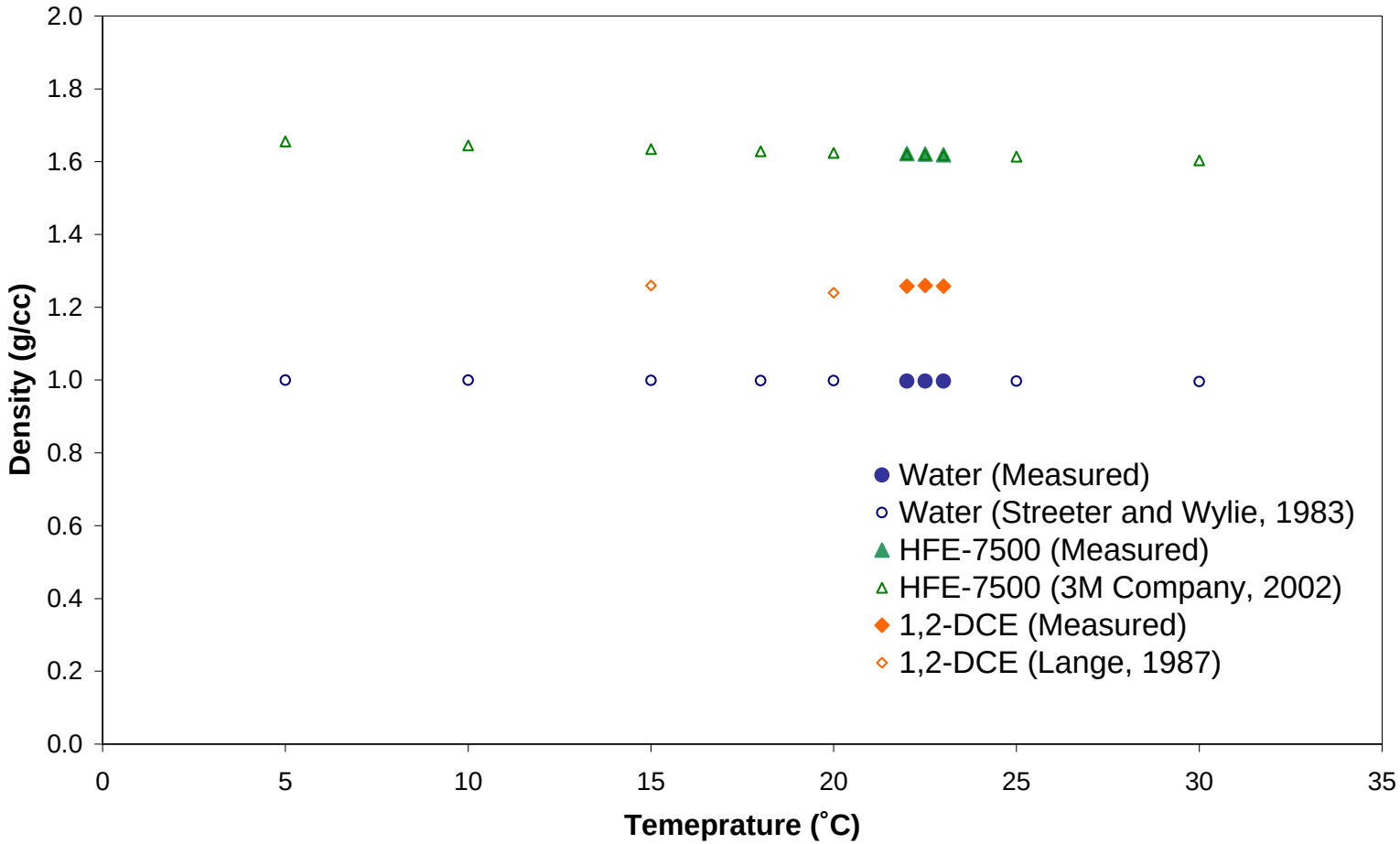

Figure A-5. Fluid density as a function of temperature.

A.3 Porous Media

Six natural sands with single mesh number grain size distributions were employed in all experiments. Referred to as the N10, N16, N20, N30, N40 and N50 sands, corresponding to the mesh number that retains each of the sands, their measured properties are presented in Table A-1. The six sands used in the experiments were separated from four different source sands. The N10 sand was separated from Leighton Buzzard DA 8/16 silica sand (WBB Minerals, Brookside Halls, Cheshire, UK), the N16 and N20 sands were separated from Chelford BS 14/22 silica sand (WBB Minerals, Brookside Halls, Cheshire, UK), the N30 and N40 sands from Chelford D30 silica sand (WBB Minerals, Brookside Halls, Cheshire, UK), and the N50 sand from Lochaline L60A silica sand (Tarmac Central Ltd., Stoke-on-Trent, Staffordshire, UK). According to documentation received from WBB Minerals and Tarmac Ltd., each of the source sands contain >97% silicon dioxide and the grain shape is classified as 'rounded'. Photomicrographs of the N10, N30 N40 and N50 sands presented in Figures A-6a through A-6d, however, reveal that the N10 sand is considerably less 'round' and has a much rougher surface than any of the other sand types examined.

Table A-1. Porous Media Utilised Throughout This Study

Parameter	Values					
	N10	**N16**	**N20**	**N30**	**N40**	**N50**
Mean Particle Diameter (μm)	2180	1295	1015	700	513	363
k_{abs} (m^2)	2.62×10^{-10}	1.90×10^{-10}	1.81×10^{-10}	7.10×10^{-11}	7.41×10^{-11}	1.84×10^{-11}
Porosity	0.35	0.38	0.34	0.33	0.31	0.36

Each of the sands was acid washed in a 0.1M HCL solution, triple rinsed with deionised water and dried prior to use in any of the experimental apparatuses, to remove any organic material or iron oxides coating the grains.

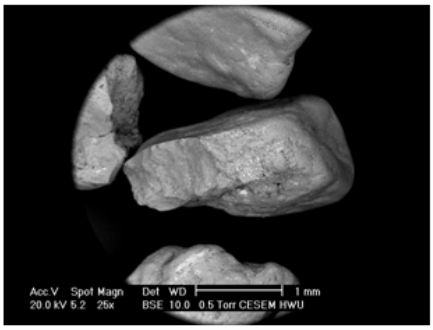

a) N10 Sand – Single Grain

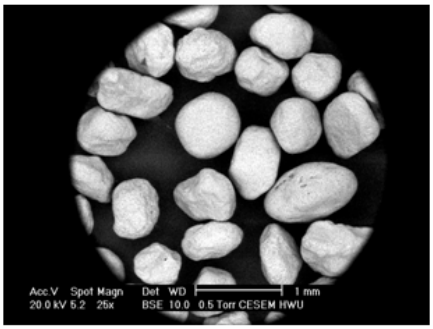

i) Numerous Grains

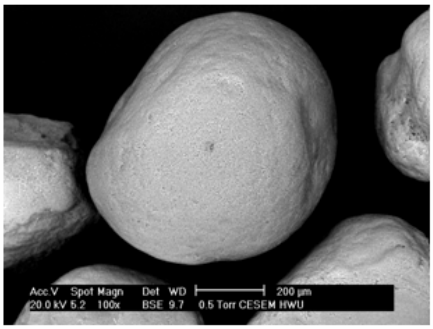

ii) Single Grain

b) N30 Sand

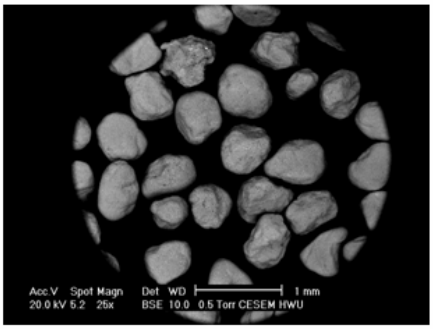

i) Numerous Grains

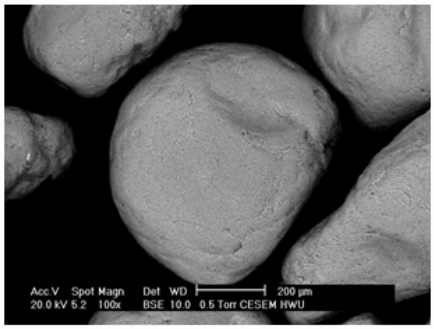

ii) Single Grain

c) N40 Sand

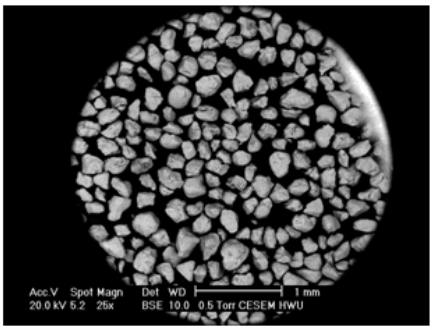

i) Numerous Grains

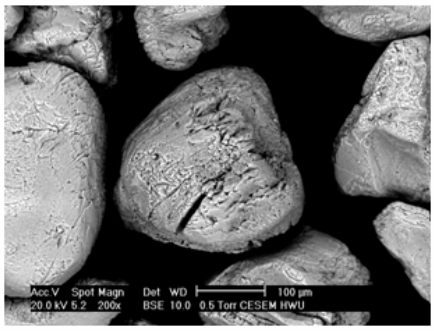

ii) Single Grain

d) N50 Sand

Figure A-6. Photomicrographs of the a) N10, b) N30, c) N40, and d) N50 sands: an overview photo of numerous grains and a close-up photo of a single grain are included for the N30, N40 and N50 sands.

A.4 Packing

A.4.1 Local Scale Apparatus

The local scale apparatus was packed with sand according to the following procedure: 1) a few grams of the selected sand was sprayed with deionised water to make it moist; 2) the moist sand was added to the cell and tamped down until fully compacted, with a tamping device that fit inside the cell with a minimal clearance, to a depth of approximately 0.5cm; 3) additional sand was added in 0.5cm 'lifts' until the fully compacted sand filled the cell; then, 4) compressed air was forced through the cell to remove the moisture from the sand prior to use. The compressed air would completely dry the apparatus between approximately two hours to two days, depending on the grain size of the sand in the cell.

A.4.2 Bench Scale Apparatus

Prior to packing the main chamber of the bench scale apparatus, the microwells were installed in the microwell chamber and the surrounding space was filled with N16 sand (see Figure A-3). This was accomplished by rotating the apparatus into its horizontal orientation, removing the top plate of glass, inserting the microwells, filling the remaining space in the microwell chamber with N16 sand to a height (thickness in the vertical orientation) of 10 mm, and replacing the glass plate on the cell and sealing it in place. The cell was then returned to its vertical orientation, ready for the main chamber sand packing procedure.

Although discretised for the purposes of numerical modelling at a scale of 1cm by 1cm, the main chamber of the apparatus was packed with sand in 5 cm by 5 cm blocks of homogeneous sand. The method for selecting the sand type emplaced in each 5 cm by 5 cm block is outlined in Chapters 3 and 5. Identical to the procedure describing the packing of sand in the local scale apparatus, each 5 cm by 5cm block

was packed in 0.5 cm lifts of moist, fully compacted sand. Two thin (1 mm thick) reinforced stainless steel dividers (1 metre long by 1 cm wide – i.e., the thickness of the space between the glass plates) were inserted into the cell to define the width of the 5 cm by 5 cm block. The height of the 5 cm by 5 cm block was defined by a grid drawn with removable ink on the front glass panel. Moist sand was dropped from the top of the apparatus and a 1 metre long tamping device was inserted between the paired dividers for each 0.5 cm lift added to the block space. The bottom row of sand was packed first, and each subsequent row of sand was packed on top of the previously emplaced row. The flow cell was packed to a total depth of 0.91 meters. Therefore, only the bottom nine of ten microwells were located within the sand pack. These nine wells will subsequently be referred to as the nine 'active' microwells in the cell.

Packing the two-dimensional bench scale apparatus was complicated by the fact that the addition of sand and water to the cell increases the pressure on the glass front and back panels which causes them to deflect in an outwards direction. This deflection not only increases the thickness of the sand pack, but also causes slumping, or a reduction in the height of the sand pack. The result is thick non-horizontal layers of sand across the apparatus. In order to approximate the stress conditions on the glass plates anticipated during the experiments, water was added to the bottom ports of the apparatus such that a watertable was maintained at a height equal to 10 cm below the working elevation of sand emplacement. By maximizing the stresses on the glass during emplacement, the effects of slumping on the sand pack could be corrected for and minimized prior to sealing the cell for the experiments.

Deflection of the glass could have been reduced by increasing the number of vertical (or horizontal) supporting beams across the front and back panels of the

apparatus (see Figure A-3), however, this would prevent the use of light transmission as a measure of NWP presence, as too much of the sand pack would be covered by the supports.

The affects of deflection (i.e., slumping) could have been reduced by increasing the thickness of the sand pack. The degree of slumping, or height loss of the sand pack is directly proportional to the thickness of the sand, as any increase in cell volume resulting from deflection, can be filled with sand across the entire thickness of the cell. However, increasing the thickness of the sand pack would again limit the efficacy of the light transmission / image analysis system.

Once the packing was completed, the cell was sealed along the top boundary with a Viton© / stainless steel barrier containing access ports, the water was drained from the cell, and compressed air was forced through the sand pack to dry it prior to re-saturation. Although the drying process took approximately three months, it was deemed necessary as numerous air bubbles were trapped within the sand pack as a results of the sand emplacement procedure.

A.5 Porosity

The porosity of the sand pack in the local scale experiments was calculated according to:

$$porosity = V_{cell} - \frac{M_{sand}}{\rho_{sand}} = V_{cell} - \frac{\left\lfloor M_{packedcell} - M_{emptycell} \right\rfloor}{\rho_{sand}} \qquad \text{(A-1)}$$

where V_{cell} [L^3] is the volume of the cell, M [M] is the mass of sand, the packed cell, or the empty cell, and ρ_{sand} is the particle density of sand.

The porosity of the sand pack in the two-dimensional bench scale experiments was not determined, however, the packing procedures were the same for both apparatuses and therefore it is unlikely that the porosity values of the sands in the

bench scale flow cell were appreciably different from those calculated in the local scale cell. Additionally, there is no indication from the data collected during the tracer test (Appendix D) or the bench scale experiment (Chapters 3 and 5) that the porosity values are appreciably different than those calculated in the local scale cell.

A.6 Water Saturation

Saturation of the sand pack in both the local scale and two-dimensional bench scale apparatuses was accomplished by first filling the pore space with an atmosphere of carbon dioxide followed by the slow addition of de-aired water. In the local scale apparatus, carbon dioxide was forced through the sand pack and all tubing attached to the apparatus (see Figure A-2) for approximately five hours prior to water addition. Carbon dioxide was forced through the bench scale apparatus for two days prior to water addition. The rate of water addition was tightly controlled to ensure a slow, smooth displacement of the carbon dioxide atmosphere. This procedure was necessary to prevent the formation of trapped bubbles; however, de-airing the water and filling the void space with high solubility carbon dioxide ensured that trapped bubbles would quickly dissolve into the water and be carried out of the system should any form during the saturation procedure.

Once water began to exit the top boundary of the sand pack, the flow rate of water addition was increased and numerous pore volumes of de-aired water were flushed through the cells to ensure the removal of any trapped bubbles not observable at the glass panels.

A.7 Single-Phase Permeability

A.7.1 Local Scale Apparatus

Single phase or intrinsic permeability's for each of the six sands employed in the experiments were calculated by establishing a series of hydraulic gradients across

the cell and measuring the resulting flow rate. The gradients were set by adjusting the relative elevations of constant head tanks attached to the top and bottom of the local scale apparatus. At least 7 repeat flow rates were measured by mass for each gradient. The ranges of gradients used are presented in Table A-2.

Table A-2. Gradients Employed in Single Phase Permeability Measurements

Sand Type	Minimum Gradient	Maximum Gradient
N10	0.24	0.82
N16	0.24	1.74
N20	0.14	1.27
N30	0.69	2.94
N40	0.80	1.83
N50	1.31	2.79

Figure A-7 presents a plot of Darcy flux as a function of hydraulic gradient for each of the sand types studied, from which intrinsic permeabilities were calculated. As can be seen in the figure, flow rate is linearly related to gradient across the entire range of gradients examined. The calculated mean permeabilities are presented in Table A-1 above.

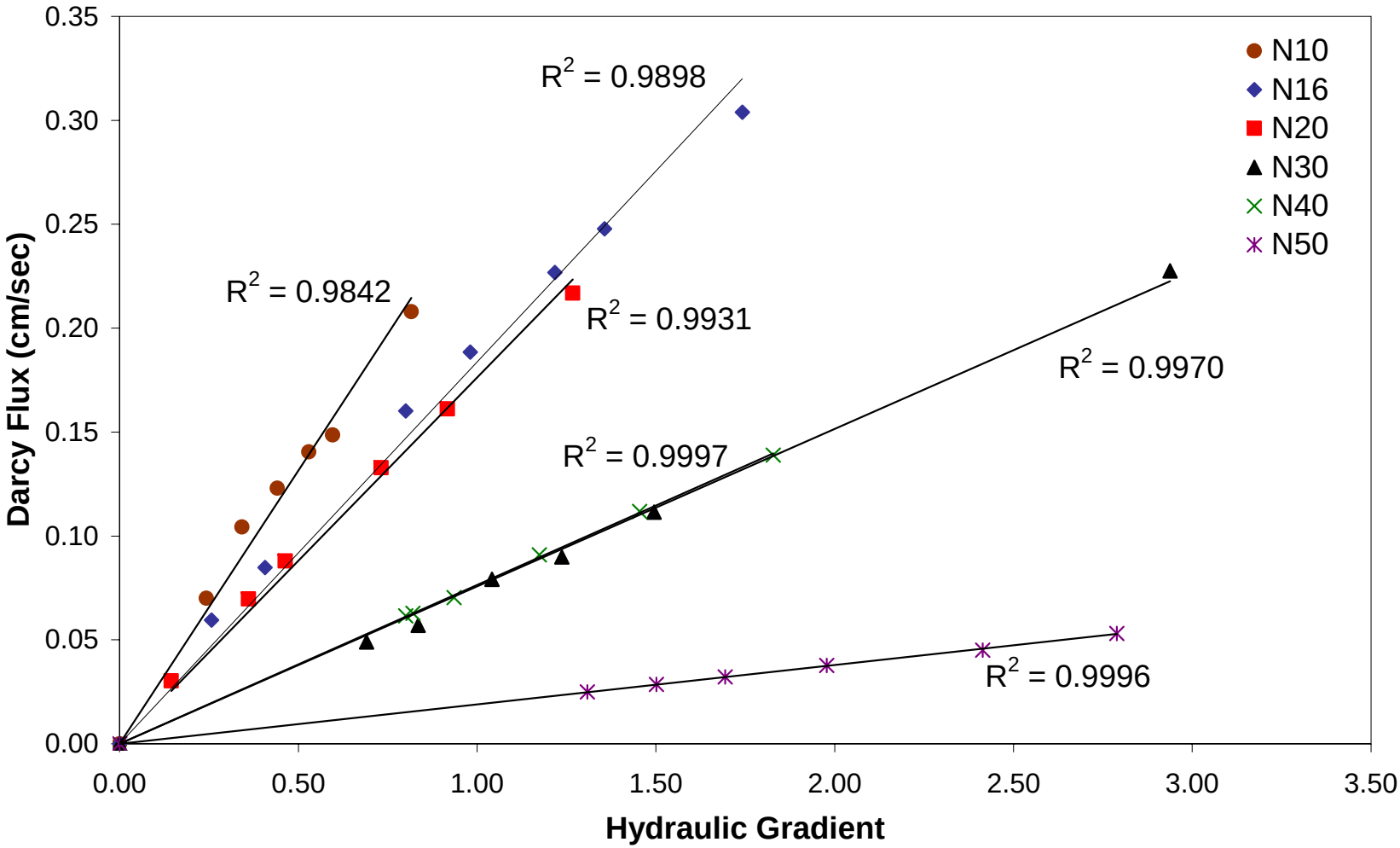

Figure A-7. Permeability measurements in the local scale apparatus.

A.7.2 Bench Scale Apparatus

The single phase average permeability of the heterogeneous sand pack in the two-dimensional bench scale apparatus was calculated from data collected from a non-reactive tracer test. The results of this test are presented in Appendix D.

A.8 Cleaning the Sand Pack Between Experiments

A.8.1 Local Scale Apparatus

Between the local scale NWP relative permeability experiments, the cell was opened, cleaned of all sands and fluids and completely dried prior to re-use. All tubing attached to the cell was drained, flushed with deionised water, and dried prior to re-use.

A.8.2 Bench Scale Apparatus

A NWP test release was performed in the two-dimensional bench scale apparatus to identify an appropriate release volume for the experiment presented in Chapters 3 and 5. Mass balance indicates that all NWP mass released to the flow cell in the trial was recovered (data not presented). However, to ensure complete removal of all pure phase and dissolved phase contaminant, the cell was flushed with more than 50 pore volumes of deionised water after the completion of the test release.

In addition, the cell was flushed with approximately 10 pore volumes of 100 ppm sodium hypochlorite solution, then three pore volumes of deionised water, followed by approximately 15 pore volumes of 100 ppm surfactant stabilised hydrogen peroxide, to discourage the growth of bacteria between the trial experiment and the full scale release experiment presented in Chapters 3 and 5. This procedure was also useful for removing the blue dye particles (see Section A.9) that were precipitated into the cell from DNAPL dissolution during the test release.

A.9 DNAPL Colouration

As an integral part of the light transmission / image analysis system, the DNAPL used in all experiments was dyed a deep blue colour. Both the 1,2-DCE used in the bench scale experiments and the HFE-7500 used in the local scale experiments were dyed to solubility with Oil Blue A powder (Octel-Starreon, Littleton, CO). Dye solubility was achieved by adding 0.01% powder by weight to the DNAPL (which is in excess of solubility) and filtering the fluid to remove powder residue.

A.10 Data Collection

A.10.1 Local Scale Apparatus

The local scale apparatus was used for the measurement of NWP relative permeability curves. As described in detail in Appendix I, the measurement of NWP flow rates at specific wetting phase saturations is integral to the calculation of NWP relative permeability. Therefore, this section will outline the data collection methods used to determine wetting phase saturation and NWP flow rate.

A.10.1.1 Saturation Change

Wetting phase saturation was set in the cell through a series of steps. Prior to the first step, or saturation change within the cell, constant head tanks containing the dyed NWP fluid were attached to the upper and lower reservoirs of the cell. The tanks were set at a suitably high pressure and a control valve was turned on to allow the advancement of the NWP / aqueous phase interface towards the top and bottom of the sand pack. Water in the tubing and the sand pack was allowed to exit through the ceramic plates on the right and left of the sand pack. Once the NWP / aqueous phase interface was deemed to be immediately adjacent to the sand pack, the experiment was ready to begin.

As seen in Figure A-2, the right and left reservoirs of the cell are connected to each other through copper tubing. The copper tubing leads to a valve where HDPE tubing transmits water to a calibrated 1.0 ml syringe. For each step or saturation change on primary drainage, the syringe level was lowered below the head of water in the cell and the syringe valve was opened until the desired volume of water had drained out of the cell into the barrel. For each step or saturation change on imbibition, the syringe level was raised above the head of water in the cell and the syringe valve was opened until the desired volume of water had imbibed out of the syringe barrel and into the cell. While the syringe valve was open, the syringe was kept horizontal to ensure a constant wetting pressure during water flow. The volume of water removed from, or added to, the cell at each step was variable depending on the proximity of the saturation in the cell to the end-points of the NWP relative permeability curve, but averaged 0.1 ml per step.

Following the removal, or addition, of wetting phase, the NWP flow rate was allowed to equilibrate for approximately two hours. The flow rate was measured repeatedly over the course of the equilibration period to ensure that a state of dynamic equilibrium existed in the cell for that saturation step. After the equilibration period, five repeat measurements of NWP flow rate were taken and an average NWP flow rate was calculated for use in determining the NWP relative permeability.

A.10.1.2 NWP Flow Rate Measurement

Due to the low vapour pressure of HFE-7500 (6 mmHg at 20ºC – Material Safety Data Sheet, 3M Company) a gravimetric method was deemed suitable and was adopted for the calculation of NWP flow rate. To determine NWP flow rate, the over flow from the downgradient NWP constant head tank was redirected to a 200 ml beaker. The flow of NWP to the beaker was timed with a stop watch. The mass of

NWP was then measured on a four-point scale and flow rate was calculated according to:

$$Q = \frac{M_{NWP}}{\rho_{NWP} \cdot T} \tag{A-2}$$

where Q [L^3T^{-1}] is the NWP flow rate, M_{NWP} [M]is the mass of NWP collected in the beaker in time, T [T], and ρ_{NWP} is the density of the NWP [ML^{-3}].

A.10.2 Bench Scale Apparatus

NWP presence / saturation history and dissolved phase concentrations were measured in the two-dimensional bench scale experiment. Details of the NWP presence / saturation history determinations are presented in Chapter 3, and details of the dissolved phase concentration sampling method are presented in Chapter 5. However, additional information regarding the detection, measurement and sampling methods are presented below.

A.10.2.1 NWP Presence / Saturation History Determination – Camera Control

Appendix B describes the light transmission / image analysis system in detail, however, additional information regarding the frequency of data collection using this system during the bench scale experiment will be presented in this section.

The collection of digital images was controlled via WIT image acquisition and processing software (Coreco, St. Laurent, Quebec). Table A-3 presents the image acquisition frequency for the bench scale flow cell experiment.

Table A-3. Image Acquisition Frequency

Experiment	Time Period	Frequency	Number of Images per Time Period	Cumulative Total Number of Images
NWP Release Experiment	0-2hr	2 min	60	60
	2hr – 24hr	10 min	132	192
	24hr – 1week	6 hours	24	216
	1week – 6week	24 hours	35	251

The schedule outlined in Table A-3 was selected to maximize the number of images collected during critical phases of the NWP migration / dissolution process without demanding extended operation of the light bank. The light bank, as described in Appendix B, is a heat source, and if left active for too long a period of time, can significantly increase temperatures in the laboratory and within the flow cell itself. Figure A-8 shows the affect of light bank operation on room temperatures as a function of time. A minimum image acquisition frequency of two minutes was determined to have no impacts on the prescribed variability of ambient temperature imposed on the laboratory throughout the experiments (22.5 ± 0.5 ºC).

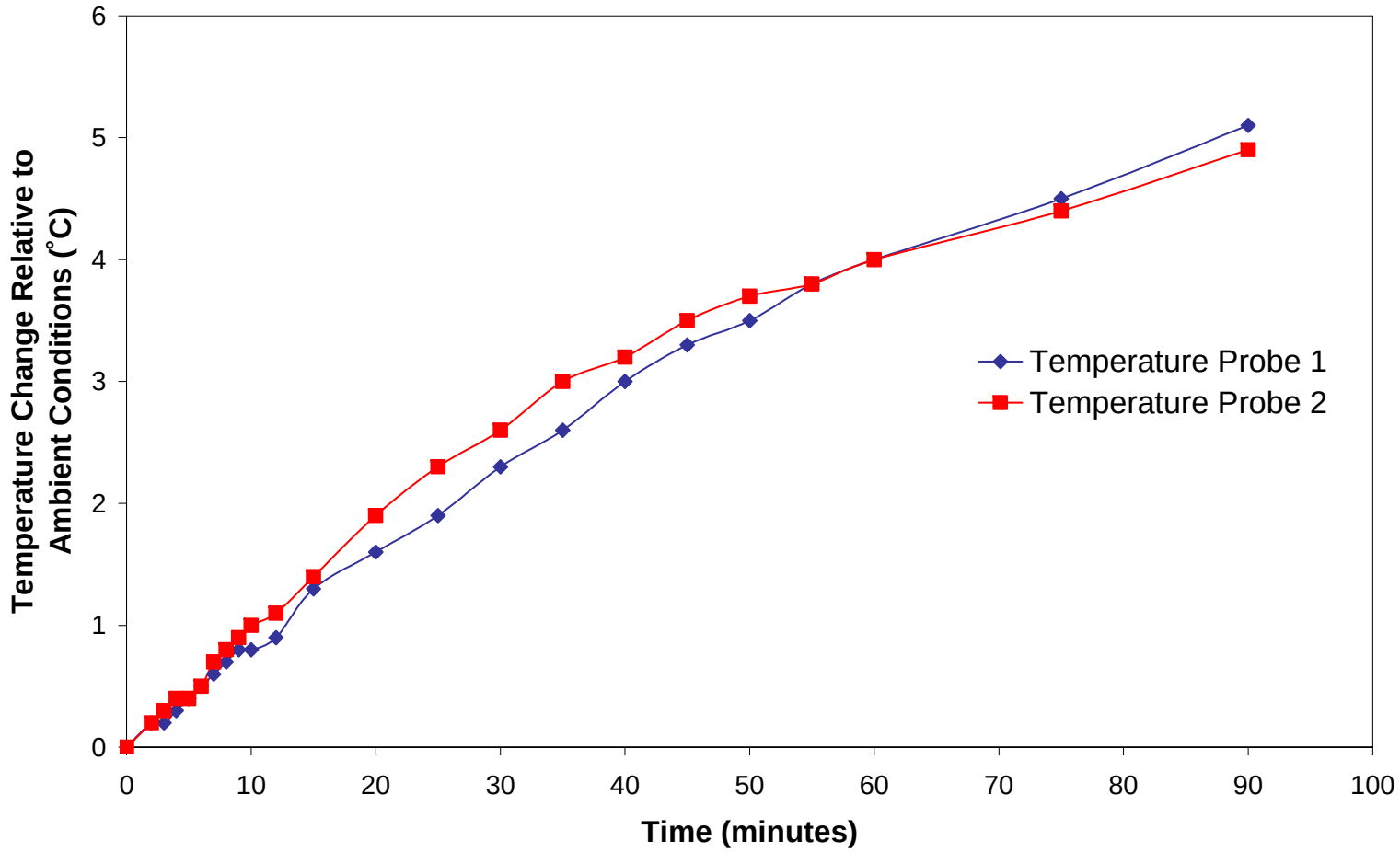

Figure A-8. The affect of light bank operation on laboratory room temperature.

A.10.2.2 Aqueous Phase Sampling

Samples of the aqueous phase were collected through the nine active microwells located near the downgradient boundary of the two-dimensional bench scale flow cell (Figure A-3). The microwell sampling system is illustrated in Figure A-9.

A 10-channel multi-channel Watson-Marlow 505s digital pump (Falmouth, Cornwall, UK) was used to pump the samples from the microwells to the sample chambers. Although the downgradient boundary condition for the cell during the experiment was constant head, the boundary condition was changed to constant flux while sampling took place. In order to prevent disruption of the flow field, the flow rate leaving the constant head boundary prior to sampling was measured and the pump rate was set to extract aqueous phase from the cell at the same rate. Therefore, while the boundary condition was changed during sampling, the effect of this action on aqueous phase flow and dissolved phase transport was negligible.

The pumping time was adjusted according to the measured flow rate so that the sample removed from the sample chamber was the same parcel of water previously at the microwell screens when pumping commenced. The materials used and the distance between the top of the screen and the sample valve is identical for each of the microwells. Thus all samples collected from each of the screened areas arrive at the sample chambers at exactly the same time.

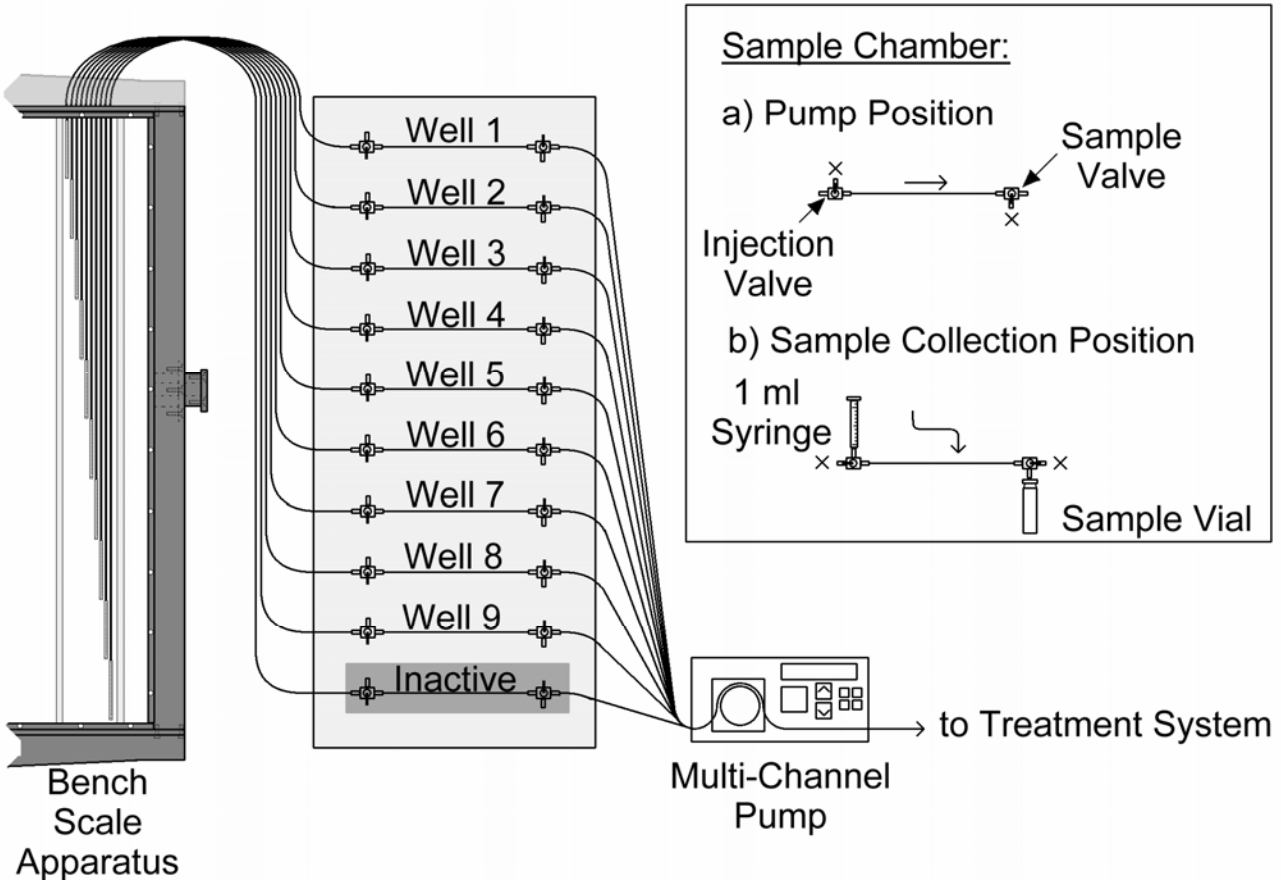

Figure A-9. Bench scale apparatus microwell sampling system.

The sample chamber volume is 1.2 ml. To collect a sample, the pump was stopped, the boundary condition was returned to constant head, and the sample chamber was isolated from the microwells by adjusting the valves at either end of the sample chamber. An empty 1 ml syringe, with the plunger extended to the 1 ml mark, was locked onto the injection valve. The injection valve was opened, a headspace sample vial was placed beneath the sample valve, the sample valve was opened, and the plunger was depressed to push a 1ml sample into the headspace vial. This process was repeated for each of the sample chambers.

The microwell method of aqueous phase sampling was adopted because it allowed for greater control of the rate and location of sample collection. A direct syringe method (such as a syringe inserted through a port installed in the glass plate) would collect a sample in a radial pattern around the location of the syringe point. This would disrupt the flow field in the cell, as each syringe would act as a point sink, and would smear the region over which the sample was collected, complicating the process of numerically simulating the laboratory results. In addition, the direct syringe method would require the installation of ports through the glass which would interfere with the light transmission system and weaken the glass plate.

Table A-4 lists the number of aqueous phase samples and sample frequency for the bench scale experiment.

Table A-4. Aqueous Phase Sampling Frequency

Interval	Sample Frequency	Number of Sampling event	Total Number of Samples
0-24hr	2 hours	12	108
24hr – 1week	12 hours	12	108
24hr – 6week	24 hours	41	369

APPENDIX B – LIGHT TRANSMISSION / IMAGE ANALYSIS SYSTEM

The light transmission / image analysis system used throughout this research is similar to the system successfully employed by Gerhard (2002). The system is described in Chapter 3, and additional information is presented in this section.

B.1 Laboratory Illumination

The backlight used for both the local scale and bench scale experiments was a light bank consisting of 40 vertically oriented 122 cm fluorescent light tubes. A plastic diffuser sheet was installed in front of the fluorescent tubes to provide an even distribution of light intensity. This light source provided the only illumination in the laboratory while images were being collected.

During the local scale experiments, the light bank was covered by a sheet of Perspex™ with a rectangular hole cut out of it. The cell and tubing used in the experiments were attached to the Perspex sheet™ such that the location of the rectangular hole corresponded to the area of the sand pack within the cell.

During the bench scale experiments, the entire light bank was exposed to the flow cell, as the cell was designed such that the size of the sand pack within the cell was equal to the size of the light bank.

B.2 System Calibration

During the NWP relative permeability experiments, images of the flow cell were collected at each saturation step. These images were analysed using WIT image acquisition and processing software (Coreco, St. Laurent, Quebec) for mean hue, mean colour saturation and mean intensity (HSI properties). While Gerhard (2002) found a good correlation between mean colour saturation and wetting phase saturation, this research found that mean intensity as a function of wetting phase

saturation gave a larger range of data and more consistent results. Other researchers have employed light transmission systems with success using either light saturation (Darnault, *et al.,* 1998) or light intensity (Glass *et al.,* 1989) as a measure of wetting phase saturation. In spite of the fact that the equipment used in this study and that of Gerhard (2002) is identical, the scale of the experiments, specifically the distance of the cameras from the cell and the number of pixels composing an image of the cell, is significantly different, and is likely the reason the 'best' light transmission parameter to be used for measuring wetting phase saturations is different for the two studies.

Mean light intensity as a function of wetting phase saturation for each of the three cameras utilised, for each of the six sand types examined, is presented in Figures B-1 through B-18. The figures include a second-order polynomial best-fit curve for each of the data sets. As can be seen in this series of figures, the calibration curves vary slightly between cameras for a given sand type and to a much greater extent, between sand types for a given camera. This is illustrated further in Table B-1 which presents the camera-averaged maximum, minimum and range of intensities for each of the sand types examined. As shown in the table, the average maximum light intensity decreases as the average grain size of the sand decreases but the average minimum and range of intensities show no such pattern.

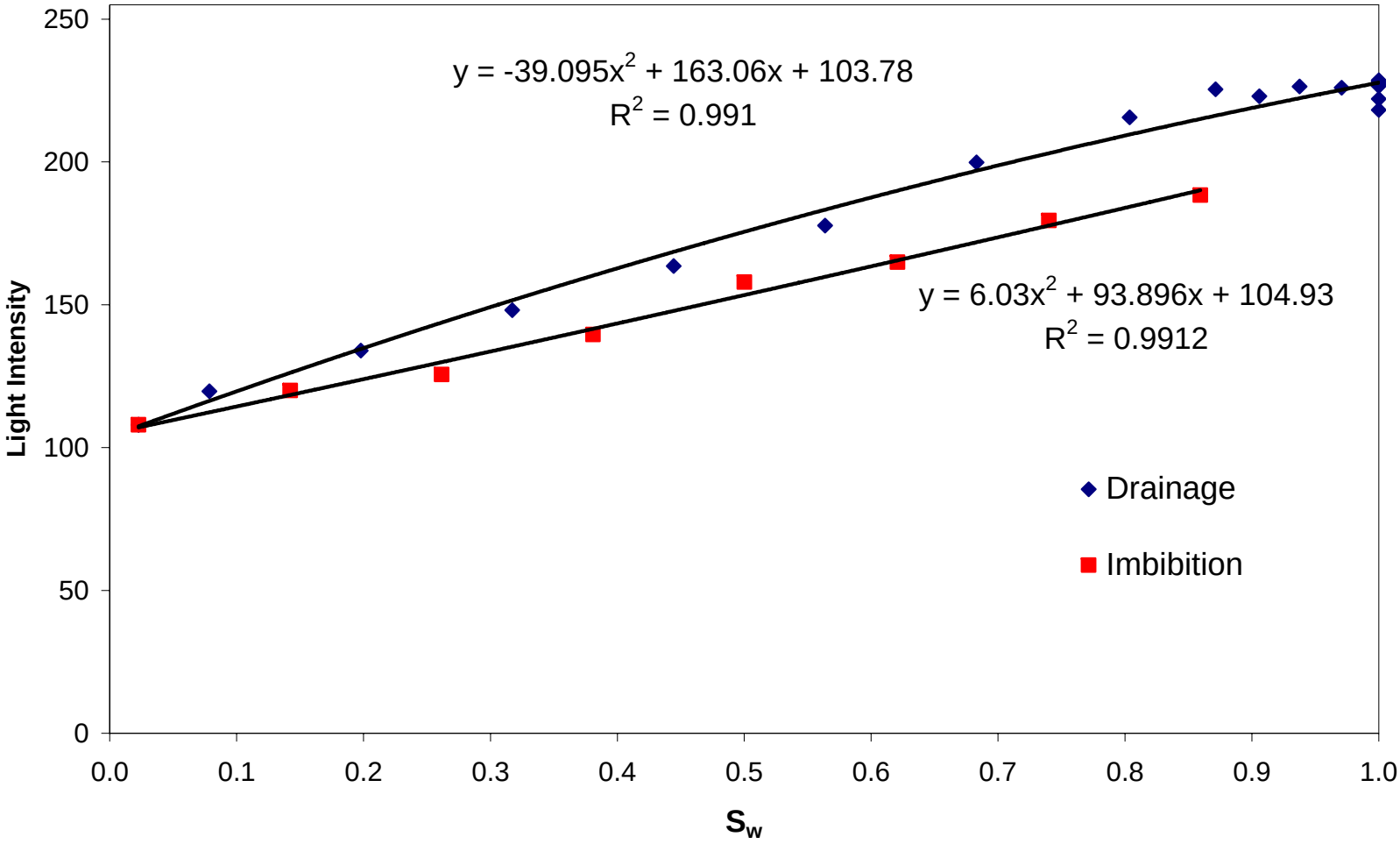

Figure B-1. Light transmission as a function of wetting phase saturation: sand N10; camera 1.

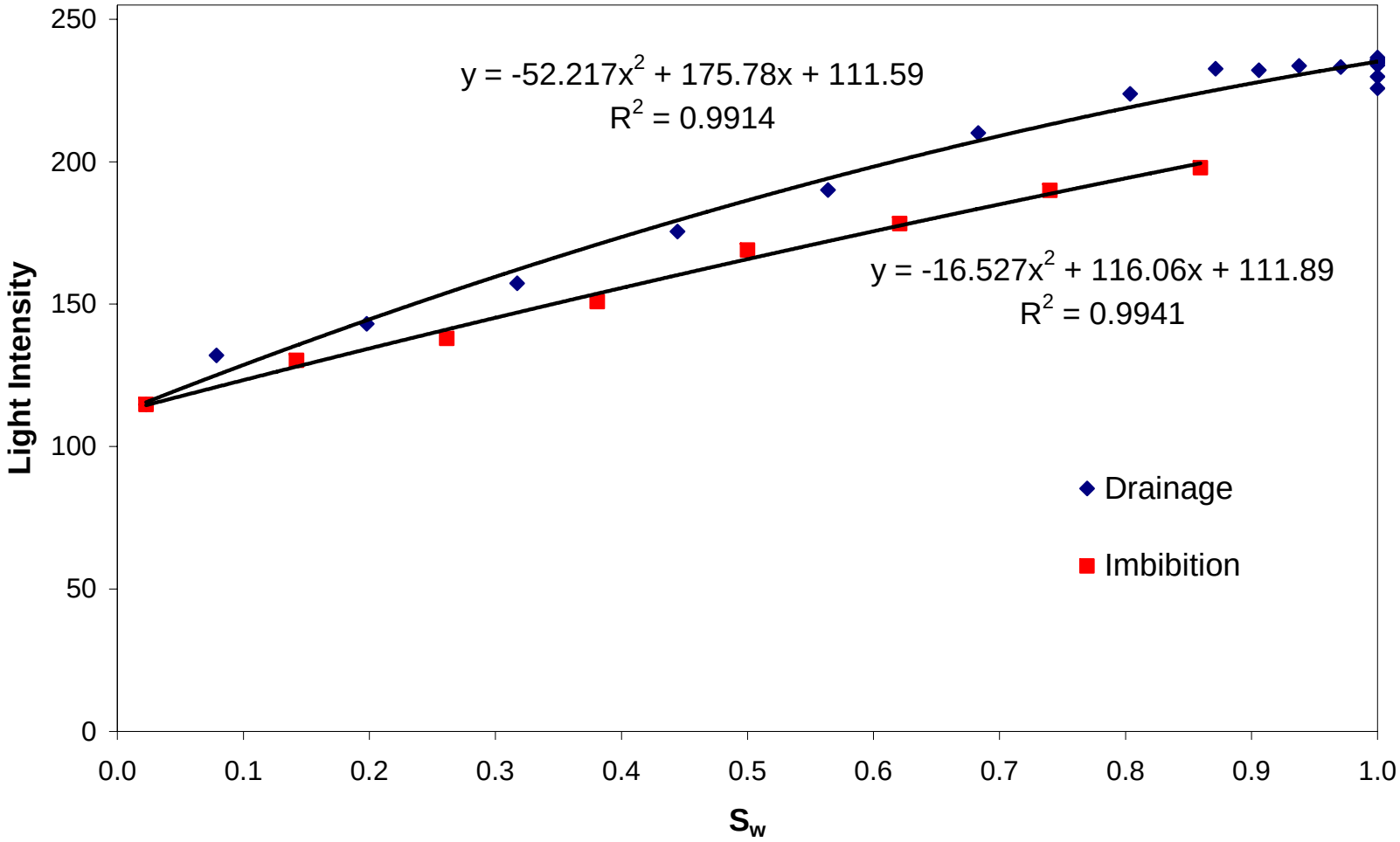

Figure B-2. Light transmission as a function of wetting phase saturation: sand N10; camera 2.

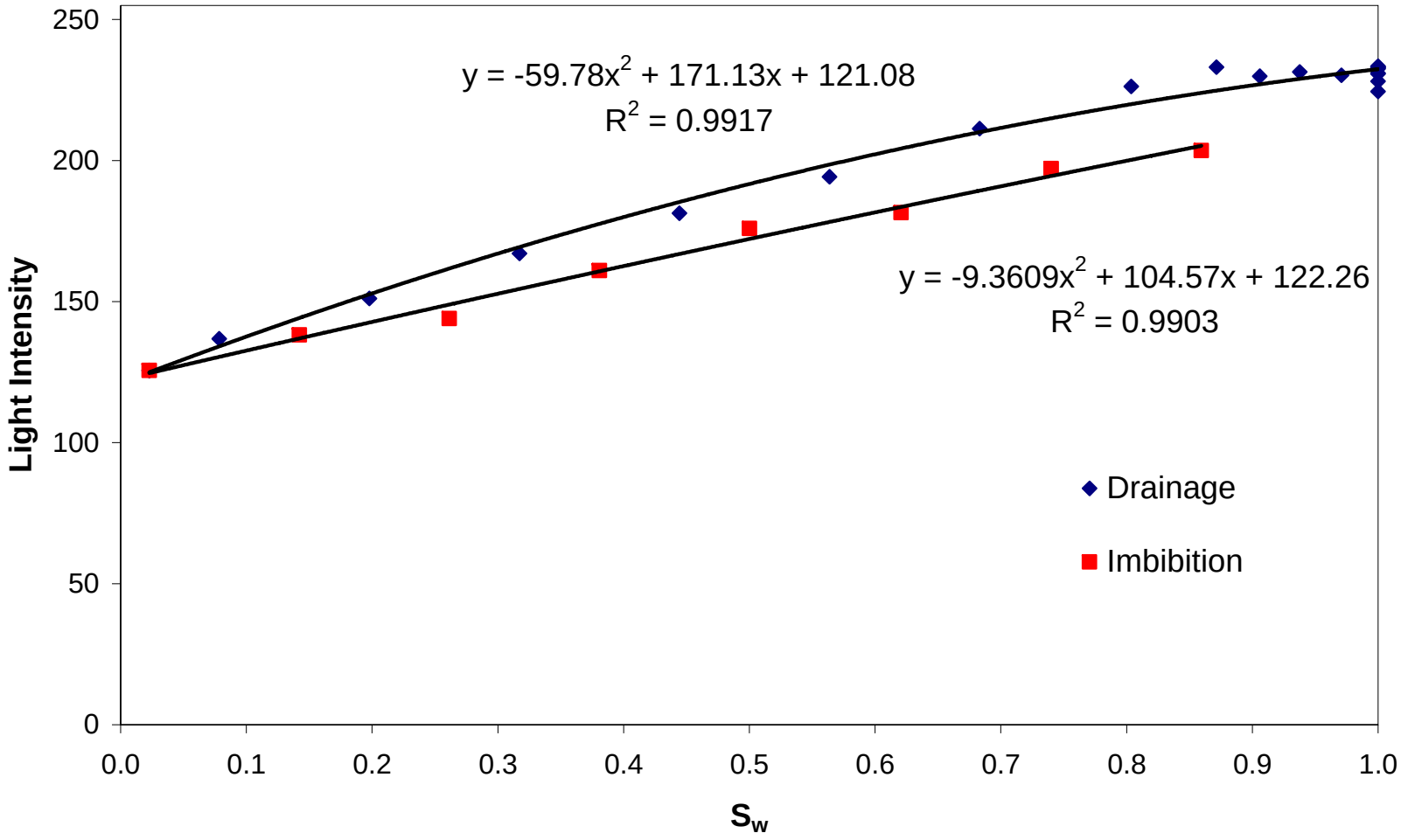

Figure B-3. Light transmission as a function of wetting phase saturation: sand N10; camera 3.

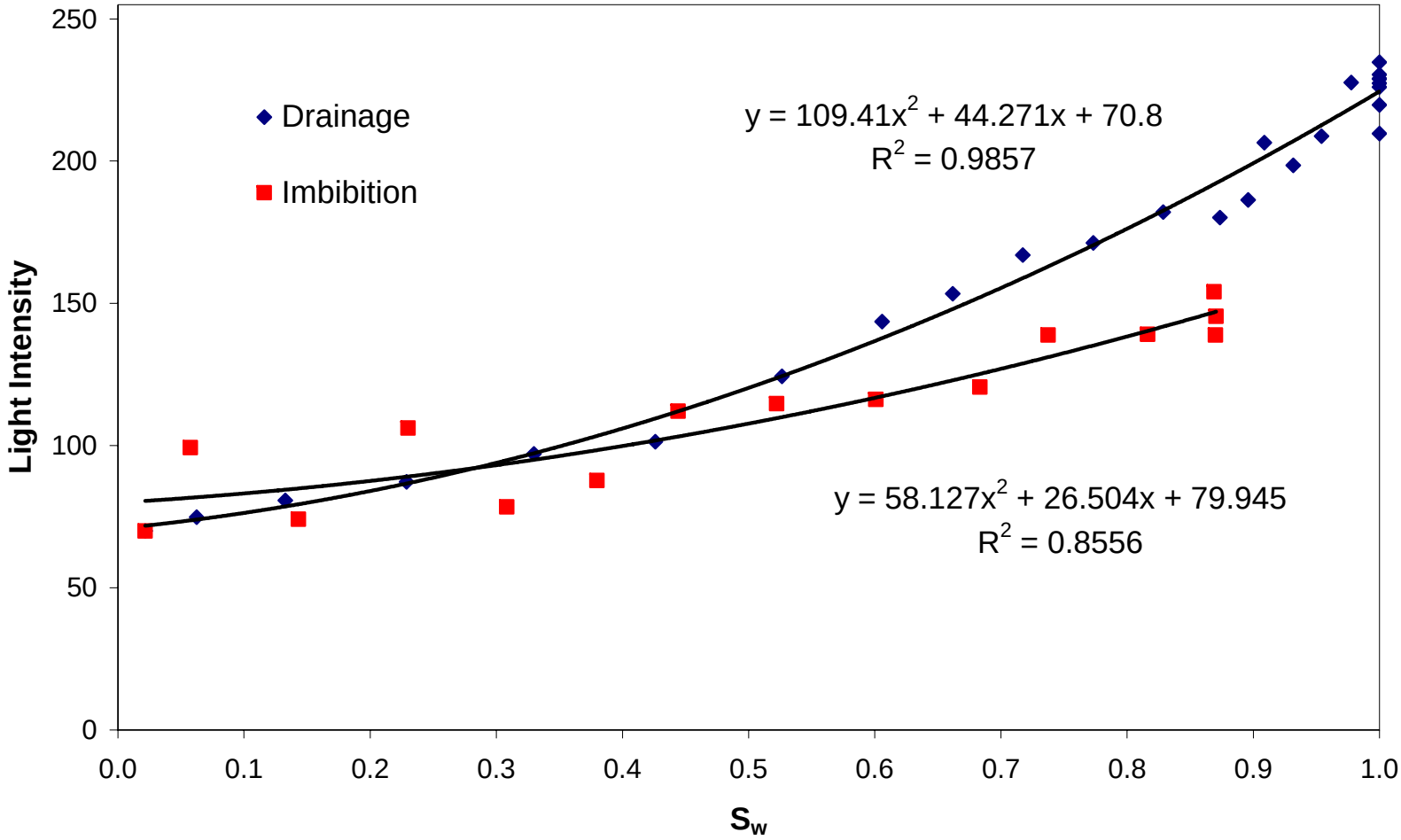

Figure B-4. Light transmission as a function of wetting phase saturation: sand N16; camera 1.

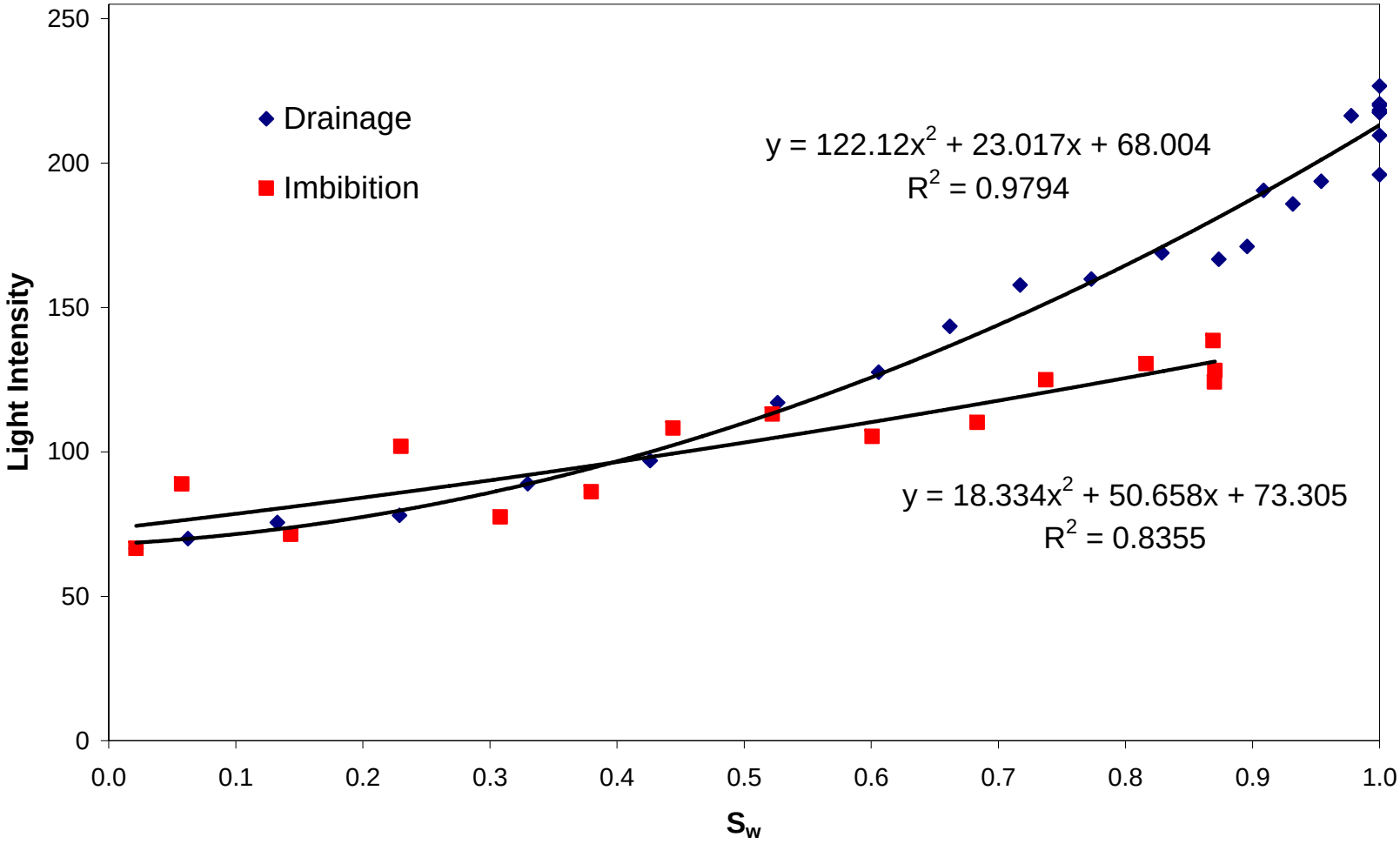

Figure B-5. Light transmission as a function of wetting phase saturation: sand N16; camera 2.

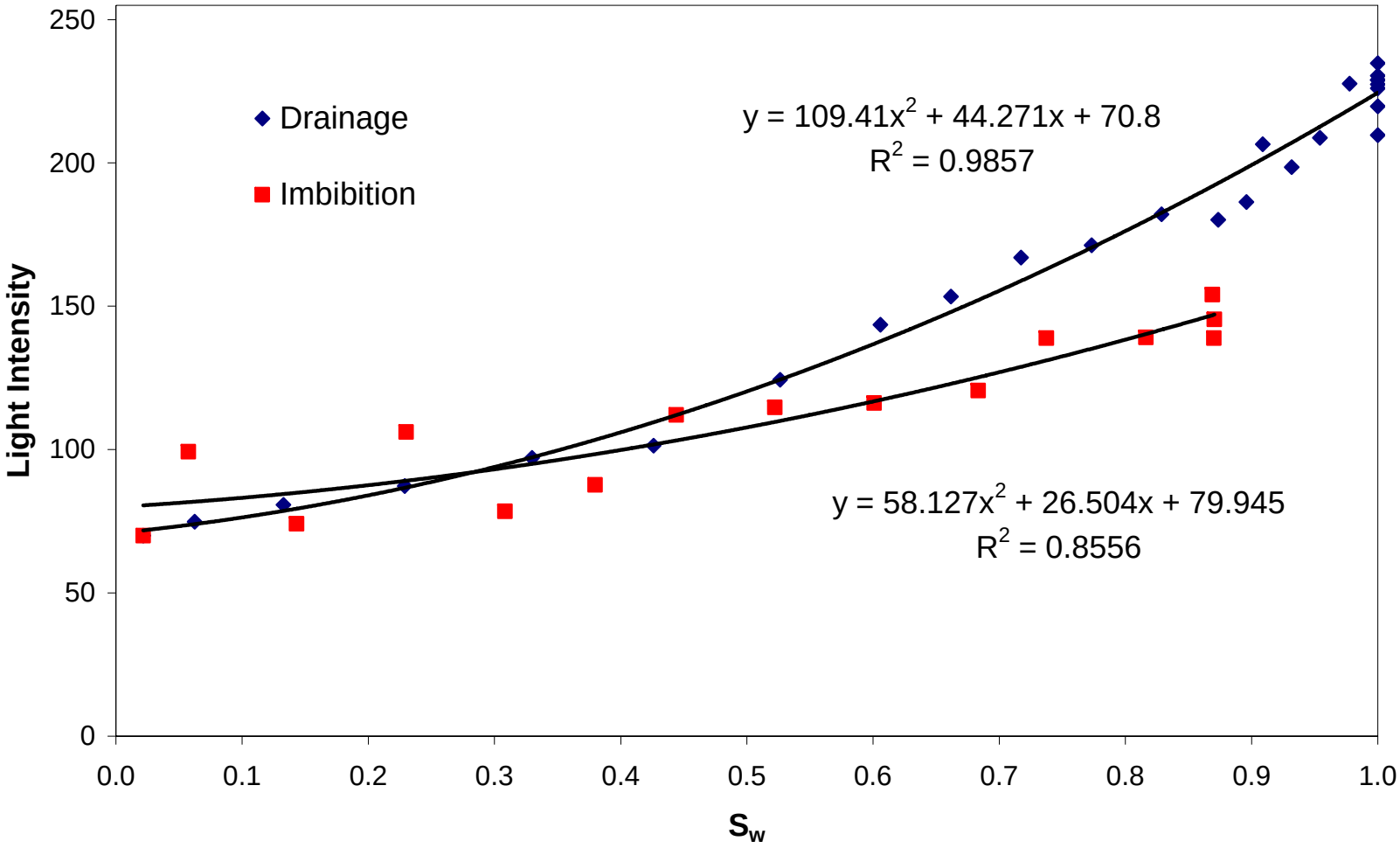

Figure B-6. Light transmission as a function of wetting phase saturation: sand N16; camera 3.

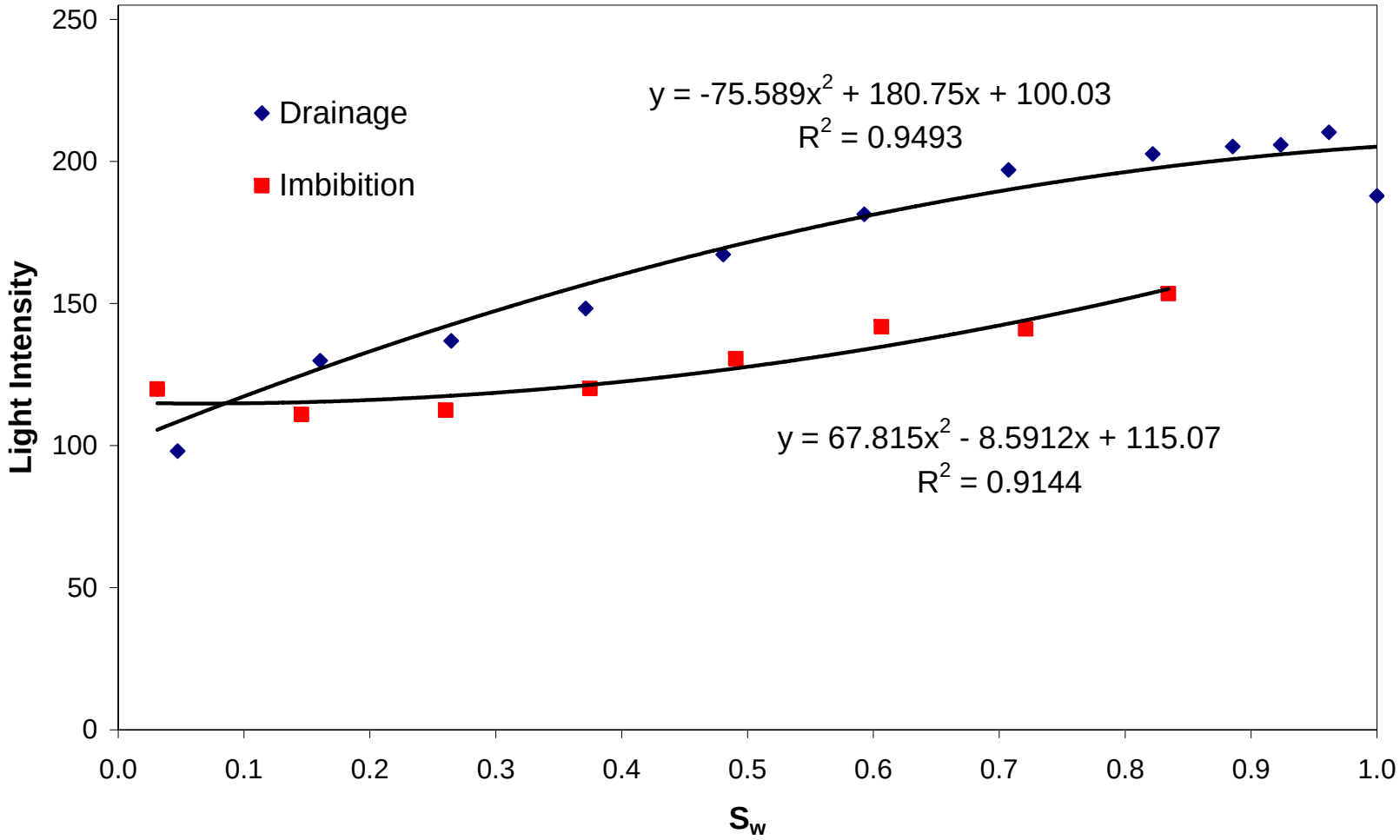

Figure B-7. Light transmission as a function of wetting phase saturation: sand N20; camera 1.

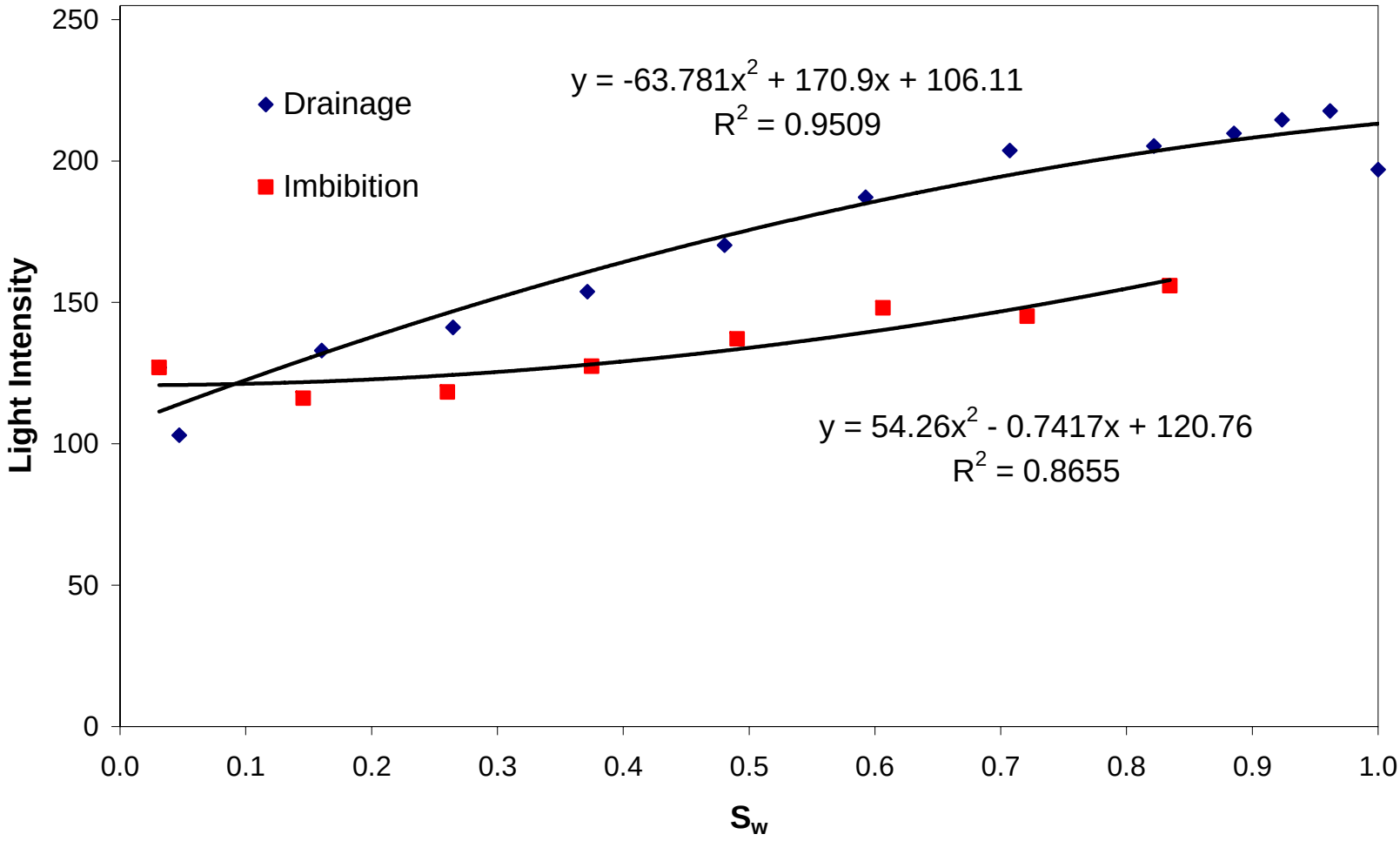

Figure B-8. Light transmission as a function of wetting phase saturation: sand N20; camera 2.

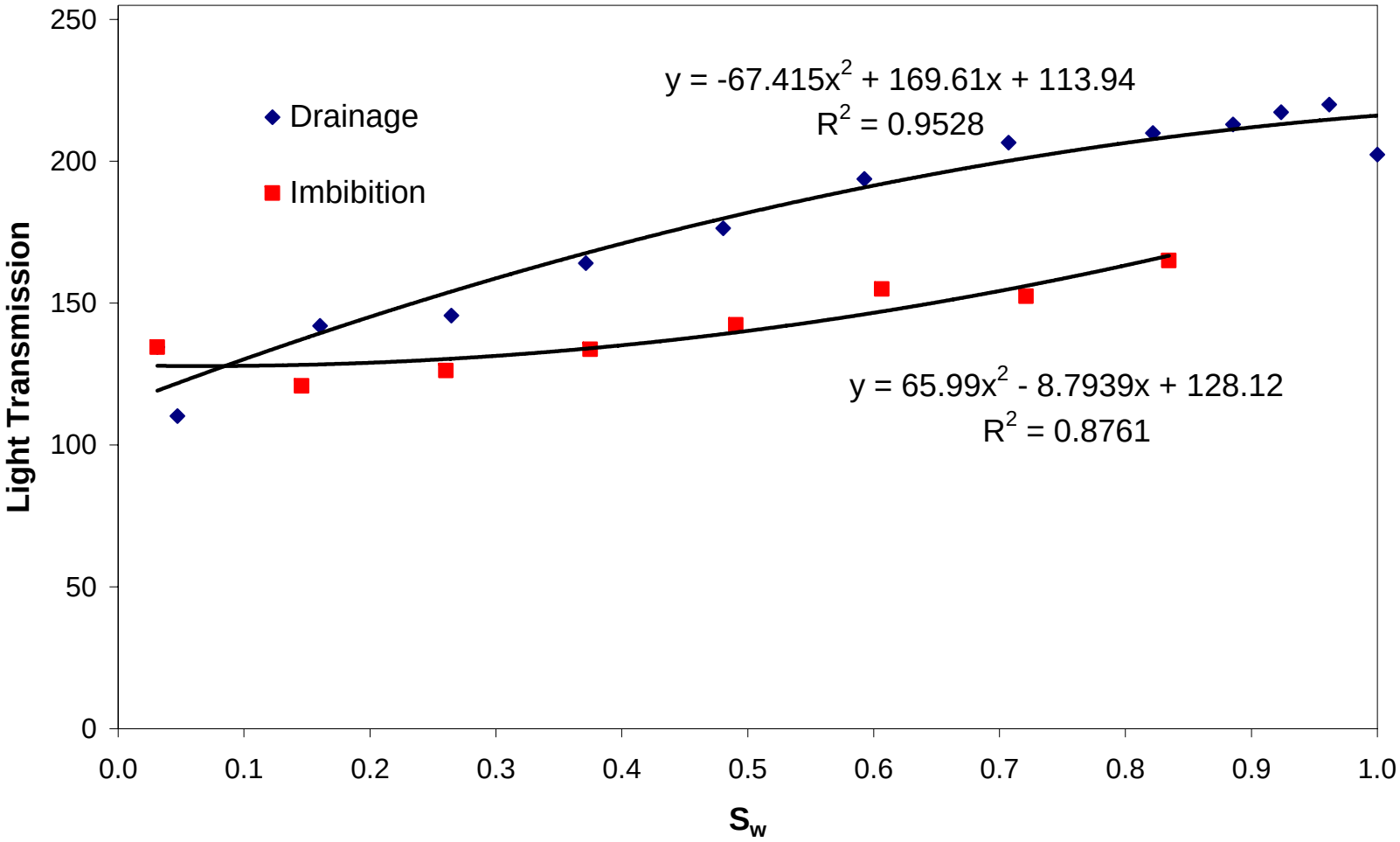

Figure B-9. Light transmission as a function of wetting phase saturation: sand N20; camera 3.

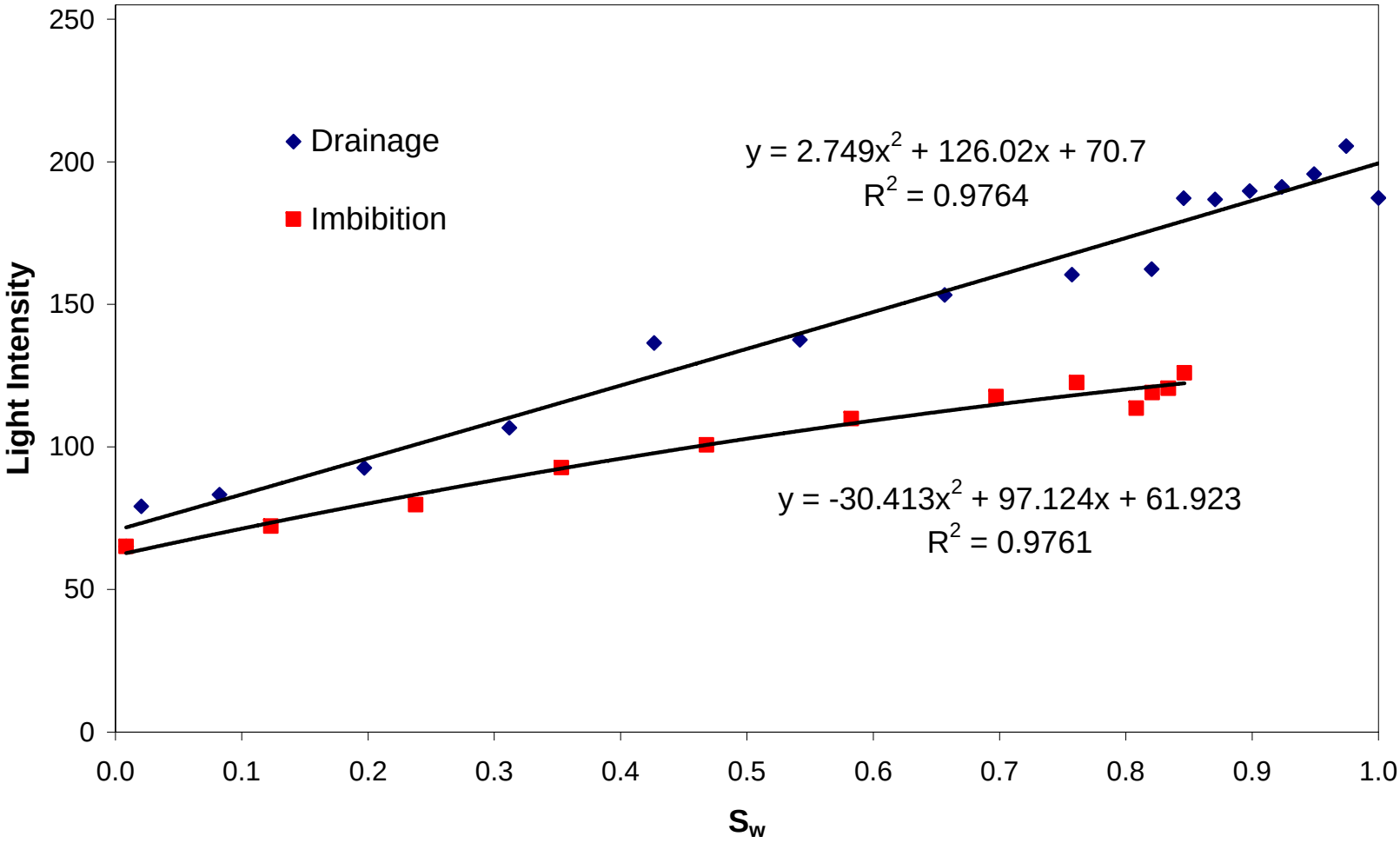

Figure B-10. Light transmission as a function of wetting phase saturation: sand N30; camera 1.

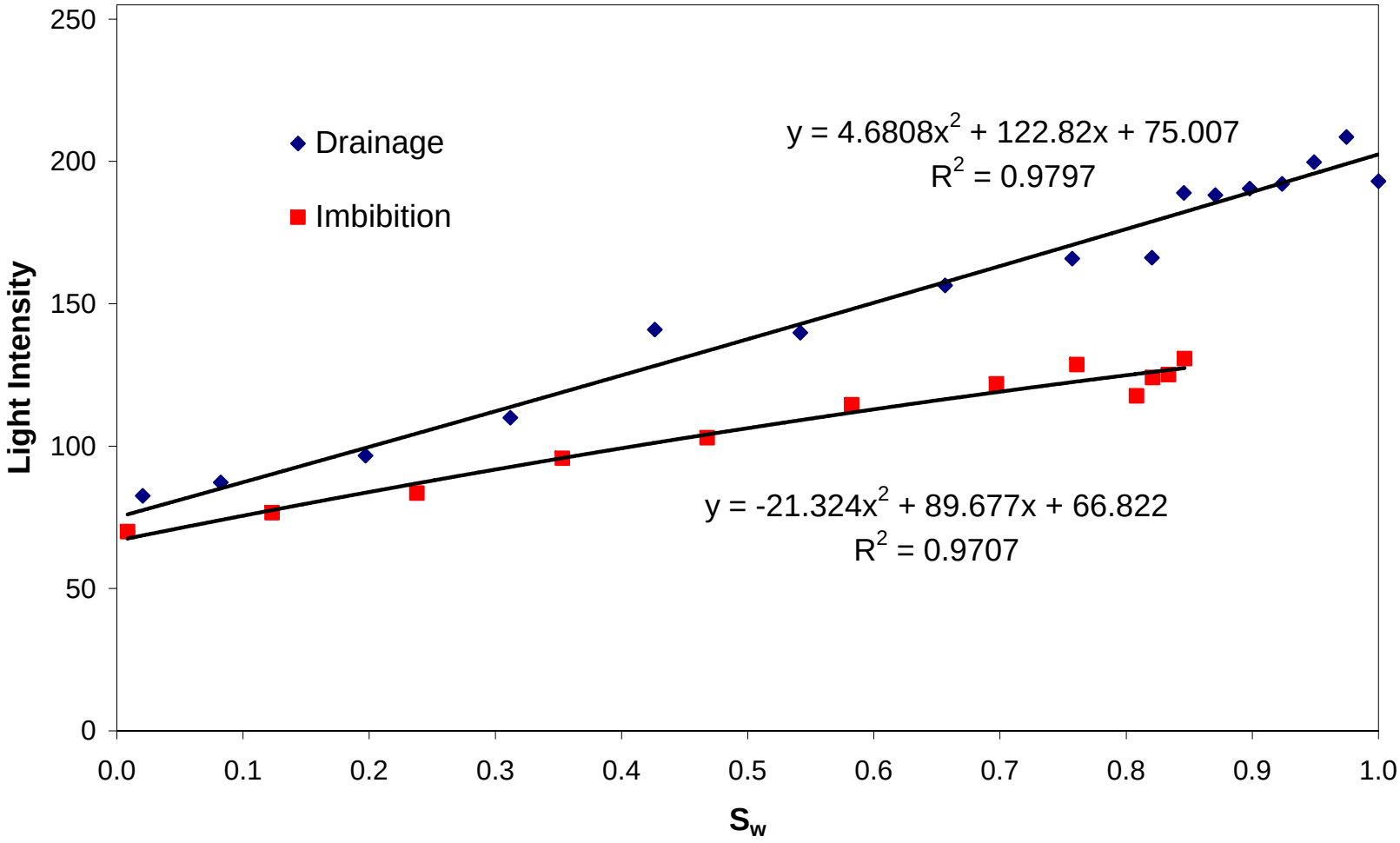

Figure B-11. Light transmission as a function of wetting phase saturation: sand N30; camera 2.

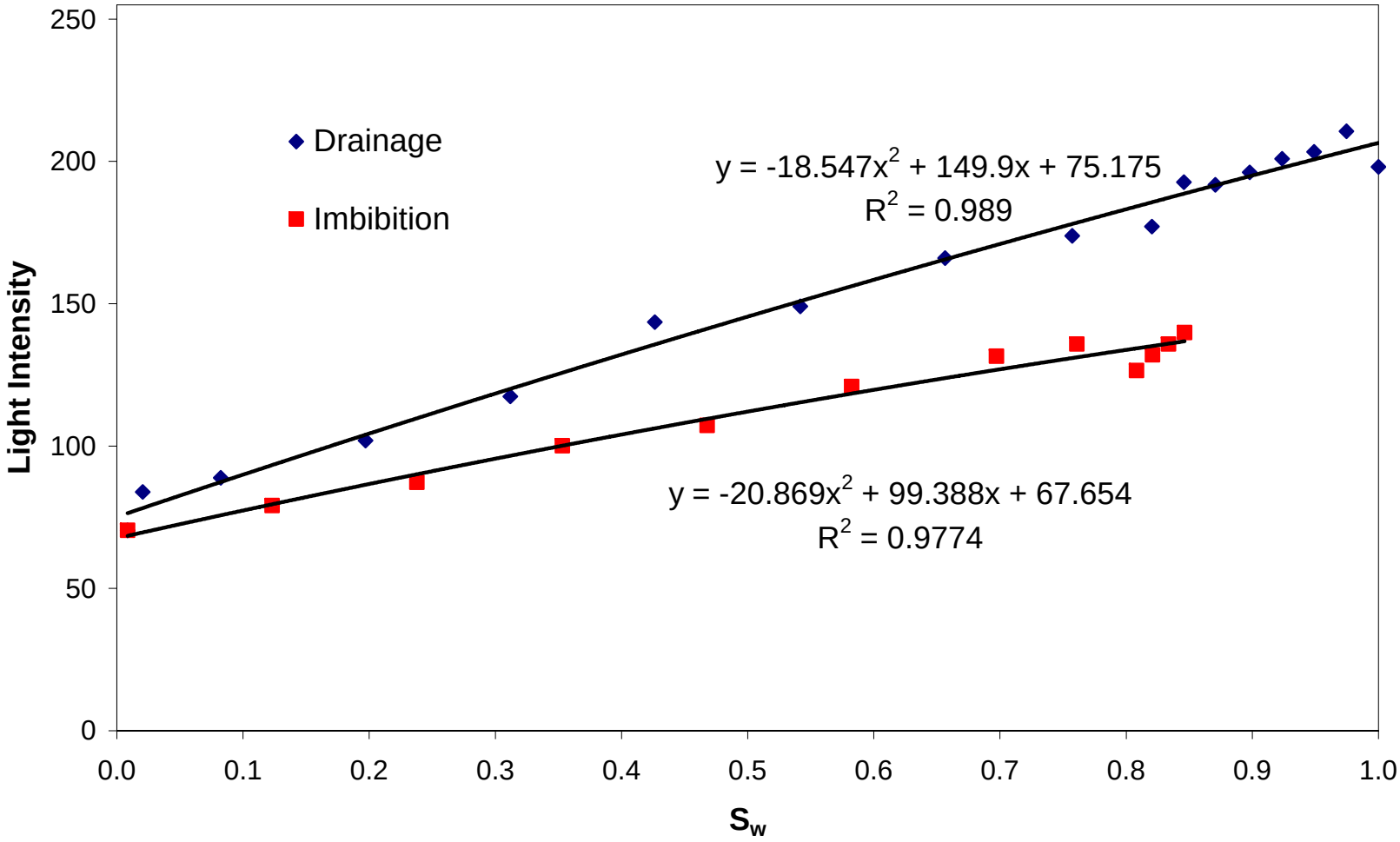

Figure B-12. Light transmission as a function of wetting phase saturation: sand N30; camera 3.

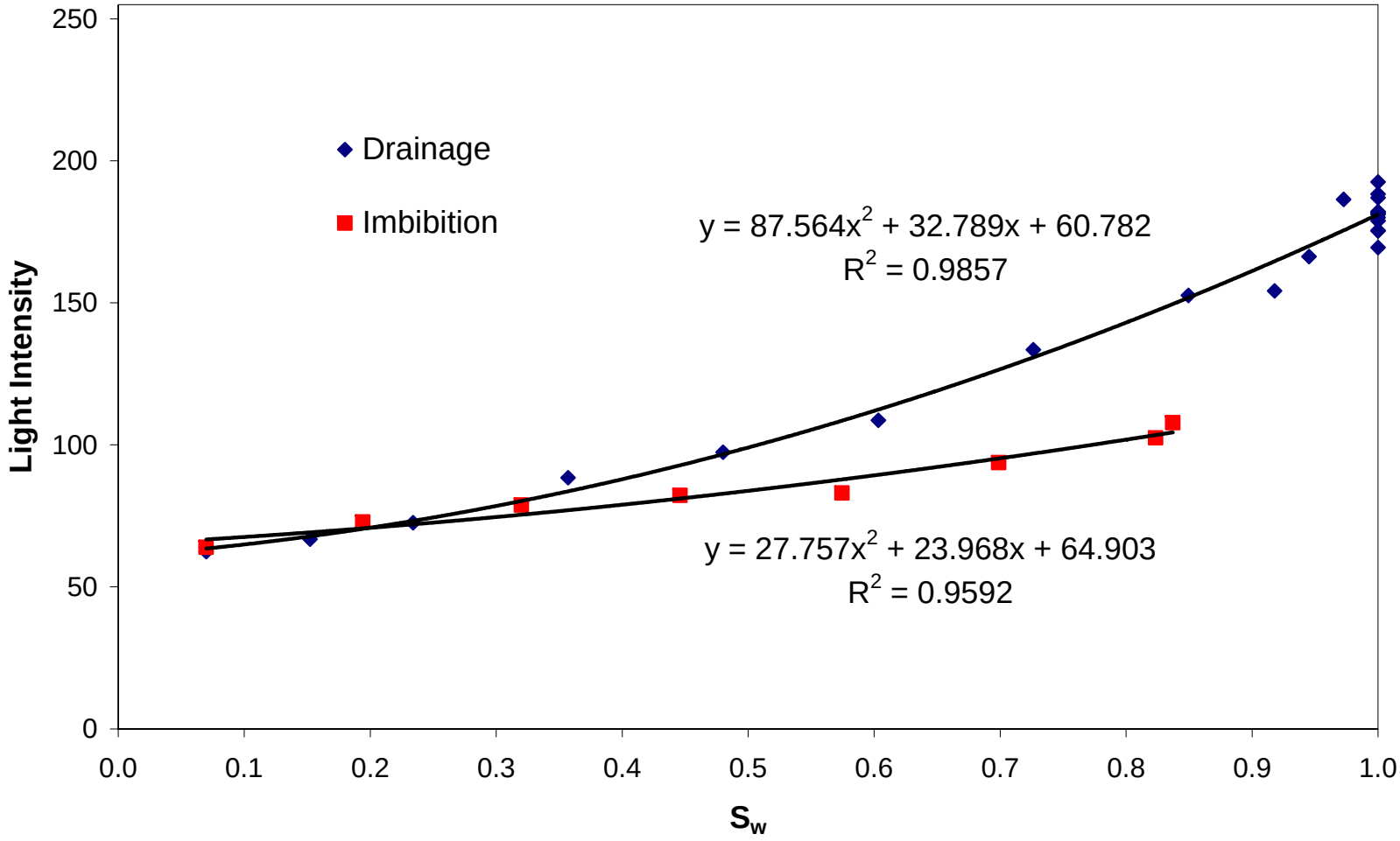

Figure B-13. Light transmission as a function of wetting phase saturation: sand N40; camera 1.

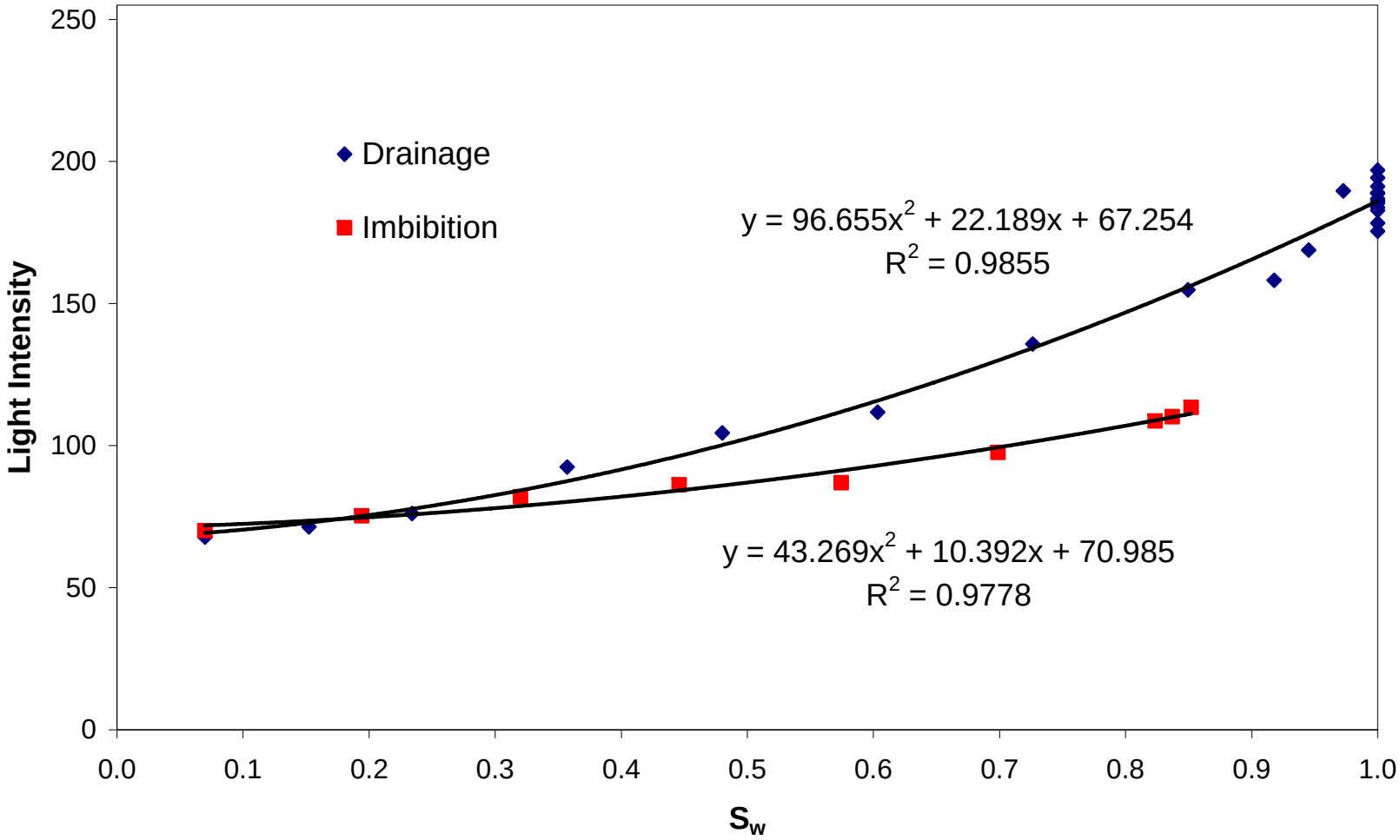

Figure B-14. Light transmission as a function of wetting phase saturation: sand N40; camera 2.

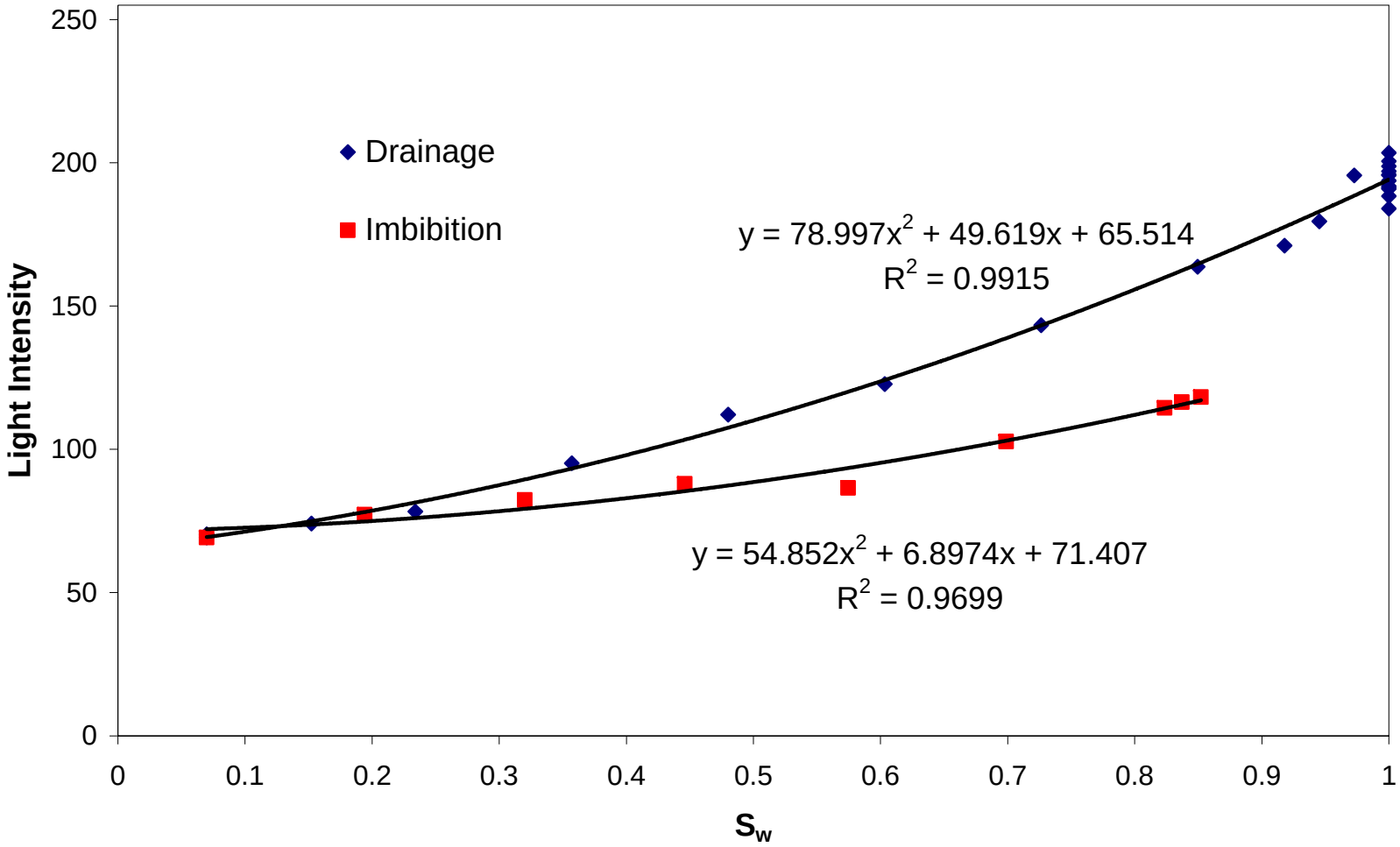

Figure B-15. Light transmission as a function of wetting phase saturation: sand N40; camera 3.

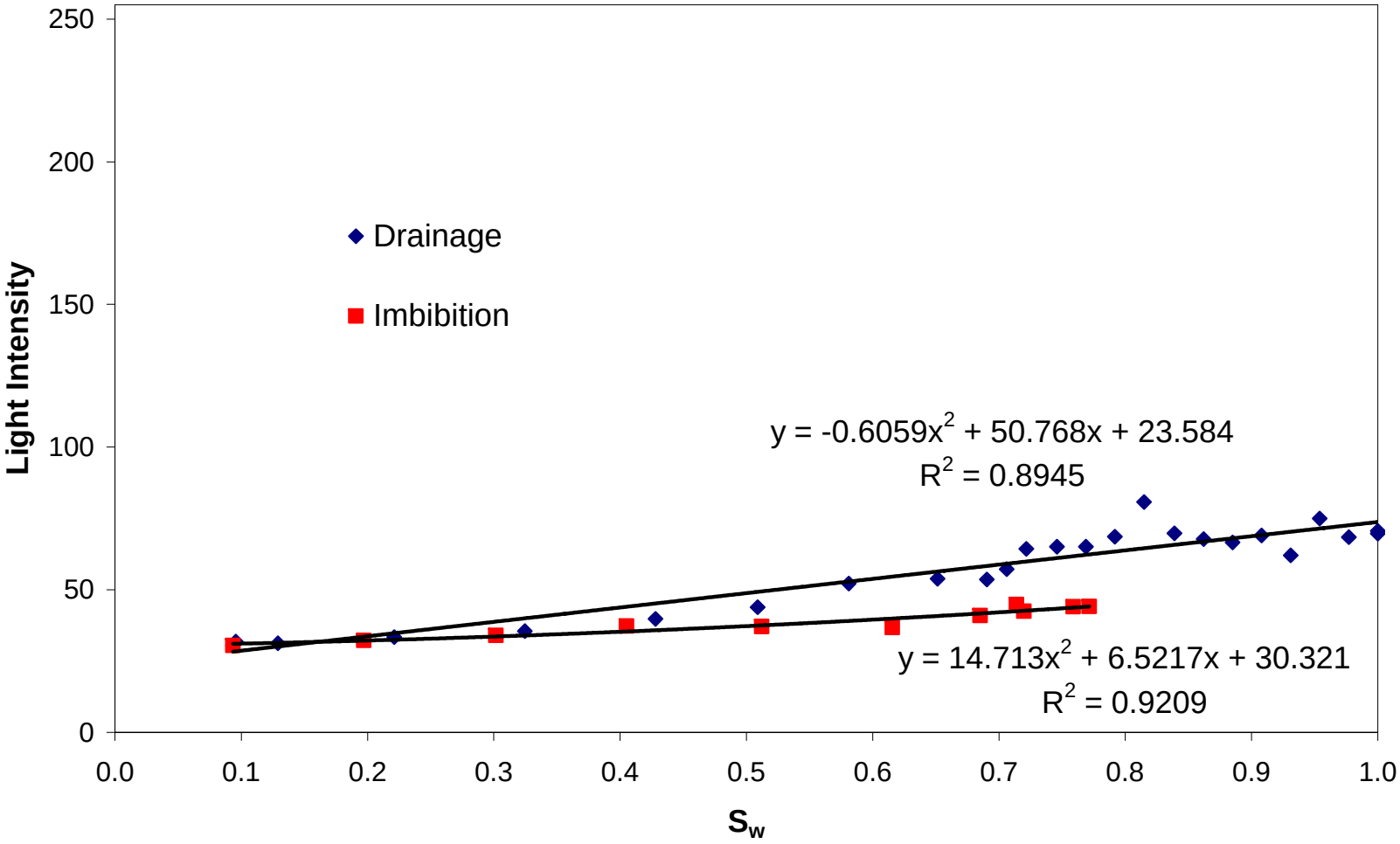

Figure B-16. Light transmission as a function of wetting phase saturation: sand N50; camera 1.

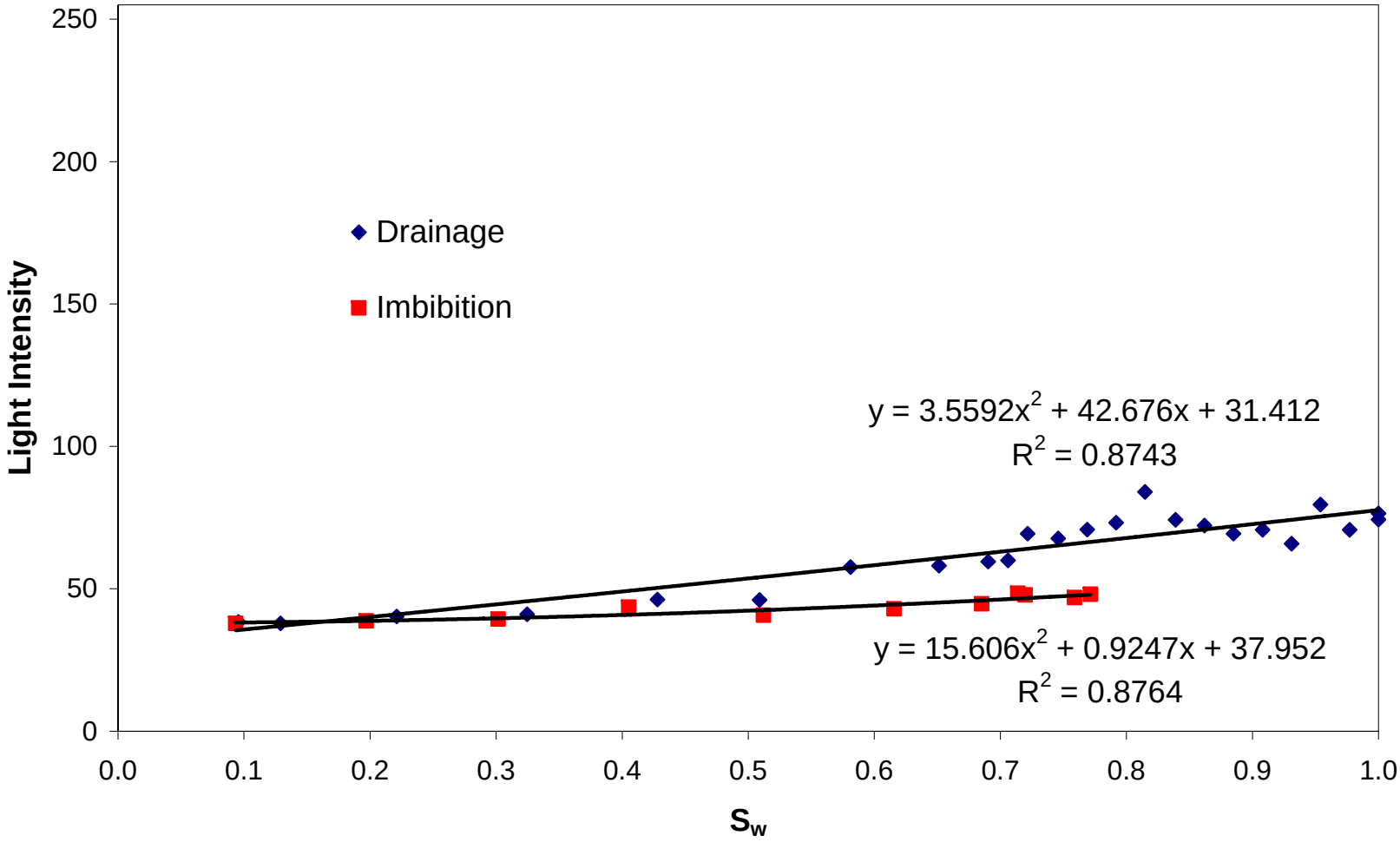

Figure B-17. Light transmission as a function of wetting phase saturation: sand N50; camera 2.

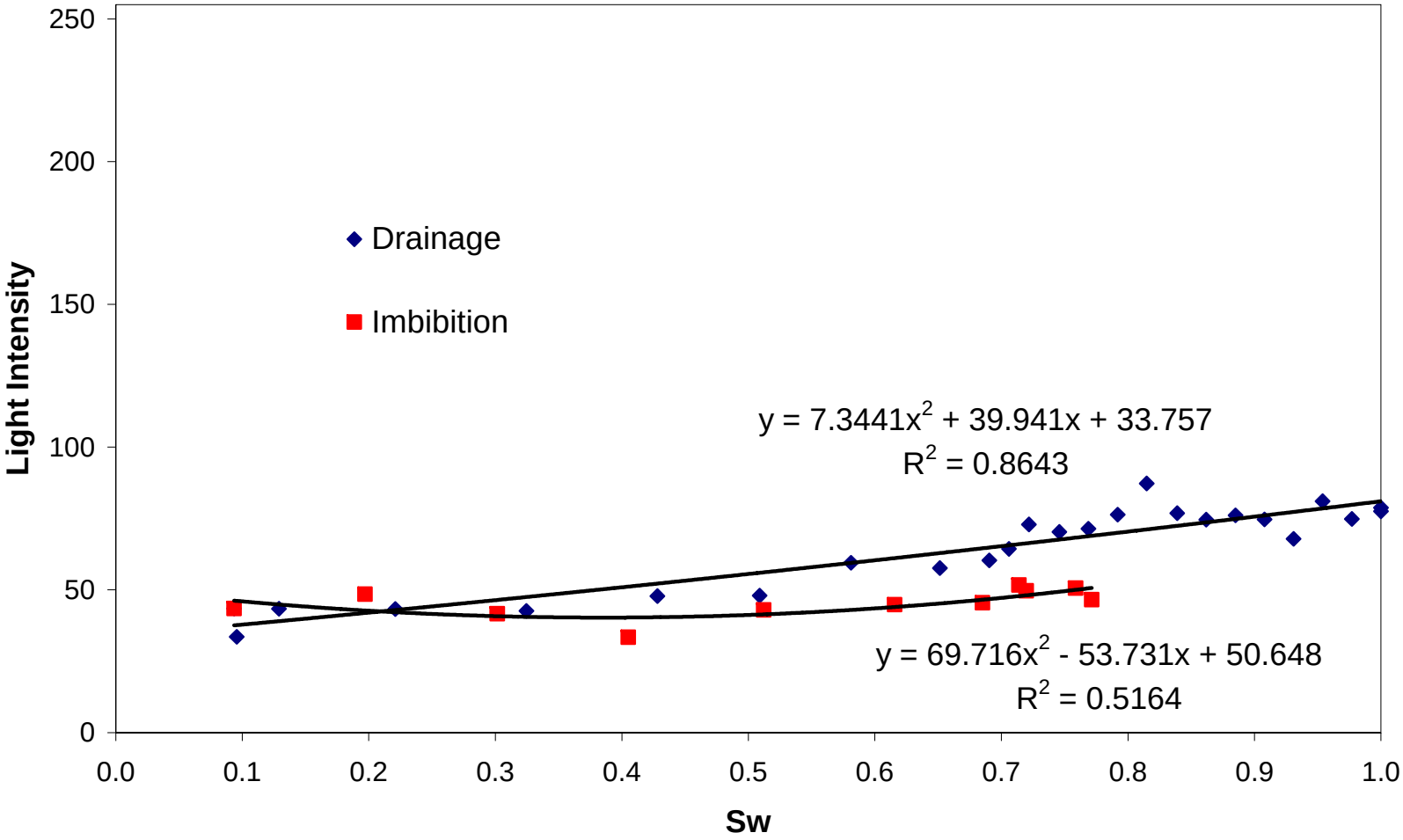

Figure B-18. Light transmission as a function of wetting phase saturation: sand N50; camera 3.

Table B-1. Average Maximum, Minimum, and Range of Intensities for the Six Sand Types Examined

Sand Type	Average Maximum Intensity	Average Minimum Intensity	Range of Intensities
N10	233	116	117
N16	232	66	166
N20	216	104	112
N30	208	68	140
N40	198	69	129
N50	84	34	50

B.3 NWP Presence / Saturation History Determination

Sand and water pressures exerted on the glass front and back plates of the flow cell caused the glass to deflect in an outwards direction, and the thickness of the sand pack to vary both horizontally and vertically across the cell (see Appendix D). Therefore, the light transmission properties of a given sand type vary in space, even prior to the addition of NWP to the system. As a result, wetting phase saturations were not calculated in the bench scale experiment using the calibration curves presented in Section B.2 above. Instead, spatial patterns of NWP distribution at various times throughout the experiment and light intensity profiles showing measured light intensity as a function of time, determined from the images collected from the light transmission / image analysis system, were used in the validation of the measured NWP relative permeability curves and constitutive relationships presented in Chapter 3.

While the light intensity profiles could also be used to delineate saturation history zones, the imprecision of the system as a result of glass deflection did not allow for the determination of specific point-by-point saturations in time and space.

B.4 References

Darnault, C.J.G., J.A. Throop, D.A. DiCarlo, A. Rimmer, T.S. Steenhuis, and J.-Y. Parlange, Visualisation by light transmission of oil and water contents in transient two-phase flow fields, *Journal of Contaminant Hydrology*, *31*, 337-348, 1998.

Gerhard, J.I., DNAPL infiltration, redistribution, and immobilization in porous media, Ph.D., thesis, Queen's Univ., Kingston, Ontario, Canada, 2002.

Glass, R.J., T.S. Steenhuis, and J.-Y. Parlange, Mechanism for finger persistence in homogeneous, unsaturated, porous media: Theory and verification, *Soil Science, 148*(1), 60-70, 1989.

APPENDIX C - HEADSPACE GAS CHROMATOGRAPH

Details regarding analytical procedures for measuring aqueous phase concentrations by headspace gas chromatograph (GC) are presented in Chapter 5. Further details regarding the operation and performance of the system will be presented in this section.

C.1 Analytical Procedure

Aqueous samples were analyzed using a headspace GC with flame ionization detection (FID). The analysis employed an Equity™-1 fused silica capillary column (Supelco, Bellefont, PA) in a Perkin-Elmer 8700 GC with a Perkin-Elmer HS-101 headspace autosampler. Because the analysis was for a single volatile species only (1,2-DCE), no oven ramping was necessary and the analysis protocol was optimized for time efficiency. The GC oven temperature was maintained at 80 ºC for 5 minutes, the injector port was set to 150 ºC and the detector port was set to 250 ºC. The employed carrier gas was ultra-high-purity helium (column pressure equal to 10 psi). The autosampler needle temperature, sample temperature and transfer temperature were all set at 25 ºC and the thermostat time was set for 5 minutes. Following this procedure, analysis time for a single sample was approximately 18 minutes.

C.2 System Performance

Matrix spike (MS) recoveries between 90 and 110% of expected values and matrix spike duplicate (MSD) differences less than 5.04% were observed for all 1-2-DCE analysis in the water/1,2-DCE system.

Figure C-1 presents a calibration curve of GC response (integrated peak area) as a function of 1,2-DCE concentration in water. Three replicate samples of five different concentrations of 1,2-DCE are plotted in this figure. As can clearly be seen,

the scatter of data for a given concentration is negligible (standard deviation between 1.1 and 5.0 percent of the measured area), and the calibration is linear over more than three orders of magnitude of concentration (R^2=0.9991). This calibration curve is representative of others generated during the analysis of samples collected from the bench scale experiment.

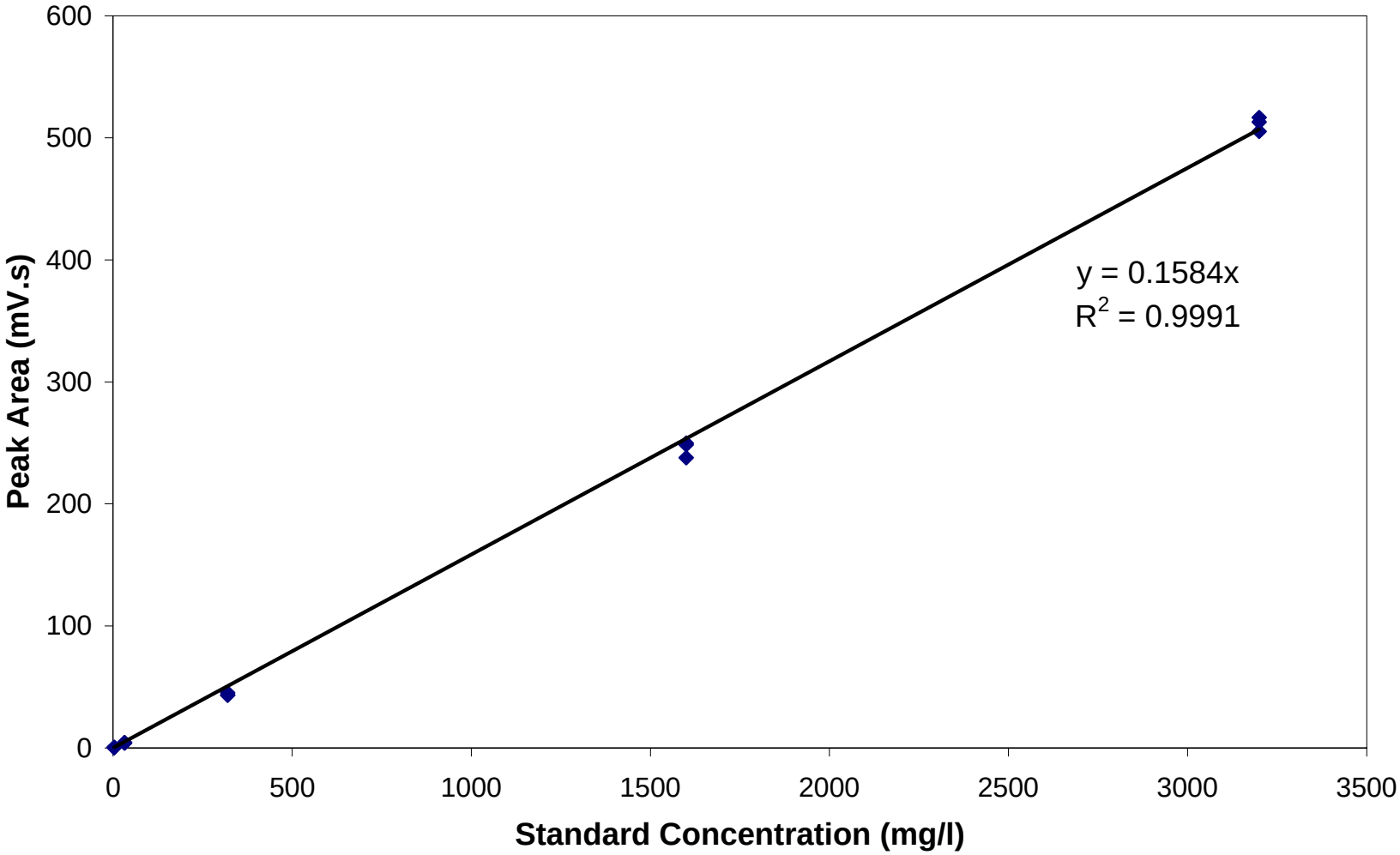

Figure C-1. Typical GC headspace calibration curve.

Method detection limits (MDLs) and limits of quantitation (LOQs) for the analytical procedure described above were calculated according to two different methods. The first method is based on a student 't' statistical analysis of data (WDNR PUBL-TS-056; 40CFR136), and the second method is based on a measure of detector 'noise' (Smith, 1999). The MDL and LOQ, as calculated by the former method, were 0.585 mg/l and 1.46 mg/l, respectively, and the MDL and LOQ, as calculated by the latter method, were 0.543 mg/l. and 1.36 mg/l, respectively.

C.3 References

40CFR136, Title 40 Code of Federal Regulations, Part 136, appendix b, revision 1.11, 2000.

Smith, R.K., *Handbook of Environmental Analysis*, Genium, Schenectady, New York, 1999.

WDNR PUBL-TS-056, Analytical detection limit guidance and laboratory guide for determining method detection limits, Wisconsin Department of Natural Resources, Laboratory Certification Program, 1996.

APPENDIX D – NON-REACTIVE TRACER TEST

A non-reactive tracer test was conducted in the bench scale apparatus to determine the average permeability of the sand pack, to assess the degree of glass plate deflection in the cell, and to determine the average dispersivity of the sand pack.

D.1 Test Procedure

A solution of 20 mg/l bromide (Br^-) was created by adding 567 mg of sodium bromide to a 22 l carboy of deionised water. The bromide solution was also dyed with blue food colouring to allow for visual tracking of the tracer throughout the experiment.

Following the method of Silliman (2001), the tracer was added as a vertically linear step increase in bromide concentration (from 0 mg/l to 20 mg/l) within the inflow reservoir. The step change in concentration was accomplished by closing the valve between the downgradient reservoir and the downgradient constant head tank to halt water flow, and flushing the upgradient reservoir with the tracer solution. The tracer was flushed through the upgradient reservoir from the bottom access port to the constant head tank port near the top of the reservoir (Figure D-1). The reservoir water was allowed to flow out the overflow of the upgradient constant head tank to a waste container. Once the reservoir water, tubing water and upgradient head tank water were determined by visual inspection (blue dye) to be at the full tracer concentration, the bottom access port was closed, the tracer was redirected by pump to the upgradient constant head tank, the valve between the downgradient reservoir and constant head tank was opened and the line source of tracer in the reservoir was allowed to flow through the cell (Figure D-2). The flow rate of tracer through the upgradient reservoir during line source emplacement was kept to a minimum to

ensure that little or no tracer was able to disperse into the sand pack prior to the commencement of the test.

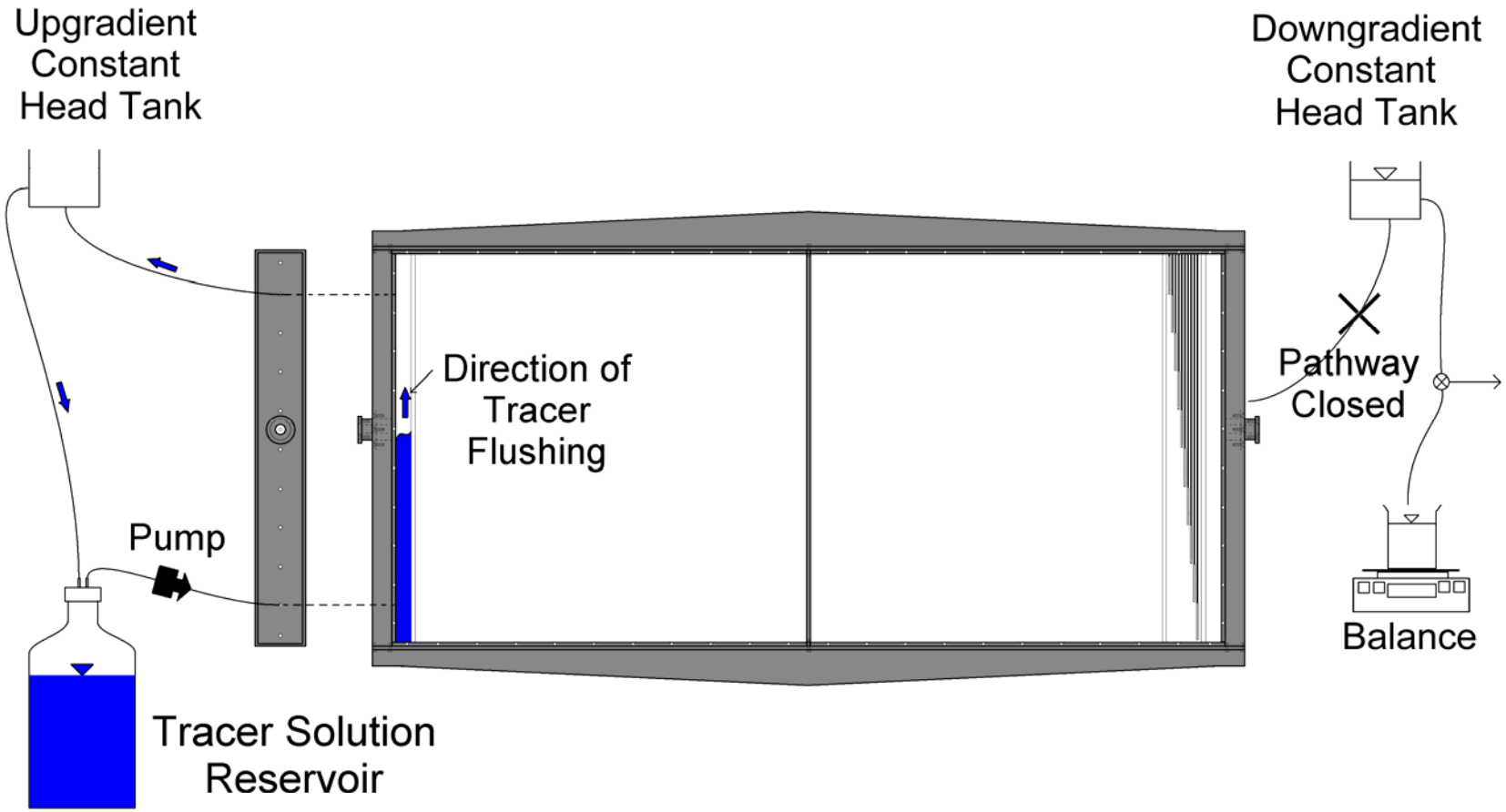

Figure D-1. Upgradient reservoir tracer flushing.

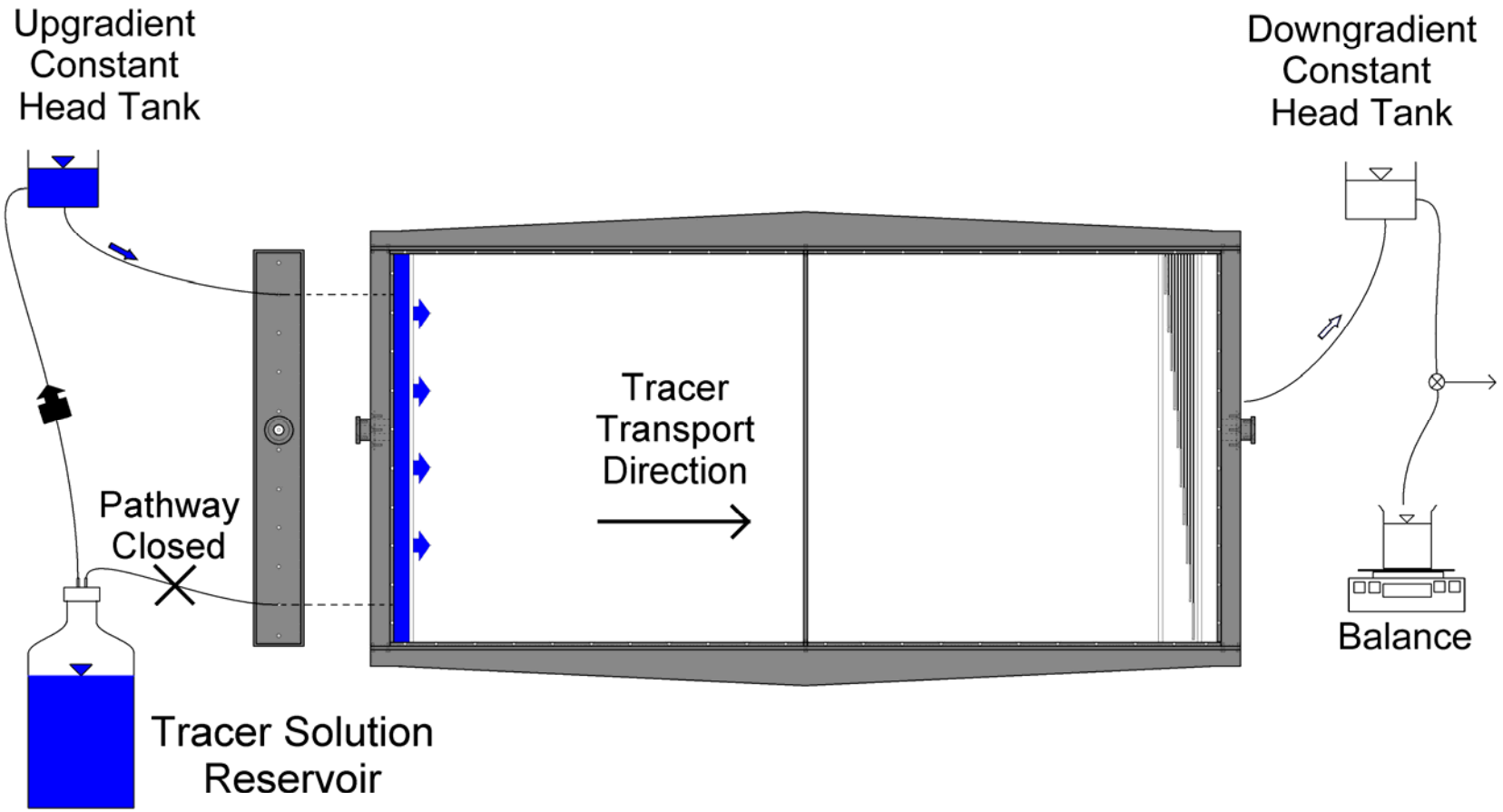

Figure D-2. Established tracer line source.

The head of the upgradient constant head tank was maintained at an elevation 1 cm above that of the downgradient constant head tank. Samples were collected at an interval of one hour from each of the nine active microwells over the course of the 26 hour test. The samples were analyzed using a Dionex LC20 ion analyzer equipped with an ED40 electrochemical detector (Sunnyvale, CA).

D.2 Test Results

D.2.1 Average Permeability Determination

Figure D-3 is a plot of total effluent bromide concentration as a function of time. This breakthrough curve (BTC) is presented in terms of relative bromide concentration, C/C_o, where C [ML^{-3}] is bromide concentration at time, t [T], and C_o [ML^{-3}] is the input bromide concentration (20 mg/l).

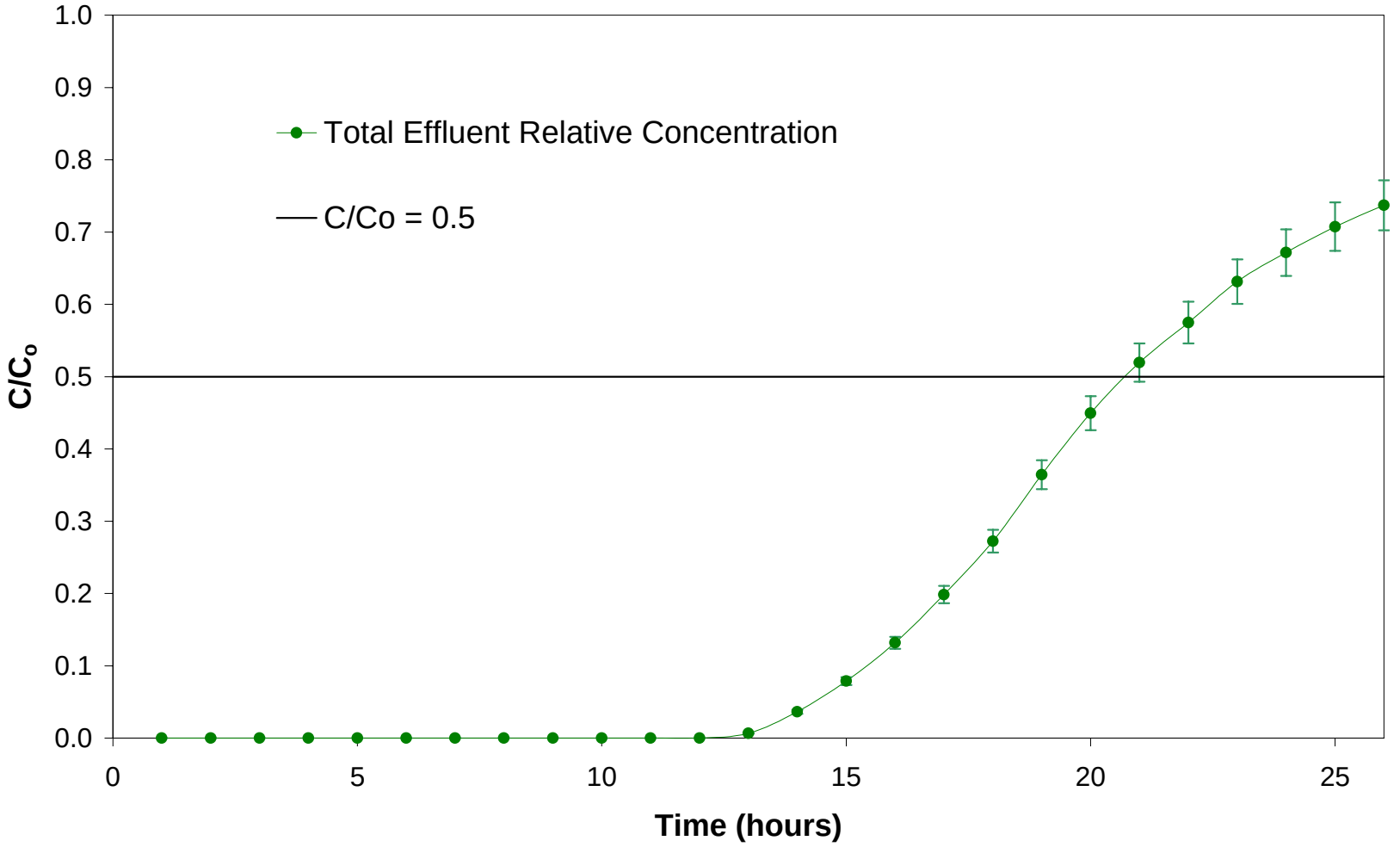

Figure D-3. Total effluent relative tracer concentration breakthrough curve.

Average aqueous phase velocity of a non-reactive tracer, V [LT^{-1}] can be calculated according to (Bear, 1972):

$$V = \frac{L}{t_{0.5}} \tag{D-1}$$

where L [L] is the total length of the sand pack and $t_{0.5}$ is the time at which C/C_o equals 0.5. For a sand pack of length, L = 2.02 m, and $t_{0.5}$ = 21.6 hr (as determined from Figure D-3), the average groundwater velocity was calculated to be, V = 2.60 x 10^{-5} m/s.

From Darcy's law, it can be shown that:

$$V = \frac{K_{avg} i}{\phi_{avg}} = \frac{k_{tracer} \rho g \cdot i}{\mu \cdot \phi_{avg}} \tag{D-2}$$

where K_{avg} [LT^{-1}]is the average hydraulic conductivity of the sand pack, i is the hydraulic gradient imposed across the sand pack, ϕ_{avg} is the arithmetic mean porosity, ρ is the density of water, g is the gravitational constant, 9.806, μ is the viscosity of water, and k_{tracer} is the tracer test determined average permeability of the sand pack. For a calculated arithmetic mean porosity of ϕ_{avg} = 0.327, and an imposed gradient of i = 0.00495 (1cm head difference across 202 cm sand pack), the average permeability at 22 ºC for the tracer test was calculated to be, k_{tracer} = 1.66 x 10^{-10} m^2.

This value is in good agreement with the arithmetic average permeability calculated to be, $k_{arithmetic}$ = 1.06 x 10^{-10} m^2. The arithmetic average permeability was calculated using the measured local scale permeability values, and the proportion of sand types emplaced in the bench scale flow cell. The tracer test calculated permeability is 1.57 times that of the arithmetic mean permeability. This slight discrepancy is likely a result of minor differences in the packing of sands between the local scale cell and the bench scale flow cell. Although the packing methods were

almost identical, the glass deflection during the bench scale flow cell packing may have caused a re-positioning of sand grains, which could account for a slight increase in permeability.

D.2.2 Degree of Glass Deflection Determination

D.2.2.1Average Deflection

The aqueous phase flow rate (Q [L^3T^{-1}]) through the flow cell during the tracer test was measured as, Q = 0.141 cm^3/s. A modified version of Darcy's law can be written:

$$Q = K_{avg} i A_{avg} \tag{D-3}$$

where A_{avg} is the average cross-sectional area of the flow cell. Using the tracer test determined average hydraulic conductivity, the imposed gradient and the measured flow rate, the average area of the flow cell was calculated to be, A_{avg} = 165.61 cm^2. The height of the sand pack was 0.91 cm, therefore, the average thickness of the cell is equal to 1.82 cm.

D.2.2.2 Shape of Deflection

While the average glass deflection can be determined quite easily, pressures exerted on the glass vary both vertically and horizontally across the cell, therefore, the exact shape of glass deflection is difficult to determine. However, logical deductions can be made to approximate the shape of the deflection:

a. The average cell thickness is approximately 1.82 cm;
b. The glass plates are held in place at a separation distance of 1cm along the outside border of the cell;
c. The glass plates are restrained by the vertical support in the centre of the flow cell;
d. Pressure increases linearly with depth; and,

e. If the slight discrepancy in measured average permeability (k_{tracer}) relative to predicted average permeability ($k_{arithmetic}$) is a result of sand grain re-positioning in response to glass deflection, then a relationship between glass deflection and permeability exists and the tracer test data can be used as a measure of deflection.

A cell thickness function was derived, through trial and error, while accounting for the above listed constraints. The proposed cell thickness function is a function of both horizontal distance (x) and vertical distance (y):

$$Thickness = \left(D_X \cdot D_y\right) + 1 \tag{D-4}$$

where D_X is the degree of deflection as a function of distance in the x-direction, and D_Y is the degree of deflection as a function of distance in the y-direction from the bottom left corner of the domain.

D_X is a forth order polynomial of the form:

$$D_x = Ax^4 + Bx^3 + Cx^2 + Dx + E \tag{D-5}$$

where A = -4.25 x 10^{-8}, B = 1.72 x 10^{-5}, C = -2.17 x 10^{-3}, D = 8.77 x 10^{-2}, and E = 3.70 x 10^{-1}, as determined by trial and error, and x is the horizontal distance from the centre line of the sand pack.

D_Y is a third order polynomial of the form:

$$D_y = Ay^3 + By^2 + Cy + D \tag{D-6}$$

where A = 5.91 x 10^{-7}, B = -7.39 x 10^{-4}, C = 5.57 x 10^{-2}, and D = 2.38 x 10^{-1}, as determined by trial and error, and y is the vertical distance from the bottom of the sand pack. The tracer test data collected from individual microwells (Section D.2.3) was used to refine the shape of the function to ensure good agreement between the degree of deflection (i.e., cell thickness) and permeability variation.

Figure D-4 is a contour map of the cell thickness function for the two-dimensional bench scale apparatus. The calculated average cell thickness of the proposed function is 1.82 cm, which is in perfect agreement with the average thickness value (1.82 cm) calculated in Section D.2.2.1.

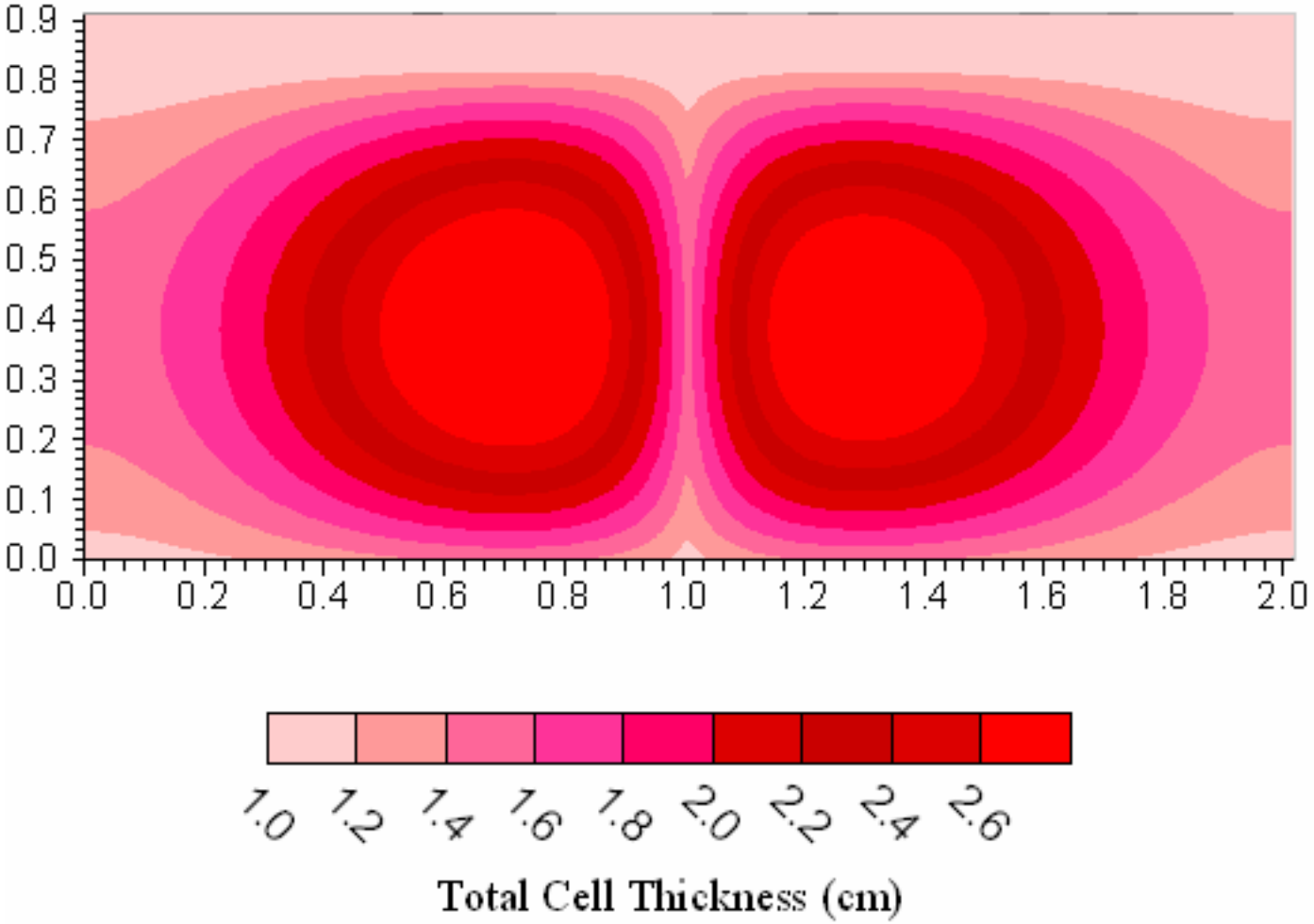

Figure D-4. Contour map of the proposed cell thickness function.

D.2.3 Average Dispersivity Determination

DNAPL3D-MT was used to simulate the tracer test experiment. The simulation assumed constant bromide concentration along the left-hand boundary of the domain, no DNAPL presence, and a hydraulic gradient of 0.00495. The model also utilised the cell thickness function presented in Equation D-4, and assumed that permeability varied linearly as a function of cell thickness.

Figure D-5 presents measured total effluent bromide relative concentration as a function of time as well as the predicted total effluent relative concentration as determined by numerical simulation. Utilising a longitudinal dispersivity value of, α = 1.5 cm and a ratio of transverse to longitudinal dispersivity of 0.001, the numerical simulation shows good agreement with the measured data.

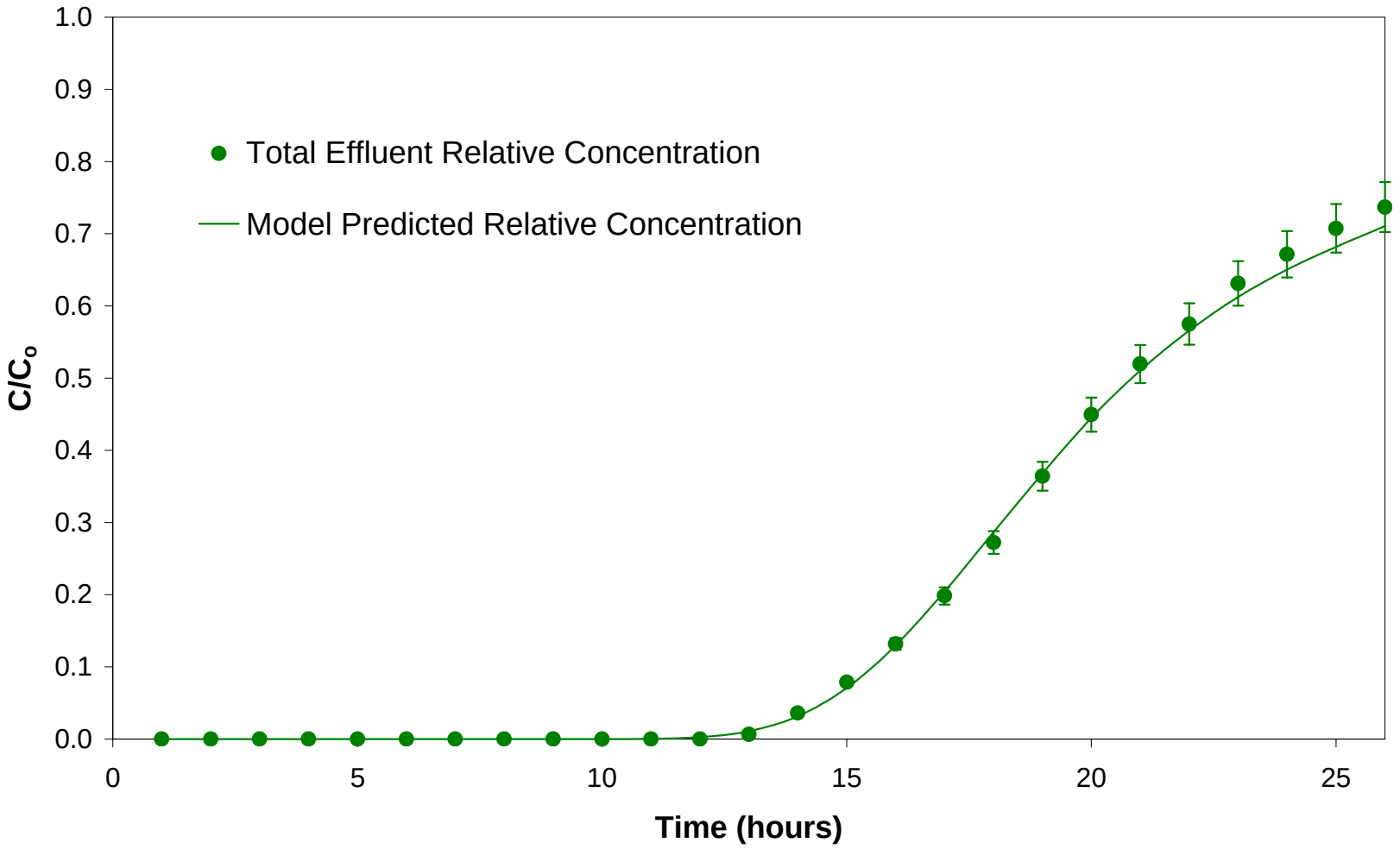

Figure D-5. Total effluent relative tracer concentration breakthrough curve including best-fit numerical model prediction.

Figures D-6 through D-14 show the individual microwell relative concentration profiles as a function of time for both the experimental results and the numerical simulation. Without any further fitting of the dispersivity parameters, the figures show good agreement between the experimental and numerical results.

Figure D-11, which presents the BTC curve of microwell #6, shows an abrupt bend in the concentration profile at approximately 18 hours that is not observed in the numerical simulation prediction. This is likely the result of an air bubble, noted in the sample tubing during the tracer test, which may have caused aqueous samples travelling to the sample chamber from the microwell to be delayed. Thus, the sample retrieved from the sample chamber was likely a parcel of lower concentration water that had arrived at microwell #6 at an early time.

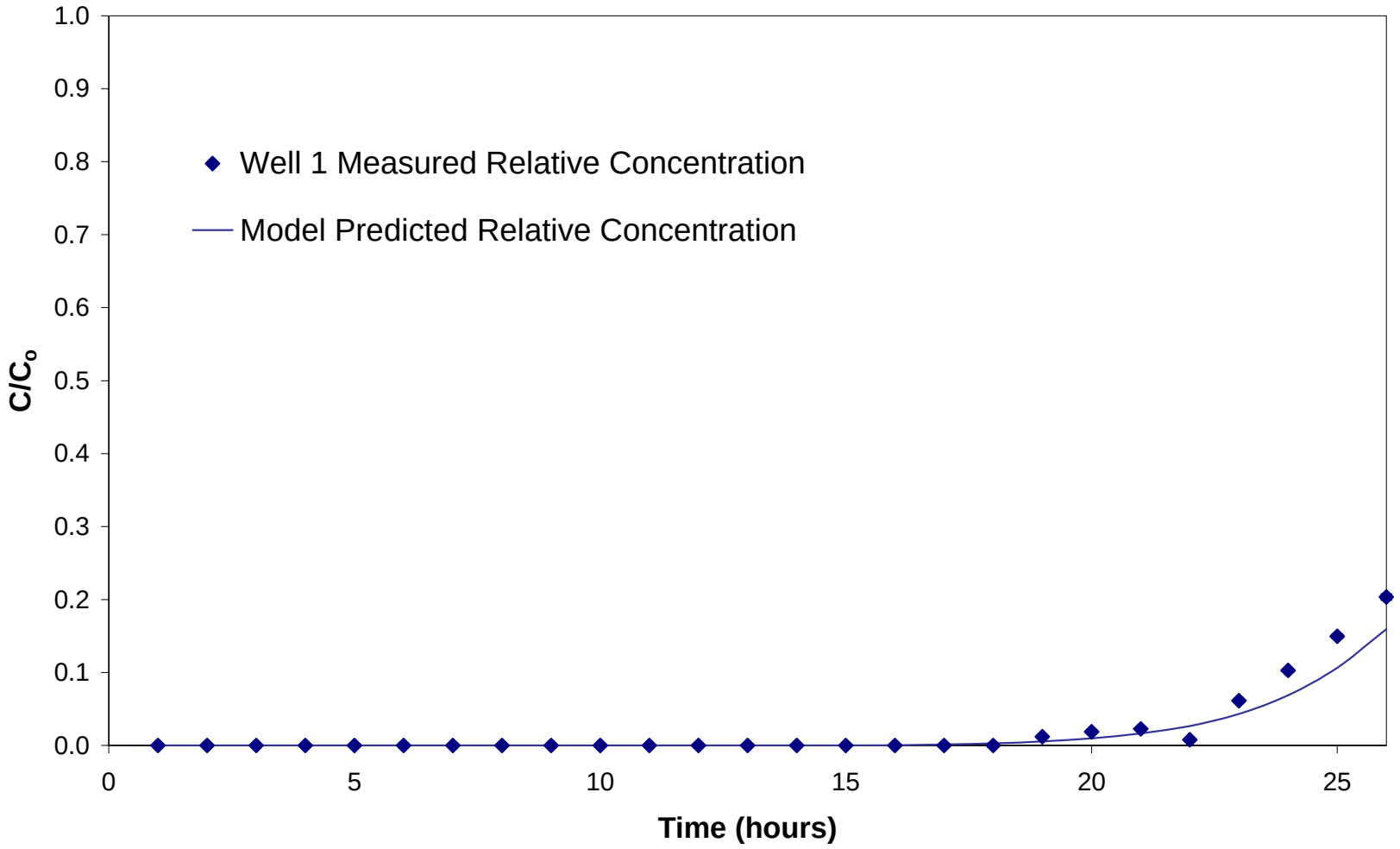

Figure D-6. Well 1 relative tracer concentration breakthrough curve including best-fit numerical model prediction.

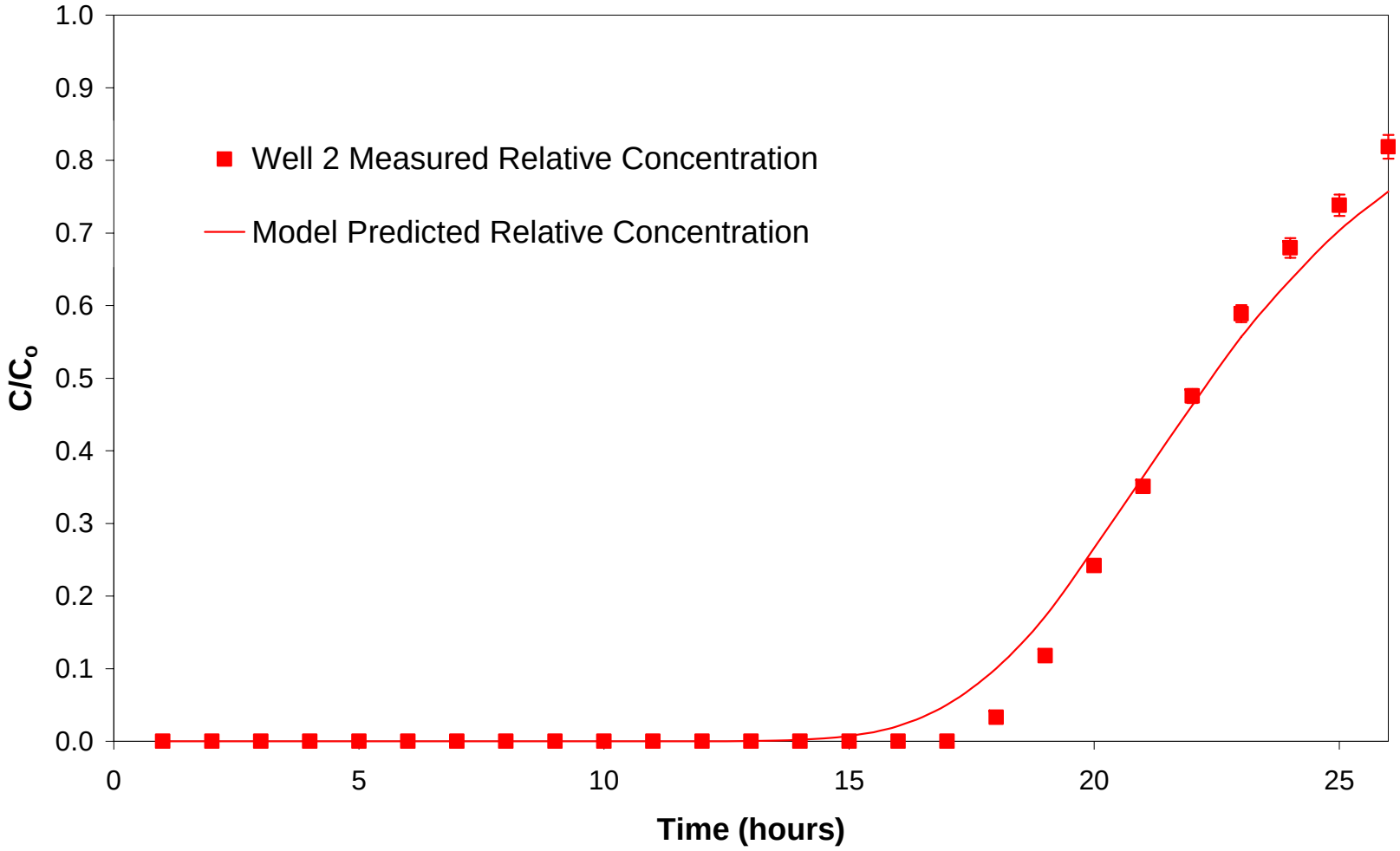

Figure D-7. Well 2 relative tracer concentration breakthrough curve including best-fit numerical model prediction.

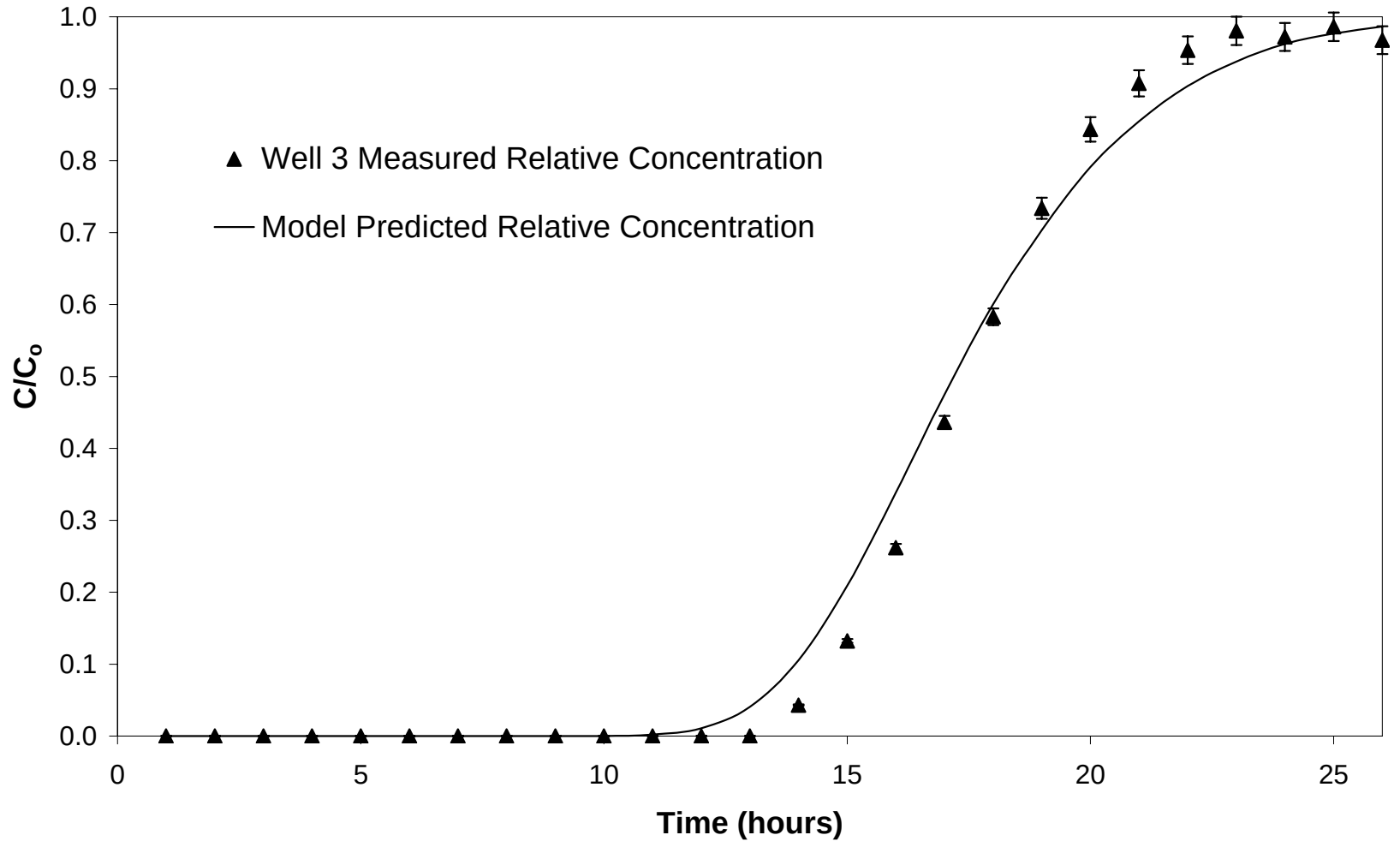

Figure D-8. Well 3 relative tracer concentration breakthrough curve including best-fit numerical model prediction.

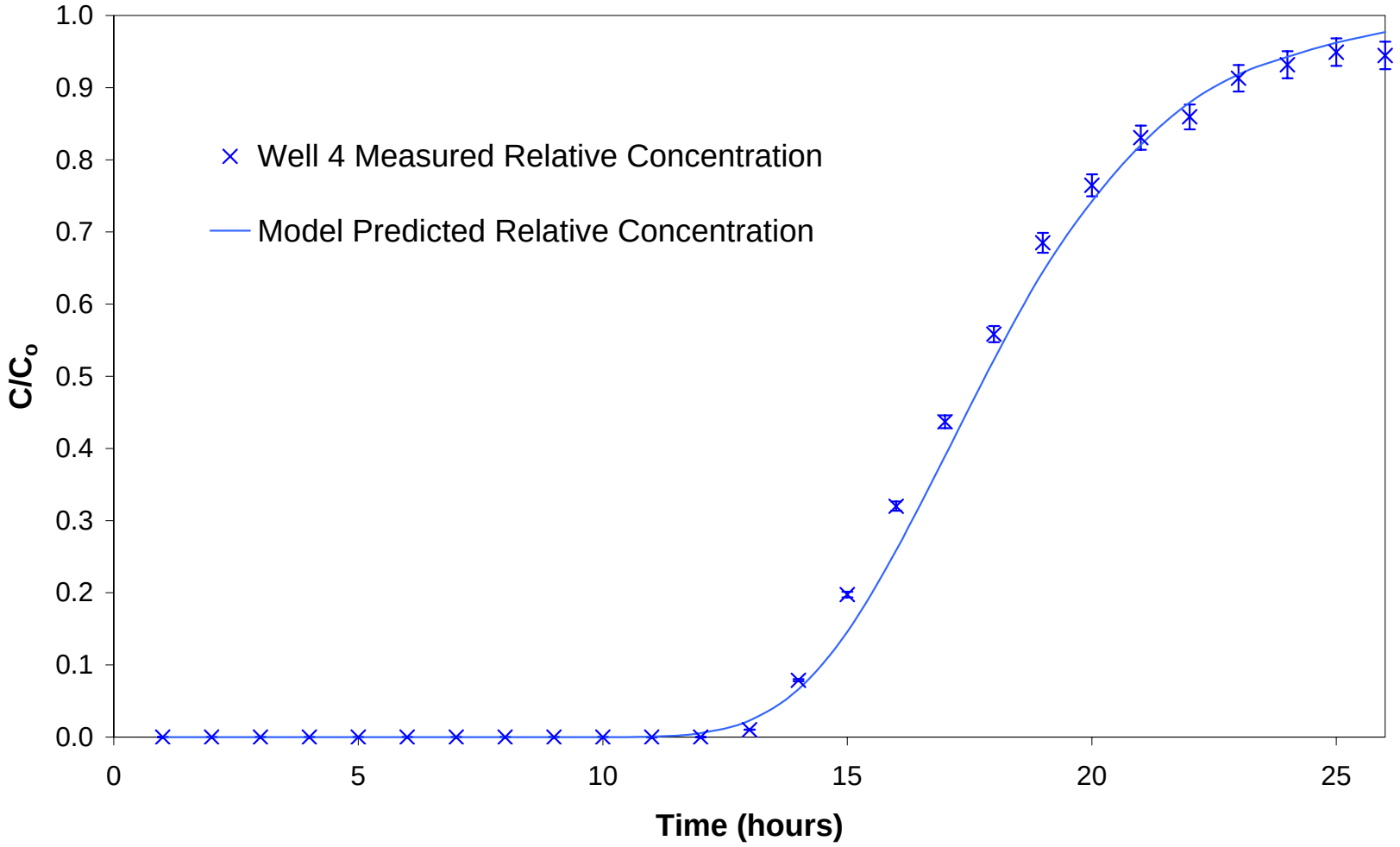

Figure D-9. Well 4 relative tracer concentration breakthrough curve including best-fit numerical model prediction.

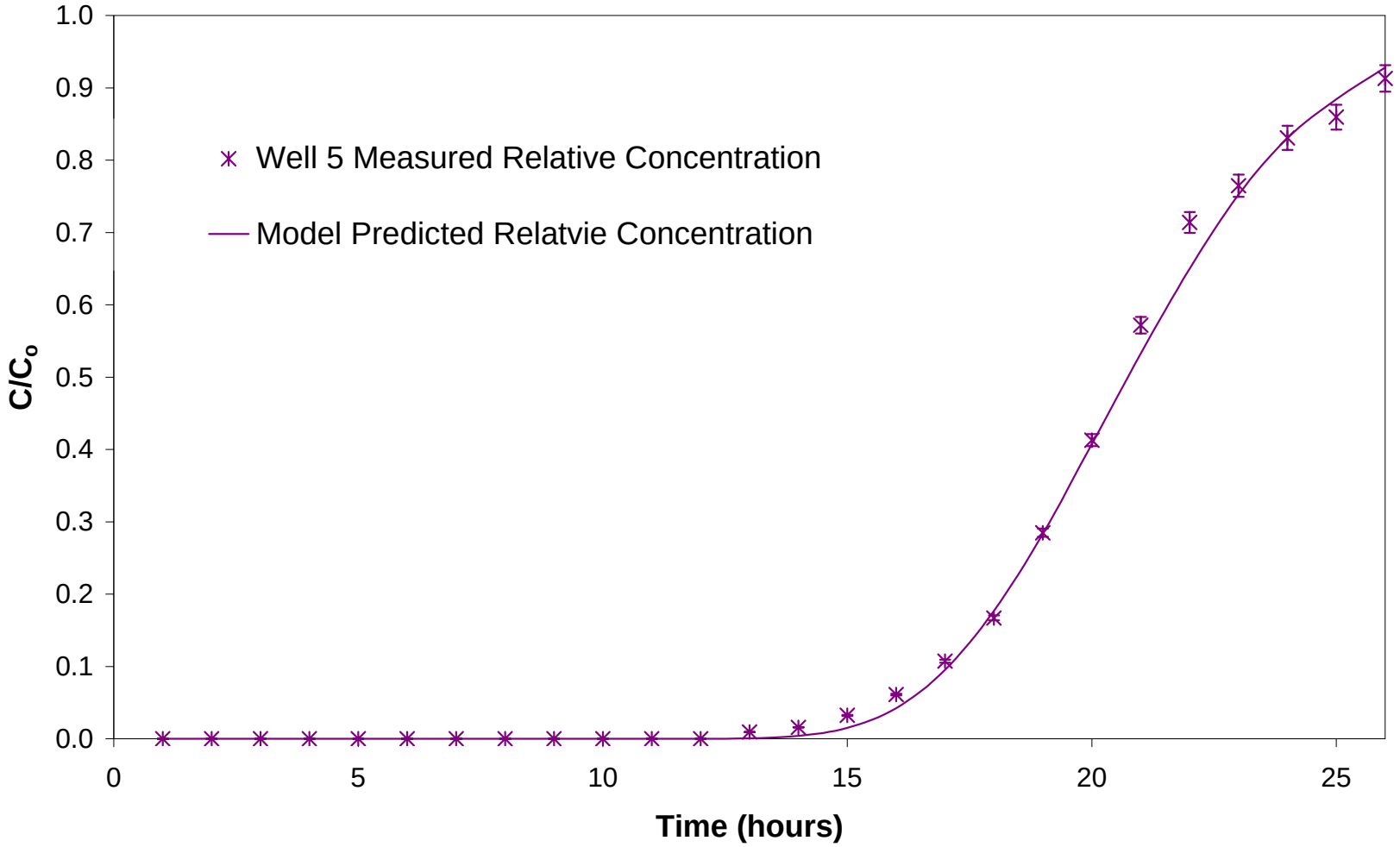

Figure D-10. Well 5 relative tracer concentration breakthrough curve including best-fit numerical model prediction.

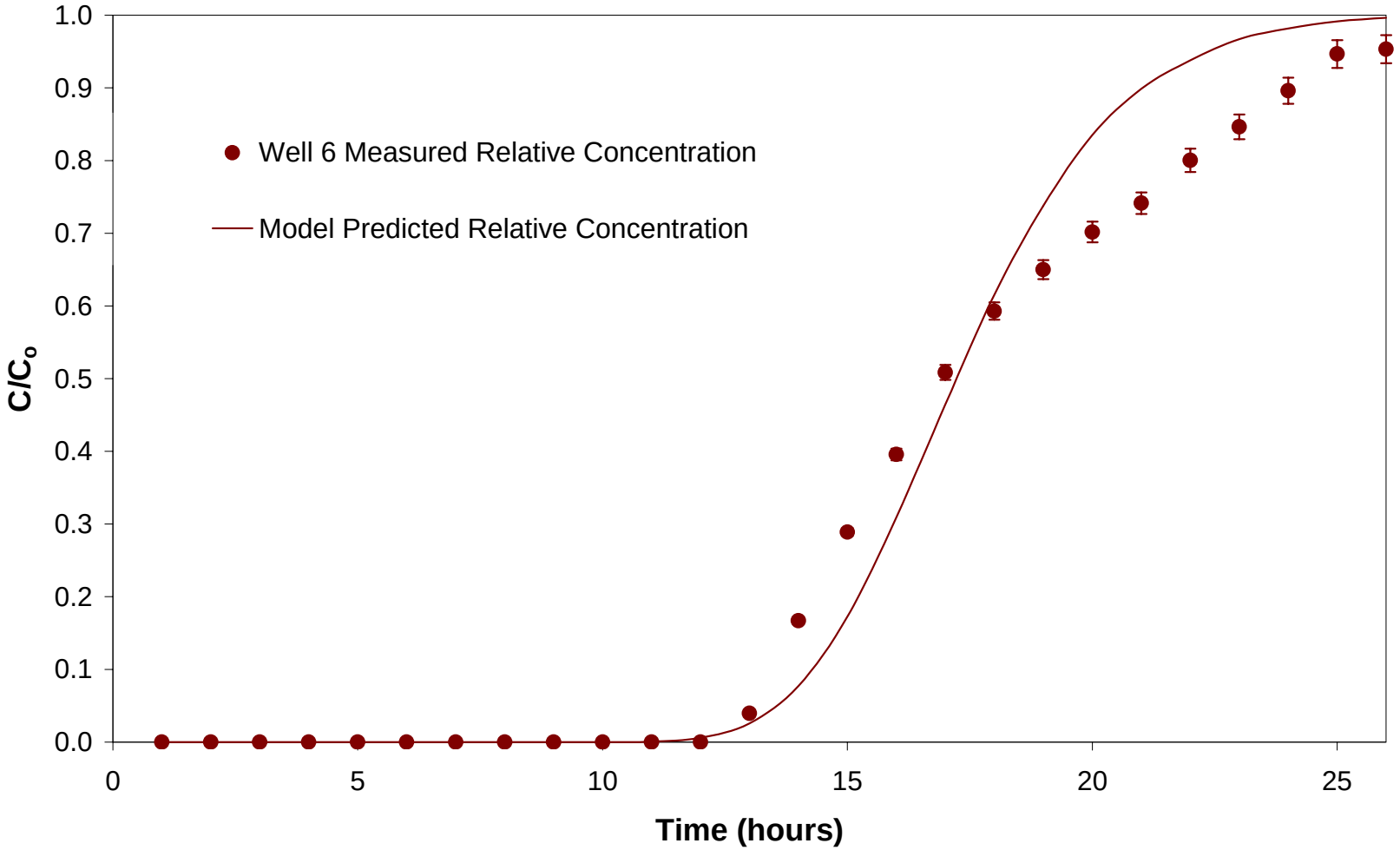

Figure D-11. Well 6 relative tracer concentration breakthrough curve including best-fit numerical model prediction.

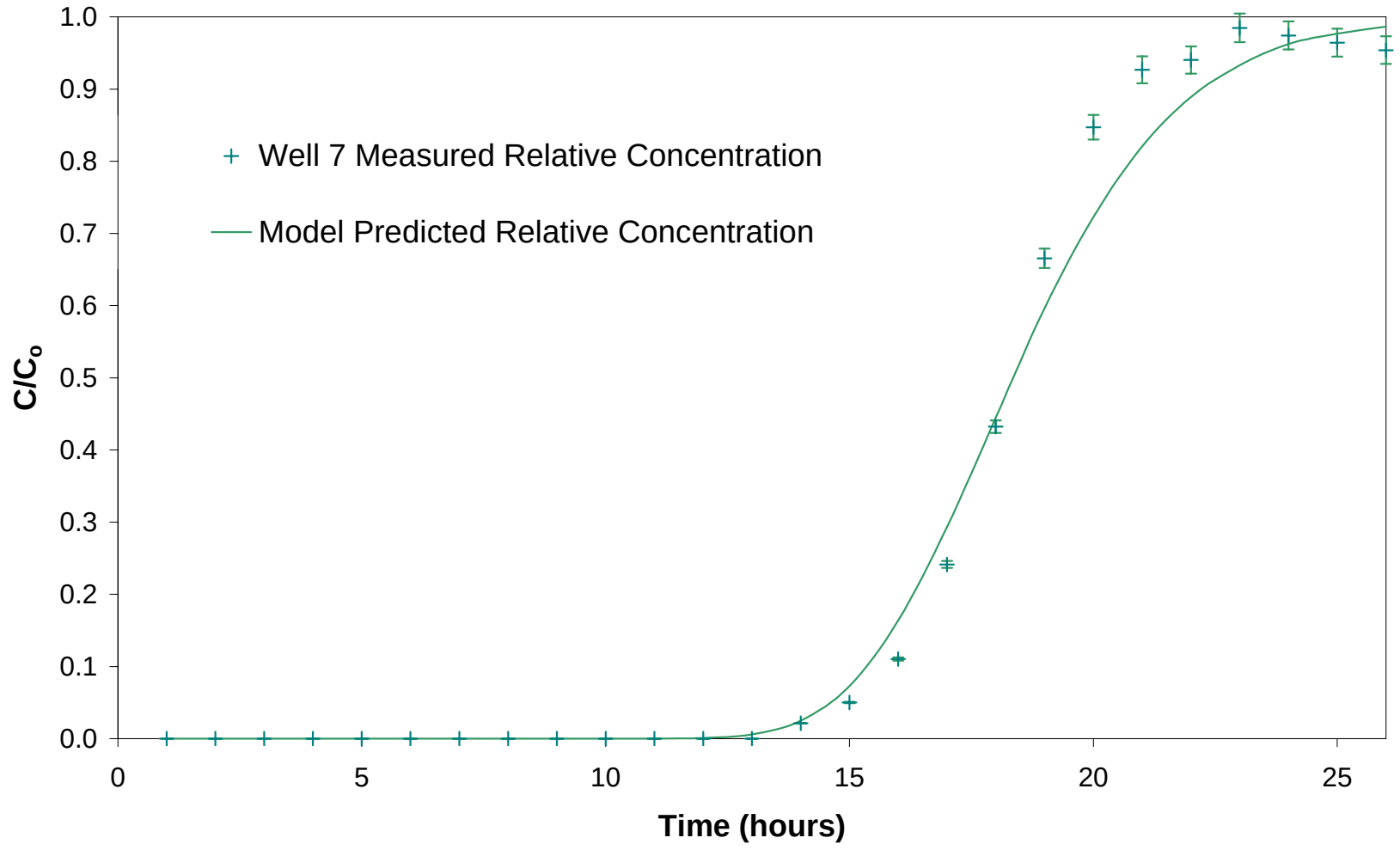

Figure D-12. Well 7 relative tracer concentration breakthrough curve including best-fit numerical model prediction.

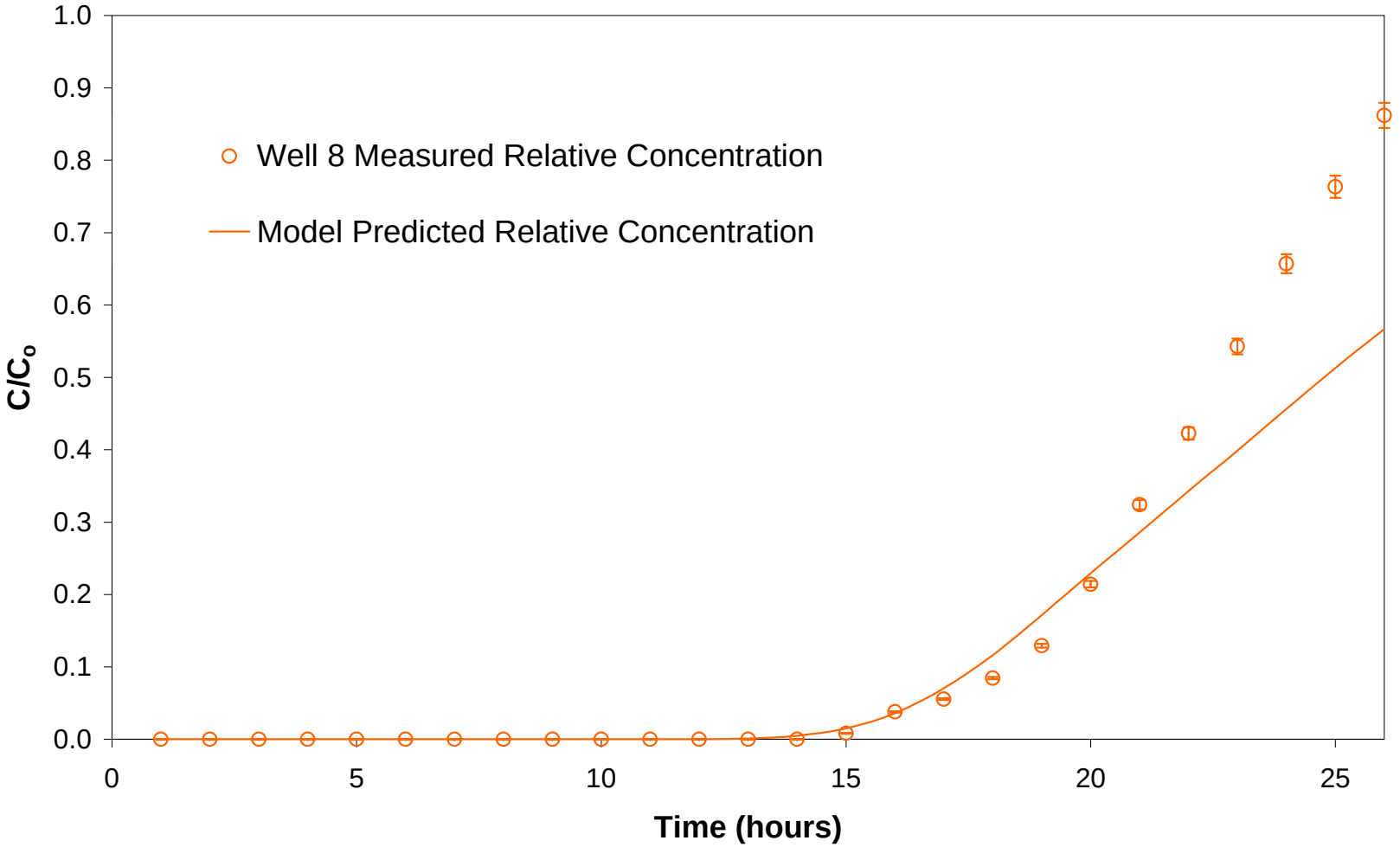

Figure D-13. Well 8 relative tracer concentration breakthrough curve including best-fit numerical model prediction.

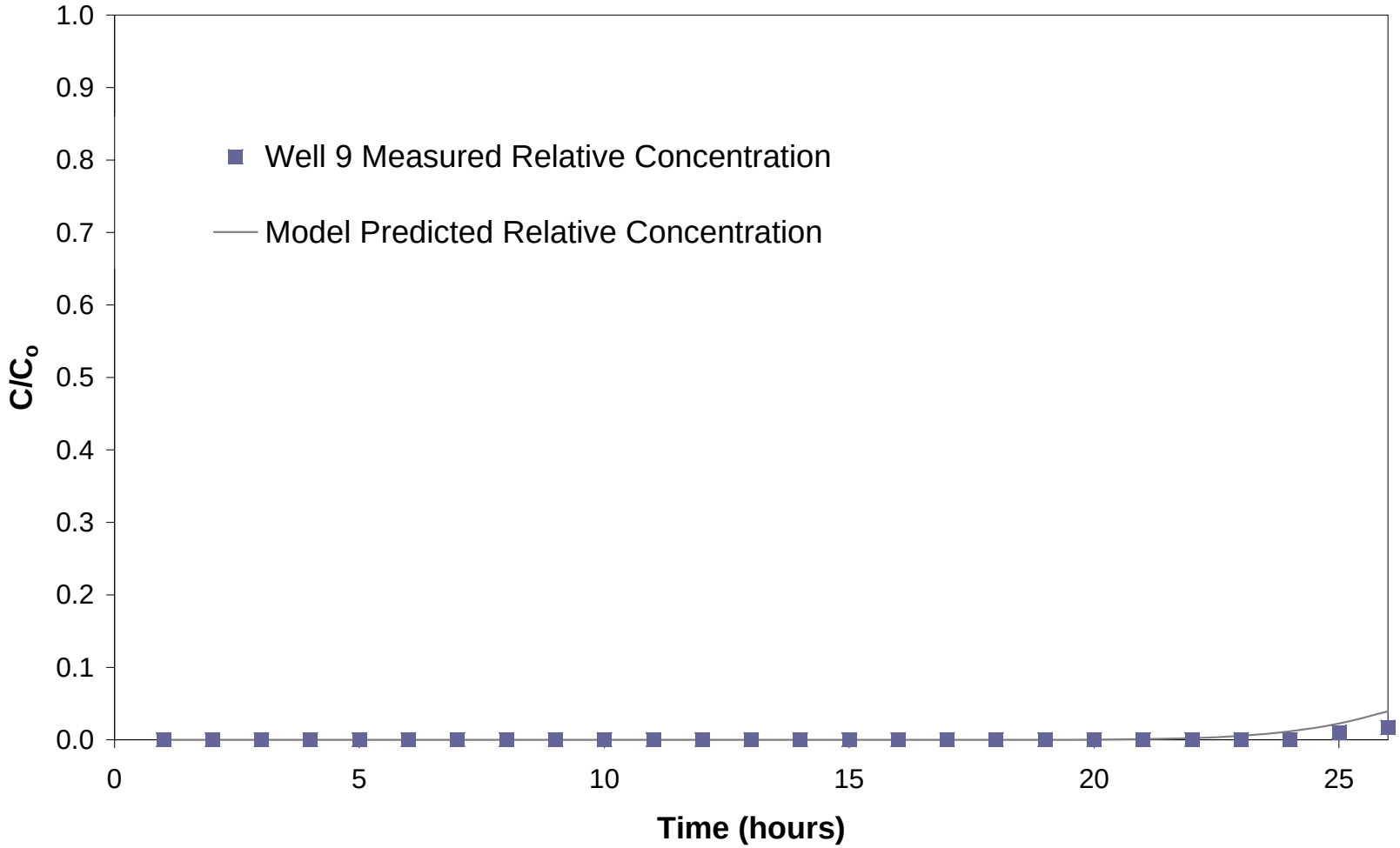

Figure D-14. Well 9 relative tracer concentration breakthrough curve including best-fit numerical model prediction.

D.3 References

Bear, J., *Dynamics of Fluids in Porous Media,* 764 pp., Dover, Mineola, N.Y., 1972.

Silliman, S.E., Laboratory study of chemical transport to wells within heterogeneous porous media, *Water Resources. Research*, *37*, 1883-1892, 2001.

APPENDIX E – NUMERICAL MODEL VERIFICATION AND PERFORMANCE MEASURES

DNAPL3D-MT was verified against a series of analytical solutions. DNAPL migration was verified against the analytical solution of McWhorter and Sunada (1990), mass transfer was verified against the analytical solution of van Genuchten and Alves (1982), and dissolved phase transport was verified against the analytical solution of Ogata (1970).

The overall performance of the model was analysed by 1) examining the mass balance of a transient DNAPL release simulation in a hypothetical two-dimensional heterogeneous bench scale apparatus; and, 2) evaluating the effects of numerical dispersion through the comparison of a number of transient DNAPL release simulations in a hypothetical two-dimensional heterogeneous bench scale apparatus.

E.1 Model Verification

E.1.1 Migration

NWP migration in DNAPL3D-MT was verified against the analytical solution for NWP migration presented by McWhorter and Sunada (1990). The analytical solution, which has been previously used to verify the migration sub-model of DNAPL3D-MT (DNAPL3D; Gerhard, 1995 and 2002), is for unidirectional displacement along a one-dimensional horizontal column containing an initially water saturated, non-deforming homogeneous porous medium and incompressible fluids that fully accounts for capillary effects.

Table E-1 presents the parameters employed in the verification simulation. Figure E-1 plots the NWP saturation profile along the length of the column at four successive times for the analytical solution and two numerical solutions. As can be seen, the accuracy of the numerical solution is a function of the domain discretisation.

The small amount of 'smearing' at the leading edge of the advancing NWP body is due to upstream weighting in the numerical model. NWP fluid mass balance in the numerical simulation never exceeded 1 x 10^{-11} m^3.

Table E-1. Parameter Values Employed During Migration Verification

Parameter	Value
Porosity (n)	0.35
Absolute Permeability (k)	5 x 10^{-11} m
Pore size Distribution Index (λ)	2
Displacement Pressure (P_d)	2000.0 Pa
Residual Wetting Phase Saturation (S_r)	0.05
Wetting Phase Viscosity (μ_w)	1 x 10^{-3} Pa.s
Nonwetting Phase Viscosity (μ_N)	0.5 x 10^{-3} Pa.s
Inflow Boundary Condition	Constant S_W = 0.525
Outflow Boundary Condition	Constant P_W = 0.0 Pa
Column Length	10 m

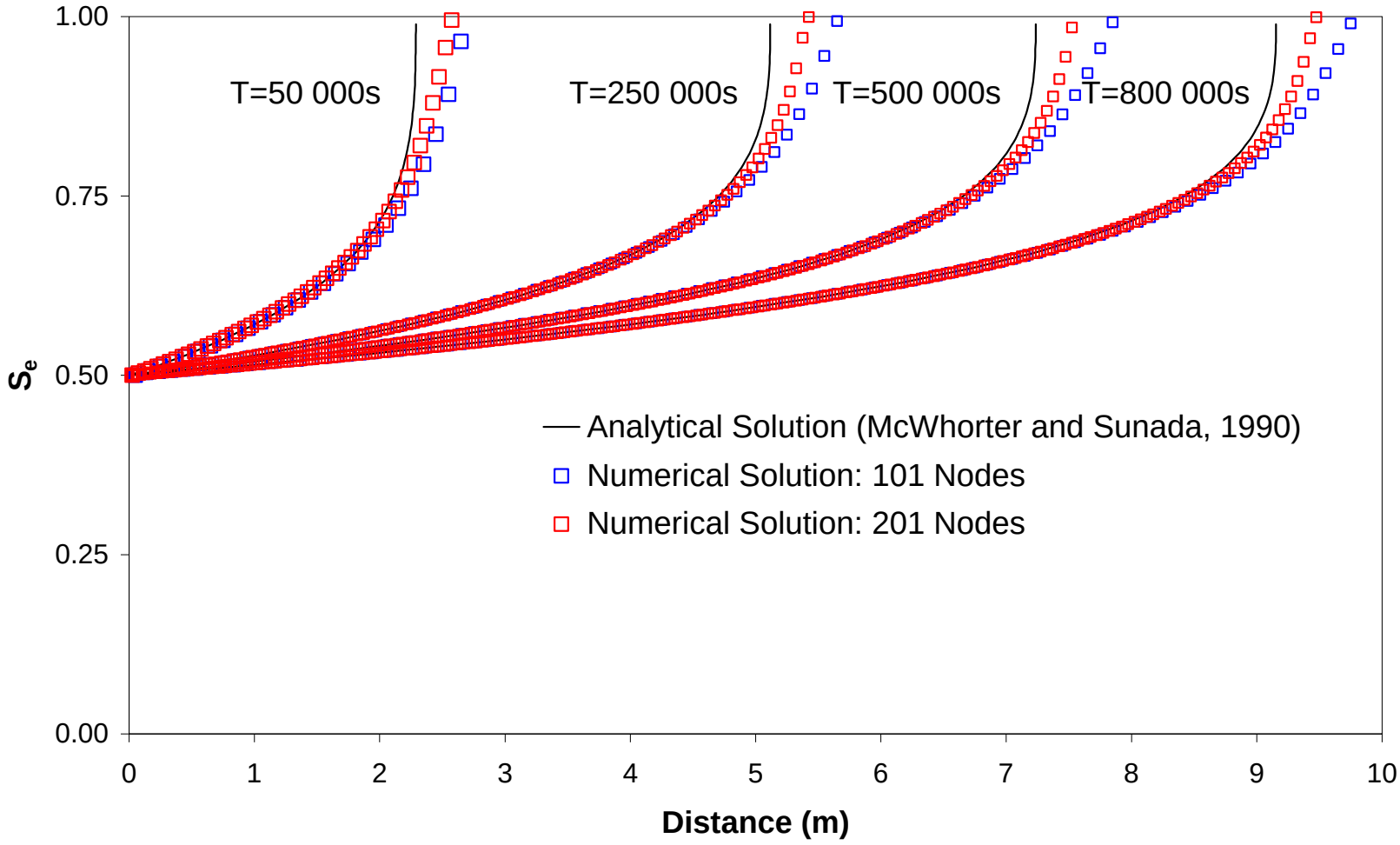

Figure E-1. Numerical and analytical solutions for one-dimensional two phase flow.

E.1.2 Mass Transfer

The mass transfer routines in DNAPL3D-MT were verified against the analytical solution of van Genuchten and Alves (1982) for advective-dispersive-reactive transport in a semi-infinite column. Following Sale and McWhorter (2001), the steady state solution of non-reactive transport through a uniform DNAPL zone can be written:

$$\frac{C(x)}{C_s} = 1 - \exp\left[\left(\frac{x}{2D_x}\right)\left(v_x - \sqrt{v_x^2 + 4D_x K_{la}}\right)\right] \qquad \text{(E-1)}$$

where C is the aqueous phase concentration, C_s is the aqueous phase solubility, x is distance along the length of the column, D_x is longitudinal dispersion, v_x is the aqueous phase velocity in the x-direction, and K_{la} is the mass transfer coefficient.

Table E-2 presents the parameters employed in the verification simulation. Figure E-2 plots the mass transfer rate, $J=K_{la}(C-C_s)$, as a function of distance along the length of the column. As can be seen, the accuracy of the numerical solution is a function of the domain discretisation.

Table E-2. Parameter Values Employed During Mass Transfer Verification

Parameter	Value
Porosity (n)	0.3
Absolute Permeability (k)	5×10^{-11} m
Solubility (C_s)	1000 mg/l
Mass Transfer Rate Coefficient (K_{la})	0.001
Dispersivity (α)	1×10^{-6} m
Diffusion Coefficient (D^*)	1×10^{-11} m^2/s
Aqueous Phase Velocity (V_w)	1×10^{-5} m/s
Wetting Phase Viscosity (μ_w)	1×10^{-3} Pa.s
Nonwetting Phase Viscosity (μ_N)	0.887×10^{-3} Pa.s
Inflow Boundary Condition	Constant $P_W = 4.26$ Pa
Outflow Boundary Condition	Constant $P_W = 0.0$ Pa
Initial Condition	$S_{NW} = 0.05$ in every node
Column Length	0.05 m

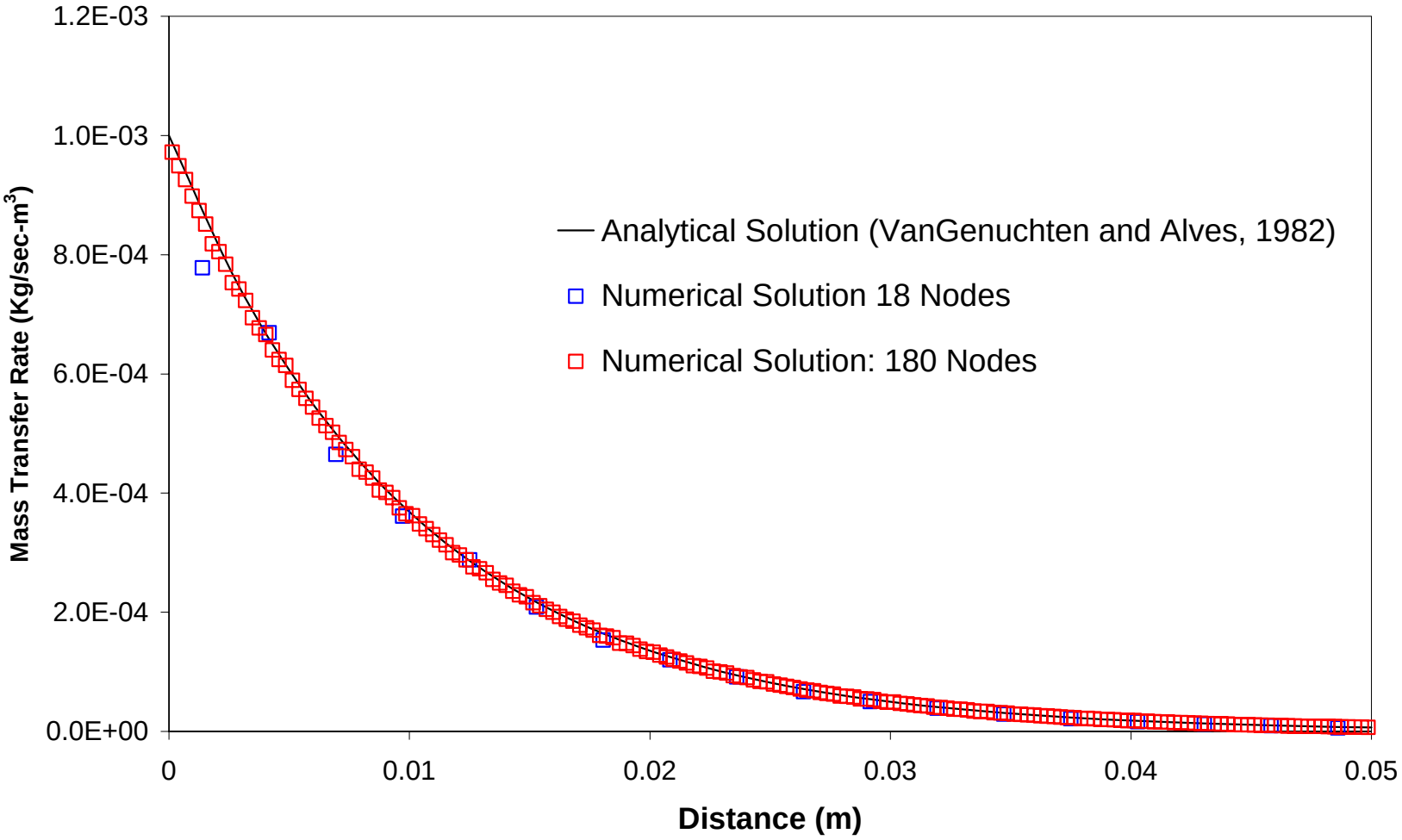

Figure E-2. Numerical and analytical solutions for mass transfer in a one-dimensional DNAPL source zone.

E.1.3 Dissolved Phase Transport

Dissolved phase transport in DNAPL3D-MT was verified against the analytical solution of Ogata (1970) for non-reactive transport in a horizontal, homogeneous, single fluid phase, one-dimensional column.

Table E-3 presents the parameters employed in the verification simulation. Figure E-3 plots dissolved phase concentration as a function of distance along the length of the column. As can be seen, the accuracy of the numerical solution is a function of the domain discretisation.

Table E-3. Parameter Values Employed During Dissolved Phase Transport Verification

Parameter	Value
Porosity (n)	0.343
Absolute Permeability (k)	4.32×10^{-6} m
Dispersivity (α)	10 m
Diffusion Coefficient (D^*)	0.0 m^2/s
Aqueous Phase Velocity (V_w)	1.235 m/day
Wetting Phase Viscosity (μ_w)	1×10^{-3} Pa.s
Inflow Boundary Condition	Constant Head = 10.1 m
Outflow Boundary Condition	Constant Head = 0.0 m
Initial Condition	Constant C =1 mg/l in first node
Column Length	1010 m

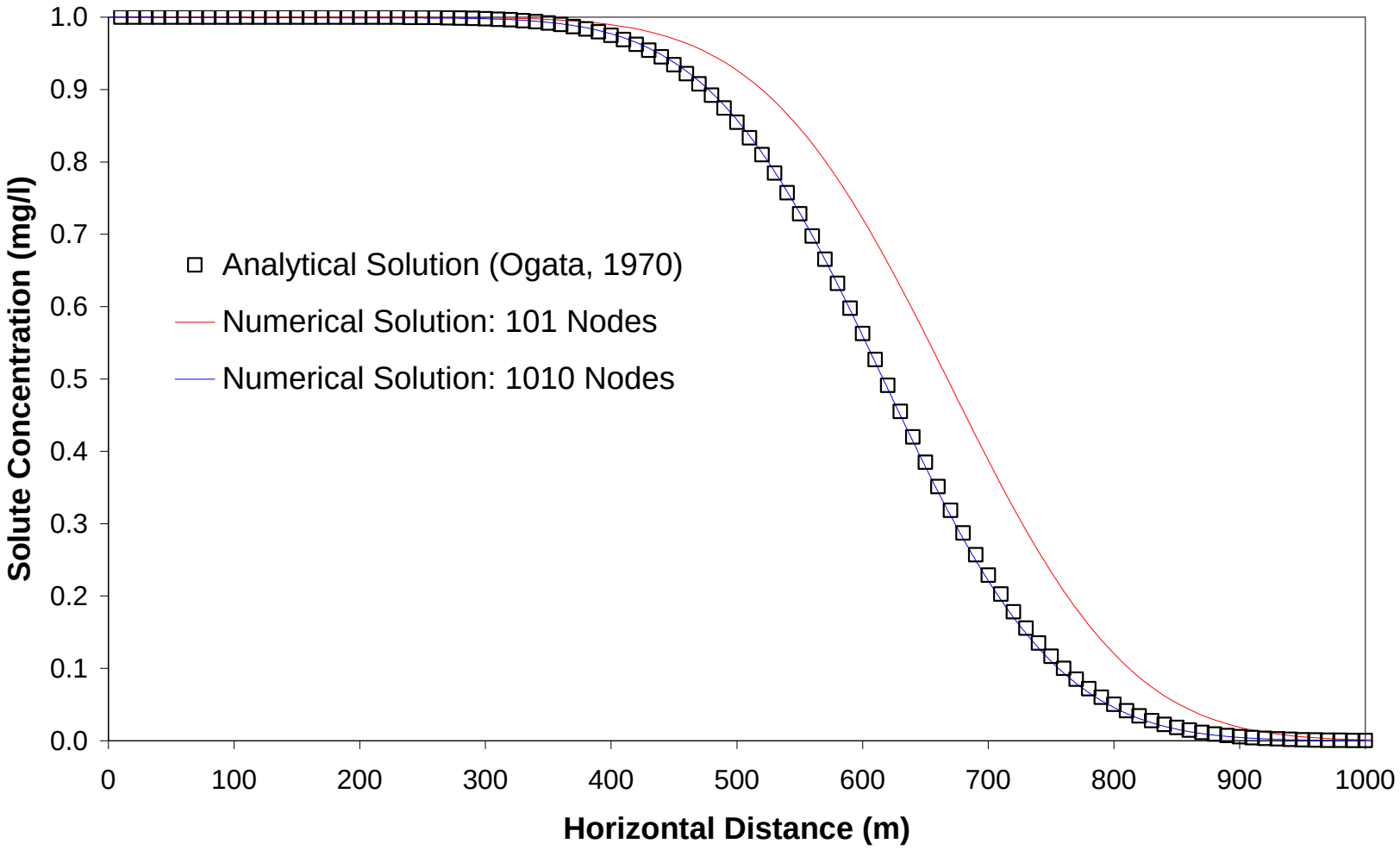

Figure E-3. Numerical and analytical solutions for dissolved phase transport in a one-dimensional column.

E.2 Model Performance

A series of DNAPL3D-MT simulations were conducted employing a hypothetical two-dimensional heterogeneous bench scale domain. Table E-4 presents the parameters used in these simulations. For each simulation, constant head boundaries were affected on the right and left boundaries of the domain to establish a hydraulic gradient of 0.01 from left to right. The lower boundary was a no-flow boundary to both the NWP and the wetting phase. A constant flux DNAPL source boundary condition, located 0.5 m from the left along the top boundary of the domain, existed for the first hour of simulation time, after which the source was turned off, and DNAPL re-distribution / dissolution was allowed to proceed until all mass had exited the downgradient (right most) boundary of the domain.

Table E-4. Numerical Model Input Parameters

Parameter	Notation	Value
Wetting phase density	ρ_W	1000 kg/m^3
Nonwetting phase density	ρ_N	1260 kg/m^3
Wetting phase viscosity	μ_W	0.001 Pa.s
Nonwetting phase viscosity	μ_N	0.000887 Pa.s
Interfacial tension	Σ	0.02 N/m
Longitudinal dispersivity	α_l	0.2 m
Transverse dispersivity	α_t	0.02 m
Molecular diffusion coefficient	D_m	5.08 x 10^{-6} m^2/s
Solubility of NWP in water	C_s	8520 mg/l
Mean ln permeability	k_i	-23.5 m^2
Variance ln permeability	k_i	0.52
Porosity	ϕ	0.32
Emergence saturation	S_W^M	0.92
Maximum NWP residual saturation (extinction saturation)	$\left(1 - S_W^X\right)$	0.09
Wetting phase residual saturation	S_r	0.13
Terminal / entry pressure ratio	κ	0.6

Brooks – Corey drainage PSD index	λ_d	6.0
Brooks - Corey imbibition PSD index	λ_i	3.0
Drainage NWP relative tortuosity exponent	τ_d	1.7
Imbibition NWP relative tortuosity exponent	τ_i	0.2
Incremental saturation target for drainage beyond emergence	ΔS_W^{*d}	0.35
Incremental saturation target for imbibition beyond extinction	ΔS_W^{*i}	0.06
Dimensionless displacement pressure	P_{CD}	0.18557
Horizontal correlation length	λ_h	0.2 m
Vertical correlation length	λ_v	0.05 m
Horizontal nodal spacing	Δx	0.02 m
Vertical nodal spacing	Δy	0.02 m
Number of nodes (horizontal)	NX	100
Number of nodes (vertical)	NY	50

E.2.1 Mass Balance

Mass balance errors are often used as a measure of the precision of a numerical simulation. Figure E-4 presents the evolution of mass within the domain throughout the entire performance evaluation simulation. This figure also presents the accumulated mass balance error as a percentage of total mass in the system, which reaches its maximum value of approximately four percent at the end of the simulation. The majority of the mass balance error is associated with the split operator (SO) routine used in DNAPL3D-MT. The SO error is proportional to the numerical time step of the discrete approximation as a result of time-lagging the transport and migration sub-models (Barry *et al.,* 2002). Time step reduction will improve mass balance precision. This is controlled in DNAPL3D-MT by limiting the amount of mass flux allowable during transport. Simulations performed in Chapter 5 were

controlled such that mass balance error was never allowed to exceed one percent of total mass in the system.

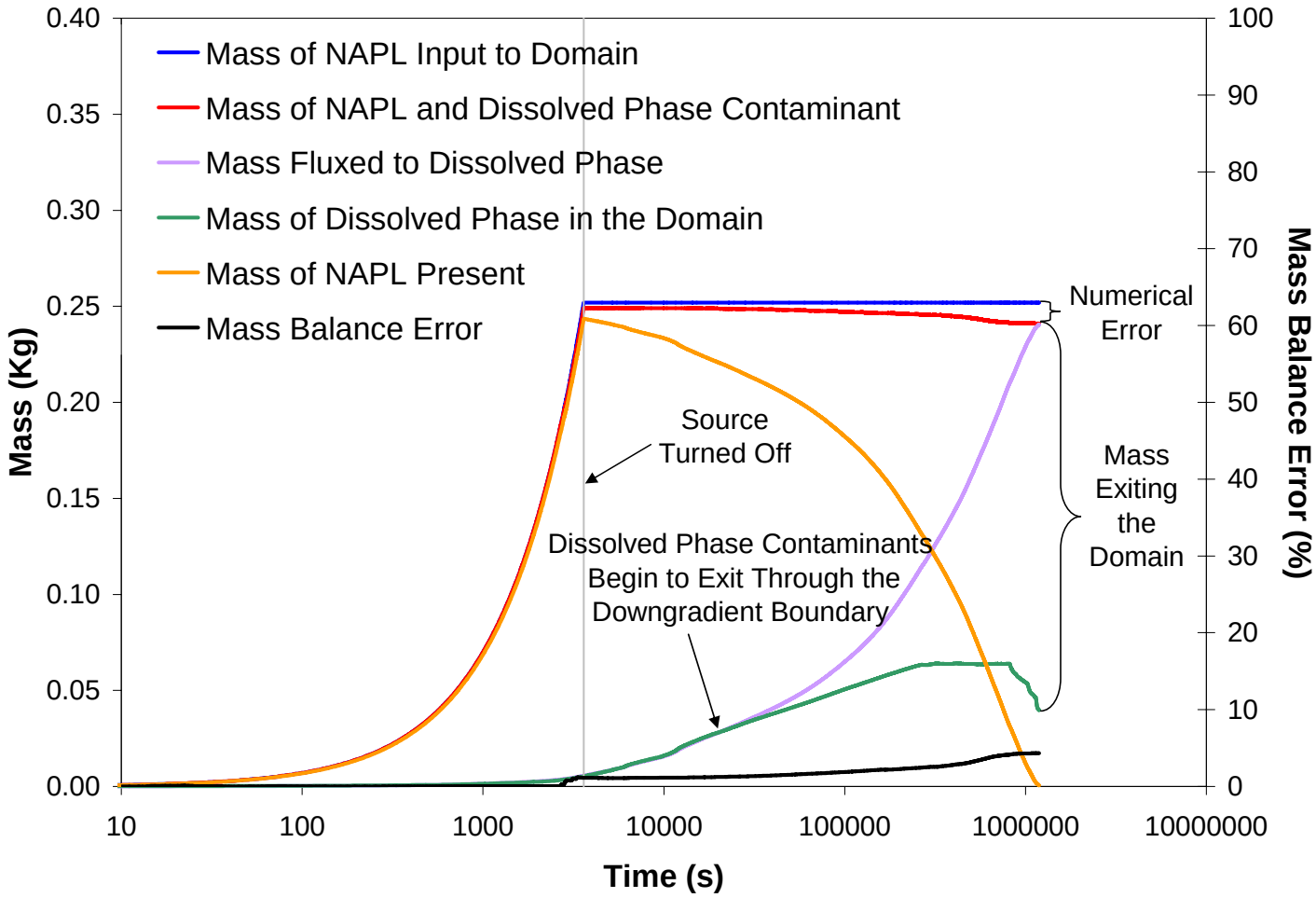

Figure E-4. Mass balance and numerical error for the test simulation.

E.2.3 Numerical Dispersion

Two tests were conducted to examine the impact of numerical dispersion on simulation results. In the first test, the results of two simulations (the base case , or performance evaluation, simulation described in Table E-4 with aqueous phase dispersion allowed, and a second simulation with aqueous phase dispersion turned off), were compared to determine if any of the dispersion observed in the base case is a result of numerical dispersion. The base case simulation exhibited mass transport upgradient of the source area as seen in Figure E-5. No mass transport upgradient of the source is seen in the second simulation (Figure E-6), indicating that the upgradient transport of mass is as a result of aqueous phase dispersion, not numerical dispersion.

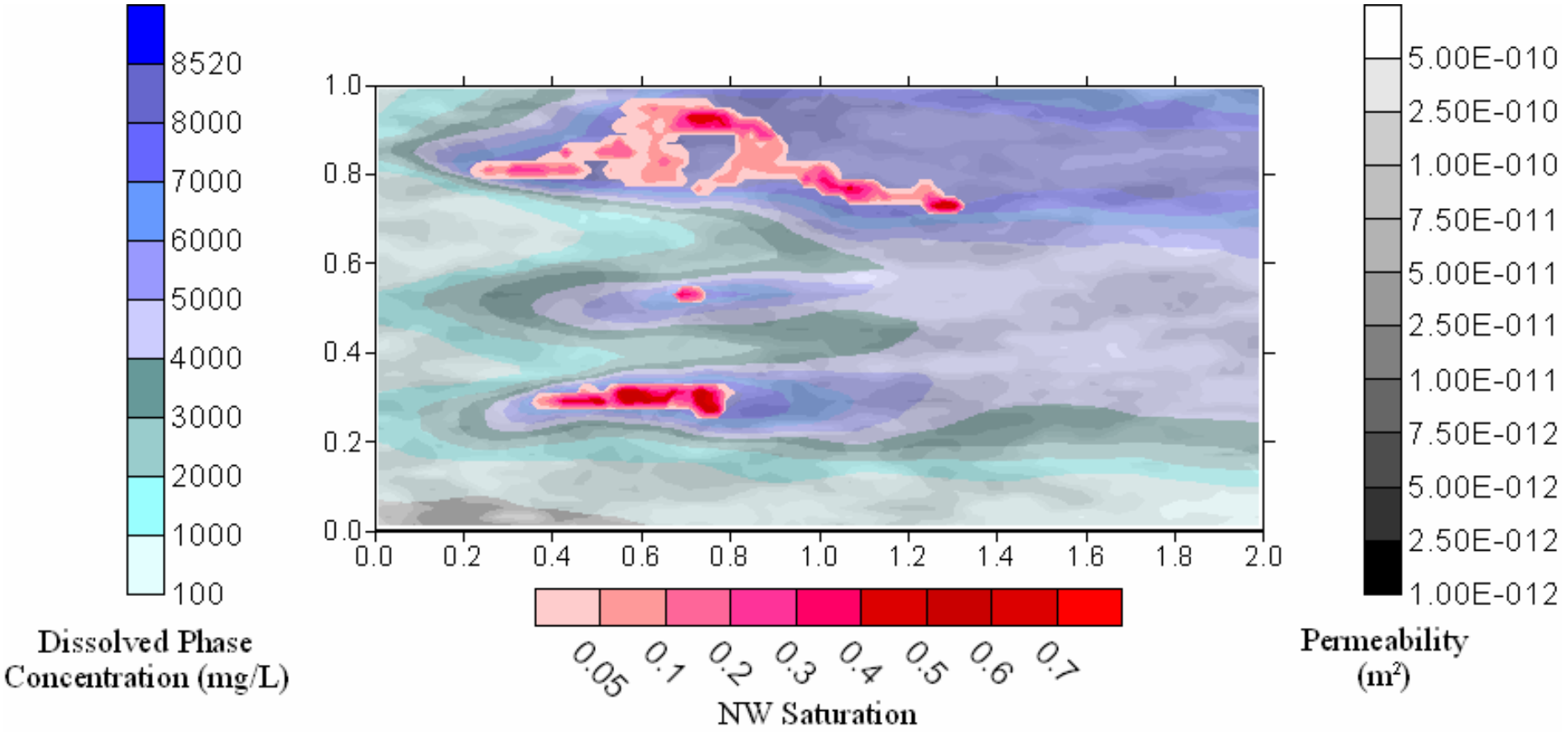

Figure E-5. Base case simulation – dispersion allowed.

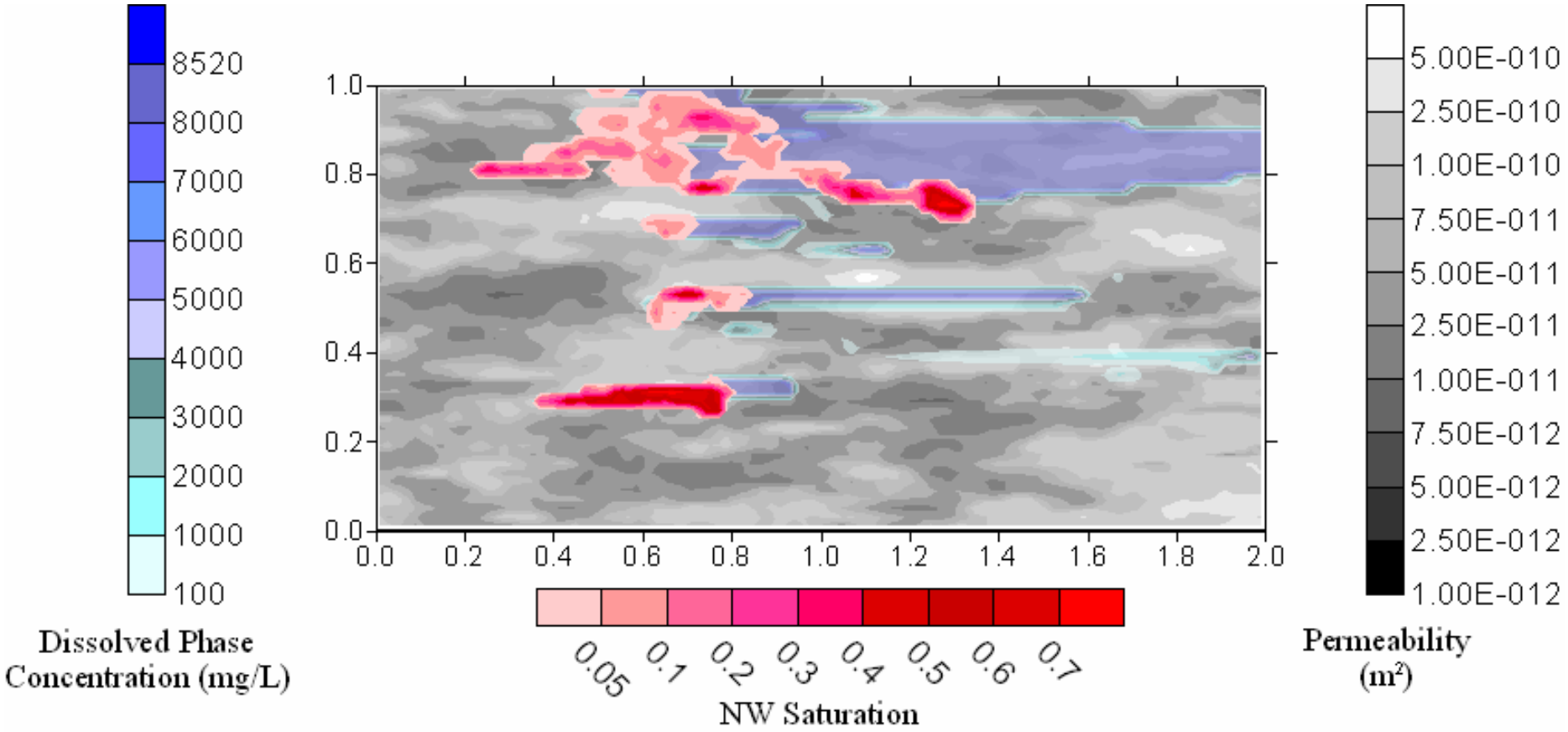

Figure E-6. Simulation results: test 1 (dispersion turned off; coarse discretisation).

The second test for numerical dispersion compared two simulations, both with aqueous phase dispersion turned off. The only difference between the two simulations during this test is that the second simulation domain is discretised at a finer scale: the domain is composed of twice as many nodes as the first simulation. Any significant difference in simulation results will likely be due to numerical dispersion. Figure E-7 is an illustration of NWP saturations and dissolved phase concentrations for the finely discretised domain. The results are very similar to those shown in Figure E-6 for a coarser discretisation. The apparent differences are likely due to contouring of the larger, more refined data set of the finely discretised domain.

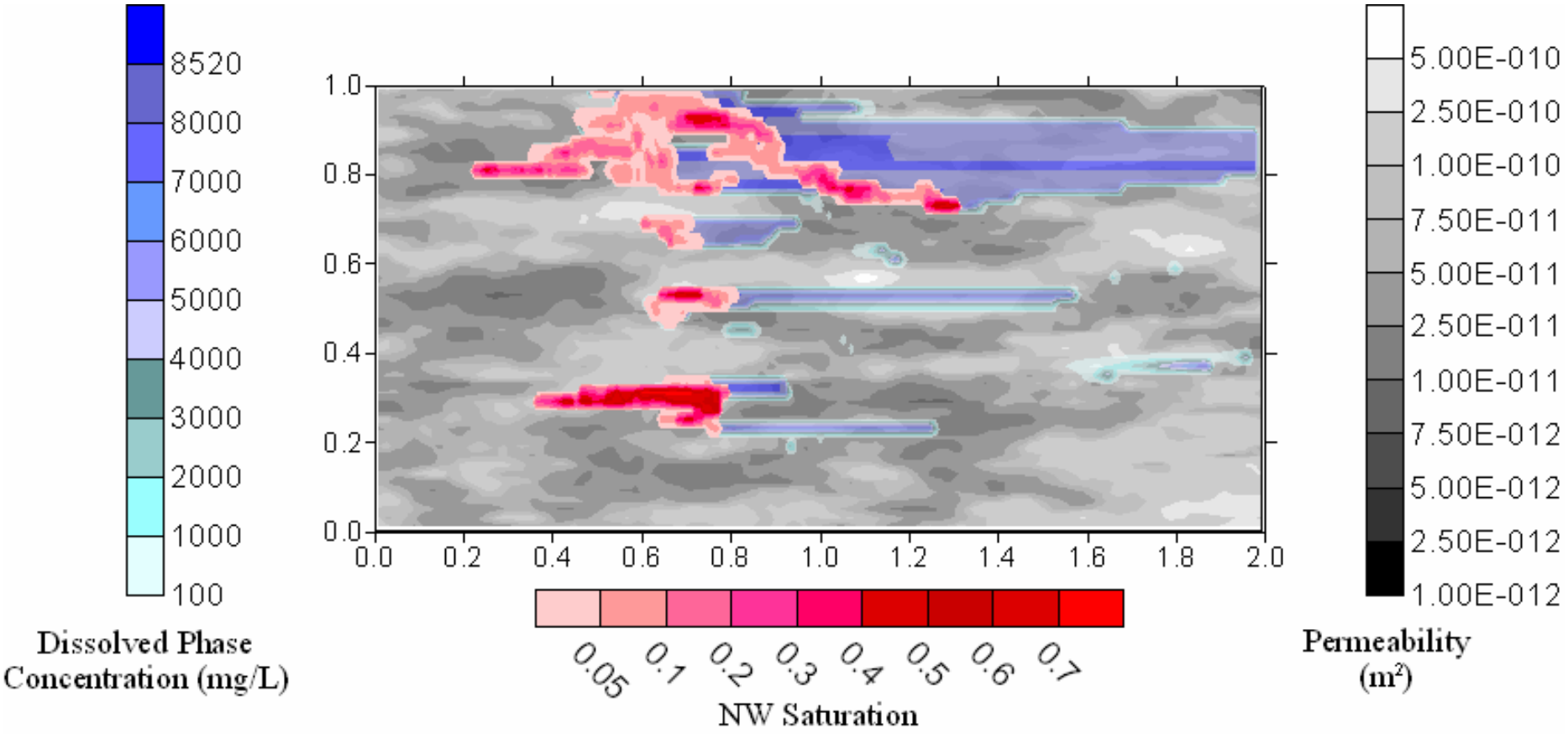

Figure E-7. Simulation results: test 2 (dispersion turned off; fine discretisation).

E.3 References

Barry, D.A., H. Prommer, C.T. Miller, P. Engesgaard, A. Brun, and C. Zheng, Modelling the fate of oxidisable organic contaminants in groundwater, *Advances in Water Resources, 25*, 945-983, 2002.

Gerhard, J.I., A three-dimensional numerical model for simulating DNAPL migration in heterogeneous porous media, Master's thesis, Queen's Univ., Kingston, Ontario, Canada, 1995.

Gerhard, J.I., DNAPL infiltration, redistribution, and immobilization in porous media, Ph.D. thesis, Queen's Univ., Kingston, Ontario, Canada, 2002.

McWhorter, D.B., and D.K. Sunada, Exact integral solutions for two-phase flow, *Water Resources Research, 23*(3), 399-414, 1990.

van Genuchten, M.T., and W.J. Alves, Analytical solution of the one-dimensional convective – dispersive solute transport equation, U.S. Department of Agriculture, Washington, D.C., 1982.

Ogata, O., A theory of dispersion in a granular medium, U.S. Geological Survey Professional Paper, *411-I*, 1970.

Sale, T.C., and D.B. McWhorter, Steady state mass transfer from single-component dense nonaqueous phase liquids in uniform flow fields, *Water Resources Research, 37*(2), 393-404, 2001.

APPENDIX F – DNAPL3D-MT SUPPLEMENTAL DESCRIPTION

Descriptions of DNAPL3D-MT can be found in Chapters 3, 4, and 5, however, this appendix will focus on the processes and information passing routines that link the sub-models of DNAPL3D-MT.

F.1 Model Description

DNAPL3D-MT is an efficient three-dimensional numerical model capable of simulating two phase flow, mass transfer and reactive transport. This model has been developed for the simulation of DNAPL infiltration and redistribution, rate limited or local equilibrium assumption (LEA) mass transfer between the non-aqueous and aqueous phases, and advective – dispersive aqueous phase transport of dissolved contaminants in heterogeneous porous media.

DNAPL3D-MT is composed of a migration sub-model (DNAPL3D: Gerhard, 1995 and 2002) and a dissolved phase transport sub-model (MT3D; Zheng, 1990) linked through a mass transfer expression. Mass transfer can be modelled according to a number of different empirically derived dissolution expressions, a local equilibrium assumption, or an explicit description of mass transfer rate using a specified mass transfer rate coefficient and an interfacial area approximation (see Chapter 5).

The linking of the sub-models follows a standard split operator (SO) approach (e.g. Barry *et al.*, 2002), whereby a time step of DNAPL migration is followed by dissolved phase transport conducted over the same time period. This time-lagging of the transport and migration sub-models introduces a source of error proportional to the numerical time step size (see Appendix E).

F.2 Sub-Model Communication

Each simulation with DNAPL3D-MT is divided into a number of time steps, the size of which (Δt) is adaptable and determined by the migration sub-model. A given time step proceeds according to the following protocol:

1. Wetting phase saturations, pressures and dissolved phase concentrations are known at time, t
2. Migration proceeds and wetting phase pressures and saturations are determined at time $t + \Delta t$.
3. Aqueous phase fluxes, saturated thicknesses and other data required by MT3D to simulate aqueous phase transport are calculated based on the presence of NWP at time $t + \Delta t$.
4. Dissolved phase concentrations at time t are determined from the distribution of NWP at time $t + \Delta t$, and the mass transfer model selected.
5. Flow field data from *step 3*, and the 'initial' concentrations at time t calculated in *step 4* are sent to the transport sub-model.
6. Transport (a complete MT3D simulation, further sub-divided by 'transport' steps) proceeds and dissolved phase concentrations are determined at time, $t + \Delta t$.
7. The amount of mass fluxed from the NWP to the wetting phase is calculated, and if:
    a. the mass flux at any given node exceeds a specified tolerance value, the time step size (Δt) is reduced and *steps 1* through *7* are repeated.

b. the amount of mass fluxed from all nodes is less than the specified tolerance, NWP pressures and saturations and wetting phase concentrations at time $t + \Delta t$ are recorded and set to the initial conditions for the next time step.

8. The current simulation time t is set to $t + \Delta t$.
9. *Steps 1* through *8* are repeated until t equals the total simulation time.

As noted in *steps 3* and *4* above, the 'initial' concentrations for transport during the time period between t and $t + \Delta t$ are based on the distribution of NWP at time $t + \Delta t$. While this may seem counter-intuitive, 'initial' concentrations for this time period were not calculated for the NWP distribution at time t because it would be possible, under this scenario, for NWP to be present at nodes containing zero aqueous phase concentrations (even if a LEA mass transfer model were being used). The differences between the two scenarios are insignificant (as the largest time steps correspond to times when DNAPL migration is minimal), except that the alternative approach would give rise to the occurrence of an impossible physical situation.

F.3 Modifications to Sub-Models

F.3.1 DNAPL3D

DNAPL3D as a sub-model of DNAPL3D-MT was modified to allow for:

a. The inclusion of variable NWP relative permeability functions;
b. The calculation of directional Darcy fluxes;
c. The determination of mass transfer rates and the resulting aqueous phase concentrations;
d. The addition of MT3D for simulating dissolved phase transport; and
e. The addition of MODPATH for particle tracking and flow path line determination.

These modifications took the form of numerous original subroutines added to the DNAPL3D code.

F.3.2 MT3D

MT3D as a sub-model of DNAPL3D-MT was modified to allow for:

f. Translation of data between the different coordinate systems of the two sub-models;

g. The input of DNAPL3D calculated Darcy fluxes, constant head fluxes, saturated thicknesses, variable porous media property values, and initial concentrations, circumventing the MT3D input files;

h. The calculation of mass fluxes and mass balances;

i. The output of aqueous phase concentrations at time intervals specified by the migration model; and,

j. The inclusion of variable porous media properties.

Modifications to MT3D were kept to a minimum where possible, to allow for the relatively simple addition of related programs such as RT3D (Reactive Transport in three-dimensions, Clement *et al.,* 1998).

F.4 References

Barry, D.A., H. Prommer, C.T. Miller, P. Engesgaard, A. Brun, and C. Zheng, Modelling the fate of oxidisable organic contaminants in groundwater, *Advances in Water Resources, 25*, 945-983, 2002.

Clement, T.P., Y. Sun, B.S. Hooker, and J.N Petersen, Modelling multispecies reactive transport in ground water, *Ground Water Monitoring and Remediation, 18*(2), 79-92, 1998.

Gerhard, J.I., A three-dimensional numerical model for simulating DNAPL migration in heterogeneous porous media, Master's thesis, Queen's Univ., Kingston, Ontario, Canada, 1995.

Gerhard, J.I., DNAPL infiltration, redistribution, and immobilization in porous media, Ph.D., thesis, Queen's Univ., Kingston, Ontario, Canada, 2002.

Zheng, C., MT3D, *USEPA Report*, 1990.

APPENDIX G - SUPPLEMENTAL STUDY: Sensitivity of Predicted DNAPL Source Zone Longevity to Mass Transfer Correlation Model

The following paper was published in *Geoenvironmental Engineering: Integrated Management of Groundwater and Contaminated Land* (ref. Grant and Gerhard, 2004). While beyond the scope of this thesis, this supplementary work was integral to the authors study of rate limited mass transfer and is included in its entirety below:

Sensitivity of Predicted DNAPL Source Zone Longevity to Mass Transfer Correlation Model

GAVIN P. GRANT and JASON I. GERHARD
Institute for Infrastructure and Environment, The University of Edinburgh, Edinburgh, UK.

ABSTRACT

Despite significant research into the topic for 20 years, the interrelationship of DNAPL source zones and downgradient aqueous-phase contaminant concentrations is poorly understood. A number of experimentally derived correlation models have been published to describe mass transfer from the non-aqueous to the dissolved phases. This study examines the sensitivity of DNAPL migration, dissolution and transport simulations in homogeneous and heterogeneous porous media to the choice of mass transfer expression using six published, experimentally derived correlation models. One-dimensional simulations illustrate the sensitivity of predicted effluent concentrations to the employed dissolution model. This sensitivity is observable in both the magnitude of dissolved phase concentrations, the length of time during which contaminated groundwater effluxes through the column, and the pattern of dissolved phase concentrations observed over time. Two-dimensional simulations of a realistic DNAPL release into a heterogeneous porous medium illustrate that the dissolution model employed significantly impacts predicted behaviour. Source zone life spans were observed to vary by greater than an order of magnitude, and maximum observed aqueous-phase concentrations were observed to vary from the solubility limit to less than one-third that value. This study suggests that attempting to infer DNAPL source configuration from downgradient concentrations or to predict site remediation times remains uncertain until such time as a comprehensive mass-transfer expression is derived and validated.

INTRODUCTION

Groundwater contamination is present throughout the industrialised world. The most ubiquitous class of organic compounds polluting groundwater are Dense Non-Aqueous Phase Liquids (DNAPLs), which includes polychlorinated biphenyl (PCB) oils, creosote, coal tar, and chlorinated solvents (Pankow and Cherry, 1996).

A conceptual model of groundwater contamination by DNAPLs is presented by Kueper and Frind (1991a). Following the release of DNAPLs at ground surface, DNAPLs *migrate* in intricate patterns through the subsurface as a separate fluid, creating a complex *source zone* composed of vertical trails of immobile *residual* blobs and horizontal accumulations of non-aqueous phase *pools*. *Dissolution* of both DNAPL residual and pools results in the evolution of dissolved-phase contaminant plumes. *Transport* of toxic, dissolved-phase constituents to environmentally sensitive receptors is the primary hazard associated with DNAPL contamination scenarios.

Numerical modelling is an effective tool for designing laboratory and field-scale experiments and can be used to perform sensitivity and uncertainty analysis in the study of DNAPL migration and remediation. Numerous multiphase flow models have been developed for use in a contaminant hydrogeology context including Lujan (1985), Faust (1985), Abriola and Pinder (1985a,b), Osborne and Sykes (1986), Kuppasamy *et al.,* (1987), Forsyth (1988), Faust *et al.,* (1989), Kueper and Frind (1991a,b), Gerhard (1995), and others. Most such models account for the migration but not the dissolution of the non-aqueous phase. Transport of aqueous-phase contaminants dissolved in groundwater is described by the Advection-Dispersion equation. Numerous transport models solving the Advection-Dispersion equation have been developed, including MT3D (Modular 3-Dimensional Transport, Zheng, 1990). However, the majority of these models do not incorporate the effects of immobile DNAPL presence or transient DNAPL flow. Some numerical models are capable of simulating multiphase flow, dissolution and contaminant transport. These include *compositional models* such as Corapcioglu and Baehr (1987), Forsyth and Shao (1991), Sleep and Sykes (1993), Huyakorn *et al.,* (1994a), Slough *et al.* (1999) and Reynolds and Kueper (2001) and decoupled flow and transport models such as Reeves and Abriola (1988). With the exception of Reeves and Abriola (1988), these

models have extremely large data requirements and are therefore of limited use for simulating field-scale scenarios.

To simulate DNAPL dissolution, numerical models rely on mathematical representations of the complex physio-chemical phenomena involved. Numerous experiments have been conducted to examine these phenomena (Miller *et al.,* 1990; Powers *et al.,* 1992; Imhoff *et al.,* 1994; Powers *et al.,* 1994; Saba and Illangasekare 2000; Nambi and Powers, 2003). Correlation models have been developed using data from these experiments to describe the process of mass transfer from the non-aqueous phase to the aqueous phase.

This study examines the sensitivity of DNAPL migration, dissolution and transport simulations in homogeneous and heterogeneous porous media to the choice of mass transfer expression using six published, experimentally derived correlation models.

NUMERICAL MODEL

A split operator (SO) approach (Barry *et al.*, 2002) was used to integrate the two phase flow model DNAPL3D (a 3-Dimsneional, 2-Phase flow model) developed by Gerhard (1995, 2001) with the dissolved-phase transport code MT3D (Zheng, 1990). The computationally efficient numerical model developed - capable of simulating two phase flow, dissolution, and dissolved-phase transport - will be referred to as DNAPL3D-MT (DNAPL3D with multiple species transport). The migration and transport sub-models are linked through a mass transfer expression, which takes one of three forms: (1) no dissolution, (2) equilibrium dissolution (i.e., mass is transferred from the non-aqueous phase to the aqueous phase instantaneously at the solubility limit of the DNAPL) and, (3) rate-limited mass transfer.

Rate-Limited Mass Transfer

A variety of models exist to describe mass transfer between phases in a multiphase system (Miller, 1990). Most assume that the rate of transfer is a function of a driving force and the interfacial area between the two phases. The mass transfer relationship is often expressed as:

$$J = k_{la} a_{na} (C_s - C) = K (C_s - C) \quad (1)$$

where J is the solute mass flux from the non-aqueous phase to the aqueous phase, k_{la} is an average mass transfer coefficient for the DNAPL-water surface, a_{na} is the interfacial area between the DNAPL and the aqueous phase, C_s is the aqueous phase solubility concentration, and C is the aqueous phase solute concentration in the bulk solution. To avoid the need to quantify entrapped DNAPL geometry, a lumped mass transfer coefficient ($K=k_{la}a_{na}$) is often used in equation (1) (Miller *et al.*, 1990). The value of K, incorporating the unspecified specific surface area between phases, is typically determined from laboratory measurements that employ a modified Sherwood number:

$$Sh = Kd_p^2 D_m^{-1} \tag{2}$$

where Sh is the Sherwood number, d_p [L] is the mean particle diameter, and D_m [L^2T^{-1}]is the molecular diffusion coefficient for the soluble constituent (Miller *et al.*, 1990). Experimental determinations of the Sherwood number are usually presented in the form of traditional dimensionless groupings such as Schmidt, Peclet, and Reynolds numbers (Sale and McWhorter, 2001).

Table 1 presents six experimentally derived correlation models and the conditions under which they are valid. In general, the expressions are only valid for residual source zones and small groundwater velocities. However, the applicability of the expressions is further limited by the experimental conditions under which they were derived. For example, each expression assumes an immobile DNAPL phase. With the exception of Saba and Illangasekare (2000) and Nambi and Powers (2003), the expressions neglect to account for the effects of flow dimensionality. With the exception of Imhoff *et al.* (1994) and Saba and Illangasekare (2000), the expressions ignore the fact that the average value of K for a source zone decreases with an increase in the length of the source zone, thus, limiting the validity of the expression to source zones with the same lengths as the laboratory columns from which they were derived (Saba and Illangasekare, 2000). With the exception of Nambi and Powers (2003), the expressions were developed from experiments conducted in homogeneous porous media. However, recent studies have indicated that the choice of dissolution rate correlation has greater influence on DNAPL dissolution in heterogeneous systems than uncertainty in DNAPL distribution or spatial heterogeneity (Unger *et al,* 1998).

Table 1. Dimensionless Sherwood Number Correlations for Interphase Mass Transfer

Exp.System	Correlation	Valid Conditions	Reference
1-D NAPL	$Sh = 12\,\mathrm{Re}'^{0.75}\,\theta_n^{0.6} Sc^{0.5}$	$0.016<\theta_n<0.07$ $0.001<Re'<0.1$ (steady state dissolution)	Miller *et al.*, 1990
1-D NAPL	$Sh = 57.7\,\mathrm{Re}^{0.61}\, d_{50}^{0.64} U_i^{0.41}$	θ_n = constant $0.012<Re<0.2$	Powers *et al.*, 1992
1-D NAPL	$Sh = 340\theta_n^{0.87}\,\mathrm{Re}'^{0.71}\left(\frac{d_{50}}{x}\right)^{0.31}$	$0<\theta_n<0.04$ $0.0012<Re'<0.021$ $1.4<x/d_p<180$	Imhoff *et al.*, 1994
1-D NAPL	$Sh = 4.13\,\mathrm{Re}'^{0.598}\,\delta^{0.673} U_i^{0.369}\left(\frac{\theta_n}{\theta_{n0}}\right)^{\varphi}$	$0.015<Re<0.23$	Powers *et al.*, 1994
2-D NAPL	$Sh = 11.34\,\mathrm{Re}'^{0.2767}\, Sc^{0.33}\left(\frac{d_{50}\theta_n}{\tau L}\right)^{1.037}$		Saba and Illangasekare, 2000
2-D NAPL	$Sh = 37.15\,\mathrm{Re}'^{0.61}\, S_n^{1.24}$	$0.1<S_n<0.35$ $0.018<Re<0.134$	Nambi and Powers, 2003

Definition of terms and variables are as follows: 1-D, one-dimensional; d_{50}, mean particle diameter [L]; *Re*, Reynolds number; *Sh*, Sherwood number; *Sc*, Schmidt number; U_I, uniformity index of the porous media; θ_n, volumetric content of DNAPL; θ_{n0}, initial volumetric NAPL content; *x*, distance from the dissolution cell entrance [L] for Imhoff *et al,*(1994); δ, normalised grain size ($=d_{50}/0.05cm$); ψ, fitting parameter which can be correlated to grain size distribution for Powers *et al.* (1994); τ, tortuosity of sand; *L*, path length inside a contaminated zone [L]; and, S_n, DNAPL saturation.

Numerical Simulations

The first suite of numerical simulations investigates the influence of correlation model selection on source zone life span and downgradient dissolved-phase concentrations in a one-dimensional (1-D) horizontal column. The column was 5 cm long, divided evenly into 18 nodes, characterised by a homogeneous sand (absolute permeability = 5.0×10^{-11}, porosity = 0.3). The first two nodes were assigned an initial amount of residual DNAPL ($S_n^{node\ 1} = 0.09$, $S_n^{node\ 2} = 0.05$) while constant head boundary conditions were employed to give a hydraulic gradient of 8.77×10^{-3} across the column.

The second suite of numerical simulations employed a two-dimensional heterogeneous porous medium to further examine the influence of correlation model selection on source zone life span and downgradient dissolved-phase concentrations. The simulation domain (representing a laboratory flow cell) was 2m wide, by 1m high, by 0.02m deep discretised into 5000 0.02m x 0.02m nodes. The top and bottom boundaries of the domain were no flow boundaries, and the left and right boundaries were constant head boundaries to give a hydraulic gradient of 0.01 across the domain. A 1,2-DCE constant flux source (200 ml input in 1 hour) was placed along the top boundary, 0.5m from the left end of the domain. The source was turned off after 1 hour and the simulation was allowed to continue until the source zone was completely dissolved. The heterogeneous permeability field employed is spatially correlated both horizontally (20 cm) and vertically (4 cm) with a mean ln(permeability) = -23.47 m^2 (variance = 0.4714 m^2). The porous medium has a porosity of 0.32 and has constant relative permeability parameters throughout: residual wetting saturation = 0.13; emergence wetting saturation = 0.92; ratio of terminal to displacement pressure = 0.6; maximum DNAPL relative permeability = 0.85; maximum residual DNAPL saturation = 0.09: main drainage DNAPL relative tortuosity exponent = 1.70: and, an imbibition DNAPL relative tortuosity exponent = 0.20 (Gerhard and Kueper, 2003a,b). Other parameters used in the simulations include: mean particle diameter = 0.5 cm; uniformity index = 1.0; Leverett dimensionless pressure coefficient = 0.18557; '*x*' for Imhoff *et al.* (1994) = 0.02m; and, *'Ψ'* for Powers *et al.* (1994) = 0.667.

Throughout this study, the DNAPL considered was dichloroethane (1,2-DCE), a common chlorinated solvent. 1,2-DCE has a density of 1260 Kg/m^3, a viscosity of 0.000887 Pa.s, solubility of 8520 mg/L, a free diffusion coefficient (in water) of $9.908x10^{-10}$ m^2/s, and an interfacial tension with water of 0.02 N/m.

For each of the 1-D and the 2-D investigations, seven simulations were conducted. Each of the first six simulations employed one of the correlation expressions presented in Table 1 for all mass transfer phenomena occurring during that simulation. The seventh simulation in each suite employed the equilibrium assumption. It is acknowledged that a single relationship may not be appropriate for all mass transfer situations within a realistic DNAPL source zone. Nevertheless, more comprehensive correlation models do not exist; furthermore, employing this assumption permits investigation into the sensitivity of predicted downgradient dissolved phase concentrations to the mass transfer function employed in the source zone.

RESULTS AND ANALYSIS

One-Dimensional Breakthrough Curve Analysis

Figure 1 is a plot of relative 1,2-DCE concentrations vs. time (logarithmic scale) at the downgradient end of the 1-D homogeneous column. This figure clearly illustrates the variability in maximum dissolved phase concentration, and length of time during which contaminated groundwater effluxes through the column, between the correlation models. The equilibrium mass transfer assumption is the only simulation that results in greater than 8% of the solubility limit at the downgradient end of the column; the dissolved phase concentrations for this simulation approach the solubility limit (8520 mg/L) of 1,2-DCE while the maximum concentration observed for any of the rate-limited mass transfer models is approximately 610 mg/L (using Miller *et al.,* 1990). For the equilibrium assumption simulation, the source has been completely dissolved and all contaminated groundwater has exited through the downgradient boundary within approximately 2.8 hours. However, the rate-limited mass transfer models all require significantly more time to achieve the same affect, with the model of Nambi and Powers (2003) requiring the longest amount of time; in excess of 1,000 hours (approximately 42 days).

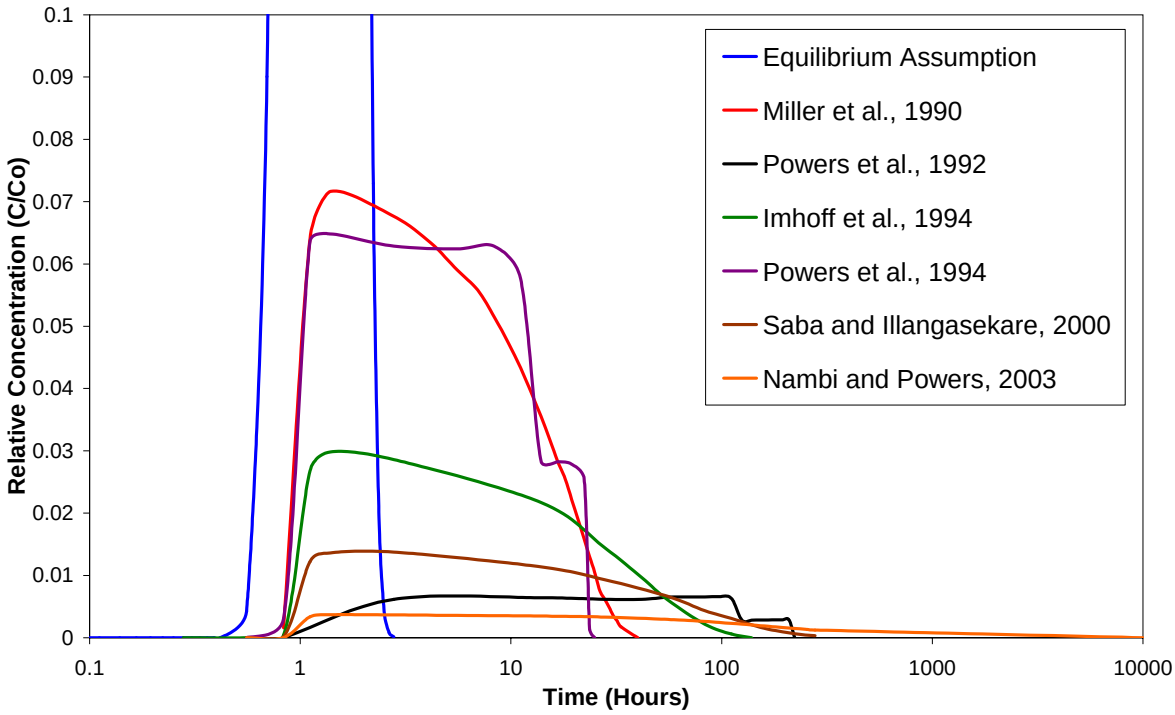

Figure 1. Simulated breakthrough curve comparison at the downgradient boundary of the one-dimensional model domain from emplaced residual DNAPL source.

Figure 1 reveals that the maximum effluent concentration for all simulations exits the domain after approximately 1.4 hours with the exception of Powers *et al.* (1992). In that latter, the maximum occurs near the end of the simulation, just after the DNAPL has completely dissolved, because this function is independent of DNAPL saturation. This correlation model exhibits an increase in mass transfer rate constant with a decrease in DNAPL saturation as a result of an increase aqueous phase velocity. The remaining correlation models were derived under non-steady state conditions (with respect to DNAPL saturation) and therefore account for the observed decrease in mass transfer rate constant as DNAPL saturations decrease. As a result, the BTC's show an increase in effluent concentration to a maximum at early time, followed by a slow decline or 'tailing' of effluent concentrations until the source zone has been completely dissolved.

Another feature observable in two of the plots (Power *et al.,* 1992 and Powers *et al.,* 1994) is a step-wise decrease in concentration near the end of curve. This feature is again a function of correlation model formulation and appears as the DNAPL input in

Node 2 of the model domain is completely dissolved prior to complete dissolution of the DNAPL input in Node 1 of the domain.

Transient DNAPL Release in a Two-Dimensional Heterogeneous Porous Medium

Figure 2 was generated from data collected from the simulation employing the equilibrium assumption mass-transfer model. This figure shows the DNAPL source zone after 10 hours of migration, and illustrates the variability of aqueous phase concentrations throughout the domain.

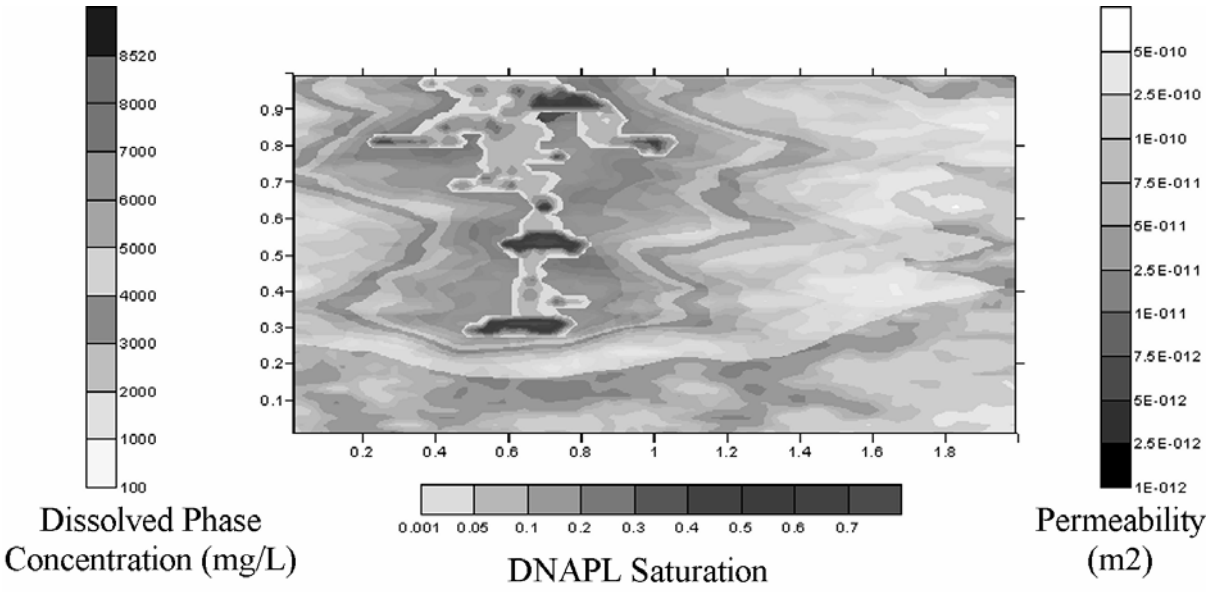

Figure 2. DNAPL saturations and aqueous-phase concentrations employing the equilibrium mass-transfer model in the simulation domain at time = 10 hours (DNAPL migration has ceased).

Figure 3 illustrates the length of time required for complete source zone dissolution as well as the maximum aqueous-phase concentration observed in the domain in the 2-D simulations. Source zone life spans range from approximately 9 days for the equilibrium dissolution model, to approximately 221 days for Powers *et al.* (1992), representing more than an order of magnitude uncertainty resulting from the choice of mass transfer model utilised in the simulation.

As illustrated in figure 3, source zone life span appears to be related to the maximum aqueous-phase concentration observed in the simulation domain. The highest maximum concentration observed corresponds to the equilibrium dissolution model at 8520 mg/L (i.e., the solubility limit of 1,2-DCE), whereas the lowest corresponds to Power *et al.* (1992) at approximately 2800 mg/L. In general, the higher the maximum aqueous-phase concentration, the shorter the source zone life span. An exception to this pattern is observed for Saba and Illangasekare (2003), where the source zone life span is disproportionately long relative to the maximum observed dissolved phase concentration. However, the aqueous-phase concentration varied significantly over time in this simulation, changing from less than 250 mg/L during the first hour, to the maximum concentration observed at approximately 1 week, to less than 400 mg/L for the remaining 40 days. Therefore, the maximum dissolved phase concentration during the majority of the simulation was significantly lower than the overall maximum concentration observed, and, as a result, the time for complete source zone dissolution was increased.

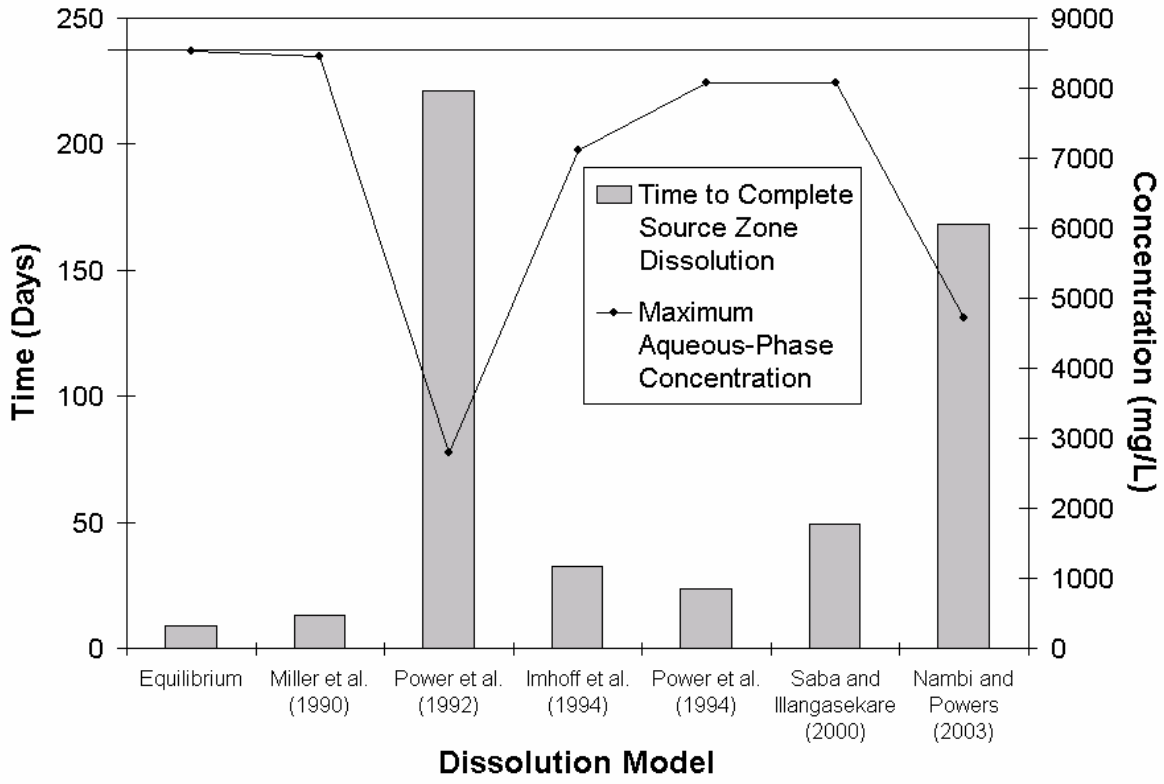

Figure 3. Time to complete source zone dissolution as well as maximum aqueous-phase concentration observed in the 2-D heterogeneous porous medium simulations

for each of the dissolution models. The horizontal line in the plot indicates the solubility limit of 1,2-DCE.

CONCLUSIONS

Numerous experimentally derived correlation expressions exist to describe mass transfer from the non-aqueous phase to the dissolved phase. The validity of most is limited to simple, specific circumstances and no comprehensive correlation model exists for simulating the range of dissolution phenomena expected in complex and evolving DNAPL source zones.

One-dimensional simulations in a homogeneous medium illustrate the sensitivity of predicted effluent concentrations to the employed dissolution model. This sensitivity is observable in both the magnitude of dissolved phase concentrations, the length of time during which contaminated groundwater effluxes through the column, and the pattern of dissolved phase concentrations observed over time. Two-dimensional simulations of a realistic DNAPL release into a heterogeneous porous medium illustrate that the dissolution model employed significantly impacts predicted behaviour. Source zone life spans were observed to vary by greater than an order of magnitude, and maximum observed aqueous-phase concentrations in the domain were observed to vary from the solubility limit to less than one-third that value. Two of the practical implications of this study are that (i) predicted dissolved phase concentrations downgradient of a realistic DNAPL release are quite sensitive to the chosen mass transfer expression, and (ii) a more robust and comprehensive correlation model is likely necessary for accurate simulations.

REFERENCES

Abriola, L.M., Pinder, G.F., Water Resou. Res. 1985a, 21, 11-18.
Abriola, L.M., Pinder, G.F., Water Resou. Res. 1985b, 21, 19-26.
Barry, D.A., Prommer, H., Miller, C.T., Engesgaard, P., Brun, A., Zheng, C., Adv. Water Resou. 2002, 25, 945-983.
Corapcioglu, M.Y., Baehr, A.L., Water Resou. Res. 1987, 23, 191-200.
Faust, C.R., Water Resou. Res. 1985, 21, 587-596.
Faust, C.R., Guswa, J.H., Mercer, J.W., Water Resou. Res. 1989, 25, 2449-2464.
Forsyth, P.A., Adv. Water Res. 1988, 11, 74-83.
Forsyth, P.A., Shao, B.Y. Numerical Simulation of Gas Venting for NAPL Site Remediation; University of Waterloo, Ontario, Res. Rep.. CS-91-06, 1991.
Gerhard, J.I. M.S. Thesis, Queen's University, Ontario, 1995.
Gerhard, J.I., Kueper, B.H., Hecox, G.R., Schwarz, E.J., Ground Water Monit. Remed. 2001, Spring, 71-88.
Gerhard, J.I. And Kueper, B.H. Water Resou. Res. 2003, 39, 1212.
Gerhard, J.I. And Kueper, B.H. Water Resou. Res. 2003, 39, 1213.
Huyakorn, P.S., Panday, S., Wu, Y.S., J. Contam. Hydrol. 1994, 16, 109-130.
Imhoff, P.T., Jaffe, P.R., Pinder, G.F., Water Resou. Res. 1994, 30, 307-320.
Kueper, B.H., Frind, E.O., Water Resou. Res. 1991a, 27, 1049-1057.
Kueper, B.H., Frind, E.O., Water Resou. Res. 1991b, 27, 1059-1070.
Kuppusamy, T., Sheng, J., Parker, J.C., Lenhard, R.J., Water Resou. Res. 1987, 24, 625-631.
Lujan, C.A., Ph.D. Dissertation, Colorado State University, Colorado, 1985.

Miller, C.T., Poirier-McNeill, M.M., Mayer, A.S., Water Resou. Res. 1990, 26, 2783-2796.
Nambi, I.M., Powers, S.E., Water Resou. Res. 2003, 39, 1030-1041.
Osborne, M., Sykes, J., Water Resou. Res. 1986, 22, 25-33.
Pankow, J.F., Cheery, J.A., Ryan, M.C. Dense Chlorinated Solvents and other DNAPLs in Groundwater, Waterloo Press: Portland, OR, 1996.
Poulsen, M, Kueper, B.H., Environ. Sci. Technol. 1992, 26, 889-895.
Powers, S.E., Abriola, L.M., Weber Jr., W.J., Water Resou. Res. 1992, 28, 2691-2705.
Powers, S.E., Abriola, L.M., Weber Jr., W.J., Water Resou. Res. 1994, 30, 321-332.
Reynolds, D.A., Kueper, B.H., J. Contam. Hydrol. 2001, 51, 41-62.
Reeves, H.W., Abriola, L.M., In Proceedings of the Seventh International Conference on Computational Methods in Water Resources: Volume 1. Modeling Surface and Subsurface Flows. Developments in Water Science, 35, 147-152.
Saba, T., Illangasekare, T.H., Water Resou. Res. 2000, 36, 971-979.
Sale, T.C., McWhorter, D.B., Water Resou. Res. 2001, 37, 393-404.
Sleep, B.E., Sykes, J.F., Water Resou. Res. 1993, 29, 1697-1708.
Slough, K.J., Sudicky, E.A., Forsyth, P.A., J. Contam. Hydrol. 1999, 40, 107-136.
Unger, A.J.A., Forsyth, P.A., Sudicky, E.A., J. Contam. Hydrol. 1998, 30, 217-242.
Zheng, C. MT3D U.S.E.P.A. Report 1990.

APPENDIX H – CAPILLARY PRESSURE - SATURATION DATA

Air / water capillary pressure / saturation curves were measured for each of the six sand types utilised in Chapters 3 and 5 by Stan Reitsma at the University of Windsor. Table H-1 presents the Brooks-Corey best-fit parameter values for each of the curves. Figures H-1 through H-6 present the capillary pressure – saturation curves for the six sand types, including Brooks-Corey best-fit curves, for primary drainage and secondary imbibition.

Table H-1. Best Fit Brooks-Corey Parameter Values for the Capillary Pressure – Saturation Curves of the Six Sand Types

Parameter	Value					
	N10	**N16**	**N20**	**N30**	**N40**	**N50**
Residual Wetting Phase Saturation (S_r)	0.080	0.127	0.099	0.119	0.100	0.124
Pore Size Distribution Index, Drainage (λ_d)	3.67	3.41	4.11	4.44	4.80	4.37
Pore Size Distribution Index, Imbibition (λ_i)	4.96	4.44	8.40	9.61	8.07	3.57
Terminal Pressure (P_t)	241 Pa	332 Pa	415 Pa	826 Pa	866 Pa	1335 Pa
Displacement Pressure (P_d)	416 Pa	563 Pa	741 Pa	1181 Pa	1604 Pa	2902 Pa
Terminal / Displacement Pressure Ratio (K)	0.58	0.59	0.56	0.70	0.54	0.46

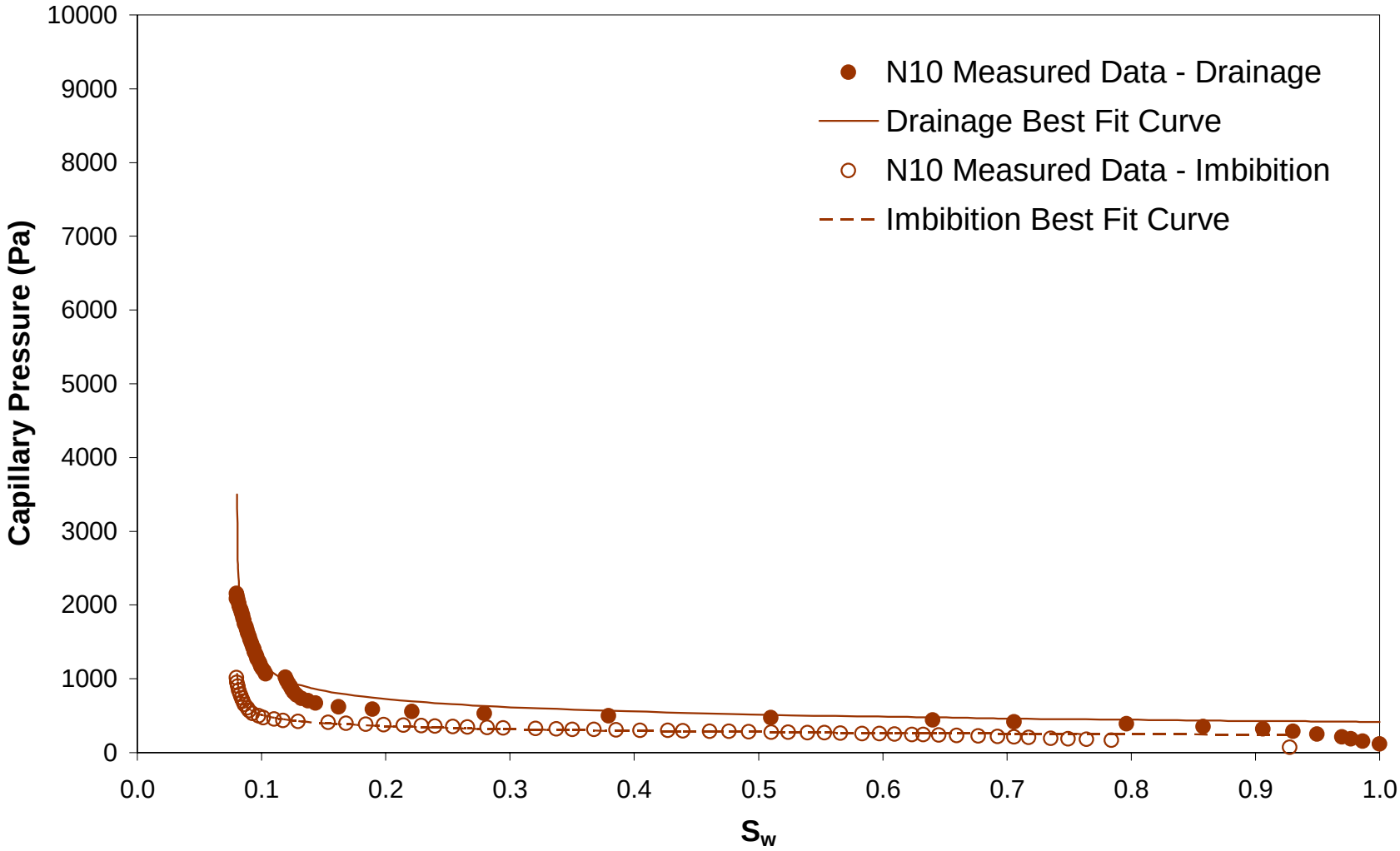

Figure H-1. Air / water capillary pressure – saturation curve for the N10 sand.

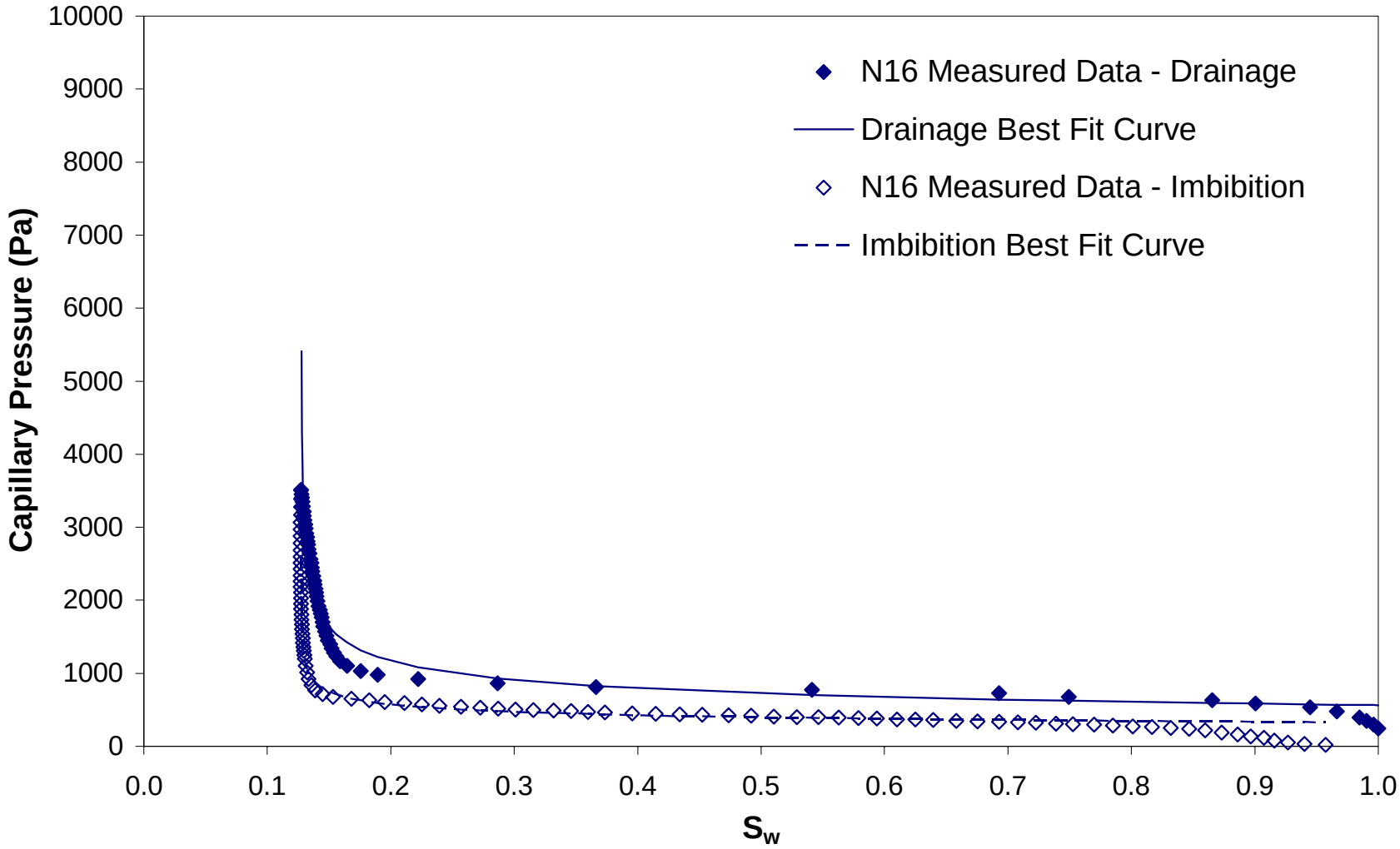

Figure H-2. Air / water capillary pressure – saturation curve for the N16 sand.

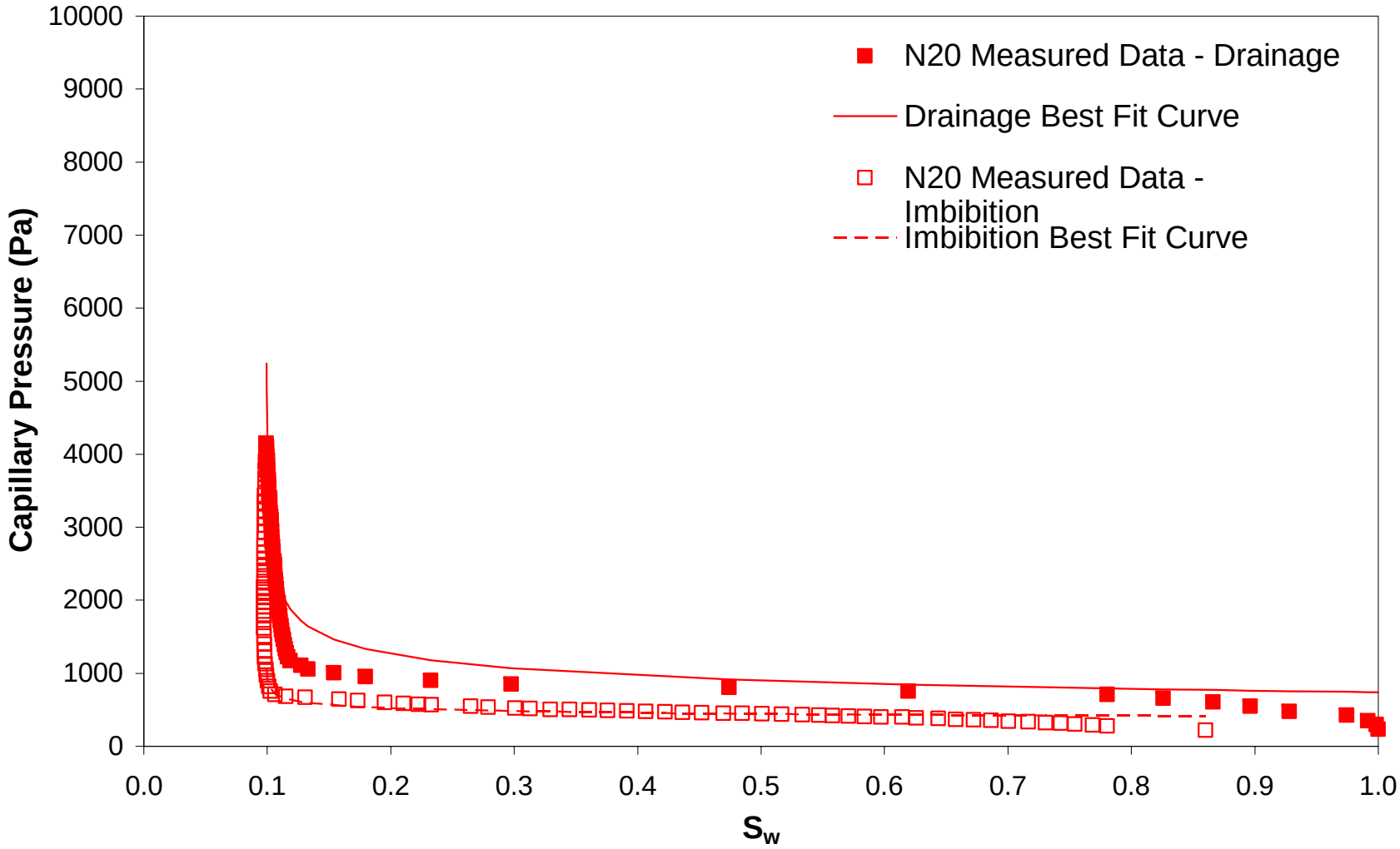

Figure H-3. Air / water capillary pressure – saturation curve for the N20 sand.

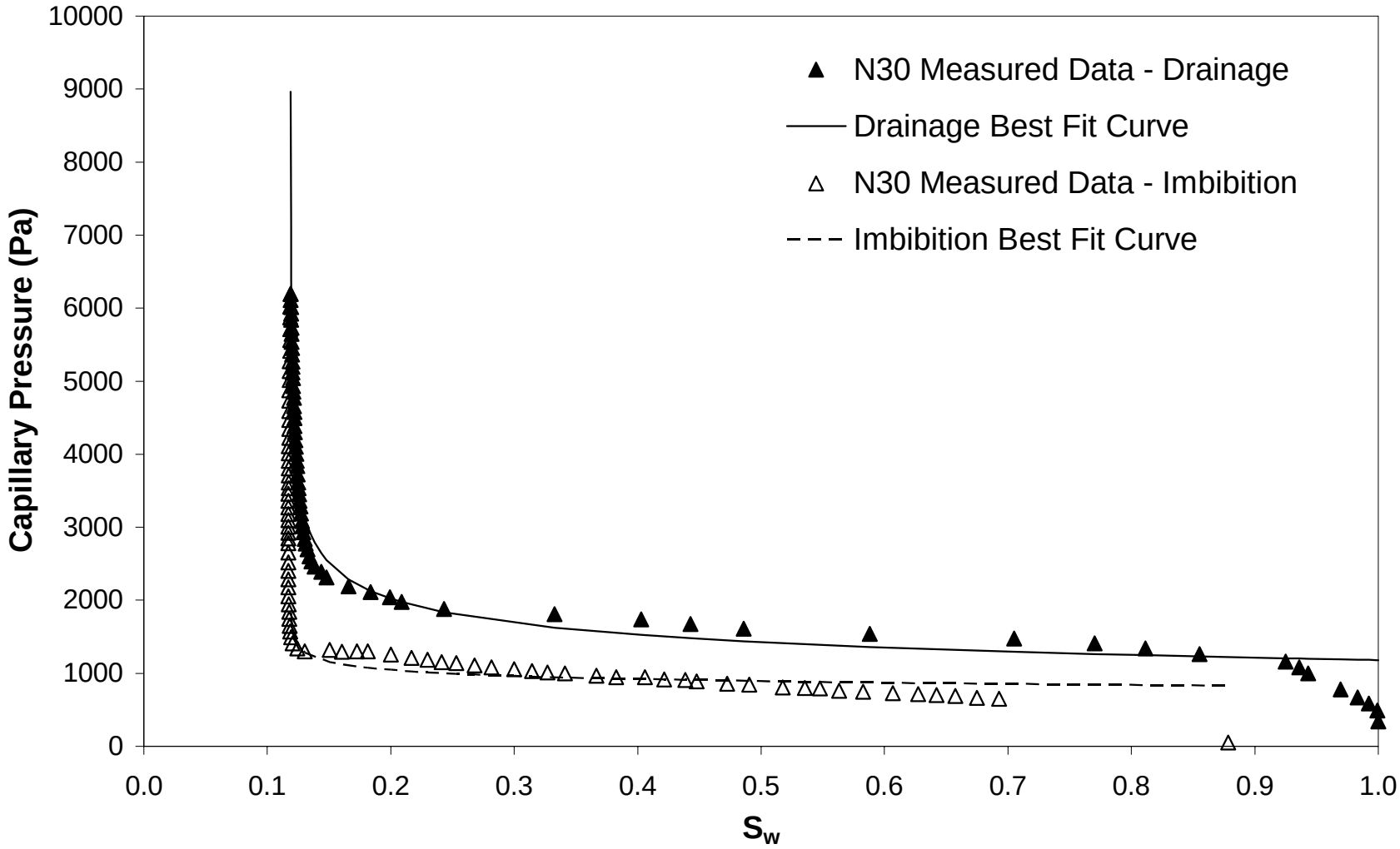

Figure H-4. Air / water capillary pressure – saturation curve for the N30 sand.

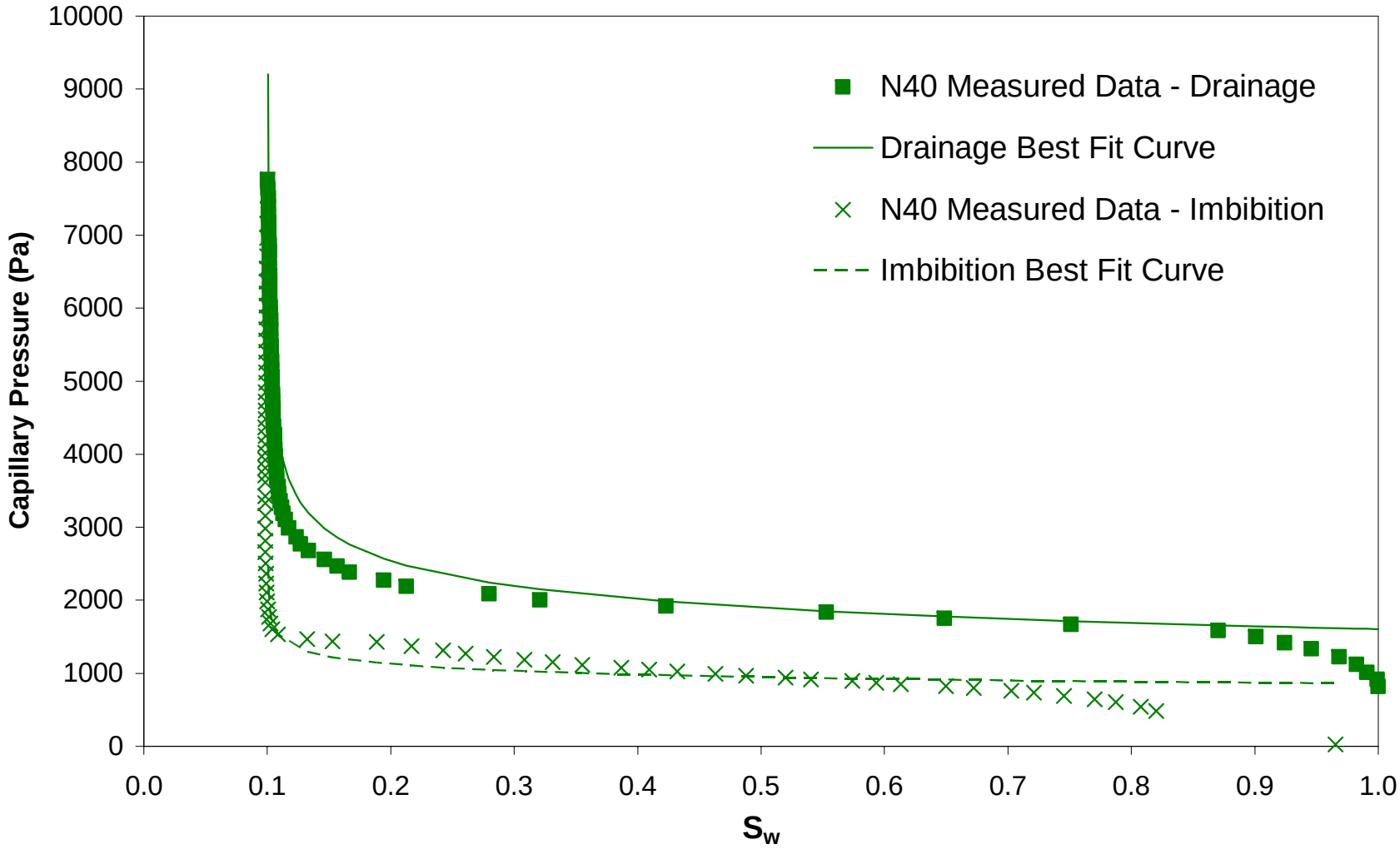

Figure H-5. Air / water capillary pressure – saturation curve for the N40 sand.

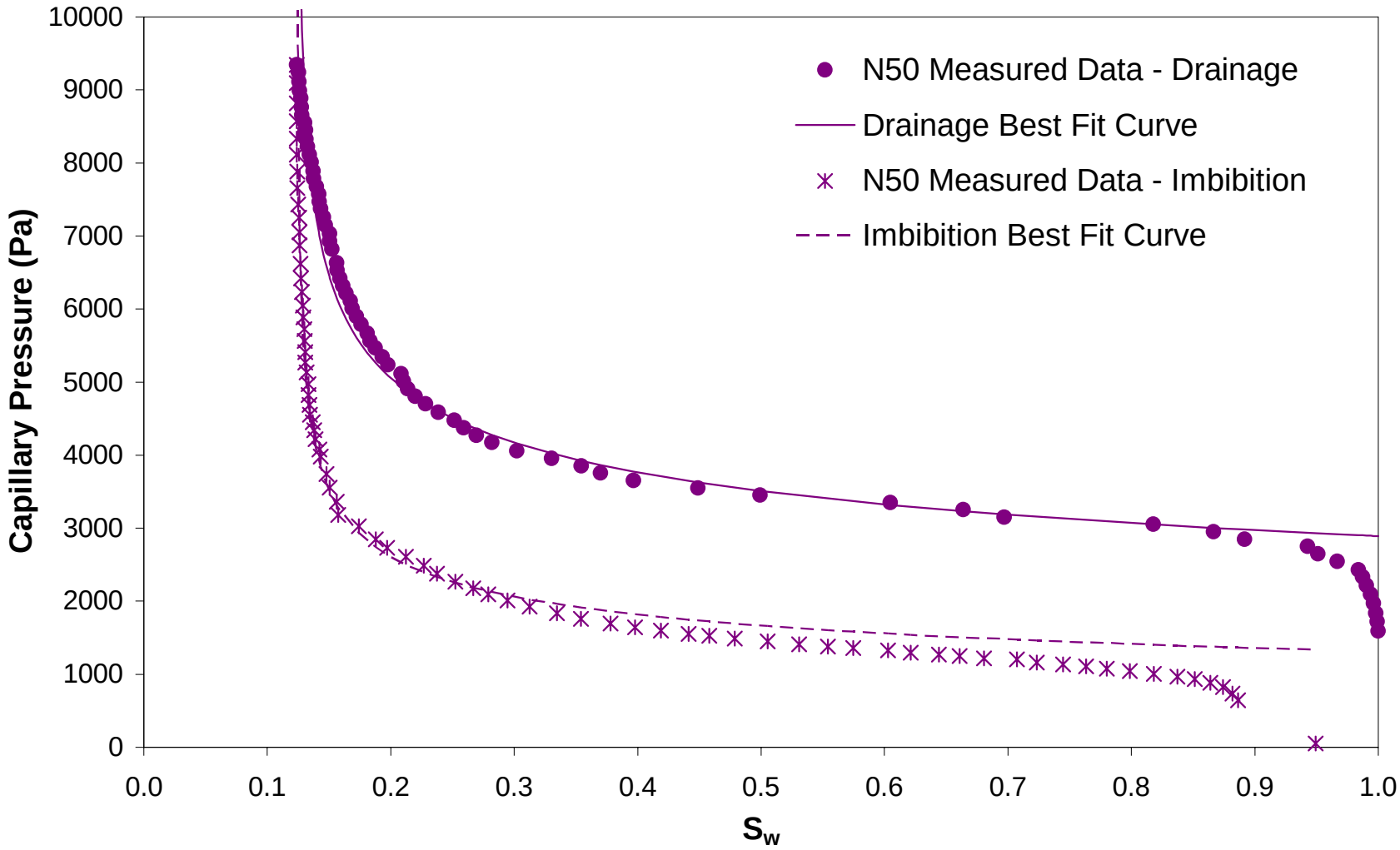

Figure H-6. Air / water capillary pressure – saturation curve for the N50 sand.

APPENDIX I – NONWETTING PHASE RELATIVE PERMEABILITY CELL THEORY

The local scale NWP relative permeability experiments followed the method developed by Gerhard (2002). This method was adapted from Dane *et al.,* (1998) and is designed to allow for the determination of saturation history – dependent NWP relative permeability through a series of steady-state steps. Each step is characterised by a flowing nonwetting phase, a static wetting phase, and a constant capillary pressure across the height of the sample. Measuring NWP flow rate allows for the determination of NWP relative permeability at each know saturation step.

I.1 NWP Relative Permeability Determination

An extension of Darcy's law for two phase flow in one dimension can be written:

$$q_w = \frac{-k_{abs}k_{r,W}}{\mu_W}\left(\frac{dP_W}{dx} + \rho_W g \frac{dz}{dx}\right) \tag{I-1}$$

$$q_N = \frac{-k_{abs}k_{r,N}}{\mu_N}\left(\frac{dP_N}{dx} + \rho_N g \frac{dz}{dx}\right) \tag{I-2}$$

where q_W and q_N are the wetting phase and NWP Darcy fluxes respectively, k_{abs} is the absolute or intrinsic permeability, $k_{r,W}$ and $k_{r,N}$ are the respective relative permeabilities, μ_W and μ_N are the respective phase viscosities, P_W and P_N are the respective phase pressures and g is acceleration due to gravity.

At steady state, capillary pressure is defined as the difference in pressure between the NWP and the wetting phase:

$$P_C = P_N - P_W \tag{I-3}$$

If the z-coordinate is assumed to be positive in the vertical direction then substituting Equation I-3 into Equation I-2 yields:

$$q_N = \frac{-k_{abs}k_{r,N}}{\mu_N}\left(\frac{d\left(P_C + P_W\right)}{dz} + \rho_N g\right) \tag{I-4}$$

If wetting phase is immobile at each steady-state saturation step, q_W = 0, water pressures are hydrostatic, and Equation I-1 becomes:

$$\frac{dP_W}{dz} = -\rho_W g \tag{I-5}$$

The NWP flow equation in the presence of an immobile, hydrostatic wetting phase can therefore be re-written as:

$$q_N = \frac{-k_{abs}k_{r,N}}{\mu_N}\left(\frac{dP_C}{dz} + \left(\rho_N - \rho_W\right)g\right) \tag{I-6}$$

While NWP is flowing, $\frac{dP_C}{dz}$ can be set to zero by manipulating the NWP constant head tanks on either side of the apparatus (Figure I-1). Therefore, Equation I-6 reduces to:

$$q_N = \frac{-k_{abs}k_{r,N}}{\mu_N} \cdot \left(\rho_N - \rho_W\right) \cdot g \tag{I-7}$$

Rearranging Equation I-7 to solve for NWP relative permeability, and substituting $q_N = \frac{Q_N}{A}$ gives:

$$k_{r,N} = \frac{-Q_N \mu_N}{A \cdot k_{abs} \cdot g \cdot \left(\rho_N - \rho_W\right)} \tag{I-8}$$

where Q_N is the NWP flow rate and A is the cross-sectional area of the local scale apparatus.

I.2 Constant Head Tank Elevations

The relative height of the NWP constant head tanks to achieve $\frac{dP_C}{dz} = 0$ can be determined by ensuring that the NWP pressure differential across the sand pack equals the wetting phase pressure differential across the sand pack, such that:

$$\frac{dP_N}{dz} = \frac{dP_W}{dz} \tag{I-9}$$

For hydrostatic water pressures in the cell:

$$\frac{dP_W}{dz} = -\rho_W g \tag{I-10}$$

Substituting Equation I-10 into Equation I-9 and integrating gives:

$$P_N(z = H) - P_N(z = 0) - \rho_w g \cdot z \tag{I-11}$$

where H is the height of the sand pack.

As seen in Figure I-1, NWP pressures are controlled by the constant head tanks, such that:

$$P_N(z = H) = \rho_N g(H_{IN} - H) \tag{I-12}$$

$$P_N(z = 0) = \rho_N g(H_{OUT}) \tag{I-13}$$

where H_{IN} and H_{OUT} are the elevations of the upstream and downstream constant head tanks, respectively. Substituting Equations I-12 and I-13 into Equation I-11 gives the elevation of the downstream constant head tank relative to the elevation of the upstream constant head tank:

$$H_{OUT} = (H_{IN} - H) + \frac{\rho_W}{\rho_N} \cdot H \tag{I-14}$$

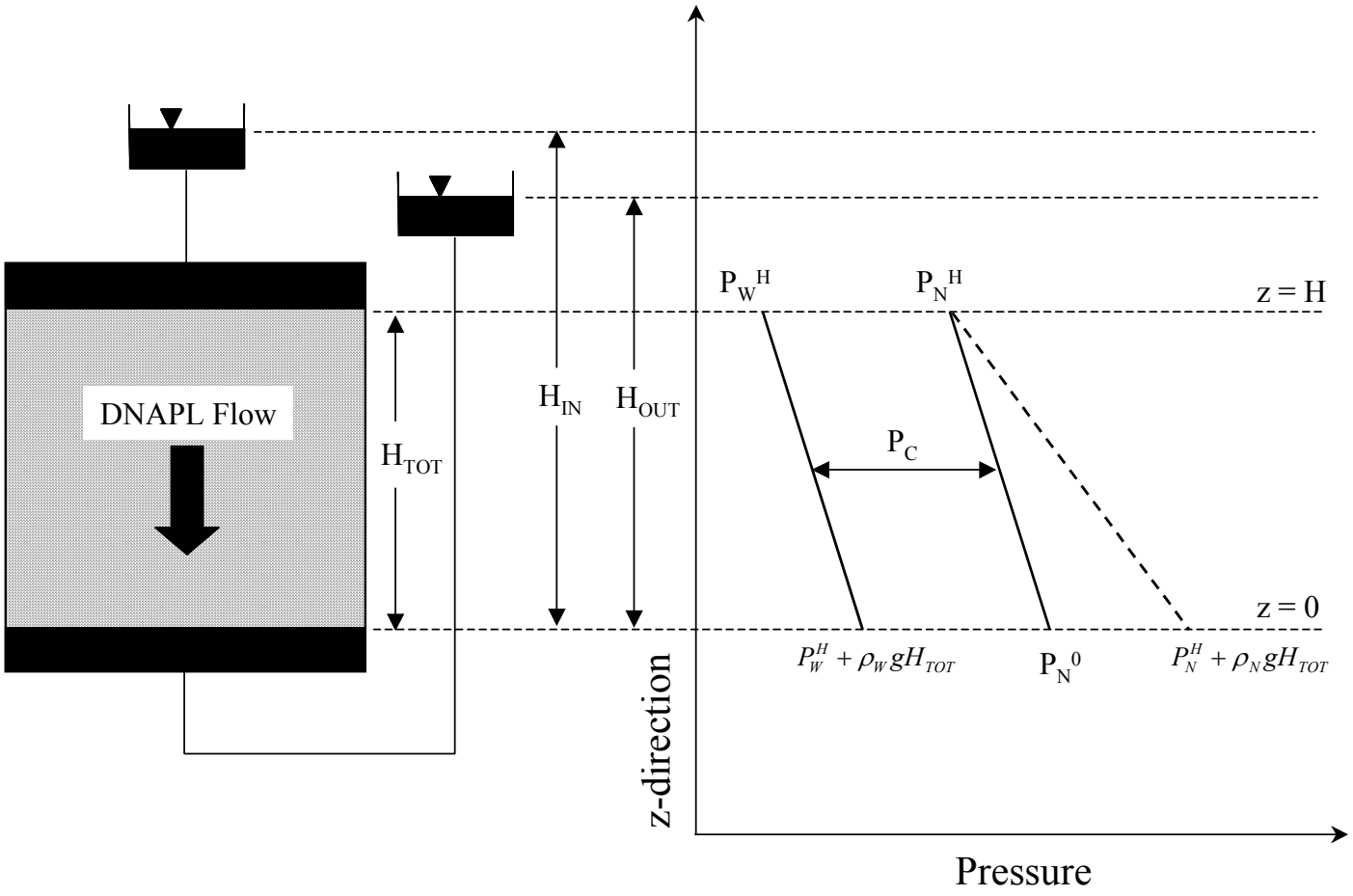

Figure I-1. Distribution of pressures in the local scale NWP relative permeability measurement apparatus.

I.3 References

Dane, J.H., C. Hofstee, and A.T. Corey, Simultaneous measurement of capillary pressure, saturation, and effective permeability of immiscible liquids in porous media, *Water Resources Research, 34*(12), 3687-3692, 1998.

Gerhard, J.I., DNAPL infiltration, redistribution, and immobilization in porous media, Ph.D., thesis, Queen's Univ., Kingston, Ontario, Canada, 2002.

APPENDIX J – UNCERTAINTY ANALYSIS

J.1 Base Sources of Error

Base sources of error are hereby defined as uncertainty resulting from limitations of the measurement devices utilised in the laboratory that are propagated throughout various calculations during data analysis. Base sources of error include density measurement uncertainty (which is a combination of mass and volume measurement uncertainty), flow cell volume measurement uncertainty (that results from physical dimension uncertainty) and syringe barrel measurement uncertainty.

As a three-point balance was used for all mass calculations, the mass uncertainty is 0.0005g. Uncertainty associated with the measurement of physical dimensions is 0.25mm, as callipers with divisions of 0.5mm were utilised for all small scale calculations of length. The 1.0 ml syringe barrel was demarked at intervals of 0.01 ml; therefore, the syringe barrel uncertainty is 0.005 ml. These mass, length, and volume errors will be propagated throughout the uncertainty analysis presented below.

J.2 Repeated Measurements

The uncertainty associated with the repeated measurement of a parameter (e.g. intrinsic permeability, flow rate, viscosity) will be taken as the standard deviation of the repeated measurement values. For example, the intrinsic permeability of the N40 sand was calculated through seven repeat measurements of flow rate giving a mean value of 7.41×10^{-11} and a standard deviation of 7.55×10^{-13}; thus, $k_{N40} = 7.41 \times 10^{-11} \pm 7.55 \times 10^{-13}$.

J.3 Local Scale Experiments

J.3.1 Saturation

The total uncertainty in the S_W of the cell at a given step is the combined uncertainty in the volume of voids in the sample and the cumulative uncertainty associated with the volume additions / subtractions performed up to that point.

The volume of voids uncertainty is the combined uncertainty associated with the mass measurement and the calculation to determine the volume of the flow cell. Therefore, the volume of voids uncertainty is a function of the base sources of error listed above and is calculated for each sand packing of the local scale flow cell (i.e., for each sand type examined).

As the volume of additions / subtractions is cumulative throughout an experiment, the total uncertainty of S_W is a function of step number (e.g. there were 34 volume changes in the N16 sand experiment). The error associated with each step is calculated using the syringe barrel volume uncertainty presented above.

Since the values of the 'volume of voids' and 'volume of additions / subtractions' uncertainties change with each step, the specific uncertainty at each step must be calculated independently. For example, the S_W uncertainty during the N16 local scale experiment varied from 0.008 for the first step, to 0.021 at the drainage / imbibition turn-around point (step 18), to 0.039 at NWP residual (step 34). This range of S_W uncertainties is typical of the local scale experiments.

J.3.2 NWP relative permeability

NWP relative permeability at each step is calculated using Equation I-8 of Appendix I. The uncertainty associated with each of the six measured properties in the expression contributes uncertainty to the final k_{rN} value. The individual uncertainties of the parameters in the equation are derived from the base sources of

error or repeated measurement sources of error presented above. Their cumulative effect on the calculated k_{rN} was examined by considering the value of k_{rN} when the individual errors resulted in a minimum k_{rN} value, and when the individual errors conspired to give a maximum k_{rN} value. It was found that the maximum possible uncertainty in k_{rN} is 8.9% of the calculated value, therefore, the error of each k_{rN} value is scaled to 8.9%, with the maximum error occurring at $k_{rN}^{\max}$.

J.4 Bench Scale Experiments

J.4.1 Tracer Test

Uncertainty associated with the tracer test bromide concentration data was calculated through 10 repeat measurements of a 20 mg/l standard. Analysis of the standard resulted in a standard deviation of concentration equal to 1.42%. As the input concentration (i.e., C_o) was set at 20 mg/l, the uncertainty of the measured concentration data was scaled to the uncertainty of the standards.

J.4.2 Gas Chromatograph Analysis of 1,2-DCE Concentrations

As in the tracer test bromide concentration data analysis, the uncertainty of the 1,2-DCE concentration measurements were scaled to the uncertainty associated with the analysis of standards. In this case, 28 repeat measurements of a series of 8000 mg/l 1,2-DCE standards resulted in a standard deviation of concentration equal to 12.9%. By utilising a series of standards instead of a single standard, and carrying out the analysis over a period of days, the standard deviation encompasses all the errors associated with the creation of the standard as well as day-to-day fluctuations in the sensitivity of the gas chromatograph detector.